University of Canterbury

Department of Electrical and Computer Engineering

Noble Metal-Oxide Schottky Contacts on Zinc Oxide

A thesis submitted in partial fulfilment
of the requirements for the Degree of

Doctor of Philosophy
in Electrical and Computer Engineering

at the
University of Canterbury

by

Alana Marie Hyland

January 2017

For my family and fiancé.

Abstract

This thesis presents a systematic investigation into the fabrication and characterisation of noble metal-oxide Schottky contacts with deliberately varied levels of oxygen incorporation to bulk single-crystal ZnO, towards the development of ZnO-based photodetectors for ultraviolet (UV) dosimetry. Noble metal and noble metal-oxide films of varied oxygen composition (as determined by Rutherford Backscattering Spectrometry) were deposited using reactive RF-sputtering (and reactive eclipse pulsed laser deposition) simultaneously with the corresponding ZnO Schottky contacts. The films were analysed for transparency, structure, surface potential, oxygen incorporation, and conductivity. The electrical characteristics of the Schottky contacts were analysed in dark conditions, under periodic exposure to visible and UV radiation, and at temperatures up to 180 °C.

The electrical characteristics of the noble metal-oxide Schottky contacts to ZnO improved dramatically in ideality factor, barrier height, and rectification ratio with increasing oxygen incorporation; for example, oxidised Pt Schottky contacts exhibited current rectification of 12 orders of magnitude and effective barrier heights of up to 1.30 eV compared to the ohmic behavior of unoxidised plain-metal contacts. In addition, a AgO_x Schottky contact produced the highest Schottky barrier to ZnO reported to date, with a barrier height of 1.42 eV, with several other AgO_x and PtO_x contacts in this work also producing very high barrier heights. A proposed model of the mechanisms responsible for the large performance gains of the oxidised noble metal-oxide Schottky contacts to ZnO in this work was developed, in which the presence of the active oxygen species during Schottky contact formation produces the following beneficial effects: (1) the removal of the hydroxyl-induced potential well and associated electron accumulation layer from the ZnO surface, (2) the passivation of interfacial oxygen vacancies, and (3) an increase in the work function and electronegativity of the oxidised Schottky contacts.

The UV photoresponse of the noble metal-oxide Schottky contacts was found to improve with respect to both response time and dark-vs-photocurrent increase with increasing oxygen incorporation, and was also found to be strongly affected by device bias. Increasingly negative device biases caused increasing levels of undesirable persistent photoconductivity (PPC). In contrast, a PtO_x Schottky contact showed a consistent square-wave photoresponse to 30 s intervals of UV (365 nm) radiation when biased at 0 V, with over 3 orders of magnitude of reproducible

current increase on UV irradiation for over 50 exposure cycles. A proposed model of the mechanisms responsible for PPC in the metal-oxide Schottky contacts is proposed, involving the desorption of atmospheric oxygen species from the surface of ZnO and the production of metastable ionised oxygen vacancies.

An IrO_x Schottky contact was found to be thermally-stable to 180 °C with a barrier height of 1.07 eV and over 6 orders of magnitude rectification at 180 °C, compared to 0.91 eV and 10 orders of magnitude rectification at room temperature, which represents the highest-reported high temperature rectification performance for ZnO Schottky contacts. A PdO_x Schottky contact heated to 180 °C was used to calculate an experimental Richardson constant of 36.4 $Acm^{-2}K^{-2}$, very close to the theoretical value of 32 $Acm^{-2}K^{-2}$.

Acknowledgements

"The Road goes ever on and on
Down from the door where it began.
Now far ahead the Road has gone,
And I must follow, if I can,
Pursuing it with eager feet,
Until it joins some larger way
Where many paths and errands meet.
And whither then? I cannot say."

– J.R.R. Tolkien, *The Fellowship of the Ring*

I would first like to thank my supervisor Assoc. Prof. Martin Allen for his support, dedication, direction, and faith in me as a student. His work-ethic and genuine enthusiasm over the scientific progress of the research has been inspiring, and his encouragement has pushed me to achieve ever-higher levels of quality and diligence in my research, and find confidence in my own observations and conclusions. I would also like to thank my co-supervisor Prof. Maan Alkaisi for his wisdom and support throughout my PhD. I have learned so much from both of you, and I will be forever grateful of your patience and teachings.

I would like to thank Helen Devereux and Gary Turner for all their help, assistance, instruction, re-instruction, and rescuing in the lab. You have both taught me so many practical skills that I will carry with me everywhere. You made the lab a home, one that you showed how to care for, respect, and innovate in. Thank you for helping me to find my confidence and independence in the lab.

I would like to thank Prof. Roger Reeves for his supervision, support, and training for my work in the Department of Physics and Astronomy. And thanks also to Dr. Ian Farrell for his assistance with the big-scary laser.

It was a great privilege to work with Dr. Holger von Wencktern, Dr. Stefan Müller, and Daniel Splith from the Universität Leipzig, Germany, and I wish them all the best on their future endeavours, and hope to meet them all again in the big world of academia.

I'd like to thank my office-mates Dr. Robert Heinhold, Dr. Salim Elzwawi, and Dr. Lynn Murray, who were my role-models from the start of my post-graduate studies, and Matthew Whiteside and Max Lynam, who started the postgraduate journey with me as fellow disciples of Martin. And thank you to Dr. Giang Dang and Dr. Saurabh Saxena, for their guidance and wisdom.

Thank you to Dr. Volker Nock for his enthusiasm and encouragement throughout my studies, and thank you to Prof. Phillipa Martin for her inspiration, support, and always having my back.

And heart-felt thanks to my colleagues and fellow-students, who have helped me throughout this journey with their wisdom, their kindness, their enthusiasm, and with their friendship. No one makes this journey alone, and I was in the best of company. Especially and in no particular order, to Claude, Azadeh, Louise, and Blair in my department, and in the far and lofty towers of the pure sciences; Chrissy, Anna, Alex, Alex, Alex, Adam, Lancia, Jonty, and Rodrigo. I was incredibly lucky to have such wonderful people with me on this journey. I will treasure the memories we built together, the Schottky contacts we fabricated, the Hall effect boards we soldered, the beers we drank and the bunny-rabbit pies we ate. Thank you all for putting up with my puns.

I would also like to thank my dear friends from 'Coffee' for supporting me through all these years; Chrissy, Beth, Dora, Jodie, Chloe, Bridget, Steph, Naomi and Ginny. I consider myself so incredibly lucky to have found such a wonderful group of people.

And finally, my greatest thanks to my family and my darling better half. I dedicate this work to my mother, father, brother, sister, and fiancé, for I am all that I am thanks to you and your love for me. Thank you.

List of Collaborators

- Professor Steven M. Durbin and Robert Makin of the Department of Electrical and Computer Engineering, Western Michigan University, United States of America.
- Professor Roger J. Reeves, Department of Physics and Astronomy, University of Canterbury, New Zealand.
- Dr Colin Doyle, Faculty of Engineering, University of Auckland, New Zealand.
- Adam Hyndman, Department of Physics and Astronomy, University of Canterbury, New Zealand.
- Dr Salim Elzwawi, Department of Electrical and Computer Engineering, University of Canterbury, New Zealand.

Table of Contents

Publications

Hyland, A., Makin, R.A., Durbin, S.M., Allen, M.W., (2017), Giant improvement in the rectifying performance of oxidized Schottky contacts to ZnO, *Journal of Applied Physics*, 121 (2), art. no. 024501.

Hyland, A., Reeves, R.J., Makin, R.A., Durbin, S.M., Allen, M.W., (2017), Thermal stability of oxidised noble metal Schottky contacts to ZnO, *Materials Science in Semiconductor Processing*, In Press.

Elzwawi, S., Hyland, A., Lynam, M., Partridge, J.G., McCulloch, D.G., Allen, M.W., (2015), Effect of Schottky gate type and channel defects on the stability of transparent ZnO MESFETs, *Semiconductor Science and Technology*, 30 (2), art. no. 024008.

Medina, G., Stampe, P.A., Kennedy, R.J., Reeves, R.J., Dang, G.T., Hyland, A., Allen, M.W., Wahila, M.J., Piper, L.F.J., Durbin, S.M., (2014), Characterization of tin oxide grown by molecular beam epitaxy, *Materials Research Society Symposium Proceedings*, 1633.

Conference Contributions

Hyland, A., Kuo, L., Allen, M.W., (2013), *MSM Ultraviolet Photodetectors on Zinc Oxide*, The 6th International Conference on Advanced Materials and Nanotechnology (AMN-6), Poster.

Hyland, A., Reeves, R.J., Allen, M.W., (2014), *The Effects of Oxygen Incorporation in Iridium Oxide Schottky Contacts on Zinc Oxide*, The 8th International Workshop on Zinc Oxide and Related Materials (IWZnO 2014), Poster.

Hyland, A., Reeves, R.J., Allen, M.W., (2014), *The Effects of Oxygen Incorporation in Iridium Oxide Schottky Contacts on Zinc Oxide*, The 10th MacDiarmid Institute Student and Postdoc Symposium 2014, Poster.

Hyland, A., Reeves, R.J., Allen, M.W., (2015), *The Effects of Oxygen Incorporation in Metal Oxide Schottky Contacts on Zinc Oxide*, The 7th International Conference on Advanced Materials and Nanotechnology (AMN-7), Poster.

Hyland, A., Reeves, R.J., Allen, M.W., (2015), *The Effects of Oxygen Incorporation in Palladium Oxide Schottky Contacts on Zinc Oxide*, The 11th MacDiarmid Institute Student and Postdoc Symposium 2015, Poster.

Hyland, A., Makin, R.A., Durbin, S.M., Allen, M.W., (2016), *Effect of Oxygen Incorporation on the performance of Noble Metal Oxide Schottky Contacts to ZnO*, The 43rd Conference on the Physics and Chemistry of Surfaces and Interfaces (PCSI-43), Poster.

Hyland, A., Reeves, R.J., Durbin, S.M., Allen, M.W., (2017), *Thermal stability of transparent, oxidised noble metal Schottky contacts to ZnO*, The 8th International Conference on Advanced Materials and Nanotechnology (AMN-8), Talk.

List of Figures

2. Background

List of Tables

Acronyms and Abbreviations

AFM	Atomic-Force Microscopy
ALD	Atomic Layer Deposition
ASR	Age-Standardised Rate
C-V	Capacitance-Voltage
CIE	Commission Internationale de l'Eclairage
CPD	Contact Potential Difference
DC	Direct Current
DNQ	Diazonaphthoquinone
EBD	Electron-Beam Deposition
GIXRD	Grazing-Incidence X-Ray Diffraction
HEMT	High Electron Mobility Transistors
HV	High Vacuum
I-T	Current-Time
I-V	Current-Voltage
I-V-T	Current-Voltage-Temperature
IGZO	InGaZnO
IPA	Isopropyl Alcohol
KPM	Kelvin-Probe Microscopy
MBE	Molecular Beam Epitaxy
MED	Minimum Erythemal Dose
MIGS	Metal-Induced Gap States
MOCVD	Metal-Organic Chemical Vapour Deposition
MSM	Metal-Semiconductor-Metal
NBIS	Negative Bias Illumination Stress
NIWA	National Institute of Water and Atmospheric Research

PL	Photoluminescence
PLD	Pulsed Laser Deposition
PPC	Persistent Photoconductivity
PPM	Parts Per Million
PVD	Physical Vapour Deposition
R-B	Roberston-Berger
RBS	Rutherford Backscattering Spectroscopy
RF	Radio Frequency
SEAL	Surface Electron Accumulation Layer
SED	Standard Erythemal Dose
SPF	Sun Protection Factor
STM	Scanning Tunneling Microscope
SZA	Solar Zenith Angle
TFT	Thin Film Transistor
UHV	Ultra-High Vacuum
UV	Ultraviolet
UVI	Ultraviolet Index
UVPS	Ultraviolet Photoresponse Selectivity
VPT	Vapour Phase Transport
XPS	X-ray Photoemission Spectroscopy
XRD	X-Ray Diffraction

1 | Introduction

The ultraviolet (UV) wavelengths from solar radiation have both a positive and negative impact on human health. Skin cancers account for one of the highest incidence rates of cancers diagnosed worldwide, however vitamin D synthesis from solar UV radiation is also the primary source of vitamin D in humans [2.1 – 2.4]. Vitamin D deficiencies contribute towards a wide range of negative health effects, including osteoporosis, multiple sclerosis, muscle weakness, hypertension, cardiovascular disease, schizophrenia, and depression [2.4]. The production of ZnO-based photodetectors for measuring UV radiation has the potential to provide a cheaper alternative to the current AlGaN photodetector-based dosimeters, both for research purposes and for personal UV dosimetry, to balance the risks and benefits of UV radiation [2.5 – 2.8].

ZnO has been a part of human history from the smelting of copper ores and the production of brass [2.35]. ZnO is commonly used today in sunscreens and cosmetics due to its UV absorption and non-toxicity to humans, as well as being used as a food additive to counter dietary zinc deficiencies in humans [2.31]. ZnO has also been used in the production of transparent conducting oxides for solar cells, liquid crystal displays, energy-saving window coatings, and has shown potential for transparent electronic displays [2.31]. Single-crystal bulk ZnO can be produced through a number of solvothermal and epitaxial methods. Hydrothermal growth is the most promising method for producing low-cost, large wafers of high quality bulk crystal ZnO [2.31 – 2.32]. Hydrothermal growth of high-quality 2-inch wafers of bulk ZnO using temperatures between 300 – 400 °C is currently a commercially viable process [2.31 – 2.32]. For this work, arrays of noble metal and noble metal-oxide Schottky contacts, as shown in Figure 1.1, were fabricated on wafers of single-crystal hydrothermal bulk ZnO from Tokyo Denpa Co., Ltd.; specifically –c-axis and +c-axis (low-lithium) bulk ZnO, using pulsed-laser deposition (PLD) and radio-frequency (RF)-sputtering. The oxygen content of the RF-sputtered noble metal-oxide Schottky contacts was controlled by varying the O_2:Ar gas flow ratio in the sputtering chamber during deposition, in order to determine the effects of oxygen incorporation on the optical and electrical characteristics of the Schottky contacts, for use as UV photodetectors in UV dosimetry. Thin films of the noble metal and noble metal-oxide material were deposited on quartz substrates simultaneously to the deposition of the Schottky contacts, to study the characteristics of the films with increasing oxygen incorporation.

A summary of Chapters 2 – 9 of this work is as follows:

Chapter 2 Background

- The health impacts of UV radiation motivating this work; skin cancer, vitamin D synthesis, and contemporary methods of recording UV radiation.
- The fundamental properties of ZnO including the crystal structure, optical and electrical properties, ohmic and Schottky contact formation, and persistent photoconductivity.

Chapter 3 Fabrication Methodologies

- Equipment and methodologies used to fabricate the noble metal and noble metal oxide Schottky contacts used in this work, including substrate preparation, photolithography, and thin film deposition.
- Details of the background and use of the thin film deposition methods including PLD, RF-sputtering, and electron-beam deposition (EBD).

Chapter 4 Characterisation Techniques

- Equipment and methodologies used to characterise the noble metal and noble metal oxide materials and Schottky contacts fabricated for this work, including the Hall effect, atomic-force microscopy (AFM), Kelvin probe microscopy (KPM), Rutherford backscattering spectroscopy (RBS), X-ray photoemission spectroscopy (XPS), and X-ray diffraction (XRD) on fabricated materials.
- Electrical characterisation of the noble metal and noble metal-oxide Schottky contacts including current-voltage (I-V) measurements with varying illumination (photoresponse tests), temperature (I-V-T), and capacitance-voltage (C-V) characterisation.

Chapter 5 Characterisation of Sputtered Metal-Oxide Films with Varied Oxygen Content

- The results and analysis of the optical and electrical characterisation of RF-sputtered noble metal and noble metal-oxide films of Ag, AgO_x, Ir, IrO_x, Pd, PdO_x, Pt, and PtO_x.
- Transmission measurements, XRD crystal structure measurements, AFM growth rate measurements, KPM surface potential measurements, XPS and RBS stoichiometry measurements, and Hall effect resistivity measurement results.

Chapter 6 Electrical Characterisation of Metal-Oxide Schottky Contacts with Oxygen Content

- The results and analysis of the electrical characterisation of RF-sputtered noble metal and metal-oxide Schottky Ag, AgO_x, Ru, RuO_x, Ir, IrO_x, Pd, PdO_x, Pt and PtO_x contacts to –c-plane and +c-plane (low-lithium) Zn-polar bulk ZnO.
- Electrical characterisation of the Schottky contacts, including dark I-V and dark C-V measurements.
- A proposed model for the formation mechanisms of the noble metal-oxide Schottky contacts to ZnO.

Chapter 7 Ultraviolet Photoresposne of Metal-Oxide Schottky Contacts with Oxygen Content

- The results and analysis of the photoresponse experiments to visual and UV light performed on noble metal-oxide Schottky contacts of AgO_x, RuO_x, IrO_x, PdO_x, and PtO_x to –c-plane and +c-plane (low-lithium) Zn-polar bulk ZnO.
- The investigation into the effects of oxygen incorporation and device bias on PPC and UV photoresponse of RF-sputtered metal-oxide contacts.
- Photoresponse measurements of were single exposures and pulsed exposures with -1 V device bias, and pulsed exposures with varying bias, using wavelengths of 365 – 625 nm.

Chapter 8 Thermal Stability of Schottky Contacts to Zinc Oxide

- The results and analysis of dark I-V-T characteristics of PLD IrO_x, and RF-sputtered AgO_x, IrO_x, PdO_x, and PtO_x Schottky contacts to bulk ZnO with temperature between 20 °C and 180 °C
- The calculation of the experimental Richardson constant of bulk hydrothermal ZnO and bulk low lithium hydrothermal ZnO.

Chapter 9 Conclusion and Suggestions for Further Investigations

- The most significant findings of this work.
- Suggestions for further investigations.

Appendix The appendices for Chapters 3 – 9.

REFERENCES

[1.1] Markovic, S.N., Erickson, L.A., Rao, R.D., Weenig, R.H., Pockaj, B.A., Bardia, A., Vachon, C.M., Schild, S.E., McWilliams, R.R., Hand, J.L., Laman, S.D., Kottschade, L.A., Maples, W.J., Pittelkow, M.R., Pulido, J.S., Cameron, J.D., Creagan, E.T., (2007), Malignant melanoma in the 21st century, part 1: Epidemiology, risk factors, screening, prevention, and diagnosis, *Mayo Clinic Proceedings*, 82 (3), pp. 364-380.

[1.2] Godar, D.E., (2005), UV doses worldwide, *Photochemistry and Photobiology*, 81 (4), pp. 736-749.

[1.3] McKenzie, R.L., Liley, J.B., Björn, L.O., (2009), UV radiation: Balancing risks and benefits, *Photochemistry and Photobiology*, 85 (1), pp. 88-98.

[1.4] Holick, M.F., (2007), Medical progress: Vitamin D deficiency, *New England Journal of Medicine*, 357 (3), pp. 266-281.

[1.5] Køster, B., Søndergaard, J., Nielsen, J.B., Allen, M., Bjerregaard, M., Olsen, A., Bentzen, J., (2016), Effects of smartphone diaries and personal dosimeters on behavior in a randomized study of methods to document sunlight exposure, *Preventive Medicine Reports*, 3, pp. 367-372.

[1.6] Køster, B., Søndergaard, J., Nielsen, J.B., Allen, M., Bjerregaard, M., Olsen, A., Bentzen, J., (2015), Feasibility of smartphone diaries and personal dosimeters to quantitatively study exposure to ultraviolet radiation in a small national sample, *Photodermatology Photoimmunology and Photomedicine*, 31 (5), pp. 252-260.

[1.7] Allen, M., McKenzie, R., (2005), Enhanced UV exposure on a ski-field compared with exposures at sea level, *Photochemical and Photobiological Sciences*, 4 (5), pp. 429-437.

[1.8] McKenzie, R., Liley, B., Johnston, P., Scragg, R., Stewart, A., Reeder, A.I., Allen, M.W., (2013), Small doses from artificial UV sources elucidate the photo-production of vitamin D, *Photochemical and Photobiological Sciences*, 12 (9), pp. 1726-1737.

[1.9] Jagadish, C., Pearton, S.J., (2006), *Zinc Oxide Bulk, Thin Films and Nanostructures – Processing, Properties and Applications*, Oxford, U.K: Elsevier Ltd.

[1.10] Maeda, K., Sato, M., Niikura, I., Fukuda, T., (2005), Growth of 2 inch ZnO bulk single crystal by the hydrothermal method, *Semiconductor Science and Technology*, 20 (4).

2 | Background

This chapter gives an overview of the motivation behind this work, the development of personal ultraviolet (UV) dosimeters on ZnO, and the fundamental properties of Schottky contacts on ZnO. The motivation behind this work covers the health impacts of UV radiation, the risk of skin cancer, vitamin D synthesis, and methods of recording UV radiation. The fundamental properties of ZnO are also covered, including the crystal structure, optical and electrical properties, ohmic and Schottky contact formation, and persistent photoconductivity.

2.1 Health Effects of Ultraviolet Radiation

Solar UV radiation exposure has both positive and negative health effects for humans. The negative health effects include developing cataracts, DNA damage, immune suppression, photoaging, erythema (sunburn), and skin cancers [2.1 – 2.3]. Skin cancers account for one of the highest incidence rates of cancers diagnosed worldwide [2.1 – 2.3]. Solar UV radiation is also the primary source of vitamin D in humans, as vitamin D is synthesised in the skin on exposure to UV radiation [2.4]. Vitamin D deficiencies contribute towards a wide range of negative health effects, including the development of osteoporosis, multiple sclerosis, muscle weakness, hypertension, cardiovascular disease, schizophrenia, and depression, highlighting the positive health effects for humans [2.4]. With the current estimates of sufficient vitamin D levels, 1 billion people worldwide are considered to be vitamin D deficient [2.4]. Affordable, personal dosimetry of radiation levels is required for further research into the relationship between UV exposure and vitamin D levels in humans [2.5 – 2.8]. The production of ZnO-based photodetectors for measuring UV radiation could provide a cheaper alternative to the current AlGaN-based dosimeters, for research purposes and personal UV dosimetry, to balance the negative and positive effects of UV radiation [2.5 – 2.8].

2.1.1 Ultraviolet Effects of Ultraviolet Radiation

Both the intensity and the spectrum of UV radiation reaching the Earth's surface is determined by solar zenith angle (SZA), season, latitude, hemisphere, altitude, stratospheric ozone

concentration, pollution, cloud cover, and surface albedo (reflectivity) of the terrain [2.2 – 2.3, 2.9 – 2.11]. The shorter UV wavelengths, UVC (200 – 280 nm), are completely blocked by Earth's upper atmosphere [2.2]. SZA has the greatest impact on UV intensity, as a larger SZA requires the solar rays to travel through a greater amount of ozone [2.2]. This scatters and absorbs UVB (280 – 315 nm) wavelengths more than UVA (315 – 400 nm), changing the intensity and spectral distribution of the UV radiation reaching the Earth's surface, as shown in Figure 2.1 [2.2 – 2.3, 2.9 – 2.11]. There is no seasonal variation in UV radiation levels at the equator, however with increasing latitudes the variation in SZA increases not only with time of day, but with day of the year [2.2 – 2.3].

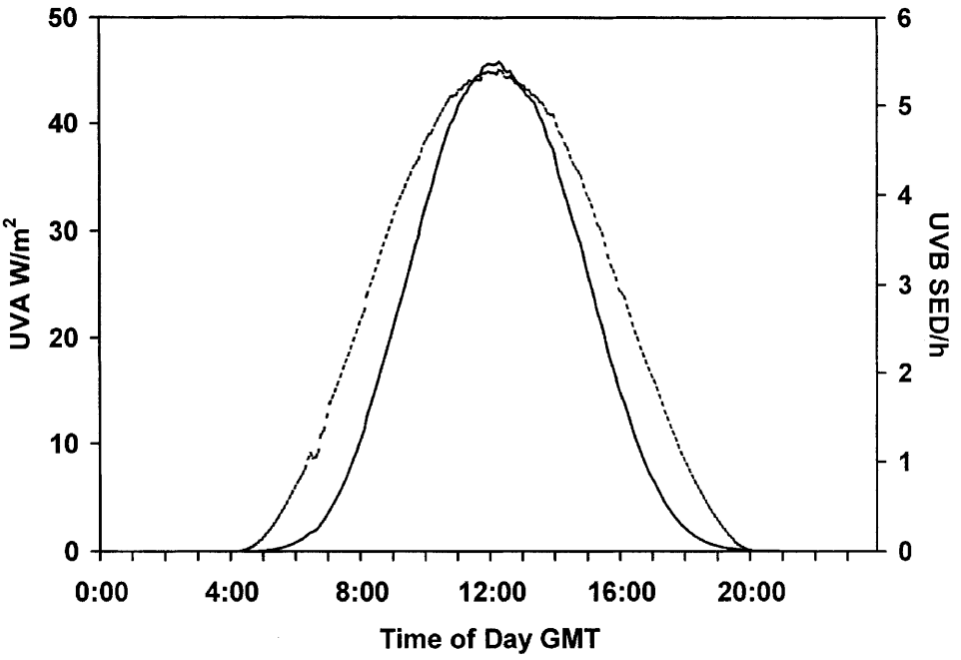

Figure 2.1: UVA (Dashed) and UVB (Solid) Radiation, United Kingdom (~55°N) [2.11]

As illustrated in Figure 2.2, at mid-latitudes (~45°) the UVB radiation level in winter is only 10% of the level received in summer [2.3]. However, latitude-based studies are complicated by geographical and pollutant variation of the sites recorded [2.2 – 2.3]. The ozone hole located over Antarctica generates ozone-poor air, which reaches countries such as New Zealand in late spring or early summer [2.3]. The ozone-poor air produces extreme UV levels, greater than an ultraviolet index (UVI) of 11, during the times of day where SZA is minimised [2.3, 2.7]. The UVI was established by the World Health Organisation as a simple scale for indicating the level of erythemally weighted UV radiation to the public in order to prevent erythemal damage, illustrated in Figure 2.3 [2.12 – 2.13]. Figure 2.2 shows the variance in UVI of a 45°S latitude [2.3].

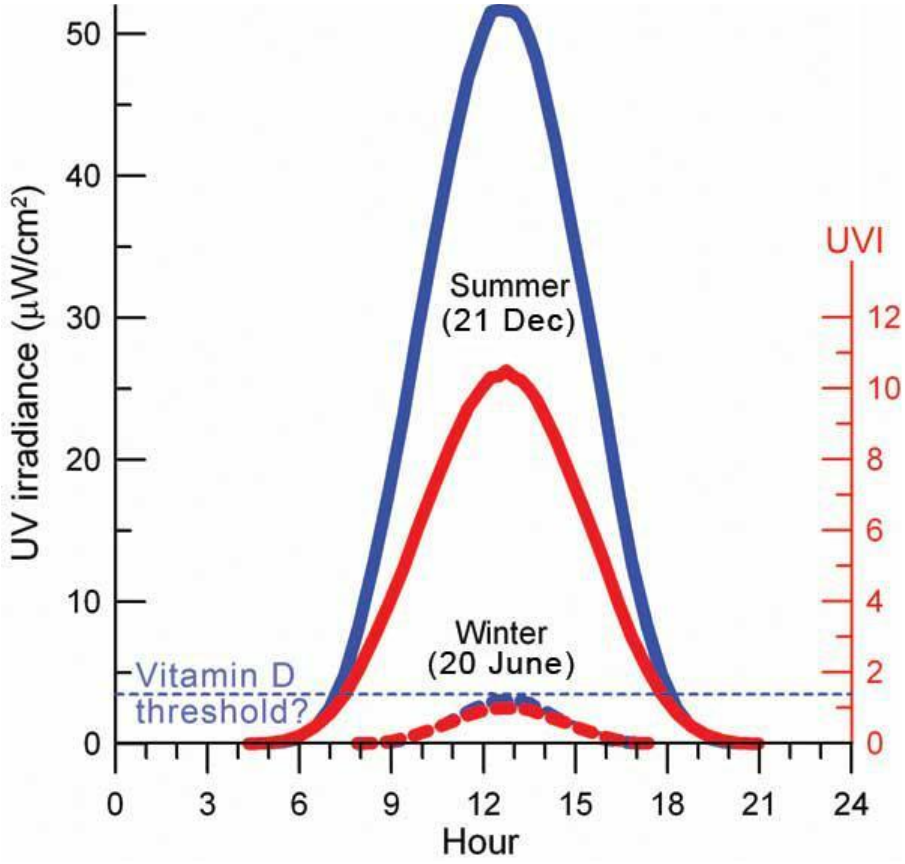

Figure 2.2: Seasonal Variation in Ultraviolet Irradiance at Lauder, New Zealand (45°S) [2.3]

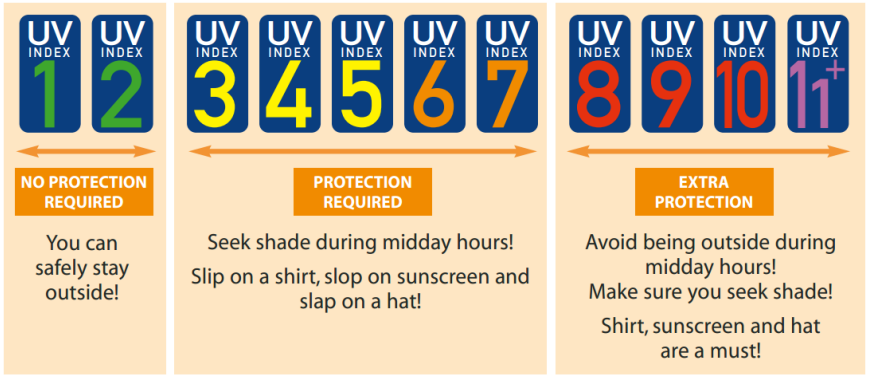

Figure 2.3: World Health Organisation Ultraviolet Index Guide, 2002 [2.12]

In order to obtain the biologically-relevant 'effective' dose, the radiation absorbed must be weighted by wavelength using the action spectra corresponding to the relevant biological effect being monitored [2.2]. Figure 2.4 shows The Commission Internationale de l'Eclairage (CIE) reference erythemal action spectrum, σ_{Ery}, the estimated CIE previtamin D action spectrum, σ_{VitD}, and the solar spectral irradiance, UV_{Sol}, were measured at 45°S latitude with clear skies at noon on

days close to the summer and the winter solstices [2.14]. Figure 2.5 shows the product of multiplying the solar spectral irradiance by the biological action spectra, producing weighted spectral irradiances, following Equations 2.1 – 2.3 listed in Table 2.1 [2.3, 2.11, 2.14 – 2.15]. However, there is still some uncertainty in the accuracy of the vitamin D synthesis action spectrum requiring further research [2.3].

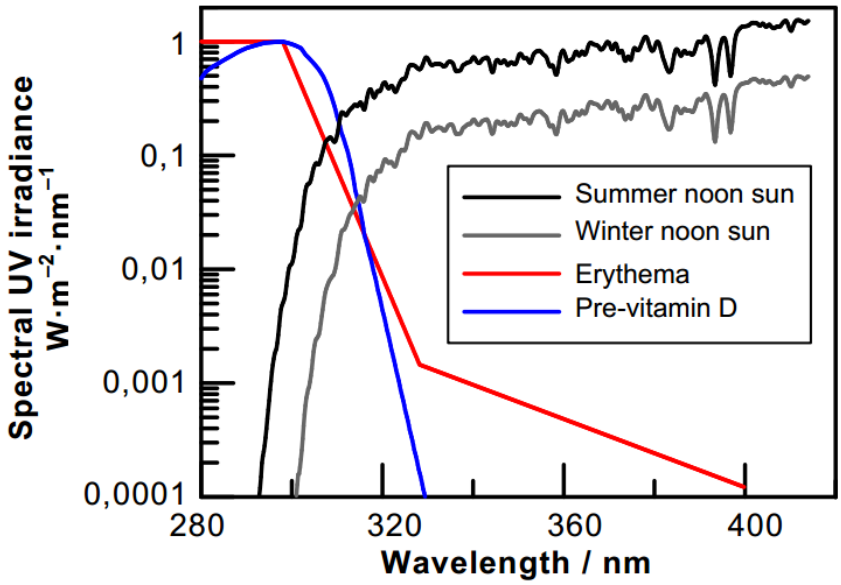

Figure 2.4: Erythemal and Previtamin D Action Spectra with Solar Spectra measured at Noon on the Summer and Winter Solstices at Lauder, New Zealand (45°S) [2.14]

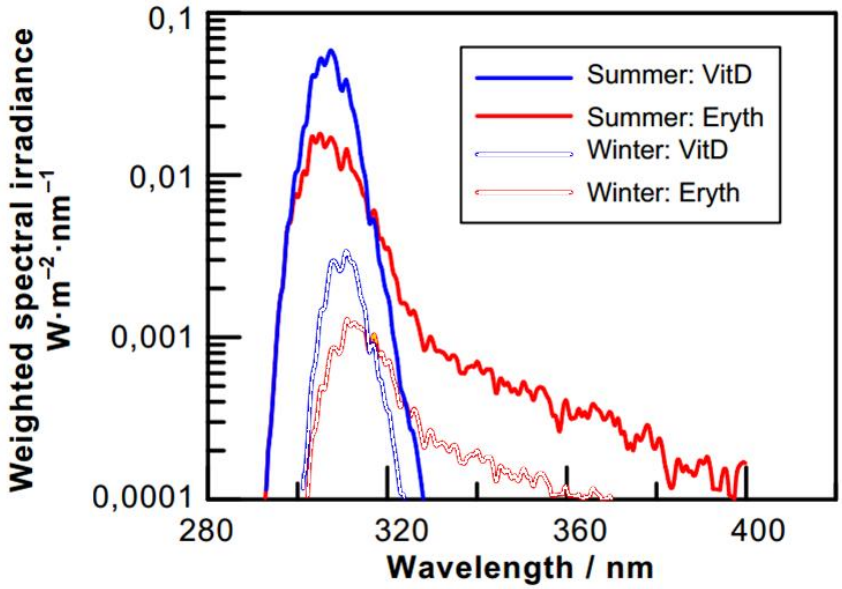

Figure 2.5: Solar Spectra measured at Noon on the Summer and Winter Solstices at Lauder, New Zealand (45°S) Weighted for Erythema and for Previtamin D Synthesis [2.14]

Table 2.1: Methods of Recording UV Radiation [2.3, 2.12, 2.15]

Parameter	Symbol	Unit	Equation	Equation Number
Vitamin D Weighted UV	UV_{VitD}	Wm^{-2}	$UV_{VitD} = \int_{\lambda=250nm}^{400nm} UV_{Sol}(\lambda) * \sigma_{VitD}(\lambda) \cdot d\lambda$	(2.1)
Erythemally Weighted UV	UV_{Ery}	Wm^{-2}	$UV_{Ery} = \int_{\lambda=250nm}^{400nm} UV_{Sol}(\lambda) * \sigma_{Ery}(\lambda) \cdot d\lambda$	(2.2)
UV Index	UVI		$UVI = 40 \cdot UV_{Ery}$	(2.3)

By integrating the exposure of erythemally weighted UV spectra over the duration of a day, the daily erythemal dose that an individual is exposed to can be calculated. The CIE standard erythemal dose (SED) is defined as an effective erythemally weighted exposure of 100 Jm^{-1} (3000 IU), half the effective dose that would produce mild erythema (skin reddening) for skin type I, extremely fair skin [2.4, 2.15]. The minimal erythemal dose (MED) is the effective dose that would produce mild erythema for the specified skin type listed in Table 2.2 [2.10 – 2.11, 2.17].

Table 2.2: Erythemal Dose Definitions [2.17]

Skin Photo Type	Sunburn Susceptibility	Tanning Ability	Classes of Individuals	MED Dose (SED)
I	High	None	Melano-compromised	1 – 3
II	High	Poor		
III	Moderate	Medium	Melano-competent	3 – 7
IV	Low	Dark		
V	Very Low	Natural Brown Skin	Melano-protected	7 – 12+
VI	Extremely Low	Natural Black Skin		

While geographic and atmospheric data can predict UV levels at a geographical location, the levels of UV radiation absorbed by an individual is also dependent on the amount of skin exposed, the orientation of the exposed skin to the sun, the melanin content of the skin, the use of sunscreen, and the age of the individual [2.1, 2.9, 2.13]. Skin pigment can reduce vitamin D synthesis by up to 99%, and the use of sunscreen can reduce of vitamin D synthesis by 92.5% for sun protection factor (SPF) 8, and by 99% for SPF 15 [2.4]. The amount of 7-dehydrocholesterol in skin decreases with age, reducing the amount of previtamin D able to be synthesised for a given UV radiation dose, as

discussed in Section 2.1.3 [2.13]. Therefore the health effects of the UV radiation depend not only on the ambient UV levels, but on the personal absorption of the available UV radiation, as well as the characteristics of the individual, making individual dosimetry essential in monitoring the health effects of UV radiation.

2.1.2 Skin Cancer from Ultraviolet Radiation

Skin cancer is increasing by 4 - 6% internationally among fair-skinned individuals, reaching 'pandemic' proportions [2.2]. Australia and New Zealand have the highest incidence rate of skin cancers worldwide; the population over 50 years of age showing an incidence rate of 1 in 19 for males, and 1 in 25 females in Queensland, Australia [2.1]. The 2009 age-standardised rate (ASR) of malignant melanoma incidences in New Zealand was 42.8 per 100,000 for men, and 33.6 per 100,000 for women [2.3, 2.16]. While the malignant cutaneous melanomas have a high cure rate, metastatic malignant melanoma has no proven effective therapy, and the incidence rate of malignant melanomas internationally is increasing rapidly [2.1].

The risk of developing malignant melanoma is increased by intermittent periods of exposure to intense UV radiation, while the risk of developing non-melanomas, basal cell carcinomas, and squamous cell carcinomas is associated with cumulative UV radiation exposure [2.1]. This makes temporally-resolved dosimetry of UV radiation crucial to properly assessing skin cancer risks. A history of erythemal skin damage, especially during childhood, doubles the risk of developing melanoma skin cancer later in life; therefore UV radiation dosimetry of younger individuals is particularly important [2.1].

2.1.3 Vitamin D Synthesis from Ultraviolet Radiation

An estimated 1 billion people internationally have been found to be vitamin D deficient or vitamin D insufficient [2.4]. Vitamin D deficiency can cause rickets, skeletal deformities, and growth issues in children [2.4]. Vitamin D deficiency also impedes the absorption of calcium and phosphorous, as only 10 – 15% of dietary calcium is absorbed without vitamin D, increasing the risk of developing osteoporosis, osteomalacia, and muscle weakness [2.4]. Studies have shown a direct relationship between vitamin D levels and bone mineral density, with serum levels greater than 40 $ngml^{-1}$ of previtamin D producing maximum density, and levels lower than 30 $ngml^{-1}$ showing reduced calcium absorption [2.4]. Levels less than 20 $ngml^{-1}$ were related to a 30 – 50% increased risk of colon, prostate, and breast cancer, as well as a higher mortality rate from the

aforementioned cancers [2.4]. A lower mortality rate from malignant melanoma was also noted for individuals with higher levels of vitamin D intake [2.4]. Vitamin D has been found to decrease cellular proliferation of both normal and cancer cells, and is potentially involved in killing off malignant cells and fighting cancer [2.4]. Low levels of vitamin D have also been associated with a higher risk of multiple sclerosis, hypertension, cardiovascular disease, schizophrenia, and depression [2.4].

The UV radiation absorbed by skin converts 7-dehydrocholesterol to previtamin D_3 [2.4, 2.13]. Several tissues and cells are capable of converting previtamin D_3 into the active form, vitamin D_3, in a heat isomerisation reaction, a process which takes hours [2.4, 2.13]. Excess vitamin D_3 and previtamin D_3 is destroyed by further UV radiation [2.4, 2.13]. The absorption and synthesis mechanics suggest that exposing a larger area of skin is more efficient in synthesising vitamin D than longer UV exposure times [2.4, 2.13]. The vitamin D synthesis mechanisms are illustrated below in Figure 2.6 [2.4]. Vitamin D_2 and D_3 can also be sourced through dietary means; such as oily fish, foods fortified with vitamin D, and dietary supplements. Both vitamin D_2 and vitamin D_3 are metabolised by the liver into 25-hydroxyvitamin D, which can be measured as vitamin D serum levels in blood [2.4, 2.13]. Artificial UV exposures from phototherapy booths and sunbeds during winter months have been shown to increase vitamin D in serum levels [2.8]. Both endogenously synthesised and dietary vitamin D are stored in fat cells, and released when necessary [2.4].

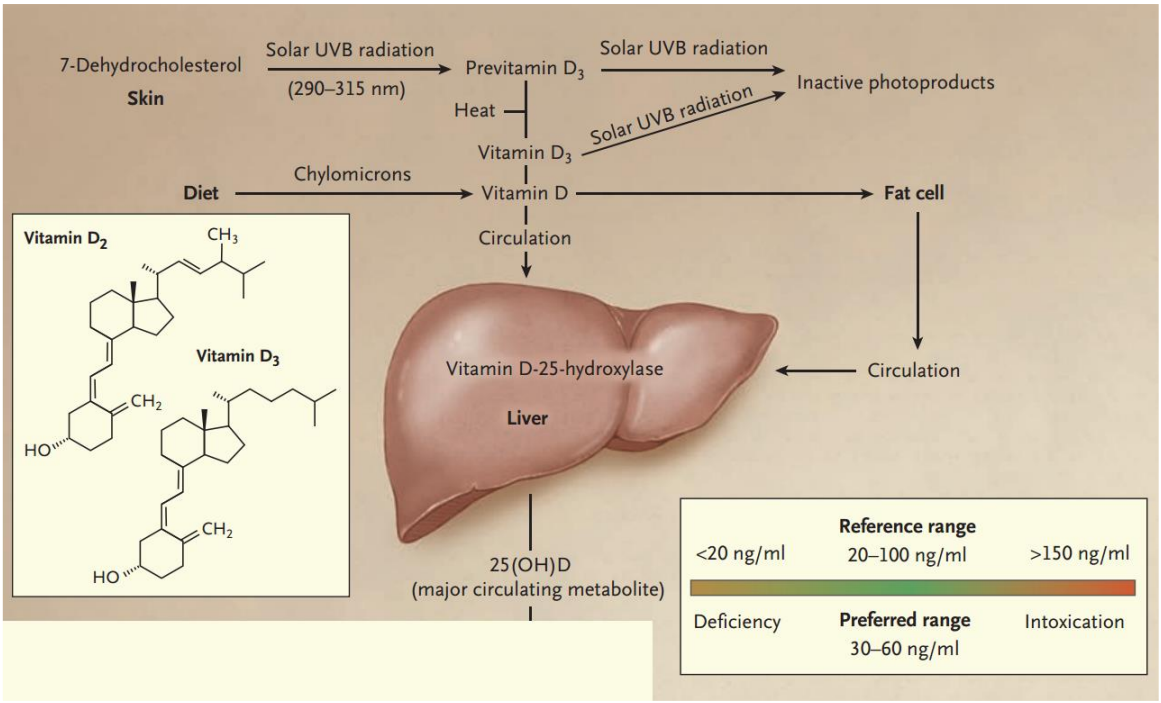

Figure 2.6: The Vitamin D Synthesis Process [2.4]

For extreme latitudes, north of 40°N and south of 40°S, the UVI levels drop below 1 during winter, therefore obtaining a sufficient dose for vitamin D synthesis during winter without risking erythema is not possible while only exposing the hands and face to direct sunlight, as shown in Figure 2.7 [2.3]. However, exposures of greater body area to direct sunlight for prolonged periods of time in winter may not be adopted by the general public. Although vitamin D has a residence time in the human body of a few weeks, maintaining sufficient levels of vitamin D in extreme latitudes during winter months is a significant issue; especially for darker skin types, as a significantly greater amount of UV radiation is required in order to synthesise vitamin D in skin with higher melanin content, from Table 2.2 [2.3, 2.18].

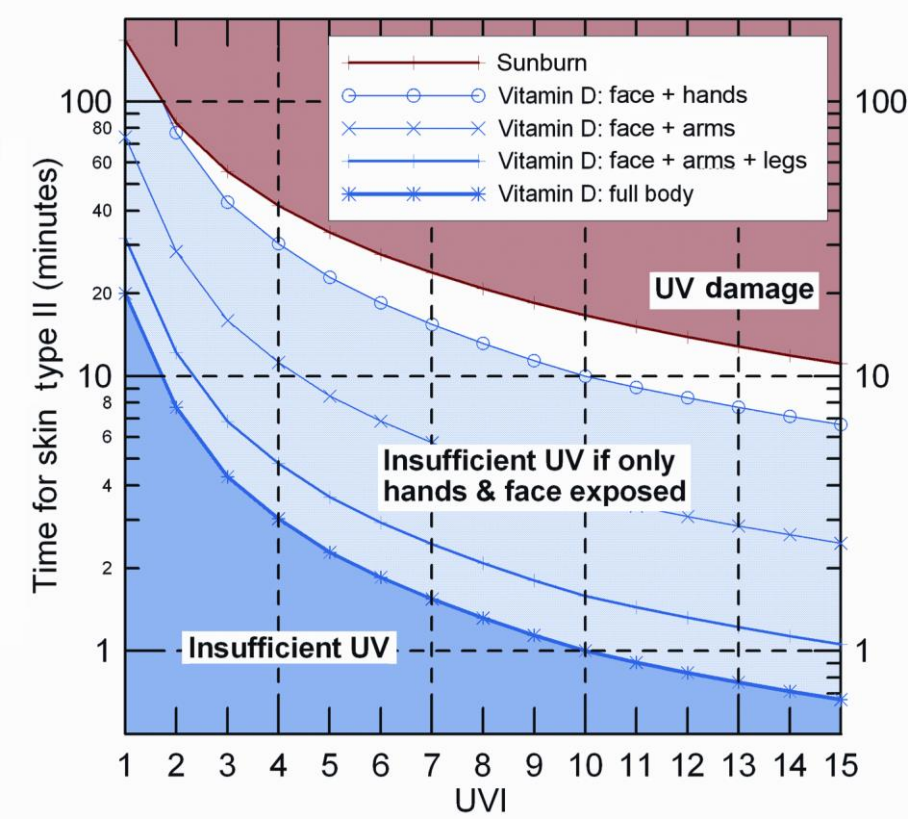

Figure 2.7: Optimal UV Radiation Exposure Times of UVI Levels for Skin Type II [2.3]

As discussed in Section 2.1.1, weighted spectral irradiances can be used to determine the level of UV radiation for previtamin D_3 synthesis. However, UVI levels cannot be used directly to forecast vitamin D synthesis, as the vitamin D action spectrum is more sensitive to UVB radiation than the erythemal spectrum, but the UVI index can be used to calculate MED [2.3, 2.10, 2.13].

The general public currently have limited tools for assessing UVI levels, especially during winter months, and general knowledge pertaining to the effects of vitamin D deficiency has been

found to be lacking [2.3, 2.19]. A survey conducted by the New Zealand Cancer Society found an increase in the use of sun-protection methods following awareness campaigns; however, only 9% of survey respondents reported taking action on improving vitamin D levels from outdoor activity [2.19]. In order to maximise the positive health effects of UV exposure and minimise vitamin D deficiency, a greater public awareness towards vitamin D production is required [2.3, 2.5, 2.15].

A study into the behaviour of individuals tracking their sun exposure over time has shown that, when given a UV dosimeter to monitor sun exposure, over 80% of participants noted being more aware of their sun exposure, and 16% of participants changed their sun exposure behaviour [2.5]. This shows a substantial potential for changing public awareness and behaviour with the availability of UV dosimeter technology. Therefore, producing cheaper photodetectors for accurately recording UV radiation over time is a promising tool for confronting both skin cancer rates, and vitamin D deficiency.

2.2 Ultraviolet Photodetection

The measurement of erythemally weighted UV radiation has been historically performed using polysulfone films, spectroradiometers, pyranometers, fluorescence systems, and photodiodes such as AlGaN and SiC [2.2, 2.7, 2.11, 2.20 – 2.22]. Meteorological equipment, such as spectroradiometers, Robertson-Berger (R-B) meters, and pyranometers, have been used to measure the UV radiation normal to a plane with very high accuracy [2.2, 2.7, 2.23]. Spectroradiometers are able to measure erythemally weighted UV radiation with only 6% uncertainty, making them the most accurate measurement method [2.23]. R-B meters filter incoming visible light, and then use a phosphor to absorb UV radiation and fluoresce discrete wavelengths, which are then measured internally by a photodiode [2.2, 2.7, 2.20]. R-B meters, such as the UVB Biometer Model 501 Radiometer, are currently used internationally for atmospheric monitoring UV radiation levels [2.2, 2.23].

Measuring the UV radiation absorbed by the exposed skin of a human body, which is dependent on the skin topology and orientation towards the sun, is a more difficult task. Estimation of the UV radiation absorbed can be made using polysulfone films, handheld UV meters, and electronic dosimeters, which are less accurate than meteorological equipment, but are portable enough for personal use [2.22 – 2.23]. Polysulfone films undergo a chemical change with UV radiation exposure and, while a cheap method of measuring personal UV radiation absorbed over a fixed period of time, do not offer temporally-resolved data, which is necessary in order to calculate peak UV levels and erythema risk [2.11, 2.21, 2.23].

2.2.1 Ultraviolet Dosimeters

Low-cost electronic UV dosimeters have been developed at the University of Canterbury, New Zealand [2.6, 2.22, 2.24]. The devices use an AlGaN Schottky photodiode to measure UV radiation [2.7, 2.22]. The spectral sensitivity of the AlGaN photodiodes can be modified by controlling the percentage of aluminium in the sensor [2.7]. The UV dosimeters developed by the University of Canterbury have used AlGaN Schottky photodiode sensors with 26% aluminium incorporation, which was found to closely match the erythemal spectrum [2.7, 2.18]. As there was at least four orders of magnitude rejection between the UV wavelengths and both the visible and infrared wavelengths, a filter was not needed as the sensor was sufficiently visible-blind to solar radiation [2.7]. The weather-proof PTFE casing was also designed to act as a UV diffuser, mimicking the cosine distribution of UV radiation entering human skin [2.18, 2.22 – 2.23]. The UV dosimeters developed by the University of Canterbury are comparable to UV-A sensor GUVA-S12SD and UV-B sensor GUVB-S11SD, with key specifications listed in Table 2.3 [2.25 – 2.26].

Table 2.3: AlGaN-Based UV-A and UV-B Photodiode Specifications [2.25 – 2.26]

Parameter	UV-A Sensor	UV-B Sensor
Operating Temperature Range	-30 – 85 °C	-30 – 85 °C
Maximum Forward Bias Current	1 mA	1 mA
Dark Reverse Bias Current (-0.1 V)	1 nA	1 nA
Photocurrent (1 $mWcm^{-2}$)	101 – 125 nA (UVA Lamp)	62 – 75 nA (UVB Lamp)
Responsivity (0 V Bias)	0.14 AW^{-1} (λ = 350 nm)	0.11 AW^{-1} (λ = 300 nm)
Spectral Detection Range (10% of Responsivity)	240 – 370 nm	240 – 320 nm
Active Area	0.076 mm^2	0.076 mm^2

The UV dosimeters were used to monitor daily UV levels, with varying time intervals between measurements in order to optimise temporally-resolved data collection and the frequency of downloading the data from the dosimeters [2.6 – 2.7, 2.18, 2.23 – 2.26]. The UV dosimeters are calibrated using a Yankee Environmental Systems Inc. broadband erythemal meter, which itself was calibrated using a spectroradiometer developed by the New Zealand National Institute of Water and Atmospheric Research (NIWA), both located at Lauder, New Zealand (45°S latitude) [2.7, 2.23]. However, the devices have shown a bandpass mismatch with the CIE erythemal spectrum, requiring further weighting in order to obtain more accurate measurements [2.23]. These UV dosimeters have

been used in studies of human exposure to UV radiation, worn on a wrist-strap, attached to clothing, and positioned stationary on a horizontal surface [2.6 – 2.7, 2.18, 2.22, 2.27].

2.3 Zinc Oxide for Ultraviolet Photodetectors

Although AlGaN photodiodes can be fabricated to match the erythemal action spectrum, the growth of high-quality AlGaN for UV photodetectors is difficult, and to date must be grown as a film on a substrate using expensive techniques such as molecular beam epitaxy (MBE), rather than in bulk crystal form [2.28 – 2.29]. The AlGaN UV photodiode used in the UV dosimeter described in Section 2.2.1 is the most expensive component of the UV dosimeter. An alternative semiconductor material for UV photodetection could allow for cheaper, more accurate UV dosimeters for both research and commercial use. A suitable semiconductor for replacing GaN and related compounds is ZnO [2.29].

ZnO is group II-VI earth-abundant semiconductor that has a high transparency in the visible spectrum, is radiation hard, stable over a wide range of temperatures, and is not biologically harmful to humans. ZnO has a wide direct band gap, (3.37 eV at 300 K), high electron mobility (~200 $cm^2V^{-1}s^{-1}$ at 300 K), large excitonic binding energy (60 meV), high melting point (1975 °C), and a high thermal conductivity (~100 $Wm^{-1}K^{-1}$ at 300 K) [2.29 – 2.31]. The wide band gap allows ZnO to operate in the UV spectrum, and have a low leakage current in rectifying devices which, along with the high electron mobility, make ZnO a promising candidate for UV photodetection [2.32 – 2.33]. ZnO also has the highest exciton binding energy for type II-VI semiconductors, 60 meV, compared to GaN with 25 meV, showing promise for optoelectronic applications, showing further potential applications for high-quality contacts to ZnO [2.33]. ZnO can also be chemically wet-etched, unlike GaN, providing more methods for device manufacturing [2.29].

Single-crystal bulk ZnO can be produced through a number of solvothermal and epitaxial methods, including hydrothermal growth, sputtering, vapour phase transport (VPT), metal-organic chemical vapour deposition (MOCVD), and MBE [2.33]. Hydrothermal growth is the most promising method for producing low-cost, large wafers of high quality bulk crystal ZnO [2.33 – 2.34]. Hydrothermal growth of high-quality 2-inch wafers of bulk ZnO using temperatures between 300 – 400 °C is currently a commercially viable process [2.33 – 2.34]. Wafers have been grown from ZnO seed crystals, as shown in Figure 2.8, with preferential growth along the +c-axis, compared to the –c-axis and m-axis [2.35].

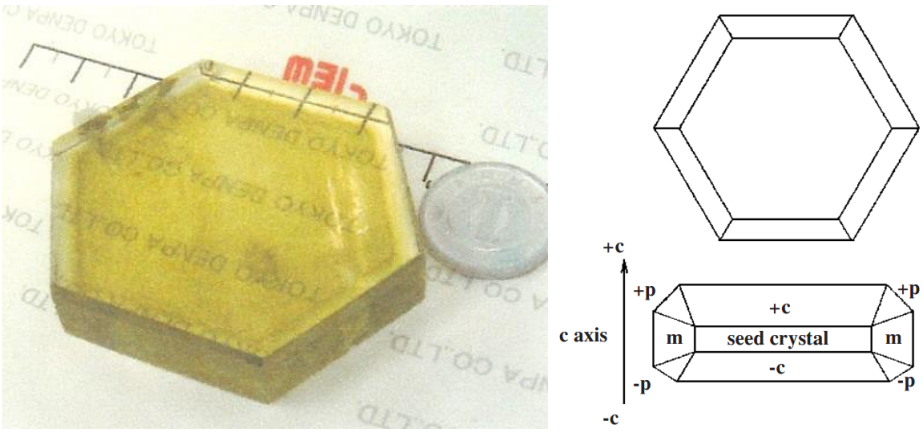

Fig 2.8: Tokyo Denpa Co., Ltd. ZnO Crystal (Left) and Growth Sectors (Right) [2.34]

For hydrothermally grown ZnO, the most common impurities were lithium, sodium, potassium, iron, and aluminium, with concentrations of the order of 0.1 – 10 parts per million (PPM) [2.33 – 2.35]. The lithium, sodium, and potassium impurities act as deep acceptors in bulk ZnO, causing increased resistivity [2.33, 2.36]. Lithium is the dominant acceptor impurity, with typically an order of magnitude larger concentration than sodium and potassium [2.36]. For high-quality hydrothermal bulk ZnO grown on the +c crystal axis, the carrier concentration was typically 10^{13} – 10^{14} cm^{-3}, with high levels of resistivity between 10^{2} – 10^{3} Ωcm [2.36]. In comparison, hydrothermal ZnO grown on the –c crystal axis shows higher impurity concentrations of aluminium and iron, attributed to differences in growth direction, producing lower bulk resistivities of 0.08 – 2.8 Ωcm [2.34 – 2.35].

Wafers of low-lithium hydrothermal ZnO have been produced by Tokyo Denpa Co., Ltd. by annealing the bulk material to temperatures of 1400 °C, causing the impurities to concentrate at the ZnO surface, which is then removed by grinding and re-polishing [2.36]. The resulting +c-axis (low-lithium) bulk ZnO wafers had carrier concentrations of between 10^{16} – 10^{17} cm^{-3}, and resistivities between 0.59 – 26 Ωcm [2.36]. The ZnO used in this work was hydrothermal bulk ZnO from Tokyo Denpa Co., Ltd., specifically –c-axis and +c-axis (low-lithium) bulk ZnO, as it was considered to be the most promising candidate for replacing AlGaN for UV photodetectors.

2.3.1 Properties of Zinc Oxide

ZnO has been a part of human history since the smelting of copper ores and the production of brass [2.37]. Alchemists formed an alloy of brass and gold with ZnO, believing they had transmuted the copper and zinc into gold [2.37]. ZnO was also produced by burning zinc in air, forming a white powder of ZnO known as ‘philosopher’s wool’, which was used in medicinal ointments [2.37].

Large-scale commercial production of ZnO began in the mid-1800s for use in the production of rubbers, ceramics, and paints [2.37]. Currently over 100,000 tons of ZnO are produced annually for industrial, medical, cosmetic, and scientific purposes [2.33].

ZnO is commonly used in sunscreens and cosmetics due to its UV absorption and non-toxicity to humans, as well as being used as a food additive to counter dietary zinc deficiencies [2.33]. In electronic applications, ZnO is used in the production of varistors and in gas sensors, due to its surface sensitivity to the presence of oxygen and hydrogen [2.33]. ZnO has also been used in the production of transparent conducting oxides for solar cells, liquid crystal displays, energy-saving window coatings, and has shown potential for transparent electronic displays [2.33]. The physical characteristics of ZnO show potential for future applications in optoelectronics, spintronics, transparent electronics, and other sensor applications [2.33].

As a semiconductor, ZnO has been widely studied since 1935, with several peaks of interest following the determination of the initial optical properties, electronic transport, and crystal structure research in the 1930s-1950s [2.33]. Renewed interest in ZnO first peaked in the 1960s with increased availability of epitaxially-grown bulk ZnO, allowing further research into ZnO band structure, doping, ferrite properties, and luminescence [2.33, 2.37]. However, the inability to realise p-type ZnO made the anticipated production of blue/UV laser-diodes using ZnO p-n junctions impossible, and interest faded in the 1980s [2.33]. The production of blue/UV laser diodes using other materials, such as GaN, as well as development in the growth and doping of ZnO, has renewed interest in ZnO and ZnO-based materials, as well as the growing interest in transparent electronics and display technology [2.33]. ZnO-based materials such as IGZO (InGaZnO) are also currently being utilised in display technology, contributing to the increase in ZnO-based research [2.33]. The self-organisation of nanostructures during ZnO growth has also prompted an increase in ZnO nanowire research [2.33].

2.3.2 Crystal Structure of Zinc Oxide

The lattice bonds in crystalline ZnO involve sp^3 hybridisation of the electron states, forming four equivalent orbitals between the zinc and oxygen atoms in a tetrahedral formation [2.33]. The wide band gap is due to the difference between the sp^3 states, the valence band, and the anti-bonding counterpart, the conduction band [2.33]. The polarity of the Zn-O bonds is strongly electronegative, bordering between covalent and ionic classification [2.33]. Due to the difference in the electronegativity of the Zn atoms, 1.65, and the O atoms, 3.44 [2.33]. The cohesive energy per bond can be up to 7.52 eV, which gives crystalline ZnO its high melting point, 1975 °C, making it a

suitable semiconductor for high-temperature electronics [2.33]. The nature of the tetrahedral bonds causes direction-dependent thermal expansion, relevant to high-temperature applications [2.33].

Due to the strong polarity of the tetrahedral bonds, under ambient conditions ZnO crystallises in the hexagonal wurtzite structure, shown in Figure 2.9, where the black spheres indicate zinc atoms, and the white spheres indicate oxygen atoms [2.33, 2.38]. Other crystal polytypes of ZnO are cubic zinc-blende and rocksalt [2.33]. The tetrahedral bonds of hexagonal wurtzite ZnO form alternating layers of zinc and oxygen atoms within the crystal [2.33]. The sequence of these layers can be used to determine the crystal orientation, as shown in Figures 2.9 – 2.10 [2.33]. The strong electronegativity of the Zn-O bonds causes a distortion in the natural wurtzite structure, bringing the alternating layers of zinc and oxygen atoms closer together than in ideal wurtzite geometry [2.33]. This further shows the impact of the bond polarisation on ZnO.

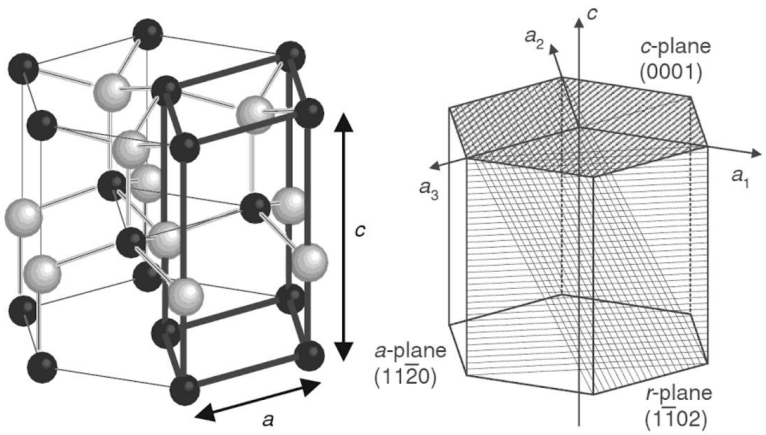

Figure 2.9: Wurtzite Crystal Structure of ZnO (Left), and Crystal Planes (Right) [2.38]

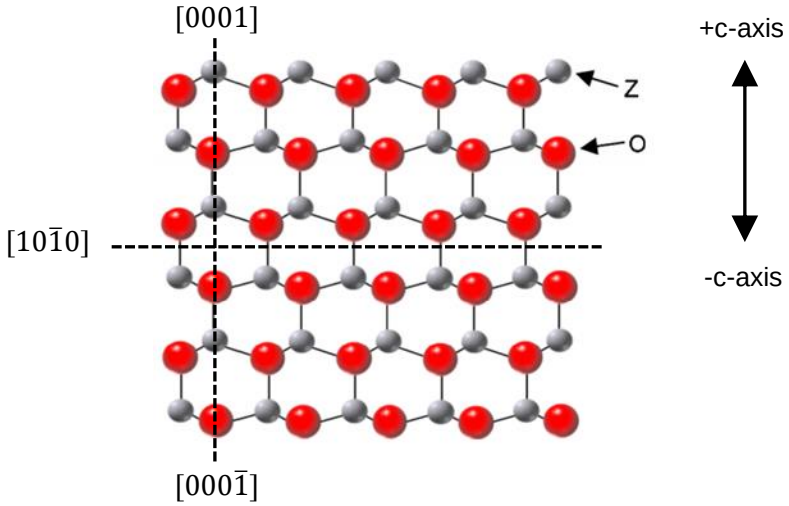

Figure 2.10: Wurtzite Crystal Axes of Zinc Oxide with Miller Indices [2.40]

As wurtzite ZnO is hexagonal, the faces are denoted by four-digit Miller indices, shown in Figure 2.10 [2.33, 2.39]. The c-axis, with a Miller index of [0001] shown in Figure 2.10, is the direction of preferential growth in wurtzite ZnO, and normal to the c-plane, (0001), shown in Figure 2.9 [2.33]. The other planes of interest are the –c-plane, $(000\bar{1})$, the a-plane, $(11\bar{2}0)$, the m-plane, $(10\bar{1}0)$, and the r-plane $(1\bar{1}02)$ shown in Figures 2.10 – 2.11 [2.33, 2.39 – 2.40].

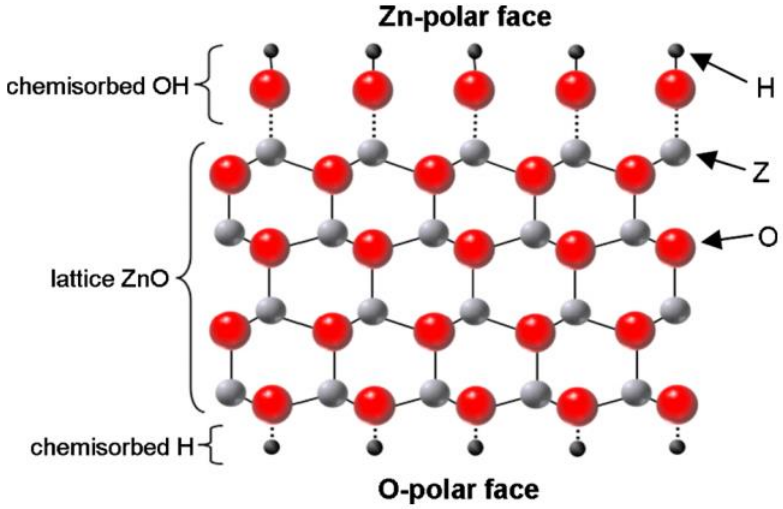

Figure 2.11: Crystal Face Terminations of Bulk ZnO (c-axis, Wurtzite) [2.40]

The c-axis is normal to the alternating double layers of zinc and oxygen atoms, therefore the terminations of the c-plane ZnO crystal have polarity [2.33]. The c-plane crystal surface, (0001), is terminated by zinc atoms (the Zn-polar face), and the –c-plane, $(000\bar{1})$, is terminated by oxygen atoms (the O-polar face), shown in Figures 2.10 – 2.11 [2.33]. The other crystal planes are of mixed-polarity [2.33]. As the monoatomic polar surfaces are not electrically stable, the c-plane faces are terminated by chemisorbed hydroxyl groups and hydrogen on the Zn-polar surfaces and O-polar surfaces, respectively, as illustrated in Figure 2.11 [2.33, 2.40]. The different faces of c-plane ZnO have different chemical reactions, etch rates, and mechanical properties, further highlighting the importance of the polarity and crystal structure of ZnO [2.33].

2.3.3 Electrical Properties of Zinc Oxide

The most significant limitation of ZnO as a semiconductor, as mentioned in Section 2.3, is the inability of the material to be doped both n-type and p-type; a common limitation for wide band gap materials [2.33]. ZnO is naturally n-type, with an unintentional undoped carrier concentration in the

order of $n \approx 10^{16}$ cm^{-3} [2.33]. The nature of the intrinsic n-type doping is believed to be caused by both intrinsic defects and hydrogen incorporation, however the roles of impurities and defects in ZnO, and their impact on the optical and electrical properties of ZnO, are still not fully understood [2.33].

The intrinsic doping is thought to be due to native point defects of zinc interstitials, Zn_I, and oxygen vacancies, V_O [2.33]. Hydrogen is always a donor in ZnO, as the electronic H^+/H^- transition level of interstitial hydrogen is in the conduction band [2.33]. Hydrogen is easily ionised, and is likely to be a dominant background donor as hydrogen is a significant residual contaminant in most deposition systems [2.33]. The substitution of hydrogen on an oxygen site, H_O, is also highly stable [2.31]. Annealing the ZnO at temperatures above 715 °C in N_2 gas has shown to deplete the ZnO of most of the hydrogen present [2.33]. The ionisation of the oxygen vacancy is also believed to contribute to the long-term effects of persistent photoconductivity, as V_O can exist in three different charge states, which affect the structure of the surrounding crystal lattice, causing relaxation towards or away from the oxygen vacancy [2.29]. Persistent photoconductivity is covered in further detail in Section 2.3.4.

ZnO can be doped as p-type, however to overcome the intrinsic n-type characteristics, the required level of doping produces p-type ZnO with very low mobility [2.33]. Hall mobility for n-type ZnO has been measured as 200 $cm^2V^{-1}s^{-1}$ at 300 K, while corresponding reports of p-type ZnO show 5 – 50 $cm^2V^{-1}s^{-1}$ [2.33]. Fabrication of ZnO homojunctions using both n-type and p-type ZnO have been reported, however the performance of these devices was significantly worse than heterojunctions involving n-type ZnO [2.33]. As producing high-conductivity p-type ZnO is still unrealised at the time of this work, the devices fabricated on ZnO were chosen to be Schottky contacts rather than p-n junctions, as Schottky contacts can be made between inhomogeneous materials.

As a direct band gap material, ZnO has a shorter minority carrier diffusion length by several orders of magnitude than indirect band gap semiconductors, as direct band gap materials allow for the recombination of electron-hole pairs without a change in momentum [2.33]. The diffusion length determines the amount of current produced from a photodiode under illumination, making it a critical parameter in the development of ZnO-based UV photodiodes [2.33]. In Schottky diodes, the non-equilibrium minority carriers are generated by the absorption of light within the bulk semiconductor and collected by the built-in field, contributing to the total electronic flow through the device [2.33]. Incident wavelengths with energies above the band gap are typically absorbed within the first 100 nm of the bulk ZnO [2.33].

The band gap of ZnO is 3.37 eV at 300 K, which corresponds to a wavelength of 370 nm, in the middle of the UVA region of the UV spectrum, as detailed in Section 2.1.1. Band gap engineering of ZnO-based materials can be used to tailor the absorption spectra of ZnO-based materials to match the erythemal action spectrum, or vitamin D action spectrum, by widening the band gap and shifting the absorption peak further towards UVB [2.33]. The band gap of ZnO can be tuned with the addition of low concentrations of oxides such as MgO and CdO[2.33]. As shown in Figure 2.12, for wurtzite $Zn_{(1-x)}Mg_xO$, where $x < 0.5$ the band gap can be varied from 3.32 eV to 4.3 eV (373 nm to 288 nm), covering both the UVA and UVB spectrum [2.33]. However, the lattice mismatch between the wurtzite ZnO and the cubic rocksalt MgO has been found to cause increasing resistivity with increasing MgO incorporation, complicating fabrication [2.33].

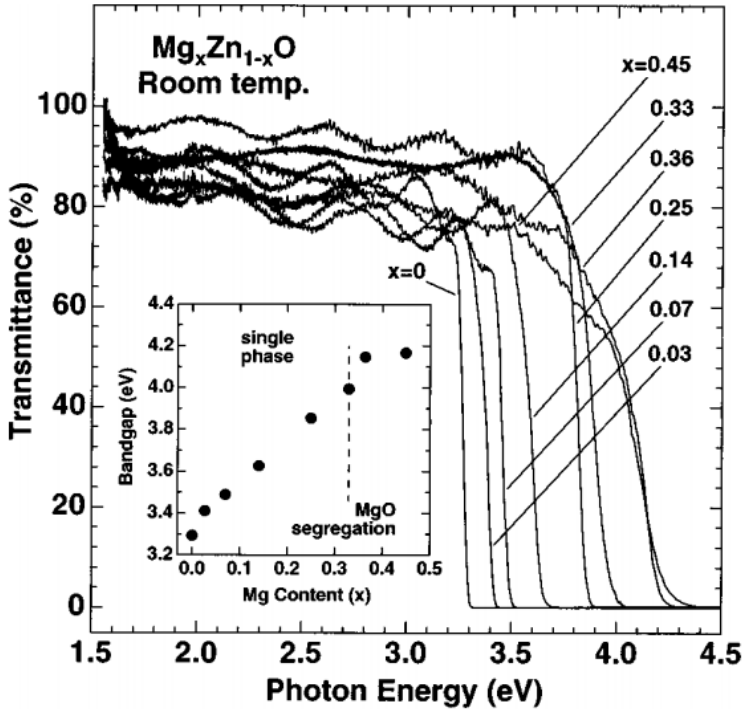

Figure 2.12: Bandgap of ZnMgO with Increasing MgO Content [2.41]

2.3.4 Ohmic and Schottky Contacts to Zinc Oxide

The first semiconductor device was made by Ferdinand Braun in 1874, who discovered the rectifying properties of a metal-semiconductor interface between a lead sulphide crystal and a thin metal wire in point contact [2.42 – 2.43]. By 1938, the formation of these contacts was explained by the Schottky-Mott model, proposing that the rectifying behaviour of the metal-semiconductor interface was caused by stable space charges in the semiconductor forming a potential barrier at the

junction, depleted of mobile charge carriers [2.32, 2.42, 2.44 – 2.45]. For this work, the analysis of metal-semiconductor contacts focuses on Schottky contacts to n-type semiconductors.

The potential barrier at a metal-semiconductor interface is caused by the different work functions of a metal, ϕ_m, and of a semiconductor, ϕ_s, shown in Figures 2.13 for a metal and an n-type semiconductor [2.42]. When brought into intimate contact and under thermal and chemical equilibrium, the Fermi levels of both materials become equal, and the vacuum levels are continuous, leading to band bending and the formation of a built-in potential, V_{bi}, with a zero bias effective barrier height, Φ_B, at the metal-semiconductor interface, shown in Figure 2.14 with accompanying Equations 2.4 – 2.5 in Table 2.4 [2.42]. The potential barrier between the semiconductor conduction band and the metal Fermi level includes the difference between the semiconductor conduction band and the Fermi level, V_n, as shown in Equation 2.6 in Table 2.4 [2.42]. It should be taken into consideration that in practical formation of metal-semiconductor junctions, the surface states at the interface have a significant impact on the formation of the potential barrier, by introducing different paths of conduction, however Equations 2.4 – 2.6 do not include surface states due to the complexity of the calculation [2.42].

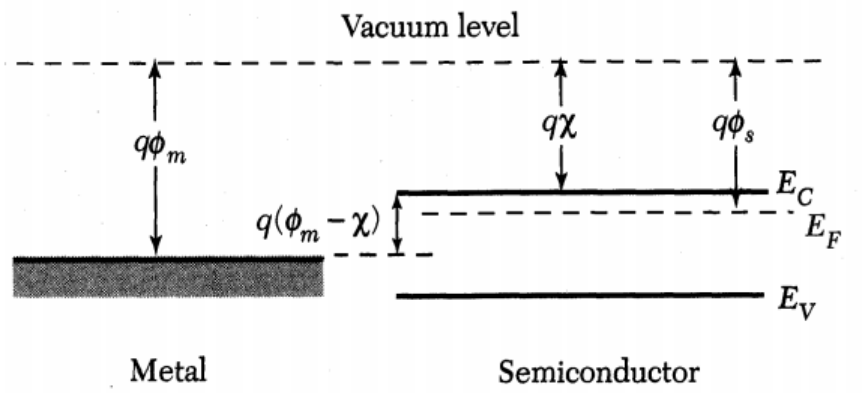

Figure 2.13: Energy Band Diagram of a Metal and an n-Type Semiconductor [2.42]

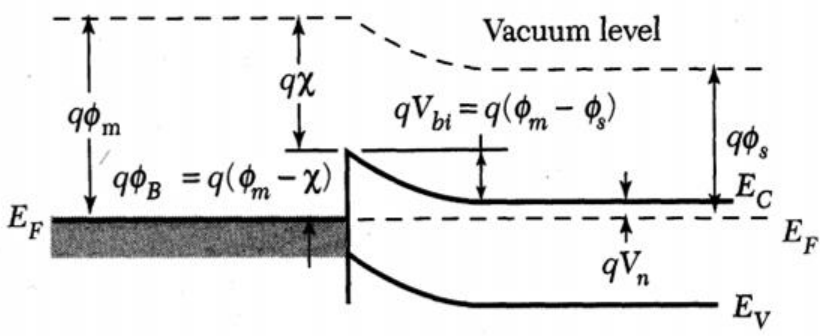

Figure 2.14: Energy Band Diagram of a Metal-Semiconductor Junction at Thermal Equilibrium, with n-Type Semiconductor [2.42]

Table 2.4: Built-In Potential and Barrier Height of Metal-Semiconductor Interfaces [2.42]

Parameter	Symbol	Unit	Equation	Equation Number
Built-in Potential	V_{bi}	V	$qV_{bi} = q(\phi_m - \phi_s)$	(2.4)
Barrier Height (n-type)	Φ_B	eV	$\Phi_B = q\phi_B = q(\phi_m - \chi)$	(2.5)
Built-in Potential (n-type)	V_{bi}	V	$V_{bi} = \phi_B - V_n$	(2.6)

Applying a bias across the metal-semiconductor interface shifts the conduction band, therefore either decreasing or increasing the barrier height, depending on the polarity of the bias, as shown in Figure 2.15 [2.42]. Applying a positive bias from the metal to the n-type semiconductor decreases the barrier height, shown in Figure 2.15 (Centre), and allows electrons to flow via thermionic emission in 'forward bias' [2.42]. Applying a negative bias across the junction increases the barrier height, preventing the conduction of charge carriers, in 'reverse bias' [2.42]. With zero bias across the junction, the device is at thermal equilibrium and the barrier height is equal to the built-in potential, V_{bi} [2.42]. In this work, the barrier height of a Schottky contact refers to the barrier height at thermal equilibrium. For large barrier heights, $\Phi_B \gg kT$, the metal-semiconductor interface is a Schottky contact, and the device is rectifying [2.42]. Small barrier heights at the metal-semiconductor interface produce ohmic contacts [2.42]. The current-voltage dynamics of a Schottky contact are explored in Section 4.2.2.

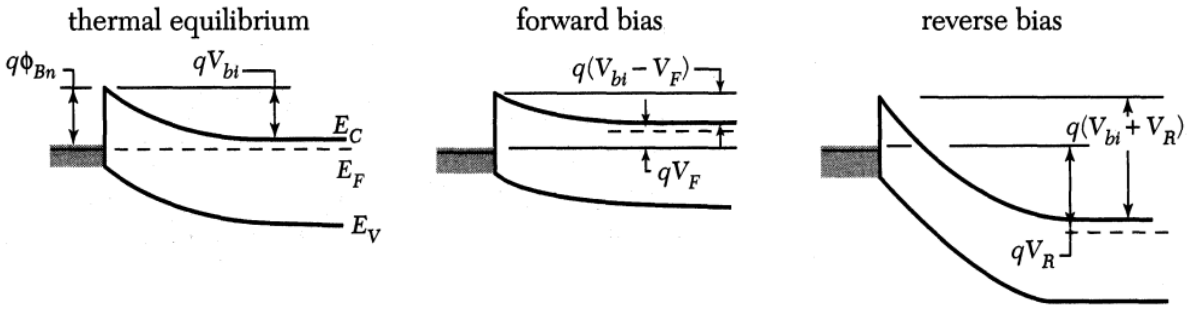

Figure 2.15: Energy Band Diagram of Metal-Semiconductor Junction, n-Type Semiconductor, with Thermal Equilibrium (Left), Forward Bias (Centre), and Reverse Bias (Right) [2.42]

The effective barrier height of the Schottky contact is also affected by the image force lowering effect [2.32]. Electrons from the semiconductor approaching the barrier are attracted by a positive 'image' charge induced in the metal, lowering the effective barrier height by $\Delta\Phi_{B(if)}$ [2.32]. $\Delta\Phi_{B(if)}$

can be calculated using Equation 2.7, where N_D is the effective doping concentration, and ξ is the energy difference between the Fermi level and the semiconductor conduction band [2.32].

Table 2.5: Schottky Contact Image Force Lowering Effect Calculations [2.32]

Parameter	Symbol	Unit	Equation	Equation Number
Image Force Lowering of Effective Barrier Height	$\Delta\Phi_{B(if)}$	eV	$\Delta\Phi_{B(if)} = \left[\left(\frac{q^3 N_D}{8\pi^2 {\varepsilon_\infty}^2 \varepsilon_s {\varepsilon_0}^3}\right)\left(\Phi_B - V - \xi - \frac{kT}{q}\right)\right]^{\frac{1}{4}}$	(2.7)
Image Force Lowering of Ideality Factor	$\frac{1}{\eta_{(if)}}$		$\frac{1}{\eta_{(if)}} = 1 - \frac{\Delta\Phi_{(if)}}{4}\left(\Phi_B - V - \xi - \frac{kT}{q}\right)^{-1}$	(2.8)

The image force lowering effect also causes an increase in the ideality factor, η, of a Schottky contact [2.32]. The ideality factor, detailed in Section 4.2.2 for current-voltage analysis of Schottky contacts, indicates the dominant carrier transport mechanism, and contact homogeneity [2.42]. Inhomogeneities in Schottky contacts are caused by variations or defects in the Schottky contact, such surface defects and regions of varying conductivity within the Schottky contact [2.32]. Schottky contacts with higher levels of homogeneity have lower ideality factors, with $\eta = 1$ being purely ideal, and have reverse bias current flow dominated by thermionic emission, independent of device bias, providing a stable reverse-bias current [2.32].

The image force lowering effect increases the lower limit of ideality factor to $\eta_{(if)}$, as shown in Equation 2.8 in Table 2.5 [2.32]. As the image force lowering effect is due to the movement of charge carriers in the Schottky contacts, the electrical measurements affected by this are current-voltage and capacitance-voltage [2.32].

Ohmic contacts conduct regardless of voltage polarity follow Ohm's law, and have negligible contact resistance and negligible voltage drop across the contact [2.42]. For sufficiently high doping concentrations, the dominant carrier transport mechanism in an ohmic contact is the tunnelling current [2.33]. Low-resistance, thermally-stable ohmic contacts are required for high-performance electronics using ZnO [2.33].

Wide band gap semiconductors generally form Schottky contacts more readily than ohmic contacts; however the opposite is true for ZnO [2.33]. Due to the high conductivity of ZnO, (~100 $Wm^{-1}K^{-1}$ at 300 K) [2.30], and the high level of intrinsic n-type doping, the fabrication of ohmic contacts on ZnO has been achieved with resistances as low as 10^{-4} Ωcm^2 using Ti/Au [2.33]. The Ti/Au ohmic contacts have a linear current-voltage characteristic, which has been shown to

improve with annealing in nitrogen [2.33]. The titanium layer has been suggested to react with oxygen species on the surface of ZnO to form TiO_2, which depletes the ohmic contact region of oxygen, and increases the electron carrier concentration [2.46]. Ohmic contacts to ZnO have also been made with In, Al/Pt, and Ti/Al/Pt/Au, with contact resistance dependent on the carrier concentration of the ZnO material used [2.33]. For this work, Ti/Au ohmic contacts were fabricated on ZnO using electron-beam deposition, detailed in Section 3.4.3, and were not varied in recipe.

2.3.5 Oxidised Noble Metal Schottky Contacts

The Schottky contacts fabricated in this work consisted of oxidised noble metals, as well as pure noble metals, in order to systematically study the effects of oxygen incorporation in noble metal Schottky contacts. The details of the Schottky contact deposition process can be found in Section 3.4.2.3. The deliberate incorporation of oxygen into noble metal Schottky contacts on ZnO was found in previous studies to significantly improve the barrier heights and ideality factors of the contacts, as shown in Figure 2.16 [2.47]. The incorporated oxygen is believed to neutralise oxygen vacancies at the interface of the metal-oxide-semiconductor interface, producing a more highly rectifying contact [2.47]. Oxidising the metal contacts is also thought to increase the work function, increasing barrier height [2.47].

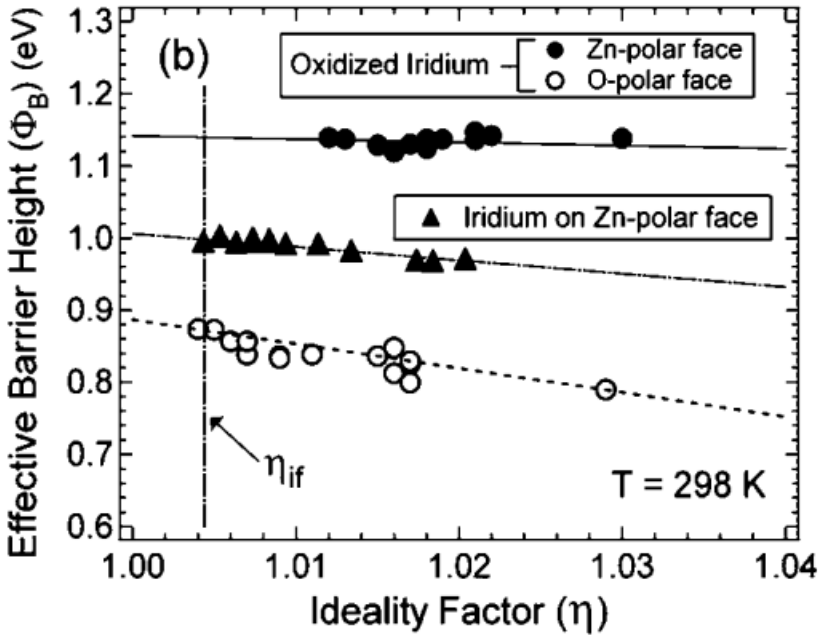

Figure 2.16: Effective Barrier Heights of Ir, IrO_x Schottky Contacts to Bulk ZnO [2.47]

2.3.6 Persistent Photoconductivity in Zinc Oxide Photodetectors

Illumination from a light source with greater photon energy than the band gap, such as UV radiation for ZnO, generates electron-hole pairs, and can cause diffusion of these photogenerated electrons and holes to the surface [2.33]. The decay time of the photoresponse of ZnO is longer than many semiconductors, with photoconductivity decaying over a period of seconds to days, as shown in Figure 2.17 [2.33, 2.48 – 2.56]. The decaying photoresponse following the removal of the illumination is known as persistent photoconductivity (PPC), and is a significant issue in the development of ZnO photodetectors [2.33, 2.48 – 2.56]. For UV dosimetry, PPC in the photodetectors would introduce a significant level of overestimation of the UV radiation absorbed, and produce unreliable measurements.

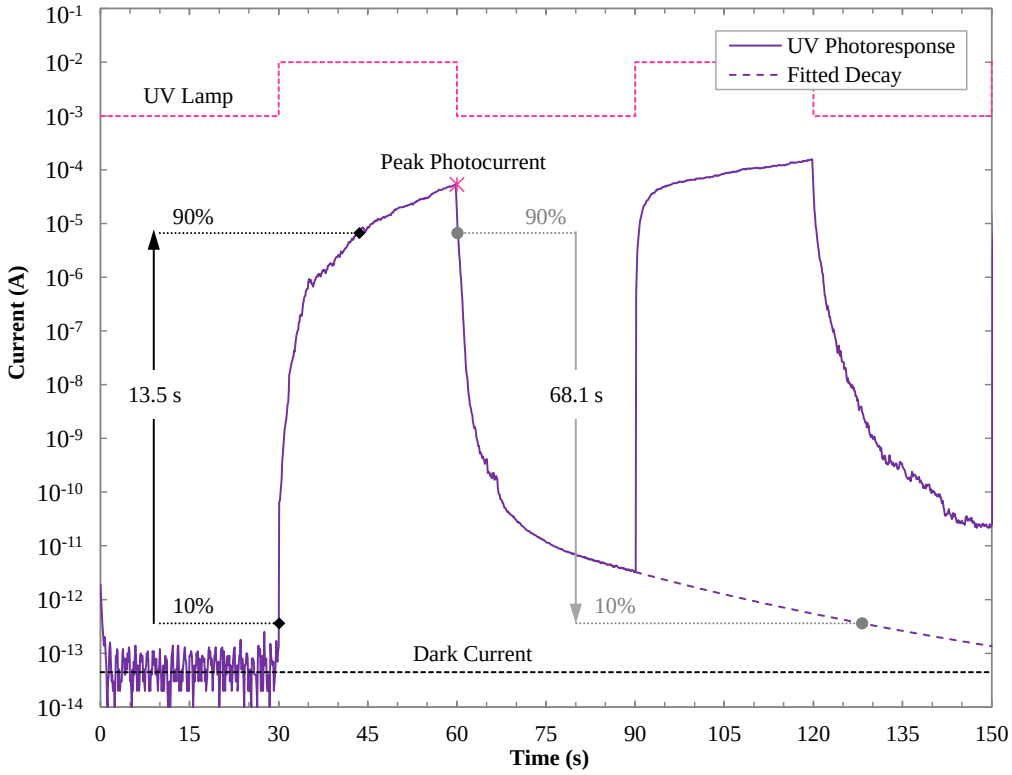

Figure 2.17: Calculation of Rise-Time and Fall-Time of Pulsed UV Response of AgO_x Contact

PPC is generally related to the ionisation of defects in semiconductor materials, and has been reported in bulk, polycrystalline, and nanowire ZnO [2.48]. The UV photoresponse of ZnO-based devices is understood to consist of two components; a fast-response, and a dominating slow-response. While the fast-response is widely accepted to be due the general photogeneration of electron-hole pairs, the cause of the slow-response has several proposed mechanisms, including

surface trap states, the ionisation of oxygen vacancies, and the desorption and re-adsorption of near-surface oxygen species [2.48 – 2.56].

A slow rise in UV photocurrent following the application of UV radiation has also been observed in ZnO photodetectors showing significant levels of PPC, as an equilibrium of photogenerated carriers is established between the conduction band and shallow trapping states, shown in Figure 2.17 for a noble metal-oxide Schottky contact to ZnO covered in this work [2.49 – 2.51]. The generated photocurrent of devices fabricated on ZnO has been observed in literature to be dependent on bias voltage, and applications of positive device bias have been shown to reduce PPC [2.52 – 2.53].

The PPC decay current has been modelled by a stretched exponential function, as shown in Equation 2.11, where β is the decay exponent ($\gamma < 1$), and τ is the decay time constant, as shown in Equation 2.12, where E_t is the potential barrier between stable and meta-stable defects [2.54 – 2.56]. This decay model has been experimentally fitted to PPC in ZnO and ZnO-based devices, and has been shown to accurately model PPC, however attempts to fit stretched exponentials to the PPC measured in this work were not successful [2.54 – 2.56]. However, long-term PPC decay in this work has been successfully fitted to a power curve, shown in Equation 2.13. The long-term PPC decay in Figure 2.17 was modelled using a power curve over the last 10 s of the decay, with a least-squares fit of $R^2 = 0.991$. In this work, power curves were used to extrapolate long-term PPC decay as opposed to the stretched-exponentials described in the literature, which were not observed to fit both the short-term and long-term PPC decay [2.54 – 2.56].

PPC Stretched Exponential Model	$I_{PPC}(t) = I_{PPC}\|_{t=0} \exp\left[-\left({}^{t}/_{\tau}\right)^{\gamma}\right]$	(2.11) [2.55 – 2.56]
PPC Decay Time Constant	$\tau \propto \exp\left({}^{E_t}/_{kT}\right)$	(2.12) [2.55]
PPC Decay Power Law	$I_{PPC}(t) = I_{PPC}\|_{t=0}(t^{-\tau})$	(2.13)

REFERENCES

[2.1] Markovic, S.N., Erickson, L.A., Rao, R.D., Weenig, R.H., Pockaj, B.A., Bardia, A., Vachon, C.M., Schild, S.E., McWilliams, R.R., Hand, J.L., Laman, S.D., Kottschade, L.A., Maples, W.J., Pittelkow, M.R., Pulido, J.S., Cameron, J.D., Creagan, E.T., (2007), Malignant melanoma in the 21st century, part 1: Epidemiology, risk factors, screening, prevention, and diagnosis, *Mayo Clinic Proceedings*, 82 (3), pp. 364-380.

[2.2] Godar, D.E., (2005), UV doses worldwide, *Photochemistry and Photobiology*, 81 (4), pp. 736-749.

[2.3] McKenzie, R.L., Liley, J.B., Björn, L.O., (2009), UV radiation: Balancing risks and benefits, *Photochemistry and Photobiology*, 85 (1), pp. 88-98.

[2.4] Holick, M.F., (2007), Medical progress: Vitamin D deficiency, *New England Journal of Medicine*, 357 (3), pp. 266-281.

[2.5] Køster, B., Søndergaard, J., Nielsen, J.B., Allen, M., Bjerregaard, M., Olsen, A., Bentzen, J., (2016), Effects of smartphone diaries and personal dosimeters on behavior in a randomized study of methods to document sunlight exposure, *Preventive Medicine Reports*, 3, pp. 367-372.

[2.6] Køster, B., Søndergaard, J., Nielsen, J.B., Allen, M., Bjerregaard, M., Olsen, A., Bentzen, J., (2015), Feasibility of smartphone diaries and personal dosimeters to quantitatively study exposure to ultraviolet radiation in a small national sample, *Photodermatology Photoimmunology and Photomedicine*, 31 (5), pp. 252-260.

[2.7] Allen, M., McKenzie, R., (2005), Enhanced UV exposure on a ski-field compared with exposures at sea level, *Photochemical and Photobiological Sciences*, 4 (5), pp. 429-437.

[2.8] McKenzie, R., Liley, B., Johnston, P., Scragg, R., Stewart, A., Reeder, A.I., Allen, M.W., (2013), Small doses from artificial UV sources elucidate the photo-production of vitamin D, *Photochemical and Photobiological Sciences*, 12 (9), pp. 1726-1737.

[2.9] Herman, J.R., (2010), Global increase in UV irradiance during the past 30 years (1979-2008) estimated from satellite data, *Journal of Geophysical Research Atmospheres*, 115 (4), art. no. D04203.

[2.10] Fioletov, V.E., McArthur, L.J.B., Mathews, T.W., Marrett, L., (2009), On the relationship between erythemal and vitamin D action spectrum weighted ultraviolet radiation, *Journal of Photochemistry and Photobiology B: Biology*, 95 (1), pp. 9-16.

[2.11] Diffey, B.L., (2002), Sources and measurement of ultraviolet radiation, *Methods*, 28 (1), pp. 4-13.

[2.12] WHO (World Health Organisation), (2002), *Global Solar UV Index: A Practical Guide*, Geneva, Switzerland: World Health Organisation.

[2.13] Webb, A.R., (2006), Who, what, where and when-influences on cutaneous vitamin D synthesis, *Progress in Biophysics and Molecular Biology*, 92 (1), pp. 17-25.

[2.14] McKenzie, R., Blumthaler, M., Diaz, S., Fioletov, V., Herman, J., Seckmeyer, G., Smedley, A., Webb, A., (2014), *Rationalizing nomenclature for UV doses and effects on humans*, (CIE 209:2014 and WMO-GAW Report No. 211), Vienna, Austria: Commission Internationale de l'Eclairage Central Bureau.

[2.15] Dowdy, J.C., Sayre, R.M., Holick, M.F., (2010), Holick's rule and vitamin D from sunlight, *Journal of Steroid Biochemistry and Molecular Biology*, 121 (1-2), pp. 328-330.

[2.16] Sneyd, M.J., Cameron, C., Cox, B., (2014), Individual risk of cutaneous melanoma in New Zealand: developing a clinical prediction aid, *BMC Cancer*, 14, 359.

[2.17] Young, A., (2006), *Scientific Committee on Consumer Products (SCCP) Opinion on Biological effects of ultraviolet radiation relevant to health with particular reference to sunbeds for cosmetic purposes*, European Commission.

[2.18] Cargill, J., Lucas, R.M., Gies, P., King, K., Swaminathan, A., Allen, M.W., Banks, E., (2013), Validation of brief questionnaire measures of sun exposure and skin pigmentation against detailed and objective measures including vitamin D status, *Photochemistry and Photobiology*, 89 (1), pp. 219-226.

[2.19] Gray, R, (2010), *Sun Exposure Survey 2010: Topline Time Series Report*, Wellington: HSC Research and Evaluation Unit.

[2.20] Berger, D.S., (1976), The sunburning ultraviolet meter: design and performance, *Photochemistry and Photobiology*, 24 (6), pp. 587-593.

[2.21] Davis, A., Deane, G.H.W., Diffey, B.L., (1976), Possible dosimeter for ultraviolet radiation, *Nature*, 261 (5556), pp. 169-170.

[2.22] Dobbinson, S., Niven, P., Buller, D., Allen, M., Gies, P., Warne, C., (2016), Comparing Handheld Meters and Electronic Dosimeters for Measuring Ultraviolet Levels under Shade and in the Sun, *Photochemistry and Photobiology*, 92 (1), pp. 208-214.

[2.23] Seckmeyer, G., Klingebiel, M., Riechelmann, S., Lohse, I., McKenzie, R.L., Ben Liley, J., Allen, M.W., Siani, A.-M., Casale, G.R., (2012), A critical assessment of two types of personal UV dosimeters, *Photochemistry and Photobiology*, 88 (1), pp. 215-222.

[2.24] Sherman, Z., (2014), Developments in electronic UV dosimeters, *NIWA UV Workshop 14-17 April 2014 Proceedings*, Auckland, New Zealand: Proceedings published on web only:

https://www.niwa.co.nz/our-services/online-services/uv-and-ozone/workshops

[2.25] Genicom, (2016), *UV-A Sensor GUVA-S12SD*, Retrieved from

http://www.geni-uv.com/download/eng/UV_Sensor/UV-A_Sensor/GUVA-S12SD.pdf

[2.26] Genicom, (2016), *UV-B Sensor GUVB-S11SD*, Retrieved from

http://www.geni-uv.com/download/eng/UV_Sensor/UV-B_Sensor/GUVB-S11SD.pdf

[2.27] Wright, C.Y., Reeder, A.I., Bodeker, G.E., Gray, A., Cox, B., (2007), Solar UVR exposure, concurrent activities and sun-protective practices among primary schoolchildren, *Photochemistry and Photobiology*, 83 (3), pp. 749-758.

[2.28] Khan, M.A., Shatalov, M., Maruska, H.P., Wang, H.M., Kuokstis, E., (2005), III-nitride UV devices, *Japanese Journal of Applied Physics, Part 1: Regular Papers and Short Notes and Review Papers*, 44 (10), pp. 7191-7206.

[2.29] Janotti, A., Van De Walle, C.G., (2009), Fundamentals of zinc oxide as a semiconductor, *Reports on Progress in Physics*, 72 (12), art. no. 126501, .

[2.30] Özgür, Ü., Alivov, Ya.I., Liu, C., Teke, A., Reshchikov, M.A., Doğan, S., Avrutin, V., Cho, S.-J., Morkọ, H., (2005), A comprehensive review of ZnO materials and devices, *Journal of Applied Physics*, 98 (4), art. no. 041301, pp. 1-103.

[2.31] Özgür, Ü., Hofstetter, D., Morkoç, H., (2010), ZnO devices and applications: A review of current status and future prospects, *Proceedings of the IEEE*, 98 (7), art. no. 5462913, pp. 1255-1268.

[2.32] Allen., M., (2008), *Schottky Contact Formation to Bulk Zinc Oxide*, PhD thesis, University of Canterbury, New Zealand.

[2.33] Jagadish, C., Pearton, S.J., (2006), *Zinc Oxide Bulk, Thin Films and Nanostructures – Processing, Properties and Applications*, Oxford, U.K: Elsevier Ltd.

[2.34] Maeda, K., Sato, M., Niikura, I., Fukuda, T., (2005), Growth of 2 inch ZnO bulk single crystal by the hydrothermal method, *Semiconductor Science and Technology*, 20 (4).

[2.35] Ohshima, E., Ogino, H., Niikura, I., Maeda, K., Sato, M., Ito, M., Fukuda, T., (2004), Growth of the 2-in-size bulk ZnO single crystals by the hydrothermal method, *Journal of Crystal Growth*, 260 (1-2), pp. 166-170.

[2.36] Heinhold, R., Kim, H.-S., Schmidt, F., Von Wenckstern, H., Grundmann, M., Mendelsberg, R.J., Reeves, R.J., Durbin, S.M., Allen, M.W., (2012), Optical and defect properties of hydrothermal ZnO with low lithium contamination, Applied Physics Letters, 101 (6), art. no. 062105.

[2.37] Brown, H.E., (1957), *Zinc Oxide Rediscovered*, New York, NY, U.S.A: New Jersey Zinc Company.

[2.38] Ellmer, K., Klein, A., Rech, B., *Transparent Conductive Zinc Oxide: Basics and Application in Thin Film Solar Cells, 2nd Edition*, (2008), Berlin, Germany: Springer-Verlag.

[2.39] Han, X.-G., He, H.-Z., Kuang, Q., Zhou, X., Zhang, X.-H., Xu, T., Xie, Z.-X., Zheng, L.-S., (2009), Controlling morphologies and tuning the related properties of nano/microstructured ZnO crystallites, *Journal of Physical Chemistry C*, 113 (2), pp. 584-589.

[2.40] Allen, M.W., Zemlyanov, D.Y., Waterhouse, G.I.N., Metson, J.B., Veal, T.D., McConville, C.F., Durbin, S.M., (2011), Polarity effects in the x-ray photoemission of ZnO and other wurtzite semiconductors, *Applied Physics Letters*, 98 (10), art. no. 101906.

[2.41] Ohtomo, A., Kawasaki, M., Koida, T., Masubuchi, K., Koinuma, H., Sakurai, Y., Yoshida, Y., Yasuda, T., Segawa, Y., (1998), $Mg_xZn_{1-x}O$ as a II-VI widegap semiconductor alloy, *Applied Physics Letters*, 72 (19), pp. 2466-2468.

[2.42] Sze, S. M., (2002), *Semiconductor Devices, Physics and Technology, 2nd Ed.*, Hoboken, N.J., U.S.A: John Wiley.

[2.43] Braun, F., (1875), Ueber die Stromleitung durch Schwefelmetalle, *Annalen der Physik*, 229 (12), pp. 556-563.

[2.44] Schottky, W., (1938), Semi-conductor theory in barrier layers, *Naturwissenschaften*, 26, 843.

[2.45] Mott, N.F., (1938), Note on the contact between a metal and an insulator or semi-conductor, *Proceedings of the Cambridge Philosophical Society*, 34 (4), pp. 568-572.

[2.46] Kim, H.-K., Han, S.-H., Seong, T.-Y., Choi, W.-K., (2000), Low-resistance Ti/Au ohmic contacts to Al-doped ZnO layers, *Applied Physics Letters*, 77 (11), pp. 1647-1649.

[2.47] Allen, M.W., Mendelsberg, R.J., Reeves, R.J., Durbin, S.M., (2009), Oxidized noble metal Schottky contacts to n -type ZnO, *Applied Physics Letters*, 94 (10), art. no. 103508.

[2.48] Litton, C.W., Reynolds, D.C., Collins, T.C., (2011), *Zinc Oxide Materials for Electronic and Optoelectronic Device Applications, 1st Edition*, West Sussex, United Kingdom: John Wiley & Sons, Ltd.

[2.49] Bayan, S., Mohanta, D., (2012), ZnO nanorod-based UV photodetection and the role of persistent photoconductivity, *Philosophical Magazine*, 92 (32), pp. 3909-3919.

[2.50] Sharma, P., Sreenivas, K., Rao, K.V., (2003), Analysis of ultraviolet photoconductivity in ZnO films prepared by unbalanced magnetron sputtering, *Journal of Applied Physics*, 93 (7), pp. 3963-3970.

[2.51] Kumar, S., Kim, G.-H., Sreenivas, K., Tandon, R.P., (2007), Mechanism of ultraviolet photoconductivity in zinc oxide nanoneedles, *Journal of Physics Condensed Matter*, 19 (47), art. no. 472202.

[2.52] Liao, Z.-M., Lu, Y., Xu, J., Zhang, J.-M., Yu, D.-P., (2009), Temperature dependence of photoconductivity and persistent photoconductivity of single ZnO nanowires, *Applied Physics A: Materials Science and Processing*, 95 (2), pp. 363-366.

[2.53] Nathan, A., Lee, S., Jeon, S., Song, I., Chung, U.-I., (2013), Transparent oxide semiconductors for advanced display applications, *Information Display*, 29 (1), pp. 6-11.

[2.54] Yu, K.M., Jeong, S.H., Bae, B.S., Yun, E.-J., (2012), The Effect of UV treatment on the recovery characteristics of a-IGZO-based thin film transistors, *Journal of the Korean Physical Society*, 61 (6), pp. 852-857.

[2.55] Kuriyama, K., Matsumoto, K., Suzuki, Y., Kushida, K., Xu, Q., (2009), Persistent photoconductivity and thermally stimulated current related to electron-irradiation induced defects in single crystal ZnO bulk, *Solid State Communications*, 149 (33-34), pp. 1347-1350.

[2.56] Li, Z., Guangsheng, F., Xiaoyun, T., Wei, Y., Heju, X., (2009), Persistent photoconductivity in undoped n-type ZnO thin films, *2009 Symposium on Photonics and Optoelectronics, SOPO 2009*, art. no. 5230089.

3 | Fabrication Methodologies

This chapter provides an overview of the equipment and methodologies used to fabricate the noble metal-oxide Schottky contacts used in this work. The methodologies include substrate preparation, photolithography, and thin film deposition. The deposition methods described include pulsed laser deposition (PLD), radio frequency magnetron sputtering (RF-sputtering), and electron-beam deposition (EBD).

3.1 Device Geometry

The Schottky devices fabricated for this work were of identical geometry, consisting of one circular Schottky and one L-shaped ohmic contact per device, shown in detail in Figure 3.1, using photolithography masks designed by David Kim [3.1]. The green area in Figure 3.1 is the Schottky contact area, and the purple area is the ohmic contact area. The photolithography masks used in fabricating these devices contained thirty-six diodes in a six-by-six array, with a separation of 60 µm between the ohmic contacts in the array, as shown in Figure A3.1 of Appendix A3.1 [3.1].

The ohmic contacts covered an active area of 66000 μm^2, and consisted of a layer of titanium 40 – 50 nm thick, covered by a layer of gold 40 – 50 nm thick. The L-shape ohmic contacts allowed for better tessellation of devices across a limited substrate area, with three enlarged square areas for probe contacts or wire bonding. The deposition techniques of both the Schottky and ohmic contacts fabricated in this work are covered in Sections 3.2 – 3.4.

In this work, an array of up to 36 Schottky diodes of identical geometry and an active area of 134000 μm^2 was fabricated simultaneously across the sample substrate in order to measure a statistical spread of device characteristics, which varied across the sample due to inhomogeneity of the Schottky contact (surface defects, stoichiometric variation in metal-oxide layer), errors in lithography (such as partial Schottky fabrication), and variation in the electrical contact between the gold capping layer and the probe during the electrical characterisation [3.2]. Early attempts were made to optimise the geometry of Schottky diodes and metal-semiconductor-metal (MSM) Schottky devices, using the interdigitated finger geometries detailed in Section 3.1.1. The variation in the electrical characteristics between identical geometries was found to be greater than the variations

due to different geometries as detailed in Section 3.1.1, and the initial investigation was discontinued. However, with the optimisation of metal-oxide Schottky material, renewed investigation into the impact of device geometry should be investigated, as the dimensions of interdigitated MSM devices have been found to significantly impact the frequency response, the transit time of photogenerated carriers, and the capacitance of the devices [3.3 – 3.5].

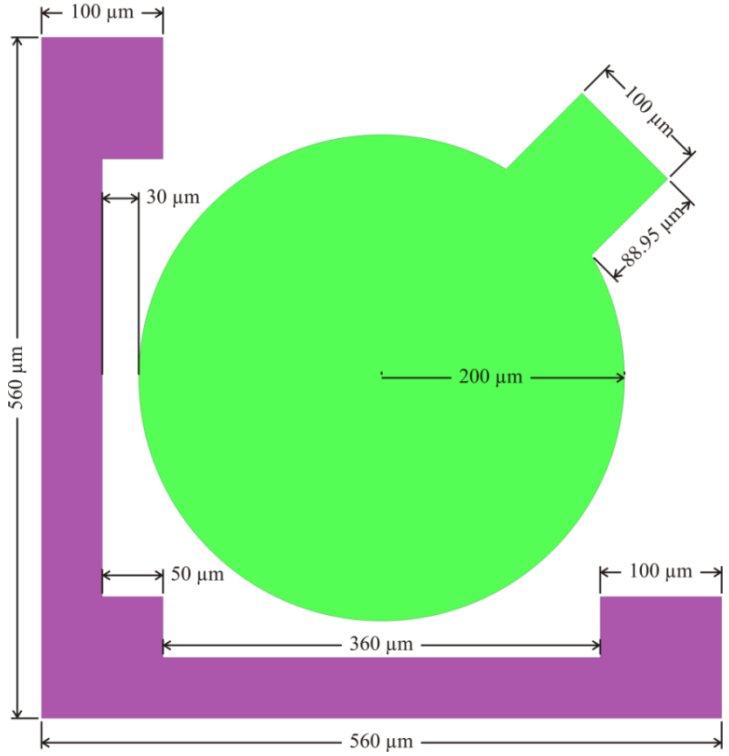

Figure 3.1: Dimensions of the Schottky Devices Fabricated

3.1.1 Interdigitated Device Geometry

Interdigitated electrode geometry has been used in a wide variety of electrical applications, including photodetectors, capacitors, and signal processing [3.6 – 3.8]. The interdigitated devices were designed to maximise the size of the Schottky contact interface by using two sets of interdigitated fingers. In order to optimise the geometry of the interdigitated devices, as well as to compare device performance with the circular diodes detailed in Section 3.1, a set of diodes was designed with identical active areas, 160000 µm^2, consisting of two combs of interdigitated fingers, each connected to a 48000 µm^2 square contact pad. The width, gap and therefore number of interdigitated fingers was varied, as detailed in Table 3.1 and shown in Figure 3.2. The limitation of the photolithography determined the smallest possible feature size of 5 µm. The mask used to fabricate these devices are included in Figure A3.2 of Appendix A3.1.

Table 3.1: Finger Gap, Width and Active Area of Interdigitated Devices

Device Name	Active Area Width (µm)	Active Area Length (µm)	Active Area (µm^2)	Contact Pad Area (µm^2)	Interdigitated Finger Width (µm)	Interdigitated Finger Gap (µm)
MS0505	400	400	160000	80000	5	5
MS1010	400	400	160000	80000	10	10
MS1020	400	400	160000	80000	10	20
MS1030	400	400	160000	80000	10	30
MS2010	400	400	160000	80000	20	10
MS2020	400	400	160000	80000	20	20
MS2030	400	400	160000	80000	20	30
MS3010	400	400	160000	80000	30	10
MS3020	400	400	160000	80000	30	20
MS3030	400	400	160000	80000	30	30
MSCI	400	400	160000	80000	10	10

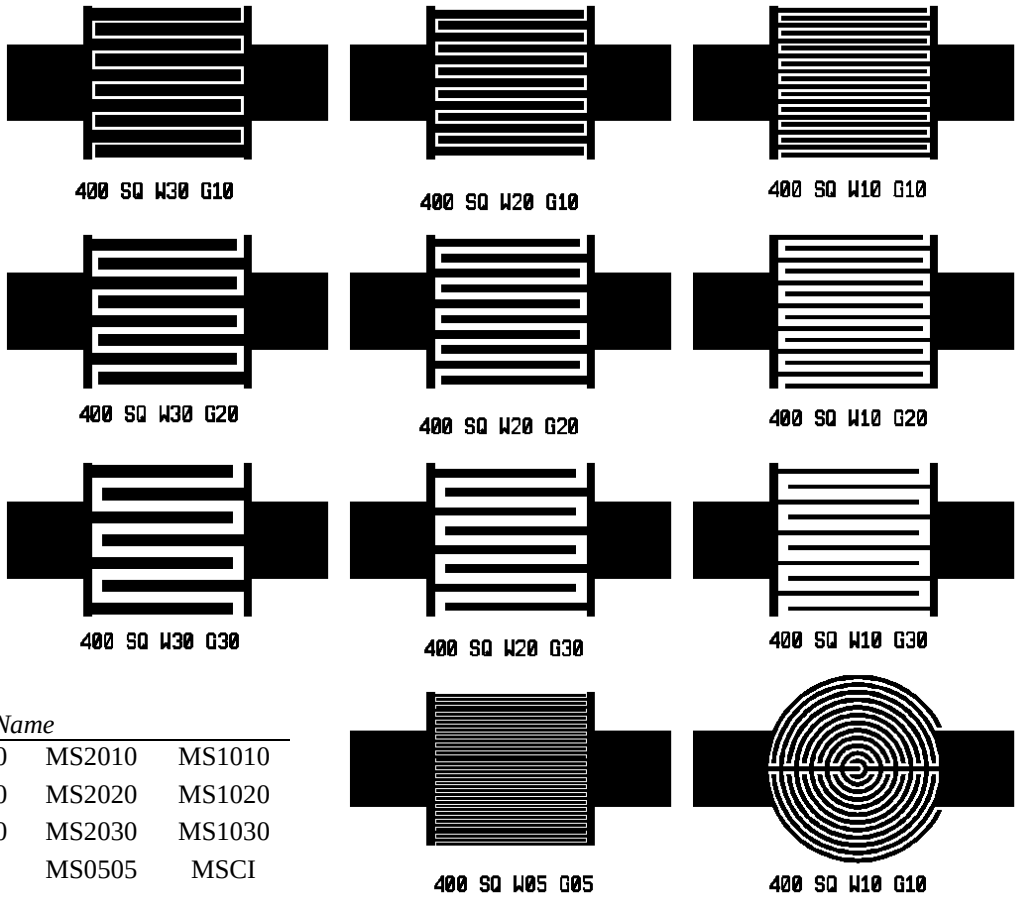

Device Name		
MS3010	MS2010	MS1010
MS3020	MS2020	MS1020
MS3030	MS2030	MS1030
	MS0505	MSCI

Figure 3.2: Interdigitated Devices with Varying Finger Gap and Width
Table Insert: Device Names as Positioned in Figure

During fabrication of the photolithography mask, device MS0505 (Figure 3.2) did not transfer completely, and produced an interdigitated device consisting of only two fingers of 5 µm width separated by 400 µm, as shown in the bottom left of Figure 3.3. The electrical characteristics on the two-fingered interdigitated device were measured and found to be within the range of the remaining interdigitated devices on the same sample. This result occurred across six different samples fabricated using the same photolithography mask. This proved that the impact of the variation in geometries explored in this study has less impact on device performance than the variation between devices due to inhomogeneity of the Schottky material, and the impact of the large contact pads used in the design. Therefore, investigations into optimising the geometry of the interdigitated devices were discontinued in favour of investigating the effect of composition on the performance of metal-oxide Schottky contacts. However, the interdigitated diodes that were fabricated showed consistently lower leakage current than most of the circular and L-shaped contact diodes fabricated using the same mask, suggesting the potential for further investigation.

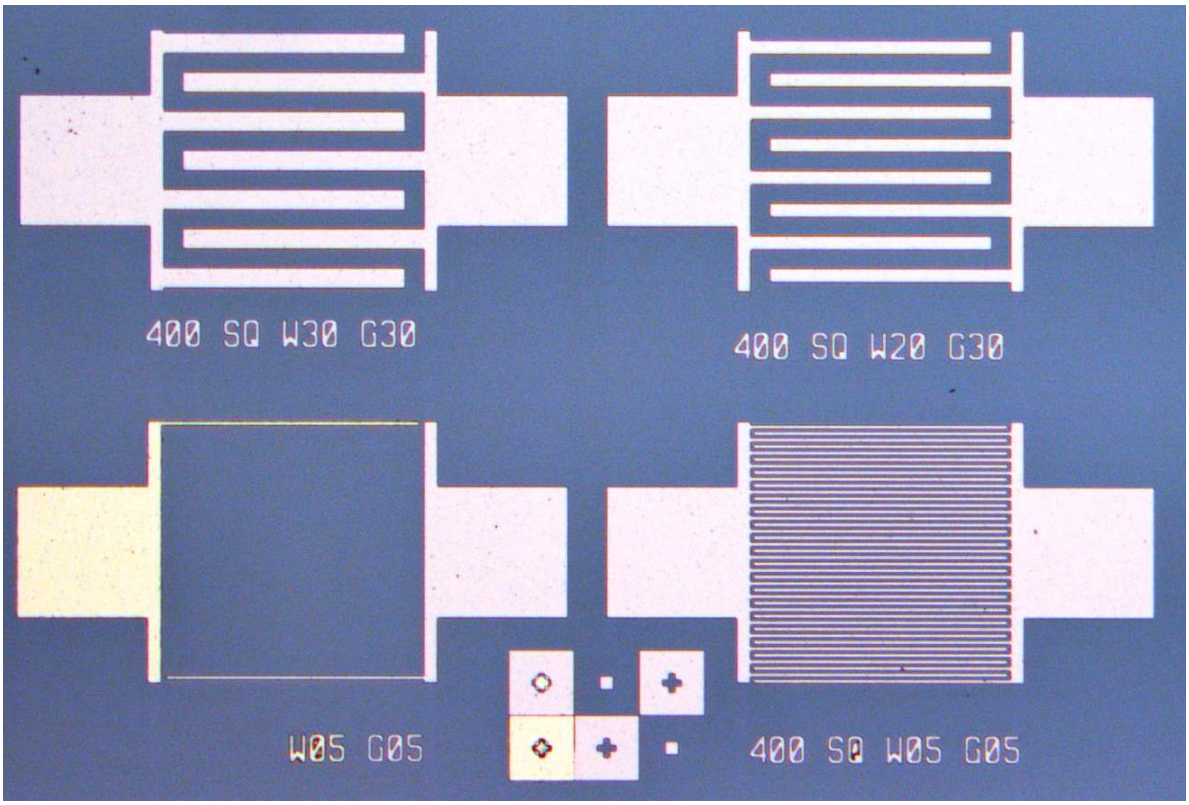

Figure 3.3: RF Sputtered AgO_x Interdigitated Devices on Bulk ZnO (0001)
(Bottom Left: Mask Write Error Producing Two-Fingered Interdigitated Device)

3.2 Substrate Preparation

In this thesis, metal-oxide Schottky contacts were fabricated on wafers of hydrothermally-grown bulk ZnO, with metal-oxide films simultaneously deposited on transparent amorphous quartz wafers for optical and electrical characterisation. The sizes and usage of each substrate are listed in Table 3.2. A complete list of the bulk ZnO substrates used can be found in Appendix A3.2, with a list of the equipment and chemicals used in the preparation and fabrication of the samples used in this work listed in Appendix A3.3.

In order to compare different metal-oxide Schottky contacts on identical ZnO substrates (10 mm x 10 mm x 0.5 mm) bulk ZnO wafers were diced into a set of identical substrates using a J.M. Industries TEMPRESS 602 Dicing Saw, pictured in Figure 3.4. The quartz substrates used for metal-oxide thin film characterisation were diced using a diamond scriber tool.

Table 3.2: Substrate Sizes and Use

Substrate	Wafer Dimensions	Substrates in Set	Substrate Size	Substrate Use
ZnO	10 x 10 x 0.5 mm	4	5 x 5 mm	Schottky devices, comparing polarity of ZnO substrate
ZnO	10 x 10 x 0.5 mm	9	3 x 3 mm	Schottky devices, comparing metal-oxide oxygen content
Glassy Quartz	10 x 10 x 0.5 mm	4	10 x 10 mm	Metal-oxide optical film analysis (transmission spectra)
Glassy Quartz	10 x 10 x 0.5 mm	16	5 x 5 mm	Metal-oxide electrical film analysis (Hall Effect)
Silicon	3 inches	-	-	Carrier wafer for dicing samples
Silicon	-	-	10 x 10 mm	Carrier wafer for photolithography

To protect the surfaces of the ZnO wafer from contamination and scratching during dicing, a layer of MicroChemicals GmbH AZ® 1518 photoresist was spin-coated (3000 – 4000 RPM) on both sides of the ZnO wafer using a Headway Research, Inc. PWM32-PS-R790 spinner, and soft-baked in a Contherm Model 2150 drying oven at 96°C for 20 minutes. The photoresist-coated wafer was then mounted on a 3 inch silicon wafer using melted wax. The silicon wafer was used as a carrier for the ZnO substrate during dicing, as the wafer saw chuck was designed for 2 – 4 inch wafers. Parfum wax was used to fix the ZnO wafer to the silicon wafer, as the wax could be later removed using xylene without dissolving the photoresist layer protecting the ZnO wafer surface. The ZnO wafers were then diced with two cut-depths using a Dicing Blade Technology resin bond

diamond dicing blade. The first cut was at a depth of one-third of the wafer thickness (0.17 mm), the second at two-thirds of the wafer thickness (0.33 mm). The two-cut process minimised stress on the saw blade, while cutting deep enough into the ZnO wafer such that the wafer could be manually broken into the 3 mm x 3 mm x 0.5 mm pieces with minimal force.

Figure 3.4: J.M. Industries TEMPRESS 602 Wafer Saw

The diced ZnO substrates were then individually cleaned in a standard sequence of solvents using an Elma Elmasonic ultrasonic cleaning unit for a duration of 2 minutes for each of the following solvents; first xylene, then acetone, then methanol, and then isopropyl alcohol (IPA). The substrates were then rinsed with IPA and dried using compressed nitrogen gas. The solvents were used in the standard order of decreasing volatility, to dissolve any residue from the evaporation of the previous solvent, with IPA being of such low volatility that drying in compressed nitrogen gas did not leave a residue. The quartz substrates were cleaned using the same sequence of solvents in the ultrasonic cleaning unit, with the exception of xylene, as the quartz was diced without wax.

Throughout all preparation steps and processing steps, every effort was taken to ensure the cleanliness of the substrates, as well as the cleanliness of tools and equipment that came into contact with the substrates to avoid contamination. Glass and metal surfaces were cleaned with acetone and rinsed with acetone, then methanol, then IPA, and dried with compressed nitrogen gas. Plastic sample holders were cleaned and rinsed with IPA and dried with compressed nitrogen gas. Photolithography was performed on substrates immediately after dicing and cleaning to prevent environmental contamination of the substrate surface.

3.3 Photolithography Process

The word ‘photolithography’ can be broken down into three components: photo, litho, and graphy; their Greek origins respectively meaning: ‘light’ (φωτός, *phōtos*), ‘stone’ (λίθος, *lithos*), and ‘writing’ (γράφειν, *graphein*) [3.9]. Photolithography can therefore be understood as the process of using light to write in stone. In the semiconductor industry, the stones are the conductors, semiconductors and insulators that are used to make devices. The writing is performed by etching the material or depositing additional material through a patterned masking layer. The mask layer is typically a thin film of light-sensitive polymer that can be patterned by exposing the polymer to a UV light source, which changes the solubility of the polymer and allows the polymer layer to be developed in a solvent that selectively dissolves the polymer that was exposed to the UV light, resulting in a patterned photoresist mask. Thus light is used to write into, or onto, stone.

Lithography can be traced back to its use in 1798 by German author Aloys Senefelder, who in order to more efficiently publish his plays, rolled sheets of paper across glass patterned with grease and water-based ink. In July of 1822, Nicéphore Niépce made his first successful photolithographic copy of an engraving of Pope Pius VII using a thin layer of bitumen of Judea (a naturally occurring asphalt) spread on a glass plate [3.10]. Where the sunlight shone through the engraving, the asphalt hardened and became insoluble to a solution of oil of lavender and turpentine, which could be used to dissolve the unexposed asphalt, thus producing a monotone photolithographic copy of the original engraving [3.11]. Further photosensitive materials used for photolithography were developed in 1839 by Mungo Ponton using a bichromate of potash on paper as the photosensitive material, and using water to dissolve the unexposed material [3.11].

Modern photoresists contain photoactive compounds that change solubility to a developer when exposed to light, divided into the categories of positive and negative photoresists, which increase and decrease the solubility of the exposed areas respectively. A common positive photoresist is a mixture of diazonaphthoquinone (DNQ) and a phenol formaldehyde resin (novolac), which is sensitive to the UV spectrum of a mercury-vapour lamp (310 – 440 nm) [3.9 – 3.12]. The unexposed DNQ-novolac photoresist is insoluble in the basic aqueous developer solvent. Exposure to UV light causes the DNQ to become a carboxylic acid, which is soluble in the developer. Exposing the photoresist to a shadow-masked UV light produces an image of soluble and insoluble regions in the photoresist. Submerging the exposed photoresist in the developer dissolves the exposed regions of photoresist, leaving behind the unexposed photoresist in the pattern of the shadow-mask.

3.3.1 Photolithography Process Steps Used in This Work

In the fabrication of Schottky devices on ZnO for this work, photolithography was used to create a patterned photoresist mask on the ZnO surface to expose selected areas of defined geometry during the deposition of a thin metal film over the masked sample. The AZ® 1518 photoresist used was a positive photoresist that, when exposed to UV light, became soluble in the MicroChemicals GmbH AZ® 326 MIF tetramethyl ammonium hydroxide developer in a process similar to analogue photography.

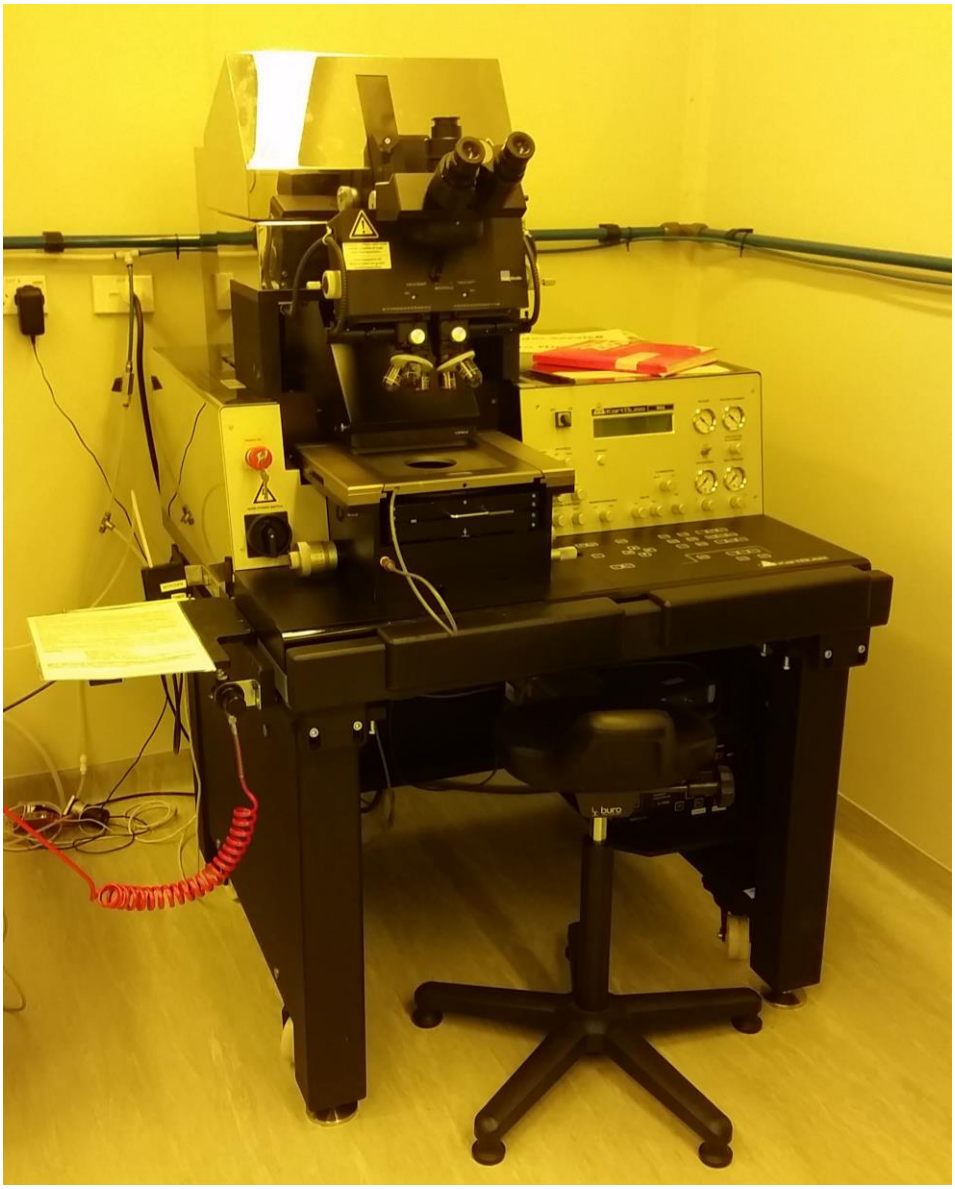

Figure 3.5: Karl Süss MA6 Mask Aligner

The ZnO substrates were first fixed to 10 x 10 x 5 mm silicon wafer chips using photoresist and soft-baked in a drying oven at 96°C for 20 minutes. This step was done to protect both the back face of the ZnO substrate, as well as for ease of handling during the photolithography process. Photoresist was then spin-coated onto the top face of the ZnO substrates, using an acceleration of 3000 RPM/s to a spin speed of 4000 RPM for 60 seconds, producing a photoresist film of 1 µm thickness, which was soft-baked in the drying oven at 96°C for 20 minutes. Photoresist-covered substrates were kept in the dark between soft-baking, mask alignment, and development to prevent photoresist deterioration.

The photoresist-covered substrates were exposed to a masked UV source using a Karl Süss MA6 Mask Aligner, and Nanofilm AZ 1518 Soda Lime Low Reflective Chrome photolithography masks. Soft vacuum contact alignment was used with an alignment gap between the mask and the substrate of 70 µm, and an exposure time of 12 seconds. The chrome masks were patterned using a Heidelberg Instruments µPG 101 mask writer. Full details of the masks used in this work can be found in Appendix A3.1. For multi-stage photolithography, where additional thin films were deposited on a substrate with existing thin film patterns, the substrate and mask were manually aligned to patterned alignment markers using the micromanipulators controlling the stage.

The substrates were then developed in AZ® 326 MIF Developer for 30 seconds with gentle agitation, rinsed in deionized water for 30 seconds, and dried with compressed nitrogen gas. The development of the photoresist was performed immediately prior to thin film deposition in order to reduce the exposure of the exposed ZnO surface to the atmosphere, as the quality of the metal-semiconductor interface was critical to the quality of the overall Schottky device. Details of the thin film deposition techniques used in this work are provided in Section 3.3.

Following thin film deposition onto the masked substrates, the photoresist mask and unwanted material was removed via a process known as ‘lift-off’, where the photoresist mask was dissolved in acetone, and the masked areas of photoresist covered in thin film material were removed by ultrasonic cleaning. The samples were submerged in a glass beaker of acetone and left to sit for approximately 5 minutes, or until the masked areas of the substrate appeared to detach slightly from the surface. The samples, still submerged in acetone, were placed in the ultrasonic unit for 10 seconds of ultrasonic cleaning. During this process, the substrates also usually detached from the silicon wafer carrier chip, otherwise the substrates were gently pushed off of the silicon wafer chip after ultrasonic cleaning. Substrates were then submerged in a glass petri dish of clean acetone and checked under a microscope to determine whether all unwanted material had been removed from the substrate surface. If unwanted material remained, further ultrasonic cleaning was required until lift-off was complete. Once all of the unwanted material was removed from the substrate and only

the patterned thin film contacts remained, the substrates were rinsed in acetone, then methanol, then IPA, and then dried with compressed nitrogen gas.

In the fabrication of Schottky diodes, two photolithographic operations were used; the first to deposit the ohmic contacts, the second to deposit the Schottky contacts. Following the lift-off and organic solvent cleaning of the ohmic contacts, the substrates were immediately fixed to clean silicon wafer chips using photoresist, soft-baked, spin-coated with photoresist, and soft baked again as described above to minimise exposure of the ZnO surface to the environment.

The UV masks for the ohmic and Schottky contact photolithography were two separate masks that were overlaid to create the complete Schottky diode geometry as shown in Figure A3.1 of Appendix A3.1. The masks used for the ohmic and Schottky contacts contained alignment markers, which were used in the optical, manual alignment of the existing ohmic contacts with the Schottky mask during the mask alignment of the second stage of photolithography.

3.4 Thin Film Deposition

For this work, three methods of thin film physical vapour deposition (PVD) were used in the fabrication of Schottky and ohmic contacts on bulk ZnO; PLD, RF-sputtering, and EBD. PLD and RF-sputtering were used to fabricate Schottky contacts, while EBD was used to fabricate standard titanium-gold ohmic contacts, and to deposit a gold capping layer on top of the fabricated Schottky contacts as an electrical contact and to prevent further oxidation.

3.4.1 Pulsed Laser Deposition

PLD is a PVD method first used in 1965 by H. M. Smith and A. F. Turner following the introduction of the first ruby laser by T. H. Maiman, and remains a robust method for growing thin films of metals, semiconductors, alloys, and compounds at room temperature [3.13 – 3.15]. PLD uses a high-powered pulsed laser to ablate a rotating target inside a high vacuum (HV) chamber.

The energy of the UV laser at the target surface, ~1 $GWcm^{-2}$, can produce an electric field within the absorption depth of the target (~10 nm depending on target material) capable of overcoming the interatomic forces in the target material [3.16]. With sufficient laser energy, depending on the target material, the absorbed radiation can induce an electric field capable of removing electrons from the atoms in the target via a non-linear process within the absorption depth and also directly vibrate the electrons to melt and vaporise atoms within the absorption depth [3.16]. The vaporised material can include ions, atoms, and macro-particles of melted material.

Inside the HV chamber, the plume of ablated material from the target condenses on a sample substrate positioned directly in front of the target. Gases such as oxygen can be added to the HV chamber to produce metal-oxides during the ablation of metal targets. Eclipse plate PLD is a variant of PLD growth where an eclipse plate is placed between the target and sample substrate to shield the sample from macro-particles ejected during ablation, but allowing the lighter particles of ablated material to diffuse around the plate and condense on the sample. A long-exposure photograph of a PLD growth with eclipse plate in Figure 3.7 shows glowing macro-particles deflecting off of the eclipse plate.

Thin films and Schottky contacts fabricated in this work using PLD were performed in the Department of Physics and Astronomy, University of Canterbury using the Lambda Physik Compex 205 248nm KrF excimer laser, and a custom-built Thermionics High Vacuum Chamber which is illustrated in Figure 3.6 below.

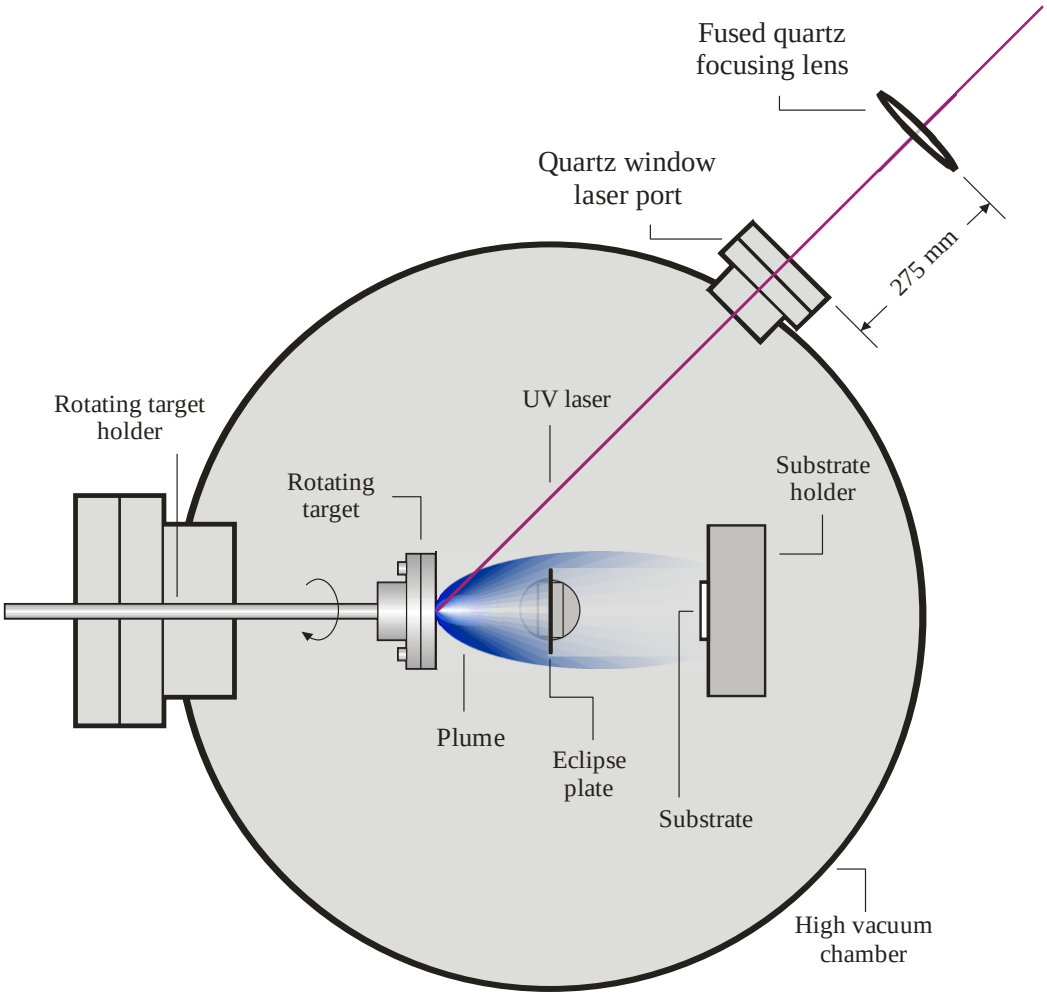

Figure 3.6: Pulsed Laser Deposition High Vacuum Chamber Diagram

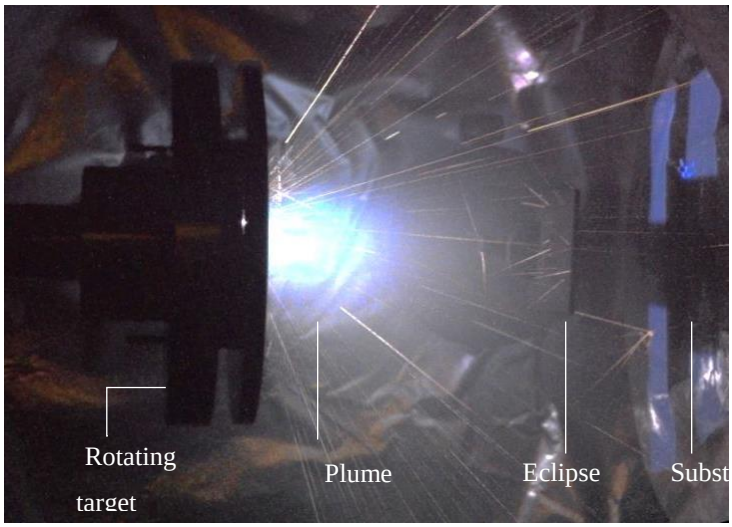

Figure 3.7: Pulsed Laser Deposition of an Iridium Target with Eclipse Plate

For the growth of PLD iridium oxide Schottky contacts on bulk ZnO, a Kurt J. Lesker Company iridium target was used in an oxygen environment to produce iridium oxide. The growth parameters for the iridium oxide Schottky contacts used in this work are listed below in Table 3.3.

Table 3.3: PLD IrO_x Schottky Contacts on ZnO Growth Conditions

Thin Film	PLD IrO_x Schottky contacts on ZnO
Growth Method	PLD
Target	Kurt J. Lesker Company Iridium Target
Target Rotation	1.08 rev/s
Focusing Lens	750 mm focal length fused-quartz lens
Lens Distance from Chamber	275 mm
Chamber Pressure (base)	1.75×10^{-5} Torr
Chamber Pressure (throttled)	1.12×10^{-4} Torr
Chamber Pressure (with O_2)	1.05×10^{-1} Torr
Laser Energy	300 mJ
Laser Discharge Voltage	26 kV
Laser Pulse Duration	10 ns
Laser Pulse Frequency	10 Hz
Growth Time	1 hour

3.4.2 Radio Frequency Magnetron Sputtering Deposition

Sir J. J. Thompson first wrote of the 'spluttering' of cathodes in vacuum tubes in 1913 as;

> "When positive rays strike against a metallic surface, the metal disintegrates and forms a deposit on the walls of the tube surrounding the metal. A well-known instance of this is the "spluttering" of the cathode in a vacuum tube…"
>
> - Sir J. J. Thompson [3.17]

Subsequent publications on the subject during 1920 – 1923 by I. Langmuir and K. H. Kingdon referred to the phenomenon as 'sputtering', omitting the 'l'. Despite General Electric Co. continuing to refer to the process as 'cathode disintegration' and efforts made by A. Guentherschulze and E. Kay to introduce the term 'impact evapouration' in 1923, the scientific community has been unable to escape the word 'sputtering' [3.18 – 3.19].

3.4.2.1 The Sputtering Process

Sputtering is a variety of vacuum deposition that uses a plasma to bombard a target with ionised gas particles, causing atomised material to be ejected from the target and deposited onto a substrate. At sufficiently low pressure, and with the addition of a partial pressure of inert gas, a power source is used to strike and maintain a plasma between the negatively charged cathode, the target, and a positively charged anode, the substrate. Noble gas ions, such as positively charged argon ions, are drawn from the plasma and accelerated across the dark space between the plasma and the target, known as the Crooke's zone, bombarding the target and causing sputtering. The bombardment is a ballistic process in which an individual ionised particle causes a cascade of binary collisions within the target, resulting in atomised material being ejected from the target, analogous to the break shot in a game of billiards [3.18 – 3.20]. The ejected material contains neutral atoms, ionised atoms, and excited atoms of the target material, which condenses on a substrate positioned within the mean free path of the ejected material, building up a layer of material on top of the substrate, atom-by-atom, as illustrated in Figure 3.8 [3.19]. Since this process predominately involves the deposition of atomised material, a smooth film is created on a smooth substrate, and there is less likelihood of 'spitting' of larger agglomerates from the target, such as in the case of PLD [3.20].

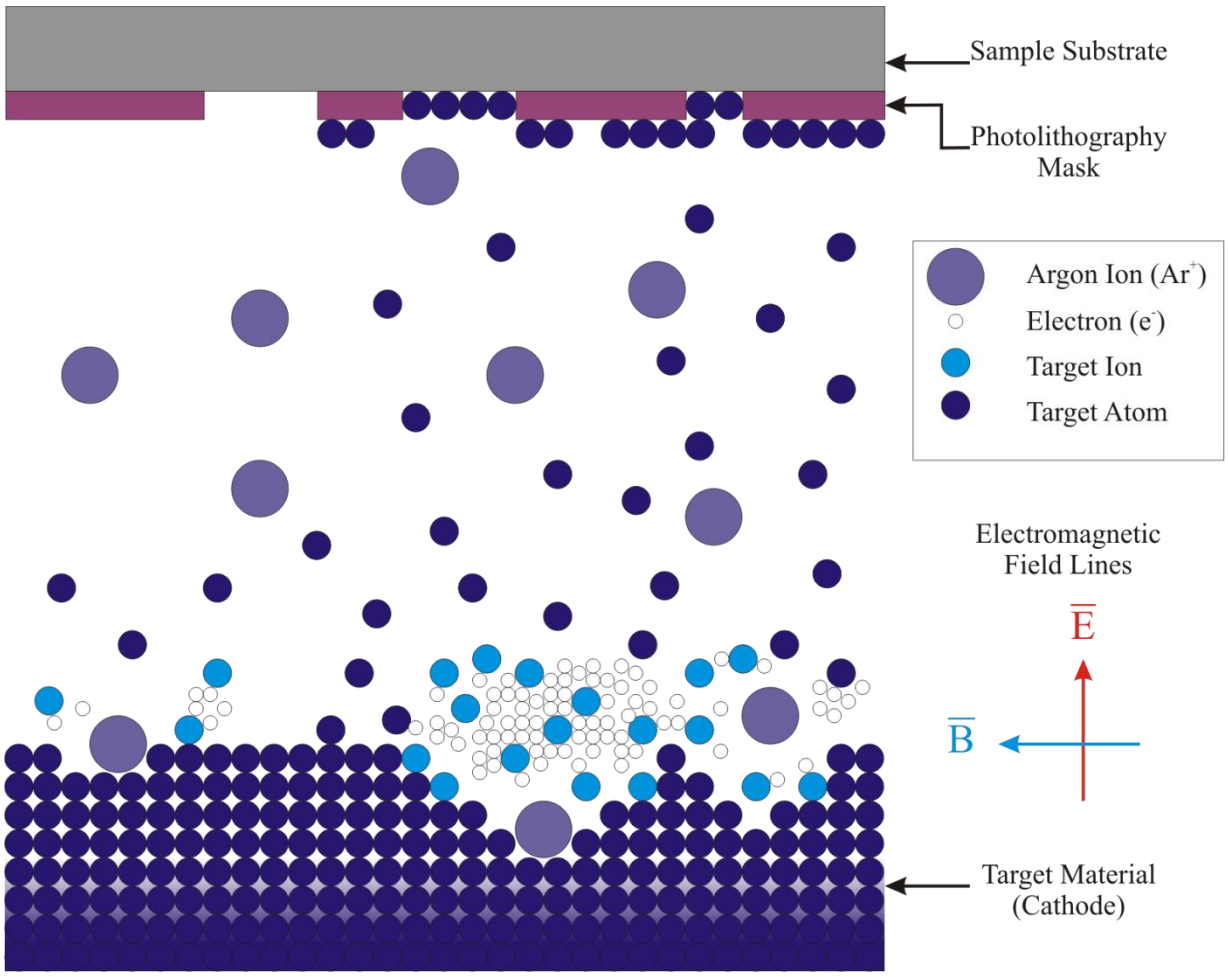

Figure 3.8: The Ballistic Process of Sputtering

Sputtering is a physical process that does not depend on the thermal conductivity or the temperature of the target material, making it a more suitable deposition process for materials with high melting points such as the noble metals palladium (1555°C), platinum (1768°C), and iridium (2447°C), and is a more commonly used deposition technique than evaporation [3.19 – 3.20]. Sputtering yield varies within only two orders of magnitude between different materials, as shown in Figure 3.9 [3.21]. Typical yield rates are 5 – 3000 nm/min, depending on the target material as well as the energy and the species of ion used in bombardment [3.19]. The variation in sputtering yields between atomic species with the sputtering gas ions (Ar^+) and power (400 eV) held constant shown in Figure 3.9 is due to the variation in interatomic bonding and variation in size ratio of the sputtering gas ions and the size of the atoms within the target material [3.21]. Using the billiards analogy; different scattering occurs when the same break-shot is used with the same cue ball and different sizes of billiards with different inter-billiard attraction.

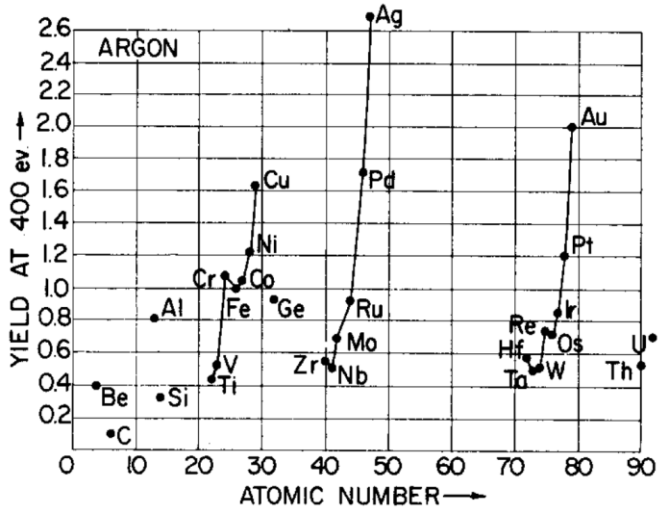

FIG. 2. Sputtering yields at 400-ev argon ion energy for 28 elements vs the element's atomic number.

Figure 3.9: Sputtering Yield in Atoms per Argon Ion at 400 eV [3.21]

Sputtering gas ions can become trapped in the target material during collisions, but are sputtered out of the material at an equilibrium determined by the sputtering energy, the target material, and the size of the sputtering gas ions relative to the structure of the target material [3.19]. Argon and krypton ions are commonly used in sputtering, as the size of the larger inert gas ions is generally much larger than the interatomic distances of both the target and growing film material, reducing the probability of interstitial gas ion entrapment [3.19 – 3.20]. Sputtering at lower energies, lower gas pressures, and increasing substrate temperature can reduce the amount of trapped gas ions [3.20].

To ensure reasonable film quality, the sputtering vacuum chamber pressure should to be less than 5 mTorr (6.67×10^{-3} mbar) without the addition of sputtering gases, to reduce contamination from atmospheric gases [3.19]. A lower chamber pressure reduces the probability of collisions between ejected atoms and neutral gas atoms, resulting in the sputtered atoms arriving at the substrate with higher kinetic energy, thus improving film quality and adhesion to the substrate. For this work, vacuum pressures less than 1.0×10^{-5} mbar were used, prior to the addition of argon and oxygen plasma processing gases.

Control of the partial pressure, or flow rates, of reactive sputtering gases through mass spectrometer feedback was patented in 1984, opening the doorway to sputtering metal-oxides with controlled stoichiometry [3.20, 3.22]. Oxygen is commonly used in reactive sputtering, chemically reacting with the sputtered target material, as well as the target itself, resulting in a deposition of metal-oxide on the substrate when sputtering from a pure metal target. The level of incorporation of

oxygen into the resulting film can be controlled by the partial pressure of the oxygen within the gas mixture flowing through the sputterer during deposition, and is related to the sticking coefficients of the oxygen and target atoms [3.20]. The level of oxygen incorporation occurring during sputtering affects both the growth rate of the film, and the parameters used to measure film thickness during growth, requiring experimental determination of film thickness [3.20].

During reactive gas sputtering, reactive gases such as oxygen can become embedded in the target and react to form oxides within the target material, such as iridium oxide forming within a solid iridium target [3.20, 3.23]. This is known as target poisoning, and can affect subsequent depositions from the same sputtering target. Trapped oxygen can also form negative ions (O^-) at the target surface when re-sputtered, and are accelerated from the target onto the substrate [3.24]. These negative ions formed at the target surface have a much higher energy than the ions formed and confined within the plasma itself, and have been observed to negatively influence the structural and electrical properties of the sputtered film, including the subplantation of O^- below the film surface [3.24]. As this work focuses on oxygen content in sputtered films; reducing the impact of negative ion bombardment was important in sputtering films with a controlled level of oxygen incorporation.

The ballistic sputtering process damages the target material with each impact, causing lattice damage and surface migration of atoms as well as removing target material for sputtering. Over time, a 'racetrack' ring-shaped etching pit will occur across the target, due to the distribution of ion current density, until it is no longer useable. The remaining target material can then be recycled [3.19 – 3.20].

3.4.2.2 The Development of RF Magnetron Sputtering

The development of sputtering as an area of research, as well as a manufacturing technique for thin film deposition, followed the advancement of other technologies integrated in the sputtering process, such as the development of vacuum systems, plasma generation, high voltage direct current (DC) power supplies, and radio frequency (RF) power supplies [3.22]. The first studied deposition of material from a glowing cathode was published by W. R. Grove in 1852, where several depositions were observed using a platinum wire and a polished silver plate in a vacuum chamber at 0.5 Torr (6.67×10^{-1} mbar) with a mixture of atmospheric and hydrogen gases [3.22, 3.25]. A dark deposit was observed around the glass tubing holding the platinum wire following a discharge in which the platinum wire was negatively charged with respect to the polished silver plate [3.19, 3.22, 3.25]. The setup used by Grove is shown in Figure 3.10 [3.25].

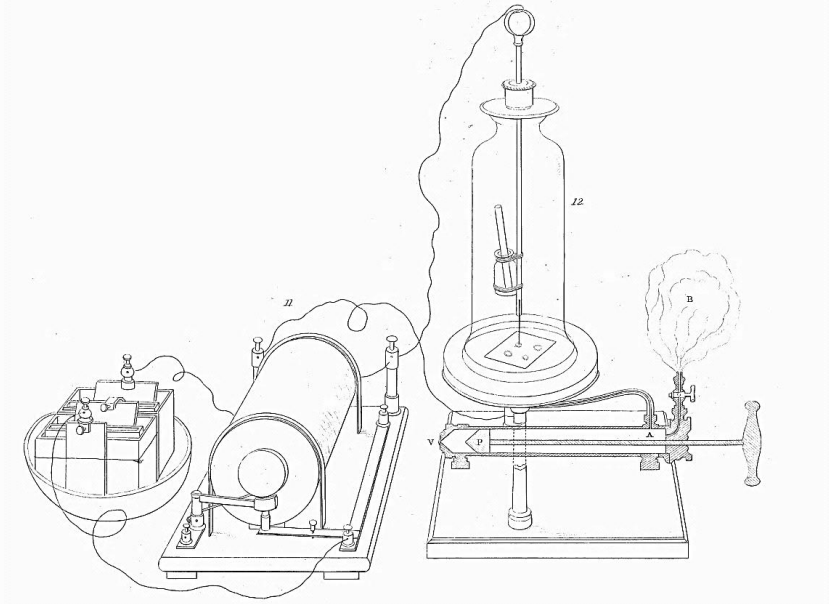

Figure 3.10: W. R. Grove's Glowing Cathode Discharge [3.25]

Important steps in the advancement of sputtering began with F. M. Penning and J. H. A. Moubis in 1940, where, using data collected by A. Güntherschulze and K. Meyer, they showed that placing a magnetic field around the cathode of the sputtering system significantly increased the rate of deposition [3.26 – 3.27].

J. D. Gow and L. Ruby demonstrated the use of electric and magnetic fields to confine and focus the sputtering plasma in 1959 [3.28]. The use of magnetic fields developed throughout the 1970s, with sputtering systems incorporating magnetic fields between 5 x 10^{-3} to 10^{-2} T parallel to the target surface [3.20, 3.22]. Secondary electrons generated by the ion collisions at the target surface were trapped within the lines of a magnetic field introduced into the plasma [3.19]. These secondary electrons posed a potential x-ray risk without containment, and also contributed to the unwanted re-sputtering of deposited films [3.19]. With the addition of the magnetic field, the confined electrons were able to ionise neutral particles during collisions, replenishing and sustaining the plasma [3.20]. The formation of cylindrical magnetrons increased plasma density, and isolated the plasma from contact with the chamber walls, where neutralisation of the ions would lower the lifetime of the plasma [3.19]. The magnetic field also increased sputtering rates with lower gas pressures, improving sputtering purity [3.20]. For planar magnetrons, such as the magnetron sputtering system used in this work, electromagnetic or permanent magnets are incorporated behind the target cathode to produce the cylindrical magnetron [3.20].

Developments in RF power supplies began in the mid-1970s, providing for an alternate means of powering the plasma source to DC systems. DC sputtering uses two oppositely charged parallel

plates, the target and the substrate, to generate the plasma. Targets used in DC sputtering must be conductive in order to dissipate the charge of the positive argon ions striking the target [3.20, 3.22]. In this work, RF magnetron sputtering has been exclusively used, despite using conducting noble metal targets, as DC sputtering requires a higher gas pressure to maintain the plasma, between 1×10^{-1} and 1×10^{-3} mbar, when lower pressures are desirable for depositions with lower contamination [3.19 – 3.20]. The lower target voltages used in the RF excitation of the plasma source have also been shown to produce films of higher uniformity compared to DC sputtering [3.24]. RF-sputtering also produces target material ions with lower maximum energy than DC sputtering, reducing the impact of negative oxygen ions bombarding the deposited film and sample substrate [3.24].

RF-sputtering uses high-frequency (1 – 30 MHz) arc discharges to strike a plasma between two electrodes by capacitively coupling an RF generator to the cathode [3.20]. The cathode, which is also the sputtering target, becomes negatively charged during the initial RF discharge and is only partially neutralised by the bombardment of positively charged argon ions during sputtering. The capacitive coupling of the RF generator prevents the conduction of negative charge on the cathode during the positive half of the RF cycle, maintaining a negative bias with respect to the plasma and thereby accelerating the sputtering argon ions across the full RF cycle [3.20]. As most of the sputtered material is accelerated away from the target, the second electrode does not have to be the substrate itself, and the substrate can be positioned normal to the direction of the ejected material [3.20]. This avoids dissipating large amounts of energy through the substrate, which could distort or re-evaporate the growing film [3.20].

The disadvantage of the planar magnetron sputtering system is that the flux of material leaving the target is not constant across the deposition area, but varies with a cosine distribution from the centre of the sputtering plasma, correlating with isotropic sputtering cascade theory [3.20]. This cosine distribution causes a variation in film deposition rate with respect to the position of the substrate to the normal of the centre of the sputtering target, limiting the available area for sputtering films with negligible thickness variation. For this work, a circular area on the substrate holder roughly 20 cm in diameter and centred directly over the sputtering target was considered to be an area of approximately even deposition rate, sufficient for producing thin film Schottky diodes and thin film samples simultaneously. The size of the useable area of the cosine distribution is limited by the size of the target and plasma, in contrast to PLD which is limited to the size of the plume of target material created by the laser, making sputtering more suitable for mass-production of semiconductor technologies due to the scalability of the technique.

3.4.2.3 RF Magnetron Sputtering Used in This Work

The vacuum chamber containing the RF-sputtering system and EBD apparatus used in this work is illustrated in Figure 3.11. The BOC Edwards Auto 500 RF, DC Sputtering and Electron-Beam Evaporation System also contained a DC sputtering unit not shown in Figure 3.11 as it was not used in this work. The technical specifications of the sputtering system, sputtering apparatus, and sputtering targets used in this work can be found in Appendix A3.3. Metal-oxide thin films of varying oxygen incorporation were deposited using RF-sputtering of noble metals including silver, ruthenium, iridium, palladium, and platinum, by controlling the proportion of oxygen and argon present during sputtering.

For every Schottky contact growth on a patterned ZnO substrate, two 5 x 5 x 0.5 mm and two 10 x 10 x 0.5 mm amorphous quartz substrates were included to simultaneously deposit thin film samples for optical and electrical measurements. The patterned ZnO substrate and amorphous quartz substrates were mounted on 10 x 10 mm silicon wafer carrier chips using photoresist, that were then fixed to the sputtering sample holder using silver tape. The 10 x 10 mm amorphous quartz substrates were directly fixed to the sample holder using silver tape on the four corners. The substrates were placed directly over the RF-sputtering gun to maximise uniformity of the sputtered film thickness.

The BOC Edwards Sputtering and Electron-Beam Evaporation System vacuum chamber was vented to atmosphere using nitrogen gas to load the sputtering target and the sample holder. Once the target and sample holder were loaded, the chamber was pumped down to a base pressure of nominally 5.0×10^{-6} mbar over the duration of 1 – 2 hours. The first mode of vacuum pumping was ‘roughing mode’, in which the chamber was sealed with the exception of the output vent, and then evacuated using the RV12 Rotary Vane Pump to a pressure of 2×10^{-1} mbar. Below that pressure, the EXT55H Compound Turbomolecular Pump was engaged in ‘fine pumping mode’ to evacuate the chamber to high vacuum pressures. For this work, base pressures up to 1.0×10^{-5} mbar were considered suitable for reactive RF-sputtering, as the sputtering environment with added processing gases exceeded 1.0×10^{-3} mbar in pressure.

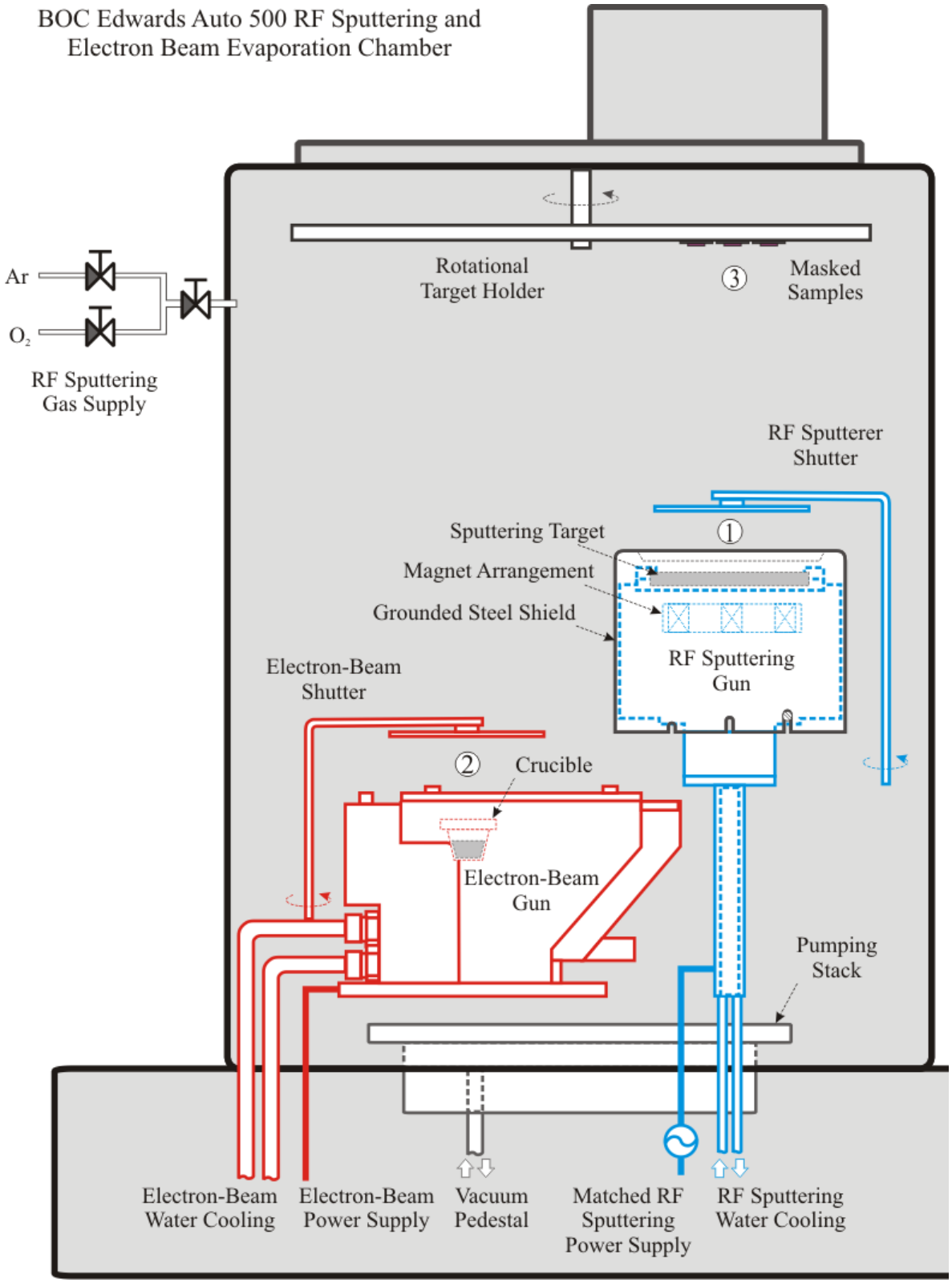

Figure 3.11: BOC Edwards RF-Sputtering and Electron-Beam Evaporation Chamber

Once the chamber had reached a sufficiently low pressure (approximately 1.0 x 10^{-5} mbar) in 'fine pumping mode', the chamber was set to 'process mode'. Process mode partially closed the gate valve of the vacuum chamber, allowing gases to flow through the chamber at a steady flow rate. The BOC Edwards Model 825 Mass Flow Controller was used to introduce a continuous, controlled flow of one or more processing gases through the chamber. The oxygen gas flow was introduced first, in order to record the partial pressure of oxygen, followed by the introduction of the argon gas. A back-flow of nitrogen gas was added to the output vent of the vacuum chamber during reactive oxygen sputtering in order to prevent vacuum pump damage. The proportion of oxygen to argon gas during sputtering was controlled by setting the flow rate of oxygen (0.5 – 10 sccm) to a fixed flow of argon (10 sccm). This produced a partial pressure ratio of between 1.0 x 10^{-4} and 3.0 x 10^{-3} mbar of oxygen to partial pressure of 3.0 x 10^{-3} mbar of argon. Argon gas (10 sccm) only was used in the sputter deposition of plain metal films.

The Cesar® Model 136 13.56 MHz RF Power Supply was used to provide a constant RF power of 50 W, with a matching network used to automatically tune the capacitive coupling of the RF power supply to the load required by the plasma, in order to minimise reflected power [3.20]. For situations where impedance detection was not available, the capacitive coupling of the RF power source was tuned manually.

After the addition of the processing gases, the plasma would not usually immediately strike when the RF power source was turned on. In this case, the control valve of the argon gas flow was fully opened for a few seconds, to provide sufficient gas pressure to strike the plasma, after which it was able to sustain itself under normal processing conditions.

A shutter was used to shield the substrates on the sample holder from the sputtered material prior to growth, allowing control of the sputter deposition time to be performed independently of the duration of the plasma. The shutter was closed during the striking of the plasma, as the initial sputtered material from the target would include surface contaminants with initial sputtering occurring at a higher pressure of argon than the desired growth conditions.

A period of five minutes pre-sputtering in pure argon gas was used between striking the plasma and opening the shutter in order to 'clean' the sputtering target by removing the first few layers of material that was likely to be contaminated by atmospheric exposure [3.20]. This pre-sputtering was performed without the addition of oxygen gas in order to remove any target poisoning from previous metal-oxide growths. For metal-oxide growths, the plasma was extinguished after pre-sputtering, the oxygen gas flow added, and the plasma was struck again.

The FTM7 Film Thickness Monitor was used to measure the approximate thickness of the sputtered films during the growth, automatically closing the shutter once the desired film thickness

had been reached. The thickness monitor used the crystal microbalance technique to determine the thickness of the film via the change in frequency of an oscillating crystal while accounting for the density and acoustic impedance of the material being deposited [3.20]. The thickness monitor was positioned beside the substrate holder, outside the maximum of the sputtering cosine distribution. A 'tooling factor' was used to account for the differences between the recorded thickness and the actual thickness of the material deposited, which was determined experimentally. Different oxygen partial pressures changed the growth rate of the metal-oxide films. The RF sputtered films in this work were grown for a standardised time of 15 minutes rather than grown to a set thickness, producing films and Schottky contacts of between 50 – 200 nm in thickness.

For every growth performed in this work, a sputtering log has been included in appendix A3.4 with the date, the source ('RF' for RF-sputtering as the source of the deposition material), the material used, the flow rates of the sputtering gases used, the power of the deposition source used, the approximate temperature inside the vacuum chamber during growth, the duration of the growth, the 'base' pressure of the vacuum chamber before the processing gasses were added, the 'process' pressures of the vacuum chamber with the addition of the argon and/or oxygen gas flows and the pressure of the processing plasma, the measured thickness of the film, and the calculated tooling factor for each level of oxygen incorporation for the crystal growth monitor.

All devices fabricated in this work involving the deposition of a Schottky contact were capped with a layer of 40 – 50 nm gold in order to provide a laterally conductive surface for characterisation, and to minimise further oxidation of the metal-oxide Schottky contacts. The layer of gold was deposited using EBD, as detailed in Section 3.4.3.

3.4.3 Electron-Beam Deposition

EBD is a PVD technique that uses a focused electron-beam to heat a crucible of source material to sufficient energy to produce a stream of atomised material onto the sample substrate, where it condenses to form a thin film [3.20]. Although less commonly used than sputtering, EBD is capable of depositing materials with high melting points, such as the titanium and gold in this work [3.20]. Titanium and gold have melting points of 1668°C and 1064°C respectively, however the vapour pressure of titanium is such that it can be both evaporated and sublimated at temperatures close to its melting point [3.22]. As evaporation rates are dependent on the vapour pressure of the material, the EBD evaporation of compounds and alloys produces a non-stoichiometric vapour compared to the composition of the source material, making EBD a more suitable technique for depositing the elemental films in this work [3.29]. The deposition area of EBD is limited by the narrow beam of

electrons, and therefore cannot be scaled up like RF-sputtering. However, the EBD crucibles require significantly less material than a 2 inch RF-sputtering target, making EBD a more cost-effective tool for research.

3.4.3.1 The Development of Electron-Beam Deposition

As early as 1857, thin layers of metal were deposited using vaporisation by M. Faraday experimenting with exploding metal wires within an inert atmosphere [3.30]. W. Crookes showed in 1879 that a focused beam of electrons from a hot cathode, deflected by a magnet, could be used in a vacuum to bring platinum to incandescence, as well as noting that, upon touching the side of his apparatus where the electron-beam was focused, he "immediately raised a blister" [3.31]. More controlled depositions of metal thin films were carried out by Nahrwold in 1887 by heating platinum wires in a vacuum [3.32]. The use of an electron beam source to evaporate metal films was reported by H. M. O'Bryan and H. W. B. Skinner in 1933 in order to study the distribution of conduction electrons, O'Bryan later describing the apparatus used in 1934 as a more energy-efficient method of evaporating metal than by using a heating element [3.33 – 3.34]. Electron-beam evaporation was used as a method for ion plating by C. T. Wan *et. al*. in 1971, evaporating metals and metal alloys in an inert gas glow discharge environment and using a plasma [3.35]. However, the presence of reactive gases and plasma during EBD was found to corrode the filament over time as well as reducing the stability of heating the evapourant [3.34 – 3.35].

EBD uses a hot cathode, usually a tungsten filament, to produce a stream of electrons that are magnetically focused and accelerated through a high voltage to bombard the surface of a source material inside a crucible [3.20]. The majority of the kinetic energy of the accelerated electron is converted into heat near the surface of the source material. This surface can exceed 3000 °C, allowing for the evaporation of most materials [3.29]. The bulk of the source material is cooled by the water-cooling system of the crucible [3.20].

As the material is heated in vacuum, typically 1.0×10^{-6} to 1.0×10^{-5} mbar in this work, a thermodynamic equilibrium is established where both the liquid and gas phase exist at the same temperature in close proximity [3.20]. At this temperature, a characteristic vapour pressure exists for the material that determines the upper limit of the practical evaporation rate [3.29]. The vapour-pressure of the material is also dependent on the vacuum chamber conditions, including residual gas levels and the rate of condensation of vaporised material with the vacuum chamber walls [3.29]. The vapour pressure increases exponentially with increasing target temperature, producing a vapour stream of atomised source material with a distribution of speeds and kinetic energies escaping the

crucible [3.20 – 3.29]. The vapour is comprised of mostly single metal atoms, with less than 0.1% of species evaporating as diatomic molecules, producing homogeneous films. The vapour condenses on a substrate in a cosine distribution centred over the centre of the point-source of evaporation within crucible, forming a thin film at a nominal rate of 1 - 10 nms^{-1} [3.20 – 3.29]. Higher rates of evaporation can cause greater variation in the film thickness across the deposition area, as well as the 'spitting' of macro particles from the source material as vapour bubbles are generated within the material, producing lower-quality inhomogeneous films [3.20].

Scanning the electron-beam in a figure-eight across the surface of the crucible can produce a more uniform source of evaporation than the point-source created by a stationary electron-beam, as well as preventing the electron-beam from boring a deep hole into the source material. As with the RF-sputtering deposition source, a circular region of roughly 20 cm in diameter on the sample holder directly above the EBD apparatus produced films of approximately uniform thickness for this work [3.20].

3.4.3.2 Electron-Beam Deposition Used in This Work

The Auto 306 EB3 Multihearth Electron-Beam Source uses a 3 kW power source to heat a tungsten filament to incandescence, providing a source of electrons. The electron-beam was accelerated using a high voltage source of 5 kV and deflected through 270° into the crucible using a permanent magnet, as shown in Figure 3.12 [3.36]. The beam power was controlled by controlling the filament current, which had a maximum current rating of 2000 mA [3.36]. The filament currents used in this work for the deposition of titanium and gold were approximately 110 mA and 60 mA.

EBD was used to deposit patterned ohmic contacts of titanium capped with a layer of gold, and also to cover Schottky contacts and thin film samples with a capping layer of gold, with the Auto 306 EB3 Multihearth Electron-Beam Source in the same vacuum chamber as the RF-sputtering system, as depicted in Figure 3.11. Titanium is known to react with the near-surface oxygen in ZnO, forming a titanium oxide interfacial phase that produces oxygen vacancies, V_O, in ZnO, which metallises the surface and increases its conductivity [3.37]. The gold capping layer was used to both prevent oxidation of the titanium layer by the atmosphere, and to provide a low resistance probe contact area for electrical characterisation on both the ohmic and Schottky contacts.

Target materials for EBD, held in Kurt J. Lesker FAMBATE® carbon crucible liners, were kept in a rotatable multihearth carousel, including the crucible of titanium and crucible of gold used in this work. This allowed titanium and gold bilayers to be deposited without breaking vacuum, which prevented unwanted oxidation of titanium by the atmosphere.

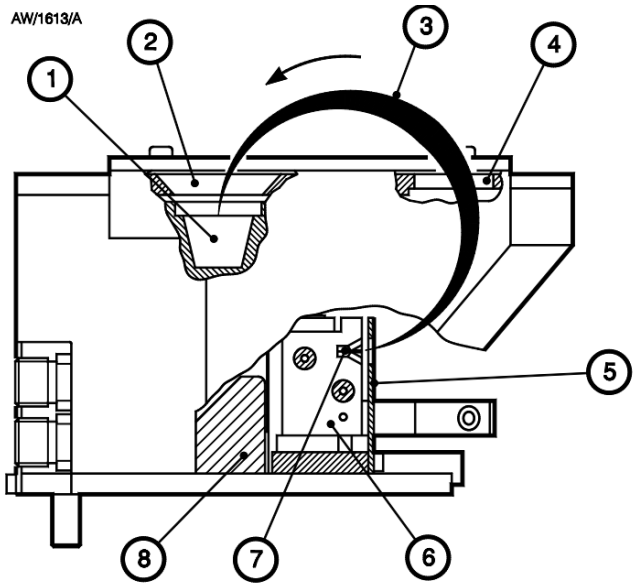

1. Crucible hearth
2. Aperture in top shield
3. Electron beam
4. Aperture in top shield
5. Anode plate
6. Emitter assembly
7. Filament
8. Permanent magnet

Figure 3.12: BOC Edwards Auto 306 EB3 Multihearth Electron-Beam Source [3.36]

The chamber was pumped down to a base pressure of nominally less than 1.2 x 10^{-5} mbar over the duration of an hour, following the same procedures detailed in Section 3.4.2 for RF-sputtering. The vacuum pressure for EBD was not as critical as the vacuum needed for RF-sputtering, as the quality of the ohmic contact was not as sensitive to residual chamber oxygen. The process of heating titanium to the vapour point also removed residual oxygen from the walls of the vacuum chamber by reacting to form titanium oxide.

The EB3 Power Supply was used to heat the titanium crucible using a figure-eight-sweeping electron-beam to produce a vapour stream of atomised titanium, ramping from 0 mA to 110 mA in steps of 10 mA every five seconds with the EBD shutter closed in order to prevent deposition during the ramping phase. The ramping was necessary in order to prevent thermal shock to the crucible and hearth liner containing the source material. During the ramping phase, the chamber pressure increased by roughly 5 x 10^{-6} mbar as the vapour pressure of the titanium increased. Between 100 mA and 110 mA, the chamber pressure dropped steadily to around 1 x 10^{-6} mbar, as residual oxygen on the chamber walls reacted with the evaporated titanium to produce titanium oxide, despite the shutter being closed. This indicated that titanium was being evaporated steadily. Once the current had reached 110 mA, the shutter was opened and the timer initialised for the

duration of the growth. Typical titanium growths were of a desired thickness of 40 – 50 nm; a trade-off between producing contacts thick enough to withstand repeated contacting from the electrical characterisation probes, and depositing too much titanium which risked hard-baking the photoresist and making lift-off difficult.

As titanium and gold were both regularly deposited using the EBD method, the tooling factor was well known, and the film thickness monitor was able to accurately control film growth to a set thickness, rather than a set time. The CAL 9900 Autotune PID Temperature Controller was used to record the chamber temperature at the beginning and end of the growth to ensure that the temperature did not rise by more than 50°C, which would risk hard-baking the photoresist.

Following the completion of the titanium deposition, the current was reduced from 110 mA to 0 mA in steps of 20 mA every five seconds to prevent thermal shock to the crucible, hearth liner and evapourant. The titanium crucible was allowed to cool for a further five minutes before the carousel was rotated to select the gold crucible. The EBD current for the deposition of gold was nominally 60 mA. The deposited thickness of the gold was also 40 – 50 nm taking approximately 3 minutes of deposition.

The gold capping layer on the ohmic contacts was deposited after the titanium layer without breaking vacuum. However, due to the relative positions of the EBD source and the RF-sputtering gun, the deposition of the gold capping layer on top of RF sputtered metal-oxide films required breaking the vacuum to move the sample substrates from the RF-sputtering sample holder to the EBD sample holder. Breaking the vacuum between depositions may have introduced contaminants between the metal-oxide layer and the gold capping layer, causing an additional series resistance, however the interface between the metal-oxide and gold layer was not considered to be as critical to the Schottky diode functionality as the interface between the metal-oxide layer and the ZnO substrate.

For every Schottky contact fabricated in this work, a 10 x 10 x 0.5 mm amorphous quartz substrate containing the same metal-oxide film was also capped with gold so that the transmission of the Schottky contact could be measured. Transmission results are discussed in Section 5.2.

For every growth performed for this work, a sputtering log has been included in appendix A3.4 with the date, the source (‘EB’ for EBD), the material used, the current of the electron-beam filament, the approximate temperature of the substrate during the growth, the duration of the growth, the ‘base’ pressure of the vacuum chamber before the EBD was started, the ‘process’ pressure of the vacuum chamber with the vapour pressure of the evaporating material, the estimated thickness of the grown film from the crystal growth monitor, and the tooling factor used in the calculation of the growth thickness estimate.

REFERENCES

[3.1] Kim, D., Department of Electrical and Computer Engineering, University of Canterbury, Christchurch, New Zealand.

[3.2] Schmitsdorf, R.F., Kampen, T.U., Mönch, W., (1997), Explanation of the linear correlation between barrier heights and ideality factors of real metal-semiconductor contacts by laterally nonuniform Schottky barriers, *Journal of Vacuum Science and Technology B: Microelectronics and Nanometer Structures*, 15 (4), pp. 1221-1226.

[3.3] Burm, J., Litvin, K. I., Schaff, W. J., Eastman, L. F., (1994), Optimization of High-speed Metal-Semiconductor-Metal Photodetectors, *IEEE Photon Technol Lett*, 6, 6, pp. 722-724.

[3.4] Averine, S.V., Chan, Y.C., Lam, Y.L. (2001), Geometry optimization of interdigitated Schottky-barrier metal–semiconductor–metal photodiode structures, *Solid-State Electronics*, 45, 3, pp. 441-446.

[3.5] Soole, J. B. D., Schumacher, H., (1990), InGaAs Metal-Semiconductor-Metal Photodetectors for Long Wavelength Optical Communications, *IEEE Trans Electron Dev*, 37, 11, pp. 2285-2291.

[3.6] den Otter, M.W., (2002), Approximate expressions for the capacitance and electrostatic potential of interdigitated electrode, Sensors and Actuators, *A: Physical*, 96 (2-3), pp. 140-144.

[3.7] Averin, S., Sachot, R., Hugi, J., De Fays, M., Ilegems, M., (1996), Two-dimensional device modeling and analysis of GalnAs metal-semiconductor- metal photodiode structures, *Journal of Applied Physics*, 80 (3), pp. 1553-1558.

[3.8] Arshak, K., Hickey, G., Forde, E., Harris, J., (2007), Development of a room temperature thin film In_2O_3, ZnO and SnO_2 ozone sensor, *IEEE International Symposium on Industrial Electronics*, art. no. 4374831, pp. 1536-1541.

[3.9] Clariant. (2013). *AZ 1500 Series Standard Photoresists*. Retrieved from http://www.microchemicals.com/micro/az_1500_series.pdf

[3.10] Hannavy, J. (2013). *Encyclopedia of Ninteeth-Centuary Photography* (reprint ed., Vol. 1, pp. 1117-1118). Oxford, United Kingdom: Routledge.

[3.11] Gernsheim, H., & Gernsheim, A. (1969). *The History of Photography from the camera obscura to the beginning of the modern era* (Revised and enlarged ed., pp. 56-57, 337). London, United Kingdom: Thames & Hudson.

[3.12] MicroChemicals. (2013). *General Properties of AZ®/ TI Photoresists*. Retrieved from http://www.microchemicals.com/technical_information/photoresist_properties.pdf

[3.13] Smith, H. M., Turner, A. F. (1965). Vacuum Deposited Thin Films Using a Ruby Laser. *Applied Optics*, 4, pp.147-148.

[3.14] Maiman, T. H. (1960). Stimulated Optical Radiation in Ruby. *Nature*, 187, 493-4.

[3.15] Castillejo, M., Ossi, P. M., Zhigilei, L. (2014). *Lasers in Materials Science*. New York, USA: Springer.

[3.16] Farrel, I. (2010). *Growth of Metal-Nitride Thin Films By Pulsed Laser Deposition*, PhD thesis, University of Canterbury, Christchurch, New Zealand.

[3.17] Thompson, J. J. (1913), *Rays of Positive Electricity And Their Application To Chemical Analyses*. London, United Kingdom: Longmans, Green & Co., Ltd.

[3.18] Kingdon, K. H., Langmuir, I., (1923), The removal of thorium from the surface of a thoriated tungsten filament by positive ion bombardment. *Physical Review*, 22 (2), 148-160.

[3.19] Wehner, G. K, Anderson, G. S., (1970), The Nature of Physical Sputtering. In L. I. Meissel & R. Glang's *Handbook of Thin Film Technology*, New York: USA: McGraw-Hill, Inc., pp. 3-33.

[3.20] Frey, H., Khan, H. R., (2015), *Handbook of Thin-Film Technology*, Berlin, Germany: Springer Berlin Heidelberg.

[3.21] Laegreid, N., Wehner, G.K., (1961), Sputtering yields of metals for ArC and NeC ions with energies from 50 to 600 eV., *J Appl Phys*, 32, pp. 365-369.

[3.22] Mattox, D. M., (2003), *The Foundations of Vacuum Coating Technology*, Norwich, NY, USA: Noyes Publications.

[3.23] Mokwa, W., Wessling, B., Schnakenberg, U., (2007), Sputtered iridium oxide for stimulation electrode coatings, *Annual International Conference of the IEEE Engineering in Medicine and Biology - Proceedings*, art. no. 4353727, pp. 6047-6050.

[3.24] Ellmer, K., Welzel, T., (2012), Reactive magnetron sputtering of transparent conductive oxide thin films: Role of energetic particle (ion) bombardment. *Journal of Materials Research*, 27 (5), pp. 765-779.

[3.25] Grove, W.R., (1852), On the Electro-Chemical Polarity of Gases, *Phil. Trans. R. Soc. Lond.*, 142, pp. 87-101.

[3.26] Penning, F. M., Moubis , J. H. A., (1940), Cathode sputtering in a magnetic field, *Proc. Kon. Ned. Akad. Wetensch*, 43, pp. 41-56.

[3.27] Guentherschulze, A., Meyer, K., (1930), *Z. Physik*, 62, pp.607.

[3.28] Gow, J. D., Ruby, L., (1959), Simple, Pulsed Neutron Source Based on Cross-Field Trapping, *Rev. Sci. Instrum*., 30(5), pp.315.

[3.29] Glang, R., (1970), Vacuum Evapouration. In L. I. Meissel & R. Glang's *Handbook of Thin Film Technology* (pp. 26-123), New York: USA: McGraw-Hill, Inc.

[3.30] Faraday, M., (1857), The Bakerian Lecture: Experimental Relations of Gold (and Other Metals) to Light, *Phil. Trans. R. Soc. Lond.*, 147, pp.145-181.

[3.31] Crookes, W., (1879), The Bakerian Lecture: On the Illumination of Lines of Molecular Pressure, and the Trajectory of Molecules, *Phil. Trans. Roy. Soc*., 170, pp. 135 – 164.

[3.32] Nahrwold, R., (1887), Ueber Luftelectricität, *Ann. Physik*, 31, 467, pp. 448-475.

[3.33] O'Bryan, H. M., Skinner, H. W. B., (1933), Experimental Determination of the Distribution of Conduction Electrons in Metals, *Phys. Rev.*, 44, pp. 602 - 603.

[3.34] O'Bryan, H. M., (1934), Evaporation Technique for Highly Refractory Substances, *Rev. Sci. Instrum..*, 5, pp. 125 - 126.

[3.35] Wan, C. T., Chambers, D. L., Carmichael, D. C., (1971), Investigation of Hot-Filament and Hollow-Cathode Electron-Beam Techniques for Ion Plating, *J. Vac. Sci. Technol.* , 8, 6, pp. 99 – 104.

[3.36] (1993), Instruction Manual AUTO 306 accessories: EB3 Multihearth Electron-Beam Source and accessories [Manual]. Crawley, West Sussex, UK: BOC Edwards, E090-72-880 Issue F.

[3.37] Kim, H.-K., Han, S.-H., Seong, T.-Y., Choi, W.-K., (2000), Low-resistance Ti/Au ohmic contacts to Al-doped ZnO layers, *Applied Physics Letters*, 77 (11), pp. 1647-1649.

4 | Characterisation Techniques

This chapter gives an overview of the equipment and techniques used to characterise the noble metal-oxide materials and Schottky contacts fabricated in this work. The techniques described include the Hall effect, Kelvin probe microscopy (KPM), Rutherford backscattering spectroscopy (RBS), X-ray photoemission spectroscopy (XPS), and X-ray diffraction (XRD) on fabricated thin films. The electrical characterisation of the Schottky contacts included current-voltage (I-V) measurements with varying illumination, temperature and ambient gases present, and capacitance-voltage (C-V) characterisation.

4.1 Material Characterisation

For each of the noble metal-oxide RF-sputtered thin film Schottky contacts deposited on bulk ZnO substrates, thin films of the same material were grown simultaneously on amorphous quartz substrates in order to optically and electrically characterise the Schottky contact material in conjunction with the performance of the Schottky contacts, as detailed in Section 3.4.2. For optical characterisation and thickness measurements, two 10 x 10 x 0.5 mm amorphous quartz substrates were fixed to the sputtering sample holder using silver tape in the four corners of each substrate, producing well-defined film boundaries on the four corners of each substrate, as shown for the 3.0:10 (O_2:Ar) IrO_x films in Figure 4.1, where the thickness of the film could be measured across the boundary. As the Schottky contacts were capped by a 50 nm layer of gold before use, one of the two samples was also capped with an identical Au layer for optical transmission measurements.

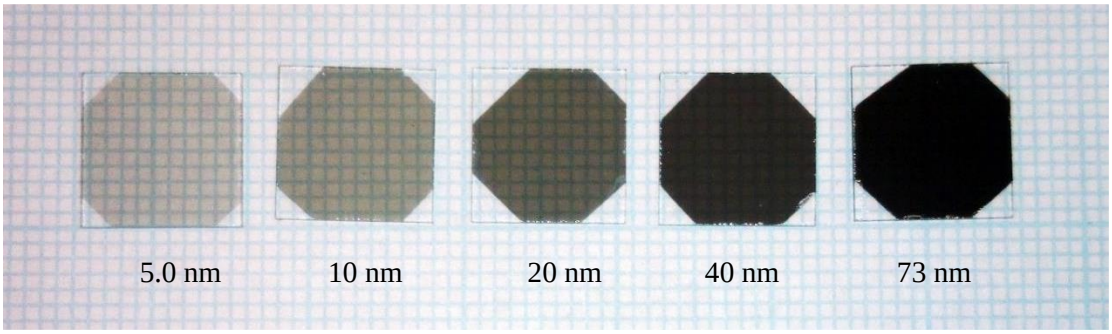

Figure 4.1: RF-Sputtered IrO_x Film Samples with Varying Thicknesses (1 mm Grid Squares)

4.1.1 Thickness Measurements

The Schottky contact layers were grown for a fixed time of 15 minutes rather than to a specified thickness, as the change in oxygen incorporation of the noble metal-oxide films affected the growth rate and caused inaccuracies in real-time thickness monitoring, due to varying material density and acoustic impedance, as detailed in Section 3.4.2. The thickness of each film was measured using either the Veeco DEKTAK 150 Profilometer, or the Veeco Dimension 3100 Atomic Force Microscope (AFM), in order to scale the optical and electrical properties of the films for comparison purposes.

For films thicker than 50 nm, the profilometer was used to measure step-height between the film and the amorphous quartz substrate using two-dimensional (2D) topography scans across the film-substrate interfaces. Three step-height measurements were made on each of the film-substrate boundaries on the four corners of the sample, and the measurements were averaged to give an estimation of the film thickness. For films thinner than 50 nm, a greater level of vertical resolution was required. Three-dimensional (3D) topographies were taken of the film-substrate boundary using the AFM, with film thickness determined from the averaged step-height across 256 2D scan lines.

4.1.1.1 Profilometer

Contact stylus profilometry has been used to study surface topography of materials from the early 1930s, by moving a stylus over a material surface and recording its vertical deflection with position to create a 2D ‘trace’ of the surface [4.1]. The development of digital collection, filtering, and analysis of the stylus deflection allowed for more accurate translation of the stylus deflection into surface topography, with the first digital surface profilometer, the Talysurf 4, developed in 1972 [4.1]. Increasing computational power made accurate, near real-time analysis of surface profilometry possible in the 1980s and 1990s, leading to three-dimensional analysis of surface topographies [4.1].

For this work, a 2D contact profilometer was used to measure the step-height between the substrate and film to determine film thickness for films thicker than 50 nm. A stylus of tip of 12.5 µm radius was traced in a 200 µm scan with 3.00 mg of force applied. A three-axis inertial sensor measures tip deflections, analysed in software to produce a surface topography with a measurement range of 6.5 µm [4.2].

For each step-height, the surface topography was levelled in software using two points on the amorphous quartz substrate. The step-height was determined from two 10 µm sections on either side of the step. An example of this is shown in Appendix A4.1.

4.1.1.2 Atomic Force Microscope

Significant advancement was made in the study of surface topography on the order of nanometer and sub-nanometer resolution, both vertically and laterally, with the development of the scanning tunnelling microscope (STM) in 1981, and the subsequent development of the AFM in 1986, by G. Binning et. al. [4.1, 4.6]. The STM and AFM are both non-optical scanning probe microscopes that use the interaction between the scanning probe and the sample surface to determine surface topography through a feedback control mechanism, rather than directly measuring vertical displacement of a probe, as is done in contact stylus profilometry.

The STM was invented by G. Binning, H. Rohrer, Ch. Gerber, and E. Weibel in 1981, and uses vacuum tunnelling to determine surface topography [4.1]. A conducting probe with a tip radius of one atom was scanned several ångströms above a conducting surface, with a bias voltage between 2 mV – 2 V applied between the probe and the surface [4.1]. The vacuum tunnelling current between the tip and the surface varied exponentially with distance, and the surface topography was measured by fixing either the height of the probe, or alternatively maintaining a constant tunnelling current, and changing the probe height as the probe is scanned across the sample surface, shown in Figure 4.2 [4.1, 4.3]. The primary limitation of the STM in measuring surface topography compared to AFM is the reliance of STM on surface conductivity.

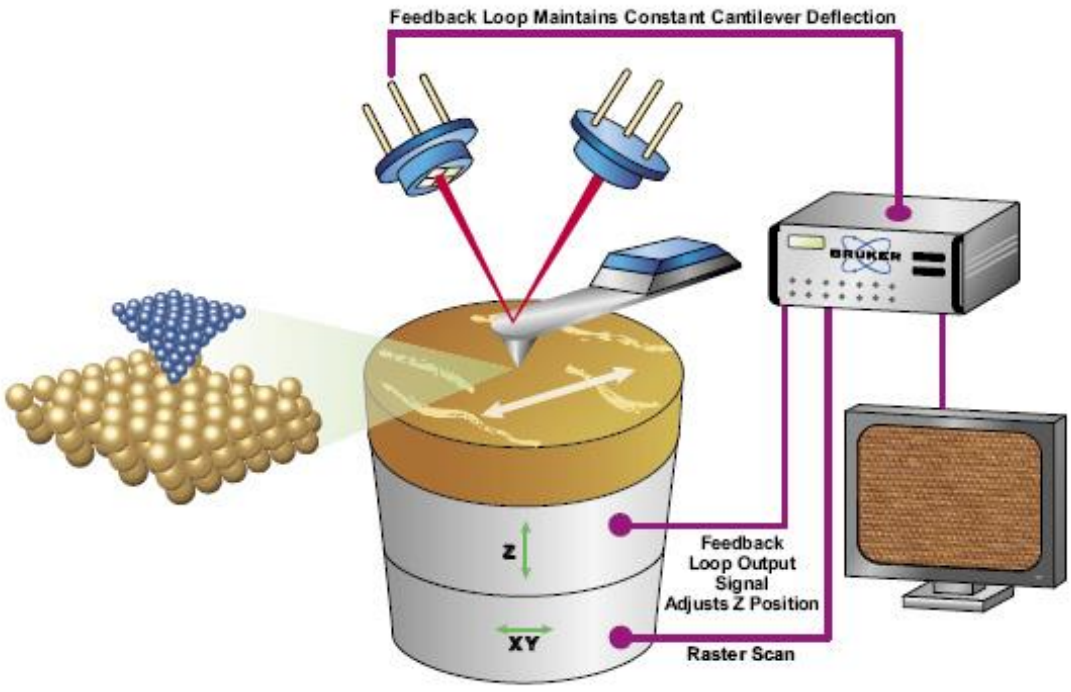

Figure 4.2: Laser Interferometer Monitoring Cantilever Position on Sample Surface Illustrating AFM Operation [4.3]

The AFM was invented by G. Binning, C. F. Quate, and Ch. Gerber in 1986 as a new system of STM capable of measuring both insulating and conducting surfaces [4.1, 4.6]. A cantilever beam with an atomically-sharp tip is scanned over a surface, as illustrated in Figure 4.2 above [4.1, 4.3]. The inter-atomic force between the cantilever tip and the sample surface deflect the cantilever vertically as it is scanned across the surface, and the deflection is translated into topography [4.1].

For this work, the Veeco Dimension 3100 Atomic Force Microscope was used in conjunction with the Veeco NanoScope Analysis Version 5 software package, shown in Figure 4.3. The AFM was operated in 'TappingMode' [4.5], where the cantilever was oscillated vertically at its resonant frequency by a piezo stack as it was scanned across the sample surface. BudgetSensors Tap300AL-G etched silicon AFM tips were used, with a resonant frequency of approximately 300 kHz, depending on the fine-tuning of the individual AFM tip.

A laser interferometer was used to measure the deflection of the cantilever by the sample surface, to determine the modulation of the amplitude and phase of the cantilever resonant frequency. This information could then be used to determine the topography, elasticity, and magnetism of the sample material [4.5]. Using a conducting probe, further measurements such as Kelvin probe microscopy (KPM) could be performed on samples, detailed in Section 4.1.4.

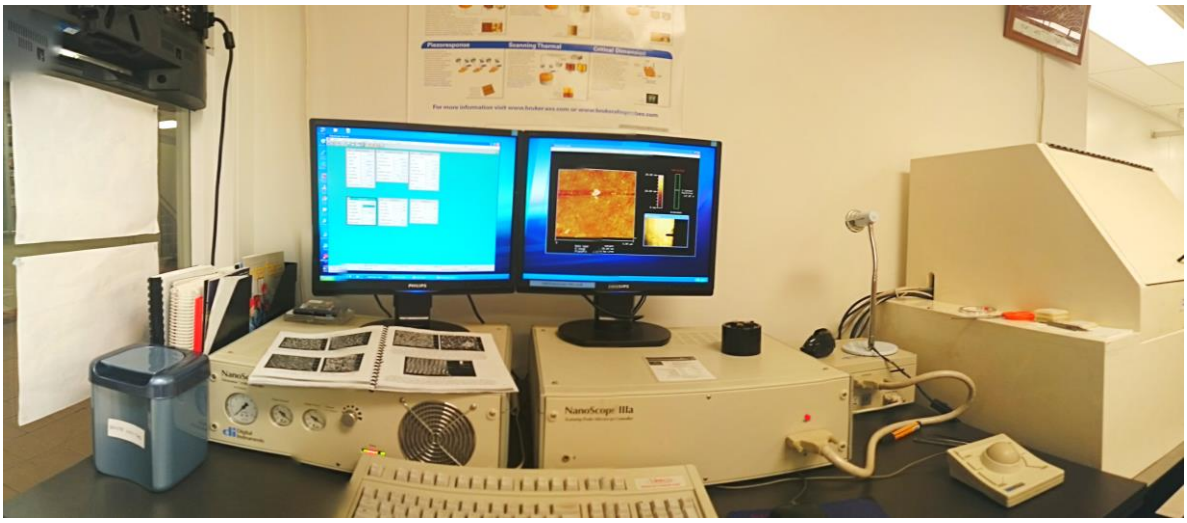

Figure 4.3: Veeco Dimension 3100 Atomic Force Microscope System

4.1.2 Transmission Measurements

The noble metal-oxide Schottky contact films grown in this work showed increasing levels of transparency with increasing oxygen content when sputtered onto amorphous quartz substrates, as well as increasing transparency with decreasing thickness, as shown in Figure 4.1. As the metal-oxide films were grown for a fixed time period, as detailed in Section 3.4.2, the transmission

measurements of the thin films were scaled to a thickness of 100 nm for comparison, as detailed in Section 5.2. Metal-oxide IrO_x and PtO_x films grown onto RF-sputtered films of platinum for Kelvin Probe spectroscopy measurements, detailed in Section 4.1.4, also showed a colour change with increasing oxidation, as shown in Figure 4.4.

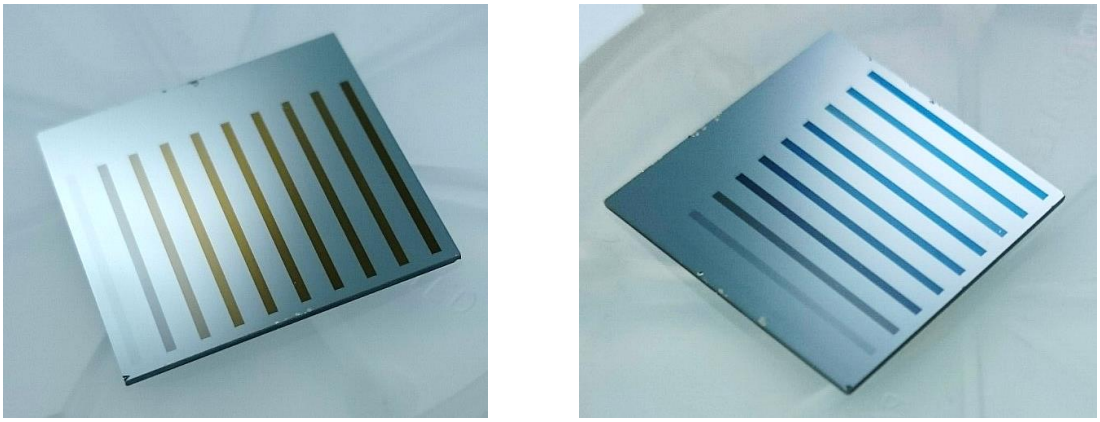

Figure 4.4: IrO_x (Left) and PtO_x (Right) Kelvin Probe Spectroscopy Samples with Metal Oxide Film Strips of Increasing Oxygen Incorporation from Left to Right

Spectrophotometry is widely used to determine the oxidation states of metal-oxides as well as other materials, the technique of analytically identifying oxides by their colour dating back to the mid-1900s [4.4]. Modern spectrophotometry measures the absorbance and transmission of electromagnetic wavelengths in the UV, visible, and near-infrared regions of the electromagnetic spectrum in materials to characterise their optical behaviour.

In order to investigate the transparency and electrochromism of the metal-oxide films, the Aglient Cary 6000i UV-Vis-NIR Spectrophotometer was used to measure the transmission of wavelengths between 200 – 800 nm through the films. The Cary used two lamps for this measurement, a deuterium UV lamp (200 – 350 nm) and a visible quartz-iodide lamp (350 – 800 nm). Initial calibration accounted for the jump in transmission from transitioning between lamps at 350 nm. The lamps produced light which was filtered through a monochromater to the selected wavelength. The monochromatic light was split into two beams; one beam passed through a bare amorphous quartz substrate, the other beam passed through an amorphous quartz substrate covered in a metal-oxide film. The light collected from each beam was used to calculate the transmission of the metal-oxide film independent of the substrate. Noble metal-oxide films with the gold capping layer on top were also tested for transparency in order to determine the filtering effect of the gold-capped Schottky contacts during UV and visible light illumination.

Two source lamps were used in order to cover the 200 – 800 nm wavelength range, the transition occurring at 350 nm. A baseline measurement was performed between two bare

amorphous quartz substrates, and with one of the substrates completely blocked, in order to calibrate 0% and 100% transmission levels, as well as to remove the jump in transmission caused by the transition between source lamps.

4.1.3 Hall Effect

In 1879 Edwin Herbert Hall published the paper 'On a New Action of the Magnet on Electric Currents', describing his discovery of an induced voltage across a conductor passing a constant current with the application of a magnetic field perpendicular to the flow of current [4.7]. As illustrated in Figure 4.5, when a magnetic field, B_Z, is applied at right angles to a conductor carrying a current, I, the current charge carriers are deflected by the Lorentz force [4.8]. The deflected charge carriers accumulate on one side of the conductor, inducing an opposing electric field, ξ_y, across the conductor in what is known as the Hall effect [4.8]. At steady-state, the magnitude of the opposing electric force exactly opposes the Lorentz force on the charge carriers [4.8]. The electric potential across the conductor due to the Hall effect can be measured, and is known as the Hall voltage, V_H [4.8].

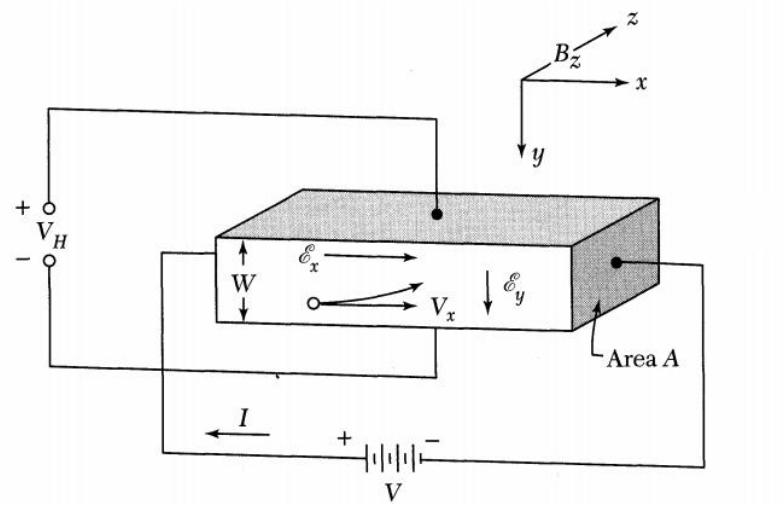

Figure 4.5: Measuring Carrier Concentration Using the Hall Effect [4.8]

The Hall effect can be used to calculate the majority carrier concentration of a semiconductor, as well as identifying the majority carrier type, and therefore whether the semiconductor material is n-type or p-type [4.8]. For this work, the EGK Corp. HEM-2000 Hall Effect System was used to measure thin films on 5 x 5 x 0.5 mm amorphous quartz substrates. The RF-sputtered thin films, either plain metal or metal-oxides, had four Au contacts deposited at the four corners of the film using EBD, detailed in Sections 3.4.2 – 3.4.3. The quartz substrates were mounted on special circuit

boards used for Hall effect measurement and ESL 1109-S polymer conductive silver paste was used to bond four wires to the gold contact, which were then soldered to the Hall effect circuit board as shown in Figure 4.6. The wire used was a single strand of a single-core multi-strand hook-up wire; 0.1 mm diameter tinned copper.

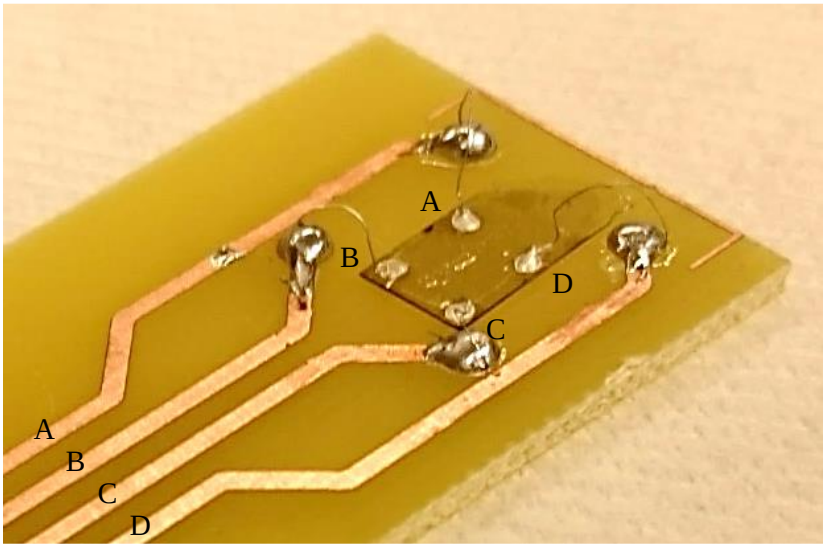

Figure 4.6: Hall Effect Circuit Board with Mounted Sample for Hall Effect Measurements with Corners A, B, C, and D Labelled

The Hall effect setup was used to measure the potential, *V*, between the four contact pads for a given DC injection current, *I*, a given sample thickness, *W*, and a given magnetic field, *B*. The Hall effect system had an upper limit to the injection current of 200 mA. The potential of each corner, labelled A, B, C, and D, was measured with respect to every other corner difference without the presence of a magnetic field. A magnetic field of 0.51 T was then applied normal to the sample in both the positive and negative direction, and the potentials of the diagonal corners re-measured.

For a positive injection current from contact A to contact B, the current was labelled I_{AB}. Similarly, a potential measured at contact A with reference to contact B was labelled V_{AB}. A magnetic field of 0.51 T was placed around the sample, with the field lines normal to the plane of the sample. The diagonal potentials, such as V_{AC}, measured with the application of the magnetic field were labelled V_{MAC} with the magnetic field in the positive direction and V_{-MAC} in the negative direction. These potentials were used by the Hall effect system to calculate the parameters listed in Table 4.1, using Equations 4.1 – 4.15. The van der Pauw formula, Equation 4.5, was solved numerically to calculate sheet resistance, R_S [4.9]. Equation 4.1 is an example of how V_{HAC}, V_{HCA}, V_{HBD}, and V_{HDB} were calculated. Equation 4.2 is an example of how R_{AB}, R_{BA}, R_{CD}, R_{DC}, R_{AD}, R_{DA}, R_{BC}, and R_{CB} were calculated. Appendix A4.2 contains all Hall Effect equations used in this work.

Table 4.1: Hall Effect Parameters, Units and Equations [4.8 – 4.9]

Parameter	Symbol	Unit	Equation	Equation Number
Hall Voltage: Contact A→C	V_{HAC}	V	$V_{HAC} = V_{MAC} - V_{-MAC}$	(4.1)
Resistance: Contact A→B	R_{AB}	Ω	$R_{AB} = \frac{V_{AB}}{I}$	(4.2)
Vertical Resistance	$R_{vertical}$	Ω	$R_{vertical} = \frac{(R_{AB} + R_{BA} + R_{CD} + R_{DC})}{4}$	(4.3)
Horizontal Resistance	$R_{horizontal}$	Ω	$R_{horizontal} = \frac{(R_{AD} + R_{DA} + R_{BC} + R_{CB})}{4}$	(4.4)
Van der Pauw Sheet Resistance	R_s	Ω	$e^{-\pi R_{vertical}/R_s} + e^{-\pi R_{horizontal}/R_s} = 1$	(4.5)
Bulk Resistivity	ρ	Ωcm	$\rho = R_S W$	(4.6)
Conductivity	σ	$\Omega^{-1}cm^{-1}$	$\sigma = \frac{1}{\rho}$	(4.7)
Hall Voltage	V_H	V	$V_H = \frac{(\lvert V_{AC}\rvert + \lvert V_{CA}\rvert + \lvert V_{BD}\rvert + \lvert V_{DB}\rvert)}{8}$	(4.8)
Sheet Carrier Concentration	N_S	cm^{-2}	$N_S = \frac{IB}{q\lvert V_H\rvert}$	(4.9)
Bulk Carrier Concentration	N_B	cm^{-3}	$N_B = \frac{N_S}{W}$	(4.10)
Mobility	μ	$cm^2V^{-1}s^{-1}$	$\mu = \frac{1}{qN_S R_S}$	(4.11)
			$\mu = \frac{\lvert V_H\rvert}{R_S IB}$	(4.12)
Hall Effect Coefficient	R_H		$R_H = \frac{W\lvert V_H\rvert}{IB}$	(4.13)
Magnetoresistance	δR	Ω	$\delta R = \frac{V_H}{I}$	(4.14)
V/H Ratio of Resistance	α		$\alpha = \frac{\sum R_{vertical}}{\sum R_{horizontal}}$	(4.15)

4.1.4 Kelvin Probe Spectroscopy

In 1991 M. Nonnenmacher *et al*. reported a technique known as Kelvin probe microscopy (KPM) to measure contact potential difference (CPD) with high spatial resolution using scanning AFM, a technique detailed in Section 4.1.1.2 [4.10]. Unlike standard topographical AFM measurements, KPM requires a conducting AFM tip, as well as a conducting sample, in order to perform scanning electrical measurements across the sample [4.10 – 4.11].

KPM uses two AFM scans over an interface of two materials to measure the CPD between one material and the other. The first AFM scan is used to determine the surface topography. During the second scan, the height of the AFM tip above the measured topography is maintained at a fixed height, while the electrical potential difference between the conducting AFM tip and the stage is measured as V_{CPD} in Equation 4.16 [4.11], where Φ_{tip} and Φ_{sample} are the respective work functions of the AFM tip and sample surface, and q is the elementary charge.

$$V_{CPD} = \frac{\Phi_{tip} - \Phi_{sample}}{-q} \qquad (4.16)\ [4.11]$$

KPM was performed across the interface between a deposited thin film of metal, or metal-oxide, and a reference film of a known work function, such as gold or platinum. The CPD difference between the thin film and reference film eliminates the dependence on tip work function and voltage between the AFM stage and the conducting substrate, as shown in Equation 4.17. The reference thin films used were gold and platinum, as the work function of these materials are well-known and they are relatively unreactive towards air.

$$V_{\Delta CPD} = V_{CPD(thin\ film)} - V_{CPD(reference)} = \frac{\Phi_{thin\ film} - \Phi_{reference}}{q} \qquad (4.17)$$

For this work, using the Veeco NanoScope Analysis software package, 512 lines of 10 µm wide scans were recorded across the interface between thin film strips of unknown work function and the reference films, in order to measure the change in work function of noble metal-oxide films with increasing oxygen incorporation. During AFM and KPM scans, the reference film was electrically connected to the sample stage using conductive tape and multi-strand hook-up wire. Figure 4.3 shows two 100 x 100 x 0.5 mm quartz substrates with a platinum reference layer and thin (~50 nm) fingers of 75 x 3 mm metal-oxide films deposited on top of the reference layer with techniques detailed in Sections 3.3.1 and 3.4.2 respectively. The photolithography mask used for KPM can be found in Appendix A3.1, Figure A3.1.3.

Figure 4.7 shows the step-height scan and the surface potential scan of a PtO_x sample film deposited on top of a gold reference film. The step-height of the sample film to the reference film was averaged over the 512 topography scan lines to determine a thickness of T = 71.8 nm, while the $V_{\Delta CPD}$ was averaged across the 512 KPM scan lines, showing $V_{\Delta CPD}$ = 0.115 V. The averaged scans used to calculate the thickness and change in surface potential across the interface can be found in Appendix A4.3.

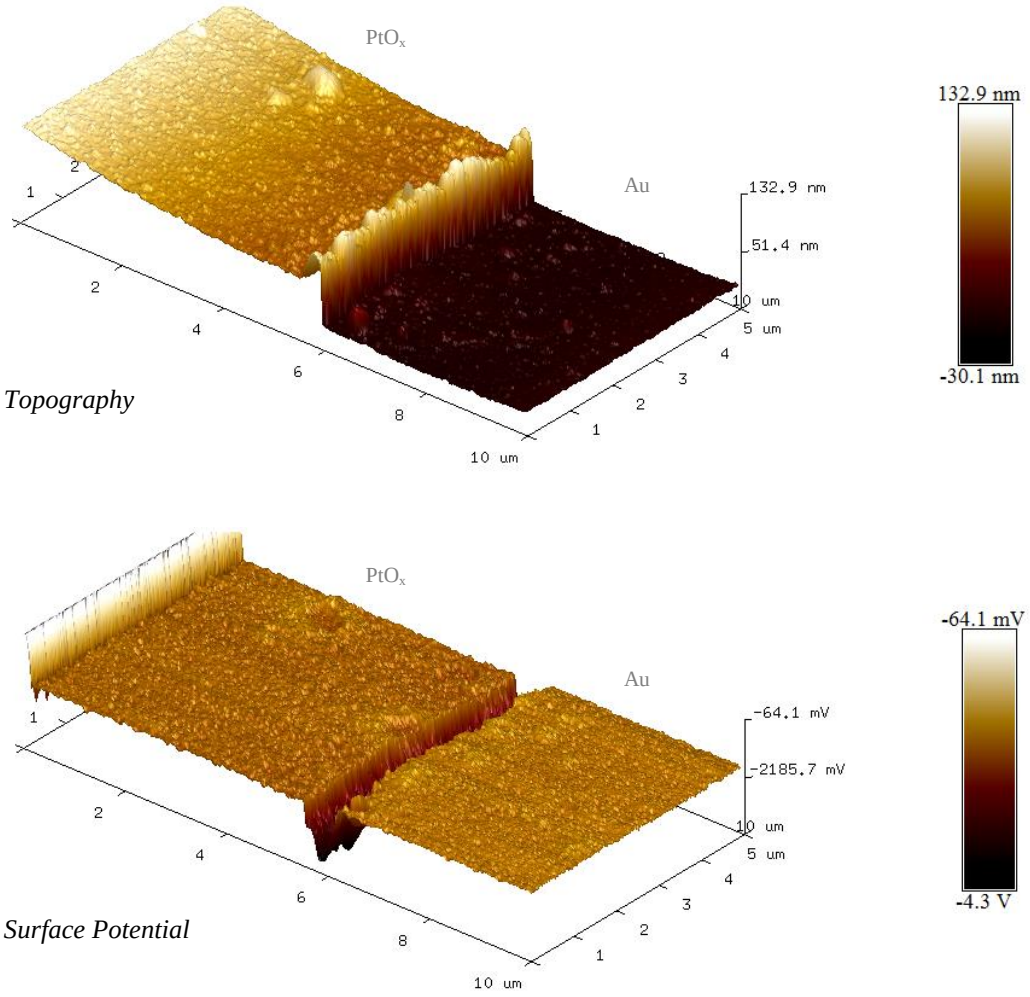

Figure 4.7: AFM (above), KPM (below) Measurements of RF-Sputtered 6.0:10 (O_2:Ar) PtO_x thin film on Au reference

For a series of metal-oxide film strips deposited on a single 100 x 100 x 0.5 mm quartz substrate, the reference surface potential was set to 0 mV in order to compare the relative CPD of the metal-oxide films of varying oxygen incorporation. Although all metal-oxide film strips were deposited within one day to reduce surface oxidation by exposure to atmosphere, the KPM measurement time of a sample was 2 – 3 days; therefore variation in surface oxidation could have affected the CPD measurements.

4.1.5 Rutherford Backscattering Spectrometry

Rutherford backscattering spectrometry (RBS) is a type of ion beam analysis commonly used to produce depth profiles of the stoichiometry and elemental composition of thin films, as it is a fast and non-destructive technique [4.15 – 4.16]. A beam of high-energy (MeV) He^{2+} ions are fired at a

thin film in a vacuum. The elastic collisions between the He^{2+} ions and the nuclei of the thin film cause a backscattering of the ions [4.15]. A nuclear particle detector is used to measure the energy of the backscattered ions at a set angle from the incident beam, which can be used to determine the mass of the nucleus involved in the elastic collision, and therefore the element [4.16]. A plot of the ion energy and detected particle counts is used to identify the elemental composition of the thin film at the surface, and the energy concentrations can be used to determine a depth profile if the geometry of the system is known [4.15 – 4.16]. Although RBS can identify atomic elements, and crystalline structures within a material, it cannot identify the chemical bonds or electronic configuration of the atoms present [4.15]. RBS is also not able to identify hydrogen or helium [4.15].

For this work, RBS measurements were made on thin films of Ir, IrO_x, Pd, PdO_x, Pt, and PtO_x deposited via RF sputtering onto 5 x 3 x 1 mm substrates of glassy carbon. The glassy carbon used was SPI Grade 11 25 x 25 x 1 mm Glassy Carbon Plates diced using the wafer saw, a technique described in Section 3.2. The RBS measurements and calculations were performed by Professor Steven M. Durbin and Robert Makin of the Department of Electrical and Computer Engineering, Western Michigan University, United States of America.

The RBS measurements used a beam of 2 MeV He^{2+} ions with a diameter of 2 mm, which ran for 50,000 counts for each sample. The RBS spectra were all taken at an angle of 150°, and the peaks fitted using the SIMNRA software package in order to calculate the ratios of metal to oxygen atoms. The resulting compositions from the RBS measurements are included in Appendix A4.4.

4.1.6 X-ray Photoemission Spectroscopy

Another technique used to quantify the elemental stoichiometry of the thin films in this work was X-ray photoemission spectroscopy (XPS). In contrast to the He^{2+} ion bombardment of RBS, XPS irradiates a thin film sample with a focused X-ray beam of a known energy and wavelength. The X-ray radiation causes excitation of the inner-shell electrons of an atom, resulting in the emission of a core level electron. The kinetic energy of the emitted electron involved can be used to calculate the binding energy of the electron, and therefore identify the atom [4.15 – 4.16].

The resulting plot of the XPS photoelectron count versus binding energy shows sharp peaks corresponding to the individual elements present in the thin film surface in different electronic configurations [4.15]. By integrating the area under the peaks, the ratio of elements present in the sample can be calculated [4.15].

Unlike RBS in Section 4.1.5, XPS is sensitive only to the surface layers of the thin film, however XPS can be used to identify the chemical bonds and electronic configurations of the material, as the chemical bonds and electronic configuration determines the inner shell structure and binding energy [4.15 – 4.16]. Depth profiles can be destructively obtained by Ar ion milling [4.15]. XPS cannot identify hydrogen or helium [4.15].

For this work, XPS measurements were made on thin films of Ir, IrO_x, Pd, PdO_x, Pt, and PtO_x deposited via RF sputtering onto 5 x 5 x 0.5 mm substrates of quartz, which were fixed to the sample bar using carbon tape and electrically connected to the sample bar using silver paste to avoid sample charging. XPS measurements of the thin films were taken before and after Ar ion milling of 180 s duration using an argon ion source. The area under the peaks of the relevant materials was calculated using the CasaXPS software package in order to obtain the ratio of metal to oxygen atoms present at the thin film surface. The XPS measurements of the iridium and platinum oxidations series was repeated twice, as the measurements were sensitive to surface oxidation of the thin film material.

The XPS measurements were performed by Dr Colin Doyle, Faculty of Engineering, University of Auckland, New Zealand. The resulting spectra from all XPS measurements are included in Appendix A4.5, Figures A4.5.1 – A4.5.7. Due to the potential surface oxidation occurring between fabrication and analysis, the spectra cannot be used to extract elemental ratios of the noble metals to oxygen. However, the relative intensity of the noble metal and oxygen peaks over a complete oxidation series does show a trend in the oxidation of the material, supporting the RBS measurements detailed in Section 4.1.5.

Surface-level stoichiometry of the ratio between oxygen and noble metals were calculated from the XPS measurements by integrating the areas under the relevant oxygen and noble metal peaks. The XPS measurements of Ir/IrO_x, Pd/PdO_x, and Pt/PtO_x in Figures A4.5.5 – A4.5.7 included separate high-resolution scans of the O 1s peak and the relevant noble metal doublet peaks (Ir $4f_{5/2}$/Ir $4f_{7/2}$, Pd $3d_{3/2}$/Pd $3d_{5/2}$, and Pt $4f_{5/2}$/Pt $4f_{7/2}$). The CasaXPS software package was used to model the area under the relevant peaks, with examples shown in Figures 4.8 – 4.9.

The area under the peaks was calculated by fitting a Shirley background to the dataset, followed by fitting overlapping Gaussian peaks to sum to the measured XPS peaks. The O 1s peak measured for all RF-sputtered films was modelled by three Gaussian peaks for O^{2-}, O^{-}, and O, as shown in Figure 4.8 [4.17 – 4.18]. The noble metal doublet peaks were modelled by six Gaussian peaks summing to three sets of doublets, as shown in Figure 4.9. The noble metal Pt/PtO_x doublet peaks were modelled as Pt, Pt^{2+}, and Pt^{4+} on the Pt $4f_{5/2}$ and Pt $4f_{7/2}$ doublet [4.18 – 4.19].

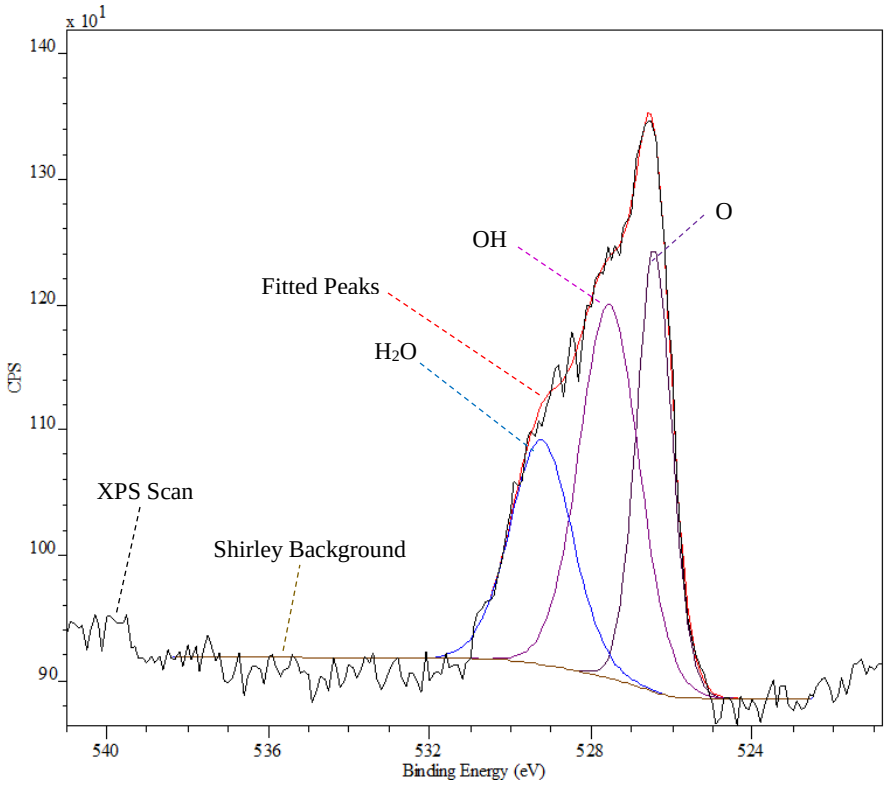

Figure 4.8: O^{2-}, O^{-}, O Fitted Peaks for O 1s of RF-Sputtered 2.0:10 (O_2:Ar) PtO_x

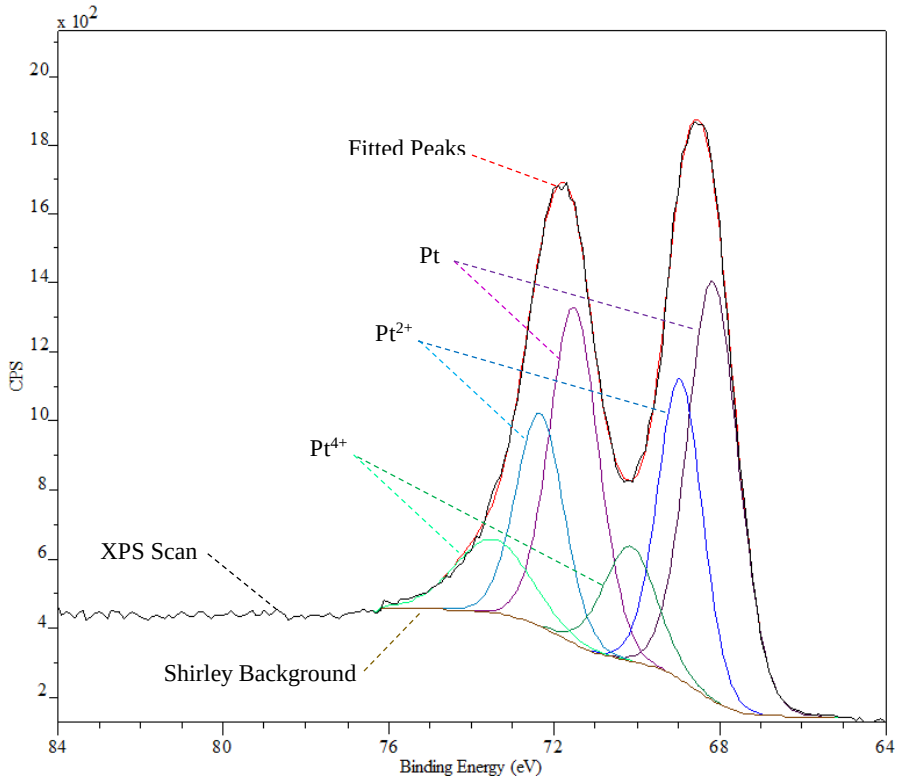

Figure 4.9: Pt $4f_{5/2}$, Pt $4f_{3/2}$ Fitted Peaks for Pt, Pt^{2+}, Pt^{4+} of RF-Sputtered 2.0:10 (O_2:Ar) PtO_x

The Ir/IrO_x doublet peaks were modelled as Ir, Ir^{2+}, and Ir^{4+} on the Ir $4f_{5/2}$ and Ir $4f_{7/2}$ doublet [4.20]. The Pd/PdO_x doublet peaks were identified as Pd, Pd^{2+} and Pd^{4+} on the Pd $3d_{3/2}$ and Pd $3d_{5/2}$ doublet [4.20]. The stoichiometric ratio of oxygen to metal species was calculated using Equation 4.18, where *A* is the area of the doublet with the corresponding oxidation (i.e. A_{PtO_2} is the summed area of the Pt^{4+} $4f_{5/2}$ and the Pt^{4+} $4f_{7/2}$ Gaussian peak); as this calculation focused only on the noble metal doublet, a yield factor was not required [4.19]. However, as XPS is a surface-level characterisation, surface-level oxidation of the RF-sputtered films can make these results unreliable.

$$\frac{O}{Pt} = \frac{2A_{PtO_2} + A_{PtO}}{A_{PtO_2} + A_{PtO} + A_{Pt}} \quad (4.18)\ [4.19]$$

4.1.7 X-ray Diffraction

X-ray Diffraction (XRD) is another non-destructive technique used to analyse the structure of thin film materials, such as identifying the presence, size, and orientation of crystal planes. A collimated beam of mono-chromatic X-rays of known wavelength, λ, is directed into a thin film of material. The X-rays are diffracted by the crystal planes within the material, and are collected at the detector in counts over time. Following Bragg's law, given in Equation 4.19, the spacing, *d*, between crystal planes can be calculated from the diffraction angle, θ, of the diffracted X-rays, and used to calculate the lattice constant of the material [4.15, 4.22].

$$n\lambda = 2d \sin\theta \quad (4.19)$$

The intensity and width of the peaks in an XRD spectrum can be used to determine the degree of crystal order orientation [4.15]. Sharp, narrow peaks in XRD spectra indicate long-range crystalline order; broad peaks indicate amorphous material [4.15]. The crystal phases identified by XRD can be used in conjunction with RBS to confirm the presence of chemical compounds by matching the chemical composition to the crystal phases identified by RBS [4.15].

As the X-rays are capable of penetrating the thin film and diffracting off deeper crystal planes, XRD can be used for characterising the bulk of the material, rather than the surface, compared to XPS [4.15]. Typical material thicknesses used for XRD of films with species of high atomic number (such as Ir, Pd, and Pt) are at least 10 – 100 µm in order to produce good diffraction patterns, due to the attenuation of the X-rays [4.15]. High Z materials thinner than 10 µm require special techniques, such as Grazing-incidence XRD (GIXRD), and rocking curves [4.15].

GIXRD limits the penetration of the X-ray beam by directing the beam at low incidence angles, 1° – 3°, while the detector was rotated through a 2θ angle of 20 – 90°, as shown in Figure 4.10. GIXRD can be used to obtain diffraction patterns on films as thin as 200 Å [4.15, 4.23 – 4.24]. The spectra produced by grazing-incidence XRD indicates whether the thin film material is polycrystalline, resulting in thin peaks, or amorphous, resulting in a single broad peak [4.22].

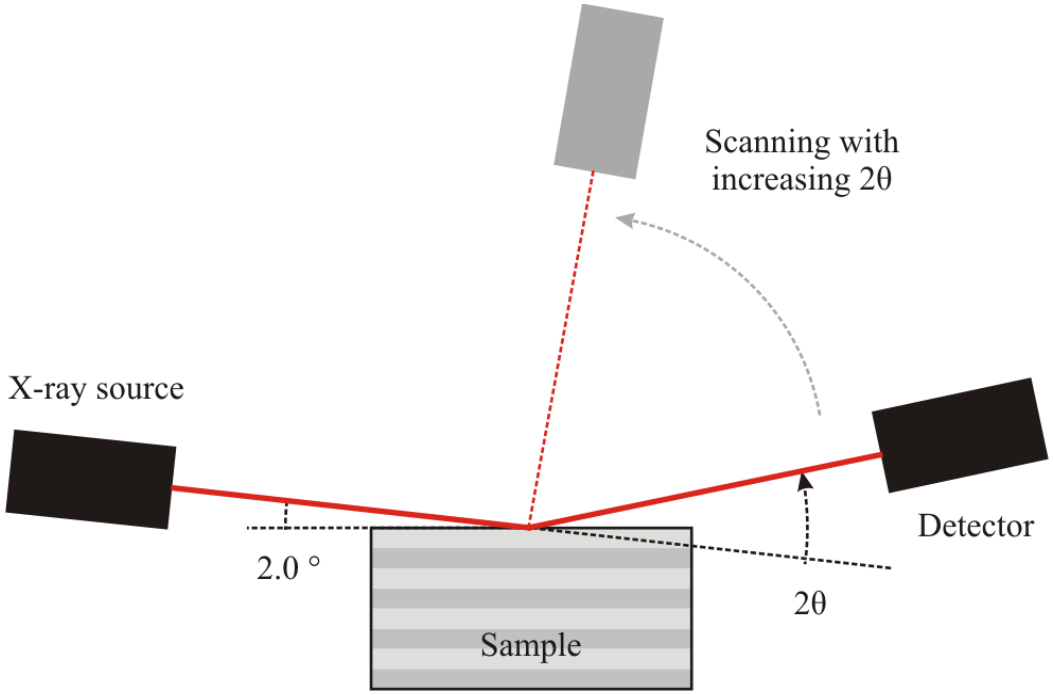

Figure 4.10: Grazing Incidence X-ray Diffraction (GIXRD) Diagram

For this work, XRD measurements were made on thin films of Ir, IrO_x, Pt, and PtO_x deposited via RF sputtering onto 5 x 5 mm substrates of quartz. The XRD measurements were performed by Adam Hyndman, Department of Physics and Astronomy, University of Canterbury, New Zealand, using a Bruker D8 Advance diffractometer with a cobalt radiation x-ray source (CoKα = 1.78897).

4.2 Schottky Contact Electrical Characterisation

The contacts fabricated in this work were characterised primarily by electrical measurements of current-voltage (I-V) characteristics under dark and wavelength-specific illumination to determine rectification ratio, R_R, ideality factor, η, and zero bias effective barrier height, Φ_B, of the fabricated contacts. Capacitance-voltage (C-V) characteristics were also measured under dark conditions.

The photoresponse of a device was characterised by measuring the current through the device over time using a fixed bias in dark conditions with intervals of visible and UV light exposure. The

fixed bias voltage was varied across multiple exposures to study the impact of negative bias stress on photoresponse. The electrical response of the devices in atmosphere was compared to their response under a constant flow of pure nitrogen gas to investigate the impact of atmospheric gases on the photoresponsivity.

4.2.1 Parameter Analyser and Probe Station

The electrical measurements of Schottky contact in this work were measured using the Hewlett-Packard 4155A Semiconductor Parameter Analyser and the Cascade Microtech, Inc. Summit™ 11000 Manual Wafer Probe Station, shown in Figure 4.11. A full list of the equipment and accessories used in this work can be found in Appendix A3.3.

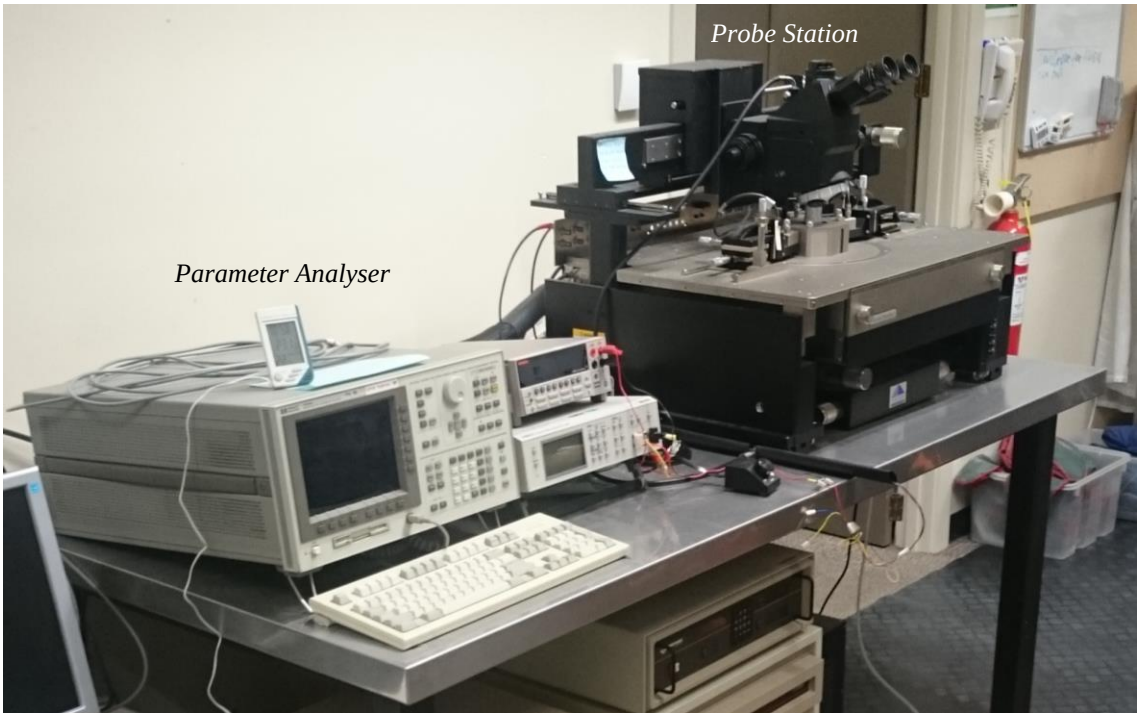

Figure 4.11: Parameter Analyser (Left) and Probe Station (Right) Equipment Setup

4.2.2 Current-Voltage Dark Measurements

Two Cascade Microtech, Inc. Model 107-158 5µm Radius Replaceable Coaxial Probes housed in two Cascade Microtech, Inc. DPP220 Probe Positioners were connected from the probe station to the parameter analyser using triaxial cable. The two probes are shown making electrical contact with an ohmic contact (left) and a Schottky contact (right) of a particular device in Figure 4.12.

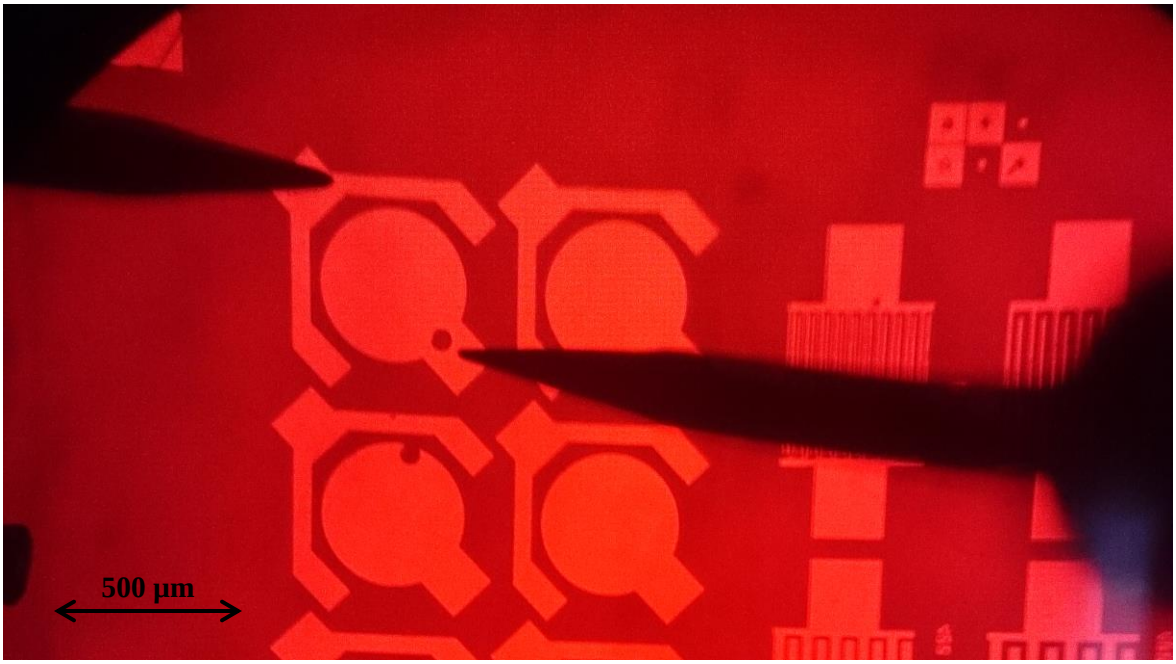

Figure 4.12: Probes in Electrical Contact with Ohmic (Left) and Schottky Contact (Right)

The ohmic contact probe was set as the 'common' channel, while the Schottky contact probe was set to the 'variable' channel, in order to bias the Schottky contact. The parameters listed in Table 4.2 were used to measure I-V characteristics under dark, atmospheric conditions. The parameter analyser was limited by a current measurement range of range of 10 fA – 100 mA. A double sweep measurement was used to measure any hysteresis present in the devices; for example, when measuring with increasing and decreasing voltage biases. An example plot of raw I-V data is shown in Figure 4.13.

Table 4.2: Dark I-V Measurement Parameters for Forward and Reverse Bias

Parameter	Forward Bias Measurement	Reverse Bias Measurement
Start	0 V	0 V
Stop	2 V	-2 V
Step	4 mV	-4 mV
Data Points	1002	1002
Sweep	Double	Double
Compliance	100 mA	100 mA

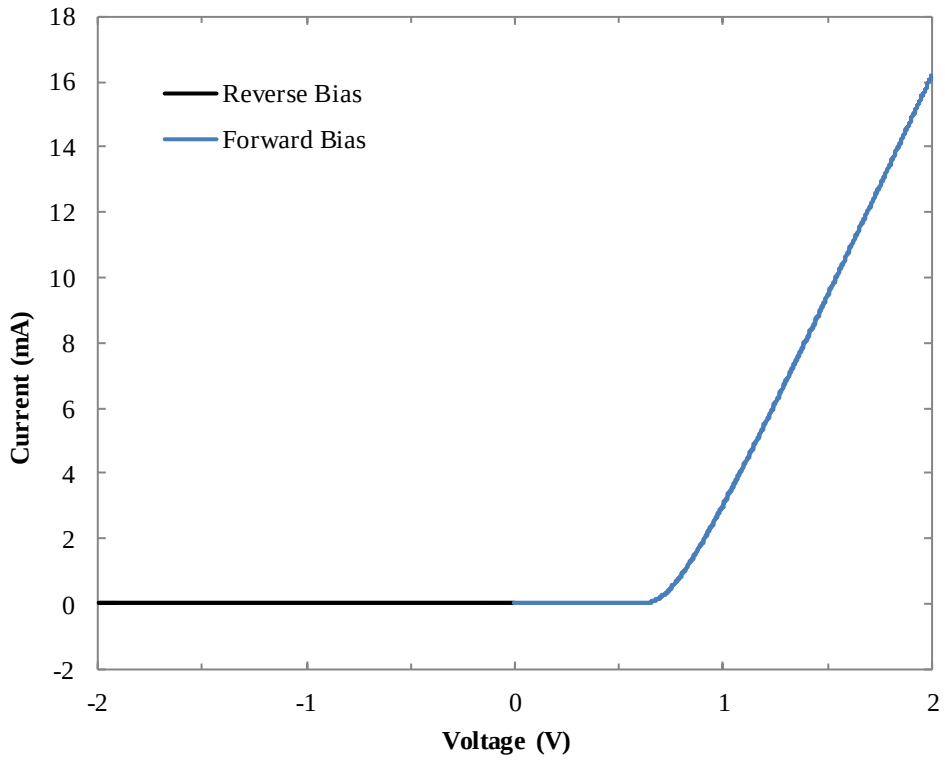

Figure 4.13: Linear Plot of Dark I-V Characteristics of 3.0:10 (O_2:Ar) PdO_x Contact 53

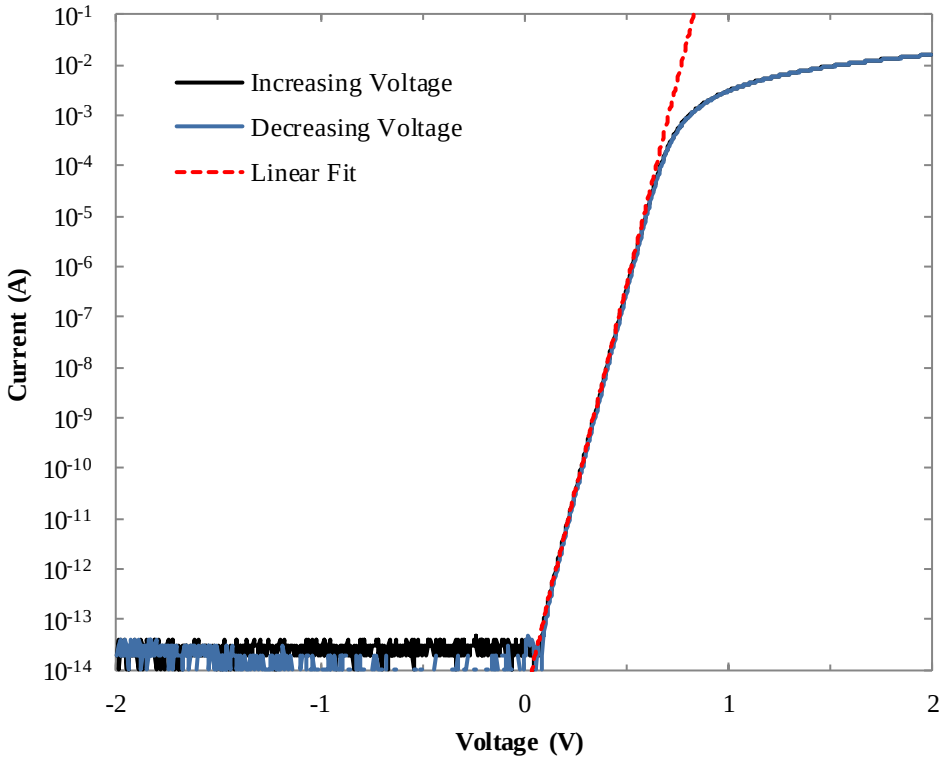

Figure 4.14: Log-Linear Plot of Dark I-V Characteristics of 3.0:10 (O_2:Ar) PdO_x Contact 53 with Least Squares Fit of the Linear Region Between $Log_{10}(I)$ and V in Forward Bias

As discussed in Section 2.3, the Schottky contact current can be modelled by pure thermionic emission in the forward bias direction and a corresponding linear trend can be observed on a graph of natural log of the current versus voltage, typically between 0 – 1 V, using Equations 4.20 – 4.21 in Table 4.3. In Table 4.3, V_D is contact voltage, I is contact current, and I_s is saturation current. The ambient temperature, T, was recorded during individual measurements in Kelvin, while Boltzmann's constant, k, was taken to be 1.38 x 10^{-23} JK^{-1} [4.8]. The theoretical Richardson Constant, A^*, of ZnO used in this work was 32 $Acm^{-2}K^{-2}$ [4.14]. The Schottky contact active area used was 134000 μm^2, as detailed in Section 3.1.

Using the assumption that the I-V characteristics of the Schottky contact could be modelled purely by thermionic emission, a least squares fit was used to determine the gradient, $\frac{\partial V_D}{\partial(\ln(J))}$, and intercept, J_s, of the linear region of the log-linear plot of the I-V characteristics as shown in Figure 4.14. The ideality factor and effective barrier height were calculated from the gradient and intercept using Equations 4.22 and 4.23 respectively. Image force lowering effect was not factored into the calculations of Φ_B. The rectification ratio was calculated as a ratio (in orders of magnitude) between the forward and reverse bias currents at ±2 V, as shown in Equation 4.24.

For this work, I-V characteristics of Schottky contacts will be presented in the format of log-linear graphs of current and voltage, and shown in Figure 4.14, in order to visually observe the rectification ratio, and the straight-line fit of the exponential forward-bias increase in current.

Table 4.3: Schottky contact I-V Characterisation, Units and Equations [4.8, 4.12 – 4.14]

Parameter	Symbol	Unit	Equation	Equation Number
Current Density	I	Acm^{-2}	$I = I_s\left(e^{\left(qV/nkT\right)} - 1\right)$	(4.20)
Saturation Current Density	I_s	Acm^{-2}	$I_s = AA^*T^2e^{\left(-q\Phi_B/kT\right)}$	(4.21)
Ideality Factor	η		$\eta = \frac{q}{kT}\left(\frac{\partial V}{\partial(\ln(I))}\right)$	(4.22)
Effective Barrier Height	Φ_B	eV	$\Phi_B = \frac{kT}{q}\ln\left(\frac{AA^*T}{I_s}\right)$	(4.23)
Rectification Ratio	R_R	Orders of magnitude	$R_R = \frac{log_{10}(I\|_{V=+2})}{log_{10}(I\|_{V=-2})}$	(4.24)

4.2.3 Capacitance-Voltage Dark Measurements

In order to verify the effective barrier height of the devices from the dark I-V measurements, dark C-V measurements were performed on a selection of Schottky contacts from each array of identical devices on the same substrate. Using the probe station described in Section 4.2.2, two probes were used to make electrical contact across a device. The probes were connected to the Philips Fluke PM6303A Automatic RCL Meter using coaxial cable. The SMU Instruments Keithley 2400 SourceMeter® was used to apply a bias across the device while the capacitance was measured by the RCL Meter. The bias applied was from -1.5 V to 0.5 V in steps of 50 mV, for a single sweep. The least squares method was used to fit a linear trend to a plot of $\frac{1}{C_j{}^2}$ against voltage, V, where C_j is the capacitance per device area, and ε_S is the effective permittivity of the material. The gradient and intercept of the least squares fit was used to calculate N_D, the net donor density, V_{bi}, the built-in potential, respectively using Equations 4.25 – 4.27. The depletion layer width, W, was calculated using Equation 4.28.

Table 4.4: Schottky Contact C-V Characterisation, Units and Equations [4.8]

Parameter	Symbol	Unit	Equation	Equation Number
Capacitance per unit Area	C_j	F·cm^{-2}	$\frac{1}{C_j{}^2} = \frac{2(V_{bi} - V)}{q\varepsilon_s N_D}$	(4.25)
Net Donor Density	N_D	atoms·cm^{-3}	$N_D = \frac{-2}{q\varepsilon_s \left(\frac{\partial}{\partial V} \left(\frac{1}{C_j{}^2} \right) \right)}$	(4.26)
Built-In Potential	V_{bi}	V	$V_{bi} = V\vert_{\frac{1}{C_j{}^2}=0}$	(4.27)
Depletion Layer Width	W	cm	$W = \sqrt{\frac{2\varepsilon_s(V_{bi} - V)}{qN_D}}$	(4.28)

A plot of a raw dark C-V measurement is shown in Figure 4.15 for 3.0:10 (O_2:Ar) RF-sputtered IrO_x Schottky contact to bulk ZnO is shown in Figure 4.15. For this work, C-V characteristics of Schottky contacts will be presented in the format of $\frac{1}{C_j{}^2}$ against voltage, such as Figure 4.16, in order to observe the intercept of V_{bi} with increasing oxygen incorporation.

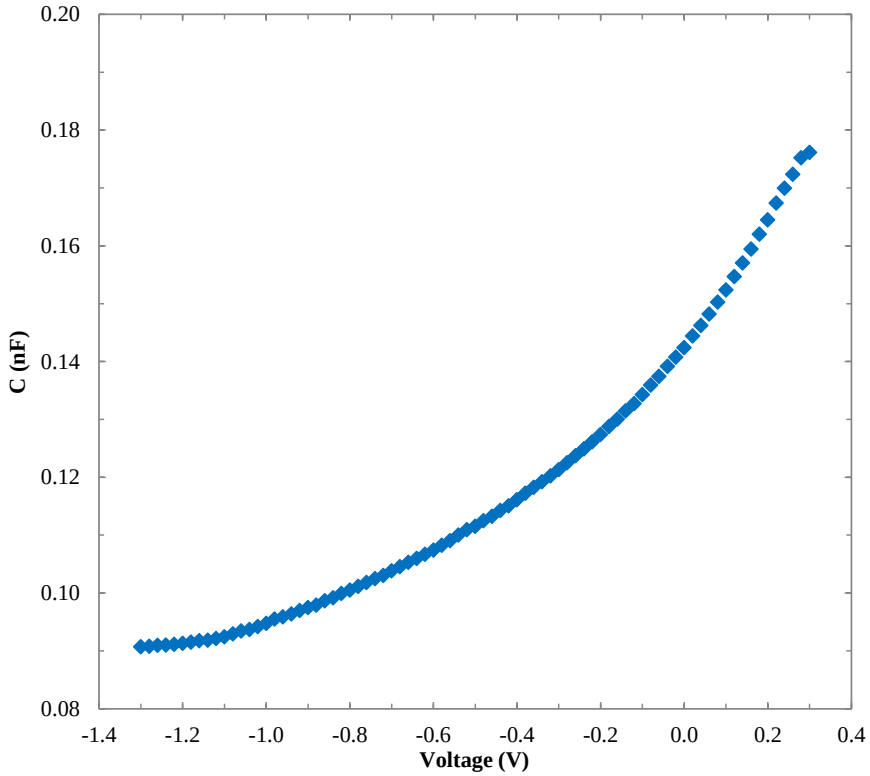

Figure 4.15: Plot of Dark C-V Characteristics of 2.0:10 (O_2:Ar) IrO_x Contact 32

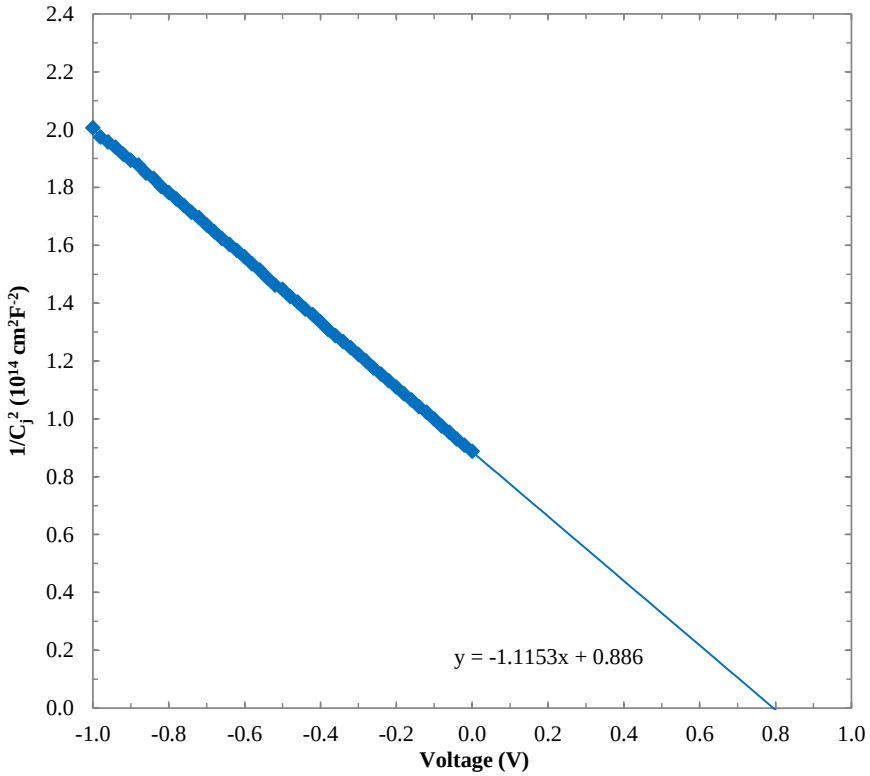

Figure 4.16: $1/C_j^2$ Plot of Dark C-V Characteristics of 2.0:10 (O_2:Ar) IrO_x Contact 32

4.2.4 Photoresponse Measurements

As one of the focuses of this work was to develop UV photodetectors on ZnO, the photoresponse of the Schottky contacts was a critical parameter. The Schottky contacts were contacted using the probe station in dark conditions, which was connected to the parameter analyser, as described in Section 4.2.2. A constant bias was applied across the contact, and the resulting current, *I*, was recorded as a function of time, *t*. The photoresponse of the contact was characterised by the change in current after the application of a particular light source, as well as the rise-time and fall-time of the photoresponse current.

The wavelengths used in this work were 625 nm (red), 610 nm (orange), 505 nm (green), 470 nm (blue), and 365 nm (UV). The visible wavelengths were applied by individual LEDs connected to a Keithley 2400 constant current source to provide an irradiation of 300 mW (2.5 Wcm^{-1}) at the contact surface, as shown in Figure 4.17. The UV light source used in this work was the Norland Products Inc. UVA Splice Lamp Model P/N 5200, with a peak emission at 365 nm. The spectral response of the UV lamp can be found in Appendix A4.6, courtesy of Dr Salim Elzwawi, Department of Electrical and Computer Engineering, University of Canterbury, New Zealand. The UV lamp provided 1 W over the substrate surface, and therefore the current response of the Schottky contacts to the LEDs was scaled by a factor of 3⅓ to match the intensity of the LED irradiation.

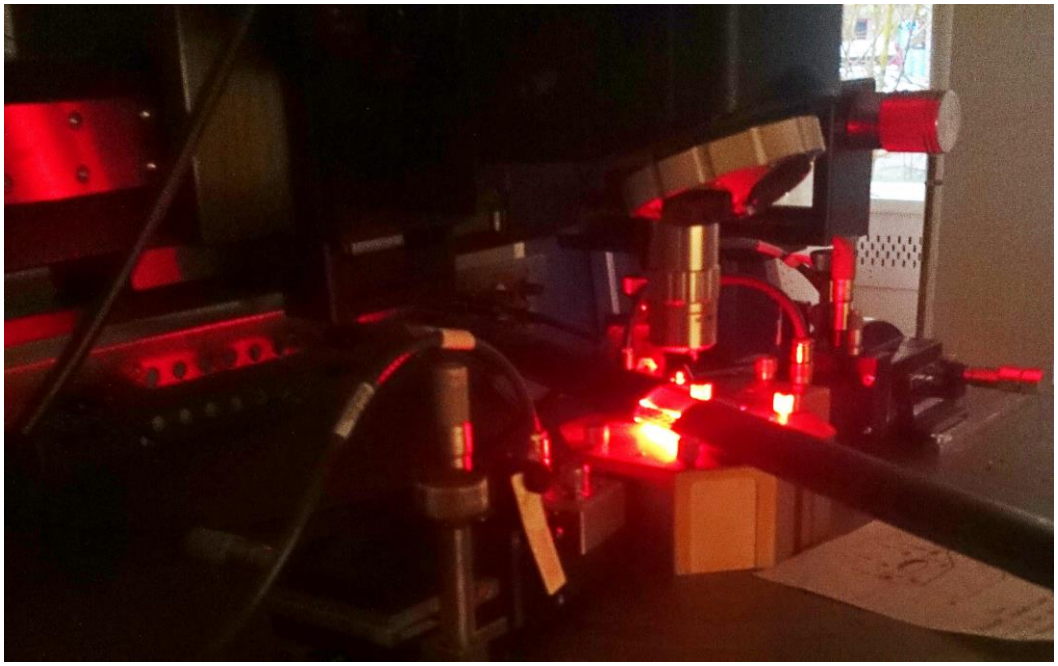

Figure 4.17: Exposure Setup of Schottky contacts to 625 nm LED Busbar Light Source (Actual Measurements Performed in Dark Conditions)

4.2.4.1 Varying Wavelength

A baseline measurement in dark conditions was performed prior to exposure to light sources. The photoresponse measurements were carried out in order of decreasing wavelength in order to minimise the effects of persistent photoconductivity (PPC), detailed in Section 2.3.4. As the photoresponse of the contacts to the visual spectrum showed no PPC, single photoresponse measurements were made for each of the four visual wavelengths with the parameters listed in Table 4.5. The photoresponse to the UV wavelength was repeated five times in immediate succession to study the cumulative effect of PPC, with parameters also listed in Table 4.5.

Table 4.5: Measurement Parameters for Single-Exposure Visual and UV Photoresponse

Parameter	LED Photoresponse Measurement	UV Photoresponse Measurement
Wavelengths	625 nm, 610 nm, 505 nm, 470nm	365 nm
Bias	-1 V	-1 V
Step	1 s	1 s
Exposure Start	30 s	30 s
Exposure End	60 s	60 s
Measurement End	600 s	600 s
Number of Measurements	1	5

To further study the effects of cumulative PPC on successive UV exposure, pulsed photoresponse measurements were performed on the devices, with parameters listed in Table 4.6. As the relaxation time between the UV pulses in the pulsed measurements was only 30 s (compared to the 540 s during the single-exposure measurements) the fall-time, t_{fall}, of the current response was calculated by extrapolation of the PPC decay curve, as shown in Figures 4.18 – 4.19. The rise-time and fall-time calculations in this work are calculated as the time from 10% to 90% of the photocurrent response on a log-linear plot of device current with time, as shown in Figure 4.19.

Table 4.6: Measurement Parameters for Pulsed UV Photoresponse

Parameter	UV Photoresponse Pulsed Measurement
Bias	-1.0 V
Step	0.5 s
Exposure Start	(60x + 30) s, (x = 0 to 19)
Exposure End	(60x + 60) s, (x = 0 to 19)
Measurement End	1800 s
Number of Exposures	20

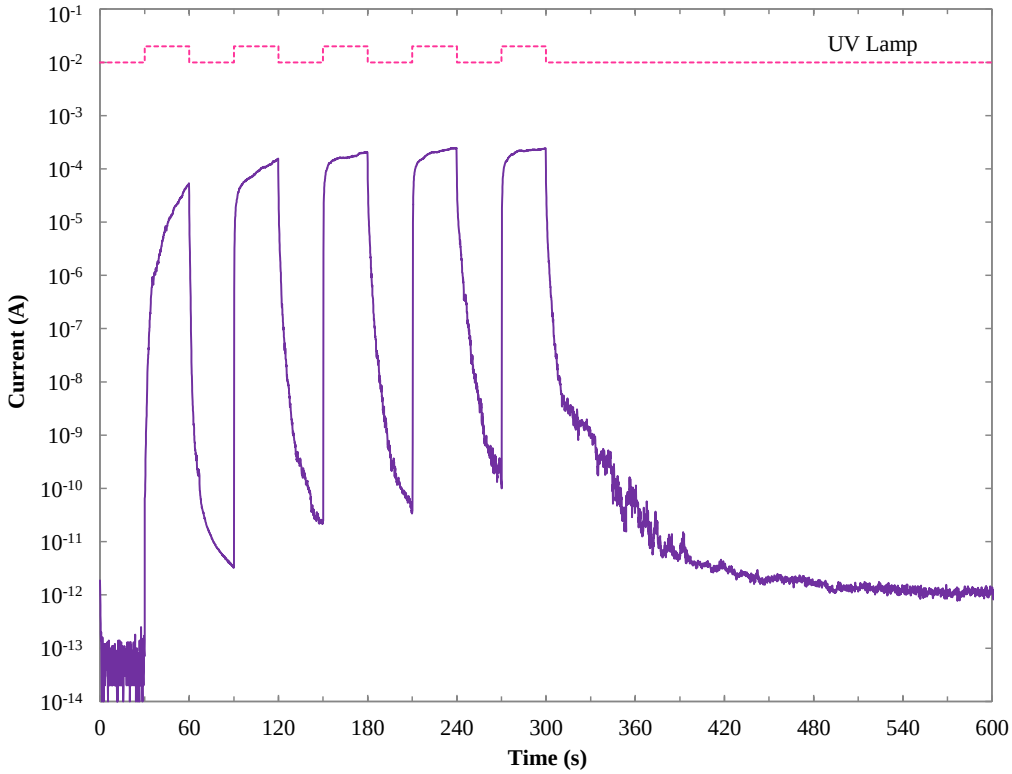

Figure 4.18: Pulsed UV Response of 4.0:10 (O_2:Ar) AgO_x Schottky Contact with -2.0 V Bias

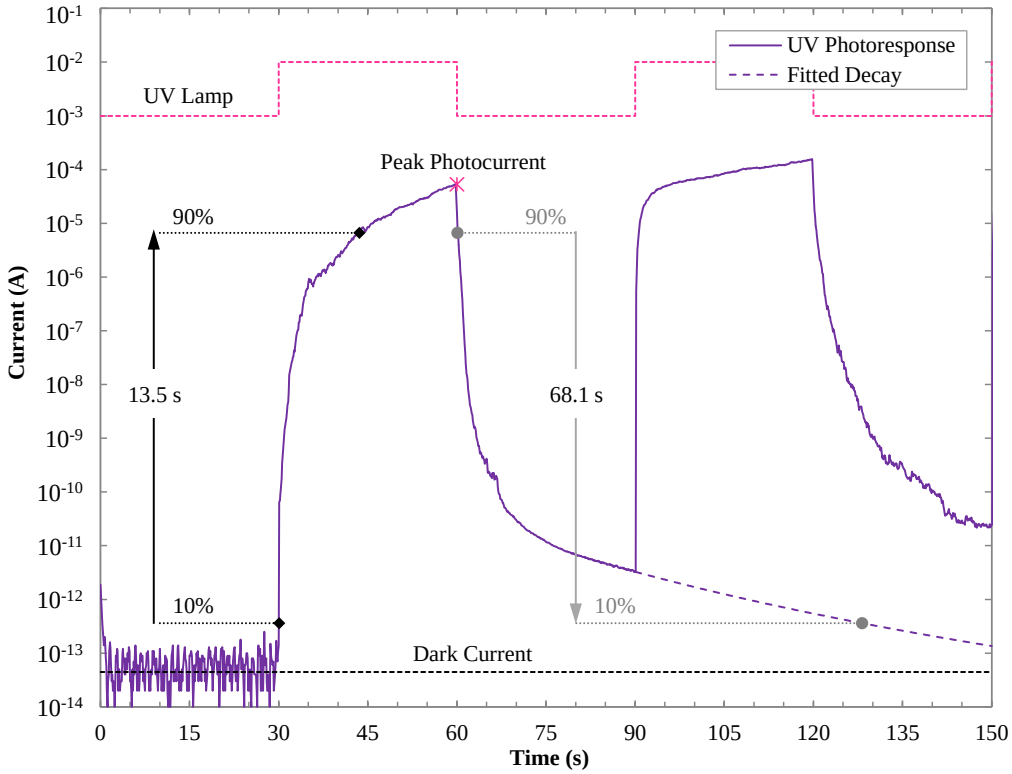

Figure 4.19: Calculation of Rise-Time and Fall-Time of Pulsed UV Response of AgO_x Contact

The UV photoresponse of a significant number of noble metal-oxide Schottky contacts showed a characteristic charging and discharging curves in a log-linear plot, shown in Figures 4.18 – 4.19. For pulsed UV exposure measurements, where the PPC did not have sufficient time to decay down to the initial dark current, a fitted decay curve was used to calculate the estimated decay time. As the curves were observed in a log-linear plot, the rise-time and fall-time was calculated from 10% to 90% of the difference of ln(I_{dark}) to ln(I_{peak}), shown in Figure 4.19. However, the level of apparent noise in the decaying current signal, as observed in Figures 4.18 – 4.19, introduces significant errors to the extrapolation of the decay curve. This is especially significant for devices with semi-permanent PPC, where the dark current does not appear to decay to initial current within the time frame of several hours.

4.2.4.2 Varying Device Bias

Although the standard photoresponse measurements in this work were performed with a -1 V bias across the contacts, the bias was varied in order to investigate the effect of contact bias on UV photoresponsivity, and particularly the PPC. For these tests, a single measurement was performed with five 30 s exposures of UV light separated by 30 s intervals, with the parameters listed in Table 4.7. A dark I-V measurement, as described in Section 4.2.2, was taken between each bias measurement in order to monitor changes in the electrical characteristics.

Table 4.7: Measurement Parameters for UV Photoresponse with Varying Bias

Parameter	UV Photoresponse Measurement with Varying Bias				
Bias	0.1 V, 0 V, -0.1 V, -0.2 V, -0.5 V, -1.0 V, -2.0 V, -4.0 V, -6.0 V, -8.0 V				
Step	1 s				
Exposure Start	30 s,	90 s,	150 s,	210 s,	270 s
Exposure End	60 s,	120 s,	180 s,	240 s,	300 s
Measurement End	600 s				
Number of Measurements	1				

4.2.4.3 Varying Gas Environment

In Section 2.3.6, a relationship was suggested between the persistent photoconductivity of ZnO devices after exposure to UV light, and the exchange of chemisorbed oxygen from the ZnO surface. To explore this relationship, UV photoresponse measurements were carried out in both atmospheric conditions, and in flowing nitrogen gas with the parameters listed in Table 4.8. Any oxygen

desorbed from the ZnO surface during UV exposure would be removed with the nitrogen gas flow, and would not be available to be reabsorbed by the ZnO surface after the removal of the UV light. A change in the persistent photoconductivity under a constant flow of nitrogen gas would support the involvement of oxygen desorption and reabsorption in this effect.

The UV photoresponse test detailed in Section 4.2.4.1 was performed under atmospheric conditions, and again under a constant flow of nitrogen. The nitrogen flow was removed after 30 min in order to observe whether the return of atmospheric gases would accelerate the decay of the persistent photoconductivity.

Table 4.8: Parameters for UV Spectrum Photoresponse in Atmosphere and in Nitrogen Gas

Parameter	UV Light Exposure in Atmosphere	UV Light Exposure in Nitrogen Gas
Bias	-1 V	-1 V
Step	1 s	1 s
Data Points	5000	5000
Exposure Start	120 s	120 s
Exposure End	150 s	150 s
Nitrogen Start	-	0 s
Nitrogen End	-	2000 s
Measurement End	5000 s	5000 s
Number of Exposures	1	5

4.2.5 High Temperature Measurements

Dark I-V characteristic measurements, described in Section 4.2.2, were also performed over a range of temperatures in order to assess the thermal stability of the Schottky contacts, and also to experimentally determine the Richardson constant for ZnO. The temperature of the Cascade Microtech, Inc. 8-inch/200mm Gold-Plated Thermal Chuck of the probe station was set by the Temptronic Corp. Model TP03000 ThermoChuck® Thermal Chuck Controller. Thermal contact was made between the thermal chuck and the bulk ZnO substrate using MR-Direct GE/IMI 7031 Varnish.

The temperature of the thermal chuck was increased from room temperature 293 K (20°C) to 453 K (180°C), and then decreased back to room temperature, in steps of 10 – 20 K. After the thermal chuck had reached its programmed temperature, the sample was left for a 10 min periods for temperature steps of 20 K to reach thermal equilibrium, before dark I-V measurements were made.

The electrical probes were disconnected from the Schottky contact surface between temperature tests to avoid damage to the contact material due to thermal expansion. However, repeated contacting of the Schottky contact was also a potential source of damage to the devices. The probes were positioned manually, and could short the Au capping layer to the ZnO surface and permanently turn the Schottky contact into an ohmic contact if too much pressure was applied and the probe penetrated the metal-oxide layer. Four Schottky contacts were tested as the temperature was increased, and two of those contacts were tested as the temperature was decreased, producing redundant series in the case of irreversible physical damage to a single contact.

4.2.5.1 Experimental Richardson Constants

In Section 4.2.2, the theoretical Richardson constant was used in the calculation of Schottky contact effective barrier height. The theoretical Richardson constant for ZnO, 32 $Acm^{-2}K^{-2}$, was calculated using Equation 4.30 in Table 4.9 [4.14, 4.25], where m^* is the effective mass of the conduction electrons in +c bulk ZnO [4.14], m_0 is the mass of an electron in free space, 9.11 x 10^{-31} kg, h is Planck's constant, 6.63 x 10^{-34} Js, and J_s is the current density.

Table 4.9: Richardson Constant Equations [4.14, 4.25]

Parameter	Symbol	Unit	Equation	Equation Number
Effective Mass of ZnO Conduction Electron	m*	kg	$m^* = 0.27m_0$	(4.29)
Theoretical Richardson Constant	A*	$Acm^{-2}K^{-2}$	$A^* = \frac{4\pi q m^* k^2}{h^3}$	(4.30)
Experimental Richardson Constant	A*	$Acm^{-2}K^{-2}$	$\ln\left(\frac{J_s}{T^2}\right) = \frac{-q\Phi_B}{kT} + \ln(A^*)$	(4.31)

The Richardson constant can be experimentally determined by measuring the dark I-V characteristics of a Schottky contact over a range of temperatures. Using the relationship in Equation 4.31, a Richardson plot can be created to fit a linear trend between $ln\left(\frac{J_0}{T^2}\right)$ and $\frac{1000}{T}$ using the least squares method. The intercept of the linear trend produces an experimental Richardson constant, following Equation 4.30. An example of a Richardson plot is given in Figure 4.20.

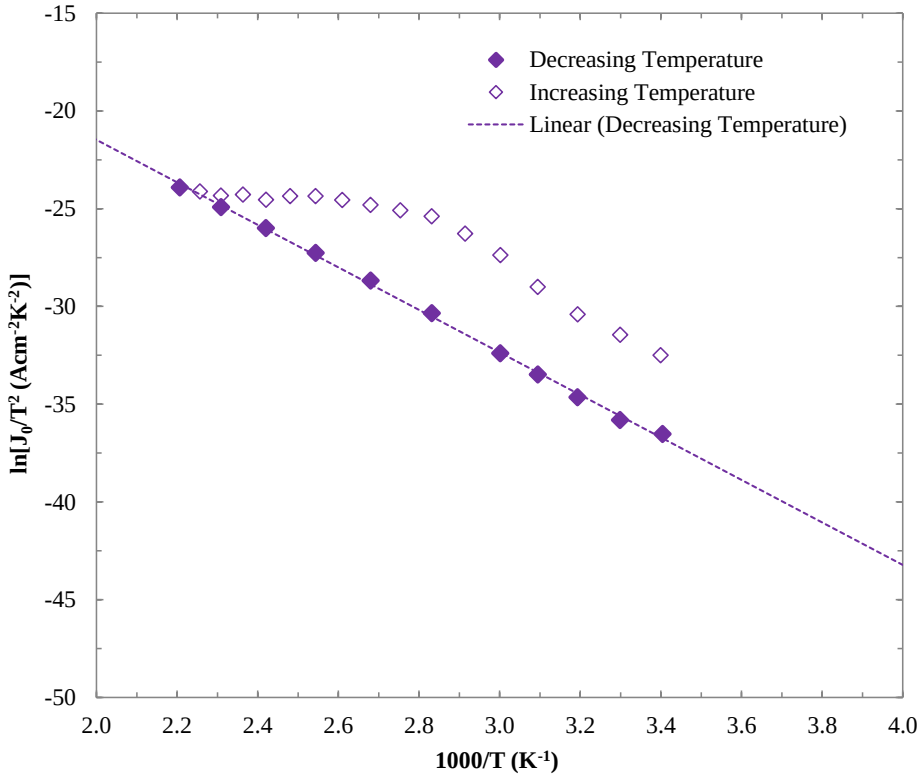

Figure 4.20: Richardson Plot of PLD IrO_x Schottky Contacts on Low-Li (0001) ZnO from Dark I-V Characteristics with Temperature Range of 293 – 453 K

Fitting a linear trend to the Richardson plot relies on a constant effective barrier height, Φ_B, over the temperature series. In this work, the range of temperatures used to determine Richardson constant was 293 – 453 K. This temperature range was observed to cause an annealing of the Schottky contacts, increasing the effective barrier height with increasing temperature. The Richardson constant analysis was therefore performed on Schottky contacts with I-V characteristics taken with decreasing temperatures from 453 – 293 K to avoid variation in the barrier height.

REFERENCES

[4.1] Stout, K. J., Blunt, L., (2000), *Three Dimensional Surface Topography*, London, U.K.: Elsevier, pp. 2-18, 70-93.

[4.2] Veeco Instruments Inc., (2009), *Dektak 150 Surface Profiler*, Retrieved from http://www.upc.edu/sct/documents_equipament/d_81_id-399.pdf

[4.3] Brooker Corporation, (2016), *p22 Contact Mode AFM main* [Image], Retrieved from http://blog.brukerafmprobes.com/guide-to-spm-and-afm-modes/contact-mode-afm/

[4.4] Marczenko, Z., Balcerzak, M., (2000), Separation, Preconcentration and Spectrophotometry in Inorganic Analysis, *Analytical Spectroscopy Library*, *Vol. 10*, Warsaw, Poland: Elsevier, pp. 26-38.

[4.5] Veeco Instruments Inc. (2004). *Dimension 3100 Manual*. Retrieved from https://www.scu.edu/media/school-of-engineering/photos/cns/Dimension3100D-Manual.pdf

[4.6] Binning, G., Quate, C. F., Gerber, Ch., (1986), Atomic Force Microscope, *Physical Review Letters*, 56 (9) pp. 930-933.

[4.7] Hall, E. H., (1879), On a New Action of the Magnet on Electric Currents, *American Journal of Mathematics*, 2 (3) pp. 287-292.

[4.8] Sze, S. M.., (2002), *Semiconductor Devices, Physics and Technology, 2nd Ed.*, Hoboken, N.J., U.S.A: John Wiley.

[4.9] van der Pauw, L. J., (1958), A Method of Measuring Specific Resistivity and Hall Effect of Discs of Arbitrary Shape, *Philips Research Reports*, 13, 1, pp. 1-9.

[4.10] Nonnenmacher, M., O'Boyle, M.P., Wickramasinghe, H.K., (1991), Kelvin probe force microscopy, *Applied Physics Letters*, 58 (25), pp. 2921-2923.

[4.11] Melitz, W., Shen, J., Kummel, A.C., Lee, S., (2011), Kelvin probe force microscopy and its application, *Surface Science Reports*, 66 (1), pp. 1-27.

[4.12] Cheung, S.K., Cheung, N.W., (1986), Extraction of Schottky contact parameters from forward current-voltage characteristics, *Applied Physics Letters*, 49 (2), pp. 85-87.

[4.13] Allen, M.W., Weng, X., Redwing, J.M., Sarpatwari, K., Mohney, S.E., von Wenckstern, H., Grundmann, M., Durbin, S.M., (2009), Temperature-dependent properties of nearly ideal ZnO Schottky contacts, *IEEE Transactions on Electron Devices*, 56 (9), pp. 2160-2164.

[4.14] Sheng, H., Muthukumar, S., Emanetoglu, N.W., Lu, Y., (2002), Schottky contact with Ag on (11$\bar{2}$0) epitaxial ZnO film, *Applied Physics Letters*, 80 (12), pp. 2132-2134.

[4.15] Exarhos, G. J., (2010), *Characterization of Optical Materials*, Materials Characterization Series, New York, N.Y., U.S.A: Momentum Press.

[4.16] Frey, H., Khan, H. R., (2015), *Handbook of Thin-Film Technology*, Berlin, Germany: Springer Berlin Heidelberg., pp. 133-167.

[4.17] Sanjinés, R., Lévy, F., Aruchamy, A., (1989), Thermal Stability of Sputtered Iridium Oxide Films, *Journal of the Electrochemical Society*, 136 (6), pp. 1740-1743.

[4.18] Abe, Y., Yanagisawa, H., Sasaki, K., (1998), Preparation of oxygen-containing Pt and Pt oxide thin films by reactive sputtering and their characterization, *Japanese Journal of*

Applied Physics, Part 1: Regular Papers and Short Notes and Review Papers, 37 (8), pp. 4482-4486.

[4.19] Bancroft, G.M., Adams, I., Coatsworth, L.L., Bennewitz, C.D., Brown, J.D., Westwood, W.D., (1975), ESCA study of sputtered platinum films, *Analytical Chemistry*, 47 (3), pp. 586-588.

[4.20] Atanasoski, R.T., Atanasoska, L.L., Cullen, D.A., Haugen, G.M., More, K.L., Vernstrom, G.D., (2012), Fuel Cells Catalyst for Start-Up and Shutdown Conditions: Electrochemical, XPS, and STEM Evaluation of Sputter-Deposited Ru, Ir, and Ti on Pt-Coated Nanostructured Thin Film Supports, Electrocatalysis, 3 (3), pp. 284-297.

[4.21] Gabasch, H., Unterberger, W., Hayek, K., Klötzer, B., Kleimenov, E., Teschner, D., Zafeiratos, S., Hävecker, M., Knop-Gericke, A., Schlögl, R., Han, J., Ribeiro, F.H., Aszalos-Kiss, B., Curtin, T., Zemlyanov, D., (2006), In situ XPS study of Pd(111) oxidation at elevated pressure, Part 2: Palladium oxidation in the 10^{-1} mbar range, *Surface Science*, 600 (15), pp. 2980-2989.

[4.22] Hyndman, A. (2009). *Growth of Thin Films by Pulsed Laser Deposition for Applications in Spin Transport Electronics*, PhD Thesis, University of Canterbury, Christchurch, New Zealand.

[4.23] Holloway, P. H., Vaidyanathan, P. N., (2009), *Characterization of Metals and Alloys*, Materials Characterization Series, New York, N.Y., U.S.A: Momentum Press.

[4.24] Nishi, Y., Doering, R., (2007), *Handbook of Semiconductor Manufacturing Technology*, Second Edition, Boca Raton, F.L., U.SA: CRC Press.

[4.25] Crowell, C. R., (1965), The Richardson constant for thermionic emission in Schottky barrier contacts, *Solid-State Electronics*, 8 (4), pp. 395-399.

5 Characterisation of Sputtered Metal-Oxide Films with Varied Oxygen Content

This chapter contains the results of the optical and electrical characterisation of RF-sputtered noble metal and noble metal-oxide films fabricated simultaneously with the Schottky contacts analysed in Chapters 6 – 8. The noble metals and metal-oxide films explored in this chapter include Ag, AgO_x, Ir, IrO_x, Pd, PdO_x, Pt, and PtO_x. The optical characterisation of the films consists of transmission measurements. The electrical and structural characterisation of the films includes analysis of the crystal structure, surface potential, stoichiometry, and resistivity of the films.

5.1 RF-sputtered Metal-Oxide Films with Oxygen Content

During the fabrication of the RF-sputtered Schottky contacts detailed in Section 3, thin films were simultaneously deposited on quartz substrates in order to perform optical and electrical characterisation on the Schottky contact material. The films were optically characterised using transmission measurements described in Section 4.1.2. The crystal structure of the films was characterised using XRD, described in Section 4.1.7. Film thickness and surface potential was characterised using AFM and KPM, described in Sections 4.1.1.2 and 4.1.4 respectively. Film stoichiometry was characterised using XPS and RBS, Sections 4.1.6 and 4.1.5, and film resistivity was characterised using Hall effect measurements, described in Section 4.1.3.

The noble metals used in the fabrication of RF-sputtered Schottky contacts on bulk ZnO in this work were chosen for the formation energies of the corresponding metal-oxides per oxygen atom, as higher formation energy was found to correlate with higher Schottky barrier height on ZnO [5.1]. Ag, Ru, Ir, Pd, and Pt have some of the highest metal-oxide formation energies, as shown in Figure 5.1 [5.1 – 5.3]. The films characterised in this chapter are RF-sputtered Ag, AgO_x, Ir, IrO_x, Pd, PdO_x, Pt, and PtO_x. RF-sputtered Ru and RuO_x Schottky contacts were also fabricated and characterised, however due to the relatively lower quality of these devices in comparison with the other metal-oxide devices, investigation into RuO_x devices was deferred in favour of investigating IrO_x, PdO_x, and PtO_x. Film characterisation of AgO_x was complicated by the tendency of the films to visibly oxidise in an inhomogeneous manner within days of deposition, discussed in Section 5.2.

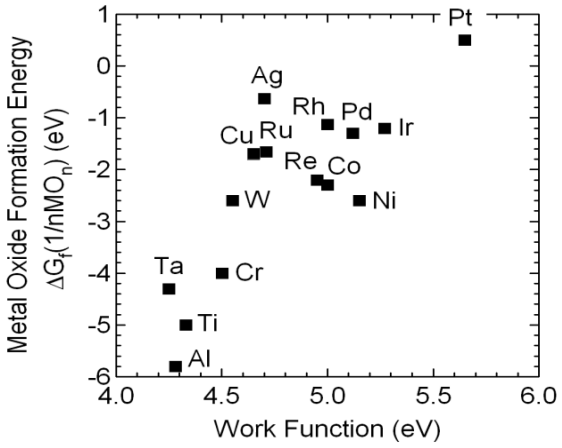

Figure 5.1: Free Energy of Metal-Oxides per Oxygen Atom [5.2, 5.4]

It has been shown by Allen *et al*., 2007, that the performance of RF-sputtered Ag Schottky contacts on bulk ZnO increased significantly with the addition of oxygen gas flow during RF-sputtering, producing AgO_x Schottky contacts with higher barrier heights (Φ_B) and lower ideality factors (η) [5.3]. The addition of oxygen gas during PLD growth of Ir, Pd, and Pt Schottky contacts on bulk ZnO also produced IrO_x, PdO_x, and PtO_x diodes with higher barrier heights, lower ideality factors, and a more pronounced polarity effect [5.5]. Plain metal Schottky contacts on bulk ZnO have previously been reported to have effective barrier heights as high as 0.6 – 1.0 eV, whereas the barrier heights of the metal-oxide Schottky contacts were reported between 0.9 – 1.2 eV [5.3, 5.5].

The increase in barrier height and diode quality with oxygen incorporation inspired the systematic investigation into RF-sputtered metal and metal-oxide Schottky contacts with controlled levels of oxygen incorporation on bulk ZnO that was performed in this work. In order to systematically investigate the effect of oxygen incorporation of the RF-sputtered films, the O_2 and Ar gas mixture present during RF-sputtering was varied by keeping the gas flow of Ar constant and increasing the gas flow of O_2. Plain metal Schottky contacts were fabricated in a 0.0:10 sccm (O_2:Ar) gas mixture, while the metal-oxide Schottky contacts were fabricated with mixtures of 0.5:10, 1.0:10 2.0:10, 3.0:10, 4.0:10, 5.0:10, and 7.0:10 sccm (O_2:Ar). An additional set of PtO_x devices were fabricated with 6.0:10, 7.0:10, 8.0:10, 9.0:10, and 10:10 sccm (O_2:Ar) gas ratios. The sputtering chamber was pumped down to a nominal 5.0×10^{-6} mbar before the addition of the reactive gases. The partial pressure of the 10 sccm Ar gas flow was typically 3.2×10^{-4} mbar. The partial pressure of 0.5 sccm to 10 sccm O_2 gas flow was 1.0×10^{-4} to 3.4×10^{-3} mbar, producing a process pressure (with RF plasma) of 3.4×10^{-3} to 6.0×10^{-3} mbar for the 0.5:10 to 10:10 (O_2:Ar) metal-oxide depositions. The RF-sputtering power was set to 50 W for all depositions. A 5 minute pre-sputter in pure Ar was completed before each deposition to clean the sputtering target surface.

5.2 Metal-Oxide Film Transparency

In order to observe the effects of oxygen incorporation in the RF-sputtered metal-oxide films, transmission measurements were performed using the Agilent Cary 600i UV-Vis-NIR Spectrophotometer, as detailed in Section 4.1.2. The transmission measurements were performed against a clean 5 x 5 x 0.5 mm quartz substrate reference sample. An initial zero-error measurement was performed between two clean reference quartz substrates before each measurement set of metal/metal-oxide films in order to remove the transmission characteristics of the quartz substrates.

Transmission measurements were performed on two samples of each metal/metal-oxide growth for Pd/PdO_x and Pt/PtO_x. One of the two samples was capped with a 40 nm Au layer on top of the metal/metal-oxide film, deposited simultaneously with the capping layer of the Schottky contacts. This was done in order to observe the amount of optical transmission received at the Schottky junction due to the filtering effect of both the Schottky contact and the gold capping layer.

The transmission measurements of the Ir, IrO_x, Ag, AgO_x, Pd, PdO_x, Pt, and PtO_x metal and metal-oxide films are shown in Figures 5.2 – 5.13. The transmission results with varied RF-sputtering O_2:Ar gas ratios have been normalised to a film thickness of 100 nm, following the Beer-Lambert Law shown in Table 5.1 [5.6]. Equation 5.1 shows the exponential relationship between the intensity of incident light, I_0, and the intensity of transmitted light, I_T, with absorption coefficient, α, and film thickness, d [5.6]. In order to normalise the transmission of the metal-oxide films to a thickness of 100 nm, Equation 5.2 was applied to the transmission results, where d is the measured thickness of the metal-oxide film. However, the metal-oxide films with identical oxygen incorporation and thickness varied between 1.0 – 73 nm were found to not follow the Beer-Lambert law, as shown in Figure 5.2, possibly due to the wide range of film thicknesses measured. Therefore the comparisons of identical oxygen incorporation and varied thickness in Figures 5.10 – 5.13 are shown without thickness normalisation. Figures 5.2 – 5.9 feature Beer-Lambert thickness normalisation to 100 nm, and are included in Appendix A5.1 without normalisation.

Table 5.1. Beer-Lambert Equations for Transmission with Film Thickness [5.6]

Parameter	Equation	Equation No.
Beer-Lambert Law	$I_T(d) = I_0 e^{(-\alpha d)}$	(5.1) [5.6]
Thickness Normalisation	$\left(\frac{I_T}{I_0}\right)^{\left(\frac{100}{d}\right)} = I_0 e^{(-\alpha \cdot 100\ nm)}$	(5.2)

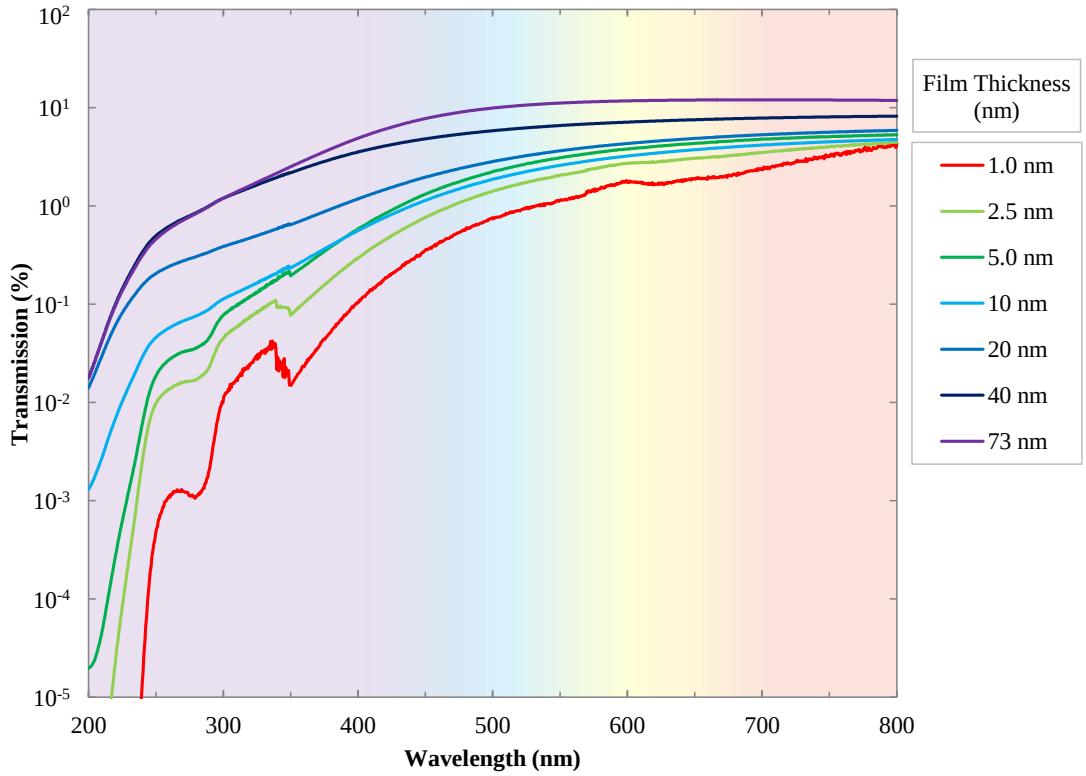

Figure 5.2: Normalised Transmission of IrO_x Films 3.0:10 (O_2:Ar) 73 – 1.0 nm Thickness

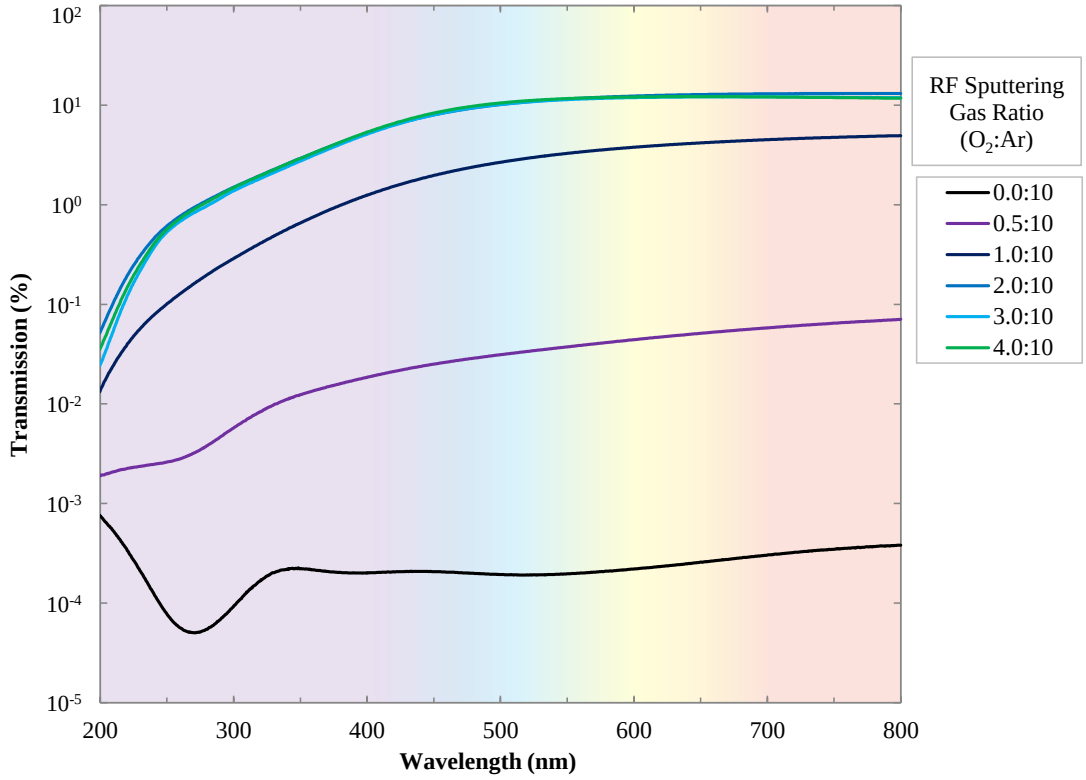

Figure 5.3: Normalised Transmission of RF-sputtered IrO_x Films 0.0:10 – 4.0:10 (O_2:Ar)

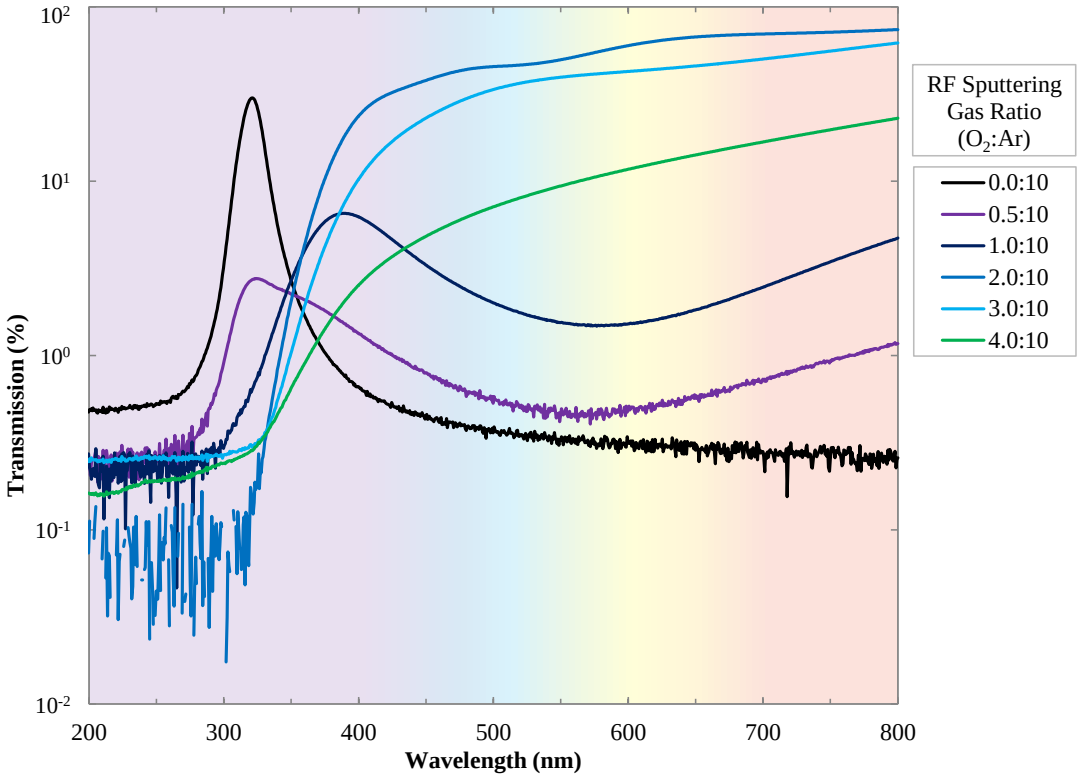

Figure 5.4: Normalised Transmission of RF-sputtered AgO_x Films 0.5:10 – 4.0:10 (O_2:Ar)

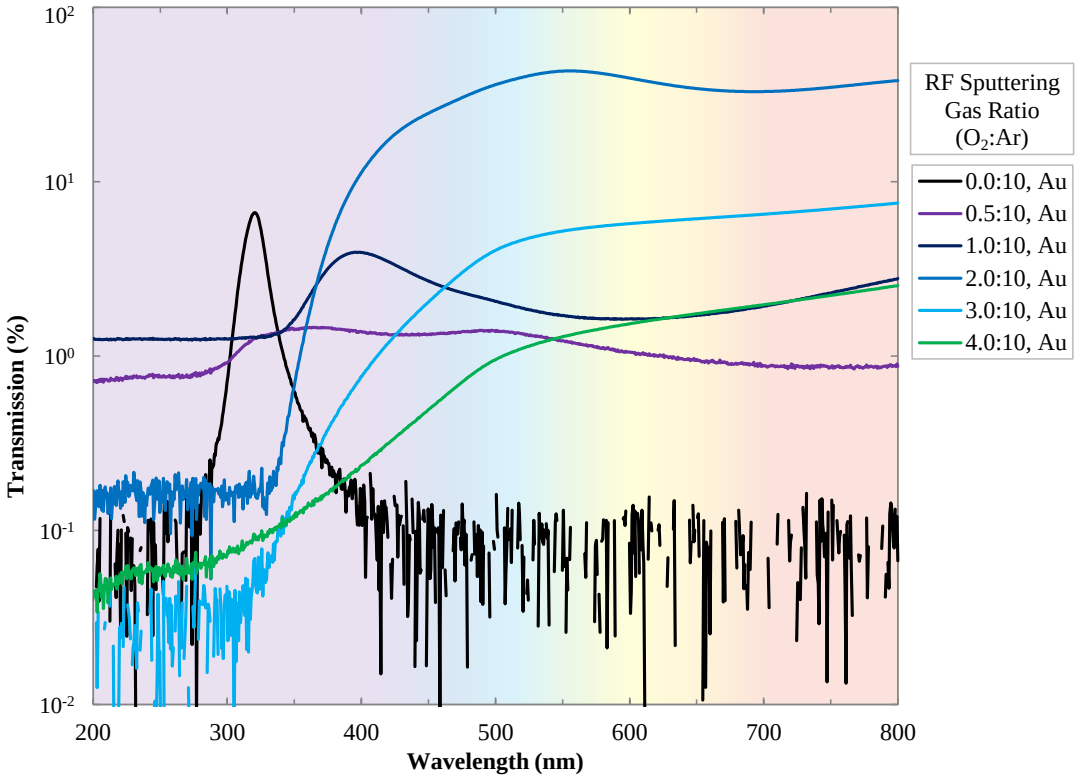

Figure 5.5: Normalised Transmission of RF-sputtered AgO_x/Au Films 0.5:10 – 4.0:10 (O_2:Ar)

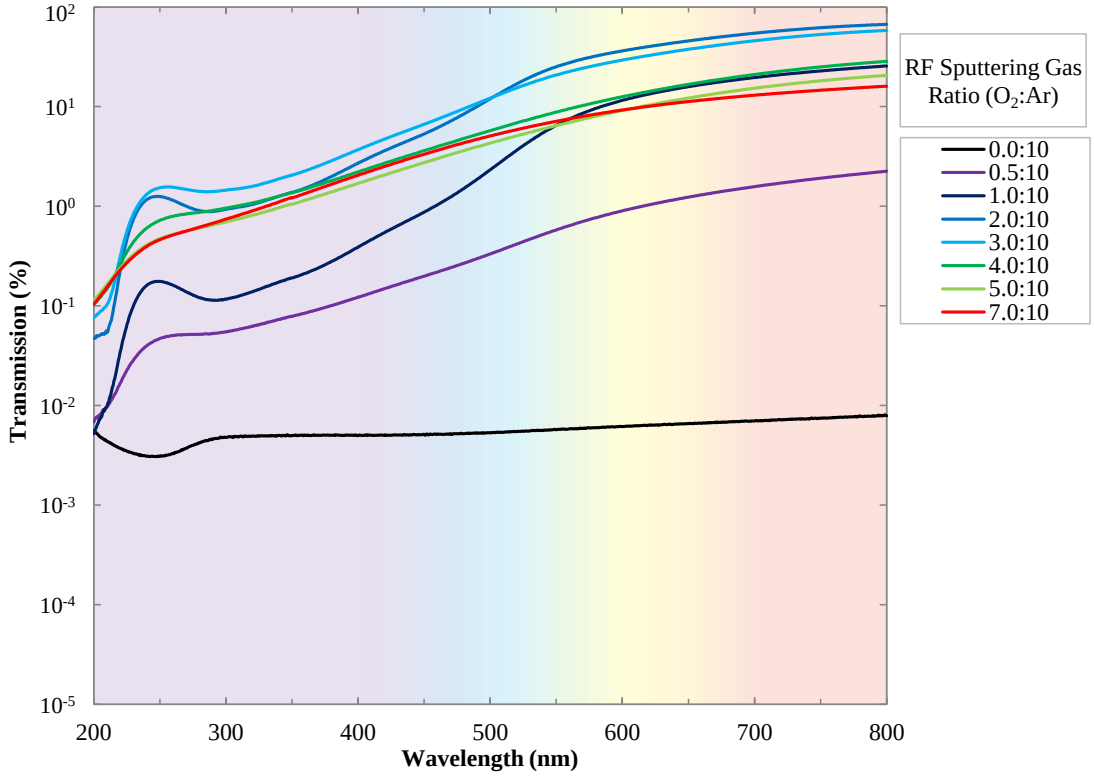

Figure 5.6: Normalised Transmission of RF-sputtered PdO_x Films 0.0:10 – 7.0:10 (O_2:Ar)

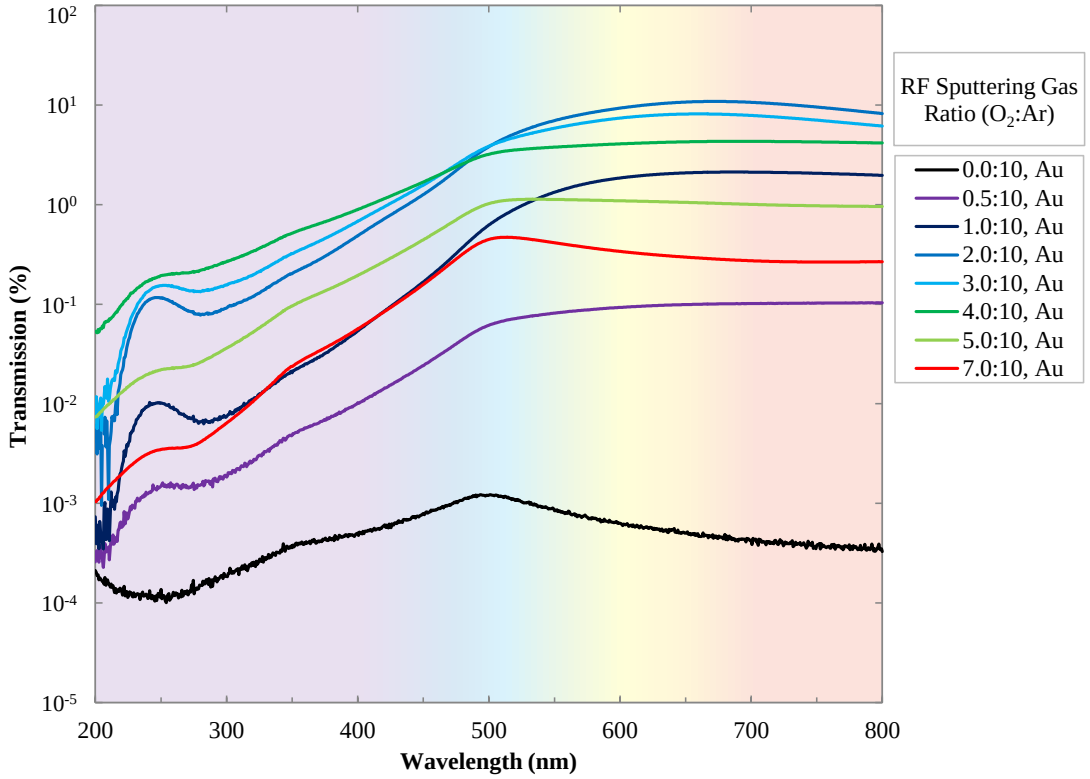

Figure 5.7: Normalised Transmission of RF-sputtered PdO_x/Au Films 0.0:10 – 7.0:10 (O_2:Ar)

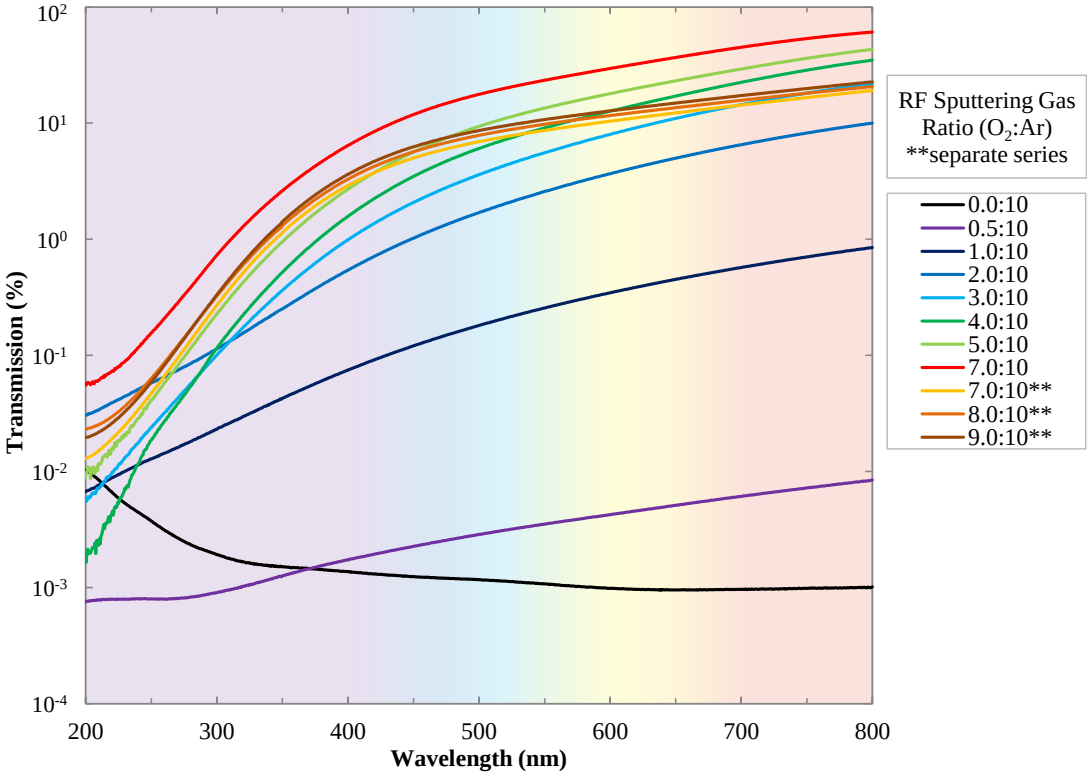

Figure 5.8: Normalised Transmission of RF-sputtered PtO_x Films 0.0:10 – 9.0:10 (O_2:Ar)

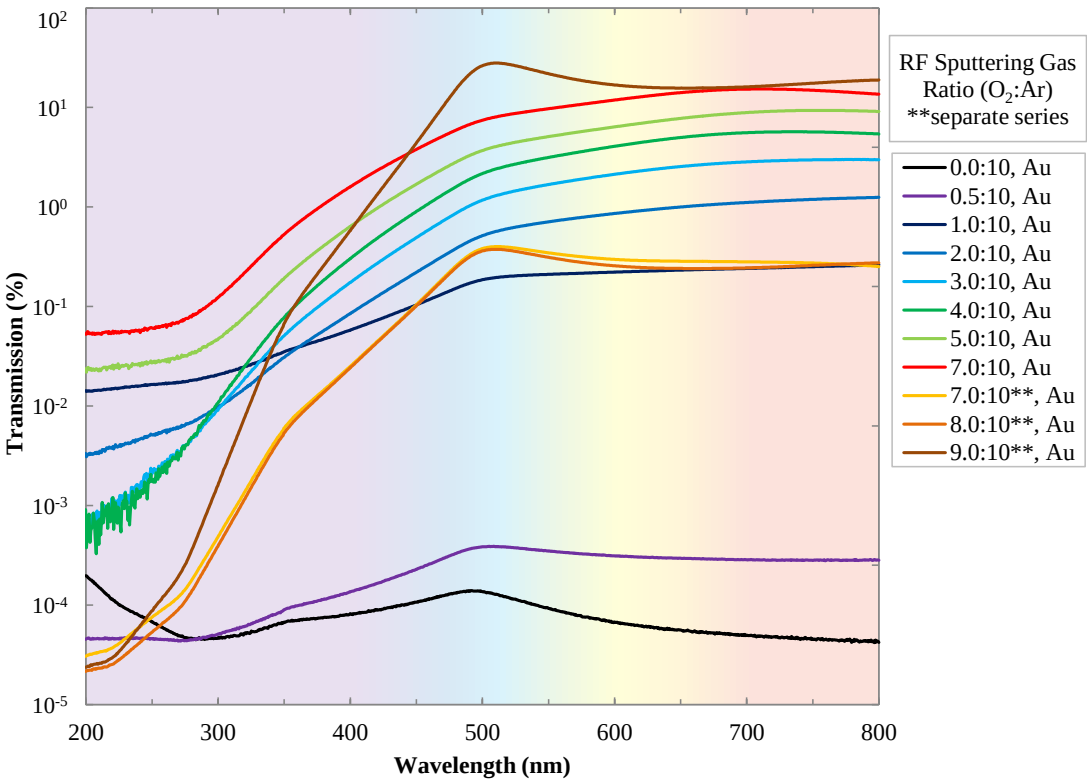

Figure 5.9: Normalised Transmission of RF-sputtered PtO_x/Au Films 0.0:10 – 9.0:10 (O_2:Ar)

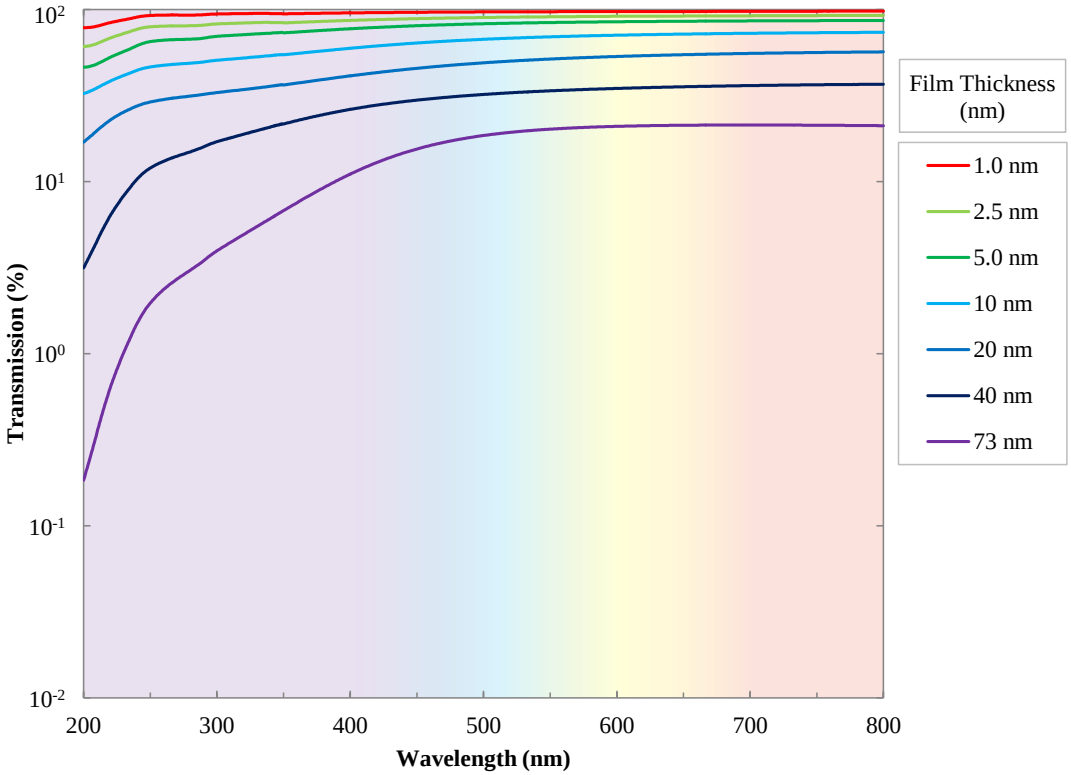

Figure 5.10: Transmission of IrO_x Films 3.0:10 (O_2:Ar) 73 – 1.0 nm Thickness

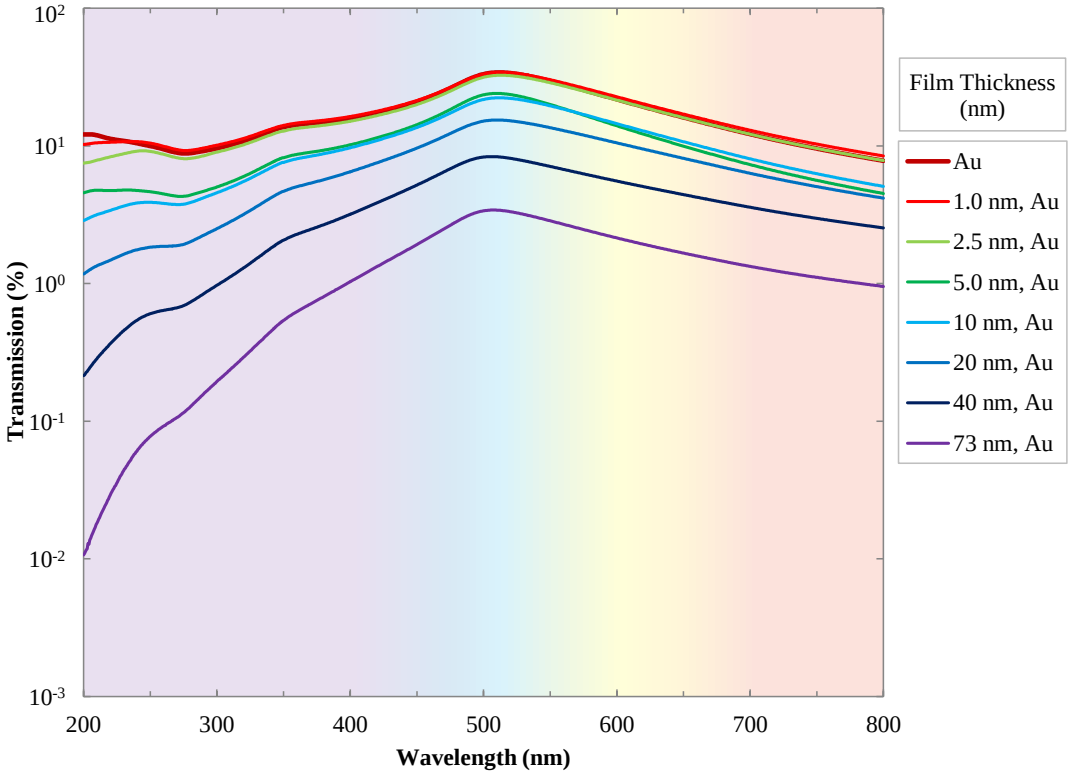

Figure 5.11: Transmission of IrO_x/Au Films 3.0:10 (O_2:Ar) 73 – 1.0 nm Thickness

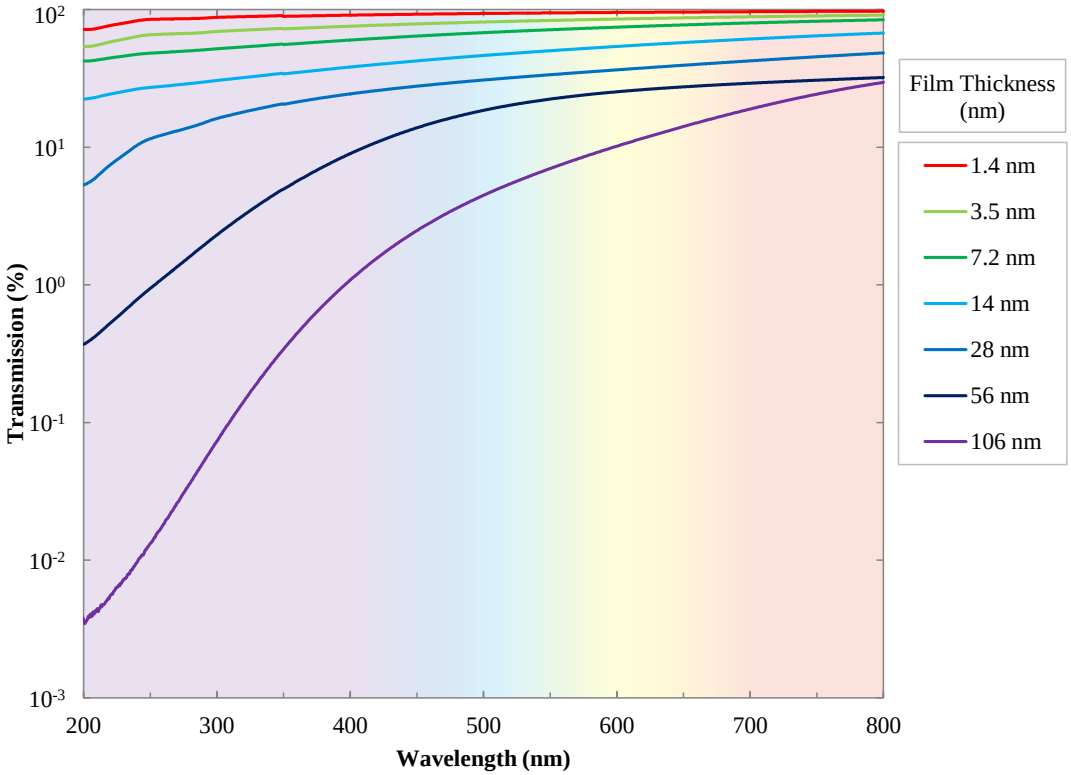

Figure 5.12: Transmission of PtO_x Films 4.0:10 (O_2:Ar) 106 – 1.4 nm Thickness

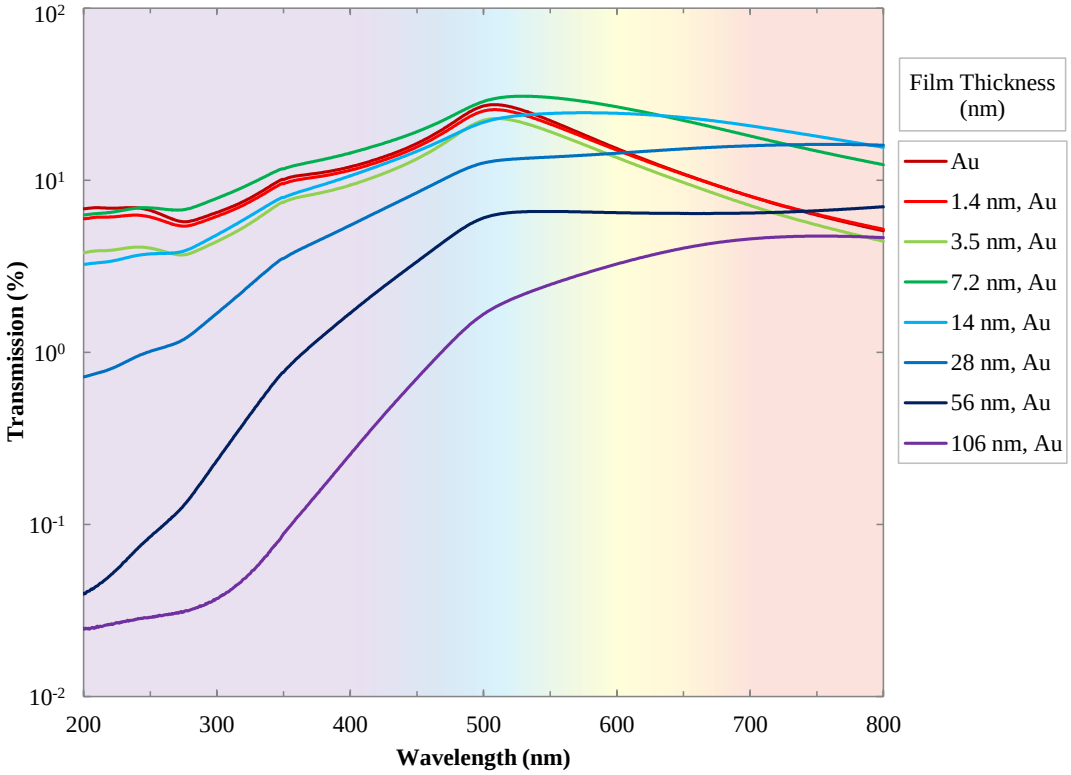

Figure 5.13: Transmission of PtO_x/Au Films 4.0:10 (O_2:Ar) 106 – 1.4 nm Thickness

Figures 5.3 – 5.9 show increasing film transmission with oxygen incorporation. Increased transmission would benefit UV sensor applications, as a greater transmission of UV wavelengths would produce devices with greater UV sensitivity. Figures 5.11 and 5.13 feature a transmission spectrum for a layer of 50 nm plain Au, with a peak at ~510 nm (2.43 eV). It can be observed from comparing the transmission spectra of the metal-oxide films to the Au-capped metal-oxide films in Figures 5.3 – 5.9 that the Au capping layer significantly attenuates the transmission of the metal-oxide films either side of the 510 nm peak as well as reducing overall transmission. The attenuation of UV wavelengths negatively affects the suitability of the material for UV sensing Schottky devices, as the selectivity of the device response to UV light over visible light is reduced.

Figure 5.3, featuring the Ir/IrO_x oxidation series transmission spectra, shows an absorption peak at 271 nm (4.56 eV) for the plain Ir film, which becomes less apparent with increasing oxygen incorporation. All IrO_x films show attenuation of transmission below 500 nm, which has been reported in literature for IrO_2 films [5.7]. The 2.0:10 (O_2:Ar), 3.0:10 (O_2:Ar), and 4.0:10 (O_2:Ar) IrO_x films show almost identical transmission spectra when scaled to 100 nm, indicating a possible upper limit to the transmission of the films, or a plateau of the oxygen incorporation for the O_2:Ar RF-sputtering gas ratios used in this work.

Ag/AgO_x films in Figures 5.4 – 5.5 show increasing transmission with increasing oxygen incorporation up to 2.0:10 (O_2:Ar), followed by a decrease in transmission to 4.0:10 (O_2:Ar). The increase in transmission with the initial increase in O_2:Ar ratio follows the trend of published transmissions of RF-sputtered Ag and AgO films [5.8 – 5.9]. While the plain Ag film has a peak at 321 nm, from Ag interband transitions, increasing oxidation appears to induce a redshift in the AgO_x films, and reduces the UV transmission peak [5.10]. As the transmission peak is located near the boundary between UV-A and UV-B wavelengths, replacing the Au capping layer with an Ag capping layer could provide a greater degree of selectivity in UV sensing photodiodes. However, as the Ag/AgO_x films were the least transparent films measured in this work, this could reduce the overall efficiency of UV sensing devices.

The Pd/PdO_x films in Figures 5.6 – 5.7 show a decrease in transmission at 250 nm (4.96 eV) for the Pd film, which becomes a transmission peak with increasing oxygen incorporation. This trend of an absorption peak becoming a transmission peak at 250 nm with increasing oxygen incorporation has been reported in literature for Pd/PdO_x films [5.11]. The transmimssion peak diminishes with higher levels of oxygen incorporation, from 4.0:10 – 7.0:10 (O_2:Ar). Despite the lower overall transmission of the PdO_x films above 3.0:10 (O_2:Ar), the 4.0:10 – 7.0:10 (O_2:Ar) PdO_x films show lower of attenuation of UV wavelengths below 250 nm than the equivalent IrO_x and AgO_x films, making 4.0:10 – 7.0:10 (O_2:Ar) PdO_x a more promising material for UV sensing applications.

The Pt/PtO_x films in Figures 5.8 – 5.9 show significant attenuation of the UV spectrum for oxygen incorporation levels of 0.0:10 – 7.0:10 (O_2:Ar). Although normalised for a thickness of 100 nm, the difference in transmittance between 134 nm 7.0:10 (O_2:Ar) and 47 nm 7.0:10** (O_2:Ar) remains significant, possibly due to the difference in film thickness of the two film series.

Figures 5.10 – 5.13 show significantly reduced attenuation of UV wavelengths with reduced Schottky contact thickness. Linear scale transmission plots of Figures 5.10 – 5.13 are also included in Appendix A5.1 Figures A5.9 – A5.12. Figure 5.13 shows increased transmission in the visible spectrum for 50 nm Au-capped metal/metal-oxide films 56 – 14 nm thick, compared with a 50 nm film of plain Au. This warrants further investigation into the effects of capping layers on transparency of thin (<10 nm) noble metal-oxide films with varied oxygen incorporation.

All RF-sputtered metal and metal-oxide films have been observed to change in transmission spectra over time, as shown in Figures 5.14 – 5.18. The transmission of the of Ag/AgO_x films over time was not recorded, as over a period of 2 – 3 days the films became inhomogeneous in transmission, with visible discolouration patterns across the films due to oxidation in atmosphere. Figure 5.15 does not show a transmission spectra for 0.0:10 (O_2:Ar) 35 days after the initial measurement as the film degraded unexpectedly.

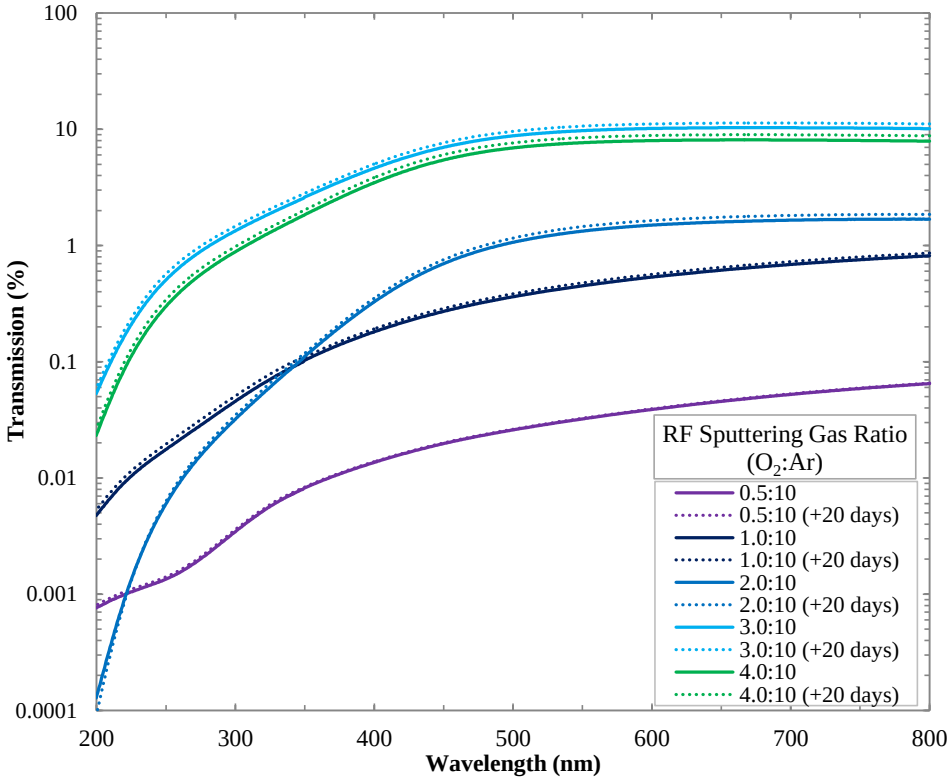

Figure 5.14: Normalised Transmission of IrO_x Films 0.5:10 – 4.0:10 (O_2:Ar) with Time

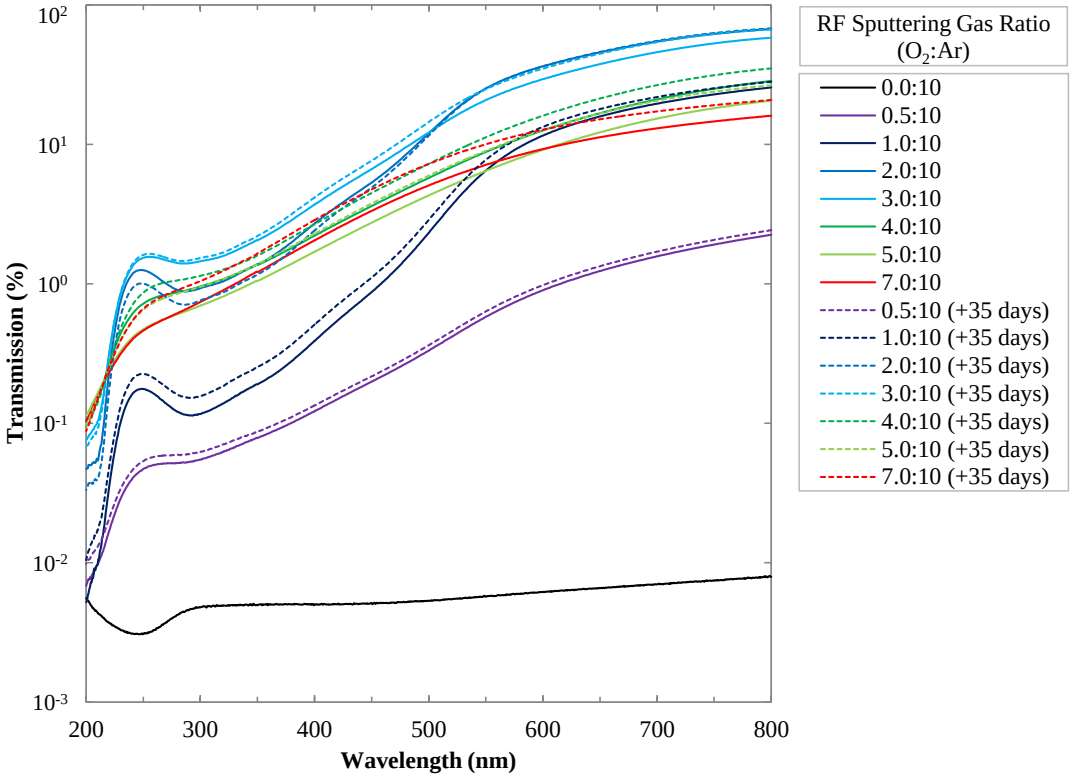

Figure 5.15: Normalised Transmission of PdO_x Films 0.0:10 – 7.0:10 (O_2:Ar) with Time

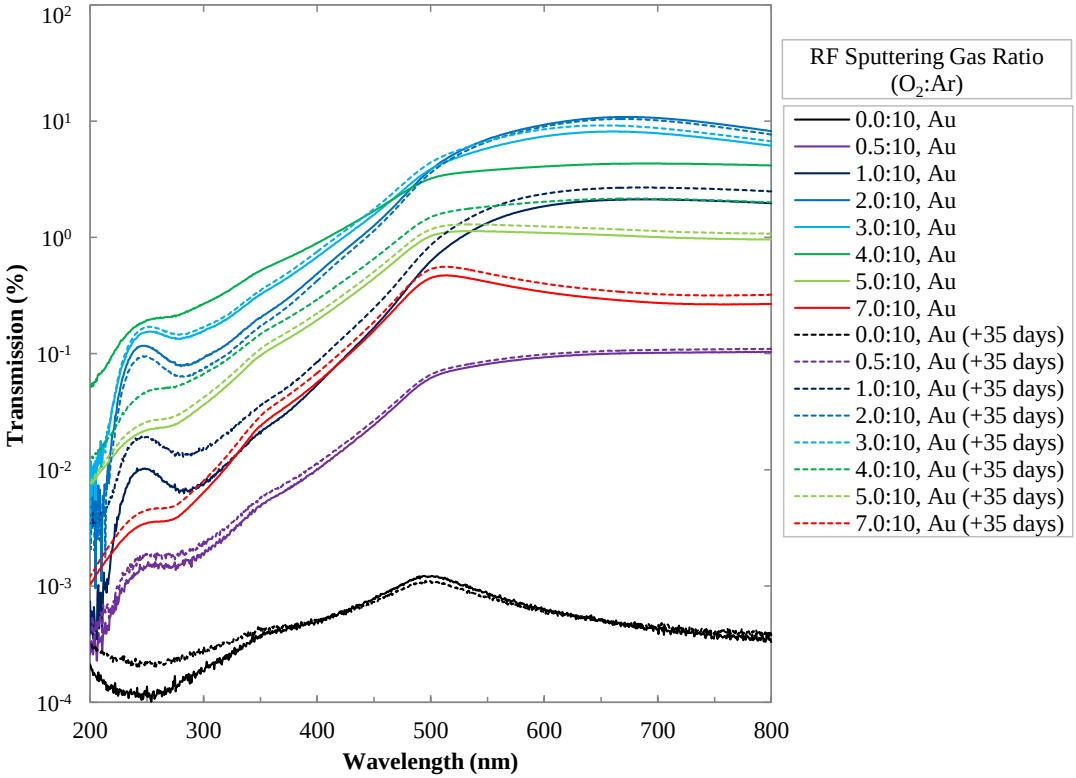

Figure 5.16: Normalised Transmission of PdO_x/Au Films 0.0:10 – 7.0:10 (O_2:Ar) with Time

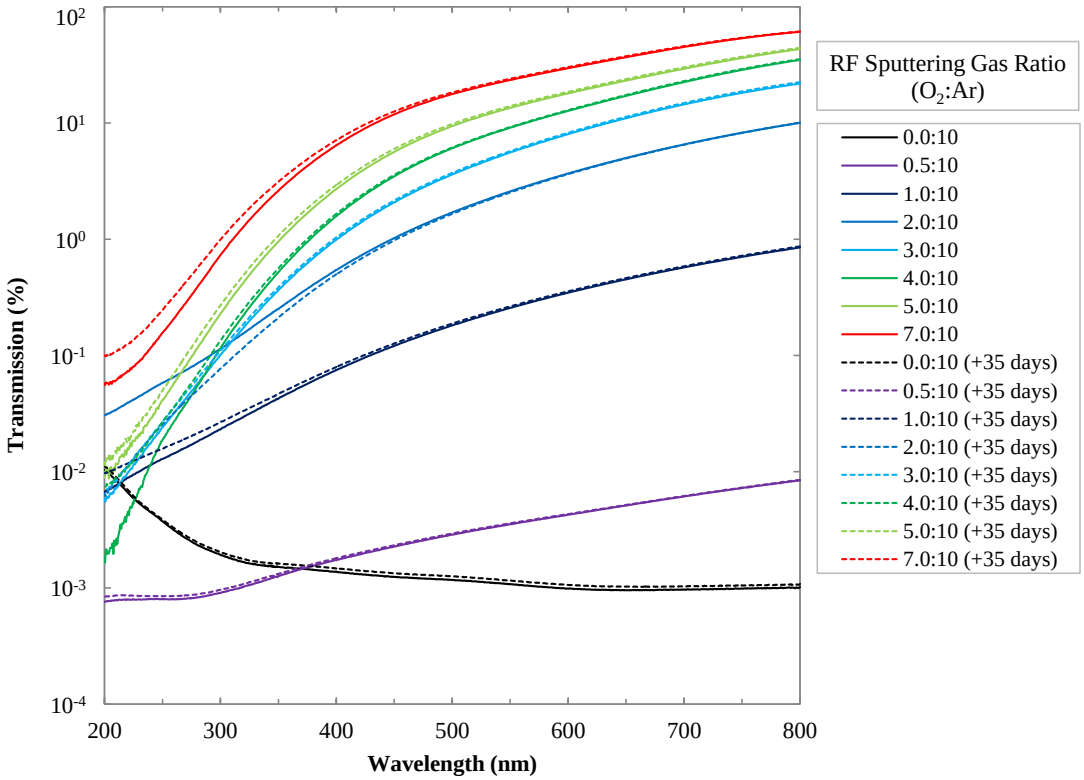

Figure 5.17: Normalised Transmission of PtO_x Films 0.0:10 – 7.0:10 (O_2:Ar) with Time

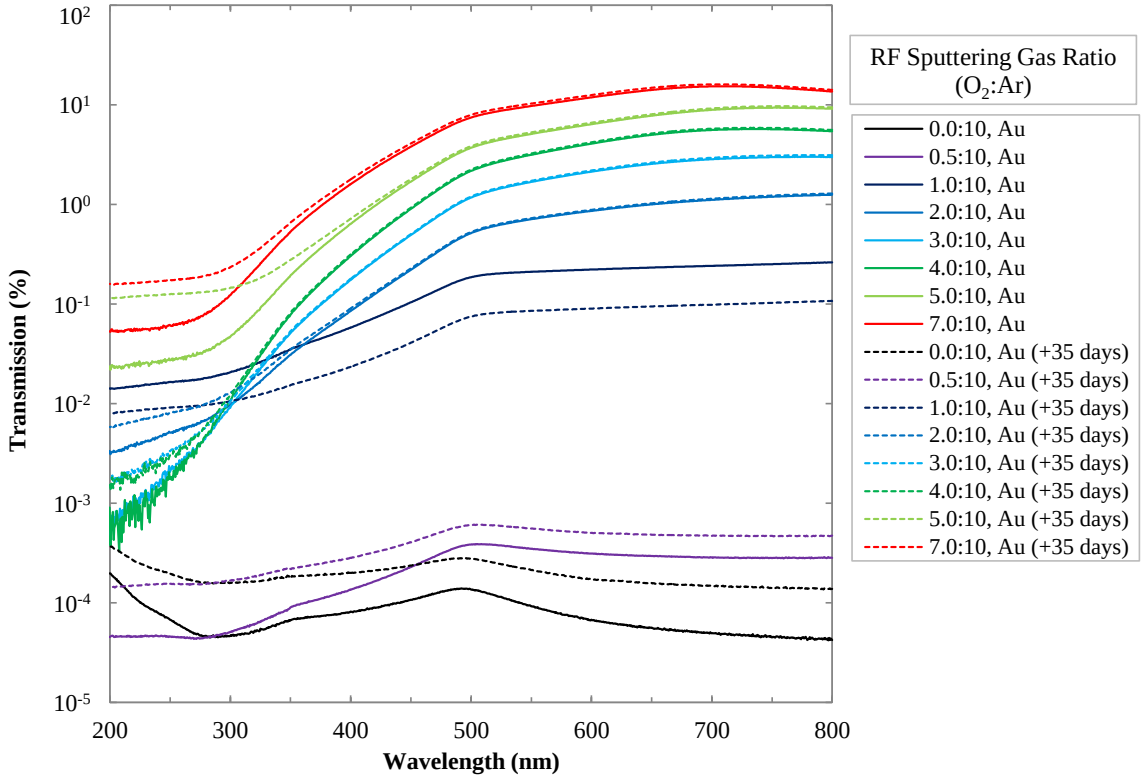

Figure 5.18: Normalised Transmission of PtO_x/Au Films 0.0:10 – 7.0:10 (O_2:Ar) with Time

Figures 5.14 – 5.18 show an increase in transmission of the metal-oxide and Au-capped metal-oxide films over time, with the exception of the 2.0:10 (O_2:Ar) PdO_x and PtO_x films. Although Figures 5.15 – 5.16 indicate that the rate of Pd/PdO_x oxidation is reduced with the Au capping layer, Figures 5.17 – 5.18 show an increase in the oxidation of the Pt/PtO_x films with the Au capping layer. However in both cases, the difference in transmission was small compared to the overall transmission of the films. The impact of the Au capping layer on post-deposition oxidations of the films is inconclusive.

5.3 Metal-Oxide Film Structure

The crystal structure of the metal and metal-oxide films was analysed using grazing incidence XRD, detailed in Section 4.1.7, to determine whether the films were crystalline, polycrystalline, or amorphous. The XRD results included in this chapter are courtesy of Adam Hyndman, Department of Physics and Astronomy, University of Canterbury, New Zealand.

Grazing incidence XRD (GIXRD) measurements were performed on the samples using a Bruker D8 Advance diffractometer with cobalt radiation x-ray source (CoKα = 1.78897). The x-ray source was set to a fixed incidence angle of 2 °, while the detector was rotated through a 2θ angle of 20 – 90 °, as shown in Figure 5.19. The samples measured were RF-sputtered films of Ir, IrO_x (1.0:10 O_2:Ar sputtering gas ratio), IrO_x (8.0:10 O_2:Ar), Pd, PdO_x (1.0:10 O_2:Ar), Pt, and PtO_x (1.0:10 O_2:Ar), with GIXRD results included in Figures 5.20 – 5.26. As the noise level of the Ir, IrO_x (1.0:10 O_2:Ar), and IrO_x (8.0:10 O_2:Ar) GIXRD scans (Figures 5.20 – 5.22) was rather high, the Pd, PdO_x (1.0:10 O_2:Ar), Pt, and PtO_x (1.0:10 O_2:Ar) GIXRD scans (Figures 5.23 – 5.26) were performed over a 12 hour period. Due to the duration of each measurement, only one metal-oxide sample was measured for the PdO_x and PtO_x oxidation series.

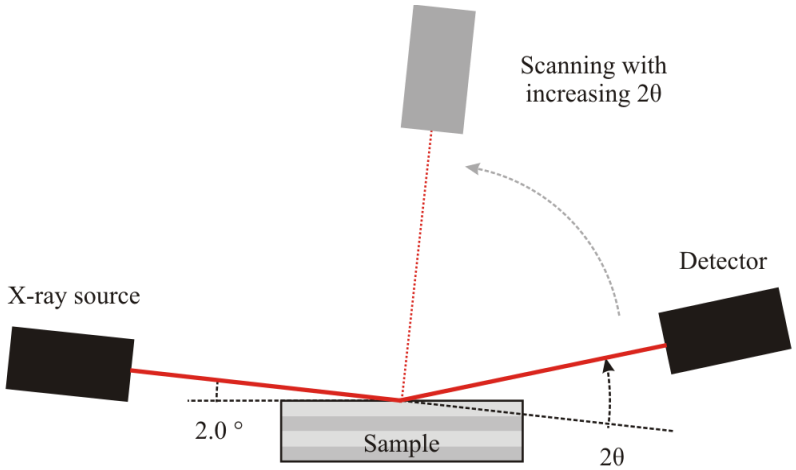

Figure 5.19: Grazing Incidence X-ray Diffraction (GIXRD) Diagram

A large broad peak is featured in all GIXRD patterns at a shallow angle of ~25 ° corresponding to the amorphous quartz substrate. Sharp peaks of the GIXRD patterns of Ir, Pd, and Pt, shown in Figures 5.20, 5.23, and 5.25 respectively, match reference peaks calculated for the noble metals from the d-spacings of their lattice planes, included in the figures with labelled Miller indices. This indicates that the RF-sputtered films plain metals are polycrystalline. The GIXRD patterns of IrO_x (1.0:10 O_2:Ar), IrO_x (8.0:10 O_2:Ar), and PtO_x (1.0:10 O_2:Ar) in Figures 5.21, 5.22, and 5.26 respectively show no distinct peaks. The IrO_x films in Figures 5.21 – 5.22 show an asymmetric shoulder at ~38 °, becoming larger with increasing oxygen incorporation. An asymmetric shoulder also appears at ~46 ° for the PtO_x film in Figure 5.26. The lack of sharp peaks indicate that the RF-sputtered metal-oxide films of IrO_x and PtO_x are amorphous or nanocrystalline. It can be inferred from the similarity of the IrO_x and PtO_x GIXRD patterns of Figures 5.21 – 5.22 and 5.26 that all RF-sputtered metal-oxide films of IrO_x and PtO_x in this work are amorphous.

In contrast to the IrO_x and PtO_x films, the GIXRD pattern of PdO_x (1.0:10 O_2:Ar) in Figure 5.24 shows sharp peaks that match the reference peaks of PdO. The presence of sharp peaks indicates that the metal-oxide film is polycrystalline in nature. GIXRD patterns of PdO_x films with higher levels of oxygen incorporation were not performed due to the time constraints.

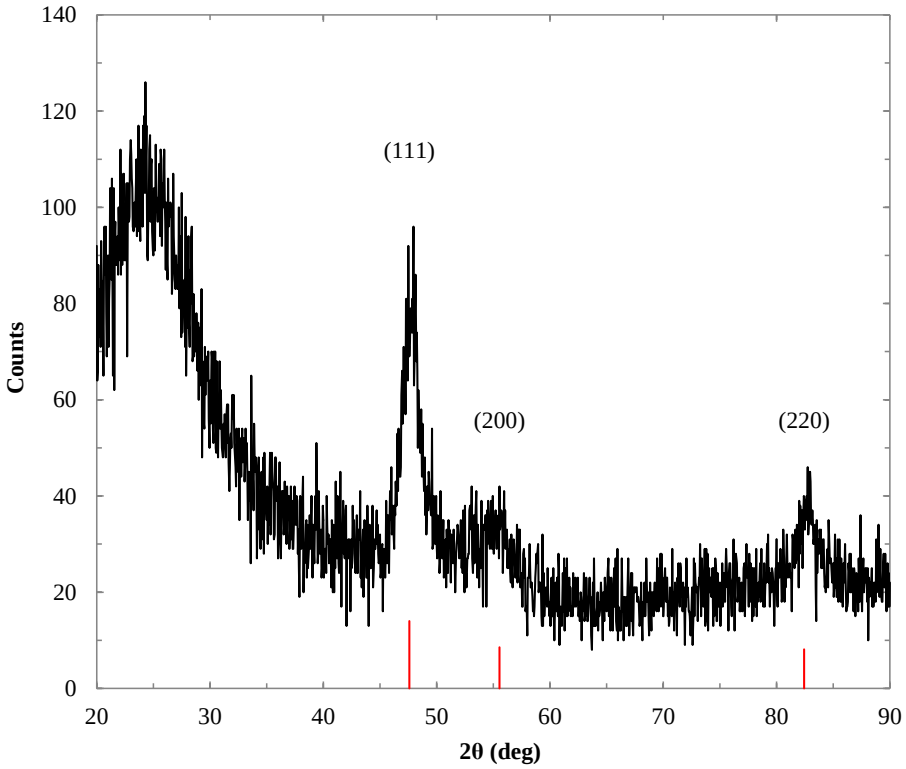

Figure 5.20: GIXRD Analysis of RF-Sputtered Iridium

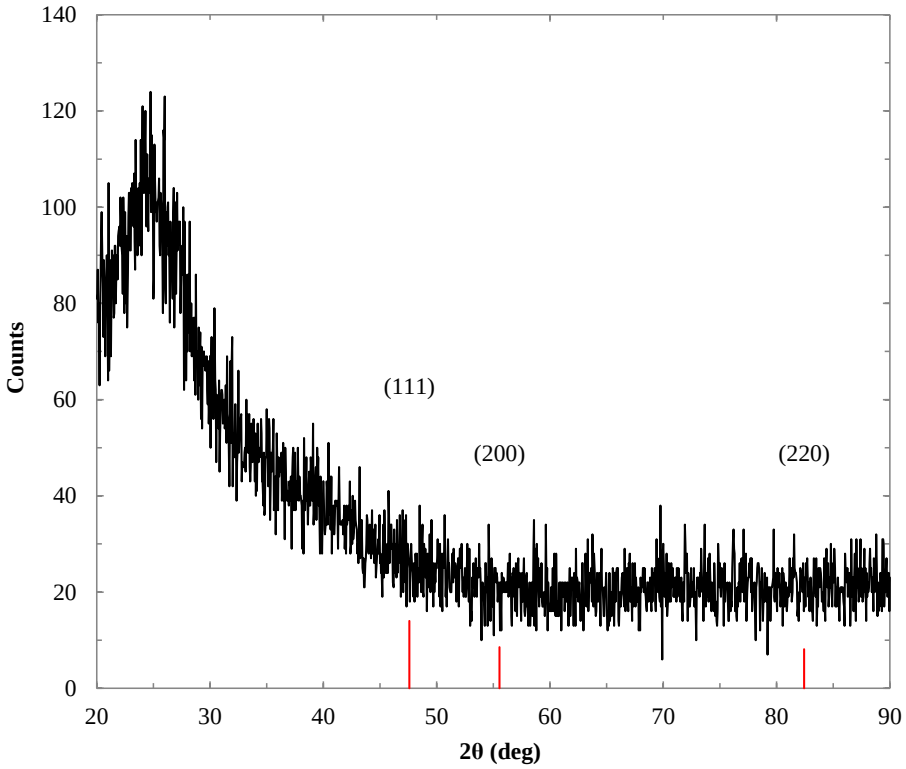

Figure 5.21: GIXRD Analysis of Iridium Oxide (1.0:10 O_2:Ar Deposition)

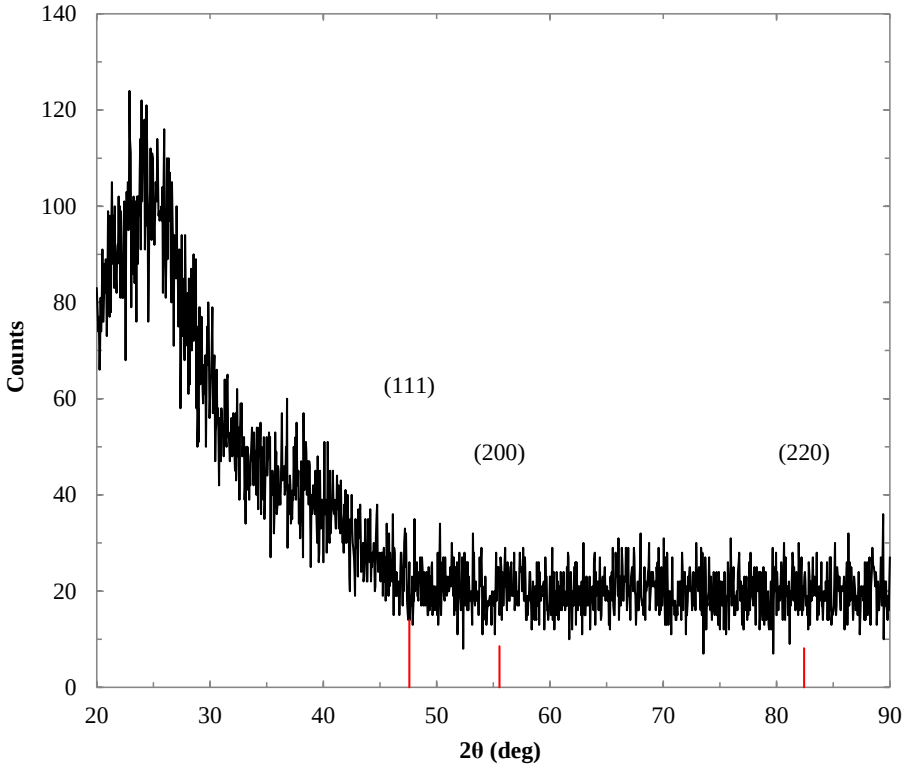

Figure 5.22: GIXRD Analysis of Iridium Oxide (8.0:10 O_2:Ar Deposition)

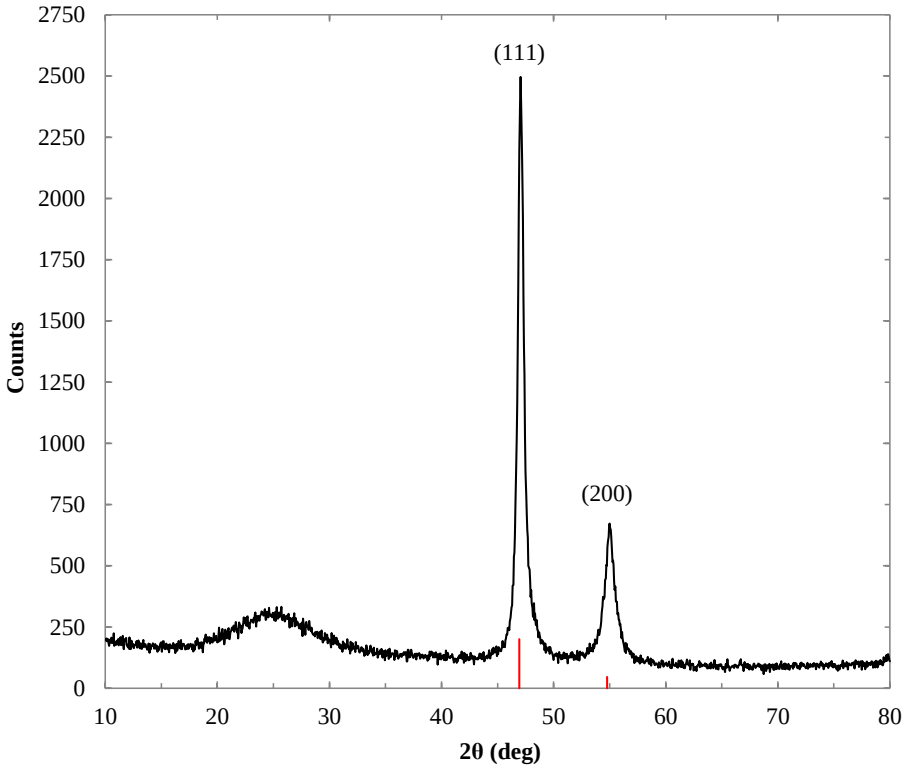

Figure 5.23: GIXRD Analysis of RF-Sputtered Palladium

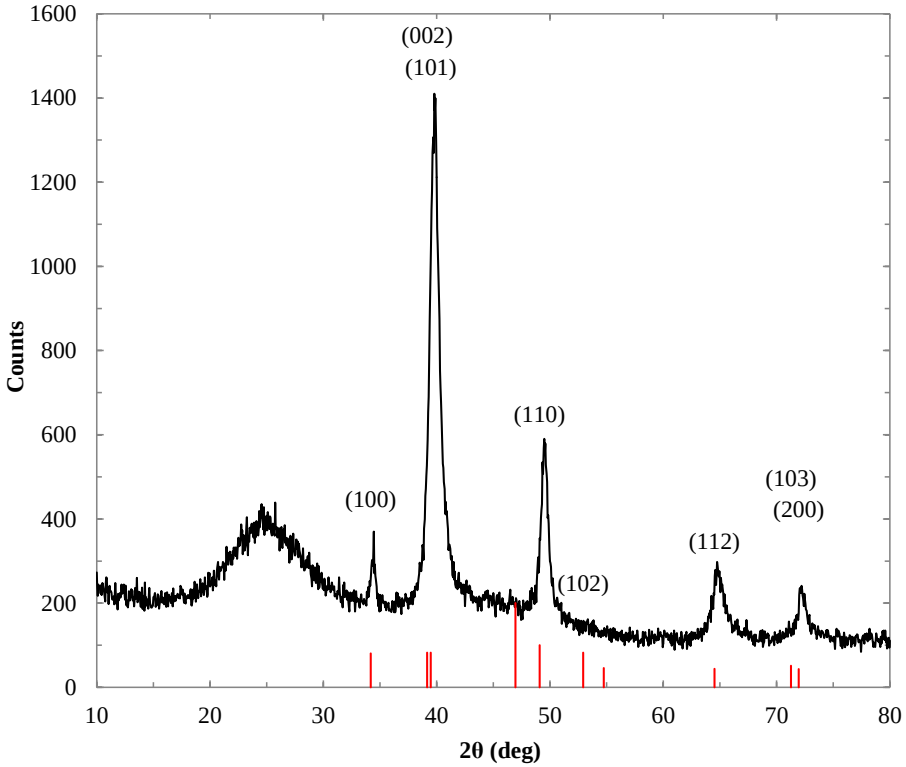

Figure 5.24: GIXRD Analysis of Palladium Oxide (1.0:10 O_2:Ar)

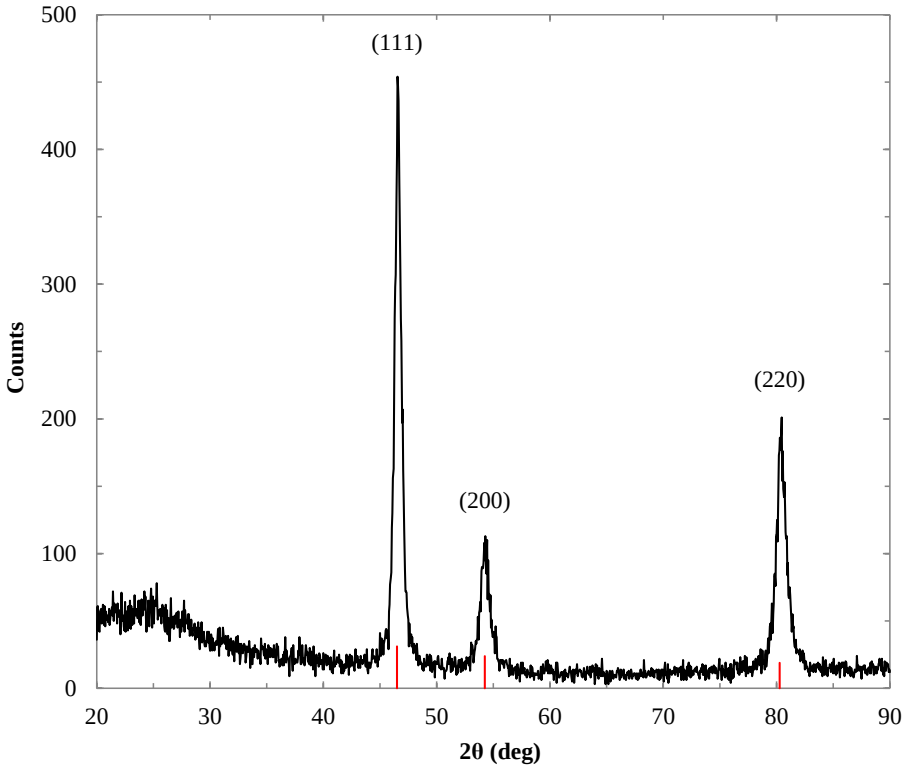

Figure 5.25: GIXRD Analysis of RF-Sputtered Platinum

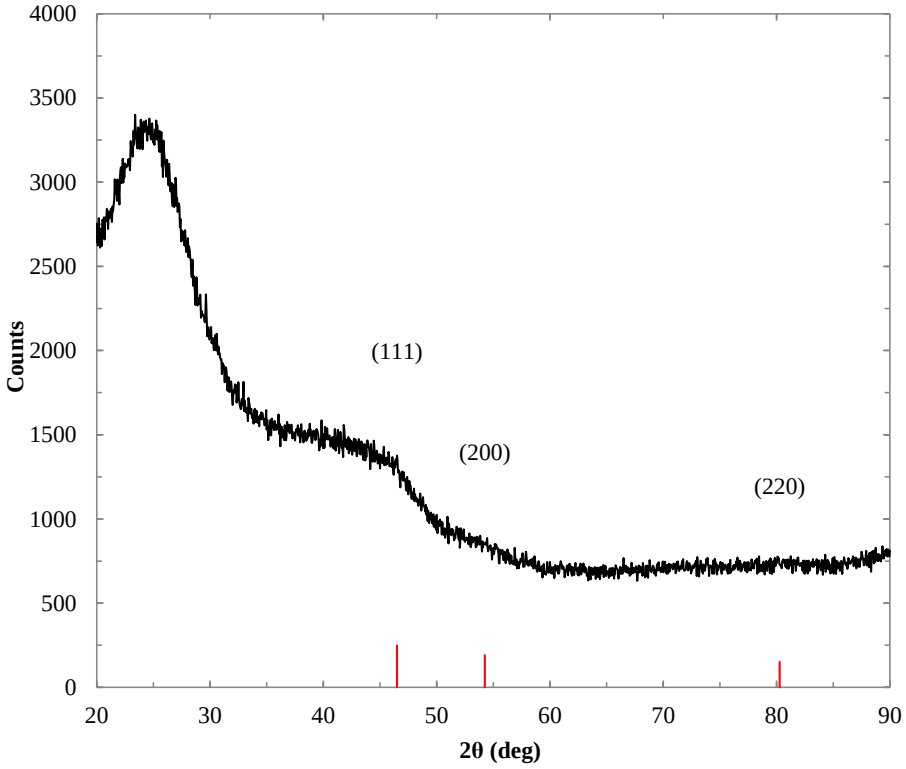

Figure 5.26: GIXRD Analysis of Platinum Oxide (1.0:10 O_2:Ar Deposition)

Studies have shown that depositing IrO_x at temperatures lower than 100 °C produced amorphous films [5.7, 5.12 – 5.13]. Atomic layer deposition (ALD) of IrO_2 at temperatures between 140 – 180 °C has been found to produce crystalline films with distinct IrO_2 peaks [5.14]. PLD IrO_x films deposited at room temperature were found to be amorphous; however films above 300 °C showed crystalline IrO_x peaks [5.7]. Amorphous sputtered IrO_x has also been shown to anneal to polycrystalline IrO_x between 350 – 400 °C in air and 150 – 200 °C in vacuum; showing potential for improving IrO_x Schottky contact crystallinity with higher deposition temperatures, or with post-deposition annealing [5.13]. Improving the crystallinity of the Schottky contact material could be advantageous for studying the effects on Schottky contact performance with changing crystallinity, especially in conjunction with the thermal stability of the Schottky contacts.

GIXRD patterns of ALD PdO_x deposited between 130 – 160 °C show polycrystalline PdO_x with increasing PdO peaks with increasing temperature [5.15]. Sputtered films of amorphous PdO_x have also been reported to crystallise above annealing temperatures of 200 °C [5.16]. Further investigation is required into the GIXRD patterns of PdO_x films.

GIXRD patterns of room temperature RF-sputtered PtO_x films were also reported to be amorphous [5.17 – 5.19]. However, RF-sputtered PtO_x with substrate temperatures 200 – 400 °C in a processing gas of pure O_2 was found to produce amorphous PtO_2 with distinct PtO GIXRD peaks [5.19]. RF-sputtering in a gas mixture of 1:1 O_2:Ar between 25 – 600 °C has also produced amorphous films of PtO_x, and pure Pt films at 700 °C [5.18]. Annealing amorphous PtO_x films at 575 – 675 °C was found to cause decomposition of the PtO_x films, showing sharp Pt peaks in the GIXRD [5.17]. This suggests a difficulty with annealing amorphous PtO_x to improve crystallinity without causing the PtO_x to decompose into pure Pt.

5.4 Metal-Oxide Film Thickness

AFM measurements were used to measure film thickness of RF-sputtered films of Ir/IrO_x and Pt/PtO_x with increasing oxygen incorporation, as described in Section 4.1.1.2. Figures 5.27 – 5.30 show thicknesses of films grown for a duration of 5 minutes, producing films of approximately 50 nm; a suitable thickness for Kelvin probe measurements. The error bars in Figures 5.27 – 5.30 show one standard deviation from the averaged calculated step-height. The films were deposited over a photolithography mask shown in Appendix A3.1, Figure A3.1.3, onto a quartz substrate that had been coated with an EBD layer of Ti/Au, as described in Section 4.1.4. The thickness of each film was measured at the edges of the film/substrate interface. The scan distances in Figures 5.27 and 5.29 are not continuous, as the scan width was only 10 µm and each film width was 100 µm.

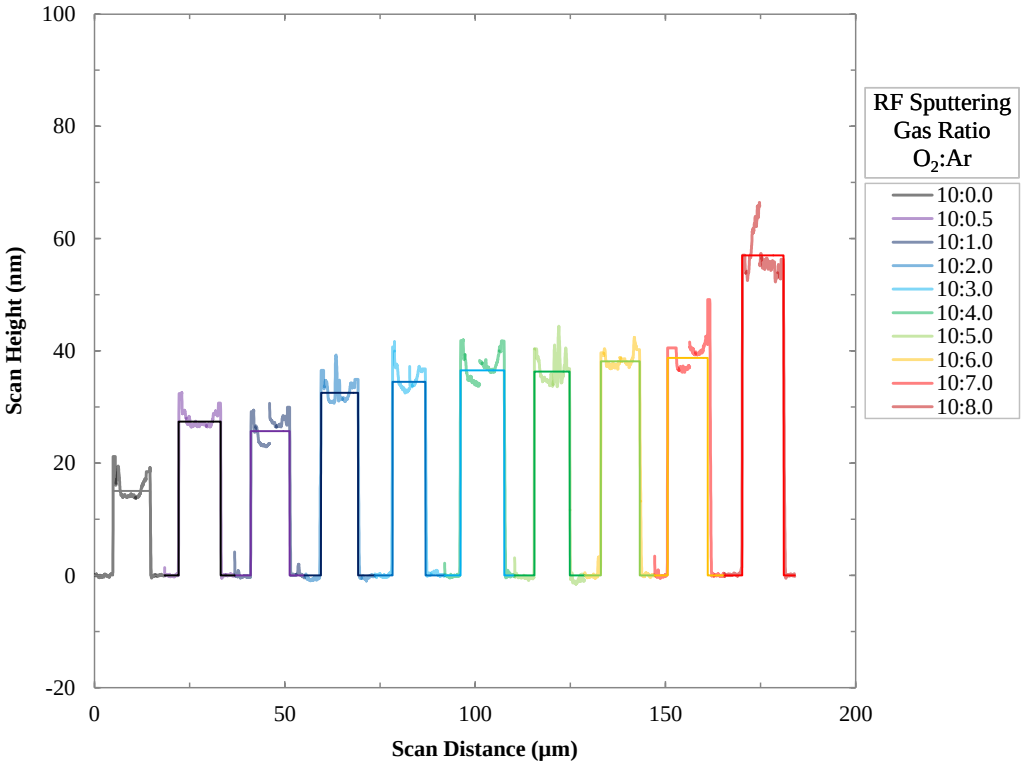

Figure 5.27: Measured, Fitted Thickness of Ir/IrO_x Films (5 Minute Deposition)

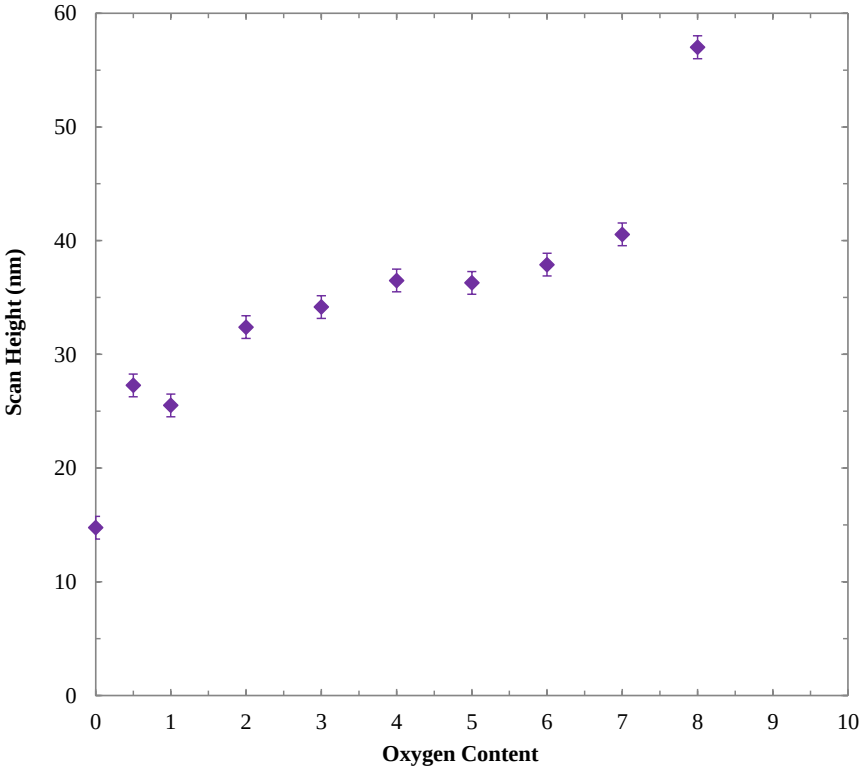

Figure 5.28: Calculated Thickness of Ir/IrO_x Films (5 Minute Deposition)

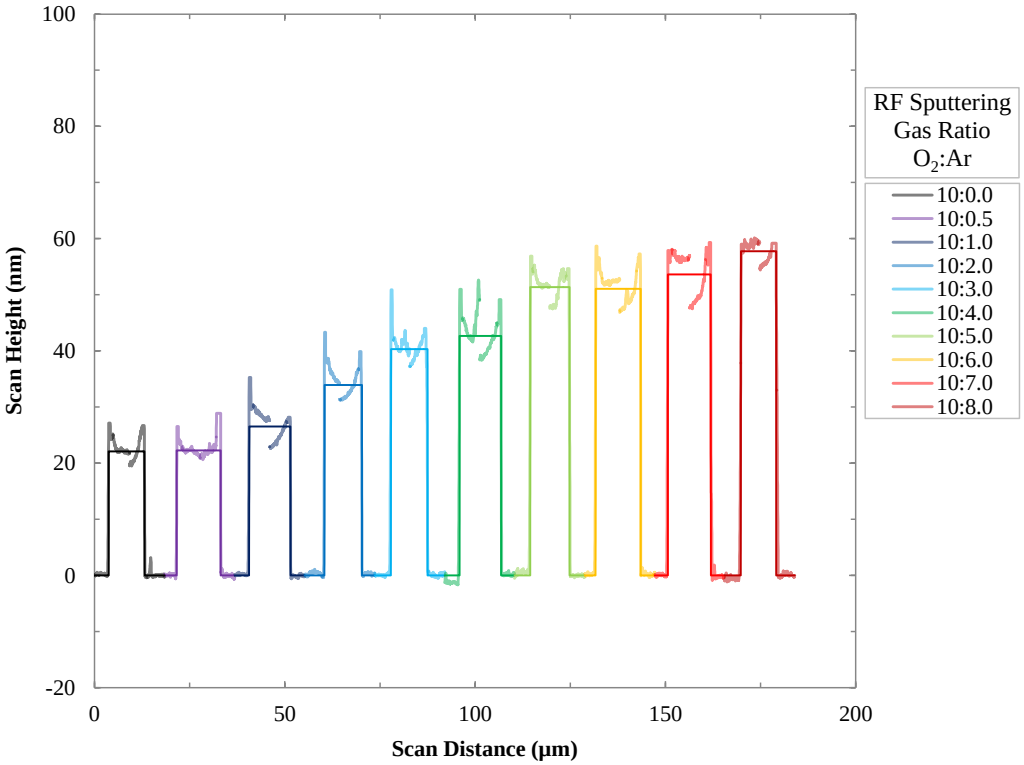

Figure 5.29: Measured, Best-Fit Thickness of Pt/PtO$_x$ Films (5 Minute Deposition)

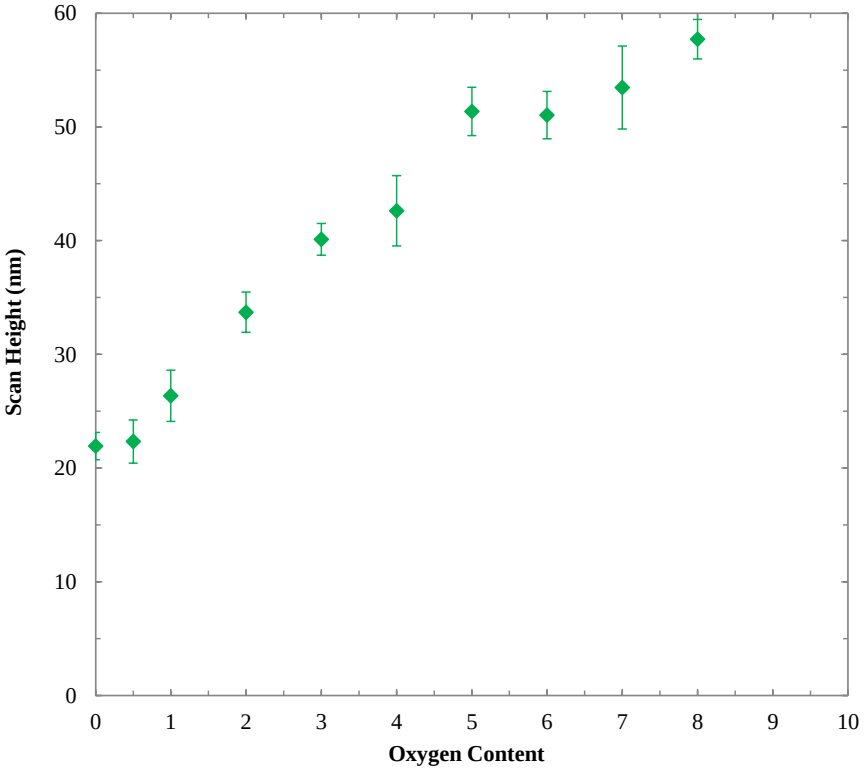

Figure 5.30: AFM Measured Calculated of Pt/PtO$_x$ Films (5 Minute Deposition)

The growth rate of the 0.0:10 – 8.0:10 (O_2:Ar) Ir/IrO_x films was calculated between 2.95 ± 0.2 to 11.4 ± 0.7 nm·min^{-1} respectively, from Figure 5.27. In literature, growth rates of 250 W RF-sputtered Ir/IrO_x with increasing O_2:Ar gas flow ratio have been reported as 5 – 30 nm·min^{-1} for 0.0:10 – 2.0:10 (O_2:Ar), 30 nm·min^{-1} between 2.0:10 – 4.0:10 (O_2:Ar), and declining to 10 nm·min^{-1} at 9.0:10 (O_2:Ar) [5.20]. The larger growth rates could be due to the higher sputtering power (250 W), compared to the 50 W power used in this work [5.20]. Figure 5.27 shows the Ir/IrO_x film growth rate plateauing between 2.0:10 – 7.0:10 (O_2:Ar).

The growth rate of the 0.0:10 – 8.0:10 (O_2:Ar) Pt/PtO_x films was calculated between 4.39 ± 0.2 to 11.5 ± 0.3 nm·min^{-1}, from Figure 5.29, similar to the growth rate range of the RF-sputtered Ir/IrO_x films in this work. Growth rates for Pt/PtO_x reported in the literature were 26 – 40 nm·min^{-1} for 50 W RF-sputtered Pt/PtO_x with gas flow ratios of 0.0:10 – 4.3:10 (O_2:Ar), and a decreasing growth rate above 4.3:10 (O_2:Ar) [5.21]. The reported growth rate is considerably larger than that calculated in this work; however there are many factors that could differ between the RF-sputtering systems, such as distance between the sputtering target and sample, and gas pumping speed. The decreasing growth rate with high levels of oxygen incorporation in literature could indicate a limitation of the RF-sputtering growth conditions above the levels of O_2:Ar explored in this work.

5.5 Metal-Oxide Film Surface Potential

The surface potential of RF-sputtered films of Ir/IrO_x and Pt/PtO_x was measured using KPM, as described in Section 4.1.4. The KPM measurements were performed simultaneously with the height measurements in Section 5.4, as KPM is an AFM-based measurement. The surface potential, $\Delta V_{surface}$, was calculated using Equation 5.3, where ϕ_{sample} is the work function of the metal or metal/oxide film with reference to the reference material (either Au or Pt) [5.22].

$$\Delta V_{surface} = \frac{\phi_{sample}}{q} \qquad (5.3)[5.22]$$

For this work, the metal and metal-oxide films were deposited onto a quartz substrate that had been coated with an EBD layer of Ti coated with an EBD layer of Au. The step difference in surface potential, $\Delta V_{surface}$, was measured between the Au layer, electrically connected to the AFM stage, and the metal/metal-oxide film. As $\Delta V_{surface}$ was measured across two different surfaces, there was no contribution from the work function of the Pt-coated AFM tip, ϕ_{tip}. The results are included in Figures 5.31 – 5.34. The scan distances in Figures 5.31 and 5.33 are also not continuous. Figure 5.35 shows the Ir/IrO_x sample used in this work for AFM and KPM measurements.

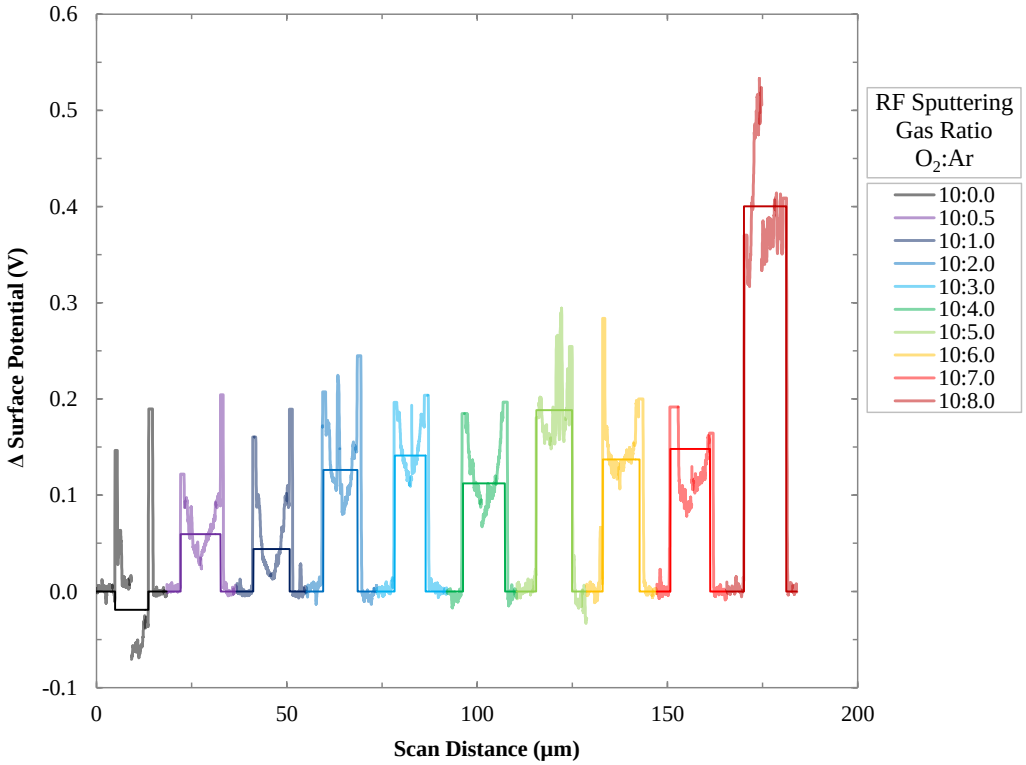

Figure 5.31: KPM Measured Surface Potential of Ir/IrO$_x$ Films (5 Minute Deposition)

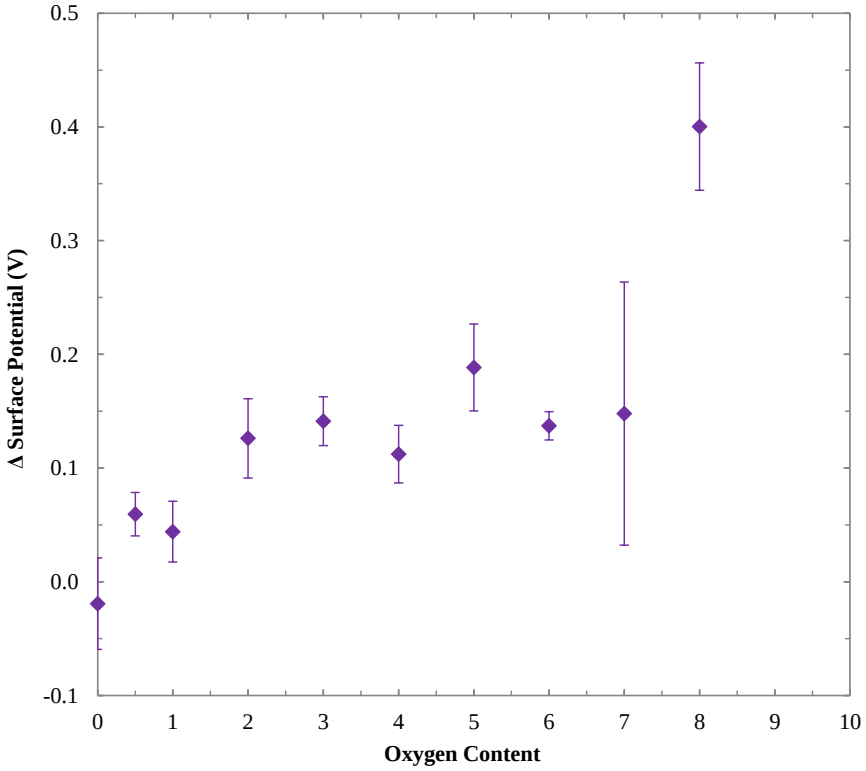

Figure 5.32: KPM Calculated Surface Potential of Ir/IrO$_x$ Films (5 Minute Deposition)

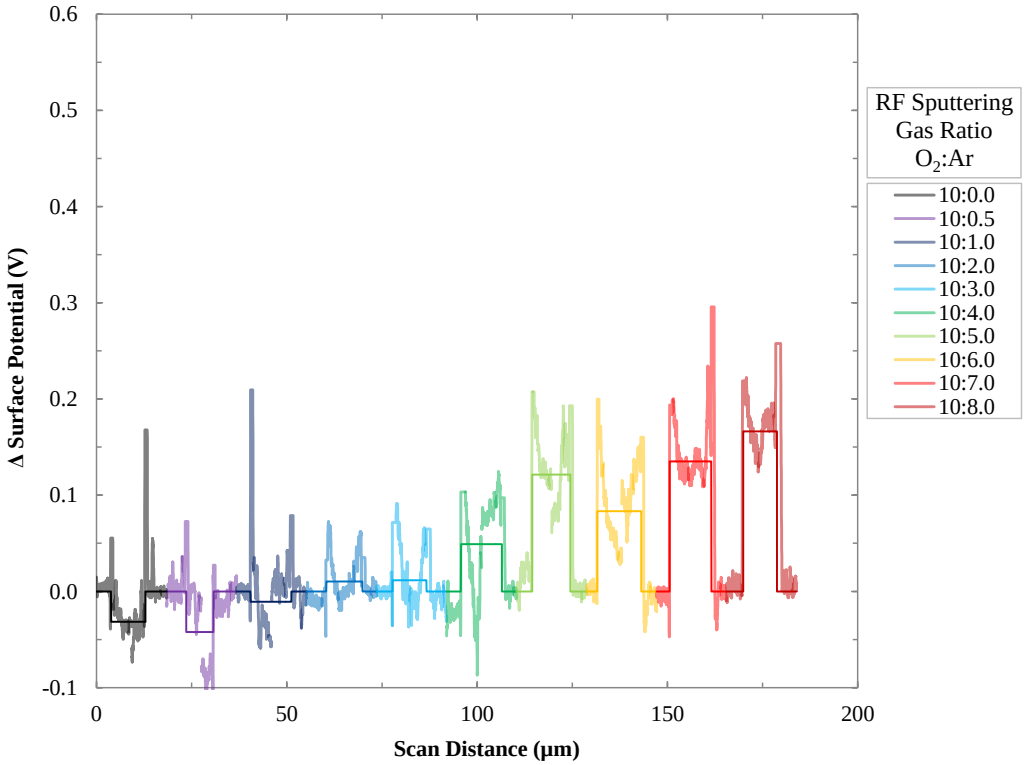

Figure 5.33: KPM Measured Surface Potential of Pt/PtO$_x$ Films (5 Minute Deposition)

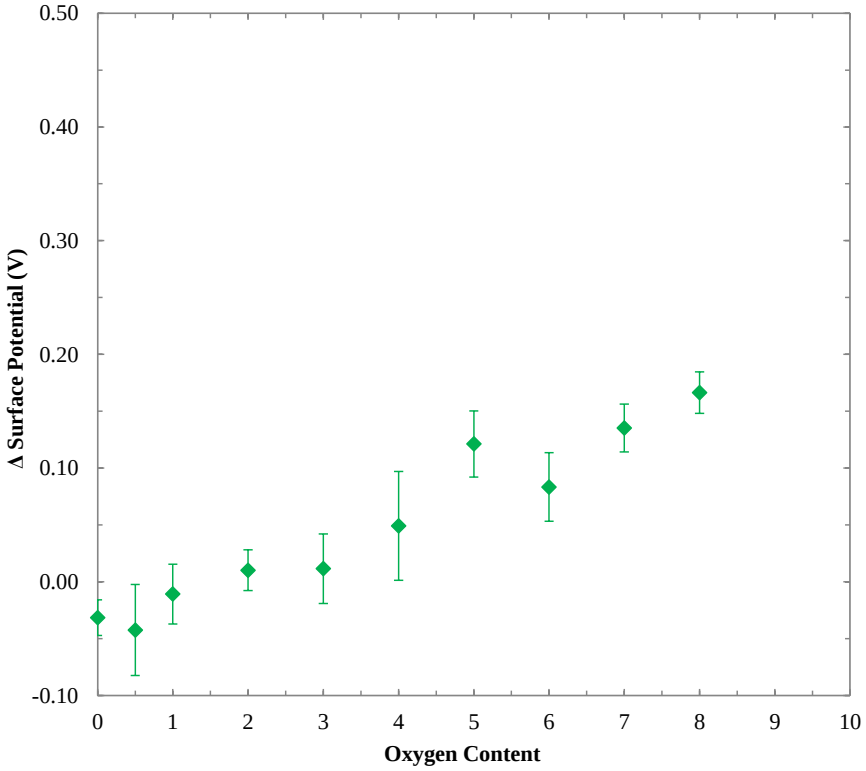

Figure 5.34: KPM Calculated Surface Potential of Pt/PtO$_x$ Films (5 Minute Deposition)

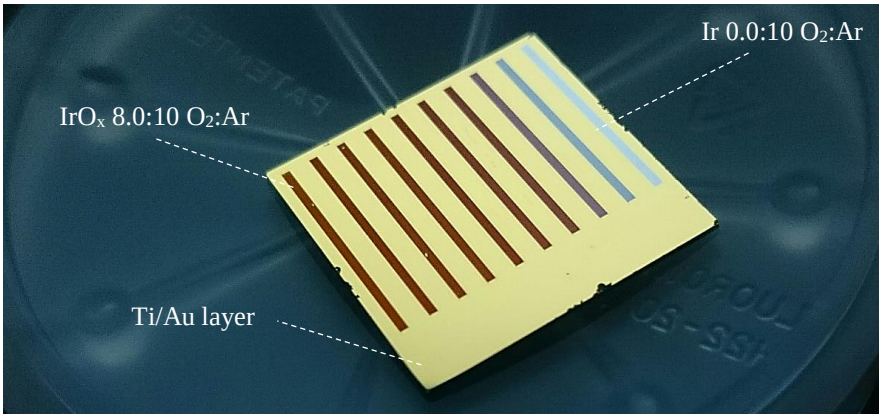

Figure 5.35: Ir/IrO$_x$ Films (5 Minute Deposition) 100 *x* 100 mm AFM Sample

The $\Delta V_{surface}$ of the 0.0:10 to 8.0:10 (O_2:Ar) Ir/IrO$_x$ films was between -19 ± 40 mV to 400 ± 60 mV, shown in Figures 5.31 – 5.32. Reported work functions of polycrystalline Au, Ir, and IrO_2 have been used to calculate theoretical $\Delta V_{surface\ potential}$ values of between -660 to 200 mV from Au to Ir, and 900 – 1270 mV from Au to IrO_2 [5.23 – 5.24]. This is higher than the $\Delta V_{surface\ potential}$ values from Au to IrO_2 measured in this work.

The $\Delta V_{surface\ potential}$ of the 0.0:10 to 8.0:10 (O_2:Ar) Pt/PtO$_x$ films was between -32 ± 15 mV to 166 ± 20 mV, shown in Figures 5.33 – 5.34. Theoretical $\Delta V_{surface\ potential}$ values calculated from reported work functions of Au and Pt range between -600 – 550 mV from Au to Pt, however KMP measurements from Au to Pt have reported a surface potential difference of -45 ± 10 mV in literature, comparable to the $\Delta V_{surface}$ of Au to Pt measured in this work [5.23, 5.25]. The difference between the theoretical and measured surface potentials has been suggested to be due to surface-absorbed atmospheric oxygen and water vapour [5.25]. Despite this difference, Figures 5.32 and 5.34 show clear trends of increasing surface potential with increasing oxygen incorporation.

5.6 Metal-Oxide Film Stoichiometry

Determining the stoichiometry of the RF-sputtered films was vital to the characterisation of the Schottky contacts. Two methods were used to determine the level of oxygen incorporation present in the RF-sputtered films, XPS and RBS, detailed in Sections 4.6 and 4.5 respectively.

XPS was performed on RF-sputtered Ir/IrO$_x$, Pd/PdO$_x$, and Pt/PtO$_x$ films, with O_2:Ar ratios of 0.0:10 – 7.0:10, and 0.0:10 – 10.0:10 for Ir/IrO$_x$, and Pt/PtO$_x$, in Figures 5.36 – 5.40. The date of fabrication and XPS scan is listed above each figure, as RF-sputtered metal-oxide films fabricated for this work have been observed to visibly oxidise over time. XPS results included in this chapter are courtesy of Dr Colin Doyle, Faculty of Engineering, University of Auckland, New Zealand.

Ir, IrO_x Films Fabricated	23/10/2015 – 28/10/2015
XPS Performed	02/02/2016

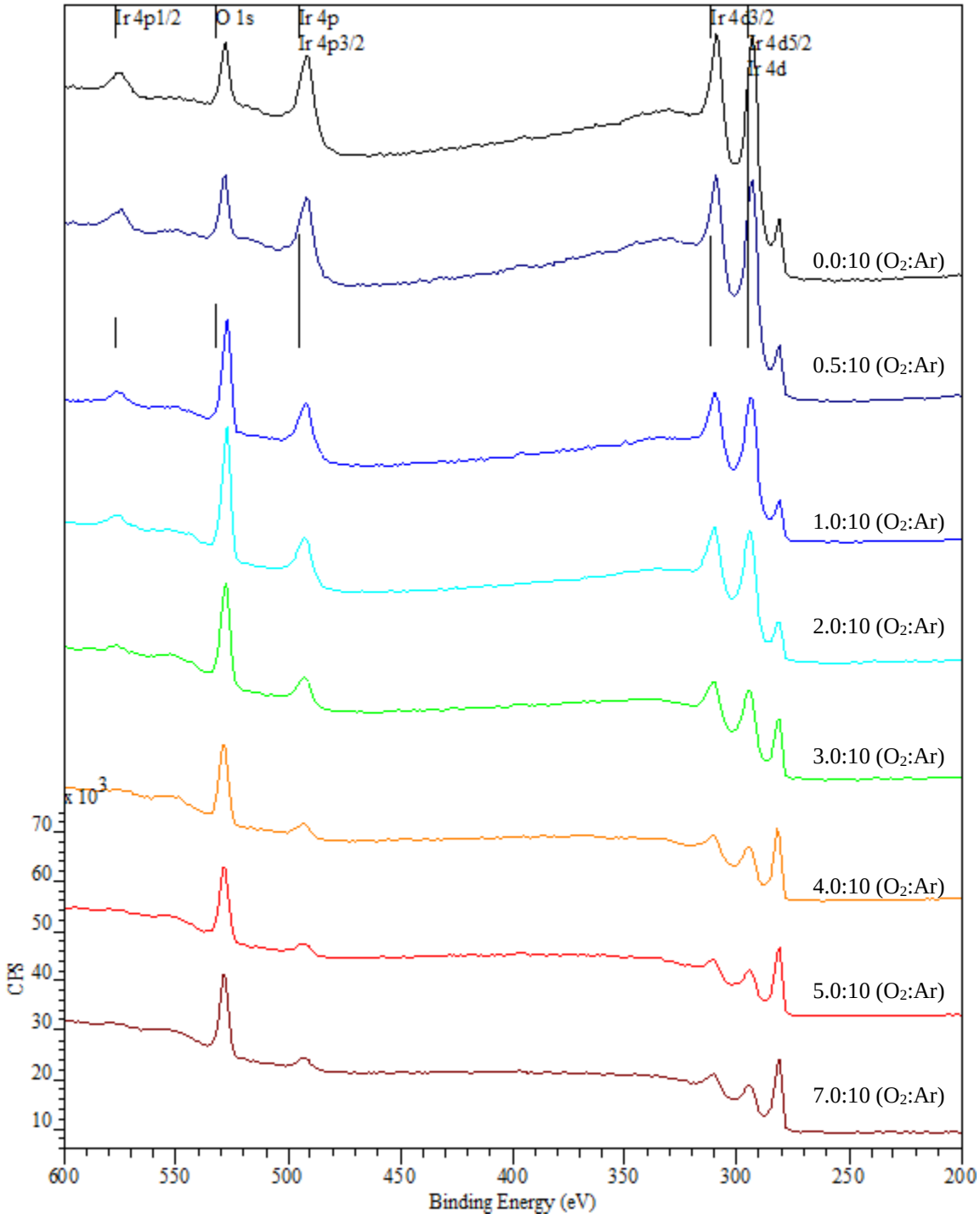

Figure 5.36: XPS Spectra of Survey 01 of Iridium Oxide Series

Ir, IrO_x Films Fabricated	03/07/2015 – 05/07/2015
XPS Performed	31/08/2015

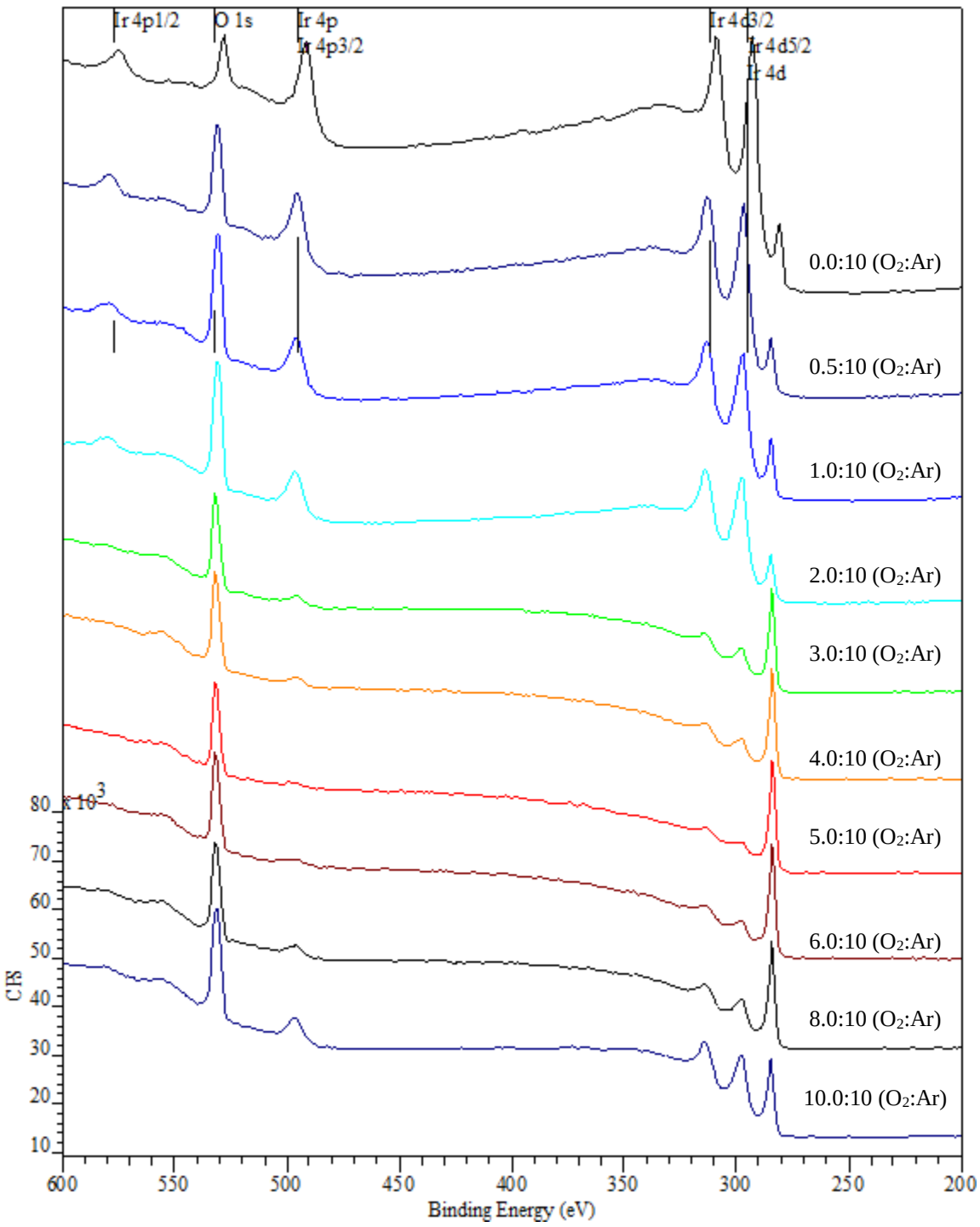

Figure 5.37: XPS Spectra of Survey 02 of Iridium Oxide Series

Pd, PdO_x Films Fabricated 23/10/2015 – 28/10/2015

XPS Performed 02/02/2016

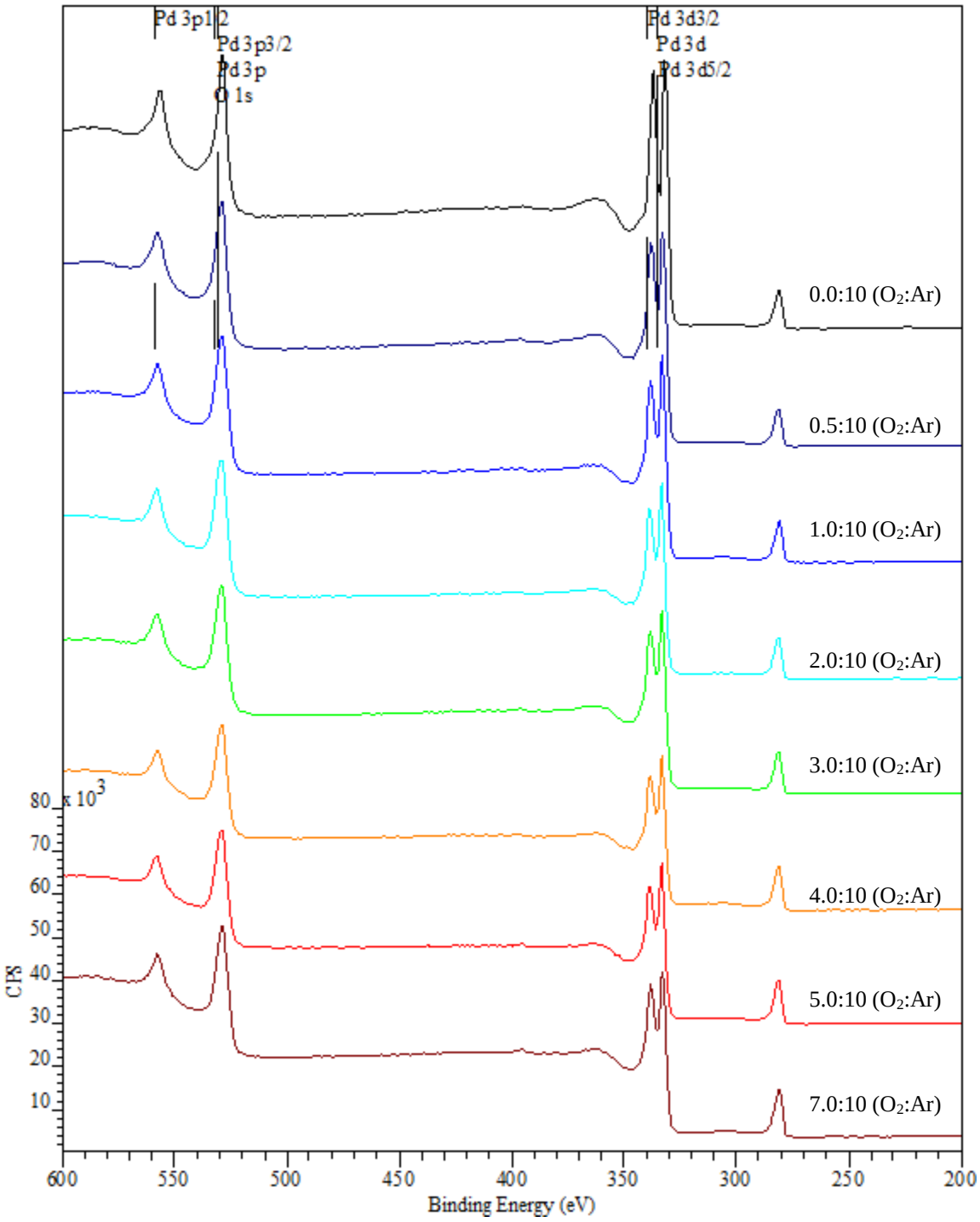

Figure 5.38: XPS Spectra of Survey 01 of Palladium Oxide Series

Pt, PtO_x Films Fabricated	23/10/2015 – 28/10/2015
XPS Performed	02/02/2016

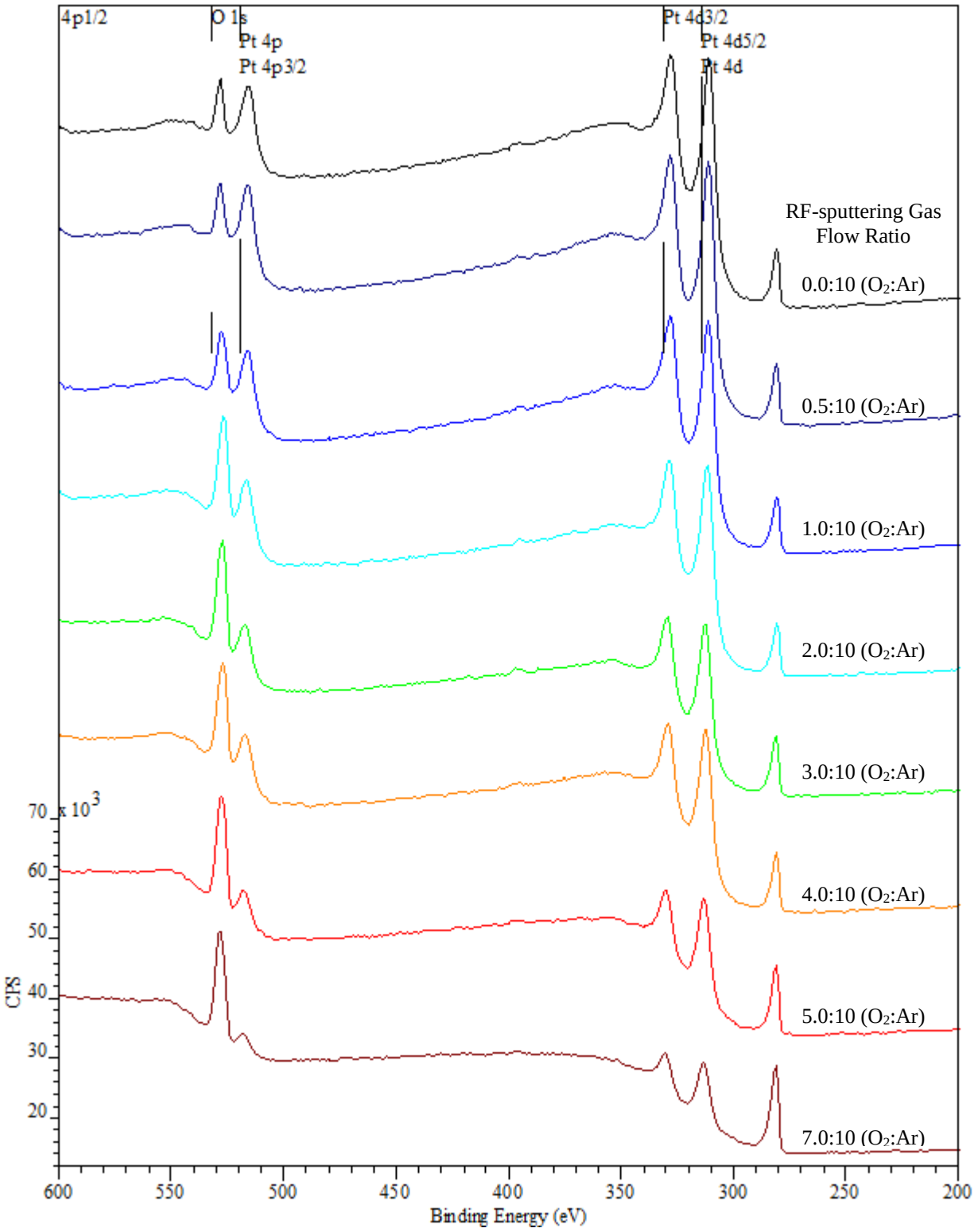

Figure 5.39: XPS Spectra of Survey 01 of Platinum Oxide Series

Pt, PtO_x Films Fabricated	03/07/2015 – 05/07/2015
XPS Performed	31/08/2015

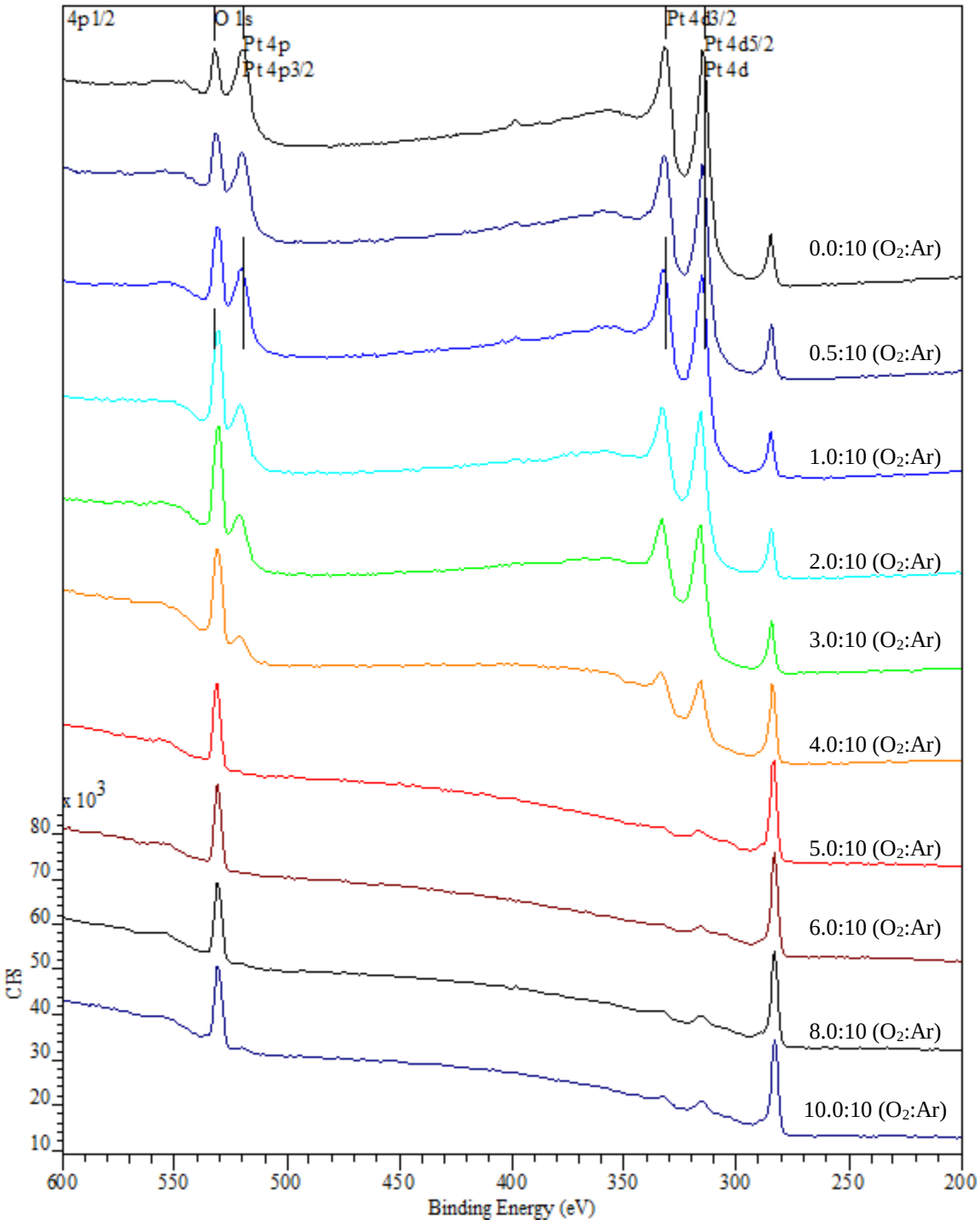

Figure 5.40: XPS Spectra of Survey 02 of Platinum Oxide Series

The XPS spectra for Ir/IrO_x, shown in Figures 5.36 – 5.37, display a clear trend of increasing peak area ratio between the O 1s peak and the Ir 4p peak with increasing oxygen flow during RF-sputtering. Figures 5.39 – 5.40, the XPS spectra for Pt/PtO_x, also show a clear trend of increasing ratio between the O 1s peak and the Pt 4p peak across the 0.0 – 7.0 and 0.0 – 10.0:10 (O_2:Ar) series. The valence band XPS spectra of all metal-oxide films measured by XPS also showed a photoemission edge near zero binding energy, indicating that the metal-oxide films still retained metallic-like characteristics.

For the XPS spectra of Pd/PdO_x, Figure 5.38, the O 1s peak is overlapped by the Pd 3p peak, therefore the oxygen content of the PdO_x films cannot be observed directly from the ratio of the O 1s peak to the Pd 3d peak. However, an enlarged scan of the O 1s/Pd $3p_{3/2}$ peaks across the Pd/PdO_x oxidation series in Figure 5.41 shows an increasing contribution from a peak at 526.7 eV with increasing O_2:Ar ratio. This peak is due to oxygen species, and is evidence of increasing oxygen incorporation in the PdO_x films [5.26 – 5.27]. The 529.4 eV peak is Pd $3p_{3/2}$ [5.26 – 5.27].

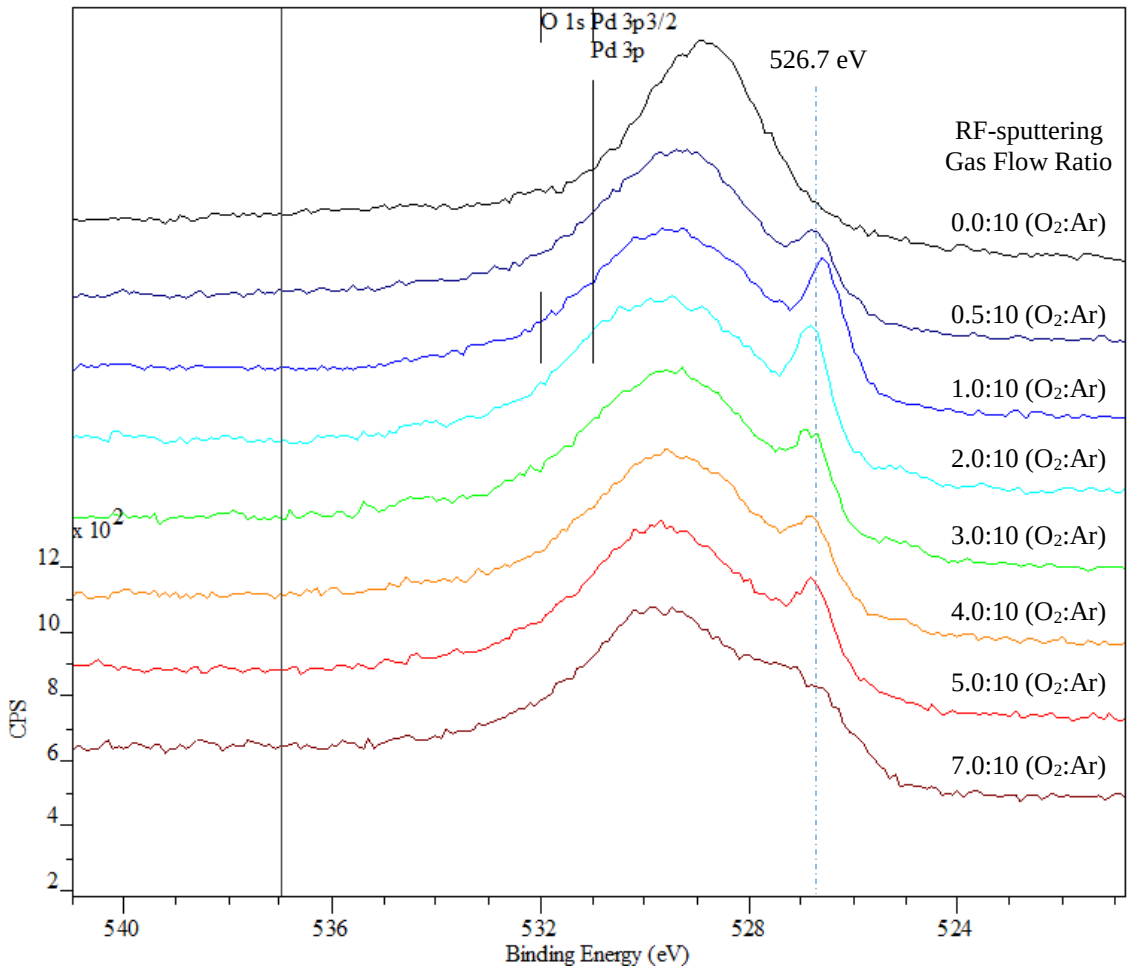

Figure 5.41: Normalised XPS Spectra of Palladium Oxide Series O 1s/Pd 3d Peak

Separate, high-resolution XPS spectra were measured over regions of interest for the Ir/IrO_x, Pd/PdO_x, and Pt/PtO_x films with 0.0:10 – 7.0:10 (O_2:Ar), from Figures 5.36, 5.38, and 5.39. These regions were the O 1s and C 1s peak of all materials, as well as the noble metal doublet peaks commonly used in chemical identification, Ir $4f_{5/2}$/Ir $4f_{7/2}$, Pd $3d_{3/2}$/Pd $3d_{5/2}$, and Pt $4f_{5/2}$/Pt $4f_{7/2}$ [5.28]. These scans were used to calculate the area of the component peaks in order to calculate the stoichiometry of the films. However, as XPS is a surface-sensitive measurement, and as the films have been observed to visibly oxidise over time, the stoichiometry calculated from XPS is unlikely to accurately reflect the stoichiometry of the Schottky contact at the metal-semiconductor interface, therefore these measurements were only used to confirm increasing oxygen incorporation with increasing O_2:Ar gas ratio during RF-sputtering.

The CasaXPS software package was used for peak-fitting and area calculation, as described in Section 4.1.6. The O 1s peaks were deconvoluted into three peaks of O, O^-, and O^{2-}. The noble metal doublets were deconvoluted into pairs of Gaussian peaks forming doublets of different charge states. Figures 5.42 – 5.44 show the doublets of the plain metal films and the 7.0:10 O_2:Ar films for Ir/IrO_x, Pd/PdO_x, and Pt/PtO_x. The binding energies of the fitted peaks in Figures 5.42 – 5.44 were calibrated using the fitted C 1s peak and reference C 1s peak value, 284.8 eV [5.7, 5.18, 5.26, 5.30].

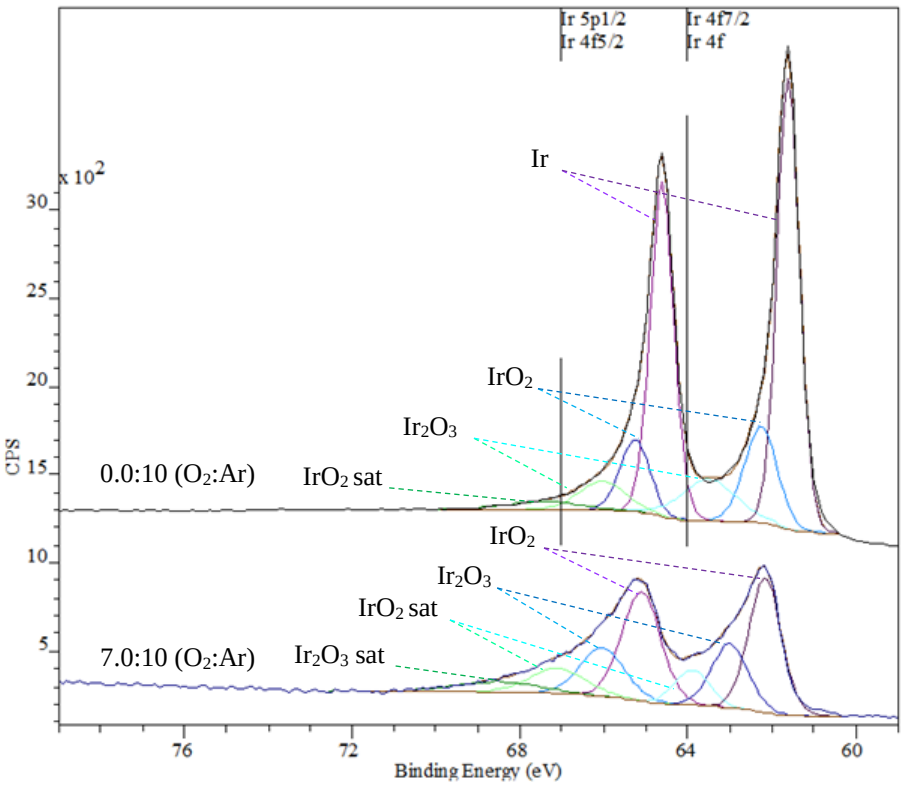

Figure 5.42: Ir $4f_{5/2}$, Ir $4f_{3/2}$ Fitted Peaks for 0.0:10 – 7.0:10 (O_2:Ar) IrO_x

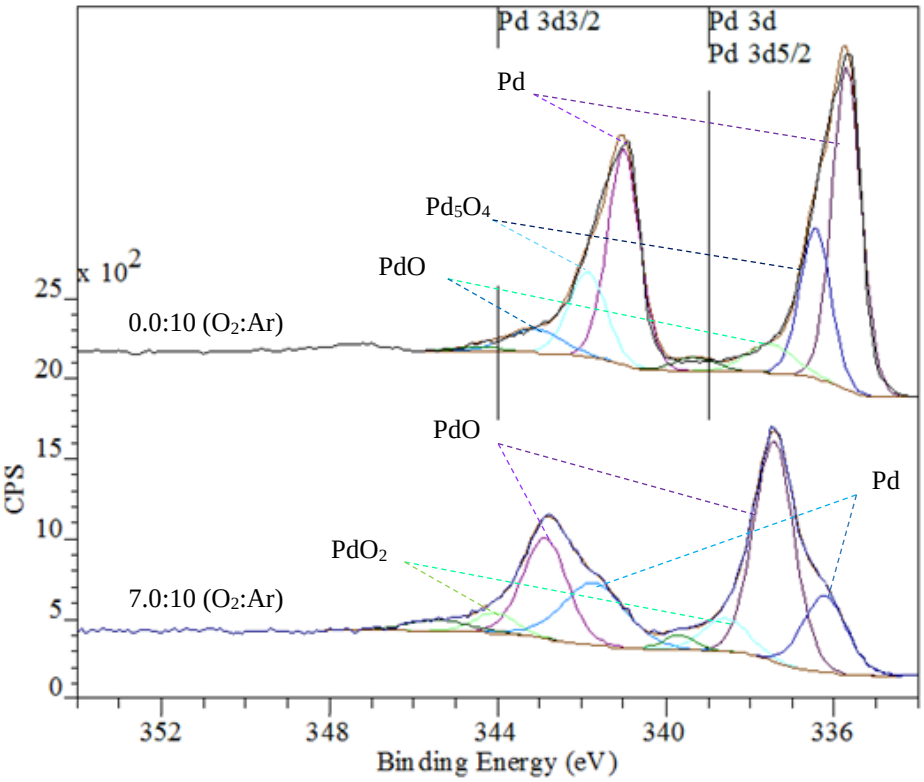

Figure 5.43: Pd $3d_{3/2}$, Pd $3d_{5/2}$ Fitted Peaks for f 0.0:10 – 7.0:10 (O_2:Ar) PdO_x

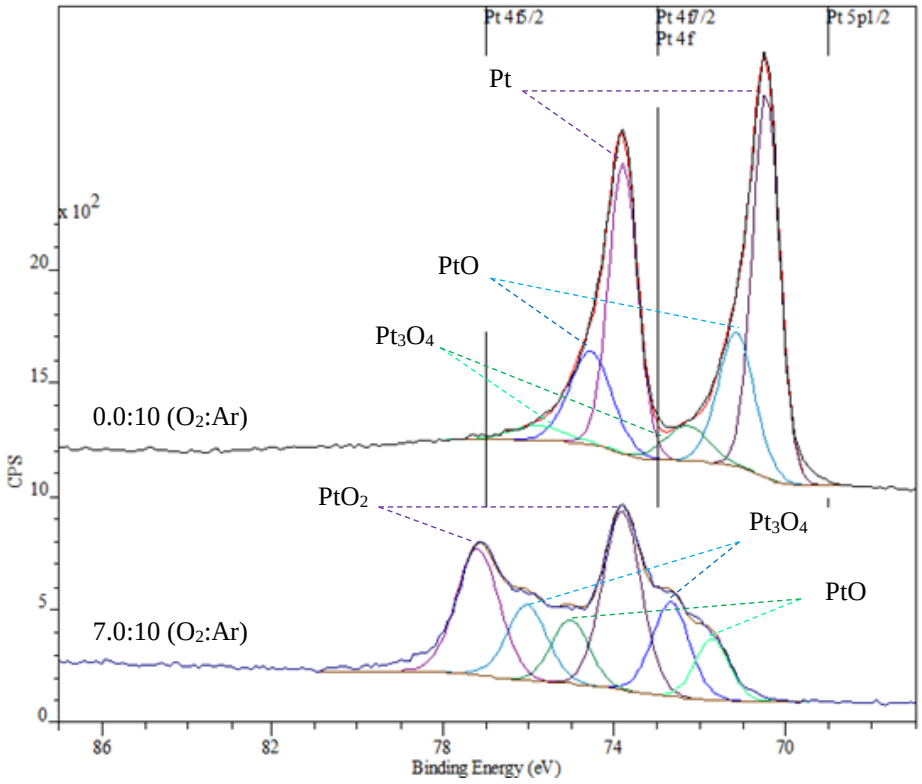

Figure 5.44: Pt $4f_{5/2}$, Pt $4f_{7/2}$ Fitted Peaks for 0.0:10 – 7.0:10 (O_2:Ar) PtO_x

Figure 5.42 shows the Ir/IrO_x $4f_{7/2}$ peak deconvoluted into peaks of Ir (60.7 eV), IrO_2 (61.6 eV), and Ir_2O_3 (62.5 eV). The IrO_x $4f_{7/2}$ is a wide peak, with the nature of the fitted components disputed in literature [5.29, 5.31]. The Ir $4f_{7/2}$ and IrO_2 $4f_{7/2}$ peaks were commonly reported as 60.8 – 60.9 eV and 61.2 – 61.9 eV respectively, which matches the fitted Ir $4f_{7/2}$ and IrO_2 $4f_{7/2}$ peaks in Figure 5.42 [5.20, 5.29, 5.31, 5.32, 5.33]. In amorphous IrO_x, doublets with higher levels of oxidation have been identified as Ir_2O_3 and an IrO_2 satellite, although the IrO_2 satellite $4f_{7/2}$ peak is lost in the overlap of the $4f_{5/2}$ peaks [5.29, 5.31]. The Ir_2O_3 $4f_{7/2}$ peak (62.3 eV) matches the fitted Ir_2O_3 $4f_{7/2}$ peak [5.29].

The Pd/PdO_x 3d doublet is most commonly used for identifying oxidation states in Pd/PdO_x [5.26]. Figure 5.43 shows the Pd/PdO_x $3d_{5/2}$ peak deconvoluted into peaks of Pd (335.5 eV), PdO (336.6 eV), PdO_2 (337.6 eV), and an unknown oxidation level PdO_x, (339.0 eV) [5.26]. These peaks match the reported values of Pd (335.4 eV), PdO (336.9 eV), and PdO_2 (337.5 eV), indicating that the modelling of the peaks was accurate [5.26, 5.28, 5.34]. The trend in XPS measurements of 0.0:10 – 7.0:10 (O_2:Ar) shows the Pd peak reducing in size and the PdO peak dominating in 7.0:10 (O_2:Ar), with traces of PdO_2 and an unknown oxidation state of PdO_x.

The Pt/PtO_x 4f doublet is commonly used for identifying oxidation states in Pt/PtO_x [5.28]. Figure 5.44 shows the Pt/PtO_x $4f_{7/2}$ peak deconvoluted into peaks of Pt (71.6 eV), PtO (72.8 eV), and PtO_2 (73.5 eV). These peaks align with reported values of Pt (71.0 eV), PtO (72.3 eV), PtO_2 (74.0 eV) [5.21, 5.28, 5.35, 5.36]. The PtO_2 $4f_{7/2}$ peak was located at a lower energy than the reported peak, however this has also been seen in other instances of RF-sputtered PtO_x, indicating the formation of a compound such as Pt_2O_3 or Pt_3O_4, rather than PtO_2 [5.18].

The oxygen content of the films was calculated using Equations 5.4 – 5.5 in Table 5.1, where *A* is the area under the doublet [5.20, 5.36]. Figures 5.45 – 5.47 show the oxygen incorporation ratios calculated using Equations 5.4 – 5.5. Figure 5.48 shows the oxygen incorporation ratio by dividing the area of the whole O 1s peak by the area of the fitted metal doublet. Although the O 1s peak was modelled by three peaks for O, O^- and O^{2-} (detailed in Section 4.1.6), the whole O 1s peak area was used in the calculations for Figure 5.48 due to modelling uncertainty [5.20, 5.36].

Table 5.1. XPS Metal/Metal Oxide Doublet Fitted Peak Oxygen Incorporation Calculation

Material	Equation	Equation No.
Ir/IrO_x	$O:Ir = \frac{\left(\frac{3}{2}\right)A_{Ir_2O_3} + 2A_{IrO_2}}{A_{Ir_2O_2} + A_{IrO_2} + A_{Ir}}$	(5.4)
Pd/PdO_x and Pt/PtO_x	$O:Pt = \frac{2A_{PtO_2} + A_{PtO}}{A_{PtO_2} + A_{PtO} + A_{Pt}}$	(5.5) [5.36]

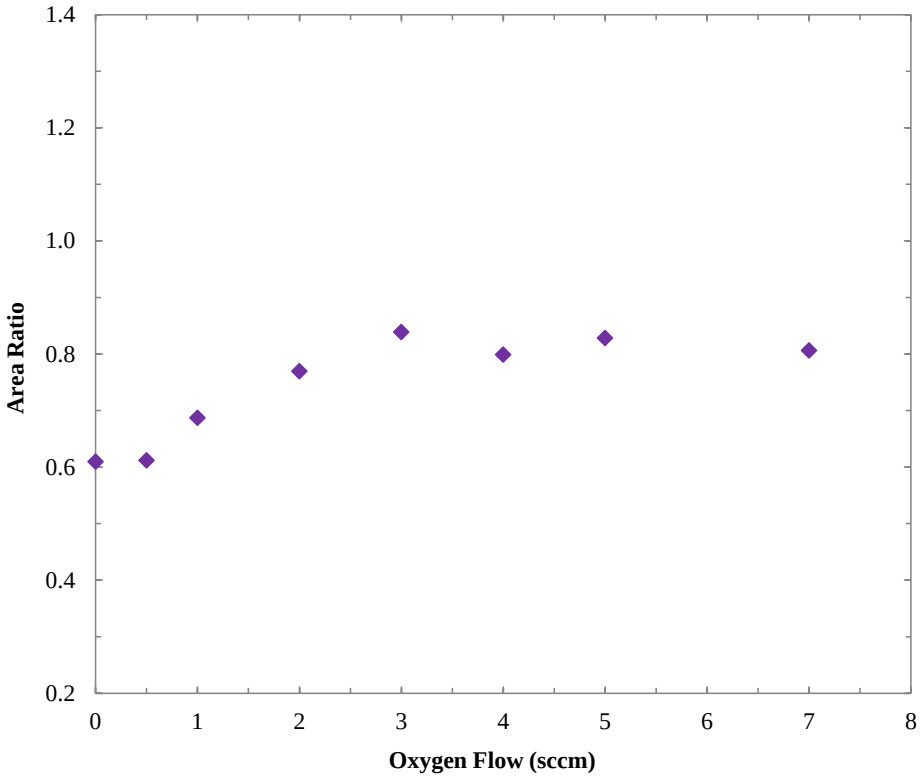

Figure 5.45: O:Ir Ratio from XPS Fitted Doublet Ir 4f for 0.0:10 – 7.0:10 (O_2:Ar) IrO_x

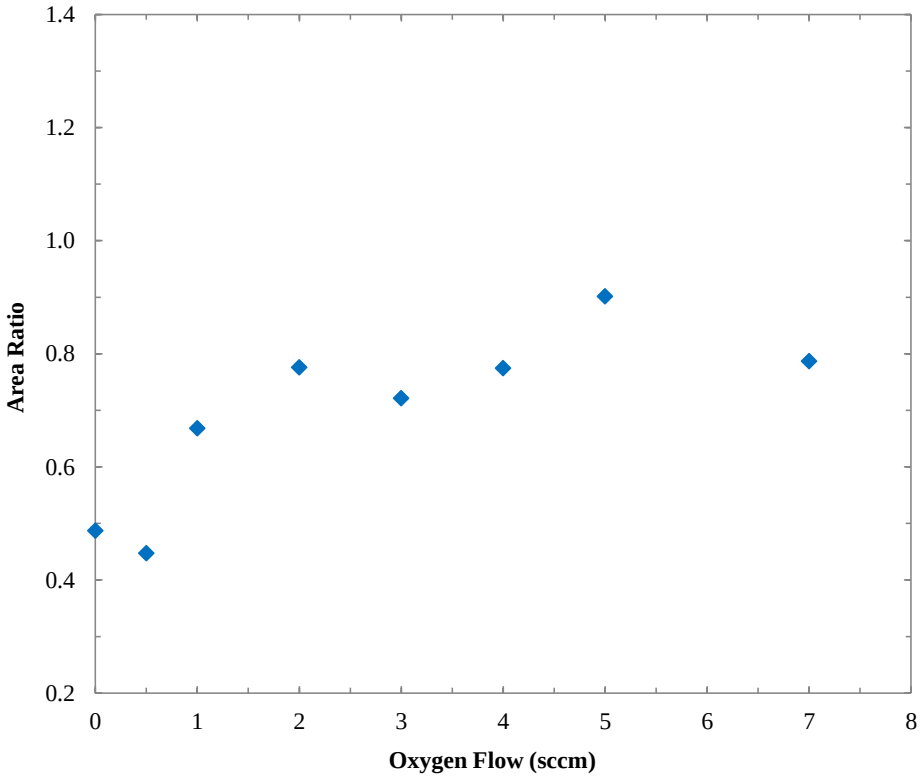

Figure 5.46: O:Pd Ratio from XPS Fitted Doublet Pd 3d for 0.0:10 – 7.0:10 (O_2:Ar) PdO_x

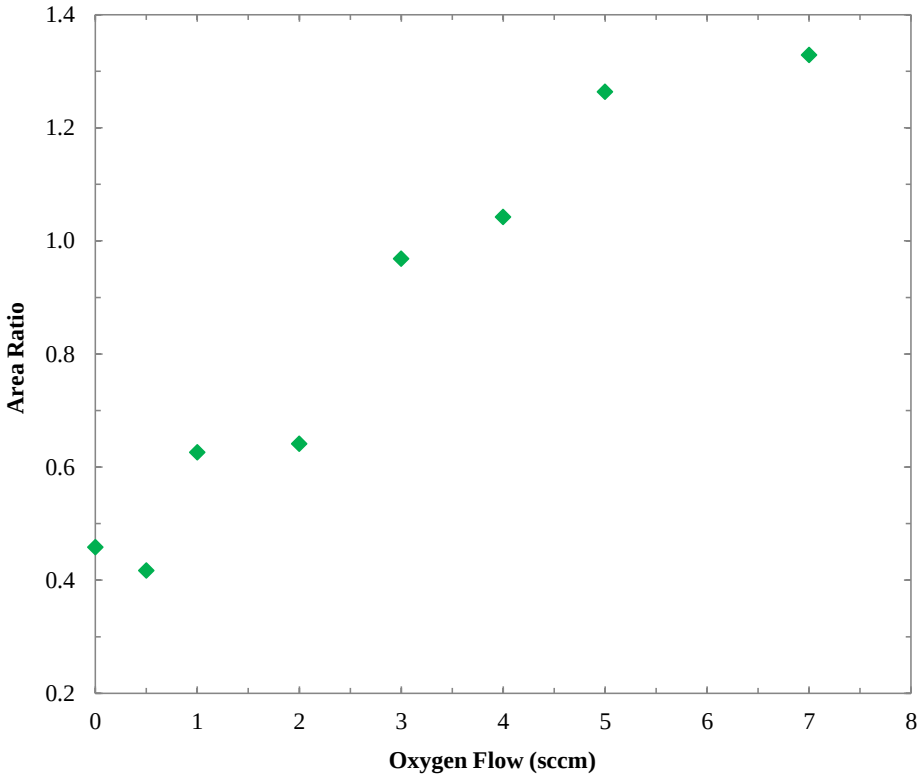

Figure 5.47: O:Pt Ratio from XPS Fitted Doublet Pt 4f for 0.0:10 – 7.0:10 (O_2:Ar) PtO_x

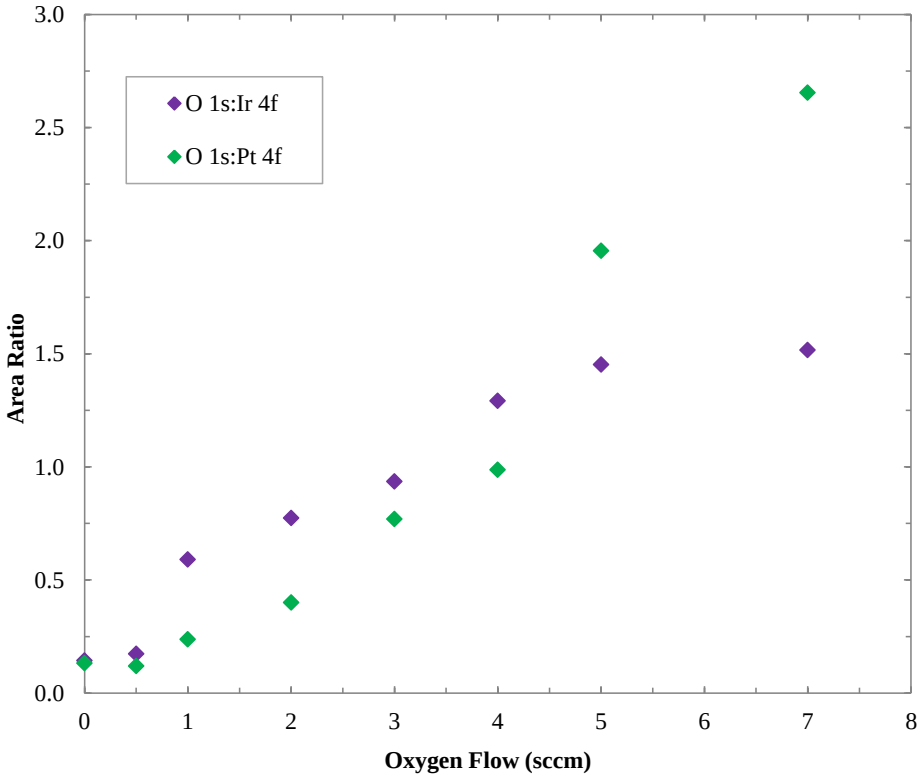

Figure 5.48: Area Ratio of O 1s Peak to Ir, Pt Doublet Peaks from XPS Spectra

Figures 5.45 – 5.47 confirm an increasing oxygen content with increasing O_2:Ar gas ratio during sputtering, with both the Ir/IrO_x and Pd/PdO_x series reaching an oxygen incorporation plateau around 3.0:10 (O_2:Ar). The Pt/PtO_x series appeared to be increasing in oxygen incorporation at 7.0:10 (O_2:Ar). The stoichiometry of the films shown in Figures 5.45 – 5.47 was not used as a measure of oxygen incorporation for the Schottky contacts, as surface-level contamination and uncertainty in the fitting of the peaks introduced an unknown level of error. However, both the ratio of areas of metal-oxides to metal doublets, and the ratio of the O 1s peak to the metal doublets in Figures 5.45 – 5.48 show clear trends of increasing oxygen incorporation.

In order to accurately obtain the stoichiometry of the films at the Schottky interface, RBS was performed on Ir/IrO_x, Pd/PdO_x, and Pt/PtO_x films deposited by RF-sputtering, a technique detailed in Section 4.1.5. The films used for RBS measurements in this work were deposited on glassy carbon substrates, as described in Section 3.4. RBS measurements and calculations were performed by Professor Steven M. Durbin and Robert Makin of the Department of Electrical and Computer Engineering, Western Michigan University, United States of America, with tabulated results in Appendix A4.4. The RBS results are shown in Figures 5.49 – 5.51, with arctangent trends identified and fitted by Robert Makin. The fitted trends are listed in Equations 5.6 – 5.8 of Table 5.2.

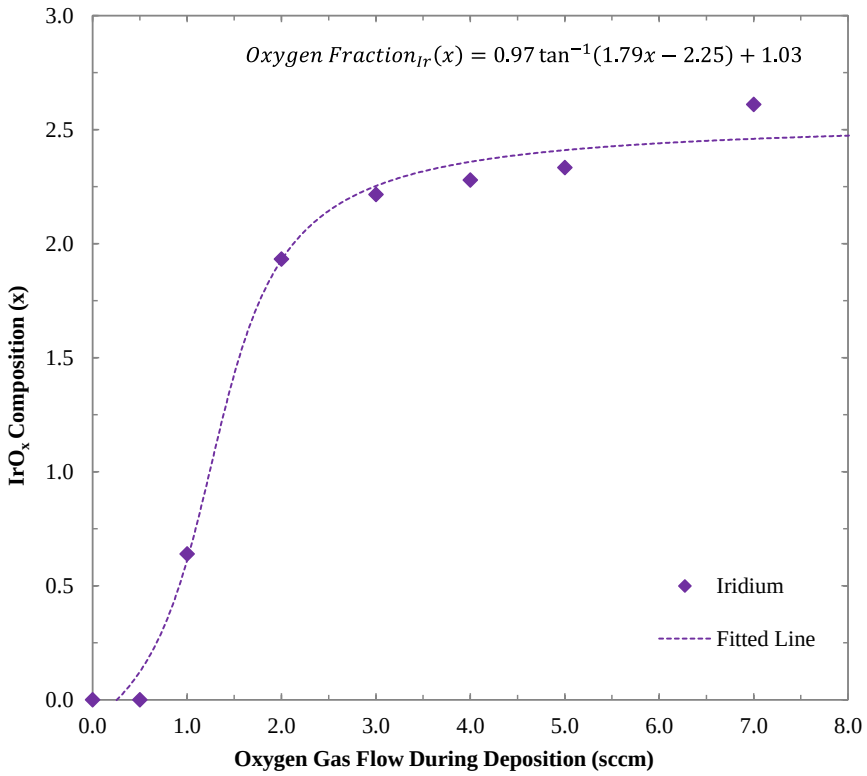

Figure 5.49: Oxygen Ratio in Iridium Oxide Films from RBS, Fitted Relationship

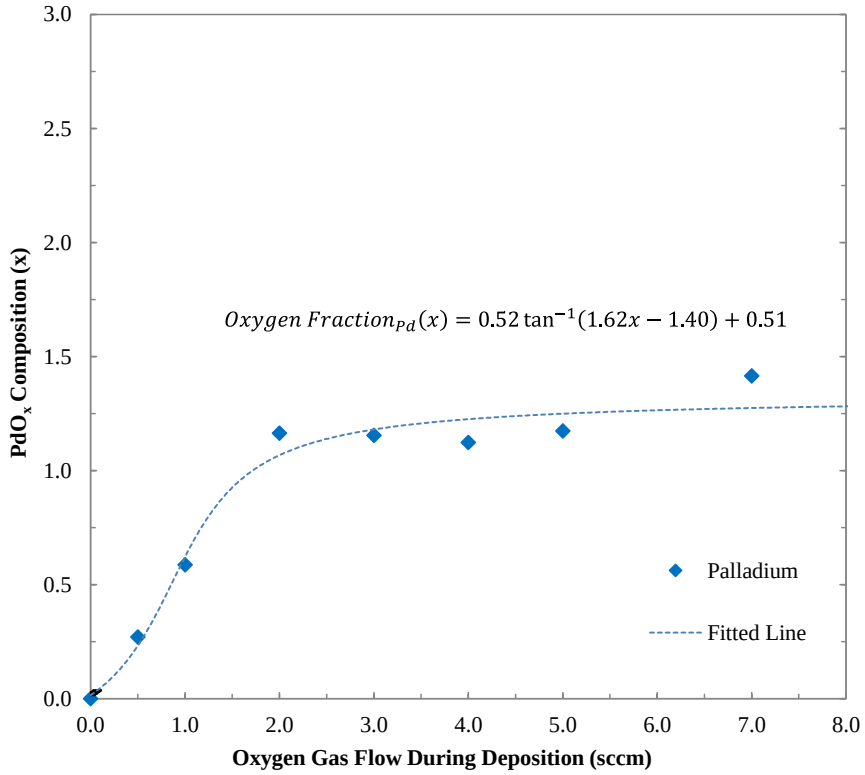

Figure 5.50: Oxygen Ratio in Palladium Oxide Films from RBS, Fitted Relationship

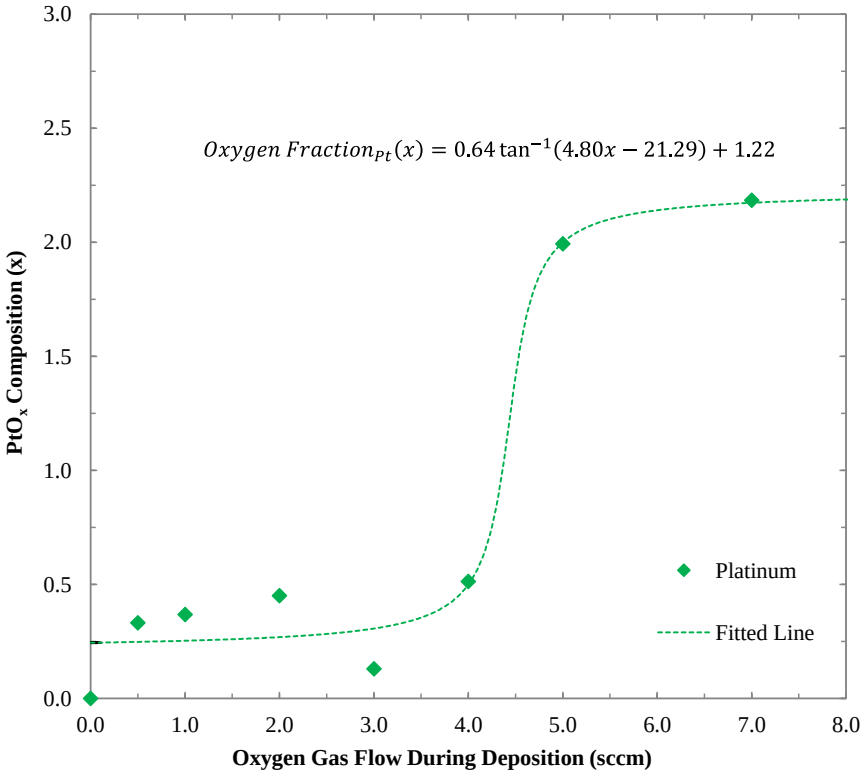

Figure 5.51: Oxygen Ratio in Platinum Oxide Films from RBS, Fitted Relationship

Table 5.2. Fitted Arctangent Trends of Rutherford Backscattering Results

Material	Equation	Equation Number
Ir/IrO_x	$Oxygen\ Fraction_{Ir} = 0.97\tan^{-1}(1.79x - 2.25) + 1.03$	5.6
Pd/PdO_x	$Oxygen\ Fraction_{Pd} = 0.52\tan^{-1}(1.62x - 1.40) + 0.51$	5.7
Pt/PtO_x	$Oxygen\ Fraction_{Pt} = 0.64\tan^{-1}(4.80x - 21.29) + 1.22$	5.8

As RBS measures bulk stoichiometry (compared to surface-sensitive XPS measurements), and as the uncertainties calculated for the RBS stoichiometry by Professor Steven M. Durbin and Robert Makin were less than 0.5%, it can be concluded that the stoichiometry values calculated from the RBS measurements were an accurate reflection of the RF-sputtered films. The outliers in Figure 5.49 of 0.5:10 (O_2:Ar) IrO_x and of 3.0:10 (O_2:Ar) PtO_x in Figure 5.51 are believed to be caused by surface contamination or physical damage to the films between fabrication and RBS measurement.

Oxygen incorporations for RF-sputtered IrO_x films with increasing O_2:Ar gas flow ratios have been reported as x = 0.62 – 1.73 for 0.7:10 – 9.0:10 (O_2:Ar) [5.20]. The RBS values in Figure 5.49 show x = 0.64 for 1.0:10 (O_2:Ar), which is close to the literature value, but larger oxygen incorporation levels of x = 1.95 – 2.60 for 2.0:10 – 7.0:10. However, both oxidation series show a plateau in oxygen incorporation above 1.0:10 – 2.0:10 (O_2:Ar) [5.20].

Oxygen incorporation for RF-sputtered PdO_x films reported in literature show x = 0.12 – 1.33 for 1.1:10 – 3.3:10 (O_2:Ar), the O:Pd ratio reaching a plateau above 3.3:10 (O_2:Ar) [5.16]. RBS values in Figure 5.50 show the same trend of plateauing oxygen incorporation of x = 1.14 – 1.41 above 2.0:10 (O_2:Ar), but a higher value of x = 0.58 for 1.0:10 (O_2:Ar) films.

Oxygen incorporation in RF-sputtered PtO_x films reported in literature show x = 0.6 – 0.9 O:Pt for 2.5:10 (O_2:Ar) and x = 1.2 – 1.4 for 10.0:10 (O_2:Ar) [5.18, 5.21]. The published results are similar to the x = 0.45 with 2.0:10 (O_2:Ar) film measured in this work, but less than the 7.0:10 (O_2:Ar) film measured in this work from RBS, x = 2.18, shown in Figure 5.51.

The RBS measurements for the RF-sputtered metal films showed no oxygen in the Ir, Pd, and Pt films, which is standard for fabrication of these films [5.18, 5.20 – 5.21]. However, the RBS measurements for the metal-oxide films showed consistently higher values of oxygen incorporation for IrO_x, PdO_x, and PtO_x films, in comparison to films sputtered in similar conditions with similar O_2:Ar gas flow ratios [5.18, 5.20 – 5.21]. This difference could be due to many different factors involved in the RF-sputtering process. However, the trends of plateauing oxygen incorporation with higher O_2:Ar RF-sputtering gas ratios validates the calculated RBS values. The plateauing IrO_x and PtO_x around x = 2 and PdO_x around x = 1 is also supported by the XPS results of the 7.0:10 O_2:Ar films in Figures 5.42 – 5.44, where the dominant peaks were IrO_2, PdO, and PtO_2, respectively.

5.7 Metal-Oxide Film Conductivity

The resistivities of RF-sputtered films of Ir, IrO_x, Pd, PdO_x, Pt, and PtO_x were measured using Van der Pauw geometry contacts at the same time as the Hall effect measurements, for which the results are shown in Figures 5.52 – 5.54. The composition of the films was measured using RBS, as discussed in Section 5.4. The composition of 3.0:10 (O_2:Ar) PtO_x film was measured to be $x = 0.130$ by RBS, which appears as an outlier in Figure 5.54. For the analysis of the resistivity in this section, and due to the lack of a complete data set on the resistivity of PtO_x, the composition of the 3.0:10 (O_2:Ar) PtO_x film was averaged to be $x = 0.482$ from the composition of 2.0:10 (O_2:Ar) PtO_x, $x = 0.451$, and 4.0:10 (O_2:Ar) PtO_x, $x = 0.513$.

Measurement of the films with higher resistivity, such as 7.0:10 (O_2:Ar) IrO_x and PtO_x, was limited by the injection current range of the Hall Effect apparatus. Measurements of low-resistivity films, such as Ir and Pt, produced short-circuits in the Hall Effect apparatus and could not be measured. Modifications to the Hall Effect apparatus, or using a different setup for four-point probe resistance measurements, could extend the range of resistivities able to be characterised for the metal/metal-oxide films.

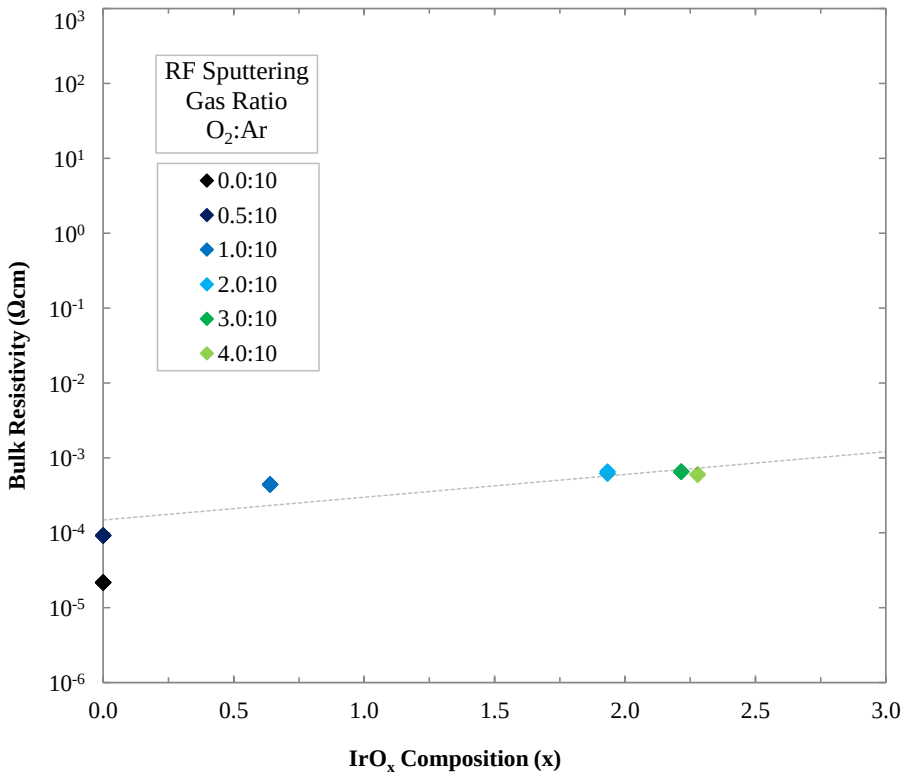

Figure 5.52: Bulk Resistivity of IrO_x Films with Composition (x)

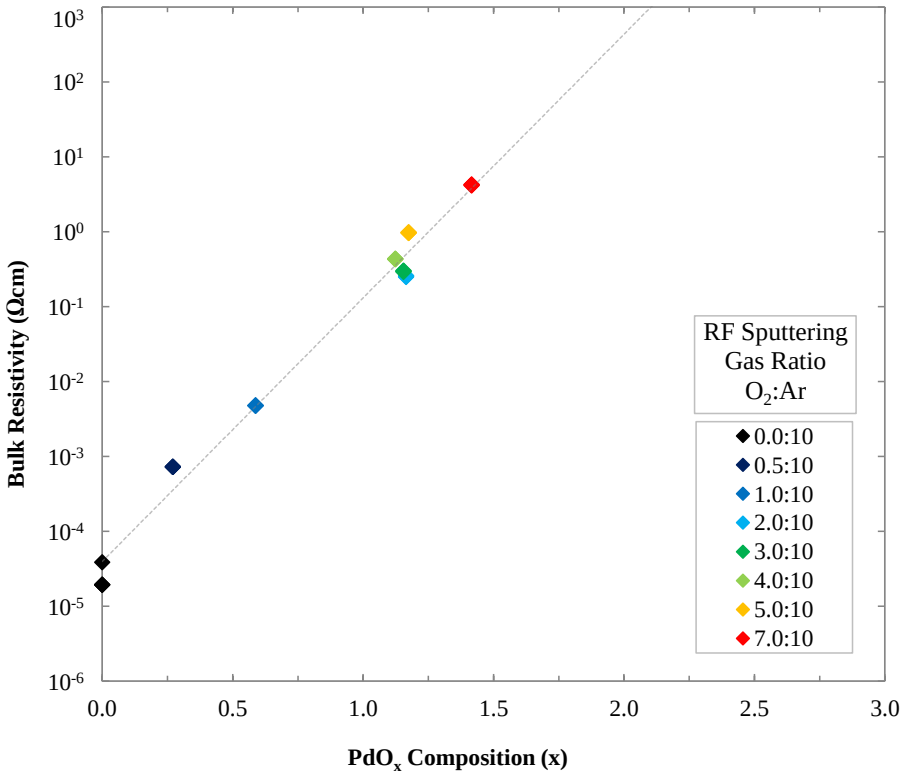

Figure 5.53: Bulk Resistivity of PdO_x Films with Composition (*x*)

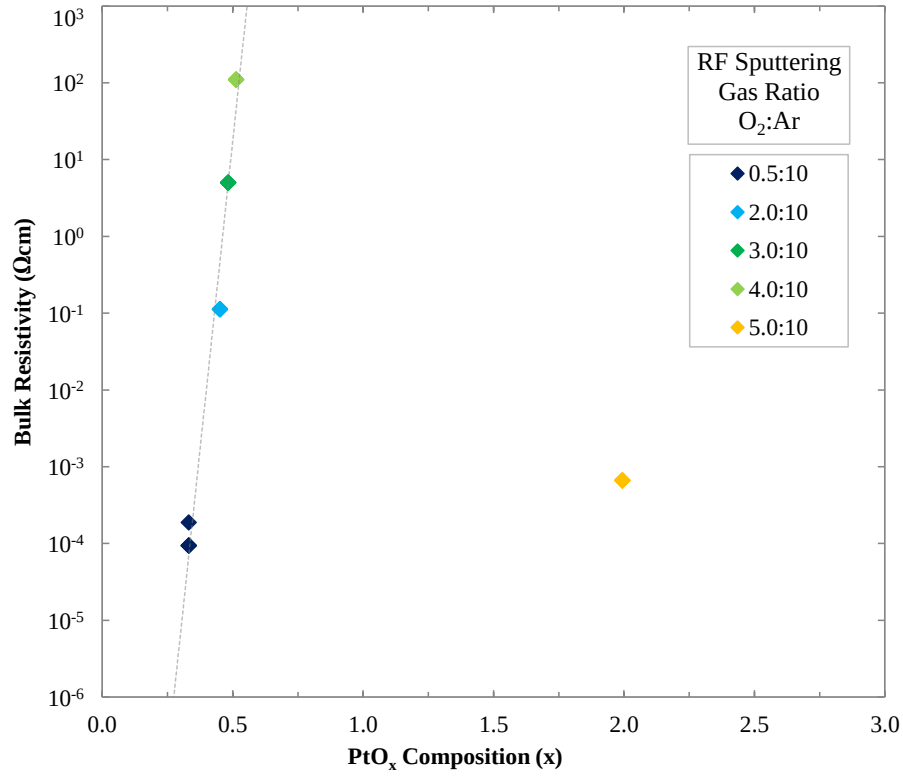

Figure 5.54: Bulk Resistivity of PtO_x Films with Composition (*x*)

The log-linear plot in Figure 5.52 shows the resistivity of the Ir/IrO_x films increasing with increasing oxygen incorporation, but remaining laterally conductive across the entire series. This behaviour is significantly different to the trends present in Figures 5.53 – 5.54, where the resistivities of the Pd/PdO_x and Pt/PtO_x films appear less laterally conductive with higher levels of oxygen incorporation. However, Pd/PdO_x and Pt/PtO_x Schottky contacts analysed in subsequent chapters in this work do not show decrease in forward bias conductivity with increasing oxygen incorporation, implying that the observed increase in resistivity with increasing oxygen incorporation of the Pd/PdO_x and Pt/PtO_x films is due to the lateral nature of the Van der Pauw measurement. The log-linear plots of Figures 5.53 – 5.54 show a clear, linear trend of logarithmic resistivity of the Pd/PdO_x and Pt/PtO_x films with increasing oxygen incorporation, indicating an exponential relationship between resistivity and oxygen incorporation, with the exception of the 5.0:10 (O_2:Ar) PtO_x film. However, the cause of the exponential relationship between the bulk resistivity and the oxygen incorporation of the metal-oxides requires further investigation.

The measured resistivity of the IrO_x films ranged from 91.3 – 655 μΩcm. This is higher than the published resistivity of bulk IrO_2, 48 μΩcm, but within an order of magnitude [5.37]. The shallow gradient in Figure 5.52 indicates that the resistivity of the IrO_x film grown in this work does not vary significantly over the range of oxygen partial pressures used. The 2:10, 3:10, and 4:10 (O_2:Ar) IrO_x films had similar stoichiometries measured by RBS, between x = 1.93 – 2.28. These films were most likely amorphous IrO_2 with a higher resistivity than the bulk form, due to the amorphous nature of low-temperature RF-sputtering observed in Section 5.1.1., an observation supported by the presence of the IrO_2 doublet from XPS measurements in Section 5.6.

Room temperature RF-sputtered IrO_x, x = 1.8 – 2.2, has been reported with resistivities between 500 – 600 μΩcm, which is within the range of resistivities of the films grown in this work [5.13]. ALD films of IrO_x grown at temperatures above 275 °C have been shown to produce polycrystalline films with resistivities between 9 – 10 μΩcm, and PLD films grown at room temperature have been shown to decrease in resistivity from 240 μΩcm to 37 μΩcm by annealing at 600 °C, indicating the potential for far lower-resistivity IrO_x films on ZnO [5.7, 5.14].

The PdO_x films show a log-linear trend across x = 0 – 1.5, indicating a mixture of oxidation phases with increasing O_2:Ar gas ratio during RF-sputtering, confirmed by the deconvoluted XPS measurements in Section 5.6. The resistivity ranged from 19.2 μΩcm – 4.25 Ωcm, with a concentration of oxygen incorporation between x = 1.12 – 1.17 with resistivities between 248 – 984 mΩcm, indicating a region of stable stoichiometry.

Single crystal PdO was reported to have resistivities between 10 – 1000 Ωcm, significantly higher than the films grown in this work, measured to be between 19.2 μΩcm – 4.25 Ωcm [5.38].

PdO_x ALD films have been reported with resistivities between 20 – 270 mΩcm [5.15]. RF-sputtered Pd films have also been oxidised into PdO by annealing the films at 700 °C in an oxygen atmosphere, with a reported PdO resistivity of 40 mΩcm [5.39]. Thermal oxidation of Pd foils has produced thin Pd/PdO films with resistivities of 19.8 – 62.1 mΩcm [5.40]. These reported resistivities were within an order of magnitude of the 248 – 984 mΩcm range of resistivities measured in this work, however the RF-sputtered PdO_x films in this work may have higher resistivities due to the amorphous nature of the films grown at room temperature, rather than a high-temperature method. As the oxygen incorporation extends beyond $x = 1$, it is likely that the PdO_x films contain an amorphous mix of Pd, PdO, and PdO_2. This is supported by the deconvoluted doublets of Pd, PdO, and PdO_2 in Section 5.6.

The PtO_x films show a steep log-linear trend across $x = 0 – 0.5$, with resistivities between 93.8 μΩcm – 110 Ωcm, with a potential outlier of 5.0:10 (O_2:Ar) with 663 μΩcm. RF-sputtered films of Pt and PtO_x have published resistivities of 10 μΩcm – 1 Ωcm with 1.1:10 – 1.0:0 O_2:Ar gas flow ratios [5.21]. Other publications have also reported RF-sputtered films with resistivities between 0.01 – 100 mΩcm with 0.0:10 – 10.0:10 O_2:Ar gas flow ratio, showing a log-linear trend of increasing resistivity with increasing oxygen incorporation [5.18]. DC sputtered films of Pt, PtO and PtO_2, have been published with resistivities between 0.01 – 10 mΩcm [5.41]. PtO_x ALD films have been produced with resistivities between 2 – 13 μΩcm [5.15].

As the oxygen incorporation values range from $x = 0 – 0.5$, the films were most likely an amorphous mix of Pt and PtO. As bulk PtO has been reported to be a metallic conductor with a resistivity of 1 – 2 mΩcm, the measured resistivities were higher than expected for the measured oxygen incorporation [5.21]. The low resistivity of the 5.0:10 (O_2:Ar) film indicates either an outlier, or an error due to the limitations of the Hall Effect apparatus for high-resistivity films. Further investigation is needed across the PtO_x series, both into the oxygen incorporation with partial pressure, and the resistivities, due to the presence of outliers.

5.8 Comparison of RF-Sputtered Metal-Oxides with Oxygen Content

Of the films characterised by transmission measurements in Figures 5.2 – 5.8, Pd/PdO_x showed the lowest attenuation of UV wavelengths, which is significant to the development of devices for UV dosimetry. However, the non-linear relationship between film thickness and transmission should be investigated for different levels of oxidation, as well as for different film materials, as thin (<10 nm) films of PtO_x and IrO_x in Figures 5.9 – 5.11 showed considerably less attenuation of UV wavelengths than the standard thickness of films. However, the Au top contact was also found

to attenuate wavelengths above 510 nm, which would cause an increase in the selectivity of the UV photodiodes fabricated in this work. Alternate top contact materials should be trialled.

Analysis of the structure of the RF-sputtered films using GIXRD found the plain metal films of Ir, Pd, and Pt to be polycrystalline, and the metal-oxide films of IrO_x and PtO_x were found to be amorphous, however 1.0:10 (O_2:Ar) PdO_x appeared polycrystalline. Further GIXRD measurements are required to characterise the degree of crystallinity in room temperature RF-sputtered PdO_x with increasing oxygen incorporation. There is evidence to suggest that room temperature RF-sputtered IrO_x films can be annealed from an amorphous to a polycrystalline state, however PtO_x films appear to decompose into Pt when annealed [5.13, 5.17 - 5.18, 5.21].

The growth rates of Ir/IrO_x and Pt/PtO_x were very similar to each other, but lower than the rates reported in literature. Many factors could account for the difference in growth rates between two RF-sputtering systems [5.20 – 5.21]. The surface potential of Ir/IrO_x and Pt/PtO_x with increasing oxygen incorporation showed a consistent decrease, as expected, however the surface potential of the oxides could not be verified due to surface contamination of chemically absorbed species of oxygen and water vapour from atmospheric conditions [5.25]. The growth rate and surface potential of Pd/PdO_x was not investigated due to time constraints.

Analysis of the XPS measurements in Section 5.6 showed that RF-sputtering of metal-oxides with higher O_2:Ar gas flow ratios during deposition produced films with higher levels of oxygen incorporation between 0:10 – 7.0:10 (O_2:Ar). Although the exact stoichiometries were considered to not reflect the stoichiometries of the RF-sputtered Schottky contacts at the Schottky interface due to increased surface oxidation compared to the bulk, the O 1s:Ir 4f and O 1s:Pt 4f trends observed from XPS measurements were similar to the trends found from the RBS measurements of O:Ir and O:Pt stoichiometry. The XPS and RBS also showed agreement in the dominant oxidation state of the noble metals for 0.0:10 (O_2:Ar), $x = 0$, and the 7.0:10 (O_2:Ar) films, with $x \approx 2$ for IrO_x and PtO_x, and $x \approx 1$ for PdO_x.

The RBS measurements for the metal-oxide films showed higher values of oxygen incorporation for IrO_x, PdO_x, and PtO_x films, compared to RF-sputtered films with similar deposition conditions in literature [5.18, 5.20 – 5.21]. This could also be caused by the differences between RF-sputtering chambers, or possibly by oxidation of the films between fabrication and RBS measurements.

The RBS measurements show a greater level of oxygen incorporation in Ir/IrO_x films. This is likely due to the preference of IrO_2 forming over IrO, compared with PtO_2/PtO and PdO_2/PdO shown in the XPS measurements of Figures 5.42 – 5.44. The XPS measurements showed a greater level of oxygen incorporation in PtO_x than IrO_x, and PdO_x showed the lowest levels of oxygen

incorporation in both XPS and RBS. The sensitivity of the Ir/IrO_x, Pd/PdO_x, and Pt/PtO_x films to O_2:Ar gas flow during RF-sputtering was within the same order of magnitude across both measurements, and showed similar trends with increasing O_2:Ar ratio. The Ag/AgO_x films showed the greatest sensitivity to O_2:Ar gas ratio during sputtering from the transmission measurements, however this sensitivity also complicated the characterisation of the films.

The conductivities of the metal/metal-oxide films were the most significant differences between the three materials tested. The range of resistivities for Ir/IrO_x, 91.3 μΩcm – 655 μΩcm, Pd/PdO_x, 19.2 μΩcm – 4.25 Ωcm, and Pt/PtO_x, 93.8 μΩcm – 110 Ωcm, varied more between materials than between oxygen incorporation. The low series resistance of Ir/IrO_x is more favourable for creating UV photodiodes. The lateral conductivity of the Ir/IrO_x Schottky contact material is also beneficial for UV photodiodes, as it would not need a complete capping layer to conduct photocurrent, allowing parts of the Schottky contact to be exposed to the UV light. The Pd/PdO_x series also showed a greater stability of conductivity with oxygen incorporation than the Pt/PtO_x series. The large change in conductivity with oxygen incorporation showed that the electrical characteristics of Pt/PtO_x Schottky contacts could change considerably over a long period of time.

In conclusion, the optical and electrical characteristics of the Ir/IrO_x, Pd/PdO_x, and Pt/PtO_x films show similar trends of increasing transmission, oxygen incorporation, and resistivity with increasing oxygen incorporation. Considering these similarities, an investigation into the characteristics of Ru/RuO_x and Ag/AgO_x should be considered, as the noble metals Ru and Ag are more earth-abundant than Ir, Pd, and Pt. Measures should also be taken to prevent the immediate oxidation of the Ag/AgO_x films, The oxidation series was generally limited to eight values between 0:10 – 7.0:10 (O_2:Ar), as each ZnO substrate used in this work could be diced into nine pieces; one of which was kept as a reference. In order to study the characteristics of the thin films, however, a wider range and a larger sample set should be used in order to reduce the impact of outliers, and to find the limitations and optimal points of oxygen incorporation.

5.9 Summary

In this chapter the optical, structural, and electrical characteristics of RF-sputtered noble metal and noble metal-oxide films fabricated simultaneously with the Schottky contacts analysed in Chapters 6 – 8, were investigated. The noble metals and metal-oxide films explored in this chapter include Ag, AgO_x, Ir, IrO_x, Pd, PdO_x, Pt, and PtO_x. Transmission measurements, XRD, AFM, KPM, XPS, RBS, and Hall effect measurements were performed on the Ir, IrO_x, Pd, PdO_x, Pt, and PtO_x films. Transmission measurements were also performed on the Ag and AgO_x films.

- The 15 minute deposition Ag, AgO_x, Ir, IrO_x, Pd, PdO_x, Pt, and PtO_x films all showed attenuation of UV wavelength transmission; an undesirable trait for UV sensors. However, a thickness series of both IrO_x and PtO_x films showed over 70% transmission for films 1 – 2 nm thick across the 200 – 800 nm spectrum, with over 90% transmission between 240 – 800 nm for a 1 nm thick film of 3.0:10 (O_2:Ar) IrO_x.

- The 40 nm Au capping layer used in this work showed very low transmission, and has not been proven to prevent further oxidation of the metal-oxide films, therefore laterally conducting films of IrO_x might benefit from not having an Au capping layer.

- The GIXRD scans of the RF-sputtered Ir, Pd, and Pt films showed polycrystalline structure. The IrO_x and PtO_x films appeared amorphous, however the 1.0:10 (O_2:Ar) PdO_x film appeared polycrystalline. Annealing room-temperature RF-sputtered films has been shown to improve the crystallinity of IrO_x and PdO_x films; however PtO_x decomposes with annealing [5.13, 5.16 – 5.17].

- AFM and KPM scans of 5 minute depositions Ir, IrO_x, Pt, and PtO_x films showed growth rates of 3.0 to 11 nms^{-1} for 0.0:10 to 8.0:10 (O_2:Ar) Ir/IrO_x, and 4.4 to 12 nms^{-1} for 0.0:10 to 8.0:10 (O_2:Ar) Pt/PtO_x, and a trend of increasing metal-oxide surface potential with increasing oxygen incorporation for both metal-oxide series.

- Deconvoluted XPS doublet peaks of Ir 4f, Pd 3d, and Pt 4f were used to calculate surface-level oxygen incorporation of Ir, IrO_x, Pd, PdO_x, Pt, and PtO_x films. All metal-oxide film series showed a trend of increasing oxygen incorporation with increasing O_2:Ar level, and a mixture of metal-oxidation states.

- RBS was used to calculate the oxygen incorporation of the Ir, IrO_x, Pd, PdO_x, Pt, and PtO_x films, showing an increasing oxygen incorporation from 0.0:10 to 7.0:10 (O_2:Ar) of x = 0.0 to 2.6 for Ir/IrO_x, x = 0.0 to 1.4 for Pd/PdO_x, and x = 0.0 to 2.2 for Pt/PtO_x.

- All Ir/IrO_x films were all laterally conductive, with resistivities of 22 to 600 μΩcm for 0.0:10 – 4.0:10 (O_2:Ar). The 0.0:10 – 7.0:10 (O_2:Ar) Pd/PdO_x and Pt/PtO_x films had lateral resistivities of 19 μΩcm to 4.14 Ωcm, and 94 μΩcm to 110 Ωcm, respectively, however this did not affect the forward bias current of the devices in Chapter 6.

REFERENCES

[5.1] Allen, M.W., Durbin, S.M., (2008), Influence of oxygen vacancies on Schottky contacts on ZnO, *Applied Physics Letters*, 92 (12), art. no. 122110.

[5.2] Robertson, J., Sharia, O., Demkov, A.A., (2007), Fermi level pinning by defects in Hf O_2 metal gate stacks, *Applied Physics Letters*, 91 (13), art. no. 132912.

[5.3] Allen, M.W., Durbin, S.M., Metson, J.B., (2007), Silver oxide Schottky contacts on n-type ZnO, *Applied Physics Letters*, 91 (5), art. no. 053512.

[5.4] Allen., M., (2008), *Schottky Contact Formation to Bulk Zinc Oxide*, PhD thesis, University of Canterbury, New Zealand.

[5.5] Allen, M.W., Mendelsberg, R.J., Reeves, R.J., Durbin, S.M., (2009), Oxidized noble metal Schottky contacts on n -type ZnO, *Applied Physics Letters*, 94 (10), art. no. 103508.

[5.6] Korotcenkov, G., (2013), *Chemical Sensors: Simulation and Modeling Volume 4: Optical Sensors, Vol. 4*, New York, NY, U.S.A: Momentum Press.

[5.7] Liu, Y., Masumoto, H., Goto, T., (2004), Electrical and optical properties of IrO_2 thin films prepared by laser-ablation, *Materials Transactions*, 45 (10), pp. 3023-3027.

[5.8] Shima, T., Tominaga, J., (2003), Optical transmittance study of silver particles formed by AgO_x thermal decomposition, *Journal of Vacuum Science and Technology A: Vacuum, Surfaces and Films*, 21 (3), pp. 634-637.

[5.9] Zhang, F., Wang, Y., Xu, W., Shi, H., Gan, F., (2005), Read-only memory disk with AgO_x super-resolution mask layer, *Chinese Optics Letters*, 3 (2), pp. 113-115.

[5.10] Yi, K.C., Hórvölgyi, Z., Fendler, J.H., (1994), Chemical formation of silver Particulate films under monolayers, *Journal of Physical Chemistry*, 98 (14), pp. 3872-3881.

[5.11] Kracker, M., Worsch, C., Rüssel, C., (2013), The effect of thermal annealing and hydrogen on the morphology and the optical properties of thin palladium layers, *Materials Letters*, 110, pp. 114-116.

[5.12] Slavcheva, E., Schnakenberg, U., Mokwa, W., (2006), Deposition of sputtered iridium oxide-Influence of oxygen flow in the reactor on the film properties, *Applied Surface Science*, 253 (4), pp. 1964-1969.

[5.13] Sanjinés, R., Lévy, F., Aruchamy, A., (1989), Thermal Stability of Sputtered Iridium Oxide Films, *Journal of the Electrochemical Society*, 136 (6), pp. 1740-1743.

[5.14] Hämäläinen, J., Hatanpää, T., Puukilainen, E., Sajavaara, T., Ritala, M., Leskelä, M., (2011), Iridium metal and iridium oxide thin films grown by atomic layer deposition at low temperatures, *Journal of Materials Chemistry*, 21 (41), pp. 16488-16493.

[5.15] Hämäläinen, J., Puukilainen, E., Sajavaara, T., Ritala, M., Leskelä, M., (2013), Low temperature atomic layer deposition of noble metals using ozone and molecular hydrogen as reactants, *Thin Solid Films*, 531, pp. 243-250.

[5.16] Arai, T., Shima, T., Nakano, T., Tominaga, J., (2007), Thermally-induced optical property changes of sputtered PdO_x films, *Thin Solid Films*, 515 (11), pp. 4774-4777.

[5.17] Mosquera, A., Horwat, D., Vazquez, L., Gutiérrez, A., Erko, A., Anders, A., Andersson, J., Endrino, J.L., (2012), Thermal decomposition and fractal properties of sputter-deposited platinum oxide thin films, *Journal of Materials Research*, 27 (5), pp. 829-836.

[5.18] Kuribayashi, K., Kitamura, S., (2001), Preparation of Pt-PtO_x thin films as electrode for memory capacitors, *Thin Solid Films*, 400 (1-2), pp. 160-164.

[5.19] McBride, J.R., Graham, G.W., Peters, C.R., Weber, W.H., (1991), Growth and characterization of reactively sputtered thin-film platinum oxides, *Journal of Applied Physics*, 69 (3), pp. 1596-1604.

[5.20] Wessling, B., Mokwa, W., Schnakenberg, U., (2006), RF-sputtering of iridium oxide to be used as stimulation material in functional medical implants, *Journal of Micromechanics and Microengineering*, 16 (6).

[5.21] Abe, Y., Yanagisawa, H., Sasaki, K., (1998), Preparation of oxygen-containing Pt and Pt oxide thin films by reactive sputtering and their characterization, *Japanese Journal of Applied Physics, Part 1: Regular Papers and Short Notes and Review Papers*, 37 (8), pp. 4482-4486.

[5.22] Melitz, W., Shen, J., Kummel, A.C., Lee, S., (2011), Kelvin probe force microscopy and its application, *Surface Science Reports*, 66 (1), pp. 1-27.

[5.23] Michaelson, H.B., (1977), The work function of the elements and its periodicity, *Journal of Applied Physics*, 48 (11), pp. 4729-4733.

[5.24] Bernhard, J.M., (1999), *Schottky Work Function Study of Iridium Oxide and Molybendum Using UPS and Simultaneous Fowler-Nordheim I-V Plots with Field Emission Energy Distributions*, PhD thesis, University of North Texas, United States of America.

[5.25] Mugo, S., Yuan, J., (2012), Influence of surface adsorption on work function measurements on gold-platinum interface using scanning Kelvin probe microscopy, *Journal of Physics: Conference Series*, 371, art. no. 012030.

[5.26] Brun, M., Berthet, A., Bertolini, J.C., (1999), XPS, AES and Auger parameter of Pd and PdO, *Journal of Electron Spectroscopy and Related Phenomena*, 104 (1-3), pp. 55-60.

[5.27] Gabasch, H., Unterberger, W., Hayek, K., Klötzer, B., Kleimenov, E., Teschner, D., Zafeiratos, S., Hävecker, M., Knop-Gericke, A., Schlögl, R., Han, J., Ribeiro, F.H., Aszalos-Kiss, B., Curtin, T., Zemlyanov, D., (2006), In situ XPS study of Pd(111) oxidation at elevated pressure, Part 2: Palladium oxidation in the 10^{-1} mbar range, *Surface Science*, 600 (15), pp. 2980-2989.

[5.28] Barr, T.L., (1978), An ESCA study of the termination of the passivation of elemental metals, *Journal of Physical Chemistry*, 82 (16), pp. 1801-1810.

[5.29] Pfeifer, V., Jones, T.E., Velasco Vélez, J.J., Massué, C., Arrigo, R., Teschner, D., Girgsdies, F., Scherzer, M., Greiner, M.T., Allan, J., Hashagen, M., Weinberg, G., Piccinin, S., Hävecker, M., Knop-Gericke, A., Schlögl, R., (2016), *The electronic structure of iridium and its oxides*, Surface and Interface Analysis, 48 (5), pp. 261-273.

[5.30] Smith, R.D.L., Sporinova, B., Fagan, R.D., Trudel, S., Berlinguette, C.P., (2014), Facile photochemical preparation of amorphous iridium oxide films for water oxidation catalysis, *Chemistry of Materials*, 26 (4), pp. 1654-1659.

[5.31] Angelinetta, C., Trasatti, S., Atanasoska, Lj.D., Minevski, Z.S., Atanasoski, R.T., (1989), Effect of preparation on the surface and electrocatalytic properties of RuO_2 + IrO_2 mixed oxide electrodes, *Materials Chemistry and Physics*, 22 (1-2), pp. 231-247.

[5.32] Peuckert, M., (1984), XPS study on thermally and electrochemically prepared oxidic adlayers on iridium, *Surface Science*, 144 (2-3), pp. 451-464.

[5.33] Atanasoski, R.T., Atanasoska, L.L., Cullen, D.A., Haugen, G.M., More, K.L., Vernstrom, G.D., (2012), Fuel Cells Catalyst for Start-Up and Shutdown Conditions: Electrochemical, XPS, and STEM Evaluation of Sputter-Deposited Ru, Ir, and Ti on Pt-Coated Nanostructured Thin Film Supports, *Electrocatalysis*, 3 (3), pp. 284-297.

[5.34] Yang, D.-J., Kamienchick, I., Youn, D.Y., Rothschild, A., Kim, I.-D., (2010), Ultrasensitive and highly selective gas sensors based on electrospun SnO2 nanofibers modified by Pd loading, *Advanced Functional Materials*, 20 (24), pp. 4258-4264.

[5.35] Lajn, A., Wenckstern, H.V., Zhang, Z., Czekalla, C., Biehne, G., Lenzner, J., Hochmuth, H., Lorenz, M., Grundmann, M., Wickert, S., Vogt, C., Denecke, R., (2009), Properties of reactively sputtered Ag, Au, Pd, and Pt Schottky contacts on n -type ZnO, *Journal of Vacuum Science and Technology B:Nanotechnology and Microelectronics*, 27 (3), pp. 1769-1773.

[5.36] Bancroft, G.M., Adams, I., Coatsworth, L.L., Bennewitz, C.D., Brown, J.D., Westwood, W.D., (1975), ESCA study of sputtered platinum films, *Analytical Chemistry*, 47 (3), pp. 586-588.

[5.37] Cordfunke, E.H.P., Meyer, G., (1962), The system iridium - oxygen I. Measurements on the volatile oxide of iridium, *Recueil des Travaux Chimiques des Pays-Bas*, 81 (6), pp. 495-504.

[5.38] Rogers, D.B., Shannon, R.D., Gillson, J.L., (1971), Crystal growth and semiconductivity of palladium oxide, *Journal of Solid State Chemistry*, 3 (2), pp. 314-316.

[5.39] Rey, E., Kamal, M.R., Miles, R.B., Royce, B.S.H., (1978), The semiconductivity and stability of palladium oxide, *Journal of Materials Science*, 13 (4), pp. 812-816.

[5.40] García-Serrano, O., Andraca-Adame, A., Baca-Arroyo, R., Peña-Sierra, R., Romero-Paredes R., G., (2011), Thermal oxidation of ultra thin palladium (Pd) foils at room conditions, *CCE 2011 - 2011 8th International Conference on Electrical Engineering, Computing Science and Automatic Control, Program and Abstract Book*, art. no. 6106122.

[5.41] Canart-Martin, M.C., Delrue, J.P., Laude, L.D., Wautelet, M., (1980), Electronic structure and reduction processes in PtO_x films, *Chemical Physics*, 48 (2), pp. 283-288.

6 | Electrical Characterisation of Metal-Oxide Schottky Contacts with Oxygen Content

This chapter provides the results from the electrical characterisation of RF-sputtered noble metal and metal-oxide Schottky contacts fabricated on c-plane Zn-polar bulk ZnO, and a proposed model for the formation mechanisms of the metal-oxide Schottky contacts to ZnO. The noble metals and metal-oxides explored in this chapter are Ag, AgO_x, Ru, RuO_x, Ir, IrO_x, Pd, PdO_x, Pt and PtO_x. The electrical characterisation of the Schottky contacts includes I-V and C-V measurements.

6.1 Electrical Characterisation of Metal-Oxide Schottky Contacts

The reproducible formation of high-quality Schottky contacts to ZnO has been reported in literature as being difficult to achieve in comparison with many other wide band-gap semiconductors [6.1 – 6.2]. However, Schottky contacts to ZnO have been attempted using a wide range of metals, including Ag, Au, In, Ir, Pd, Pt, Ru, and W [6.1, 6.3 – 6.5]. Reported zero bias effective barrier heights, Φ_B, of the metal Schottky contacts to ZnO ranged between < 0.3 – 1.2 eV, with and ideality factors, η, of 1.01 and above, from dark I-V measurements [6.3 – 6.5]. The barrier heights of Schottky contacts to Zn-polar bulk ZnO specifically range between 0.53 – 1.2 eV from dark I-V measurements [6.3]. The rectification ratios, R_R, of the metal Schottky contacts to Zn-polar bulk ZnO ranged between 2 – 9 O_{Mag} (orders of magnitude) at ±2 V [6.3].

Metal-oxide Schottky contacts to ZnO have also been reported, using AgO_x, IrO_x, PdO_x, and PtO_x [6.4, 6.6 – 6.7]. The ideality factors of the metal-oxide Schottky contacts have been reported as 1.005 – 1.14, notably lower than for the plain metal contacts [6.4, 6.6 – 6.7]. The rectification ratios of metal-oxide contacts also ranged between 8 – 10 O_{Mag}, showing greater potential for highly-rectifying devices [6.6 – 6.7]. The relationship between the level of oxidation of the metal-oxide Schottky contacts to ZnO and the electrical characteristics of the contacts had not been reported in literature. A systematic analysis of the electrical characteristics of Schottky contacts to ZnO with controlled, systematic levels of oxygen incorporation was therefore required to better understand the variation of the rectification ratio, barrier height, and ideality factors of metal-oxide Schottky contacts to ZnO and the formation mechanisms responsible for their high performance.

In this work, the effects of oxygen incorporation on metal-oxide Schottky contacts were studied using arrays of identical Schottky contacts deposited on samples of c-plane Zn-polar bulk ZnO, as shown in Figure 6.1, with electrical characterisation methodologies detailed in Section 4.2.

In order to minimise variations between ZnO substrates across a Schottky contact oxygen incorporation series, a single 10 x 10 x 0.5 mm substrate of bulk ZnO was diced into nine identical 3 x 3 x 0.5 mm samples, as described in Section 3.2. This provided identical substrates for eight different levels of oxygen incorporation, and one reference sample for further analysis. This limited the number of samples available for different O_2:Ar ratios used for each oxygen incorporation series. The substrate could not be diced into smaller sizes, as the edge bead of the lithography mask, described in Section 3.3.1, became a significant issue for sample areas smaller than 5 x 5 mm.

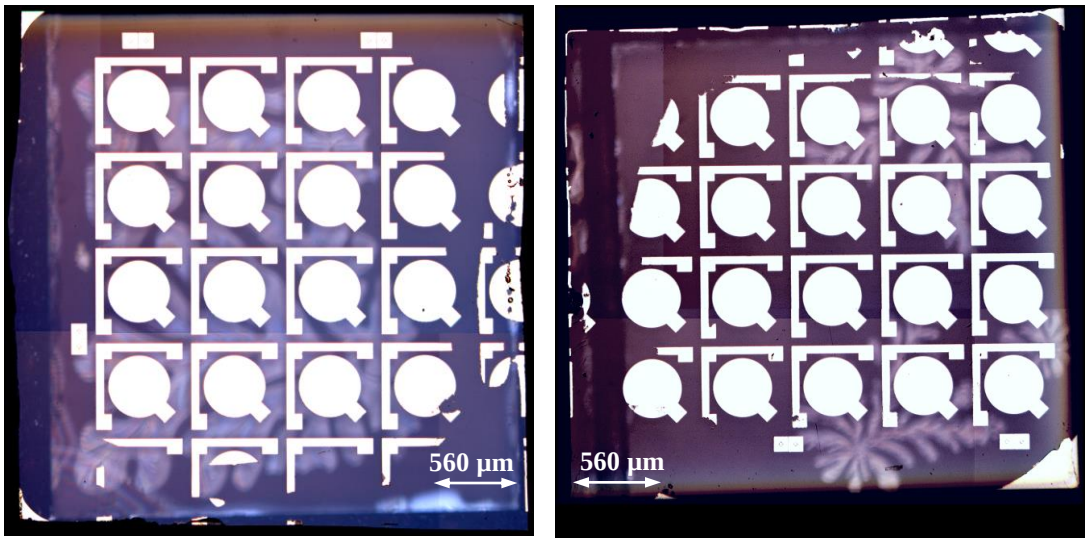

Figure 6.1: RF-Sputtered 7.0:10 (O_2:Ar) PdO_x (Left), and 0.5:10 (O_2:Ar) PtO_x (Right)

The lithography masks used in the fabrication of the Schottky contacts, detailed in Section 3.3, were designed for a 5 x 5 mm sample. When used on 3 x 3 mm samples, partial Schottky contacts were often deposited near the edges of the samples, as shown in Figure 6.1. The number of Schottky contacts produced varied between 16 – 25 contacts per sample. The lithography masks used in this Chapter are included in Figure A3.1 of Appendix A3.1.

Unintentional lateral inhomogeneities in the Schottky contacts produced variation in the electrical characteristics of the individual Schottky contacts, as mentioned in Section 2.3.3. These inhomogeneities were mainly due to mainly due to surface defects in the bulk ZnO at the Schottky contact interface, but also due to lateral inhomogeneous regions of the metal-oxide (such as conductivity or stoichiometry), and possible surface contamination between the development and

sputtering processes described in Section 3.3. For an array of Schottky contacts fabricated on a single substrate, a plot of the barrier heights against ideality factors of all contacts shows a strong linear correlation, as the barrier heights are reduced with increasingly non-ideal Schottky contacts [6.8 – 6.9]. Therefore the Schottky contact with the highest barrier height of the devices with a strong linear correlation indicates the most laterally homogeneous Schottky contact of the array, and the ideality factor can be used to reflect the homogeneity of the Schottky contact [6.8 – 6.9].

For Schottky contacts containing significant lateral inhomogeneities, a double-barrier can be observed in the log-linear plot of the dark I-V characteristics, as shown in Figure 6.2, and in separate plots in Figures A6.1 – A6.3 of Appendices 6.1 – 6.2. The dark I-V characteristic of *DI42* in Figure 6.2 shows two distinct linear regions in the log-linear plot between 0 – 2 V; matching the blue and red dashed lines in Figure 6.2. This is characteristic of two different barrier heights (0.99 eV and 0.73 eV respectively) present in *DI42*; one barrier height matching *DI24*, and a second barrier height characteristic of a weakly-rectifying Schottky contact with a high level of reverse-bias leakage current dominating the I-V characteristics for V < 0.5 V. A double-barrier causes a 'bulge' outward from the linear region of the forward-bias I-V characteristic, seen in Figure 6.2.

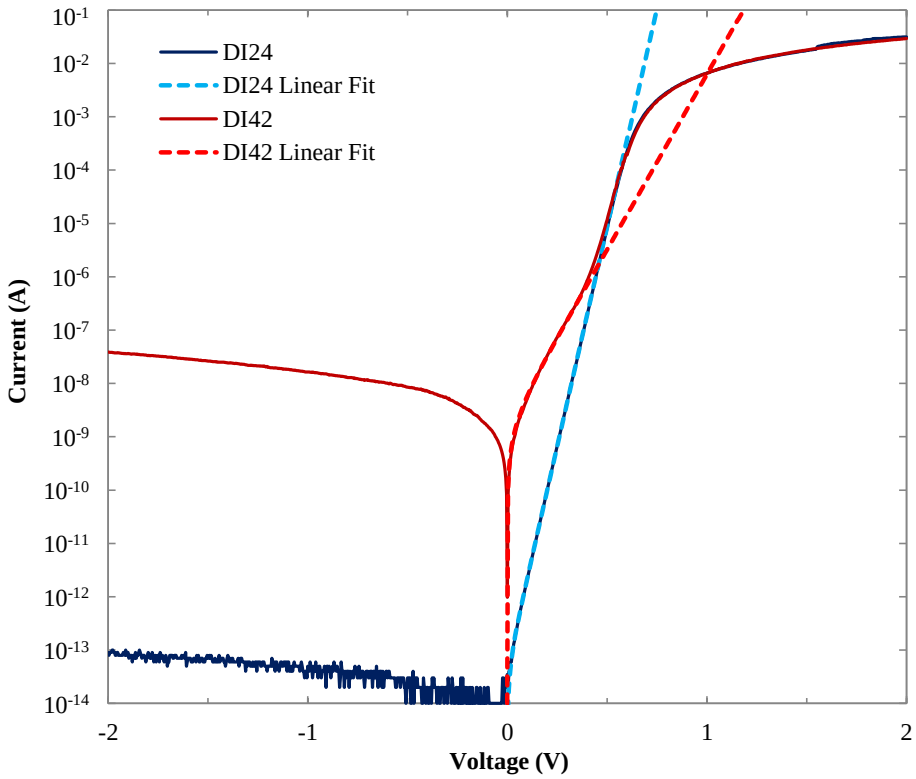

6.2: Log-Linear Plot of Dark I-V Characteristics of 3.0:10 (O_2:Ar) PdO_x Contact DI24 (Single-Barrier) and DI42 (Double-Barrier) with Least Squares Fit of the Linear Region

Dark I-V measurements are more sensitive to lateral inhomogeneities in the Schottky contacts than dark C-V measurements. This is due to the I-V current response being dominated by the region of lowest barrier height in an inhomogeneous Schottky contact as a path of least resistance. In comparison, the overall C-V capacitance of the Schottky contact is averaged across all regions of varied barrier height [6.9]. A comparison of the Schottky contact barrier height calculated from dark I-V measurements, $\Phi_{B,\,I\text{-}V}$, and the barrier height calculated from dark C-V measurements, $\Phi_{B,\,C\text{-}V}$, can be used to verify the level of homogeneity in the Schottky contact, as $\Phi_{B,\,I\text{-}V} << \Phi_{B,\,C\text{-}V}$, for significantly inhomogeneous contacts that contain a large standard deviation of the distribution of barrier heights [6.9]. The level of inhomogeneity in the Schottky contacts could be reduced by improving the quality of the ZnO surface by removing surface defects. Other methods include reducing the Schottky contact size, and fabricating the Schottky contacts in a higher standard of clean-room to avoid surface contamination between development and Schottky contact deposition.

To electrically characterise the Schottky contact of the metal or metal-oxide to the bulk ZnO, dark I-V characteristics of all of the contacts on a single sample were measured in order to obtain the most accurate linear fit of barrier height and ideality factor, as well as the dark C-V characteristics of several Schottky contacts. Due to the small size of the ZnO substrate, and the position of the substrate relative to the RF-sputtering source, it is a reasonable assumption that the Schottky contacts were of uniform thickness and oxygen incorporation across the individual samples, following the methodology detailed in Section 3.4.

The level of oxygen incorporation in the RF-sputtered Schottky contacts was varied by controlling the ratio of O_2:Ar processing gas flow in the chamber during RF-sputtering, as described in Section 3.4.2.1. For the eight levels of oxygen incorporation during RF-sputtering, the gas ratios used were 0.0:10, 0.5:10, 1.0:10, 2.0:10, 3.0:10, 4.0:10, 5.0:10 and 7.0:10 sccm (O_2:Ar). Thin films deposited simultaneously with the Schottky contacts were deposited onto 5 x 5 x 0.5 mm quartz substrates, and analysed in Chapter 5 to determine the optical, structural, and electrical characteristics of the films with increasing oxygen incorporation. The RBS results of the oxygen incorporation of RF-sputtered films of Ir/IrO_x, Pd/PdO_x, and Pt/PtO_x with these gas ratios are shown in Figure 6.3, from the analysis performed in Section 5.6. The RBS measurements and calculated results in Figure 6.3 are courtesy of Professor Steven M. Durbin and Robert Makin of the Department of Electrical and Computer Engineering, Western Michigan University, United States of America, with tabulated results included in Appendix A4.4. The arctangent trends of oxygen incorporation with RF-sputtering O_2:Ar gas ratio were identified and fitted by Robert Makin. Although a model relating the arctangent trend to the oxygen incorporation was not proposed, all three noble metal oxidation series follow the arctangent trend closely.

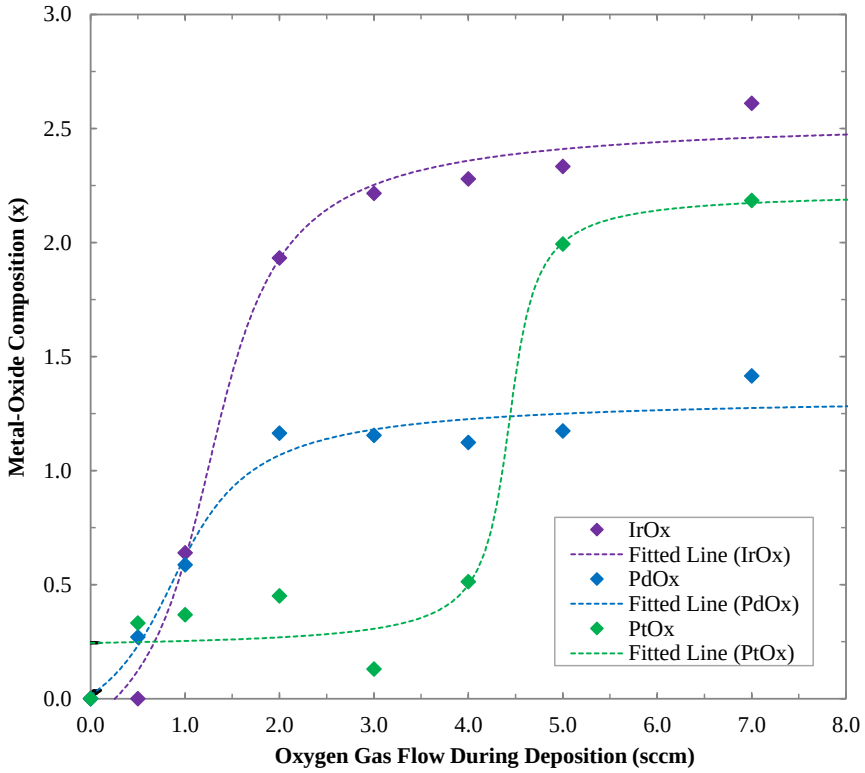

Figure 6.3: Oxygen Incorporation of RF-Sputtered Films with O_2:Ar Ratio from RBS

6.2 Electrical Characterisation of Silver Oxide Schottky Contacts

RF-sputtered AgO_x Schottky contacts with varying levels of oxygen incorporation were deposited on +c-plane Zn-polar (low-lithium) bulk ZnO, following a 5 minute pre-sputter in Ar gas to clean the target surface of contaminants and oxide species from previous sputtering depositions. The deposition gas ratios used during RF-sputtering were 0.0:10, 0.5:10, 1.0:10, 2.0:10, 3.0:10, and 4.0:10 sccm (O_2:Ar). Two sets of contacts were also fabricated with 0.5:10 and 1.0:10 (O_2:Ar) gas flow ratios, but with the oxygen supply closed during the deposition process, so that the only available oxygen was the initial O_2 in the gas line. Despite this error in fabrication, the Schottky contacts fabricated with the oxygen supply closed showed a surprising level of rectification, and were included in this analysis, denoted in this Chapter as '0.5*:10' and '1.0*:10' (O_2:Ar). The substrate and deposition details for the AgO_x contacts are included in Appendices A3.2, and A3.4.

The complete optical analysis of AgO_x films is included in Section 5.2. Figure 6.4 shows the transmission measurements of the 0.0:10, 0.5*:10, 1.0*:10, 0.5:10, and 1.0:10 (O_2:Ar) AgO_x films. The 0.5*:10 and 1.0*:10 (O_2:Ar) films show the same characteristic transmission curve as the pure Ag film, indicating that the majority of the films were plain Ag.

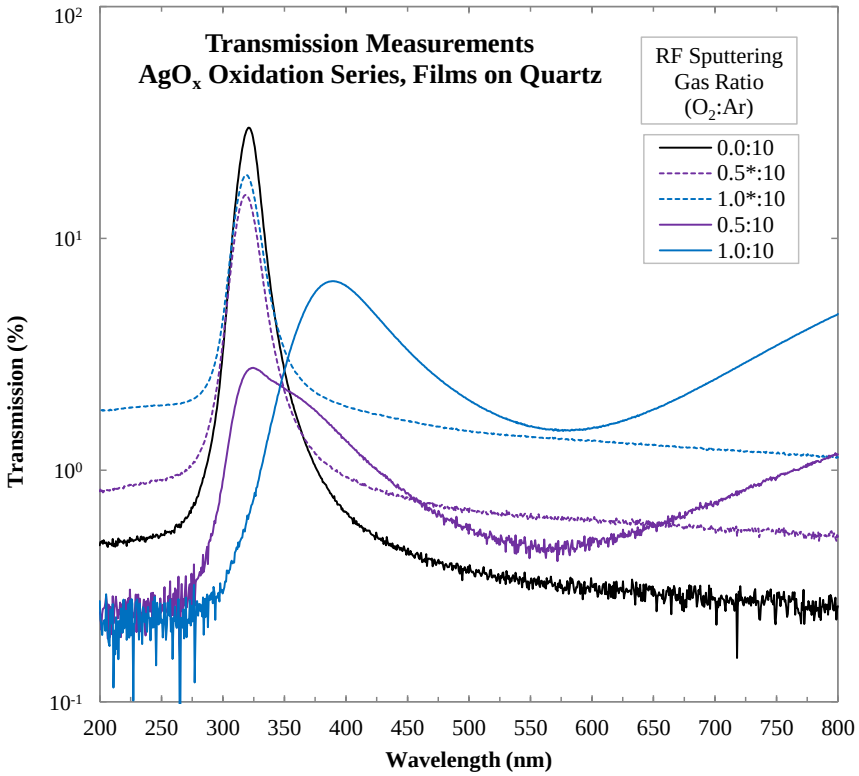

Figure 6.4: RF-Sputtered AgO_x Film Transmission Spectra, *O_2 Gas Line Closed

The partial pressure of the O_2 flow recorded for the growths of 0.5*:10 and 1.0*:10 (O_2:Ar) AgO_x was 0.0 sccm, shown in Appendix A3.4, indicating that there was no additional gas flow during the deposition process, however there was a positive fluctuation in chamber pressure from enabling the O_2 gas supply before the ignition of the plasma, indicating that there was an initial O_2:Ar level at the beginning of the deposition. It is likely that the deposited Schottky contacts from the 0.5*:10 and 1.0*:10 (O_2:Ar) growths consist of a thin layer of AgO_x, capped by a significantly thicker layer of Ag, which would account for the similar film transmission to plain Ag.

The dark I-V characteristics of the AgO_x contacts representative of the 0.0:10 – 4.0:10 (O_2:Ar) oxygen incorporation levels are shown in Figure 6.5. The representative contact of each oxidation series was selected as the most laterally-homogenous (lowest ideality factor) contact from the sample with a barrier height typical of the sample. The barrier heights and ideality factors of the complete set of the 0.0:10 – 4.0:10 (O_2:Ar) AgO_x Schottky contacts with varying oxygen incorporation levels are shown in Figure 6.6. The significant increase in rectification ratio and barrier height between the 0.0:10 (O_2:Ar) Ag contacts and the 0.5*:10 and 1.0*:10 (O_2:Ar) AgO_x contacts was a surprising result. The similarity between the 0.5:10 and 0.5*:10 (O_2:Ar) dark I-V characteristics in Figure 6.5 suggests that the performance of the Schottky contact is dominated by the composition of the material at the interface of the ZnO and the Schottky contact material.

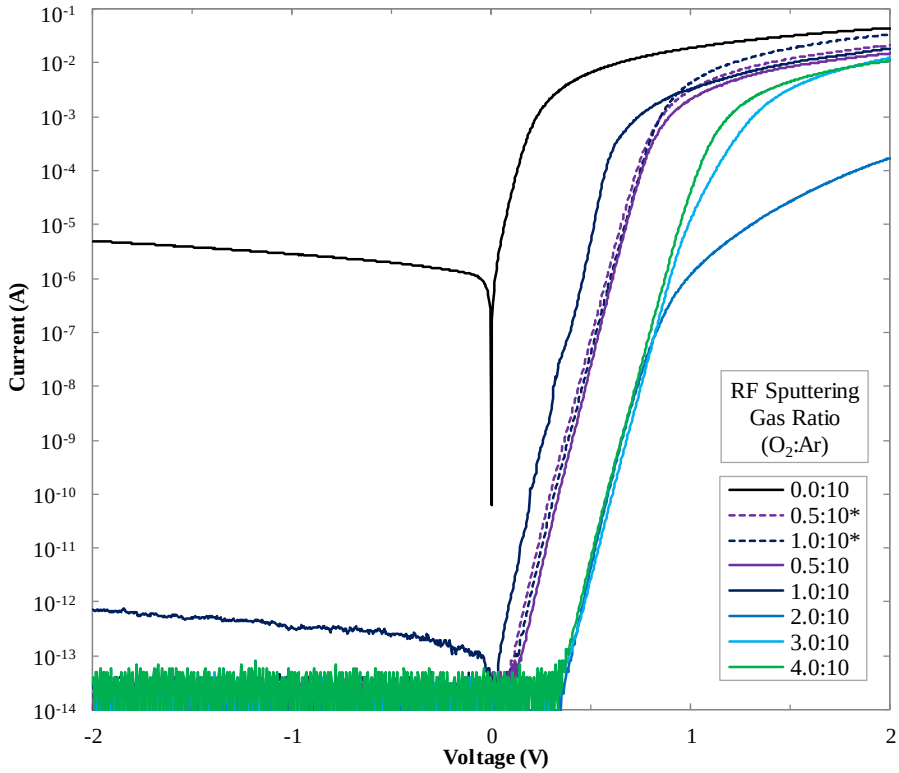

Figure 6.5: RF-Sputtered AgO_x Schottky Contacts Dark I-V Characteristics

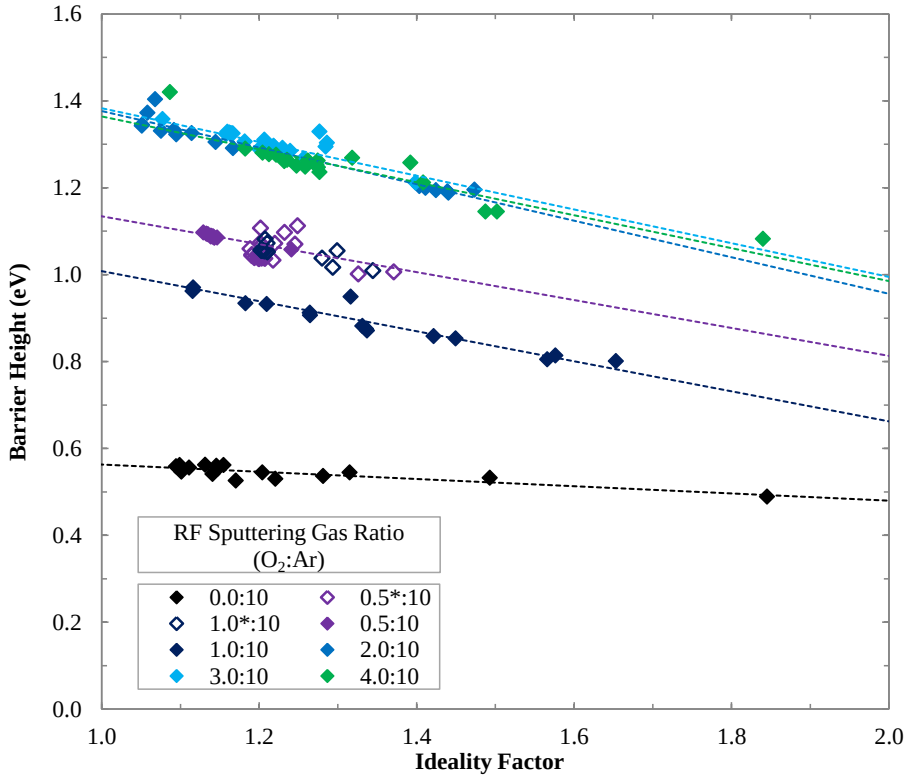

Figure 6.6: RF-Sputtered AgO_x Schottky Contacts Ideality Factors and Barrier Heights

Figures 6.5 – 6.6 show an overall inconsistent set of results for the 0.0:10 – 4.0:10 (O_2:Ar) RF-sputtered AgO_x Schottky contact dark I-V characteristics. The 1.0:10 (O_2:Ar) AgO_x contacts show barrier heights between the 0.0:10 (O_2:Ar) Ag and 0.5:10 (O_2:Ar) AgO_x contacts, and the forward bias current of the 2.0:10 (O_2:Ar) AgO_x contacts appears significantly lower than the rest of the series. Despite these two outliers, the overall trends show increasing barrier heights and rectification ratios with increasing oxygen incorporation during RF-sputtering. Figure 6.6 shows the linear correlation between the barrier height and ideality factors for multiple Schottky contacts for each of the oxygen incorporation levels, characteristic of inhomogeneous Schottky contacts [6.8 – 6.9].

The 1.0:10 (O_2:Ar) AgO_x contacts showed significantly lower quality than expected, with 14 of the 16 fabricated devices showing the formation of a double-barrier and a significant reduction in rectification ratio, as shown in Appendix A6.1. The two devices that did not have a double-barrier, *DI14* and *DI43* in Figure A6.1, showed rectification ratios of 10.2 – 10.4 O_{Mag}, compared with the median rectification ratio of 6.68 for the rest of the 1.0:10 (O_2:Ar) AgO_x contacts. The formation of a double-barrier in most devices has been attributed to potential surface contamination of the interface by Ag during pre-sputtering. Despite the RF-sputtering shutter between the RF-sputtering source and the sample during pre-sputtering, it is possible that a small amount of atomised Ag within the sputtering chamber could have been deposited on the exposed ZnO surface prior to the deposition of the Schottky contact. As the characteristics of the AgO_x Schottky contacts appear dominated by the species present at the interface, small quantities of unoxidised Ag could have a significant impact on the 1.0:10 (O_2:Ar) Schottky contacts.

The 2.0:10 (O_2:Ar) AgO_x contacts showed a significant forward bias series resistance, with an average of 0.168 mA at +2 V, compared with 21.0 mA and 5.28 mA for 1.0:10 and 3.0:10 (O_2:Ar) AgO_x contacts respectively. As all of the 2.0:10 (O_2:Ar) AgO_x contacts showed the same low forward bias current, and no other devices in the AgO_x oxygen incorporation series showed the same drop, the increased series resistance was also attributed to contamination during fabrication.

The dark I-V characteristics of the 0.0:10, 0.5:10, 3.0:10, and 4.0:10 (O_2:Ar) AgO_x contacts in Figures 6.5 – 6.6 show a trend of increasing barrier height, and increasing rectification ratio, with increasing oxygen incorporation. Figure 6.5 shows that, with an O_2:Ar as low as 0.5:10 present during sputtering, RF-sputtered AgO_x Schottky contacts to ZnO were produced with 12.2 O_{Mag} rectification. The improvement was substantial, compared to the plain metal Ag contacts with 3.37 O_{Mag} rectification. In literature, the rectification ratio of Ag contacts to ZnO ranged between 4 – 9 O_{Mag}, with AgO_x contacts to ZnO producing rectification ratios of 9 – 10 O_{Mag} [6.3, 6.6 – 6.7]. The AgO_x contacts produced in this work have significantly improved on the AgO_x contacts to ZnO published in literature [6.3 – 6.5].

Ideality factor approaches unity for a perfectly homogeneous Schottky contact. A linear regression of the barrier heights with ideality factor across multiple Schottky contacts from the same sample can be used to extrapolate the homogeneous barrier height, Φ_B^{homo}. The homogeneous barrier height of an oxidation series is a better tool for comparing the barrier heights of different oxidation series, as it represents an ideal, laterally-homogeneous contact for the metal-oxide Schottky contacts to ZnO.

The homogeneous barrier height increased significantly from the 0.0:10 (O_2:Ar) AgO_x contacts of 0.563 eV, to the 0.5:10 (O_2:Ar) AgO_x contacts of 1.13 eV. The improvement in barrier heights with oxygen incorporation were observed to plateau between 2.0:10 – 4.0:10 (O_2:Ar) AgO_x in Figure 6.6, with homogeneous barrier heights of 1.36 – 1.38 eV. This could indicate a maximum oxygen incorporation for the RF-sputtering conditions used in this work. The highest barrier height fabricated in this work was 1.31 eV for a 2.0:10 (O_2:Ar) AgO_x contact. This is comparable to barrier heights of AgO_x contacts fabricated in literature; 1.1 – 1.2 eV, from dark I-V measurements [6.6 – 6.7]. Plain Ag contacts to ZnO have been reported to have barrier heights of 0.66 – 1.02 eV, which is comparable to the Ag contacts fabricated in this work [6.3].

6.3 Electrical Characterisation of Ruthenium Oxide Schottky Contacts

RF-sputtered RuO_x Schottky contacts with varying levels of oxygen incorporation were deposited on –c-plane Zn-polar bulk ZnO with a resistivity of 0.09 Ωcm. This resistivity was significantly lower than the resistivities of the +c-plane (low-lithium) ZnO, 0.89 – 5.12 Ωcm.

For the RuO_x contacts, the gas ratios used were 0.5:10, 1.0:10, 2.0:10, 3.0:10, 4.0:10, 5.0:10, and 7.0:10 sccm (O_2:Ar). The substrate characteristics and deposition conditions for the RuO_x contacts are included in Appendices A3.2 and A3.4. Unlike the fabrication of the AgO_x, IrO_x, PdO_x, and PtO_x, the RF-sputtering of the RuO_x Schottky contacts did not include the 5 minute pre-sputter stage in pure Ar, as described in Section 3.4.2.3, which has been used in subsequent metal-oxide contact fabrication to clean the metal sputtering target. The oxygen content of the RuO_x contacts in this work was therefore subject to error. A repeat series of RuO_x contacts was proposed, but due to the relatively low Schottky barrier heights measured in this work, the completion of the repeat series was deferred. The pre-sputter stage was used in subsequent oxygen incorporation series.

The dark I-V characteristics of the RuO_x contacts representative of the 0.5:10 – 7.0:10 (O_2:Ar) oxygen incorporation levels are shown in Figure 6.7. The barrier heights and ideality factors of the RuO_x Schottky contacts are shown in Figure 6.8.

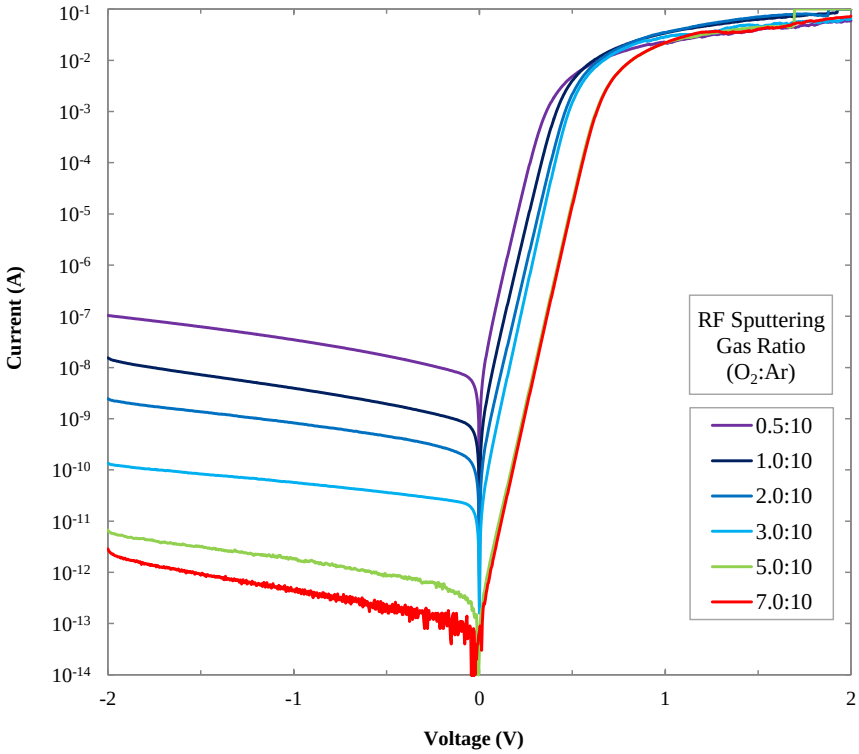

Figure 6.7: RF-Sputtered RuO_x Schottky Contacts Dark I-V Characteristics

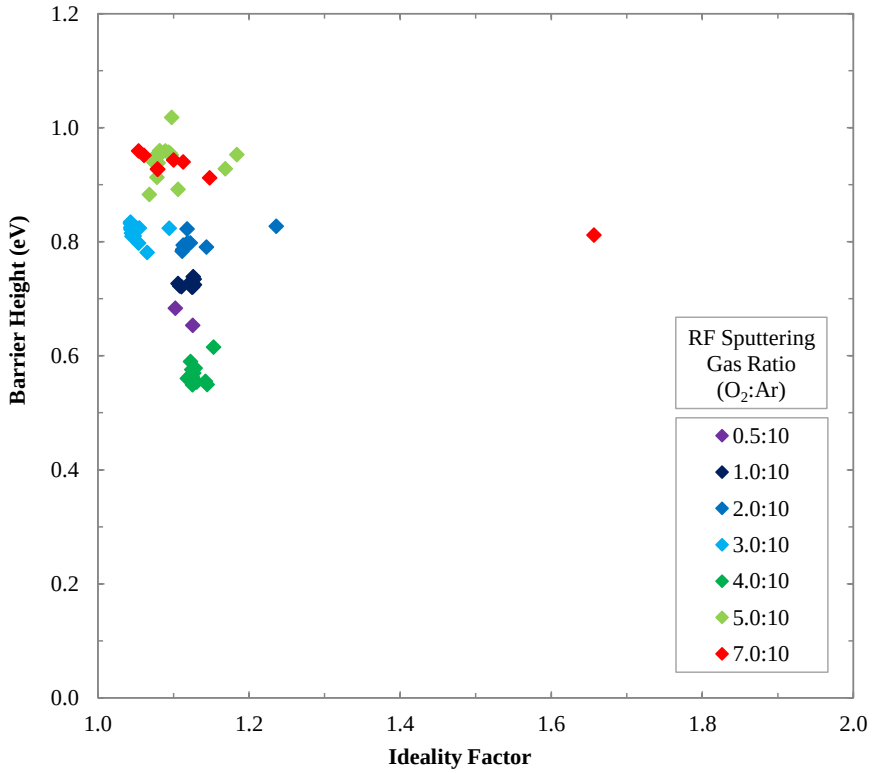

Figure 6.8: RF-Sputtered RuO_x Schottky Contacts Ideality Factors and Barrier Heights

Figure 6.7 does not show a representative dark I-V characteristic for the 4.0:10 (O_2:Ar) RuO_x contacts, as all contacts were found to have unusually high levels of leakage current due to possible contamination during fabrication. The ±2 V rectification ratios of the representative 4.0:10 (O_2:Ar) RuO_x contacts was 4.25 O_{Mag}, compared to 5.76 O_{Mag} from the representative 0.5:10 (O_2:Ar) RuO_x contact. Figure 6.8 also shows that the barrier heights of the 4.0:10 (O_2:Ar) RuO_x contacts were significantly lower than the rest of the RuO_x series. The unexpected behaviour of the 4.0:10 (O_2:Ar) RuO_x contacts was most probably due to surface contamination, as the low barrier height was constant across the sample set of Schottky contacts in Figure 6.8.

Figure 6.7 shows a clear trend of increasing barrier height and rectification ratio with increasing oxygen incorporations of the representative 0.5:10 – 7.0:10 (O_2:Ar) RuO_x contacts, with the exception of the 4.0:10 (O_2:Ar) sample. Unlike the AgO_x series in Section 6.2, the reverse bias leakage current of the RuO_x contacts did not drop below 1 pA at -2.0 V. This is likely due to the difference in the impurity concentration of the substrates, as the Schottky contacts were deposited on different types of hydrothermally-grown bulk ZnO wafers [6.3, 6.5]. The RuO_x contacts were deposited on –c-plane bulk ZnO, with typical resistivities between 0.08 – 2.8 Ωcm [6.10 – 6.11]. For the RuO_x contacts in this work, –c-plane ZnO substrate had a resistivity of 0.09 Ωcm. The +c-plane (low-lithium) bulk ZnO used in this work as a substrate for AgO_x, IrO_x, PdO_x, and PtO_x contacts had resistivities between 0.59 – 26 Ωcm, significantly higher in resistivity of the –c-plane ZnO, indicating lower levels of impurity concentrations, as discussed in Section 2.3 [6.12].

The range of barrier heights for the 0.5:10 – 7.0:10 (O_2:Ar) RuO_x contacts in Figure 6.8, with the exception of the 4.0:10 (O_2:Ar) RuO_x contacts, is 0.654 – 1.02 eV. Schottky contacts of plain Ru to ZnO have been reported in literature with a barrier height of 0.91 eV, higher than the RuO_x contacts in this work [6.3]. Compared to the AgO_x contacts barrier heights in Section 6.2, 0.489 – 1.42 eV, the RuO_x contacts showed less potential for producing high-quality Schottky contacts.

Linear trends between barrier height and ideality factor are not included in Figure 6.8, as the spread of the data points for each series made an accurate linear fit difficult for most RuO_x contact series. This incoherence of barrier height and ideality factor is most likely due to the lack of pre-sputtering before the deposition of the Schottky contacts producing a non-uniform level of oxygen incorporation across the devices.

6.4 Electrical Characterisation of Iridium Oxide Schottky Contacts

RF-sputtered IrO_x Schottky contacts with varying levels of oxygen incorporation were deposited on –c-plane Zn-polar bulk ZnO and on +c-plane Zn-polar (low-lithium) bulk ZnO in two

separate oxygen incorporation series. The first series, deposited on –c-plane bulk ZnO, had deposition gas ratios of 0.5:10, 1.0:10, 2.0:10, 3.0:10, 4.0:10, 5.0:10, and 7.0:10 (O_2:Ar). The second series, deposited on the +c-plane (low-lithium) bulk ZnO, had deposition gas ratios of 0.0:10, 0.5:10, 1.0:10, 2.0:10, 3.0:10, and 4.0:10 (O_2:Ar). The Ir/IrO_x deposition conditions are included in Appendix A3.4. For the 2.0:10 (O_2:Ar) IrO_x deposition of the first series, a sample of +c-plane ZnO was also used to deposit identical Schottky contacts on both types of ZnO. Substrate details of the ZnO used for IrO_x Schottky contacts from Appendix A3.2 are listed in Table 6.1.

Table 6.1: Tokyo Denpa Co., Ltd. C-Plane Wafer Details for IrO_x Schottky Contacts

IrO_x Series	Contacts Fabricated	Wafer Number	ZnO Type	Resistivity (Ωcm)
1	0.0:10 – 7.0:10 (O_2:Ar)	CGZ-1209-09	–c-plane	0.10
1	2.0:10 (O_2:Ar)	CGZ-0937-06	+c-plane (low-lithium)	0.85
2	0.0:10 – 4.0:10 (O_2:Ar)	XGZ-0196-17	+c-plane (low-lithium)	1.18

As with the RuO_x series in Section 6.5, the first IrO_x contact series was deposited without the pre-sputtering process, therefore the oxygen incorporation of this series is subject to error. The second series was deposited with a 5 minute pre-sputtering of the Ir target before each Ir/IrO_x Schottky contact growth. However, only six samples were available for Schottky contact fabrication from the +c-plane (low-lithium) ZnO substrate. The gas ratios 5.0:10 and 7.0:10 (O_2:Ar) were omitted, as it had been observed in the first IrO_x series that the 4.0:10 – 7.0:10 (O_2:Ar) IrO_x contacts had similar barrier heights and rectification ratios. Analysis of identical films of IrO_x with increasing oxygen incorporation can be found in Chapter 5. The electrical characterisation of the second series of IrO_x contacts included dark C-V measurements, as detailed in Section 4.2.3.

Representative dark I-V characteristics of the 0.5:10 – 7.0:10 (O_2:Ar) IrO_x contacts on –c-plane ZnO are shown in Figure 6.9, with barrier heights and ideality factors in Figure 6.10. Representative dark I-V characteristics of 0.0:10 – 4.0:10 (O_2:Ar) IrO_x contacts on +c-plane (low-lithium) ZnO are shown in Figure 6.11, with barrier heights and ideality factors in Figure 6.12. Plots of homogeneous barrier height and rectification ratio with metal-oxide incorporation from RBS measurements of the IrO_x contacts to +c-plane (low-lithium) ZnO are shown in Figures 6.13 – 6.14. Representative dark C-V characteristics of 0.0:10 – 4.0:10 (O_2:Ar) IrO_x contacts on +c-plane (low-lithium) ZnO are shown in Figure 6.15, with the comparison of averaged barrier heights and standard deviations from I-V and C-V measurements shown in Figure 6.16.

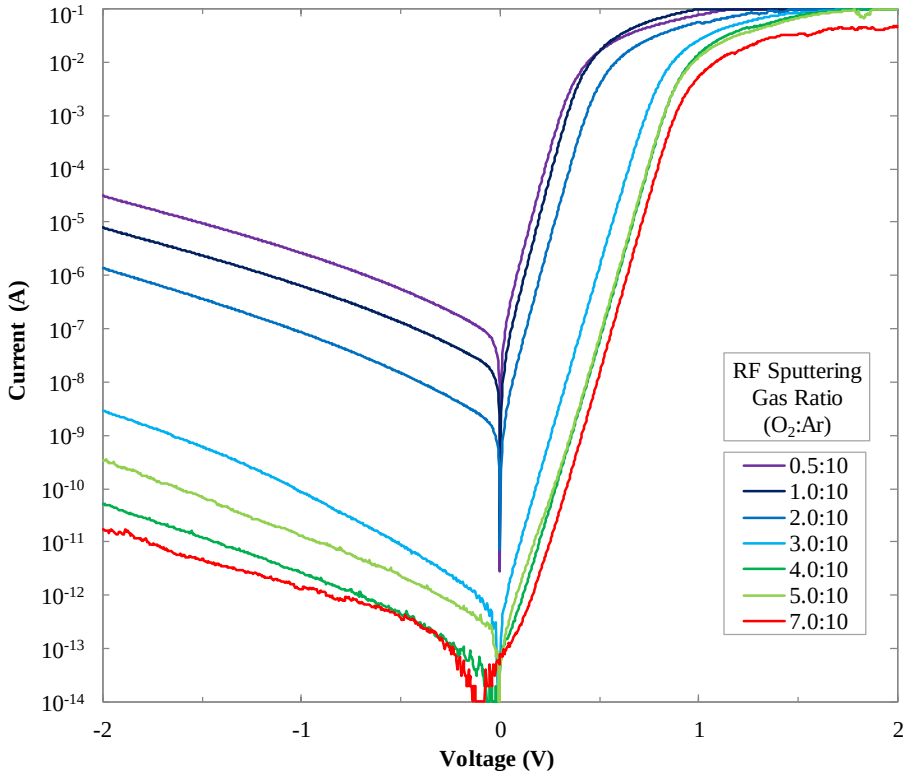

Figure 6.9: RF-Sputtered IrO_x Schottky Contacts Dark I-V, –c-plane ZnO

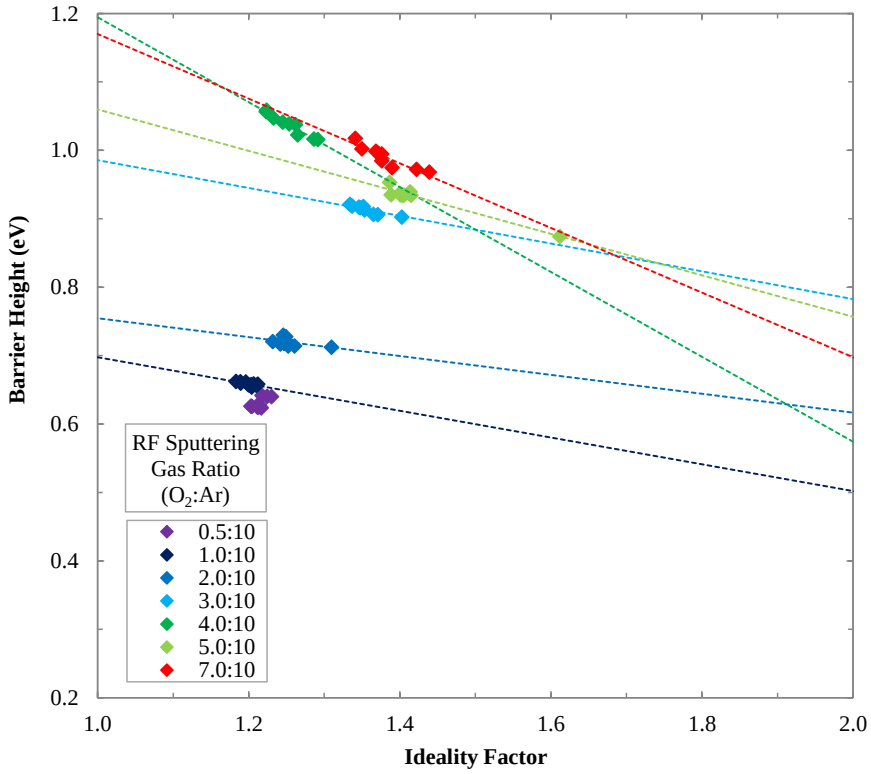

Figure 6.10: RF-Sputtered IrO_x Schottky Barrier Heights, –c-plane ZnO

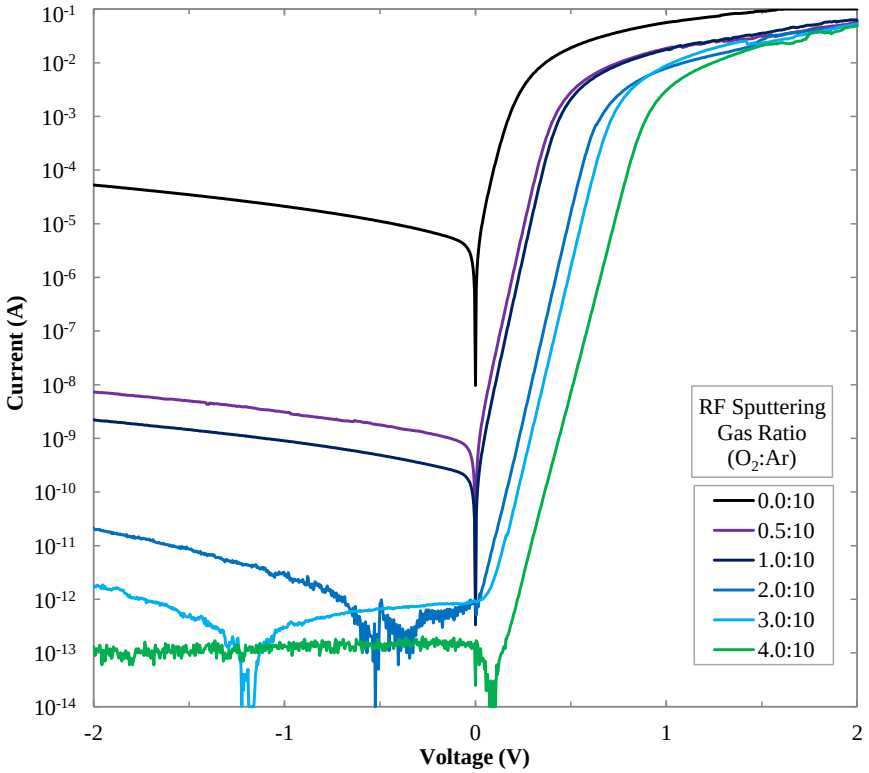

Figure 6.11: RF-Sputtered IrO_x Schottky Contacts Dark I-V, +c-plane (low-Li) ZnO

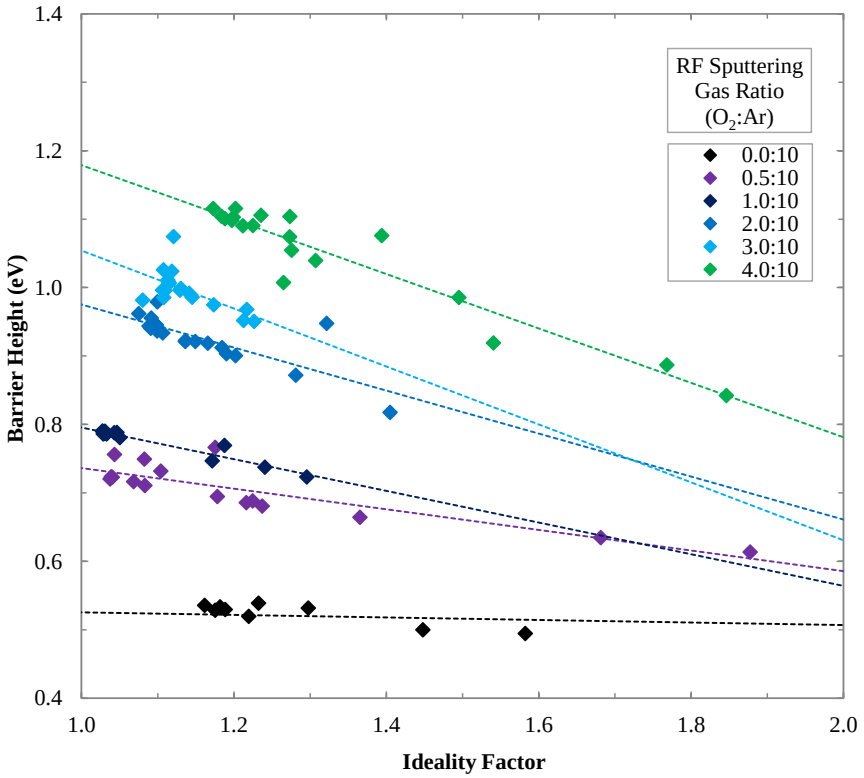

Figure 6.12: RF-Sputtered IrO_x Schottky Barrier Heights, +c-plane (low-Li) ZnO

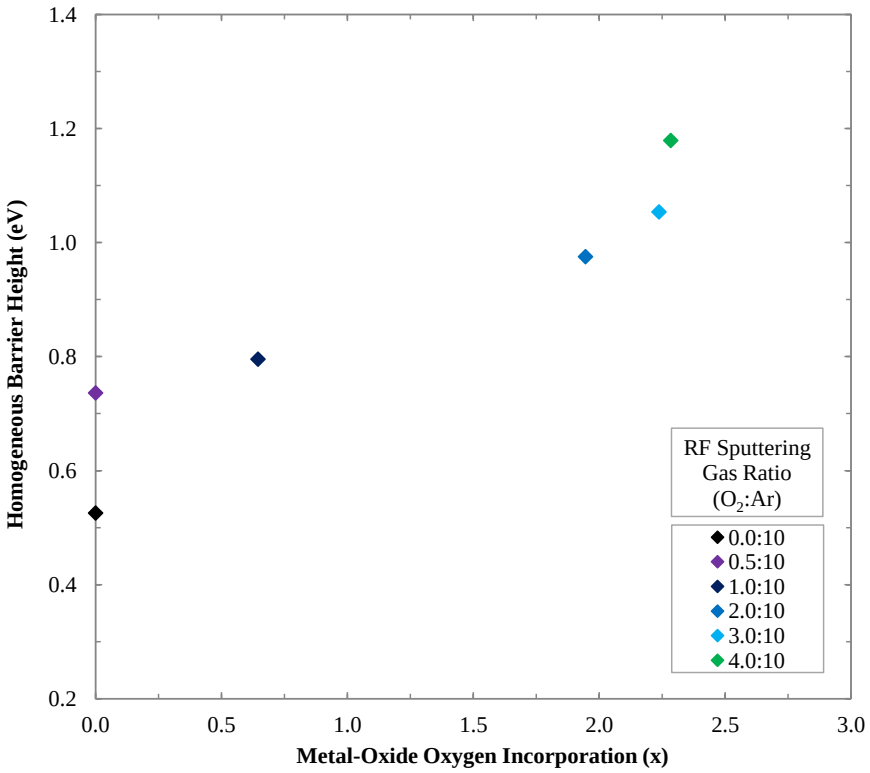

Figure 6.13: RF-Sputtered IrO_x Homogeneous Barriers with *x*, +c-plane (low-Li) ZnO

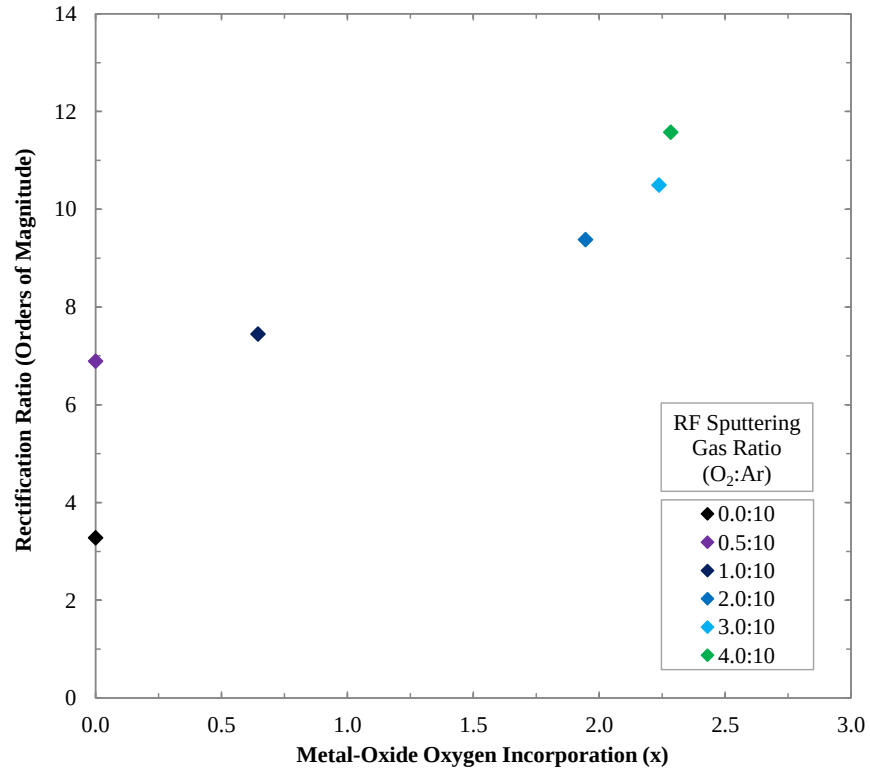

Figure 6.14: RF-Sputtered IrO_x Rectification Ratios with *x*, +c-plane (low-Li) ZnO

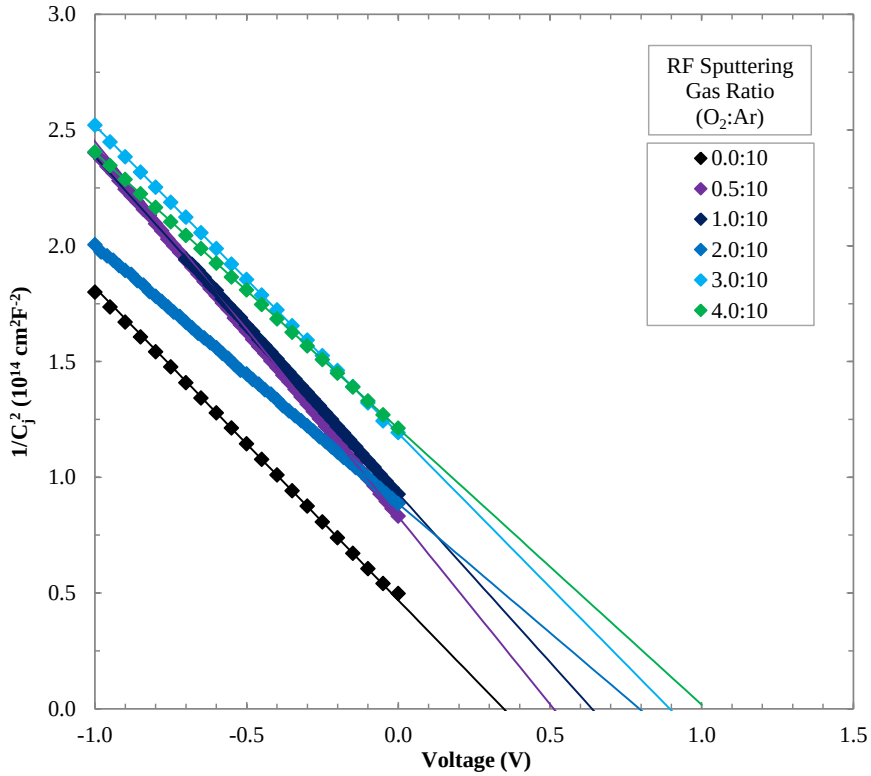

Figure 6.15: RF-Sputtered IrO_x Schottky Contacts Dark C-V, +c-plane (low-Li) ZnO

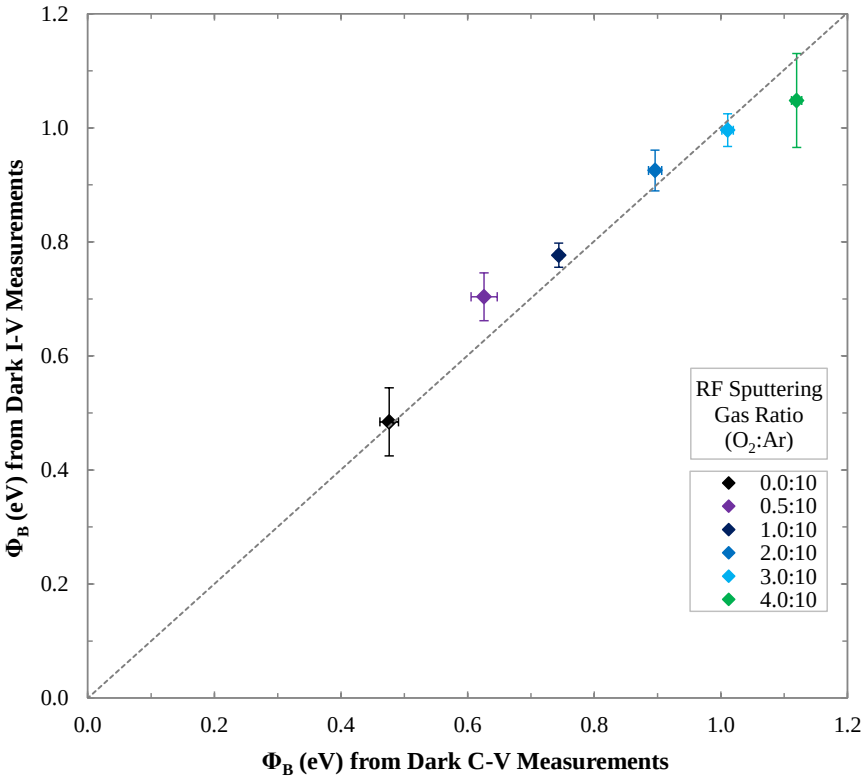

Figure 6.16: Barrier Heights of IrO_x Contacts from I-V and C-V, +c-plane (low-Li) ZnO

The dark I-V characteristics of the IrO_x series on –c-plane ZnO in Figure 6.9 show significantly higher reverse leakage current than the IrO_x series on +c-plane (low-lithium) ZnO in Figure 6.11. This is likely due to the different level of impurities present in the ZnO substrate types, with resistivities listed in Table 6.1. Lower resistivity has been linked to the increase in impurities such as aluminium and iron in the bulk ZnO grown along the –c-axis, as detailed in Section 2.3 [6.10 – 6.11].

Higher concentration of impurities also cause a narrowing of the Schottky contact potential barrier height, shown in Figure 6.17, allowing for a greater level of electron tunnelling current in reverse-bias [6.13]. The reverse-bias current of Schottky contacts to semiconductors with low concentrations of impurities is dominated by thermionic emission, also shown in Figure 6.17 [6.13]. The electron tunnelling current is more strongly dependent on device bias than thermionic emission, therefore the reverse-bias current of a device dominated by electron tunnelling current increases steeply with increasingly negative device bias [6.13]. Comparatively, devices dominated by thermionic emission show a relatively constant reverse-bias leakage current with increasingly negative device bias before reaching breakdown voltage [6.13]. This can be seen in a comparison between the reverse-bias leakage currents in Figure 6.9 and Figure 6.11, where the IrO_x contacts to –c-plane ZnO show a steeper increase in reverse bias leakage current with increasingly negative device bias than the IrO_x contacts to +c-plane ZnO.

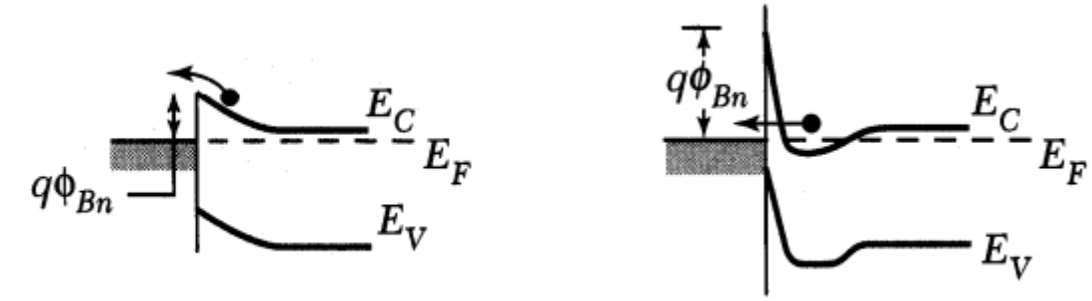

Figure 6.17: Thermionic Emission (Left) and Electron Tunnelling (Right) [6.13]

During the deposition of the 2.0:10 (O_2:Ar) IrO_x contacts on –c-plane ZnO, Schottky contacts were also deposited on a sample of +c-plane (low-lithium) ZnO to directly compare the –c-plane and +c-plane ZnO. The comparison of the dark I-V characteristics of the Schottky contacts is shown in Figure 6.18. It is important to note that the 2.0:10 (O_2:Ar) IrO_x contacts in Figure 6.18 are from a different +c-plane ZnO substrate to the 2.0:10 (O_2:Ar) IrO_x contacts in Figure 6.12, with both resistivities listed in Table 6.1. The reverse-bias leakage currents of the Schottky contact to –c-plane ZnO and +c-plane ZnO in Figure 6.18 show a significant difference in dependence on device bias

with substrate material, supporting the assertion that the IrO_x contact to –c-plane ZnO reverse-bias leakage current increase is due to the dominance of electron tunnelling current due to the higher concentration of impurities [6.13]. The higher forward-bias current of the IrO_x contact to –c-plane ZnO can be attributed to the lower resistivity of the –c-plane ZnO wafer listed in Table 6.1.

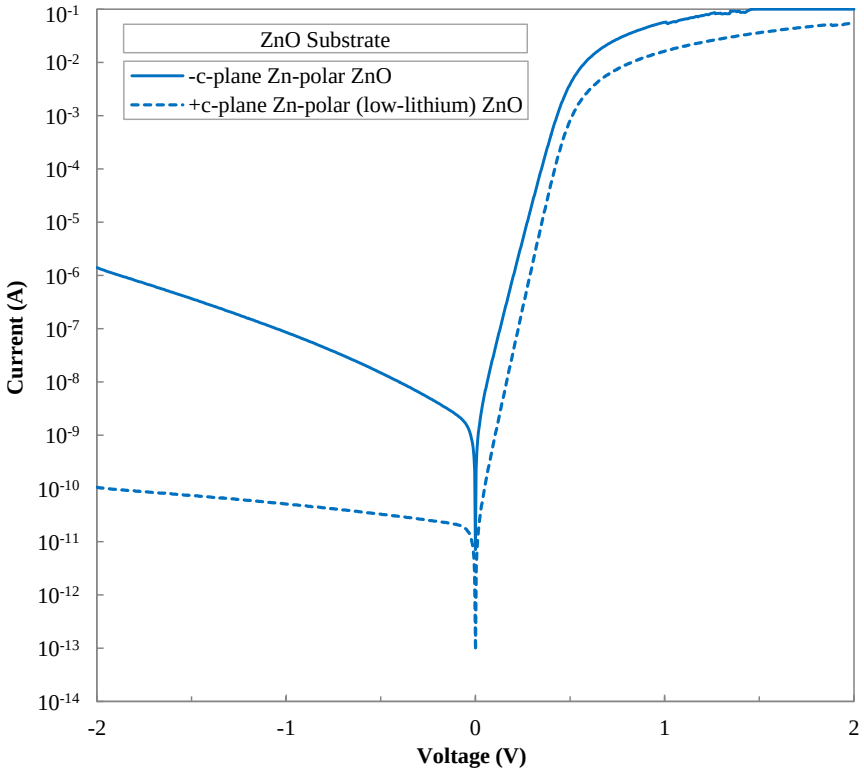

Figure 6.18: RF-Sputtered 2.0:10 (O_2:Ar) IrO_x Schottky Contacts on Varied ZnO Substrates

Figure 6.18 shows that the +c-plane (low-lithium) ZnO contacts have a greater rectification ratio, but lower forward bias current. The ideality factors of the representative IrO_x contacts in Figure 6.18 were calculated to be 1.25 and 1.06 respectively, with barrier heights of 0.718 eV and 0.829 eV, respectively. From this result, +c-plane (low-lithium) ZnO was chosen as the substrate for the second oxygen incorporation series of IrO_x contacts, as well as for the PdO_x and the PtO_x contacts.

It can be seen in Figure 6.3 of Section 6.1 that the IrO_x oxygen fraction has a steep transition between gas ratios of 0.5:10 to 3.0:10 (O_2:Ar) of $x \approx 0$ to $x > 2$. This shows that the IrO_x contacts are very sensitive to variations of gas ratio over this range, resulting in the representative barrier heights of the 2.0:10 (O_2:Ar) IrO_x contacts to both types of ZnO being either closer in value to the 1.0:10 or 3.0:10 (O_2:Ar) IrO_x contacts, as shown in Figures 6.10 and 6.12. The transition from $x \approx 0$ to $x > 2$

in the 0.0:10 – 4.0:10 (O_2:Ar) IrO_x contacts can also be seen in Figures 6.13 – 6.14, with barrier heights greater than 0.975 eV, and rectification ratios above 9.4, apparent only after the transition. Both homogeneous barrier height and rectification ratio of the IrO_x contacts continue to increase for $x > 2$.

The dark I-V characteristics of both IrO_x oxygen incorporation series in Figures 6.9 – 6.12 show an increasing rectification ratio and barrier height with increasing oxygen incorporation. The IrO_x series on –c-plane ZnO increased in rectification ratio from 3.50 to 9.42 O_{Mag}, and in barrier height from 0.625 to 0.975 eV from 0.5:10 to 7.0:10 (O_2:Ar). The IrO_x series on +c-plane (low-lithium) ZnO increased in rectification ratio from 3.28 to 11.6 O_{Mag}, and in barrier height from 0.534 – 1.12 eV from 0.0:10 to 4.0:10 (O_2:Ar). The highest homogeneous barrier height for each series was calculated to be 1.19 eV for IrO_x to –c-plane ZnO and 1.17 eV for IrO_x to +c-plane (low-lithium) ZnO. Plain Ir Schottky contacts to ZnO have been reported with rectification ratios of 7 – 9 O_{Mag}, and barrier heights of 0.54 – 1.0 eV [6.3 – 6.4]. IrO_x Schottky contacts to bulk ZnO have also been reported with 9 O_{Mag} rectification and 0.88 – 1.14 eV barrier heights, comparable to the IrO_x contacts fabricated and measured in this work [6.3 – 6.4, 6.7].

The increase in IrO_x diode performance appears to be gradual over the O_2:Ar range, with the exception of the transition from IrO_x from $x \approx 0$ to $x > 2$. This is likely caused by the amorphous nature of the IrO_x films, as discussed in Section 5.3, containing a mixture of Ir, IrO_2, and a possible higher oxidation state of IrO_x. Both IrO_x oxygen incorporation series also show an apparent plateau of increasing barrier height with increasing O_2:Ar gas flow at 4.0:10 (O_2:Ar) and above.

Figure 6.15 shows the C-V curves of representative contacts from the second IrO_x series. The intercept of the fitted linear trends in Figure 6.15 was used to determine the built-in potential, V_{bi}, described in Section 4.2.3. Figure 6.15 shows increasing V_{bi} with increasing oxygen incorporation, from 0.347 V to 0.794 V with 0.0:10 to 4.0:10 (O_2:Ar), confirming the observations from the dark I-V measurements. Figure 6.16 shows the comparison of barrier heights calculated by dark I-V measurements and dark C-V measurements. The barrier height was calculated for the C-V measurements using Equations 6.1 – 6.2 in Table 6.2, where ξ is the energy difference between the Fermi-level and the conduction band minimum, N_C is the conduction band effective density of states (2.94×10^{18} cm^{-3} for ZnO [6.15]), and N_D is the net doping density, taken to be the carrier density, $n \approx 2.0 \times 10^{16}$ cm^{-3}, for the +c-plane low-lithium ZnO used in this work [6.12].

Table 6.2: Dark C-V Measurement and Analysis Equations [6.12, 6.14 – 6.15]

Parameter	Symbol	Unit	Equation	Equation Number
Barrier Height from C-V Measurements	$\Phi_{B,\,C\text{-}V}$	eV	$\Phi_B = qV_{bi} + \xi$	(6.1)
Energy from Fermi-Level to Conduction Band	ξ	eV	$\xi = \frac{kT}{q} ln\left(\frac{N_C}{N_D}\right)$	(6.2)

The barrier heights calculated from all dark I-V measurements from all Schottky contacts on a single sample were averaged, producing $\bar{\Phi}_{B,I-V}$ with a standard deviation for each sample. Averaged barrier heights from the dark C-V measurements of each sample, $\bar{\Phi}_{B,C-V}$, with standard deviations were also calculated. The averaged values were used in favour of representative or homogeneous barrier heights in order to include the spread of inhomogeneous Schottky contacts.

The averaged barrier heights calculated from the dark I-V measurement and dark C-V measurements for the 0.0:10 – 4.0:10 IrO_x contacts on +c-plane low-lithium ZnO show excellent agreement, with a linear fit of $\Phi_{B,\,I\text{-}V} = \Phi_{B,\,C\text{-}V}$ producing an R^2 value of 0.940. The barrier heights calculated from dark I-V measurements are susceptible to lateral inhomogeneities in Schottky contact material, as the DC current flows preferentially through the region of lowest barrier height [6.9]. As calculated barrier heights from dark C-V measurements are less sensitive to lateral inhomogeneities, and are typically higher than barrier heights calculated from dark I-V measurements, the similarity between the $\Phi_{B,\,I\text{-}V}$ and $\Phi_{B,\,C\text{-}V}$ in this work indicates that the Ir/IrO_x Schottky contacts fabricated have an overall high level of lateral homogeneity [6.8 – 6.9].

6.5 Electrical Characterisation of Palladium Oxide Schottky Contacts

RF-sputtered PdO_x Schottky contacts with varying levels of oxygen incorporation were deposited onto +c-plane Zn-polar (low-lithium) bulk ZnO, with gas ratios of 0.0:10, 0.5:10, 1.0:10, 2.0:10, 3.0:10, 4.0:10, 5.0:10, and 7.0:10 sccm (O_2:Ar). The Pd target was pre-sputtered before each deposition. The substrate characteristics and Pd/PdO_x deposition conditions for the contacts are included in Appendices A3.2 and A3.4. Representative dark I-V characteristics of 0.0:10 – 7.0:10 (O_2:Ar) PdO_x contacts on +c-plane (low-lithium) ZnO are shown in Figure 6.19, with barrier heights and ideality factors in Figures 6.20 – 6.21. Homogeneous barrier heights and rectification ratios with increasing oxygen fraction *x* from RBS measurements are shown in Figures 6.22 – 6.23. Representative dark C-V characteristics of 0.0:10 – 7.0:10 (O_2:Ar) PdO_x contacts on +c-plane (low-lithium) ZnO are shown in Figure 6.24, with the comparison of $\Phi_{B,\,I\text{-}V}$ and $\Phi_{B,\,C\text{-}V}$ in Figure 6.25.

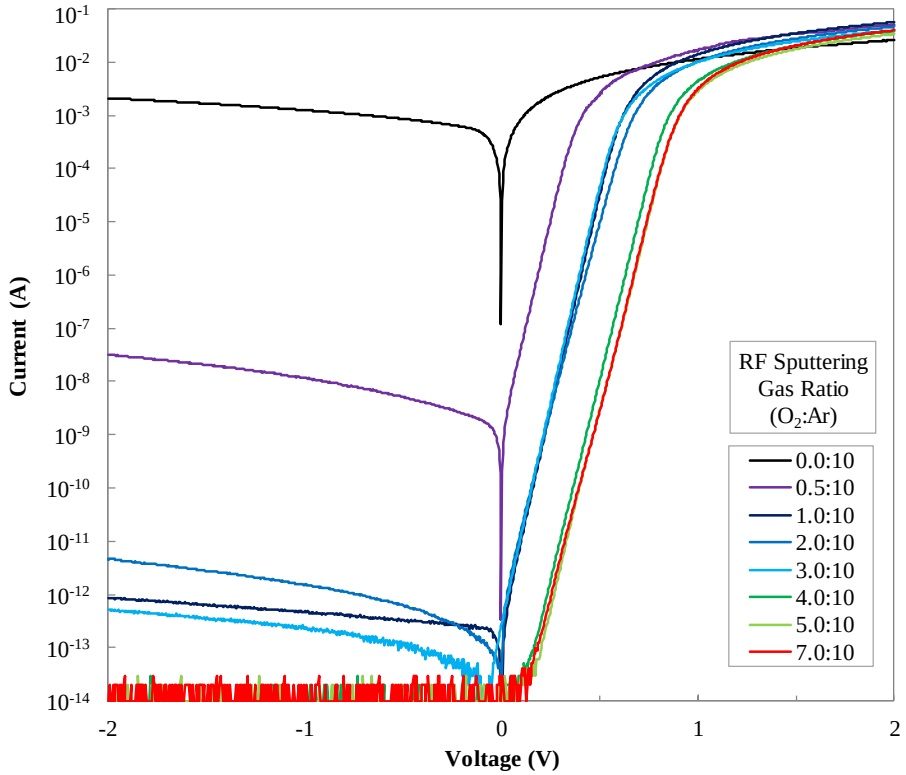

Figure 6.19: RF-Sputtered PdO_x Schottky Contacts Dark I-V Characteristics

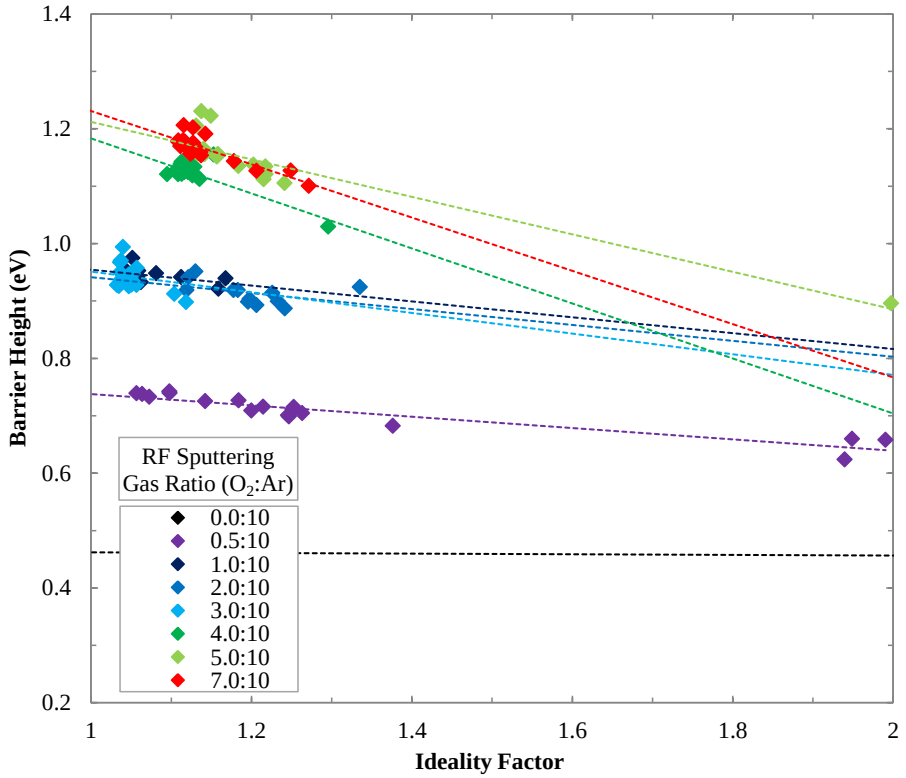

Figure 6.20: RF-Sputtered PdO_x Schottky Contacts Ideality Factors and Barrier Heights

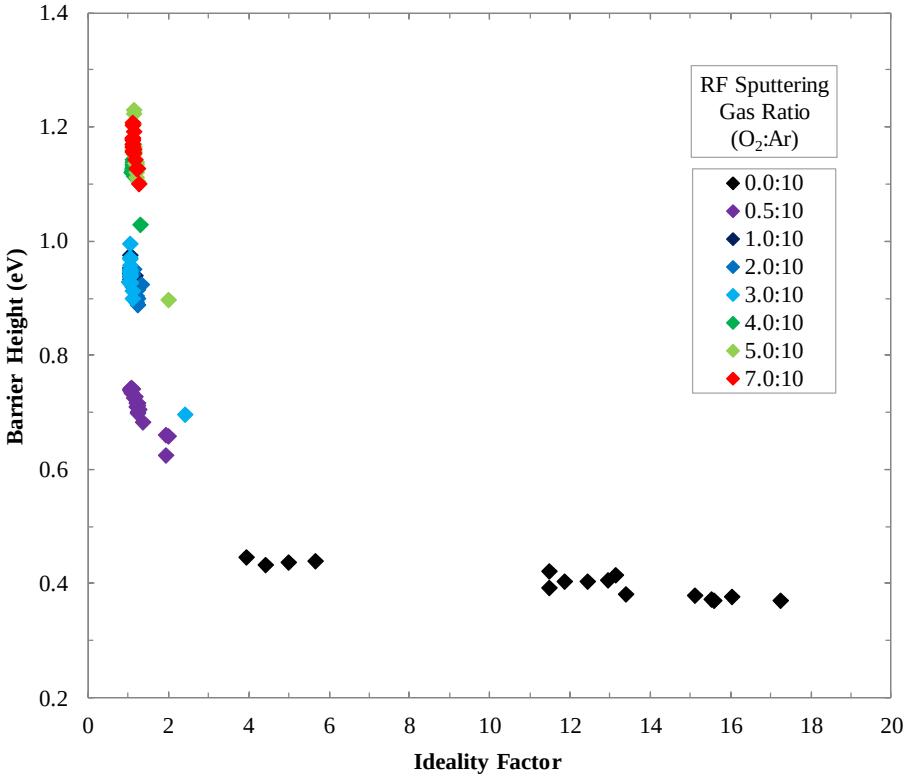

Figure 6.21: RF-Sputtered PdO_x Schottky Contacts Ideality Factors and Barrier Heights

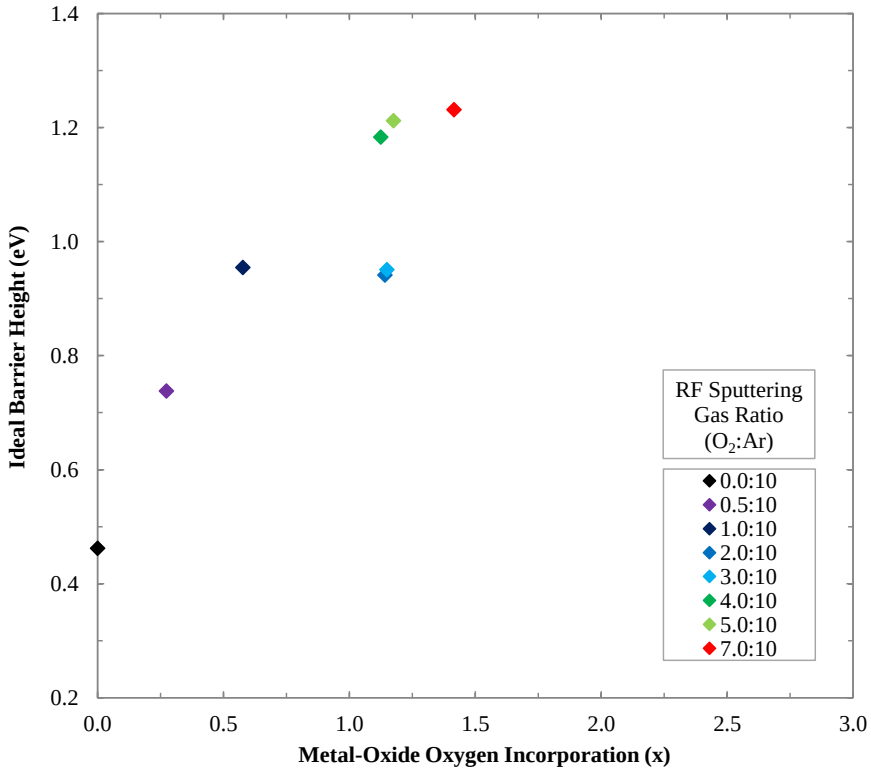

Figure 6.22: RF-Sputtered PdO_x Schottky Contacts Homogeneous barrier Height with *x*

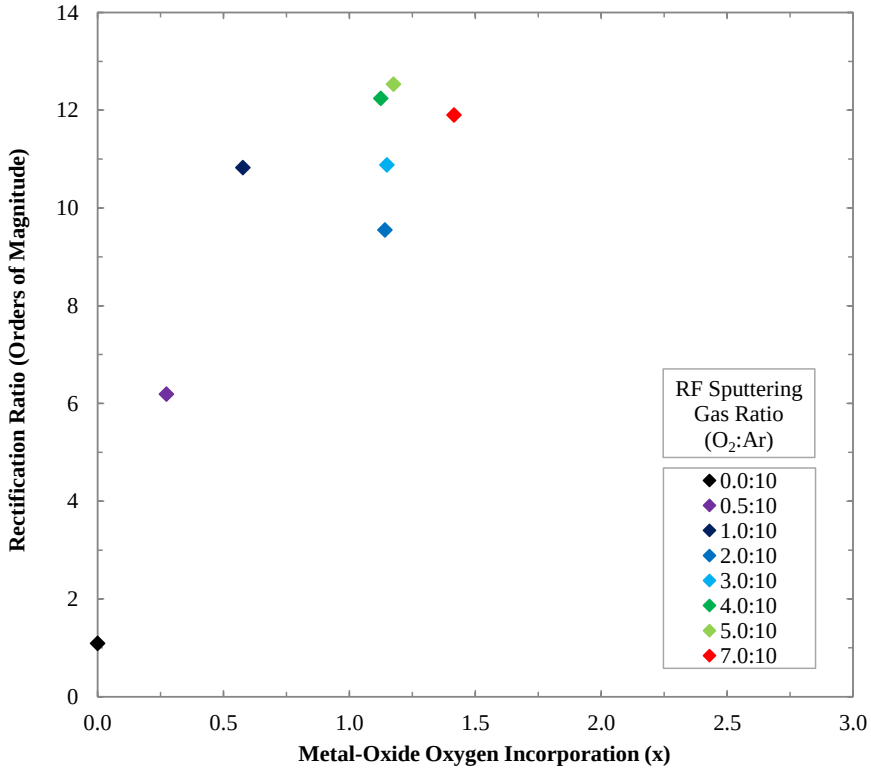

Figure 6.23: RF-Sputtered PdO_x Schottky Contacts Rectification Ratio with *x* (RBS)

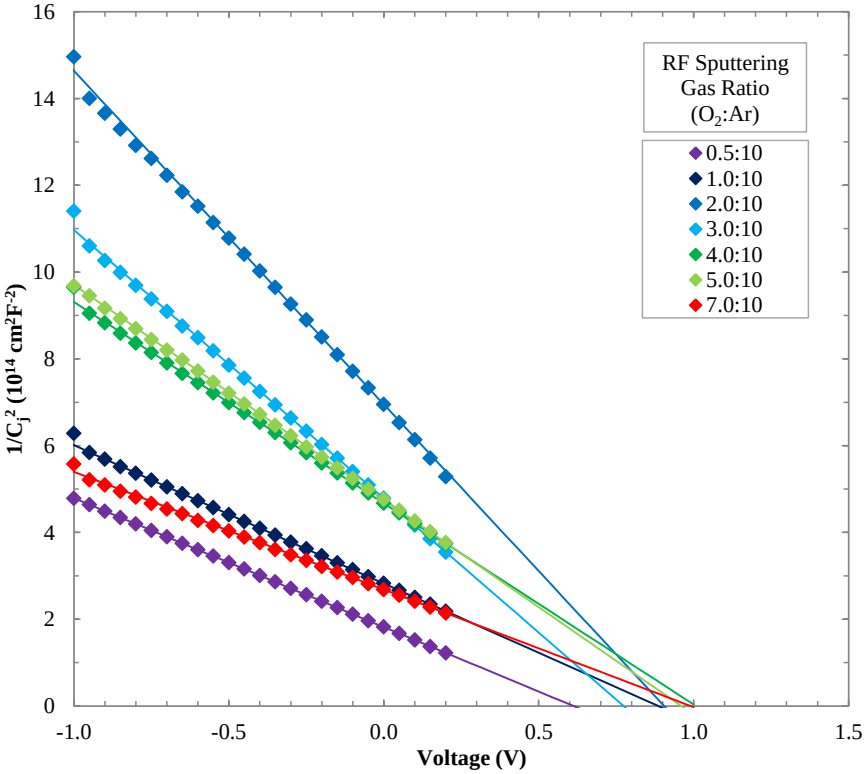

Figure 6.24: RF-Sputtered PdO_x Schottky Contacts Dark C-V Characteristics

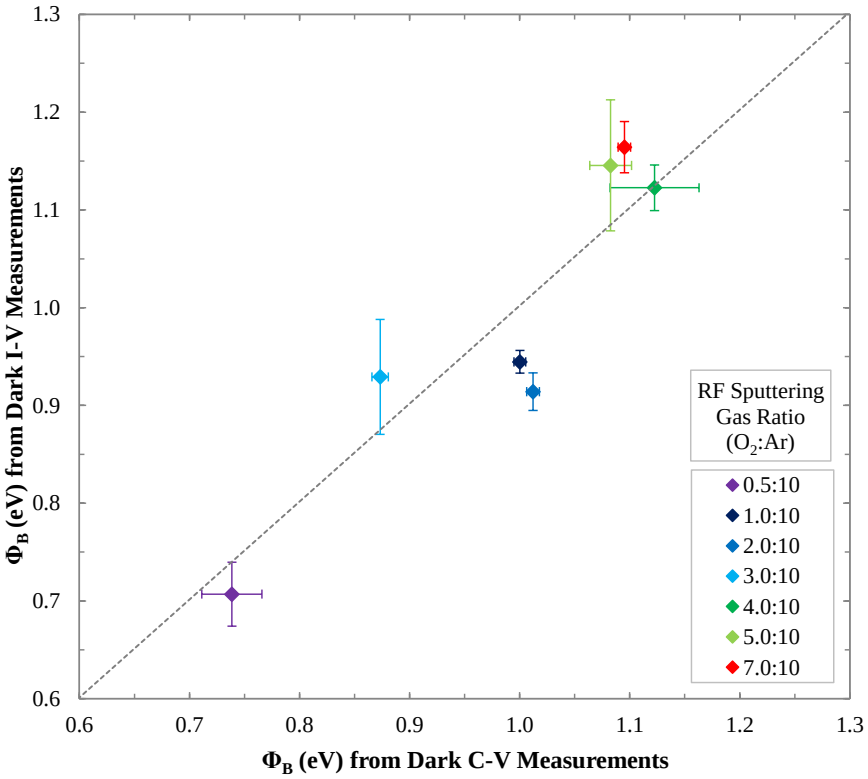

Figure 6.25: RF-Sputtered PdO_x Schottky Contacts Dark C-V Built-In Potential

The dark I-V characteristics of the PdO_x contacts in Figure 6.19 show a significant increase in rectification ratio and barrier height. Between 0.0:10 to 7.0:10 (O_2:Ar) gas flow during sputtering; the rectification ratio has increased from 1.09 to 11.9 O_{Mag} at ±2 V, and barrier heights has increased from 0.373 to 1.10 eV, as shown in Figures 6.19 – 6.21. The extension of Figure 6.20 in Figure 6.21 contains the ideality factors and barrier heights of the 0.0:10 (O_2:Ar) PdO_x contacts with ideality factors greater than 2, showing a significant improvement in ideality factor with the addition of O_2 gas flow during sputtering. Plain Pd Schottky contacts to ZnO have been reported with rectification ratios of 2 – 10 O_{Mag} and barrier heights between 0.55 – 1.2 eV; significantly higher than the plain Pd contacts fabricated in this work [6.3 – 6.4]. However, reported values of the barrier heights of PdO_x Schottky contacts to ZnO ranged between 0.89 – 1.1 eV, comparable to the PdO_x contacts fabricated in this work [6.3, 6.7].

The reverse bias leakage current of the representative 2.0:10 and 3.0:10 (O_2:Ar) PdO_x contacts in Figure 6.19 appears higher than the 1.0:10 (O_2:Ar) PdO_x contact. The cause of the leakage is most likely Schottky contact inhomogeneity, as discussed in Section 6.1.

The dark I-V characteristics and ideality factors with barrier height in Figures 6.19 – 6.20 show grouping between 1.0:10 – 3.0:10 and 4.0:10 – 7.0:10 (O_2:Ar) PdO_x contacts. Barrier height

grouping was also observed in AgO_x contacts in Figures 6.5 – 6.6, and to some extent in IrO_x contacts deposited on –c-plane ZnO in Figures 6.9 – 6.10. While the grouping of the IrO_x contacts was shown to be related to the transition of $x \approx 0$ to $x > 2$, the grouping in the PdO_x contacts does not follow the trend of oxygen fraction in Pd/PdO_x films in Figure 6.3. The RBS measurements show a plateau of x = 1.12 – 1.18 in PdO_x films fabricated with 2.0:10 – 5.0:10 (O_2:Ar) gas flow, and x = 1.42 for the 7.0:10 (O_2:Ar) PdO_x film. This grouping of oxygen fraction levels is likely caused by polycrystalline nature of the PdO_x films, observed in Section 5.3, producing largely homogenous ratios of O:Pd over a range of O_2:Ar levels.

Despite the grouping of oxygen fractions of PdO_x shown in Figure 6.2, the homogeneous barrier heights appear to vary significantly between $1.0 < x < 1.5$ in Figure 6.22. With the exception of the 2.0:10 and 3.0:10 (O_2:Ar) homogeneous barrier heights, the overall trend of the PdO_x Schottky contacts shows an increasing homogeneous barrier height that reaches a plateau above 1.2 eV. The rectification ratios also increase to plateau around 12 O_{Mag} in Figure 6.23, however this is due to the low current measurement limitations of the parameter analyser, 10 fA, in the reverse bias direction.

The dark C-V characterisation of the PdO_x contacts in Figures 6.24 – 6.25 shows an increasing V_{bi} of 0.612 – 0.991 V with increasing oxygen incorporation, with the exception of the 3.0:10 (O_2:Ar) PdO_x contact, supporting the observations made from the dark I-V measurements in Figures 6.19 – 6.20. Figure 6.25 shows a strong correlation between barrier heights calculated from dark I-V and dark C-V measurements, with a linear fit of $\Phi_{B,\,I\text{-}V} = \Phi_{B,\,C\text{-}V}$ producing an R^2 value of 0.844.

6.6 Electrical Characterisation of Platinum Oxide Schottky Contacts

RF-sputtered PtO_x Schottky contacts with varying levels of oxygen incorporation were deposited onto +c-plane Zn-polar (low-lithium) bulk ZnO in two sets. The first set consisted of 0.0:10, 0.5:10, 1.0:10, 2.0:10, 3.0:10, 4.0:10, 5.0:10, and 7.0:10 (O_2:Ar) gas ratios; the second set of 6.0:10, 7.0:10, 8.0:10, 9.0:10, and 10.0:10 (O_2:Ar) gas ratios. The Pt target was pre-sputtered in pure Ar before each deposition. The substrate characteristics and Pt/PtO_x deposition conditions for the contacts are included in Appendices A3.2 and A3.4. Representative dark I-V characteristics, ideality factors, and barrier heights of 0.0:10 – 7.0:10 (O_2:Ar) PtO_x contacts are shown in Figures 6.26 – 6.28. Homogeneous barrier heights and rectification ratios with oxygen fraction x from RBS measurements are shown in Figures 6.29 – 6.30. Representative dark C-V characteristics of the 0.0:10 – 7.0:10 (O_2:Ar) PtO_x contacts on are shown in Figure 6.31, with the comparison between $\Phi_{B,\,I\text{-}V}$ and $\Phi_{B,\,C\text{-}V}$ shown in Figure 6.32. Representative dark I-V characteristics, ideality factors, and barrier heights of the 6.0:10 – 10.0:10 (O_2:Ar) PtO_x contacts are shown in Figures 6.33 – 6.34.

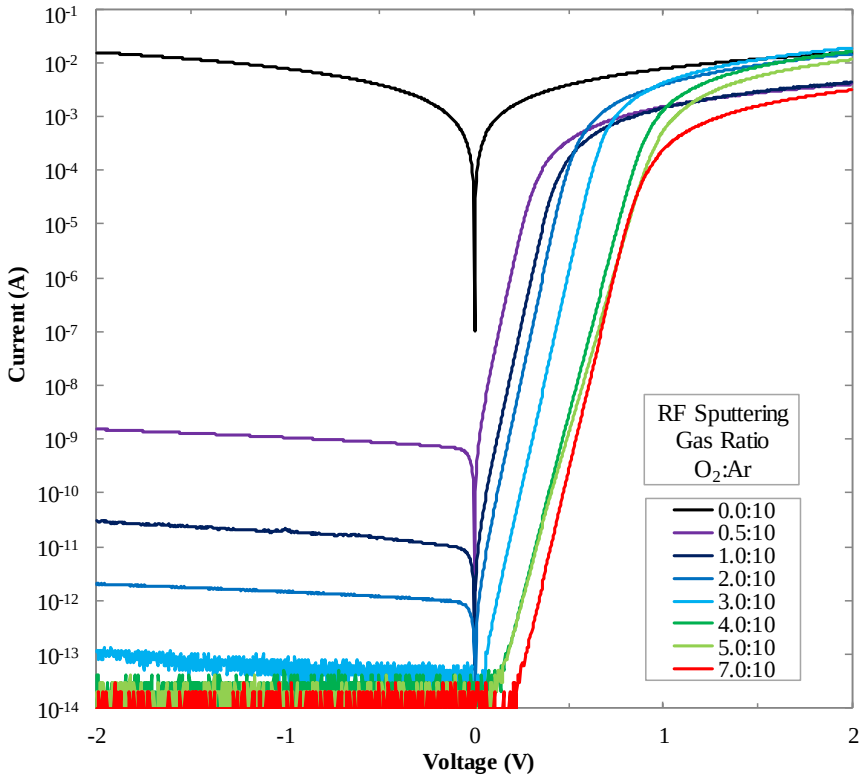

Figure 6.26: RF-Sputtered PtO_x Schottky Contacts Dark I-V Characteristics

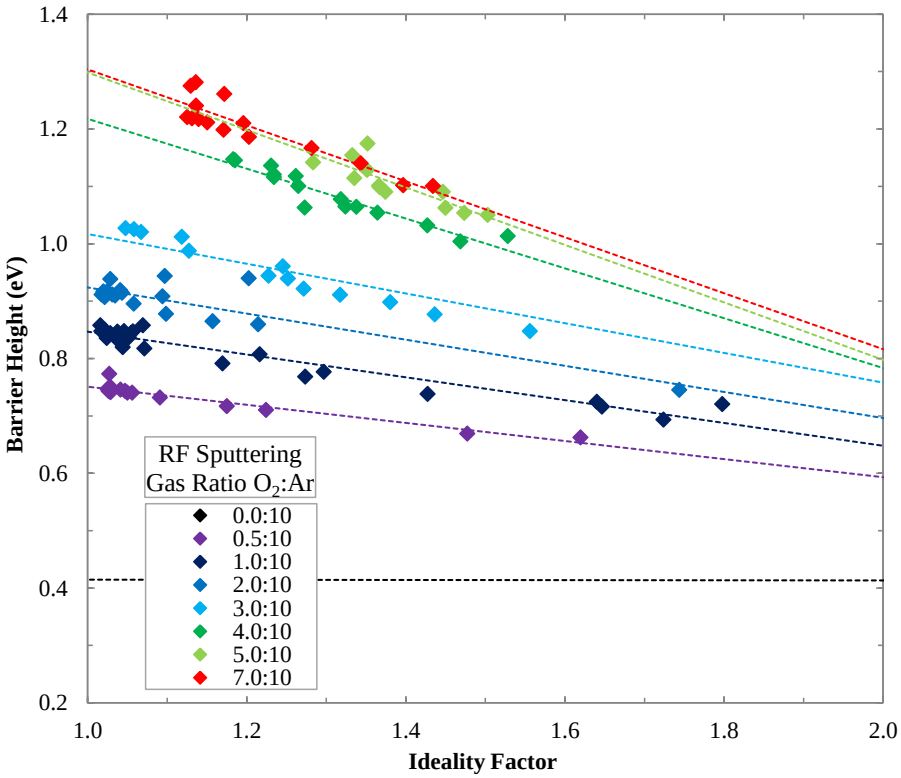

Figure 6.27: RF-Sputtered PtO_x Schottky Contacts Ideality Factors and Barrier Heights

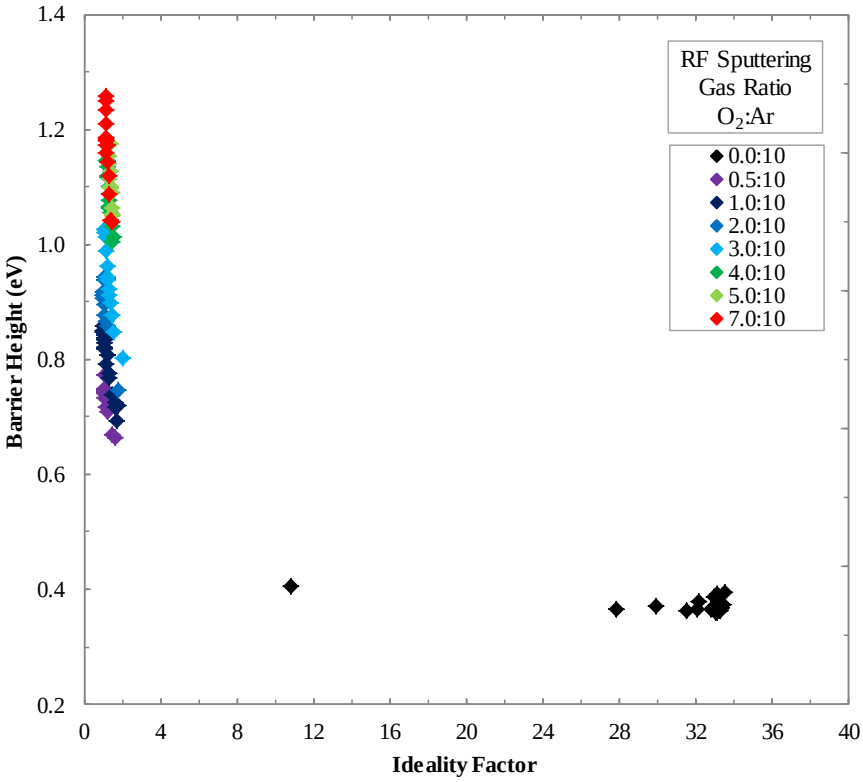

Figure 6.28: RF-Sputtered PtO_x Schottky Contacts Ideality Factors and Barrier Heights

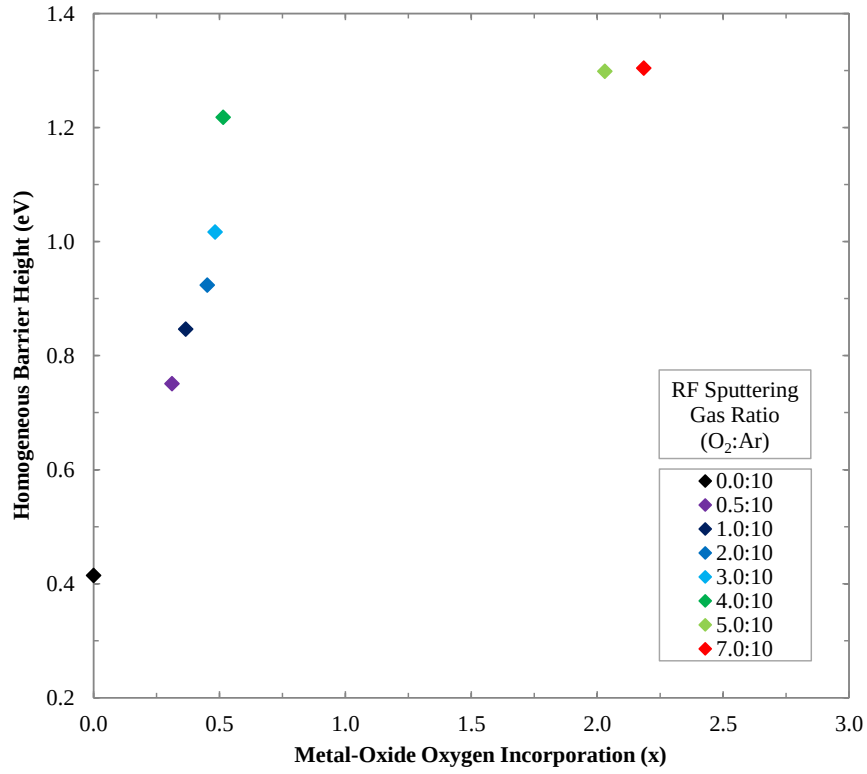

Figure 6.29: RF-Sputtered PtO_x Schottky Contacts Homogeneous Barrier Height with *x*

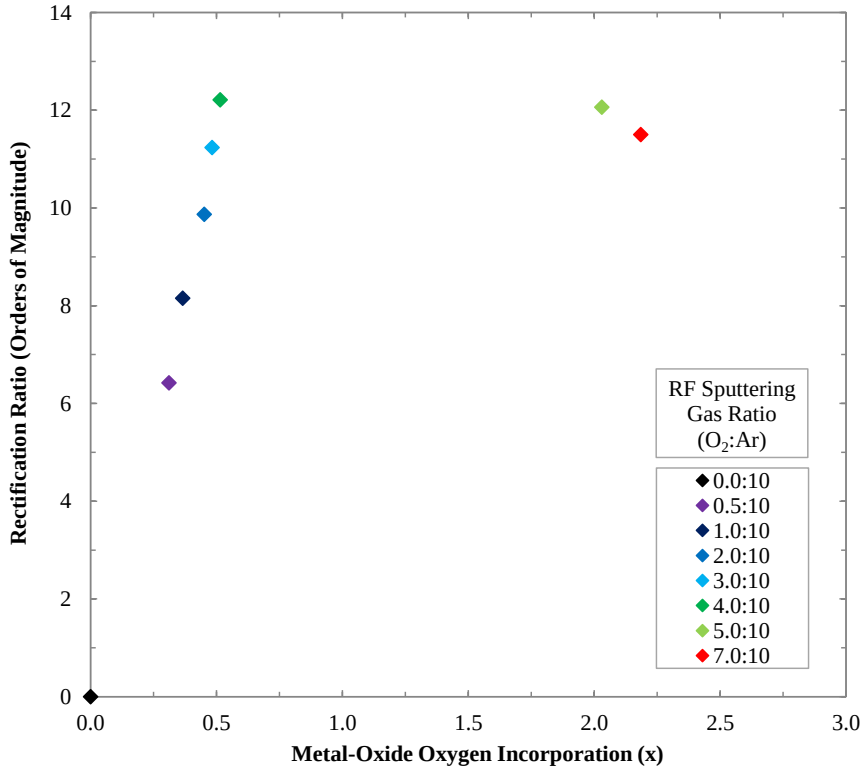

Figure 6.30: RF-Sputtered PtO_x Schottky Contacts Rectification Ratio with *x* (RBS)

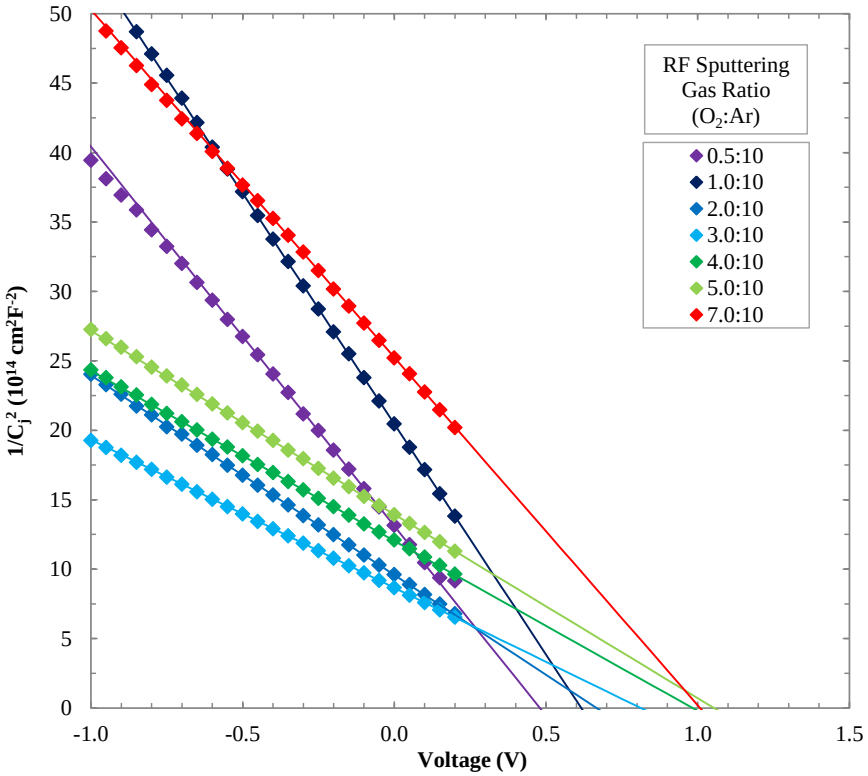

Figure 6.31: RF-Sputtered PtO_x Schottky Contacts Dark C-V Measurements

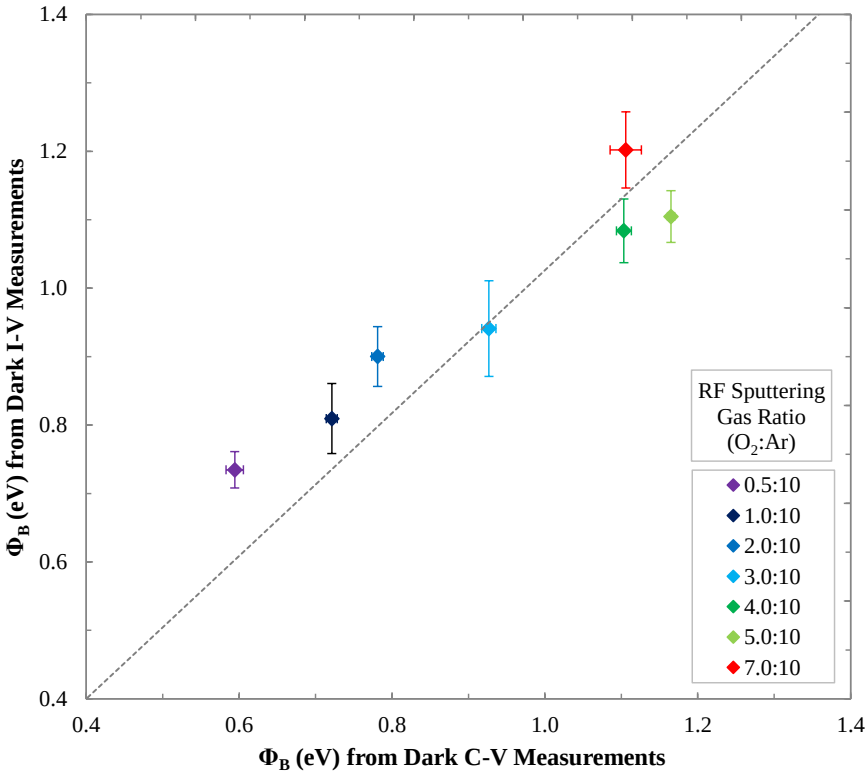

Figure 6.32: RF-Sputtered PtO_x Schottky Contacts Dark C-V Built-In Potential

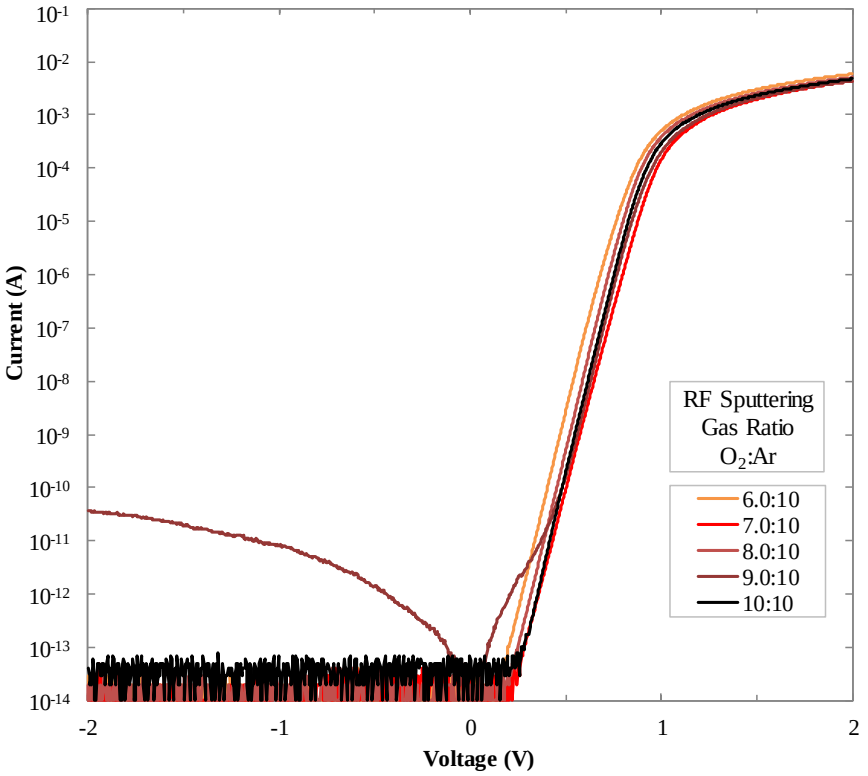

Figure 6.33: RF-Sputtered PtO_x Schottky Contacts Dark I-V Characteristics

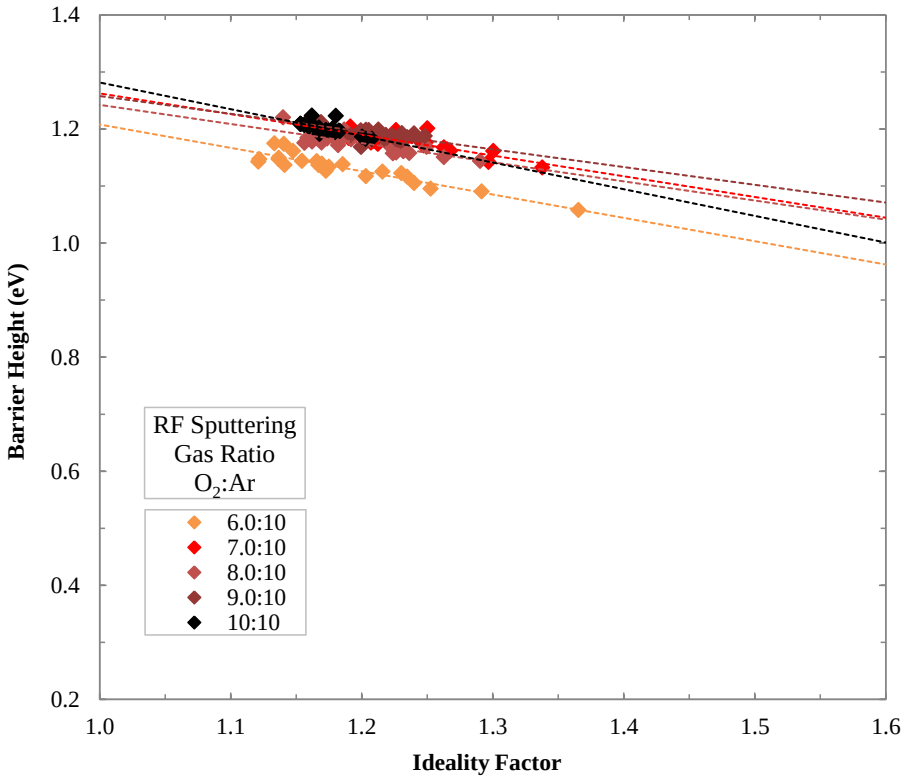

Figure 6.34: RF-Sputtered PtO_x Schottky Contacts Ideality Factors, Barrier Heights

The dark I-V characteristics of the PtO_x contacts in Figures 6.26 – 6.28 show increasing rectification ratio and barrier height with increasing oxygen incorporation, as has been seen for all of the metal-oxides studied in this work. For the 0.0:10 – 7.0:10 (O_2:Ar) PtO_x representative contacts in Figure 6.26, the rectification ratio increased from 0.0 to 12.2 O_{Mag}, and the barrier height increased from 0.362 – 1.22 eV. It is significant that the Pt were completely ohmic, compared to the rectifying behaviour of the PtO_x contacts. In literature, plain Pt contacts to ZnO have been reported with rectification ratios between 2 – 5 O_{Mag} and barrier heights between 0.39 – 1.08 eV, which are comparably better than the plain Pt contacts fabricated in this work [6.3, 6.5]. PtO_x contacts to ZnO have also been reported in literature, with barrier heights between 0.98 – 1.20 eV, lower than the barrier heights achieved in this work [6.5, 6.7].

The PtO_x oxygen incorporation series with 6.0:10 – 10:10 (O_2:Ar) gas flow during RF-Sputtering in Figure 6.33 did not show a significant improvement in rectification ratio or barrier height. With the exception of the 9.0:10 (O_2:Ar) PtO_x contacts, which showed an anomalously high leakage current, the rectification ratio of the 6.0:10 – 10:10 (O_2:Ar) PtO_x contacts ranged between 11.4 – 11.5 O_{Mag} in Figure 6.33. However, as the reverse bias current was below the measurement limitation of the parameter analyser, 10 fA, the exact rectification ratio is at least this large. The

barrier heights of the representative 6.0:10 – 10:10 (O_2:Ar) PtO_x contacts in Figure 6.34 ranged between 1.18 – 1.21 eV. For the sputtering conditions used in this work, the improvement in PtO_x Schottky contact performance with increasing O_2:Ar ratio plateaued above 5.0:10 (O_2:Ar).

The O:Pt ratio for 0.0:10 – 7.0:10 (O_2:Ar) PtO_x films measured by RBS in Figure 6.3 of Section 6.1 shows a distinct jump in oxygen fraction between the 4.0:10 and 5.0:10 (O_2:Ar) PtO_x films from x = 0.513 to x = 1.99, indicating that the films fabricated with 5.0:10 (O_2:Ar) and above consisted mostly of PtO_2. This jump can also be seen in Figures 6.29 – 6.30, where the homogeneous barrier height and rectification ratio appear to increase linearly with increasing oxygen fraction below $x \approx 0.5$, before plateauing above $x > 2$. The oxygen fraction, x, of the 6.0:10 – 10:10 (O_2:Ar) PtO_x contacts is not known, however as the homogeneous barrier heights range from 1.21 to 1.28 eV and the rectification ratios did not exceed 11 O_{Mag}, it can be concluded that the plateau above $x > 2$ extends from 5.0:10 (O_2:Ar) PtO_x to 10:10 (O_2:Ar) RF-sputtered PtO_x contacts.

The 0.0:10 – 7.0:10 (O_2:Ar) PtO_x oxygen incorporation series did not show barrier height grouping prior to the plateau above 5.0:10 (O_2:Ar), as was observed in Section 6.5 for the 0.0:10 – 7.0:10 (O_2:Ar) PdO_x oxidation series. This is likely due to the amorphous nature of the PtO_x contacts containing a mix of PtO and PtO_2, similar to the IrO_x contacts in Section 6.4.

It can be observed from Figure 6.27 that the lowest ideality factors of the 3.0:10 – 7.0:10 (O_2:Ar) PtO_x contacts are slightly higher than the lowest ideality factors of the 0.5:10 – 2.0:10 (O_2:Ar) PtO_x contacts. A similar trend can be seen in both the IrO_x contacts to +c-plane (low-lithium) ZnO in Figure 6.12 for O_2:Ar ratios above 2.0:10, and in the PdO_x contacts for O_2:Ar ratios above 4.0:10 in Figure 6.20. As the distribution of the ideality factors depends on the barrier height inhomogeneity, these trends indicate that there is a lower probability of producing Schottky contacts with high levels of lateral homogeneity becomes less likely with higher O_2:Ar ratios. However, this is likely caused by the higher total pressure of the O_2 and Ar gas flows during deposition increasing from 3.2 x 10^{-3} to 4.6 x 10^{-3} mbar with 0.0:10 to 7.0:10 (O_2:Ar) gas flow ratios, as the Ar flow is a constant 10 sccm for all growths. RF-sputtering at higher processing pressures produces lower-quality films and adhesion to the substrate, as the sputtered atoms have a higher probability of colliding with gas particles and arriving at the substrate with lower kinetic energy.

The dark C-V characterisation of the PtO_x contacts in Figures 6.31 – 6.32 shows a trend of increasing V_{bi}, supporting the observation of increasing barrier height from the dark I-V measurements. Figure 6.32 shows a correlation between the barrier heights from both the dark I-V and dark C-V measurements, with a linear fit of $\Phi_{B,\,I\text{-}V} = \Phi_{B,\,C\text{-}V}$ producing an R^2 value of 0.747. The similarity of the $\Phi_{B,\,I\text{-}V}$ and $\Phi_{B,\,C\text{-}V}$ values indicate an overall high level of lateral homogeneity across the PtO_x Schottky contacts, despite the lack of low-ideality contacts with high O_2:Ar ratios.

6.7 Comparison of Metal-Oxide Contacts with Varying Oxygen Content

All RF-sputtered metal-oxide Schottky contacts fabricated on c-plane ZnO in this work showed a significant increase in rectification ratio and barrier height with an increasing ratio of O_2:Ar during RF-sputtering. All oxygen incorporation series of metal-oxide Schottky contacts fabricated on +c-plane (low-lithium) ZnO achieved Schottky contacts with rectification ratios above 11 O_{Mag}, with measurements limited by the lower current limitations of the parameter analyser, 10 fA.

The AgO_x contacts showed the greatest sensitivity to the addition of O_2 gas during deposition, and produced the contacts with the highest barrier height values; 1.31 eV measured for a 2.0:10 (O_2:Ar) AgO_x contact on +c-plane (low-lithium) ZnO. The RuO_x contacts showed the lowest barrier heights with increasing oxygen incorporation, with the highest barrier height measured to be 0.960 eV for a 7.0:10 (O_2:Ar) RuO_x contact on –c-plane ZnO.

The PdO_x contact oxidation series showed significant grouping of both barrier height and oxygen fraction from RBS measurements, which is likely caused by the polycrystalline nature of the films explored in Section 5.3. Higher crystallinity Schottky contacts appear to produce contacts that are less sensitive to fluctuations in O_2:Ar gas ratios, which allows for greater reproducibility. In comparison, the 2.0:10 (O_2:Ar) IrO_x contacts to –c-plane and +c-plane (low-lithium) ZnO in Section 6.4, varied significantly in oxygen fraction and barrier height in relation to the 1.0:10 and 3.0:10 (O2:Ar) IrO_x contacts from the respective series.

In order to compare the dark I-V characteristics of the different metal-oxides explored in this work, the homogeneous barrier height and rectification ratio have been plotted against the RF-sputtering O_2:Ar gas ratios used, as well as against the RBS oxygen fraction values for the Ir/IrO_x, Pd/PdO_x, and Pt/PtO_x films that were discussed in Section 5.6.

The calculated homogeneous barrier heights of the RF-sputtered AgO_x, RuO_x, IrO_x, PdO_x, and PtO_x contacts with increasing O_2:Ar gas ratio are shown in Figure 6.35, and with increasing oxygen fraction *x* from RBS measurements for the IrO_x, PdO_x, and PtO_x contacts, in Figure 6.36. The representative rectification ratios of RF-sputtered AgO_x, RuO_x, IrO_x, PdO_x, and PtO_x Schottky contacts to +c-plane (low-lithium) ZnO with increasing O_2:Ar gas ratio are shown in Figure 6.37, and with increasing oxygen fraction *x* from RBS measurements for the IrO_x, PdO_x, and PtO_x contacts in Figure 6.38. It is important to note that the RuO_x, and IrO_x Schottky contacts deposited on –c-plane ZnO were not deposited after a pre-sputter cleaning of the metal target, therefore there was a significant level of uncertainty in the oxygen incorporation.

Tabulated statistical analysis of the variation of the barrier heights and ideality factors of each set of metal/metal-oxide Schottky contacts explored in this chapter is included in Appendix A6.3.

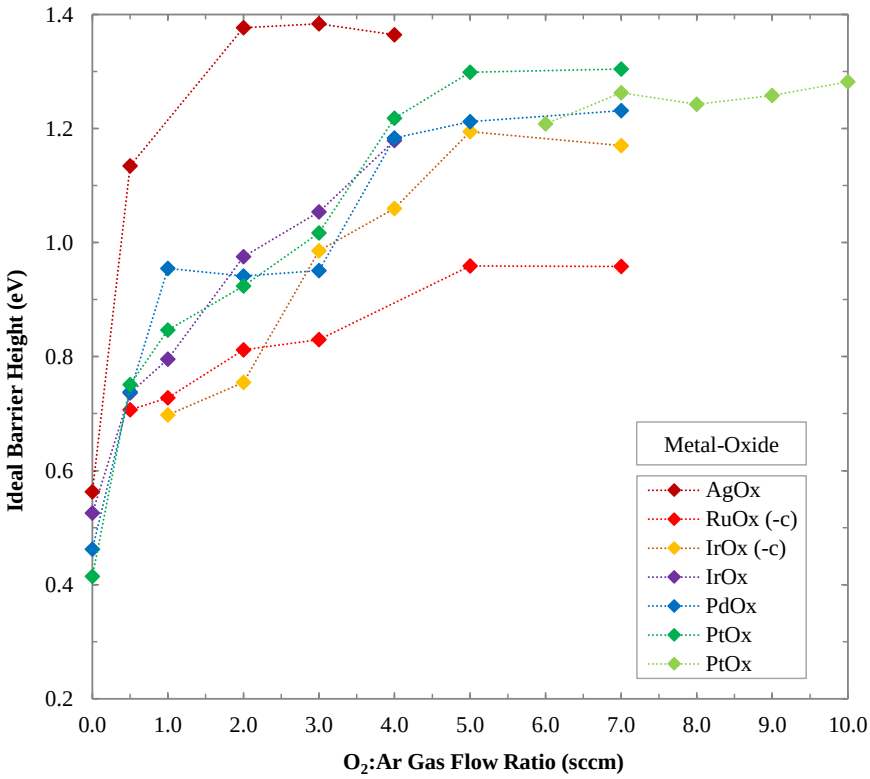

Figure 6.35: Metal-Oxide Contacts Homogeneous barrier Heights with O_2:Ar Ratio

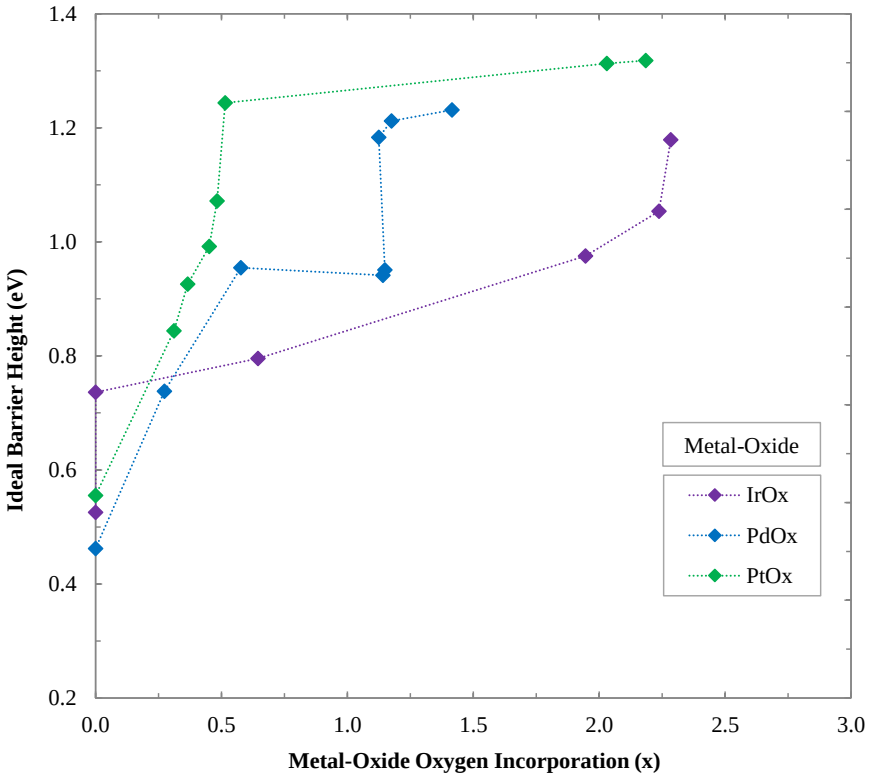

Figure 6.36: Metal-Oxide Contacts Homogeneous barrier Heights with *x* (RBS)

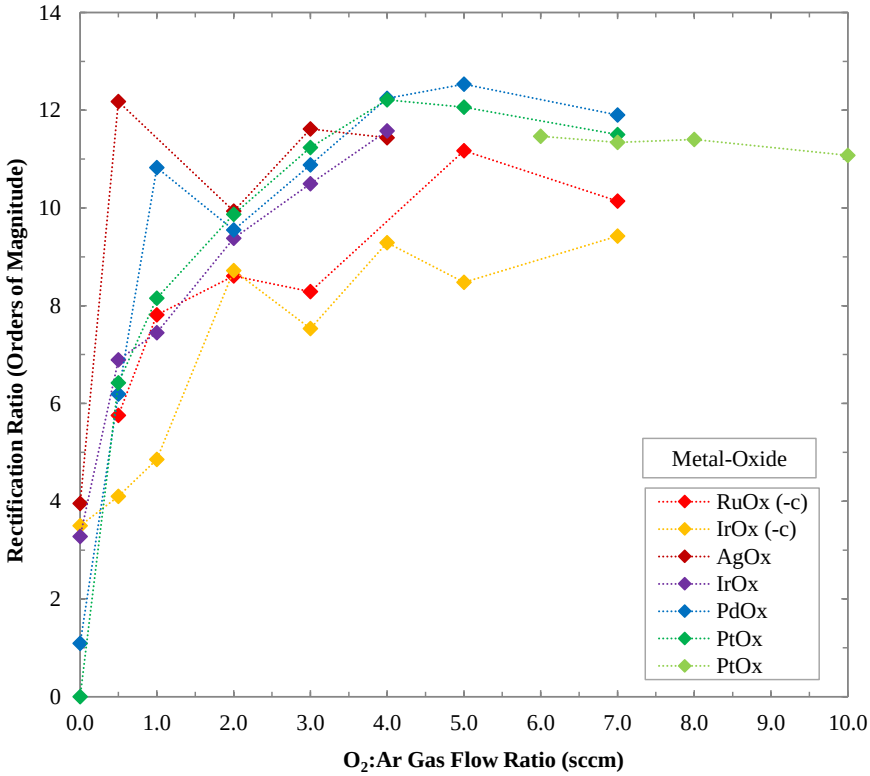

Figure 6.37: Representative Metal-Oxide Contacts Rectification Ratios with O_2:Ar Ratio

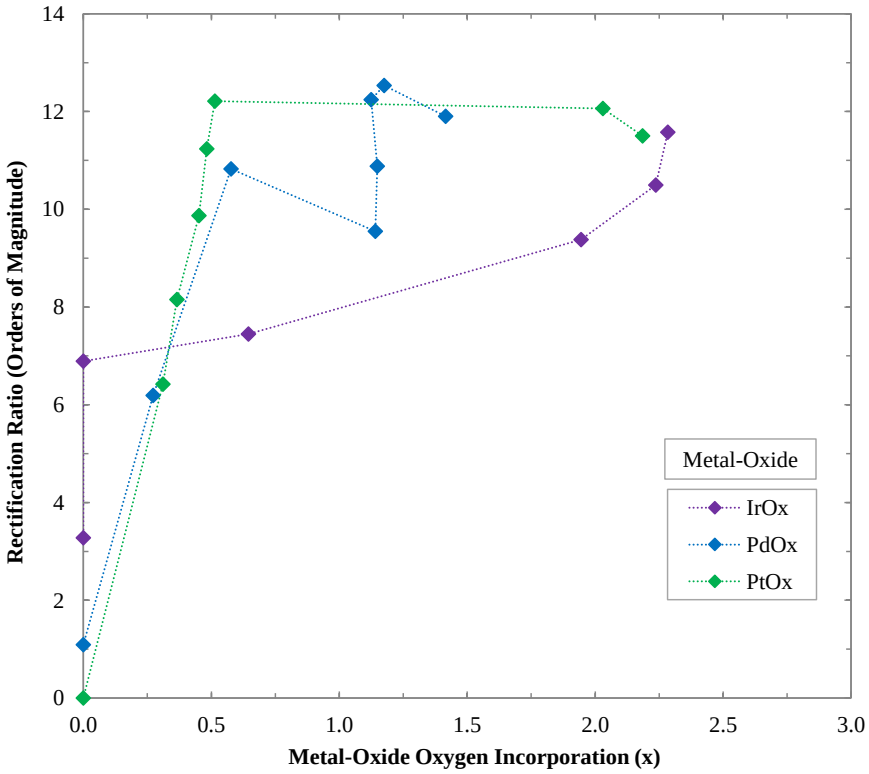

Figure 6.38: Representative Metal-Oxide Contacts Rectification Ratios with *x* (RBS)

The calculated laterally-homogeneous barrier heights of the metal-oxide Schottky contacts in Figure 6.35 show a trend of increasing barrier height with increasing O_2:Ar ratio. The trend appears to reach an upper limit of 1.2 – 1.3 eV reached between 5.0:10 – 7.0:10 (O_2:Ar) gas flow for PdO_x and PtO_x, and with IrO_x contacts to +c-plane (low-lithium) ZnO following the same trend towards a similar upper limit. The homogeneous barrier heights with oxygen fraction *x* show a similar trend in Figure 6.36, with the exception of the 2.0:10 and 3.0:10 (O_2:Ar) PdO_x contacts. However, the IrO_x series does not appear to increase in homogeneous barrier height as rapidly as PdO_x and PtO_x with increasing oxygen incorporation.

The representative metal-oxide Schottky contacts to +c-plane Zn-polar (low-lithium) ZnO in Figure 6.37 shows a trend of increasing rectification ratio with increasing oxygen incorporation, reaching a plateau around 12 O_{Mag} rectification. However, the upper limit of the rectification ratio was limited by the noise floor of the parameter analyser, 10 fA. With the exception of 2.0:10 and 3.0:10 (O_2:Ar) PdO_x, which showed unexpectedly high levels of reverse-bias leakage current, the plot of rectification ratio with oxygen fraction *x* in Figure 6.38 also shows a trend of increasing rectification ratio to the upper limits of 11 – 12 O_{Mag}.

The rectification ratio of the representative metal-oxide contacts in Figure 6.37 increased from between 0.0 – 4.0 O_{Mag} for the plain metal contacts to between 11 – 12 O_{Mag} for 7.0:10 (O_2:Ar) RF-sputtered metal-oxide contacts, showing a significant improvement in Schottky contact behaviour. The lower rectification ratios of the RuO_x and IrO_x contacts on –c-plane ZnO in Figure 6.37 are likely due to the increased conductivity of the –c-plane ZnO substrates of 0.09 to 0.1 Ωcm, compared to 0.89 – 5.12 Ωcm for the +c-plane (low-lithium) ZnO substrates used in this work, which is understood to be caused by the increased carrier concentration in –c-plane ZnO [6.10 – 6.12]. A higher carrier concentration would cause an increased image force lowering effect, as discussed in Section 2.3.4, lowering the barrier height and increasing the ideality factor.

In order to compare the barrier heights and ideality factors of the metal-oxide Schottky contacts to ZnO fabricated in this work to values published in literature, tabulated barrier heights and ideality factors of metal and metal-oxide Schottky contacts to ZnO from Müller et. al., Brillson and Lu, and Özgür et. al. were plotted in Figure 6.39, representing 74 Schottky contacts to ZnO from 41 individual publications [6.3 – 6.5]. Figure 6.40 shows the barrier heights and ideality factors of the representative Schottky contacts from this work against the Schottky contacts to ZnO from Figure 6.39 [6.3 – 6.5]. The Schottky contacts in Figure 6.39 include contacts that were deposited following the use of pre-deposition or post-deposition treatments for improving the performance of Schottky contacts, including the use of O_2 plasma, O_2/He plasma, H_3PO_4/HCl acid, and boiling H_2O_2 surface treatments, which could oxidise the metal Schottky contacts [6.3 – 6.4].

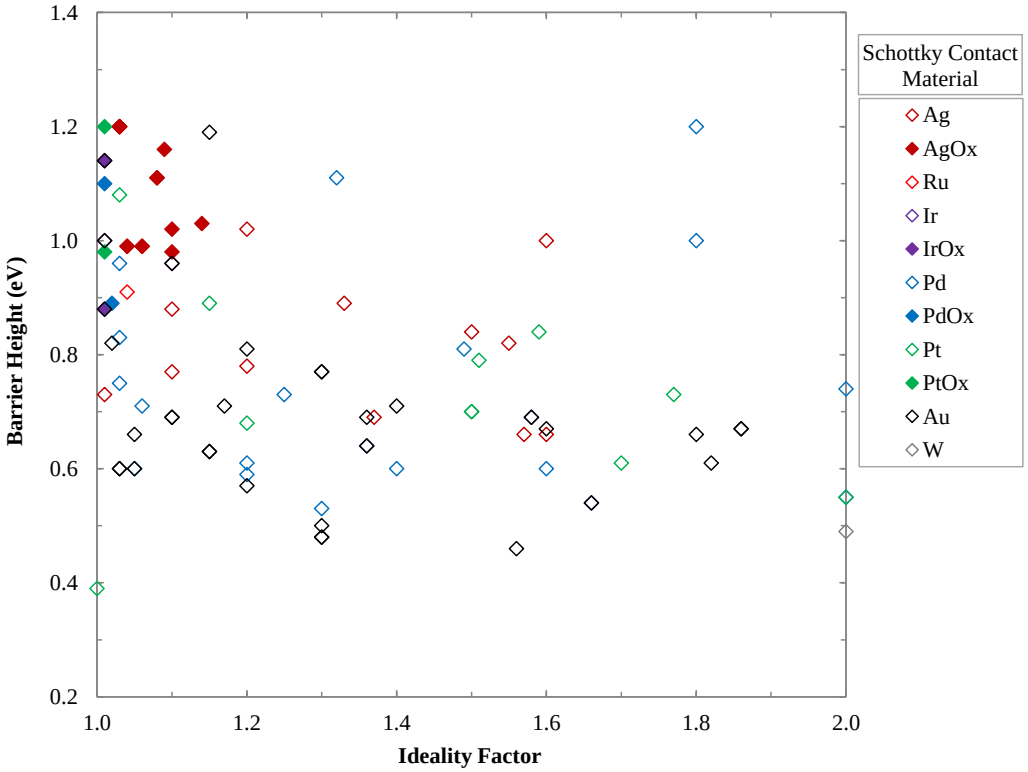

Figure 6.39: Barrier Heights, Idealities of Schottky Contacts to ZnO in Literature [6.3 – 6.5]

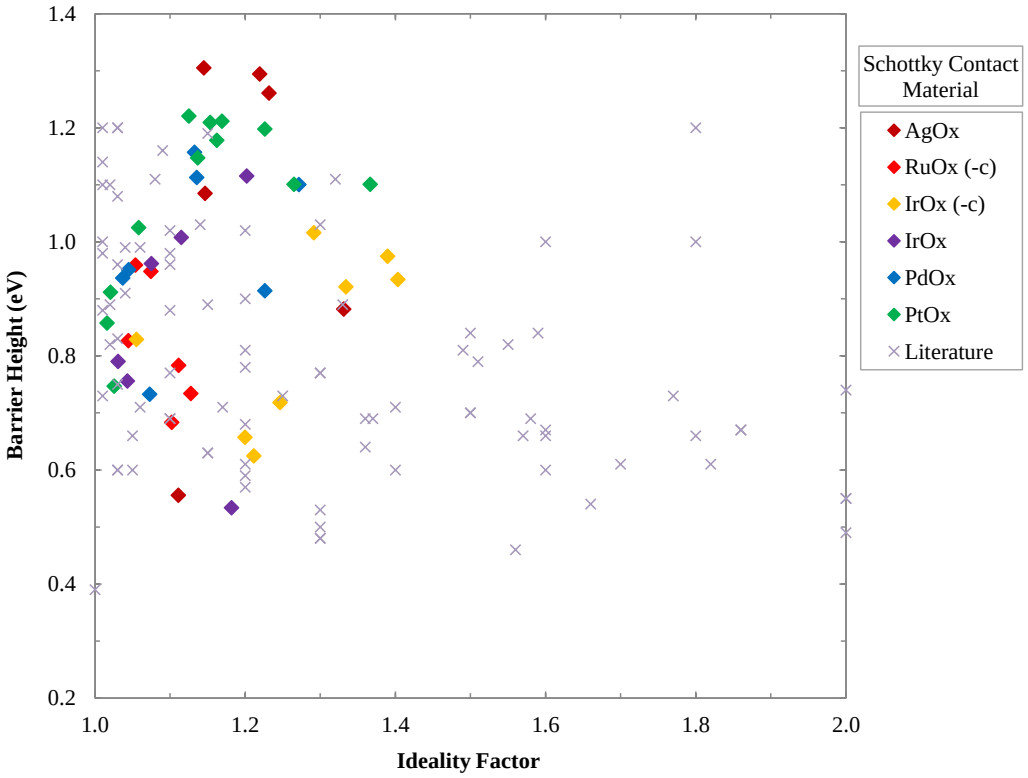

Figure 6.40: Barrier Heights of Schottky Contacts to ZnO: This Work, Literature [6.3 – 6.5]

Figure 6.40 shows that AgO_x and PtO_x Schottky contacts from this work have higher barrier heights from dark I-V measurements than the Schottky contact devices reported in the literature from S. Müller et. al., L. J. Brillson and Y. Lu, and Ü. Özgür et. al. [6.3 – 6.5]. However, the ideality factors of these Schottky contacts are higher than the contacts reported in literature. The ideality factors and barrier heights of plain metal Schottky contacts in literature are significantly better than the plain metal Schottky contacts fabricated in this work, which is unexpected as hydrothermally-grown +c-plane bulk ZnO is reportedly the highest quality ZnO grown [6.12].

XPS and RBS analysis in Section 5.6 of RF-sputtered films of 0.0:10 – 7.0:10 (O_2:Ar) IrO_x, PdO_x, and PtO_x have shown that, for the sputtering conditions used, the IrO_x and PtO_x films exceeded oxygen fractions of $x = 2$, likely reaching an upper limit of the oxygen incorporation and therefore barrier height. However, the PdO_x films did not reach $x = 2$, therefore higher levels of oxygen incorporation could be possible, producing contacts with higher barrier heights.

6.8 Metal-Oxide Schottky Contact Formation Mechanism Analysis

A model that explains the giant improvement in barrier height and rectification ratios of the Schottky contacts has been proposed in this work combining separate, previously observed effects into a consistent model that includes the following three mechanisms. Firstly, the removal of the hydroxyl-induced surface potential well and electron accumulation layer of the ZnO [6.3, 6.15 – 6.21]. Secondly, the passivation of intrinsic interfacial oxygen vacancies, V_O, in ZnO, and the prevention of extrinsic V_O at the metal-semiconductor interface causing Fermi-level pinning [6.3, 6.16]. And thirdly, the increase in work function and electronegativity of the Schottky contacts [6.3, 6.17 – 6.20].

6.8.1 Zinc Oxide Surface Treatments

Unlike many other wide band gap semiconductors, ZnO has been found to form ohmic contacts more readily than Schottky contacts [6.1]. From persistent difficulty in forming reliable Schottky contacts, surface treatments including remote O_2 plasma, remote O_2/He plasma, UV-ozone, and H_2O_2 have been found to improve Schottky contact performance from ohmic to rectifying behaviour [6.3 – 6.4, 6.15 – 6.21]. The improvement has been attributed to the reduction of deep-level defects, such as Zn interstitials, Zn_I, and V_O, and the reduction of near-surface conductivity.

UV-ozone plasma treatment of ZnO was found to remove surface-layer contaminants, such as carbon, contributing to an improvement in Schottky contact quality [6.18]. Photoluminescence (PL)

spectroscopy on H_2O_2–treated ZnO observed a reduction of donor defects such as Zn_I and V_O, believed to be caused by the oxidation of the ZnO surface reacting with Zn_I to form ZnO, neutralising V_O, and as producing Zn vacancy, V_{Zn}, acceptor defects [6.19 – 6.21].

Remote O_2 and O_2/He plasma treatments of Au, Ir, and Pt contacts to bulk ZnO have been reported to create a conversion from ohmic to Schottky behaviour in the contacts, a process that was found to be reversible with the application of remote Ar plasma treatment [6.15 – 6.16]. The improvement in rectification behaviour, barrier height and ideality factor, was attributed to a reduction of deep level defects in the ZnO, as well as the removal of surface hydroxyl groups [6.15 – 6.17, 6.19]. The presence of ~2 monolayer hydroxyl groups attached to the surface layer of ZnO has been reported, occurring on many crystal faces under normal laboratory conditions [6.23 – 6.26]. The hydroxyl groups have been associated with downward band bending at the surfaces, creating a potential well trapping a 2-dimensional surface electron accumulation layer (SEAL) as illustrated in Figure 6.41, where V_{bb} is the downward band bending [6.23 – 6.28]. The downward band bending severely hinders the formation of rectifying Schottky contacts, which require upward band bending to create a region of (depleted) positive space charge [6.3].

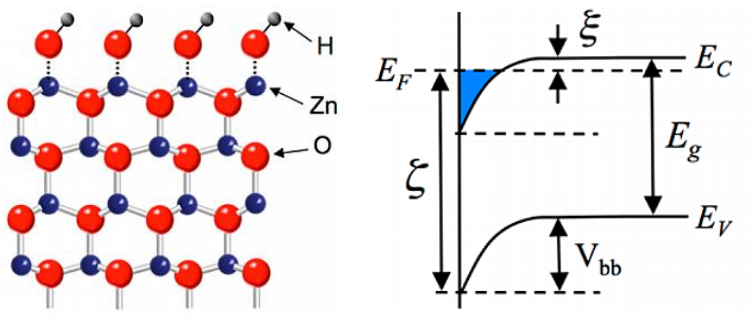

Figure 6.41: Hydroxyl Termination of ZnO (Left), Surface Potential Well (Right) [6.23]

The SEAL causes the surfaces of ZnO to be metallic in nature, which could account for the ohmic behaviour of plain metal Pt contacts to ZnO in this work [6.24 – 6.28]. Heating of the ZnO under ultra-high vacuum (UHV) to 750 °C has shown to remove hydroxyl groups from the surface of c-plane bulk ZnO, resulting in a reduced level of downward band bending on the Zn-polar face of bulk ZnO, and therefore reducing the surface potential well and the SEAL [6.25].

In this work, the increasing O_2:Ar ratio of gas flow during RF-sputtering of the metal-oxide Schottky contacts could be increasingly neutralising the Zn_I and V_O defects in the near-surface ZnO. During RF-sputtering deposition, the ZnO surface is bombarded with the sputtered noble metal ions, as well as O^{2-} and Ar^+ ions, in a ballistic process described in Section 3.4.2.1 [6.22]. The bombardment of O^{2-} ions, as well as the incorporation of oxygen species in the Schottky material,

could be providing a source of oxygen for the neutralisation of the donor defects, improving Schottky rectifying behaviour. The presence of oxygen in the Schottky contact material could also be preventing the creation of more oxygen vacancies, especially with noble metals of high formation energies such as Ag and Pt [6.19]. The bombardment of O^{2-} ions could also be reacting with the surface hydroxyl groups, producing H_2O, and removing them from the ZnO surface, and cleaning the surface of other contaminants before deposition. Increasing ratios of O_2:Ar would account for greater removal of the hydroxyl groups, which has been shown to improve contact quality from ohmic to Schottky behaviour [6.15 – 6.17, 6.19]. However, increased ballistic damage to the ZnO surface from RF-sputtering at higher pressures could be causing the lack of low-ideality factor Schottky contacts for O_2:Ar ratios above 5.0:10, as mentioned in Section 6.7. The initial rapid increase in Schottky contact quality with O_2:Ar sputtering gas ratio indicates that the removal of the surface hydroxyl groups is occurring with low O_2:Ar gas ratios, as the removal of the SEAL is crucial to the formation of a rectifying contact [6.24 – 6.28].

6.8.2 Fermi-Level Pinning

The Schottky-Mott model of metal-semiconductor rectifying contacts predicts a barrier height determined exclusively by the work function of the metal, ϕ_m, and the electron affinity of the semiconductor, χ, which is 4.2 eV in the case of ZnO [6.4, 6.29 – 6.30]. From Equation 6.3, the expected barrier heights of Ag, Ru, Ir, Pd, and Pt Schottky contacts to ZnO are 0.06, 0.51, 1.07, 0.92, and 1.45 eV, respectively [6.13 - 6.31]. However, published barrier heights of plain metal Schottky contacts to ZnO without the use of ZnO surface treatments were typically between 0.6 – 0.8 eV [6.3 – 6.5, 6.32]. This has been attributed to the Fermi-level pinning by intrinsic defect states, such as V_O, and interfacial metal-induced gap states (MIGS) created by the metal-semiconductor contact [6.32]. ZnO, as a wide band gap semiconductor, should be only weakly dependent on MIGS, however the oxygen vacancies has been shown to pin the Fermi-level close to the V_O (+2, 0) defect level, 0.7 ± 0.2 eV below the conduction band minimum, E_C, accounting for the limit of typical barrier heights of plain metal Schottky contacts to ZnO [6.3, 6.32]. Oxygen vacancies appear to be formed at the Schottky contact interface immediately upon contact formation, from chemical reactions between the ZnO and Schottky contact metal, in addition to the intrinsic oxygen vacancy concentration [6.32]. The resulting Schottky barrier formation band diagram with the Fermi-level pinned to the V_O (+2, 0) defect level is shown in Figure 6.42 [6.32].

$$q\Phi_{Bn} = q(\phi_m - \chi) \qquad (6.3)[6.13]$$

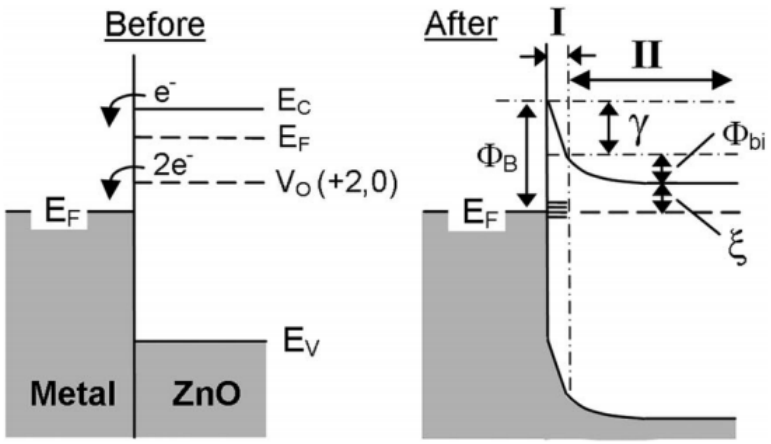

Figure 6.42: Band Diagrams of V_O Influence on Schottky Barrier Formation to ZnO [6.32]

Figure 6.42 shows two distinct regions of positive space charge following the formation of the Schottky contact, due to the Fermi-level pinning of the V_O (+2, 0) defect level [6.32]. While region II is typical for an n-type Schottky contact, the addition of the narrow (few-nanometer thickness) positive space charge region I allows for a greater amount of electron-tunnelling reverse bias leakage current, resulting in higher ideality factors and lower rectification ratios, as shown for plain metal Schottky contacts in this work [6.32]. However, the metal-oxide Schottky contacts with low levels of oxygen incorporation and barrier heights between 0.6 – 0.8 eV in this work still had surprisingly low ideality factors, indicating a low level of V_O (+2, 0) defect Fermi-level pinning.

The rapid improvement of the Ag/AgO_x and Pt/PtO_x Schottky contacts with O_2:Ar ratio in Figures 6.37 – 6.38 could be due to the high metal-oxide formation energies of Pt and Ag compared to Ir, Pd, and Ru, as discussed in Section 5.1 [6.31, 6.33]. In the formation of a Schottky contact, a metal with higher metal-oxide formation energy would be less likely to chemically react with the ZnO interface to produce oxygen vacancies, as it would be less energetically-favourable [6.32].

6.8.3 Metal-Oxide Work Function

The work function of the Ir/IrO_x and Pt/PtO_x films was investigated using KPM, a technique described in Section 4.1.4, measuring change in surface potential, $\Delta V_{surface}$, between an Au reference layer and uncapped films of Ir/IrO_x and Pt/PtO_x. The plots of $\Delta V_{surface}$ from Ir/IrO_x and Pt/PtO_x films to the Au reference with increasing oxygen incorporation, and with oxygen fraction x from RBS measurements, as shown in Figures 6.43 – 6.44, with standard deviations. The results of the KPM measurements are detailed in Section 5.5. The surface potential of the films shown in Figures 6.43 – 6.44 directly relates to the work function of the films, as shown in Equation 6.4 [6.34].

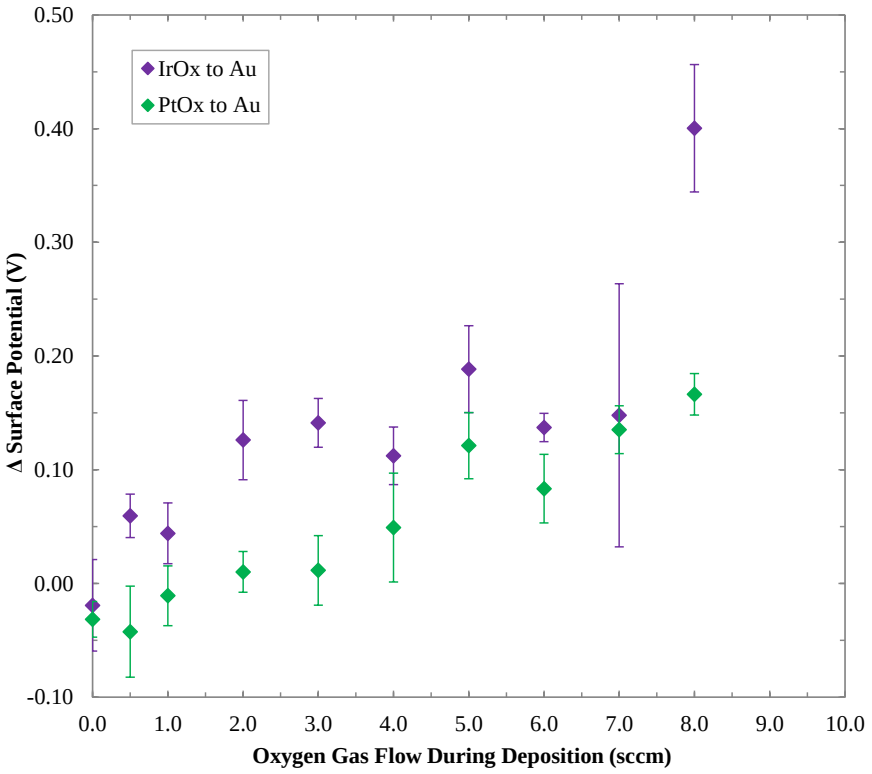

Figure 6.43: Surface Potential of RF-Sputtered Films with O_2:Ar Sputtering Gas Ratio

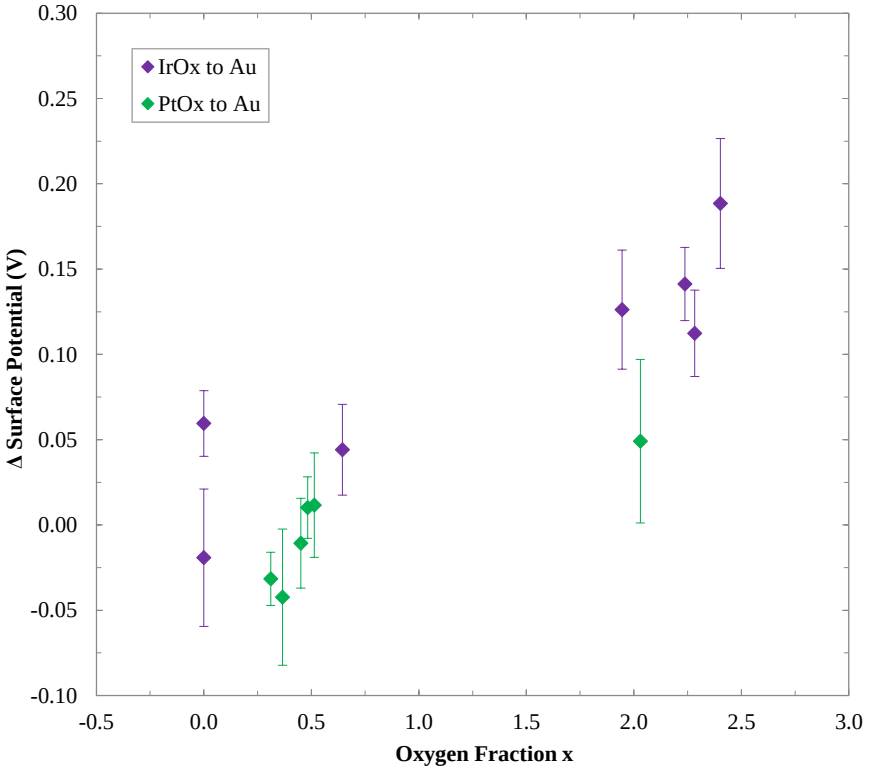

Figure 6.44: Surface Potential of RF-Sputtered Films with Oxygen Fraction *x* (RBS)

$$\Delta V_{surface} = \frac{\phi_{sample}}{q} \quad (6.4)[6.35]$$

Although the expected work function of plain Pt is 5.65 eV, published KPM measurements of $\Delta V_{surface}$ from plain Pt to Au using a Pt-coated AFM tip have shown a value of -45 ± 10 mV, comparable to the -32 ± 16 mV measured in this work [6.35]. The significant difference in $\Delta V_{surface}$ between theoretical and measured results is believed to be caused by surface absorption of contaminants across the sample, as the potentials were measured under atmospheric conditions [6.35]. The trend of increasing surface potential with increasing RF-sputtering O_2:Ar gas ratio and oxygen fraction, as seen in Figures 6.43 – 6.44, is evidence of increasing work function in the RF-sputtered films with increasing oxygen incorporation. However, the trend of increasing work function is not as steep as the trend of increasing homogeneous barrier height in this work, as shown in Figure 6.45. The work function values from dark I-V measurements used in Figure 6.45 were calculated using Equation 6.3, homogeneous barrier heights of the 0.0:10 – 4.0:10 (O_2:Ar) IrO_x series and 0.0:10 – 7.0:10 (O_2:Ar) PtO_x series, and the electron affinity for the ZnO used in this work, 4.2 eV [6.4, 6.13]. The work function values from KPM were calculated by adding the $\Delta V_{surface}$ to the work function of the reference material, Au (5.1 eV) [6.35].

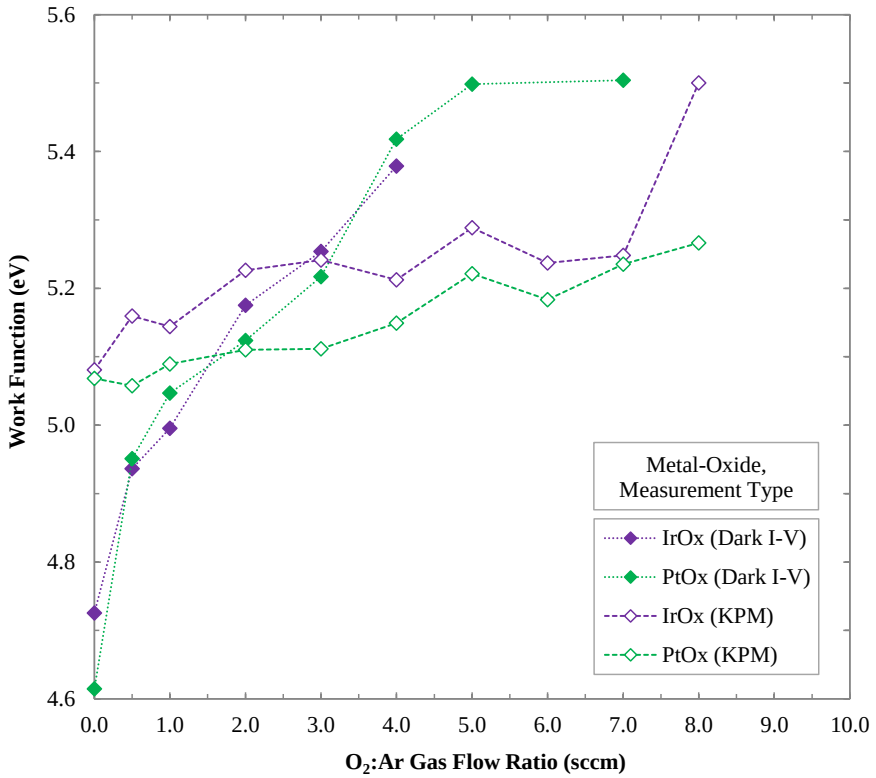

Figure 6.45: Calculated Work Functions of RF-Sputtered Ir/IrO_x and Pt/PtO_x Films

The Schottky-Mott model described by Equation 6.3 has been found to consistently overestimate $d\Phi_B/d\phi_m$, where ϕ_m is the work function of the RF-sputtered metal or metal-oxide film, for ZnO and other semiconductors, which could account for the significantly steeper trend of ϕ_m from dark I-V calculations in Figure 6.40 [6.36]. Overall, the KPM measurements provide significant evidence of increasing work function of the RF-sputtered films fabricated in this work.

Metal and metal-oxide Schottky contacts to ZnO have been shown to form barrier heights that show a stronger correlation to the metal (Meidema) electronegativity of the Schottky contact material, as opposed to correlation between barrier height and work function [6.36]. As oxygen is strongly electronegative, the steep increase in barrier height with oxygen incorporation could be due to the increasing electronegativity of the oxygen-rich metal-oxide Schottky material [6.36].

6.9 Summary

In this chapter, the electrical characteristics of RF-sputtered noble metal and metal-oxide Schottky contacts to –c-plane and +c-plane (low-lithium) Zn-polar bulk ZnO were investigated, using dark I-V and dark C-V measurements to determine the ideality factors, barrier heights, and rectification ratios of the Schottky contacts. The noble metals and metal-oxides explored were Ag, AgO_x, Ru, RuO_x, Ir, IrO_x, Pd, PdO_x, Pt and PtO_x. The formation mechanics of the Schottky contacts were explored using the oxygen incorporation of the films from RBS (Section 5.6), and the surface potential of the films from KPM (Section 5.5).

- Ag/AgO_x Schottky contacts showed the fastest increase in Φ_B with increasing O_2:Ar ratio, from Φ_B = 0.56 eV (η = 1.11) to Φ_B = 1.09 eV (η = 1.15) with 0.0:10 to 0.5:10 (O_2:Ar), and rectification ratios increasing from 4 to 12+ O_{Mag}.

- Ag/AgO_x Schottky contacts showed the greatest improvement in barrier height in this work, as well as producing contacts with the largest barrier heights reported to date, with Φ_B = 1.42 eV (η = 1.09) for 4.0:10 (O_2:Ar), and a rectification ratio of 11 O_{Mag} [6.3 – 6.5].

- AgO_x Schottky contacts were formed with an initial supply of O_2 gas only, with transmission measurements suggesting mostly Ag films, of Φ_B = 1.06 eV (η = 1.21) and 12 O_{Mag} rectification, implying that the Schottky behaviour is dominated by the species present at the Schottky interface.

- RuO_x and IrO_x Schottky contacts fabricated on –c-plane ZnO had higher leakage current and lower barrier heights compared to Schottky contacts fabricated on +c-plane (low-lithium) ZnO, due to higher levels of defects in –c-plane ZnO.

- RuO_x Schottky contacts to –c-plane ZnO improved in quality with increasing O_2:Ar from Φ_B = 0.68 eV (η = 1.10) to Φ_B = 0.96 eV (η = 1.05) with 0.5:10 to 7.0:10 (O_2:Ar), and associated rectification ratios increasing from 6 to 10 O_{Mag}.

- IrO_x Schottky contacts to –c-plane ZnO improved in quality with increasing O_2:Ar from Φ_B = 0.62 eV (η = 1.21) to Φ_B = 0.97 eV (η = 1.39) with 0.5:10 to 7.0:10 (O_2:Ar), and associated rectification ratios increasing from 4 to 9 O_{Mag}.

- Ir/IrO_x Schottky contacts to +c-plane (low-lithium) ZnO improved with increasing O_2:Ar from Φ_B = 0.53 eV (η = 1.18) to Φ_B = 1.12 eV (η = 1.20) with 0.0:10 to 4.0:10 (O_2:Ar), and with rectification ratios increasing from 3 to 12+ O_{Mag}.

- Pd/PdO_x Schottky contacts to +c-plane (low-lithium) ZnO improved with increasing O_2:Ar from Φ_B = 0.37 eV (η > 2) to Φ_B = 1.27 eV (η = 1.27) with 0.0:10 to 7.0:10 (O_2:Ar), and with rectification ratios increasing from 1 to 12+ O_{Mag}.

- Pt/PtO_x Schottky contacts to +c-plane (low-lithium) ZnO improved with increasing O_2:Ar from Φ_B = 0.36 eV (η > 2) to Φ_B = 1.22 eV (η = 1.12) with 0.0:10 to 7.0:10 (O_2:Ar), and with rectification ratios increasing from 0 to 12+ O_{Mag}. A second Pt/PtO_x oxidation series to 10:10 O_2:Ar found no further increase in Schottky performance.

- Dark C-V measurements of Ir/IrO_x, Pd/PdO_x and Pt/PtO_x Schottky contacts produced $\Phi_{B,\ C\text{-}V}$ values strongly correlated to $\Phi_{B,\ I\text{-}V}$ from dark I-V measurements, indicating a high level of lateral homogeneity in all Schottky contacts [6.9].

- KPM measurements showed a trend of increasing surface potential of the RF-sputtered Ir/IrO_x, Pd/PdO_x and Pt/PtO_x films with increasing O_2:Ar ratio; evidence of increasing work function of the metal-oxide films with increasing oxygen incorporation.

- Metal-oxide Schottky contacts fabricated with higher levels of O_2:Ar produced few low-ideality Schottky contacts. The high total RF-sputtering pressure could be causing increased Schottky contact inhomogeneity through damage to the ZnO substrate.

- Reported Φ_B of plain metal Schottky contacts to ZnO in literature were significantly higher than the ones measured in this work. This could be due to the pre-deposition surface treatments employed in many of the publications, including O_2/He plasma and H_2O_2 treatments, which provide a source of oxygen during the formation of the Schottky contacts [6.3 – 6.5].

- A proposed model of the mechanisms responsible for the giant improvement in barrier height and rectification ratio of the noble metal and metal-oxide Schottky contacts in this work involves the removal of surface hydroxyl layers on the ZnO surface and the associated SEAL, the reduction of V_O forming at the Schottky interface associated with Fermi-level pinning and Φ_B < 0.8 eV, and the increase of the work function and electronegativity of the Schottky contact material with increasing oxygen incorporation [6.4, 6.23 – 6.28, 6.32 – 6.33, 6.36].

- The rapid increase in barrier height improvement of the AgO_x and PtO_x Schottky contacts could be related to the high level of metal-oxide formation energy of Pt and Ag compared to the other noble metals in this work.

- The RBS measurements of the Ir/IrO_x, Pd/PdO_x and Pt/PtO_x films showed that, while IrO_x and PtO_x had exceeded x = 2 with 7.0:10 (O_2:Ar), PdO_x did not exceed x = 1.4, implying that higher levels of oxygen incorporation of PdO_x may be possible.

REFERENCES

[6.1] Jagadish, C., Pearton, S.J., (2006), Zinc Oxide Bulk, *Thin Films and Nanostructures – Processing, Properties and Applications*, Oxford, U.K: Elsevier Ltd.

[6.2] Pearton, S.J., Norton, D.P., Ip, K., Heo, Y.W., Steiner, T., (2005), Recent progress in processing and properties of ZnO, *Progress in Materials Science*, 50 (3), pp. 293-340.

[6.3] Müller, S., Von Wenckstern, H., Schmidt, F., Splith, D., Heinhold, R., Allen, M., Grundmann, M., (2014), Method of choice for fabrication of high-quality ZnO-based Schottky diodes, *Journal of Applied Physics*, 116 (19), art. no. 194506.

[6.4] Brillson, L.J., Lu, Y., (2011), ZnO Schottky barriers and Ohmic contacts, *Journal of Applied Physics*, 109 (12), art. no. 121301, .

[6.5] Özgür, Ü., Alivov, Ya.I., Liu, C., Teke, A., Reshchikov, M.A., Doğan, S., Avrutin, V., Cho, S.-J., Morkǫ, H., (2005), A comprehensive review of ZnO materials and devices, *Journal of Applied Physics*, 98 (4), art. no. 041301, pp. 1-103.

[6.6] Allen, M.W., Durbin, S.M., Metson, J.B., (2007), Silver oxide Schottky contacts on n-type ZnO, *Applied Physics Letters*, 91 (5), art. no. 053512.

[6.7] Allen, M.W., Mendelsberg, R.J., Reeves, R.J., Durbin, S.M., (2009), Oxidized noble metal Schottky contacts to n -type ZnO, *Applied Physics Letters*, 94 (10), art. no. 103508.

[6.8] Mönch, W., (1999), Barrier heights of real Schottky contacts explained by metal-induced gap states and lateral inhomogeneities, *Journal of Vacuum Science and Technology B: Microelectronics and Nanometer Structures*, 17 (4), pp. 1867-1876.

[6.9] Werner, J.H., Güttler, H.H., (1991), Barrier inhomogeneities at Schottky contacts, *Journal of Applied Physics*, 69 (3), pp. 1522-1533.

[6.10] Maeda, K., Sato, M., Niikura, I., Fukuda, T., (2005), Growth of 2 inch ZnO bulk single crystal by the hydrothermal method, *Semiconductor Science and Technology*, 20 (4).

[6.11] Ohshima, E., Ogino, H., Niikura, I., Maeda, K., Sato, M., Ito, M., Fukuda, T., (2004), Growth of the 2-in-size bulk ZnO single crystals by the hydrothermal method, *Journal of Crystal Growth*, 260 (1-2), pp. 166-170.

[6.12] Heinhold, R., Kim, H.-S., Schmidt, F., Von Wenckstern, H., Grundmann, M., Mendelsberg, R.J., Reeves, R.J., Durbin, S.M., Allen, M.W., (2012), Optical and defect properties of hydrothermal ZnO with low lithium contamination, Applied Physics Letters, 101 (6), art. no. 062105.

[6.13] Sze, S. M.., (2002), *Semiconductor Devices, Physics and Technology, 2nd Ed.*, Hoboken, N.J., U.S.A: John Wiley.

[6.14] Exarhos, G. J., (2010), *Characterization of Optical Materials*, Materials Characterization Series, New York, N.Y., U.S.A: Momentum Press

[6.15] Mosbacker, H.L., Strzhemechny, Y.M., White, B.D., Smith, P.E., Look, D.C., Reynolds, D.C., Litton, C.W., Brillson, L.J., (2005),Role of near-surface states in ohmic-Schottky conversion of Au contacts to ZnO, *Applied Physics Letters*, 87 (1), art. no. 012102.

[6.16] Brillson, L.J., Mosbacker, H.L., Hetzer, M.J., Strzhemechny, Y., Jessen, G.H., Look, D.C., Cantwell, G., Zhang, J., Song, J.J., (2007), Dominant effect of near-interface native point defects on ZnO Schottky barriers, *Applied Physics Letters*, 90 (10), art. no. 102116.

[6.17] Coppa, B.J., Davis, R.F., Nemanich, R.J., (2003), Gold Schottky contacts on oxygen plasma-treated, n-type ZnO$(000\bar{1})$, *Applied Physics Letters*, 82 (3), pp. 400-402

[6.18] Ip, K., Gila, B.P., Onstine, A.H., Lambers, E.S., Heo, Y.W., Baik, K.H., Norton, D.P., Pearton, S.J., Kim, S., Laroche, J.R., Ren, F., (2004), Improved Pt/Au and W/Pt/Au Schottky contacts on n-type ZnO using ozone cleaning, *Applied Physics Letters*, 84 (25), pp. 5133-5135.

[6.19] Gu, Q.L., Cheung, C.K., Ling, C.C., Ng, A.M.C., Djurišic, A.B., Lu, L.W., Chen, X.D., Fung, S., Beling, C.D., Ong, H.C., (2008), Au/n-ZnO rectifying contact fabricated with hydrogen peroxide pretreatment, *Journal of Applied Physics*, 103 (9), art. no. 093706.

[6.20] Kim, S.-H., Kim, H.-K., Seong, T.-Y., (2005), Effect of hydrogen peroxide treatment on the characteristics of Pt Schottky contact on n-type ZnO, *Applied Physics Letters*, 86 (11), art. no. 112101, pp. 1-3.

[6.21] Schifano, R., Monakhov, E.V., Grossner, U., Svensson, B.G., (2007), Electrical characteristics of palladium Schottky contacts to hydrogen peroxide treated hydrothermally grown ZnO, *Applied Physics Letters*, 91 (19), art. no. 193507.

[6.22] Wehner, G. K, Anderson, G. S., (1970), The Nature of Physical Sputtering. In L. I. Meissel & R. Glang's *Handbook of Thin Film Technology*, New York: USA: McGraw-Hill, Inc., pp. 3-33.

[6.23] McNeill, A.R., Hyndman, A.R., Reeves, R.J., Downard, A.J., Allen, M.W., (2016), Tuning the Band Bending and Controlling the Surface Reactivity at Polar and Nonpolar Surfaces of ZnO through Phosphonic Acid Binding, *ACS Appl. Mater. Interfaces*, 8 (45), pp 31392–31402.

[6.24] Allen, M.W., Swartz, C.H., Myers, T.H., Veal, T.D., McConville, C.F., Durbin, S.M., (2010), Bulk transport measurements in ZnO: The effect of surface electron layers, *Physical Review B - Condensed Matter and Materials Physics*, 81 (7), art. no. 075211.

[6.25] Heinhold, R., Williams, G.T., Cooil, S.P., Evans, D.A., Allen, M.W., (2013), Influence of polarity and hydroxyl termination on the band bending at ZnO surfaces, *Physical Review B - Condensed Matter and Materials Physics*, 88 (23), art. no. 235315.

[6.26] Coppa, B.J., Fulton, C.C., Kiesel, S.M., Davis, R.F., Pandarinath, C., Burnette, J.E., Nemanich, R.J., Smith, D.J., (2005), Structural, microstructural, and electrical properties of gold films and Schottky contacts on remote plasma-cleaned, n -type ZnO{0001} surfaces, *Journal of Applied Physics*, 97 (10), art. no. 103517.

[6.27] Ozawa, K., Mase, K., (2011), Comparison of the surface electronic structures of H-adsorbed ZnO surfaces: An angle-resolved photoelectron spectroscopy study, *Physical Review B - Condensed Matter and Materials Physics*, 83 (12), art. no. 125406, .

[6.28] Piper, L.F.J., Preston, A.R.H., Fedorov, A., Cho, S.W., Demasi, A., Smith, K.E., (2010), Direct evidence of metallicity at ZnO $(000\bar{1})$ - (1×1) surfaces from angle-resolved photoemission spectroscopy, *Physical Review B - Condensed Matter and Materials Physics*, 81 (23), art. no. 233305.

[6.29] Schottky, W., (1938), Semi-conductor theory in barrier layers, *Naturwissenschaften*, 26, 843.

[6.30] Mott, N.F., (1938), Note on the contact between a metal and an insulator or semi-conductor, *Proceedings of the Cambridge Philosophical Society*, 34 (4), pp. 568-572.

[6.31] Michaelson, H.B., (1977), The work function of the elements and its periodicity, *Journal of Applied Physics*, 48 (11), pp. 4729-4733.

[6.32] Allen, M.W., Durbin, S.M., (2008), Influence of oxygen vacancies on Schottky contacts to ZnO, *Applied Physics Letters*, 92 (12), art. no. 122110.

[6.33] Robertson, J., Sharia, O., Demkov, A.A., (2007), Fermi-level pinning by defects in HfO_2 - metal gate stacks, *Applied Physics Letters*, 91 (13), art. no. 132912.

[6.34] Melitz, W., Shen, J., Kummel, A.C., Lee, S., (2011), Kelvin probe force microscopy and its application, *Surface Science Reports*, 66 (1), pp. 1-27.

[6.35] Mugo, S., Yuan, J., (2012), Influence of surface adsorption on work function measurements on gold-platinum interface using scanning Kelvin probe microscopy, *Journal of Physics: Conference Series*, 371, art. no. 012030.

[6.36] Allen, M.W., Durbin, S.M., (2010), Role of a universal branch-point energy at ZnO interfaces, *Physical Review B - Condensed Matter and Materials Physics*, 82 (16), art. no. 165310.

7 | Ultraviolet Photoresponse of Metal-Oxide Schottky Contacts with Oxygen Content

This chapter provides the results from the photoresponse experiments performed on noble metal-oxide Schottky contacts, explores the effects of persistent photoconductivity (PPC) on UV photodetection, and proposes a model explaining the mechanisms responsible for the UV PPC in devices measured in this work. The metal-oxide contacts used in these experiments were RF-sputtered AgO_x, RuO_x, IrO_x, PdO_x, and PtO_x. The range of wavelengths used was 625 nm – 365 nm. The photoresponse measurements performed in this work were single exposures and pulsed exposures with -1 V device bias, and pulsed exposures with varying device bias.

7.1 Ultraviolet Photoresponse of Metal-Oxide Schottky Contacts

The focus of this work was to produce UV photodetectors suitable for UV dosimetry by fabricating noble metal-oxide Schottky contacts to ZnO. Ideally, the contacts should have a high selectivity of UV over visible wavelengths, produce a large UV photocurrent, and have a fast response-time to the application and removal of UV radiation. In order to characterise the effectiveness of the metal-oxide Schottky contacts as UV photodetectors, the contacts were exposed to light sources of varied wavelength for varied durations with varied device biases. The photoresponse to visible wavelengths was measured using LED light sources with spectral peaks in 625 nm (red), 610 nm (orange), 505 nm (green), and 470 nm (blue), with 300 mW (2.5 $mWcm^{-1}$ irradiance) measured at the sample surface, as detailed in Section 4.2.4.1. The photoresponse to UV wavelengths was measured using the Norland Products Inc. UVA Splice Lamp Model P/N 5200 (known hereafter as the ‘UV lamp’), with a spectral peak of 365 nm. The spectral response of the UV lamp is included in Appendix A4.6, courtesy of Dr Salim Elzwawi, Department of Electrical and Computer Engineering, University of Canterbury, New Zealand. The photoresponse to both visible and UV wavelengths was compared to measure the selectivity of the devices to UV wavelengths. A photoresponse to visible wavelengths is undesirable for UV dosimetry, as it introduces a significant source of error.

Three different current-time (*I-T*) measurements were used to characterise the UV photoresponse of the noble metal-oxide Schottky contacts in this work; single exposure, pulsed exposure, and varied bias exposure. All *I-T* measurements were performed in dark conditions. The single exposure was to a visible or UV light source of 30 s duration with a -1.0 V bias, as shown in Table 7.1. A bias of -1.0 V was chosen as the typical operating voltage for the devices in this work. The pulsed exposure measurement used 20 UV light pulses of 30 s or 60 s duration, with 30 s or 60 s darkness between UV pulses and -1.0 V bias, shown in Tables 7.2 – 7.3. The varied bias measurement used 5 UV light pulses of 30s duration, with device bias varied from 0.1 to -8.0 V, as detailed in Table 7.4.

Table 7.1: Measurement Parameters for Single-Exposure Visual and UV Photoresponse

Parameter	LED Photoresponse Measurement	UV Photoresponse Measurement
Wavelengths	625 nm, 610 nm, 505 nm, 470nm	365 nm
Bias	-1 V	-1 V
Step	1 s	1 s
Exposure Start	30 s	30 s
Exposure End	60 s	60 s
Measurement End	600 s	600 s
Number of Measurements	1	5
AgO_x Devices Tested (O_2:Ar)	-	4.0:10
RuO_x Devices Tested (O_2:Ar)	-	1.0:10 – 7.0:10
IrO_x Devices Tested (O_2:Ar)	3.0:10	0.0:10 – 4.0:10, 0.5:10 – 7.0:10
PdO_x Devices Tested (O_2:Ar)	0.5:10 – 7.0:10	0.5:10 – 7.0:10
PtO_x Devices Tested (O_2:Ar)	0.0:10 – 7.0:10	0.0:10 – 7.0:10

Table 7.2: Measurement Parameters for 30 Second Pulsed UV Photoresponse

Parameter	UV Photoresponse Pulsed Measurement
Bias	-1.0 V
Step	1.0 s
Exposure Start	(60x + 120) s, (x = 0 to 19)
Exposure End	(60x + 150) s, (x = 0 to 19)
Measurement End	1800 s
Number of Exposures	20
AgO_x Devices Tested (O_2:Ar)	4.0:10

Table 7.3: Measurement Parameters for 60 Second Pulsed UV Photoresponse

Parameter	UV Photoresponse Pulsed Measurement
Bias	-1.0 V
Step	1.0 s
Exposure Start	(120x + 120) s, (x = 0 to 9)
Exposure End	(120x + 180) s, (x = 0 to 9)
Measurement End	1800 s
Number of Exposures	10
AgO_x Devices Tested (O_2:Ar)	4.0:10

Table 7.4: Measurement Parameters for UV Photoresponse with Varying Bias

Parameter	UV Photoresponse Measurement with Varying Bias				
Bias	0.1 V, 0 V, -0.1 V, -0.2 V, -0.5 V, -1.0 V, -2.0 V, -4.0 V, -6.0 V, -8.0 V				
Step	0.1 s				
Exposure Start	30 s,	90 s,	150 s,	210 s,	270 s
Exposure End	60 s,	120 s,	180 s,	240 s,	300 s
Measurement End	600 s				
Number of Exposures	5				
AgO_x Devices Tested (O_2:Ar)	4.0:10				
RuO_x Devices Tested (O_2:Ar)	3.0:10				
IrO_x Devices Tested (O_2:Ar)	4.0:10				
PdO_x Devices Tested (O_2:Ar)	0.5:10 – 7.0:10				
PtO_x Devices Tested (O_2:Ar)	0.0:10 – 6.0:10				

The repeated exposure tests were used to investigate accumulative PPC effects, and the change in responsivity with repeated exposure of the noble metal-oxide Schottky contacts. The responsivity of the contacts was measured using rise-time, t_{rise}, and fall-time, t_{fall}, as shown in Figure 7.1 and detailed in Section 2.3.6 and Section 4.2.4.1. The rise-time was defined as the time required for the photocurrent to increase from 10% to 90% of the difference between the initial dark current (I_{dark}) and the maximum photocurrent (I_{peak}) reached with 30 s exposure to UV light, in a log-linear plot of *I-T*, as shown in Equation 7.1 of Table 7.5, and illustrated in Figure 7.1. Fall-time was calculated in a similar method from 90% to 10% of the difference between I_{dark} and I_{peak}, following the removal of the UV source, shown in Equation 7.2.

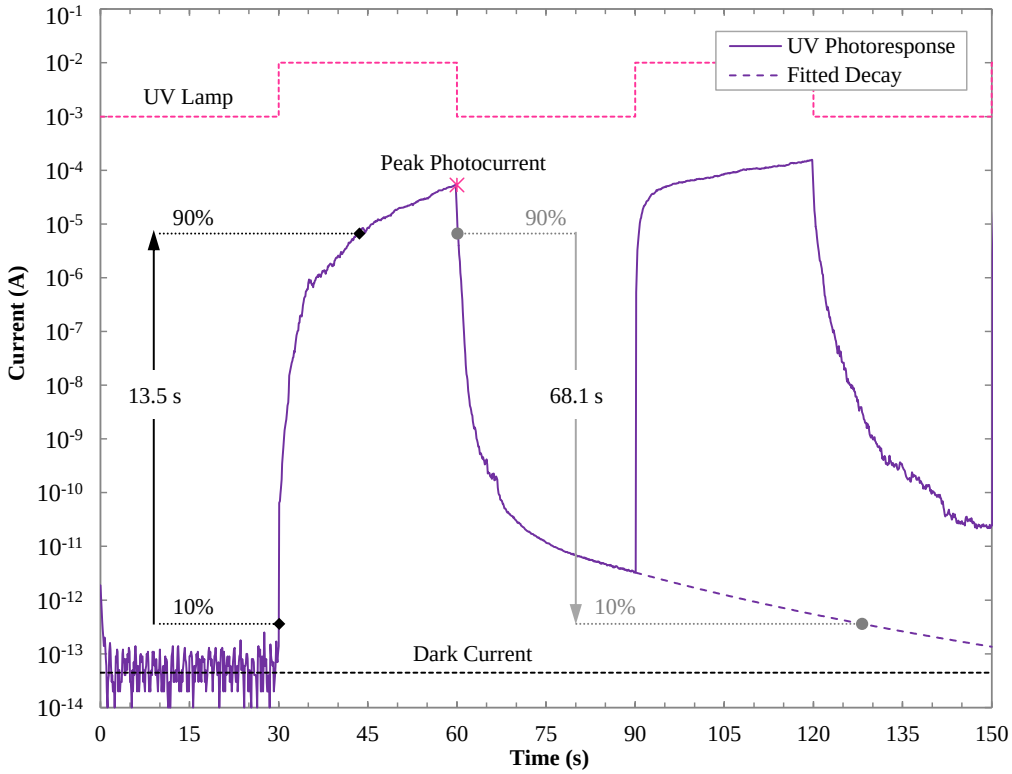

Figure 7.1: Calculation of Rise-Time, Fall-Time of Pulsed UV Response of AgO_x Contact

Table 7.5: Rise-Time and Fall-Time Equations

Parameter	Symbol	Unit	Equation	Equation Number
Rise-Time	t_{rise}	s	$t_{rise} = t\|_{90\%[Ln(I_{peak})-Ln(I_{dark})]} - t\|_{10\%[Ln(I_{peak})-Ln(I_{dark})]}$	(7.1)
Fall-Time	t_{fall}	s	$t_{fall} = t\|_{10\%[Ln(I_{peak})-Ln(I_{dark})]} - t\|_{90\%[Ln(I_{peak})-Ln(I_{dark})]}$	(7.2)

In the case of repeated and pulsed UV photoresponse measurements, the relaxation time between UV exposures, 30 s, was often insufficient for the photocurrent to decay down to $t|_{10\%[Ln(I_{peak})-Ln(I_{dark})]}$ due to the level of PPC. In order to calculate fall time, a decay trend was fitted to the last 20 s of the decay curve using a power law and least squares fit, as shown in Figure 7.1. The decay trend was only fitted to the last 20 s of the decay, as the power law did not model the initial decay of PPC accurately. Due to the limited data points used to fit the decay trend, and the noise present in the decaying current curve, the extrapolation of the fitted decay curve is subject to error. The rise-time and fall-time of the photoresponse was calculated on a log-scale.

The analysis of each UV photoresponse in this work includes the rise-time, fall-time, maximum photocurrent, and current increase from the initial dark current ($I_{increase}$) in orders of magnitude (O_{Mag}), in order to characterise the suitability of the devices for UV dosimetry. The maximum UV photocurrent and current increase measurement were two different and significant measurements, as the current increase was found to be dependent on the rectification ratio of the devices, which was found to be related to the oxygen incorporation of the Schottky contact, as discussed in Chapter 6.

For the measurement of UV photoresponse with varying device bias, the dark I-V characteristics measured between each UV photoresponse measurement were used to investigate the effects of bias-dependent PPC on device performance and the electronic characteristics of the devices. The varying bias was typically measured in the order; +0.1, 0.0, -0.1, -0.2, -0.5, -1.0, -2.0, -4.0, -6.0, -8.0, as well as 0.0 V and +0.1 V repeated following the negative bias measurements.

As UV dosimetry was the focus of this work, the results presented in this chapter cover all noble metal-oxides used for Schottky contacts fabricated in this work. Sections 7.2 – 7.6 focus on the UV photoresponse results of the AgO_x, RuO_x, IrO_x, PdO_x, Pt/PtO_x contacts measured in this work, respectively. Sections 7.7 – 7.8 focus on comparison of the results in this work to literature, and the proposed mechanics involved in the measured UV photoresponses.

7.2 Ultraviolet Photoresponse of Silver Oxide Schottky Contacts

The photoresponse tests performed on a RF-sputtered 4.0:10 (O_2:Ar) AgO_x Schottky contact to +c-plane (low-lithium) ZnO consisted of pulsed exposures with -1 V bias, and exposures with varying device bias. The pulsed UV photoresponse measurements, as detailed in Tables 7.2 – 7.3, consisted of 20 pulses of 30 s UV light, followed by 30 s darkness, and in a separate test of 10 pulses of 60 s UV light, followed by 60 s darkness, both experiments using a device bias of -1.0 V. The UV photoresponse to 5 pulses of 30 s UV exposure with varied device bias between 0.1 and -4.0 V was also measured, as detailed in Table 7.4. Dark I-V characteristics were measured between each pulsed UV exposure during this test, allowing for 600 s in dark conditions between UV exposures. Details on dark I-V characterisation can be found in Section 4.2.2 with pre-UV electrical characterisation results in Chapter 6.

The 30 s pulsed UV photoresponse of the 4.0:10 (O_2:Ar) AgO_x contacts is shown in Figure 7.2. The 60 s pulsed UV photoresponse is shown in Figure 7.3. The overlaid photoresponse to each UV pulse from the 30 s and 60 s pulsed exposures in Figures 7.2 – 7.3 is shown in Figures 7.4 – 7.5. Plots of the rise-time, fall-time, maximum photocurrent, and current increase (in O_{Mag}) of both the 30 s and 60 s UV photoresponse measurements are shown in Figures 7.6 – 7.9.

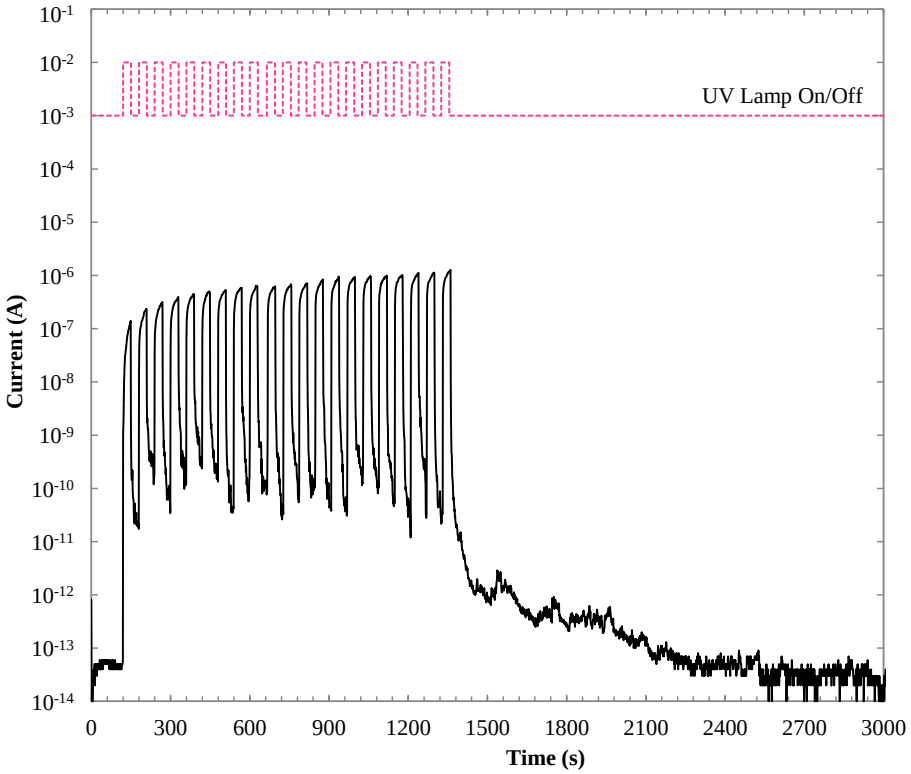

Figure 7.2: 4.0:10 (O_2:Ar) AgO_x 30 s UV Pulsed Photoresponse with -1.0 V Bias

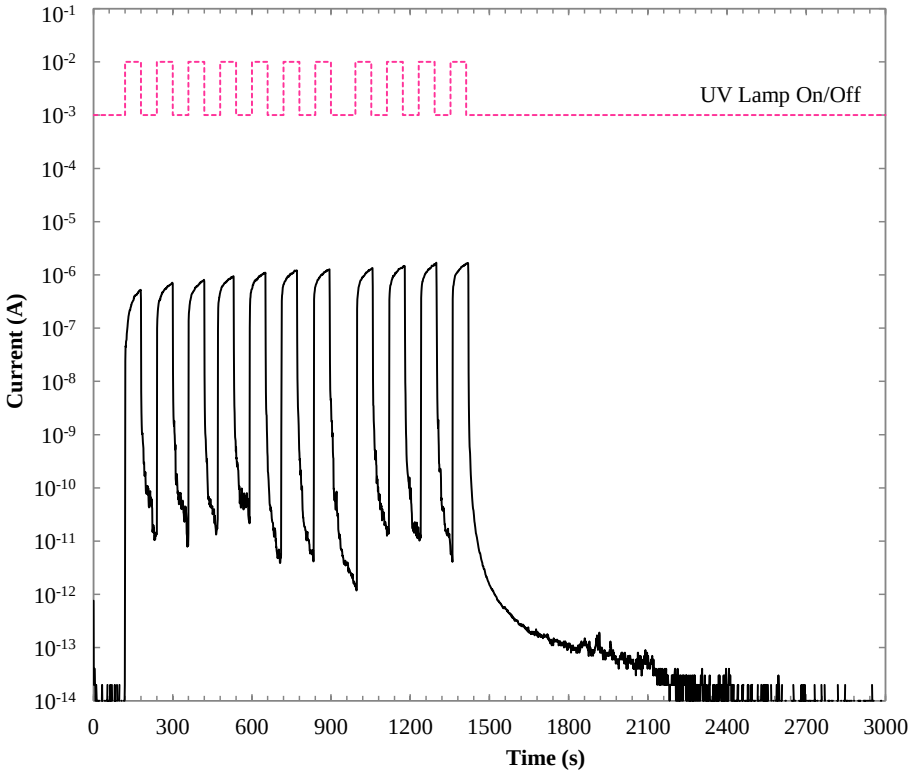

Figure 7.3: 4.0:10 (O_2:Ar) AgO_x 60 s UV Pulsed Photoresponse with -1.0 V Bias

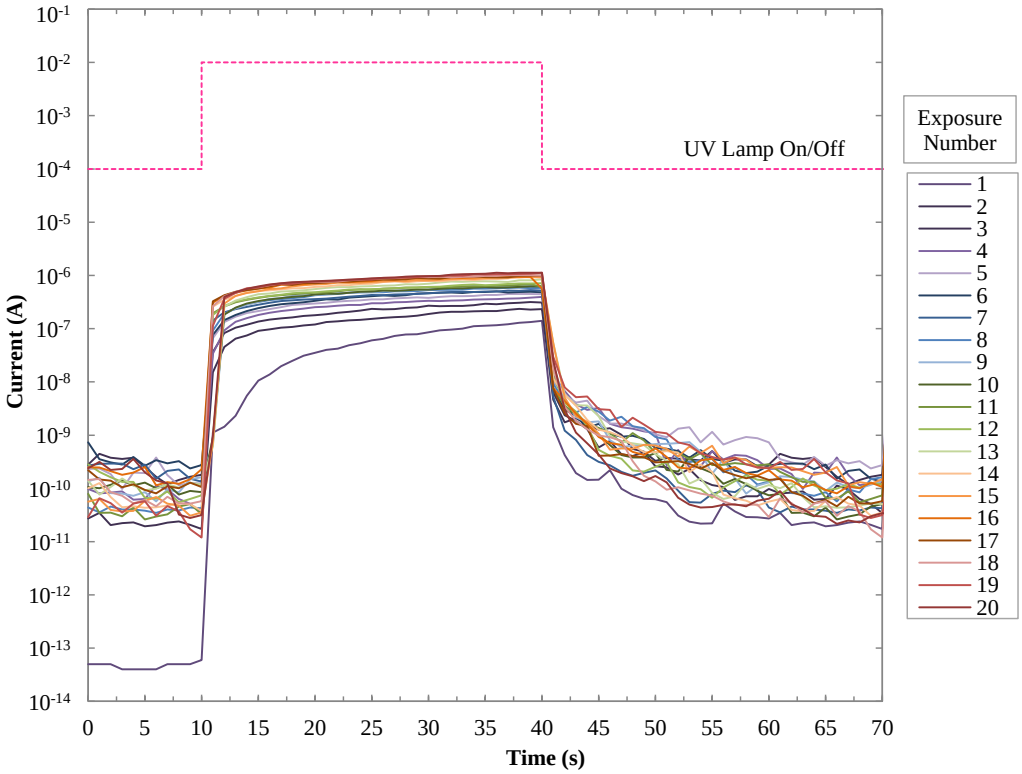

Figure 7.4: 4.0:10 (O_2:Ar) AgO_x Overlaid 30 s UV Pulsed Photoresponse with -1.0 V Bias

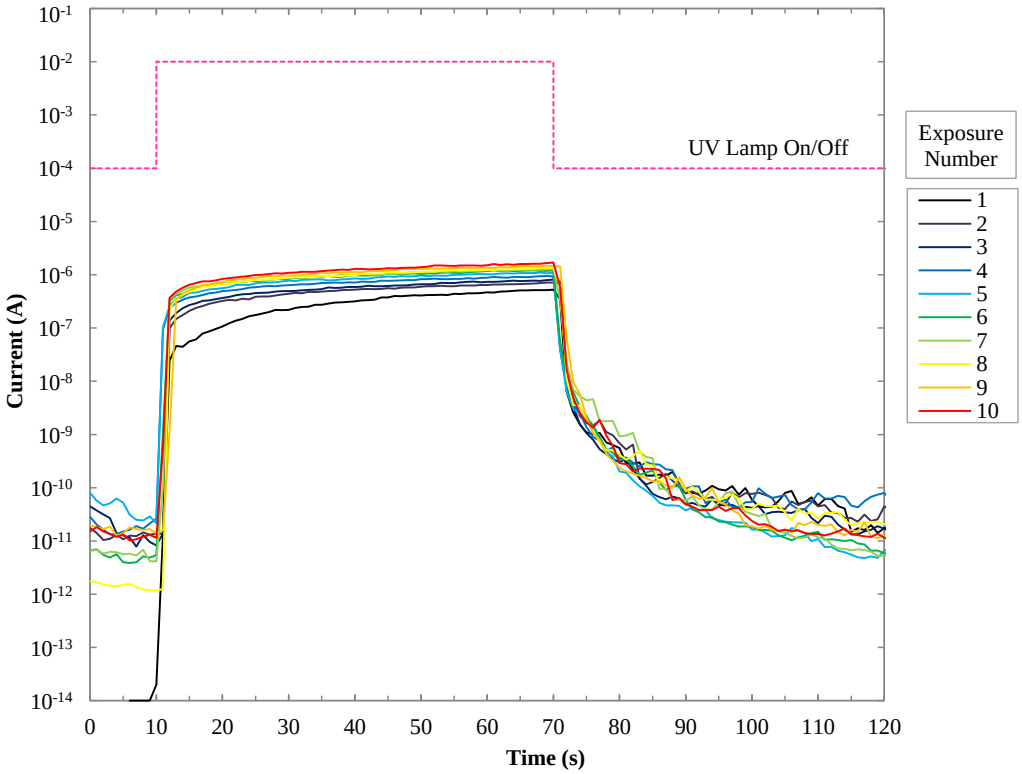

Figure 7.5: 4.0:10 (O_2:Ar) AgO_x Overlaid 60 s UV Pulsed Photoresponse with -1.0 V Bias

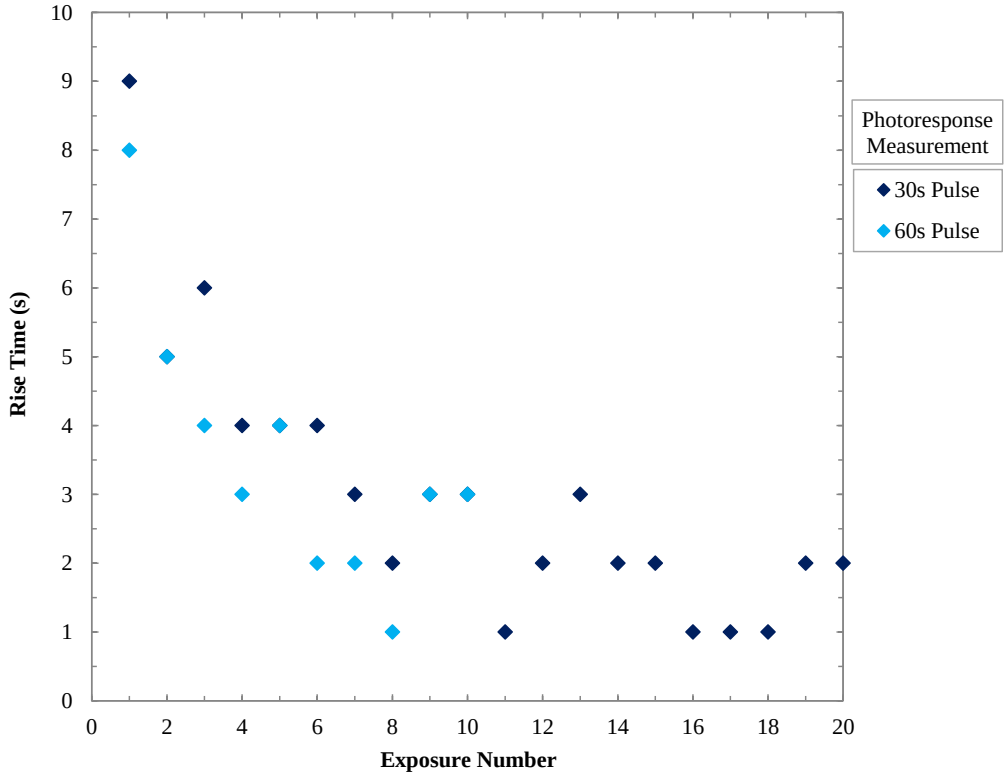

Figure 7.6: 4.0:10 (O_2:Ar) AgO_x 30 s, 60 s UV Photoresponse with -1.0 V Bias, Rise-Time

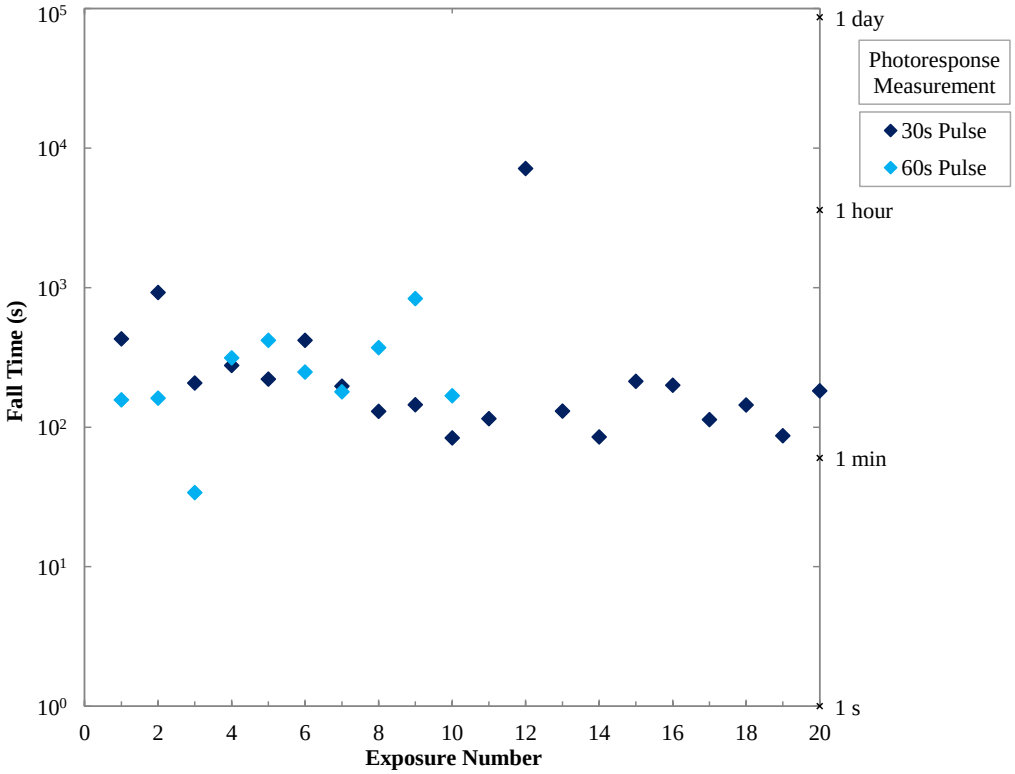

Figure 7.7: 4.0:10 (O_2:Ar) AgO_x 30 s, 60 s UV Photoresponse with -1.0 V Bias, Fall-Time

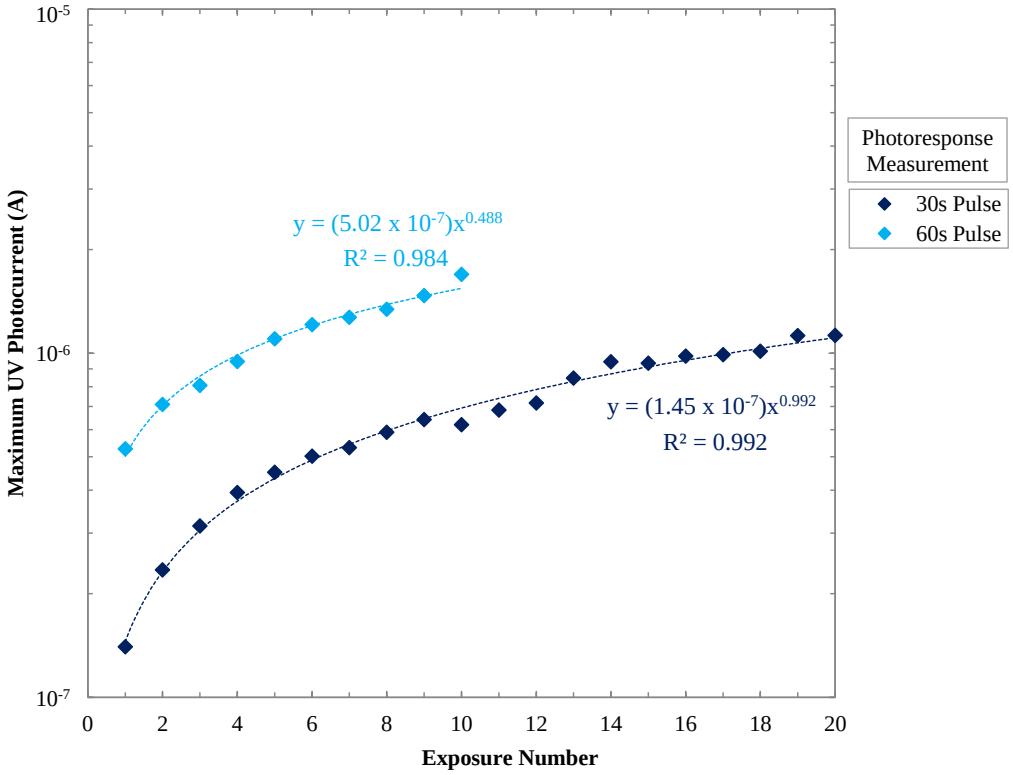

Figure 7.8: 4.0:10 (O_2:Ar) AgO_x 30 s, 60 s UV with -1.0 V Bias, Maximum Photocurrent

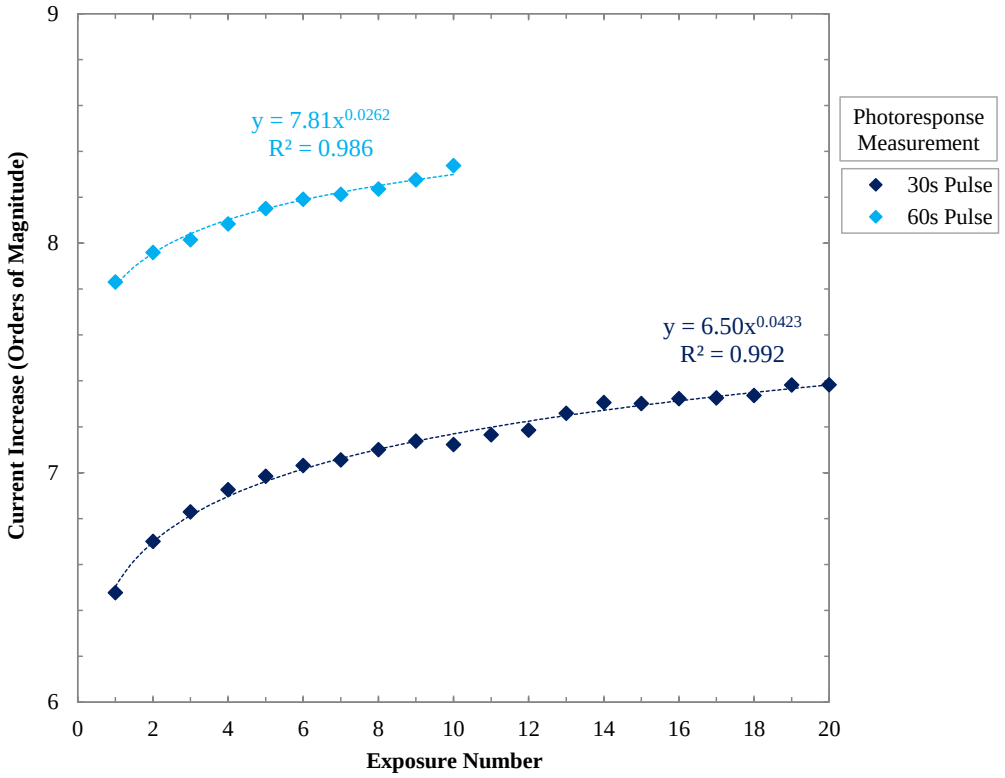

Figure 7.9: 4.0:10 (O_2:Ar) AgO_x 30 s, 60 s UV with -1.0 V Bias, Current Increase

Figures 7.2 – 7.5 show that, for both 30 s and 60 s exposures, the UV photoresponse did not have the desired square-wave response to a square wave input of switching the UV lamp on and off for 30 s (or 60 s) intervals. There was a latency in every UV photoresponse in Figures 7.2 – 7.5, appearing as a build-up of increasing photocurrent with time. The amount of response latency in this work has been measured as rise-time, and is undesirable for UV dosimetry.

From the overlaid photoresponses in Figures 7.4 – 7.5, it can be observed that the initial photoresponse had a significantly longer rise-time than subsequent measurements. This is confirmed in Figure 7.7, where the rise-time of both 30 s and 60 s exposures decreases significantly following the first 5 – 6 exposures to a steady-state rise-time of ~2 s for both the 30 s and 60 s exposures. Figure 7.8 shows that the fall-time of the 30 s and 60 s exposures was significantly higher than the rise-time (34 – 7100 s), with high variance between exposures. The long fall-time indicates a severe level of PPC from the UV photoresponse of the AgO_x contact. To be used as a UV sensor, the device would only be able to make one UV measurement every 5 – 10 minutes without introducing substantial levels of error.

The similar trends between the rise-time and fall-time of the 30 s and 60 s exposures in Figures 7.7 – 7.8 indicate a consistent trend of increasing and decreasing photocurrent over the 30 – 60 s photoresponse timeframe. From this observation, it has been concluded that 30 s illumination measurements were sufficient to characterise the photoresponse of the RF-sputtered metal-oxide Schottky contacts.

Figures 7.8 – 7.9 show fitted power law trends to the maximum UV photocurrent and the current increase (in O_{Mag}) at -1.0 V. The fitted trends have R^2 values of 0.948 – 0.992, indicating a good fit between the data and the power law. The power law relationship between the total UV dose with time is useful in determining a model of the UV photoresponse of the metal-oxide Schottky contacts. However, the increase in photocurrent from successive exposures at -1.0 V indicates a further source of error in applying the power law model.

In order to investigate whether the high rise-time, fall-time, and variation in photocurrent was related to the device bias, an identical AgO_x contact was subjected to 5 pulses of 30 s UV with 30 s darkness between each pulse, with device bias varied from 0.1 to -4.0 to 0.1 V, with dark I-V characteristics measured immediately after each UV photoresponse. The UV photoresponse with varying bias is shown in Figure 7.10. The dark I-V characteristics measured immediately after each pulsed UV photoresponse are shown in Figure 7.11. Plots of the rise-time, fall-time, maximum photocurrent, and current increase are included in Figures 7.12 – 7.15. The full UV photoresponses of the AgO_x contact with bias is also included in Figure A7.1 of Appendix A7.1 to show the long-term PPC of the device following UV exposures with varying device bias.

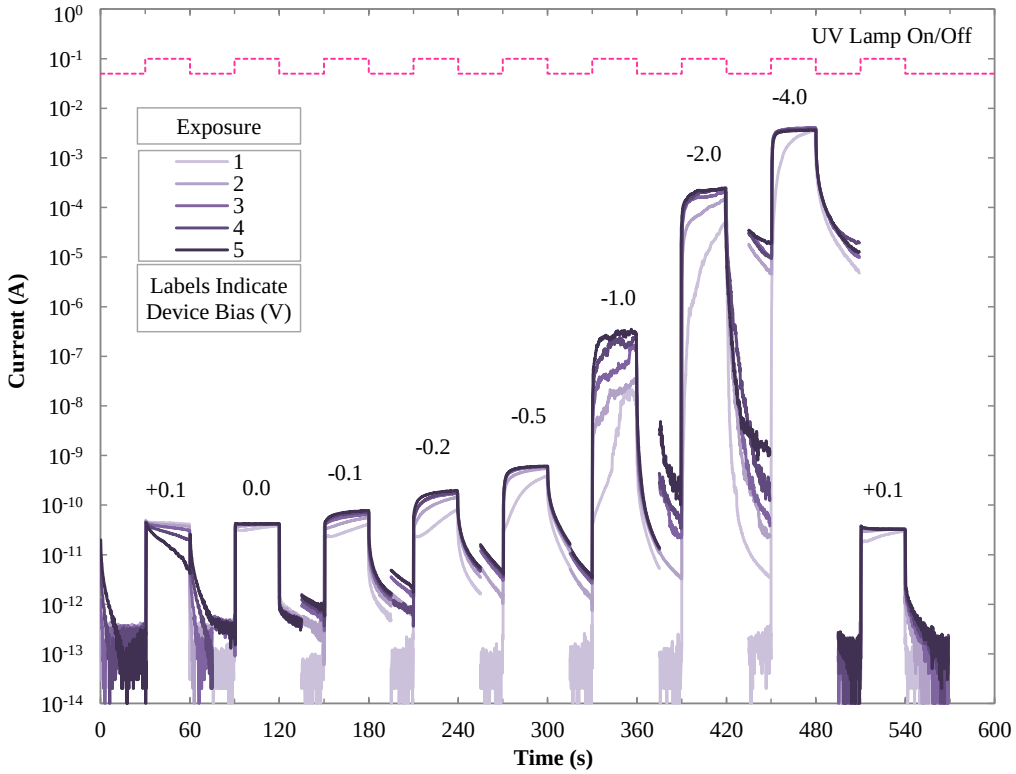

Figure 7.10: 4.0:10 (O_2:Ar) AgO_x 30 s Overlaid UV Pulsed Photoresponse, Varied Bias

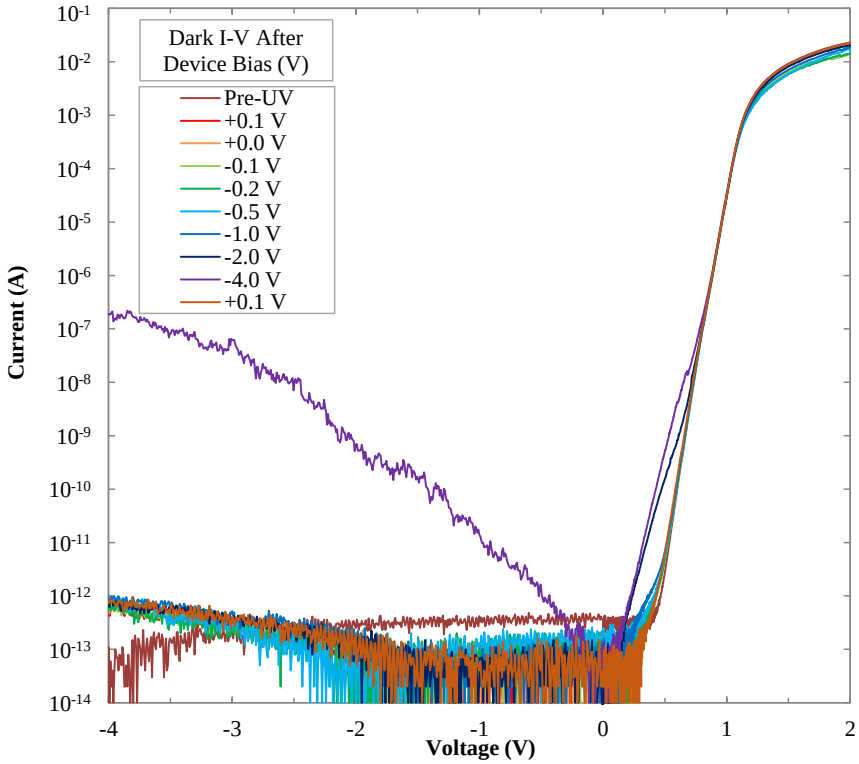

Figure 7.11: 4.0:10 (O_2:Ar) AgO_x Dark I-V After Each UV Photoresponse Bias Test

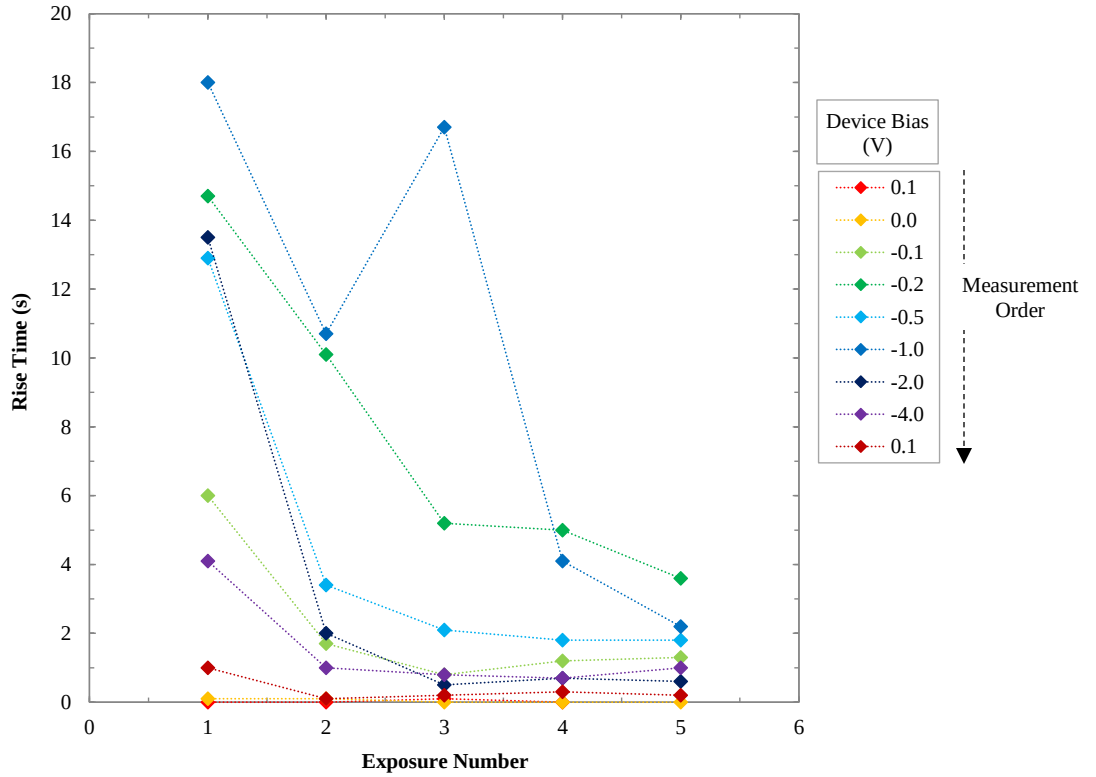

Figure 7.12: 4.0:10 (O_2:Ar) AgO_x 30 s UV Photoresponse with Bias, Rise-Time

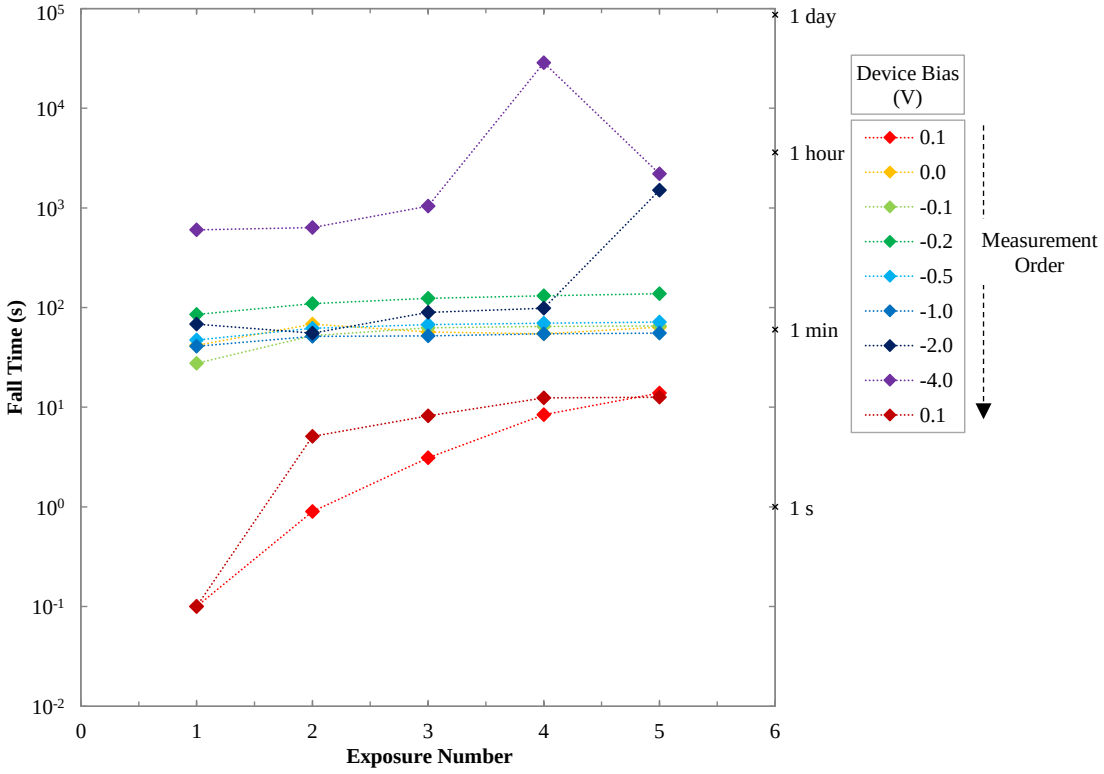

Figure 7.13: 4.0:10 (O_2:Ar) AgO_x 30 s UV Photoresponse with Bias, Fall-Time

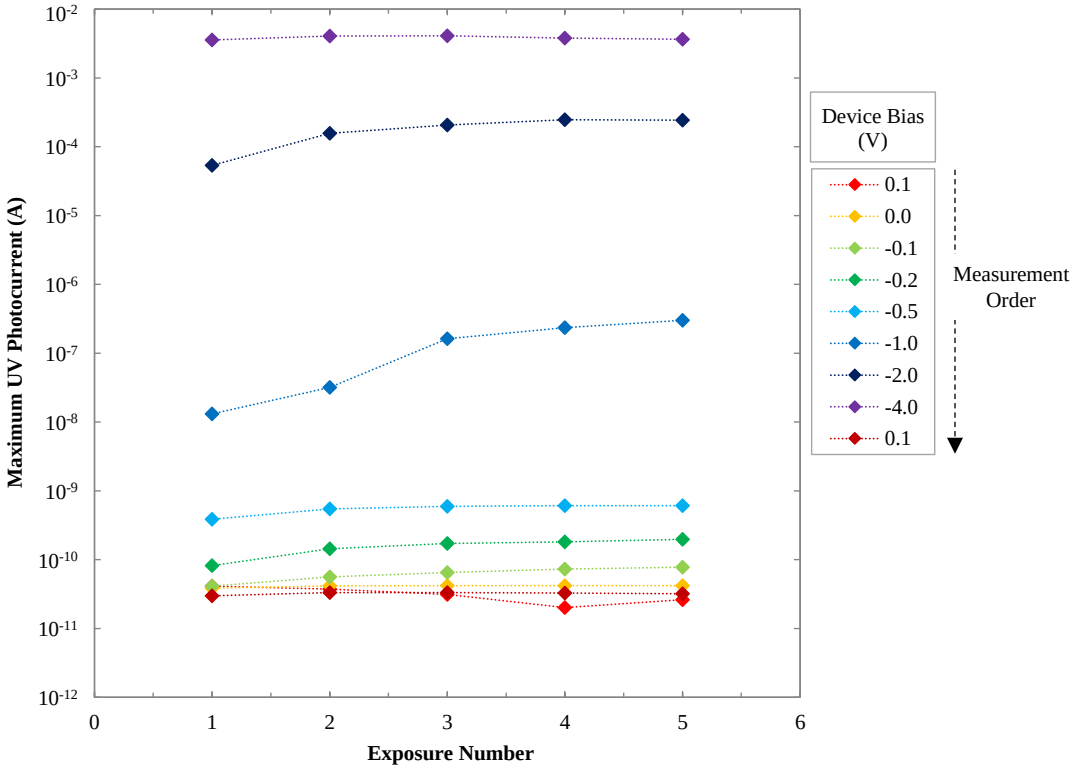

Figure 7.14: 4.0:10 (O_2:Ar) AgO_x 30 s UV Photoresponse with Bias, Maximum Photocurrent

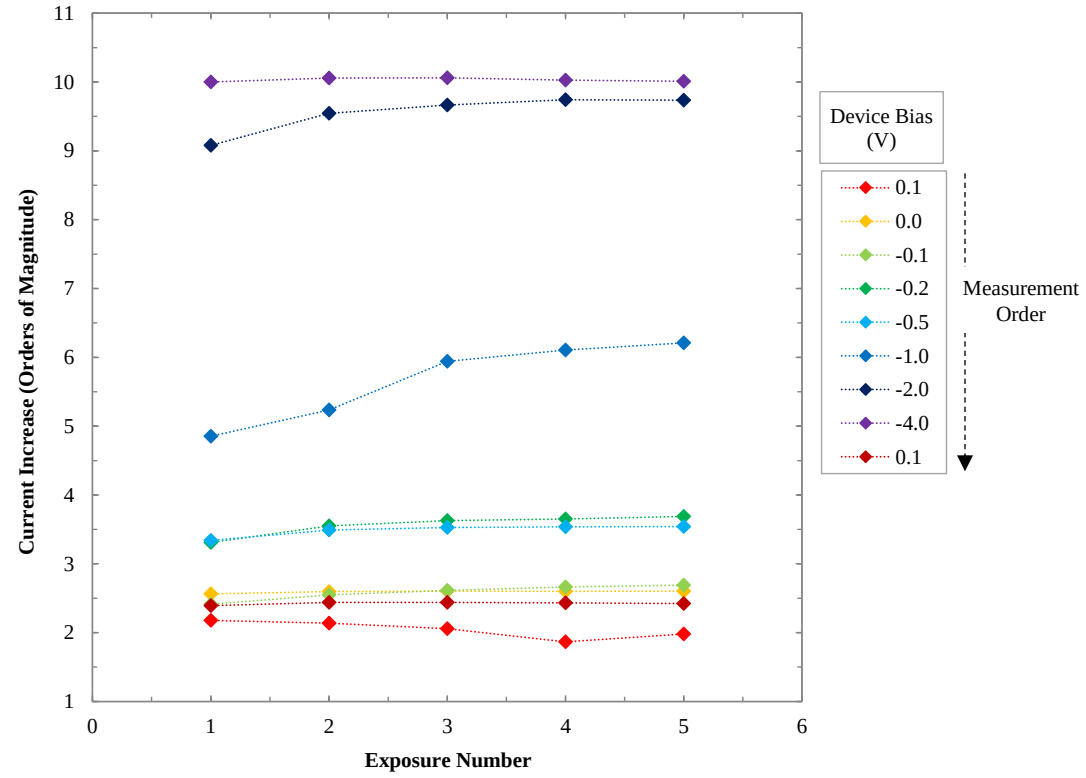

Figure 7.15: 4.0:10 (O_2:Ar) AgO_x 30 s UV Photoresponse with Bias, Current Increase

Figure 7.10 shows significant increase in UV photoresponse and a significant increase in PPC with increasingly negative device bias. The long-term PPC from t = 300 s to 600 s for the UV photoresponses shown in Figure 7.10 is included in Figure A7.1. The most significant result from Figure 7.10 is that the square-wave photoresponse with 0 V has the smallest rise-time and PPC, indicating a possible mechanistic correlation between the rise-time and fall-time and PPC.

Figure 7.11 shows that the -2.0 V and -4.0 V bias tests created a double-barrier in the dark I-V characteristics of the AgO_x contact, with a significant increase in reverse-bias leakage current following the -4.0 V bias test, indicating the formation of a double-barrier. However, the dark I-V characteristic returned to its original state before the second 0.1 V bias UV photoresponse, as it was left for 30 min for the PPC to dissipate. This shows that the induced double-barrier and reverse bias leakage current formed by the negative-bias UV photoresponse was not permanent in nature.

Figure 7.12 shows a reduction from the initial rise-time of up to 18 s to a steady-state rise time of 0 – 6 s. However, Figure 7.13 shows that the fall-time of the devices increases significantly from 0.1 s with 0.1 V bias to > 1 hr with -4.0 V bias. The 0.1 V bias UV photoresponse shows a square-wave response to the UV, with < 1 s rise time, and < 10 s fall-time, showing potential for dosimetry.

Figures 7.14 – 7.15 show that both the maximum photocurrent and the current increase of the 0.1 V bias device were the lowest of all biases measured, with 41.1 pA and 2.6 O_{Mag}, respectively. In comparison, the maximum photocurrent and current increase with -4.0 V bias was 3.83 mA, and 10 O_{Mag}, respectively. A trade-off therefore exists between the response time and response current of the 4.0:10 (O_2:Ar) RF-sputtered AgO_x Schottky contact measured in this work. However, higher response currents also have a higher rise-time, as the PPC causes a build-up of UV photocurrent over time, introducing more error in UV dosimetry.

7.3 Ultraviolet Photoresponse of Ruthenium Oxide Schottky Contacts

To investigate the effect of oxygen incorporation on UV photoresponse in 1.0:10 – 7.0:10 (O_2:Ar) RF-sputtered RuO_x contacts, one contact from each level of oxygen incorporation was used to measure UV photoresponse to 5 pulses of 30 s UV radiation with a device bias of -1.0 V, as described in Table 7.1. The UV photoresponse to 5 pulses of 30 s UV radiation of the 3.0:10 (O_2:Ar) RuO_x contact was also measured with device bias varying from 0.1 and -2.0 V, as described in Table 7.4. Dark I-V characteristics were measured between each pulsed UV exposure during this test. The UV photoresponse of the RuO_x devices with varying oxygen incorporation is shown in Figure 7.16. Plots of the rise-time, fall-time, maximum photocurrent, and current increase are included in Figures 7.17 – 7.20.

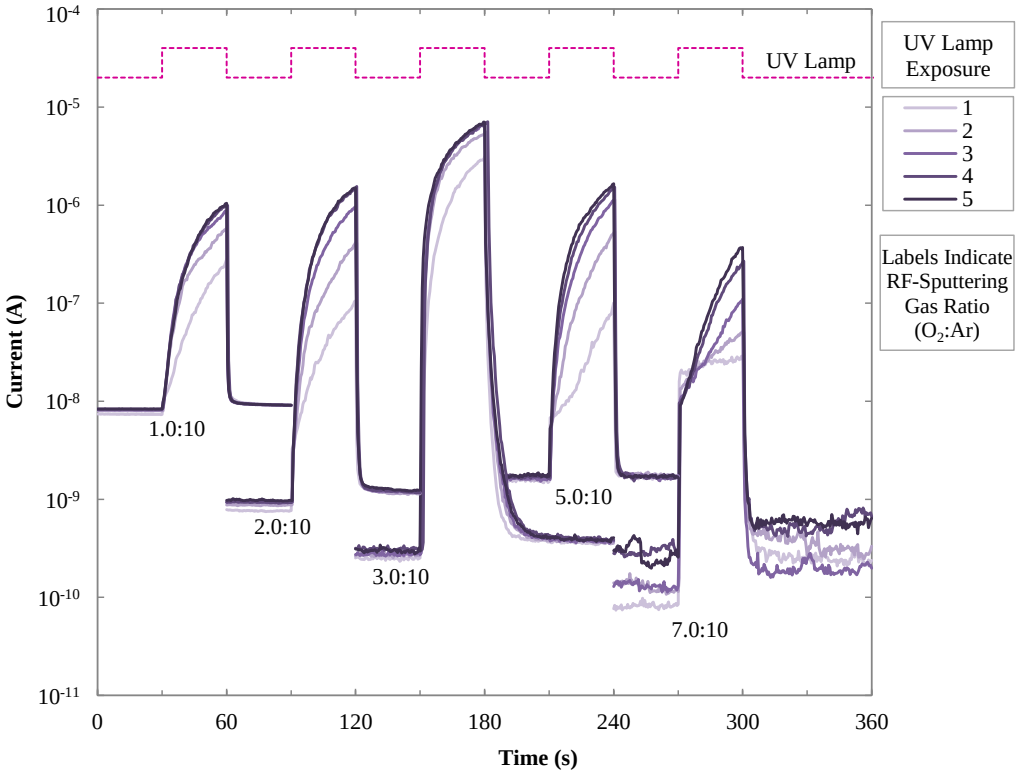

Figure 7.16: 1.0:10 – 7.0:10 (O_2:Ar) RuO_x 30 s UV Photoresponse with -1 V Bias

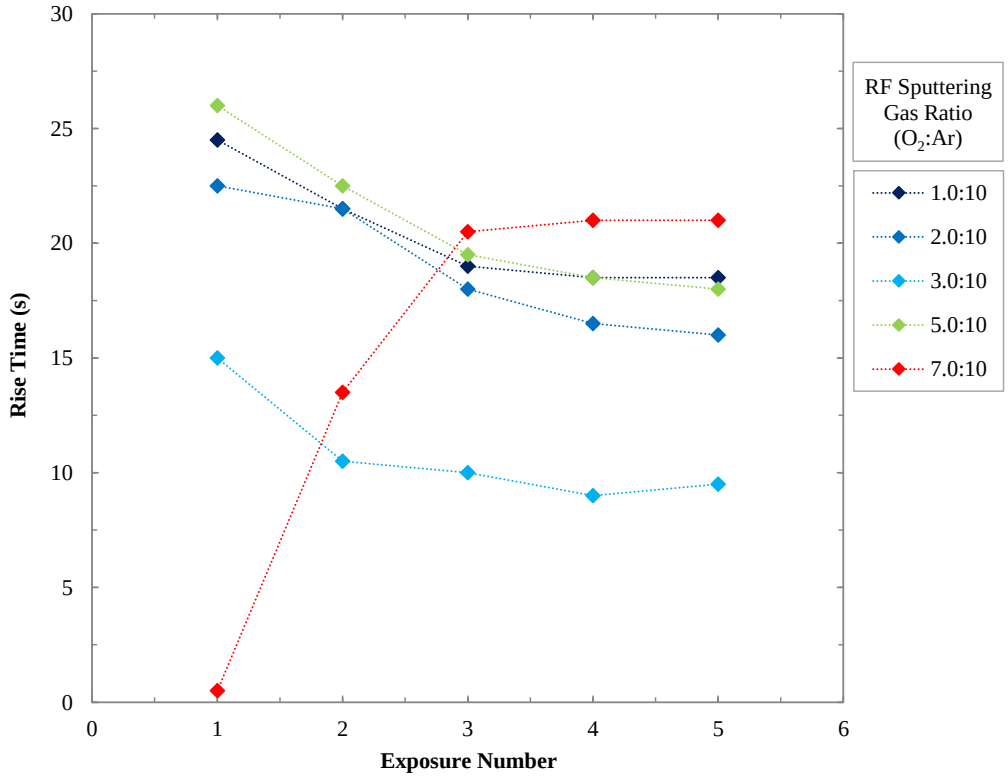

Figure 7.17: RuO_x 30 s UV Photoresponse with -1 V Bias, Rise Time

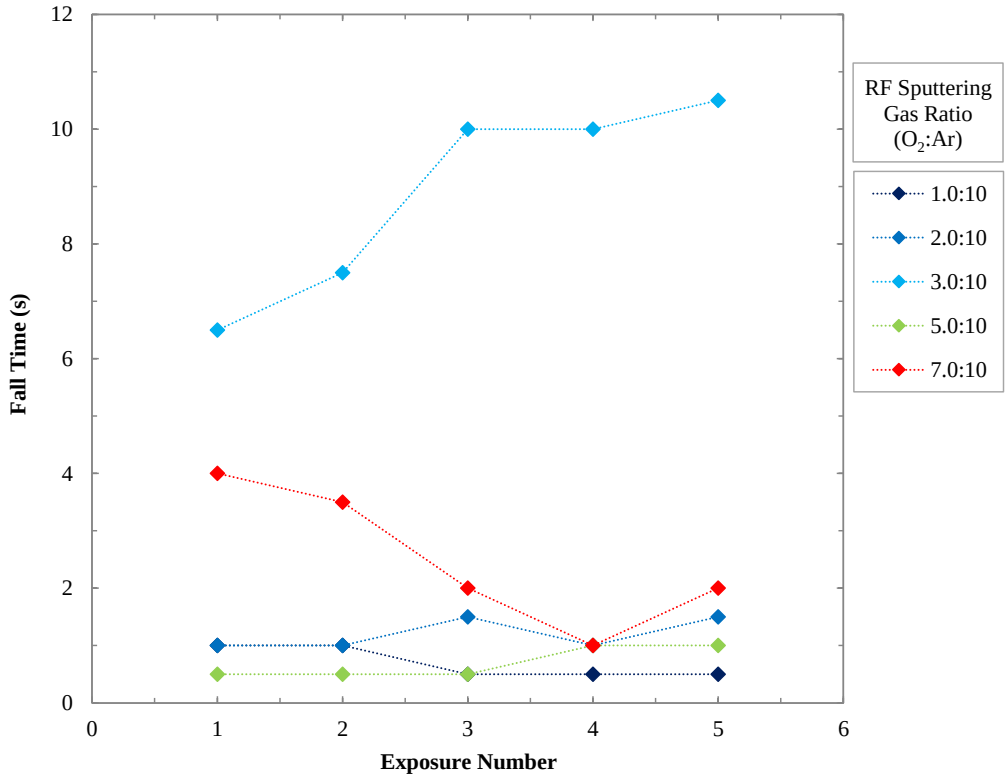

Figure 7.18: RuO_x 30 s UV Photoresponse with -1 V Bias, Fall Time

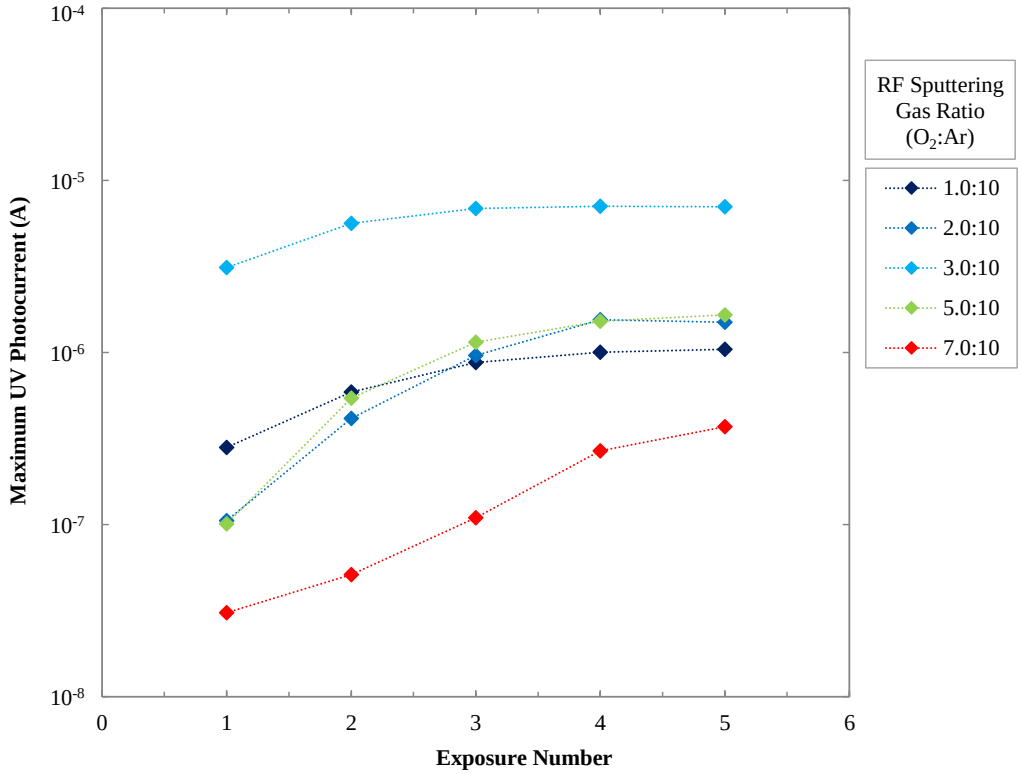

Figure 7.19: RuO_x 30 s UV Photoresponse with -1 V Bias, Maximum Current

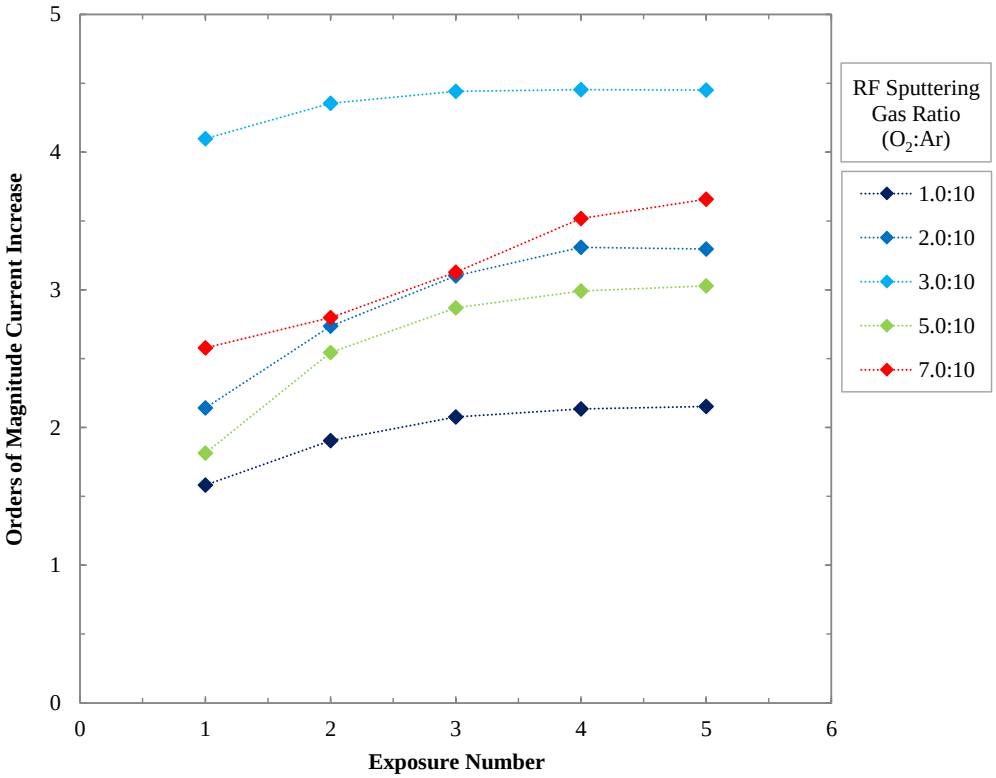

Figure 7.20: RuO_x 30 s UV Photoresponse with -1 V Bias, Current Increase

The 3.0:10 (O_2:Ar) RuO_x contact exhibited the highest photoresponse, with a maximum current of 7.03 µA and 4.5 O_{Mag} current increase, as shown in Figures 7.19 – 7.20. Figure 7.17 also shows the 3.0:10 (O_2:Ar) RuO_x contact having the shortest rise-time of the RuO_x series, with 9.0 – 11 s after an initial rise time of 15 s. However, Figure 7.18 shows that the 3.0:10 (O_2:Ar) RuO_x contact also had the longest fall-time of the RuO_x series, with 6.5 – 11 s, increasing with subsequent exposures. In comparison, the 1.0:10, 4.0:10, and 5.0:10 (O_2:Ar) RuO_x contacts had fall-times of < 1 s. These were significantly lower than the fall-times of the AgO_x contacts, likely due to the resistivity of the –c-plane ZnO, 0.09 Ωcm. ZnO type differences are discussed in Section 2.3.2.

To investigate the effect of device bias on the RuO_x contacts, the UV photoresponse of the 3.0:10 (O_2:Ar) RuO_x contact was measured with device bias varied from 0.1 to -2.0 to 0.0 V, with results and dark I-V measurements shown in Figures 7.21 – 7.22. Plots of the rise-time, fall-time, maximum photocurrent, and current increase are shown in Figures 7.23 – 7.26. The full UV photoresponses of the RuO_x contact with bias is also included in Figure A7.2 of Appendix A7.2 to show the long-term PPC of the device. Rise-times and fall-times of '0 s', were plotted on logarithmic plots as 0.01 s, in order to appear below 0.1 s, the lower limit of the time resolution, determined by the time resolution of the parameter analyser measurement.

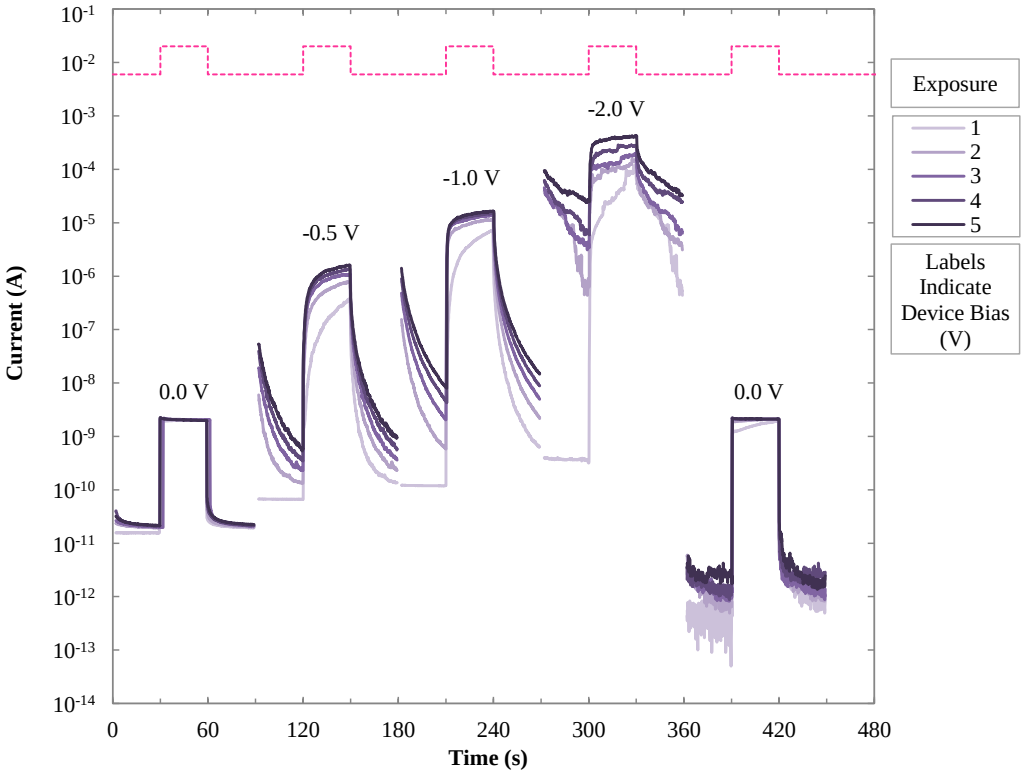

Figure 7.21: 3.0:10 (O_2:Ar) RuO_x 30 s UV Pulsed Photoresponse with Varied Bias

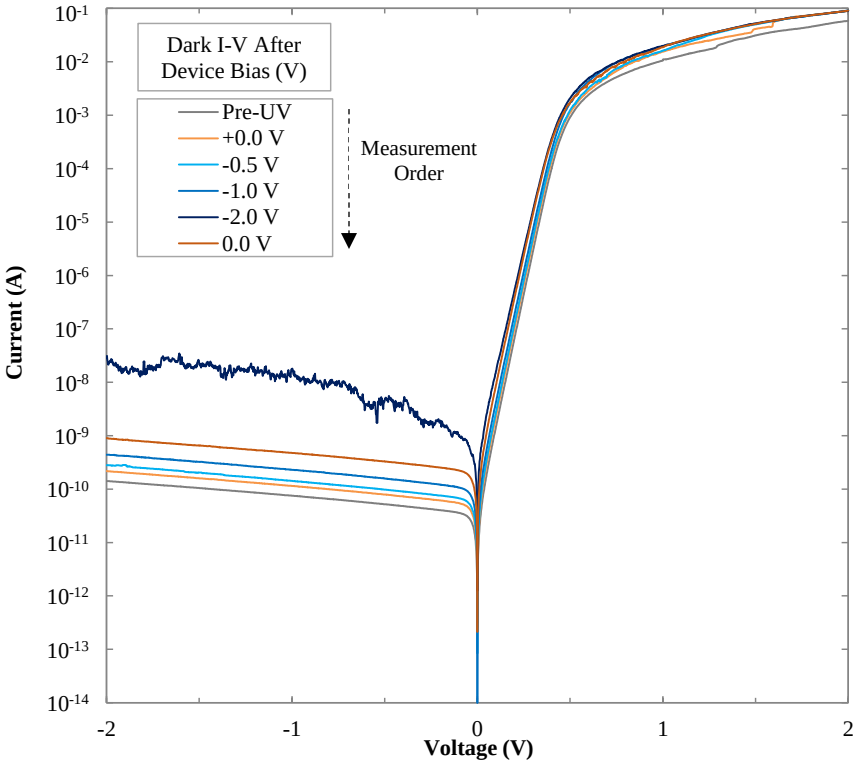

Figure 7.22: 3.0:10 (O_2:Ar) RuO_x Dark I-V After Each UV Photoresponse Bias Test

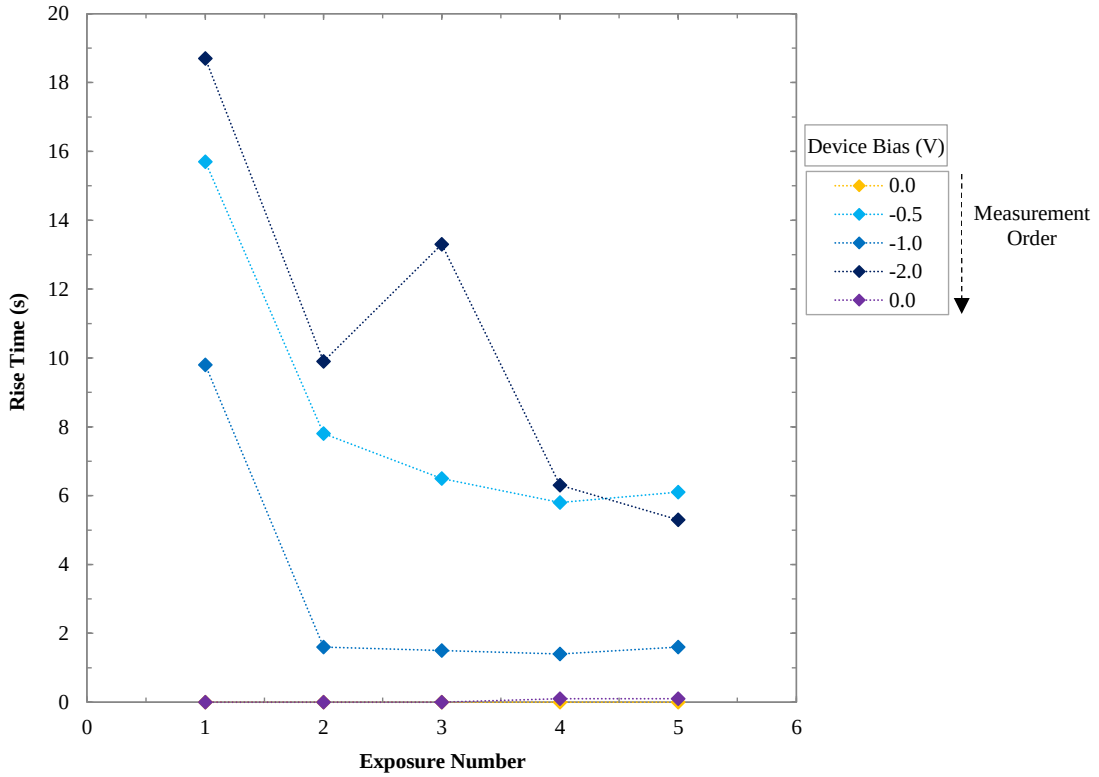

Figure 7.23: 3.0:10 (O_2:Ar) RuO_x 30 s UV Photoresponse with Bias, Rise-Time

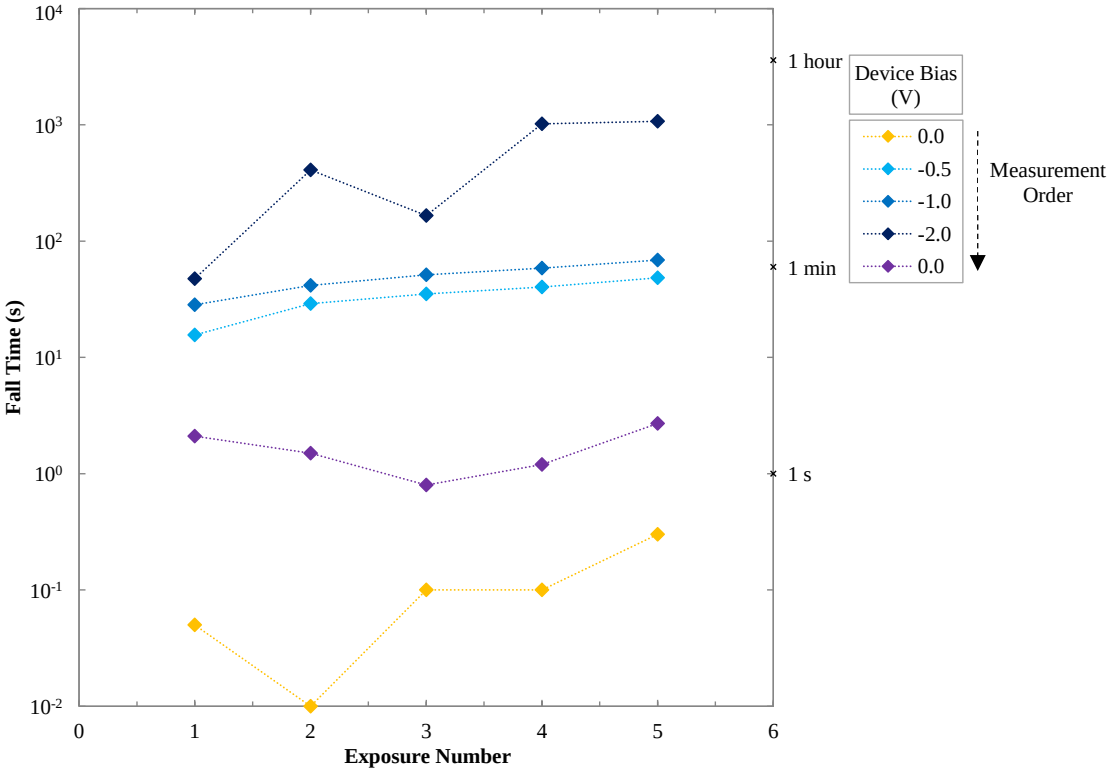

Figure 7.24: 3.0:10 (O_2:Ar) RuO_x 30 s UV Photoresponse with Bias, Fall-Time

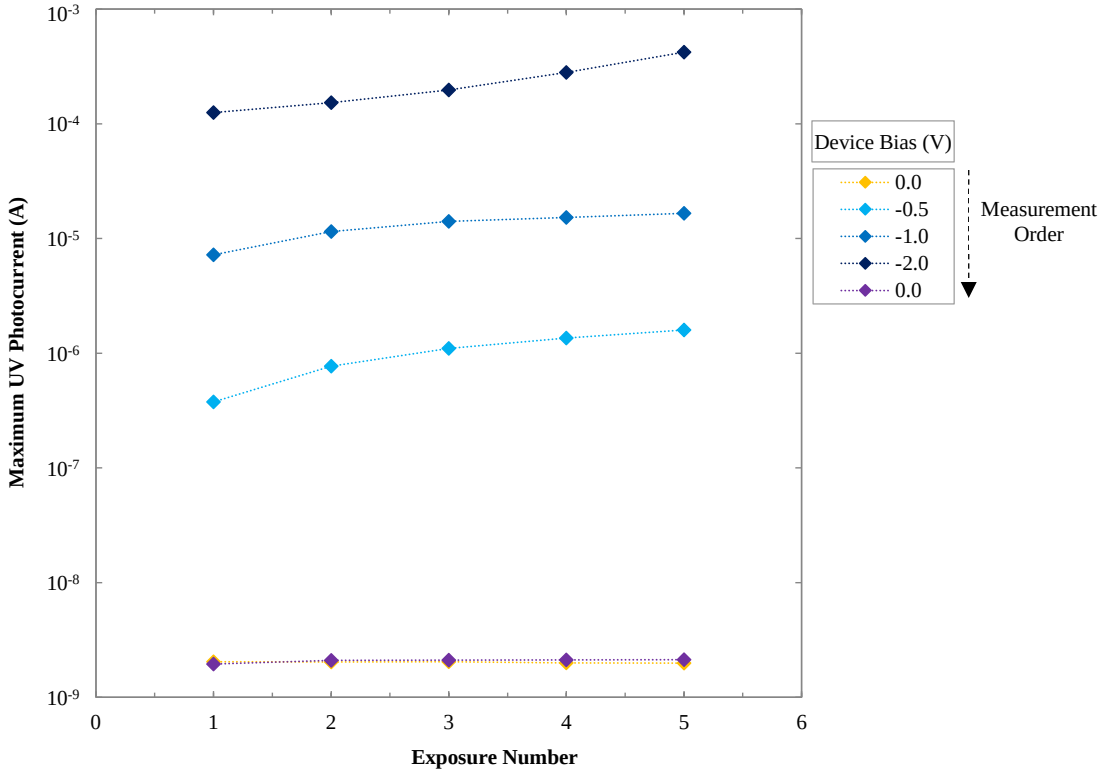

Figure 7.25: 3.0:10 (O_2:Ar) RuO_x 30 s UV Photoresponse with Bias, Maximum Photocurrent

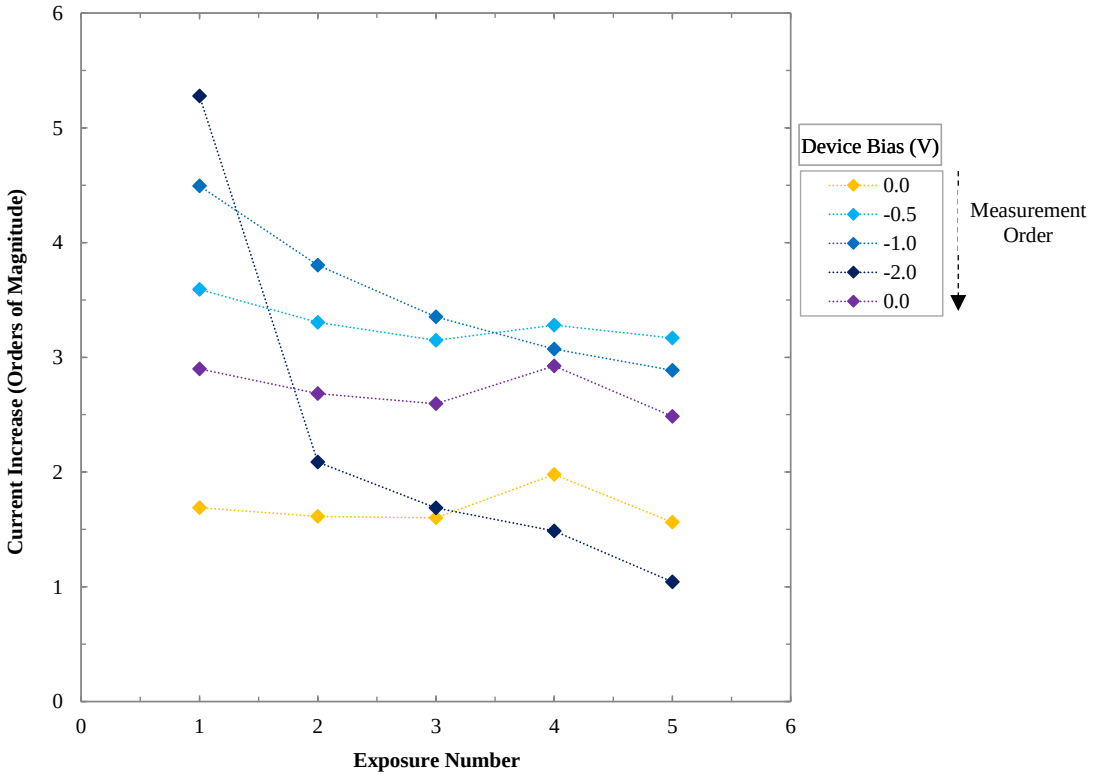

Figure 7.26: 3.0:10 (O_2:Ar) RuO_x 30 s UV Photoresponse with Bias, Current Increase

The 3.0:10 (O_2:Ar) RuO_x contact in Figures 7.21 – 7.26 shows a trend of increasing rise-time, fall-time, maximum current, and current increase with increasingly negative device bias, similar to the AgO_x device in Section 7.2. However, a device bias of -2.0 V produced an unstable photoresponse, with estimated fall-times as high as 18 min from significant PPC, as shown in Figure 7.24. The long-term PPC from t = 300 s to 600 s is included in Figure A7.2.

Figure 7.22 shows the dark I-V measurements following each UV photoresponse with a trend of increasing reverse-bias leakage current with increasingly negative device bias, peaking in the I-V measurement after the -2.0 V bias test, and partially recovering after the second 0.0 V bias test. This indicates a semi-permanent increase in reverse bias leakage current following UV measurements.

As with the AgO_x contact, the UV photoresponse with 0 V bias showed the lowest rise-time and fall-time, < 1 s, but also the lowest maximum photocurrent, 2.05 nA, and current increase, 1.98 O_{Mag}. A trade-off has been shown between the response time and response current of the 3.0:10 (O_2:Ar) RF-sputtered RuO_x contact and the 4.0:10 (O_2:Ar) RF-sputtered AgO_x contact.

7.4 Ultraviolet Photoresponse of Iridium Oxide Schottky Contacts

Two series of RF-sputtered IrO_x Schottky contacts were fabricated on –c-plane ZnO and +c-plane (low-lithium) ZnO, as discussed in Section 6.4. The first series comprised of 0.5:10 – 7.0:10 (O_2:Ar) IrO_x contacts to a –c-plane ZnO wafer with a resistivity of 0.10 Ωcm. The second series comprised of 0.0:10 – 4.0:10 (O_2:Ar) IrO_x contacts to a +c-plane (low-lithium) ZnO wafer with a resistivity of 1.18 Ωcm. In Section 6.4, the higher-resistivity–c-plane ZnO wafer was shown to produce Schottky contacts with higher reverse-bias leakage current, and lower barrier heights. In this section, the UV response of the IrO_x Schottky contacts to –c-plane and +c-plane (low-lithium) ZnO is compared with UV photoresponse measurements of 5 pulses of 30 s UV light, with a device bias of -1.0 V.

Figures 7.27 – 7.28 show the visual spectrum and UV photoresponse of 30 s illumination for a 3.0:10 (O_2:Ar) IrO_x Schottky contact to +c-plane (low-lithium) ZnO. Figure 7.28 exhibits significant selectivity of the IrO_x contact, with 5.8 O_{Mag} current increase to the UV photoresponse, which was scaled to the same low incident illumination power (2.5 $mWcm^{-1}$ irradiance), compared to the 1.3 – 1.5 O_{Mag} current increase from the visual spectrum. The level of UV selectivity indicates significant potential for use in UV dosimetry. Figures 7.29 – 7.30 show the UV photoresponse of the IrO_x series to –c-plane and +c-plane (low-lithium) ZnO, respectively. The rise-time, fall-time, maximum UV photocurrent, and current increase of both the IrO_x series to –c-plane and +c-plane (low-lithium) ZnO are included in Figures 7.31 – 7.38.

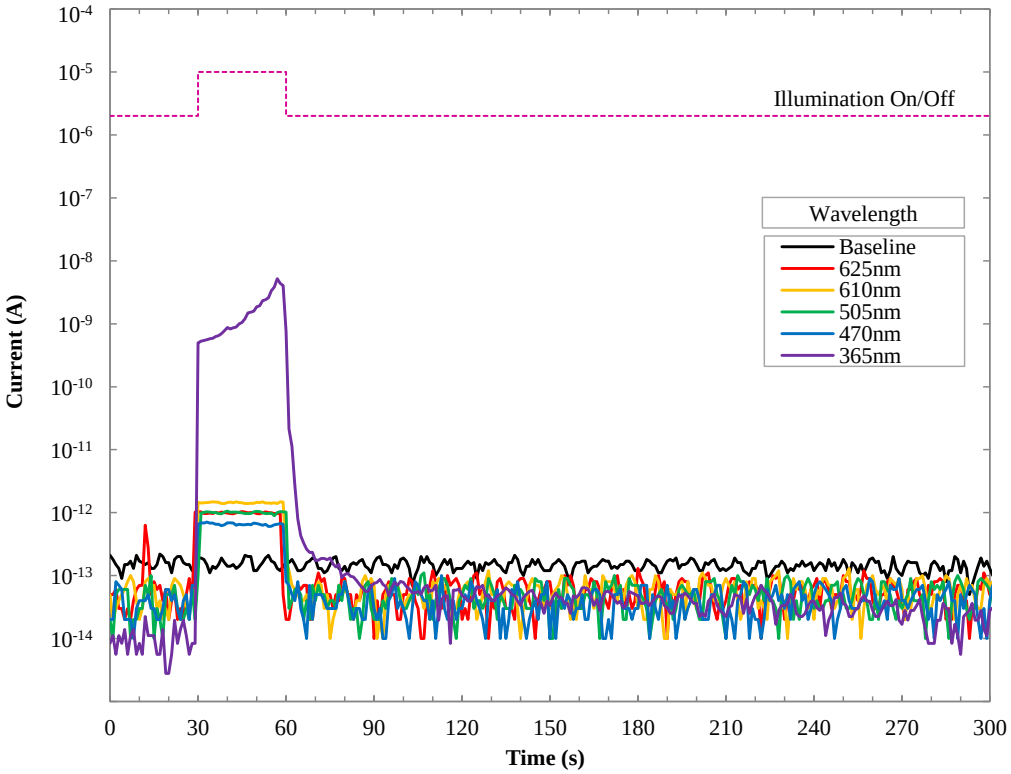

Figure 7.27: 3.0:10 (O_2:Ar) IrO_x 30 s Visual Spectrum and UV Photoresponse, -1 V Bias

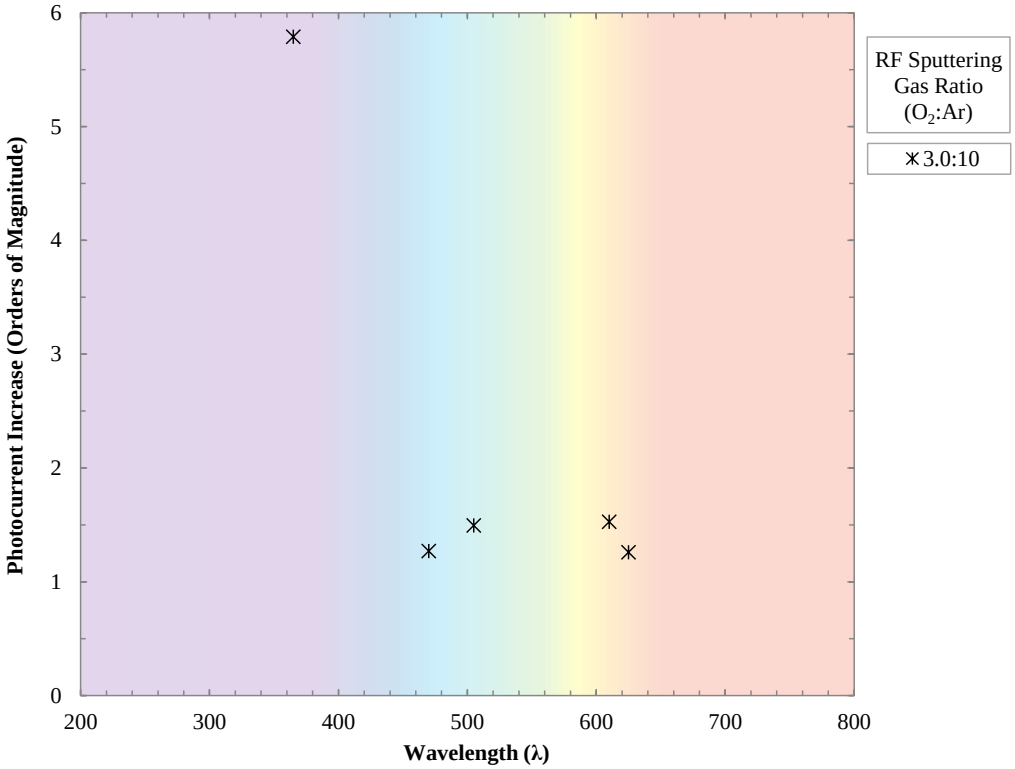

Figure 7.28: 3.0:10 (O_2:Ar) IrO_x 30 s Visual Spectrum and UV Responsivity, -1 V Bias

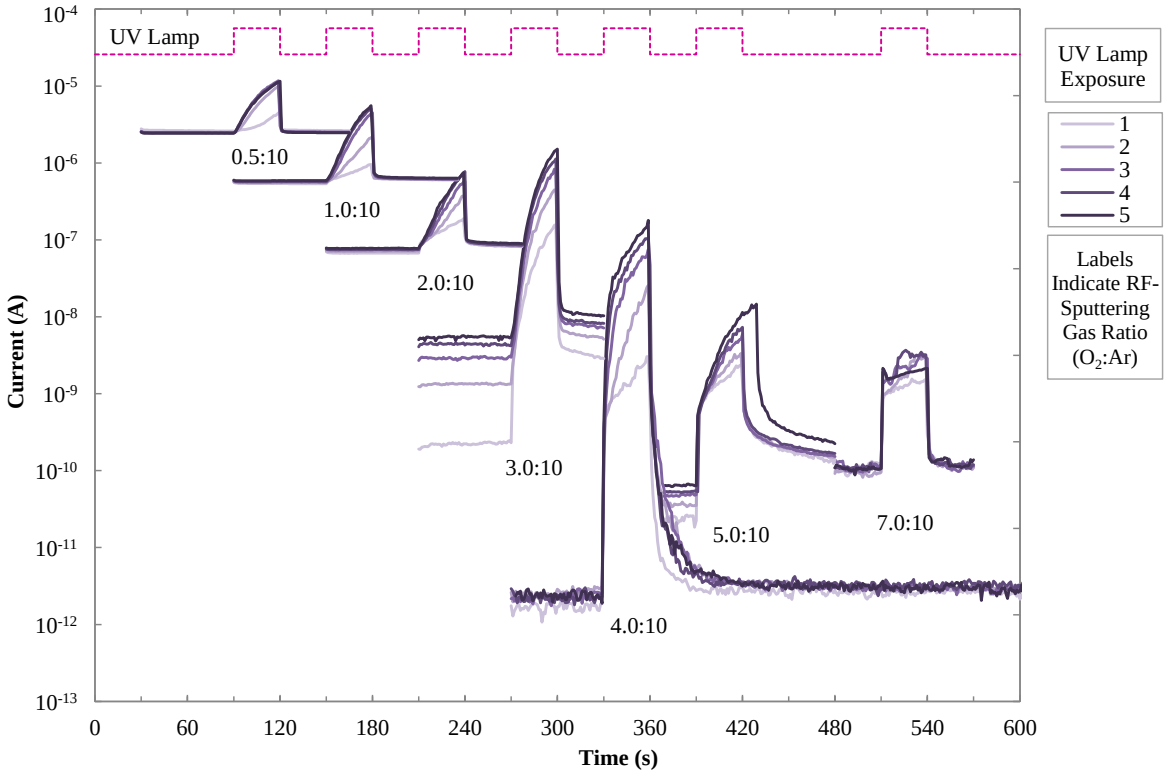

Figure 7.29: 0.5:10 – 7.0:10 (O_2:Ar) IrO_x (–c-plane ZnO) 30 s UV Photoresponse, -1 V Bias

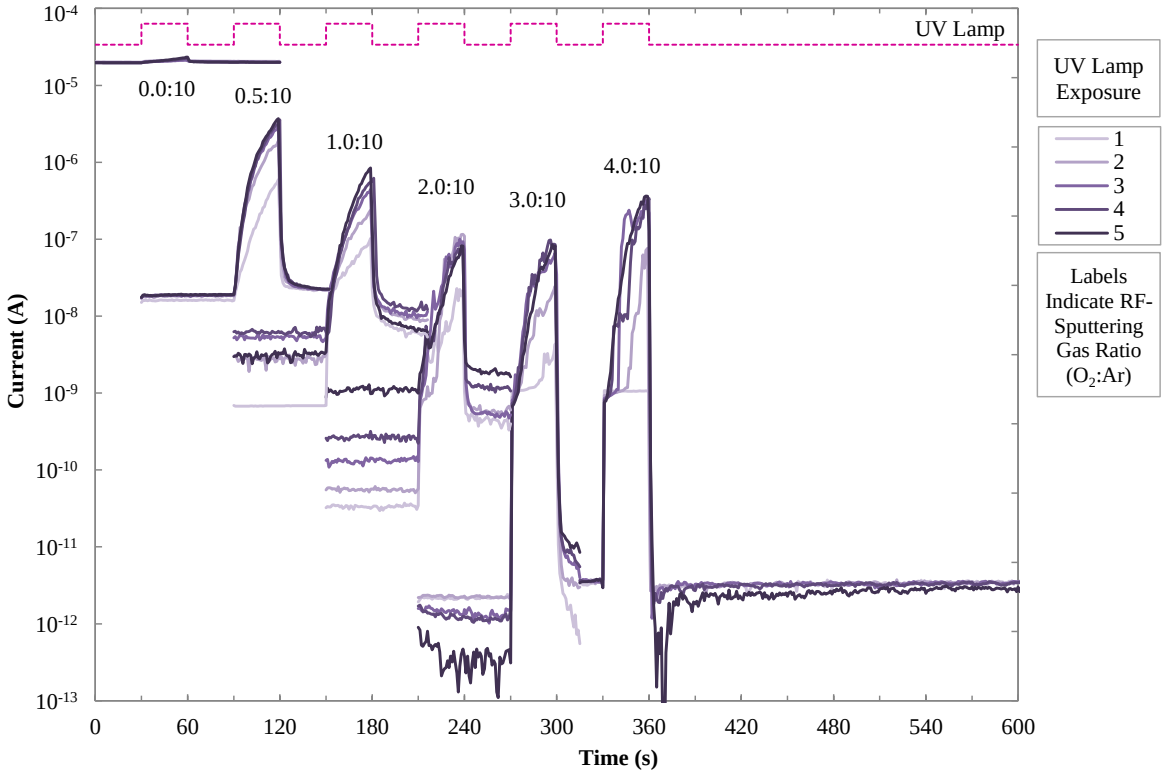

Figure 7.30: 0.0:10 – 4.0:10 (O_2:Ar) IrO_x (+c-plane low-Li ZnO) 30 s UV Response, -1 V Bias

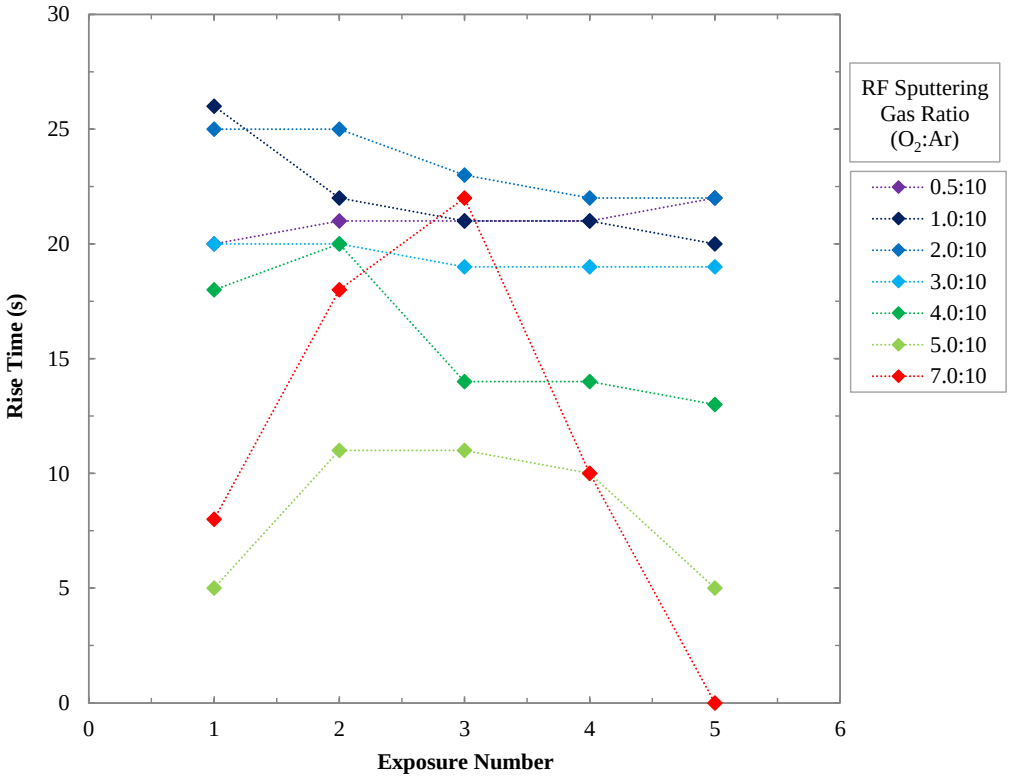

Figure 7.31: IrO_x (–c-plane ZnO) 30 s UV Photoresponse, Rise Time

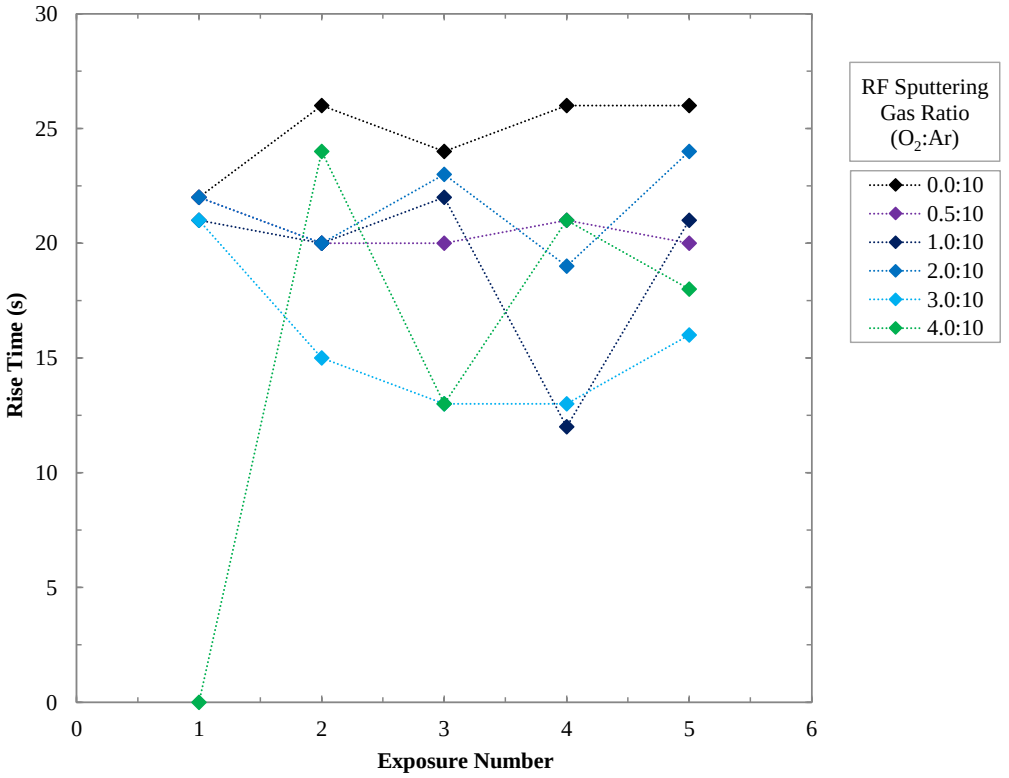

Figure 7.32: IrO_x (+c-plane low-lithium ZnO) 30 s UV Photoresponse, Rise Time

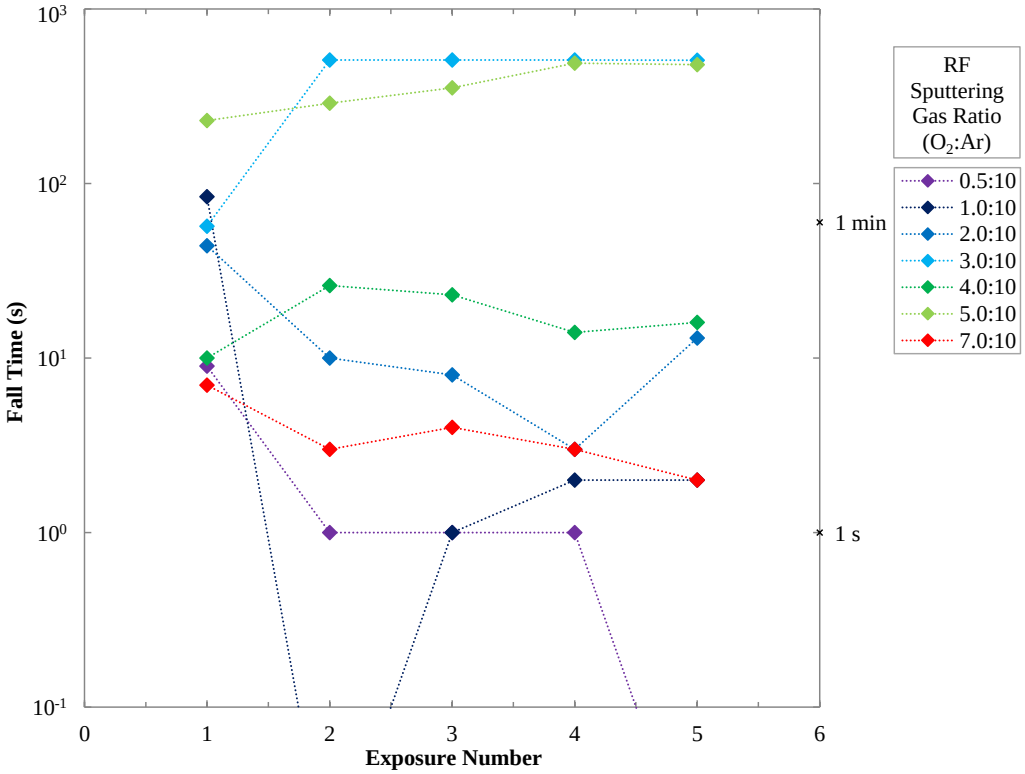

Figure 7.33: IrO_x (–c-plane ZnO) 30 s UV Photoresponse, Fall Time

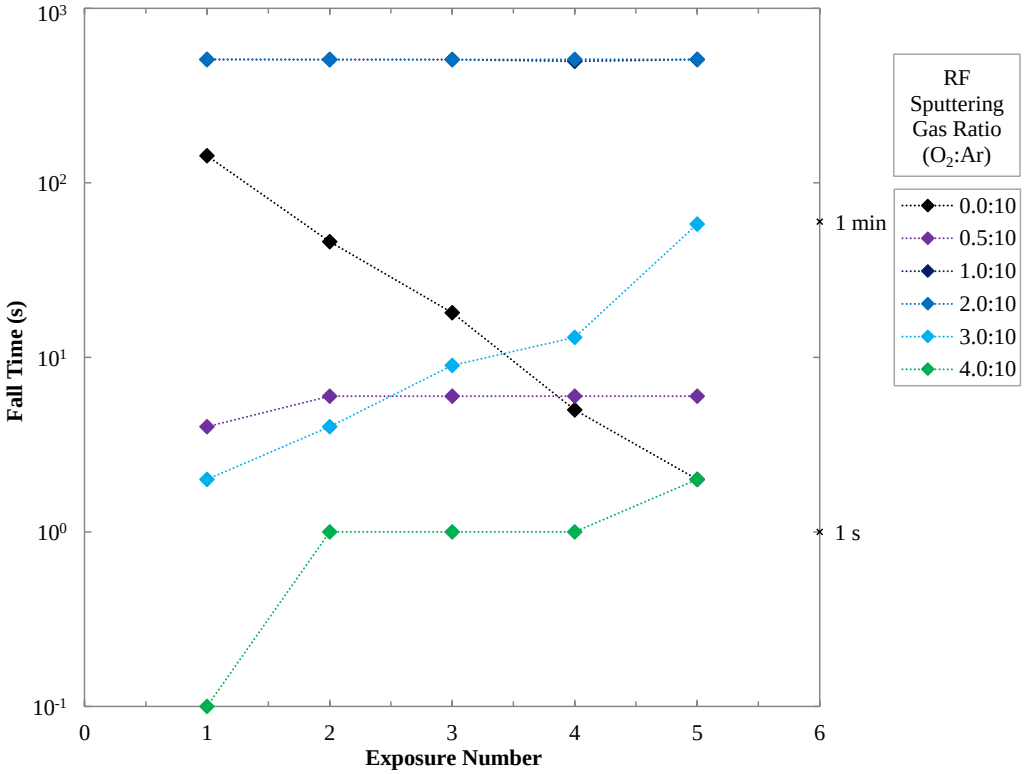

Figure 7.34: IrO_x (+c-plane low-lithium ZnO) 30 s UV Photoresponse, Fall Time

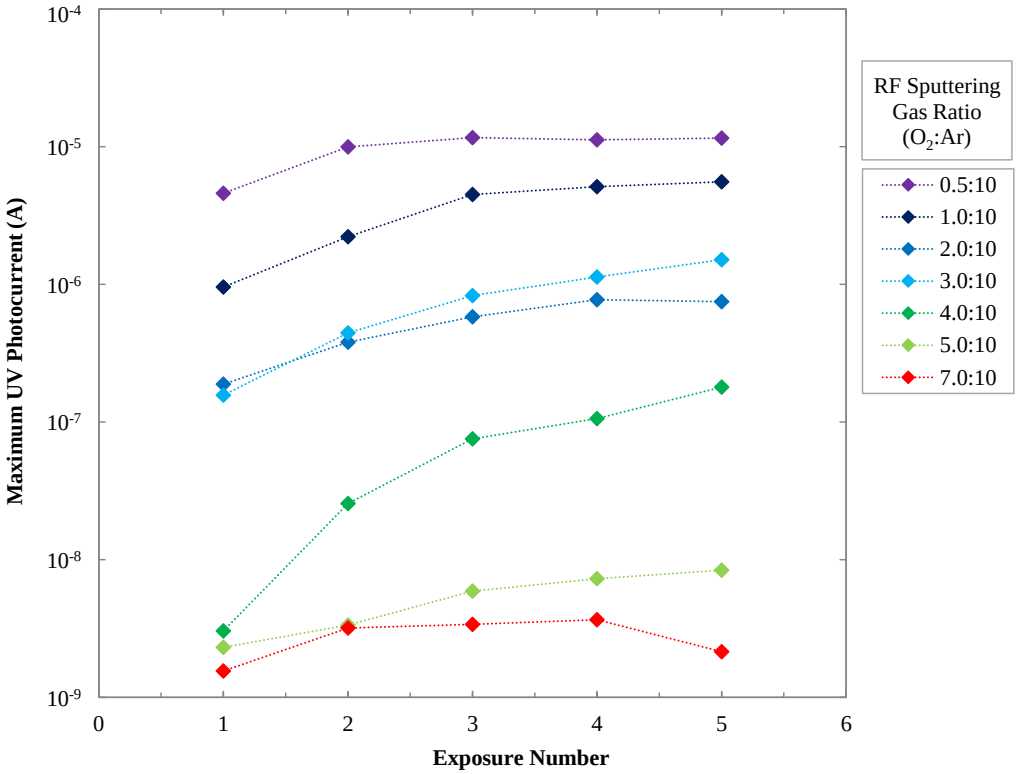

Figure 7.35: IrO_x (–c-plane ZnO) 30 s UV Photoresponse, Maximum Current

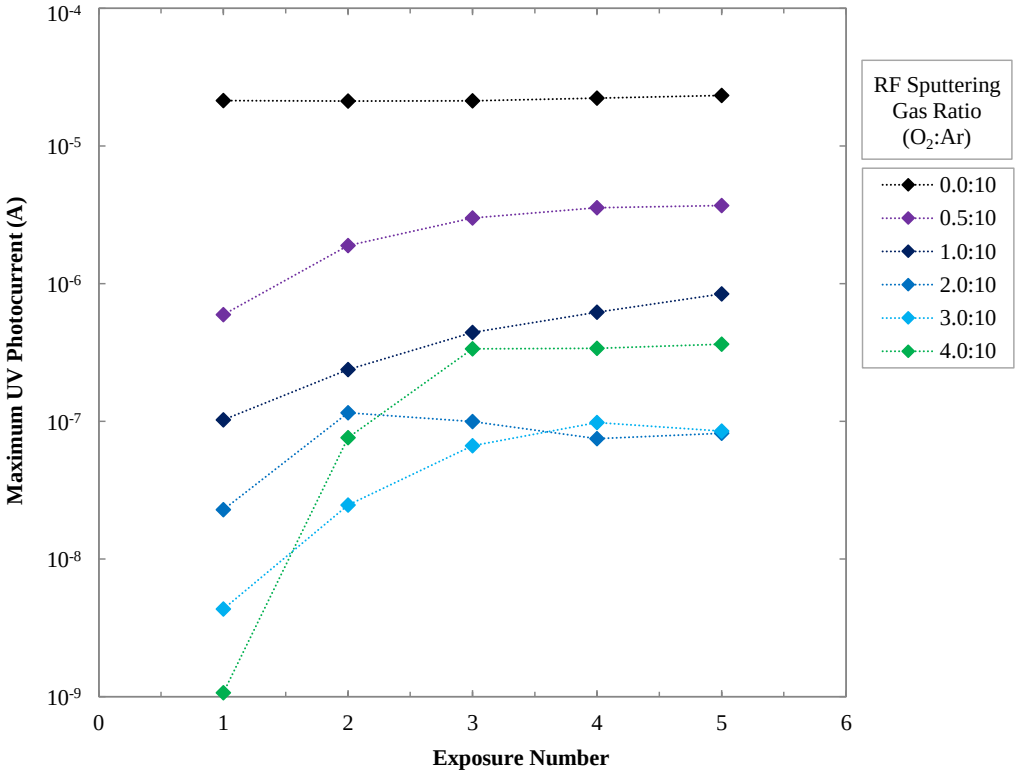

Figure 7.36: IrO_x (+c-plane low-lithium ZnO) 30 s UV Photoresponse, Maximum Current

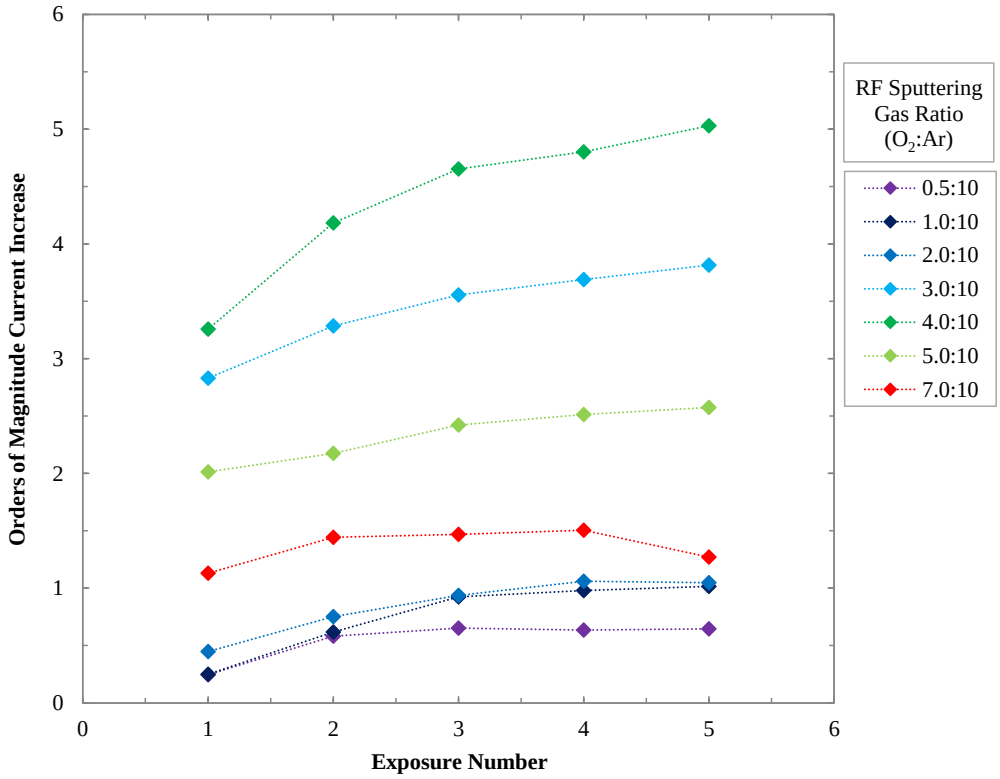

Figure 7.37: IrO_x (–c-plane ZnO) 30 s UV Photoresponse, Current Increase

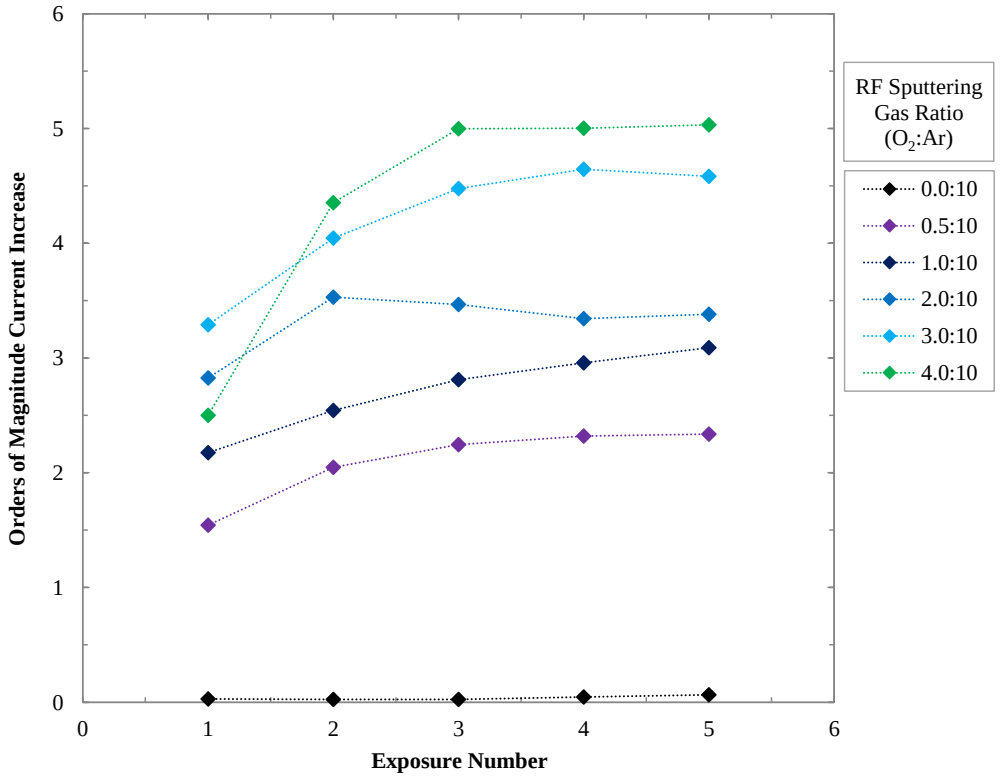

Figure 7.38: IrO_x (+c-plane low-lithium ZnO) 30 s UV Photoresponse, Current Increase

The UV photoresponse of the IrO_x devices to –c-plane and +c-plane (low-lithium) ZnO in Figures 7.29 – 7.30 show similar trends in UV photoresponse with increasing levels of oxygen incorporation. With the exception of the 4.0:10 (O_2:Ar) IrO_x contact to +c-plane (low-lithium) ZnO, the maximum photocurrents appear to decrease with increasing oxygen incorporation. In contrast, the current increase with UV radiation increases with increasing oxygen incorporation, peaking with the 4.0:10 (O_2:Ar) IrO_x contacts of both series with 5.0 O_{Mag}, before decreasing again for the 5.0:10 and 7.0:10 (O_2:Ar) IrO_x contacts to +c-plane (low-lithium) ZnO, as shown in Figures 7.31 – 7.32, to 1.1 – 2.6 O_{Mag}.

A decrease in rise-time with increasing oxygen incorporation can be observed in the UV photoresponse in Figures 7.29 – 7.30, with calculated values shown in Figures 7.31 – 7.32. The rise time of the 7.0:10 (O_2:Ar) IrO_x contact in Figure 7.32 shows a high level of variability, due to the instability of the UV photocurrent, as observed in Figure 7.29. Despite this, the 7.0:10 (O_2:Ar) IrO_x contact appears to have a UV photoresponse closest to that of a square-wave.

Figures 7.32 – 7.33 show that the fall-time of the IrO_x contacts appears to increase with increasing oxygen incorporation, with maximum fall-times for both series around 500 s. The exception to this is the 7.0:10 (O_2:Ar) IrO_x contact, with a maximum fall-time of 7 s, which appeared to decrease with subsequent UV exposures. In Figure 7.29, it can be observed that the decaying PPC for the 2.0:10 and 5.0:10 (O_2:Ar) IrO_x contacts follow two separate trends; an immediate drop in UV photocurrent, followed by a longer decay back down to the original dark current. This separation of PPC decay trends was not observed for the AgO_x and RuO_x contacts, and indicates at least two mechanisms responsible for the UV PPC. This effect can also be observed for the 1.0:10 – 3.0:10 (O_2:Ar) IrO_x contacts in Figure 7.30. The proposal of a model for PPC decay is introduced in Section 7.8, following the photoresponse results of the devices measured in this work.

The UV photoresponse of the AgO_x and RuO_x contacts with varying bias showed a similar trade-off between the response signal and response time with increasingly negative device bias. The IrO_x oxidation series shows a similar trade-off, implying that increased levels of oxygen incorporation could be reducing the sensitivity of the contacts to the negative bias, which would be advantageous for UV dosimetry. With the trade-off considered, the 4.0:10 (O_2:Ar) IrO_x contact on +c-plane (low-lithium) ZnO was used to explore the effects of device bias on UV photoresponse.

The UV photoresponse was measured with device bias varied from 0.1 to -6.0 V, with results and dark I-V characteristics in Figures 7.39 – 7.40. Rise-time, fall-time, maximum photocurrent, and current increase are shown in Figures 7.41 – 7.44. The full UV photoresponses of the IrO_x contact with bias is also included in Figure A7.2 of Appendix A7.3 to show long-term PPC.

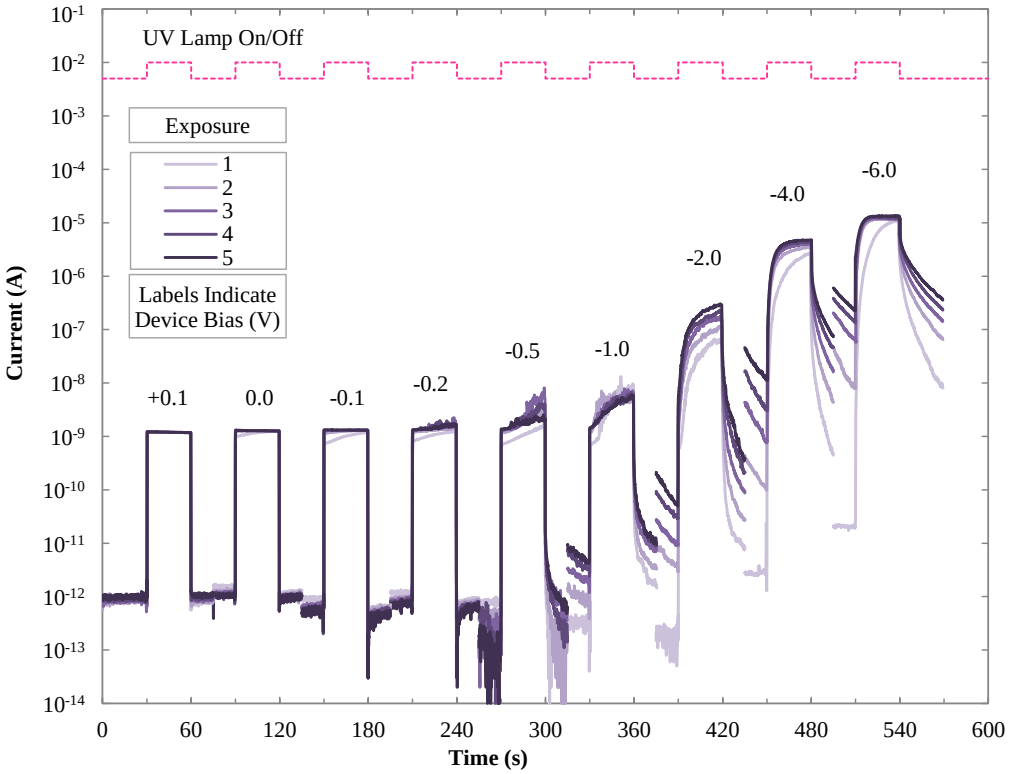

Figure 7.39: 4.0:10 (O_2:Ar) IrO_x (+c-plane low-lithium) 30 s UV Response, Varied Bias

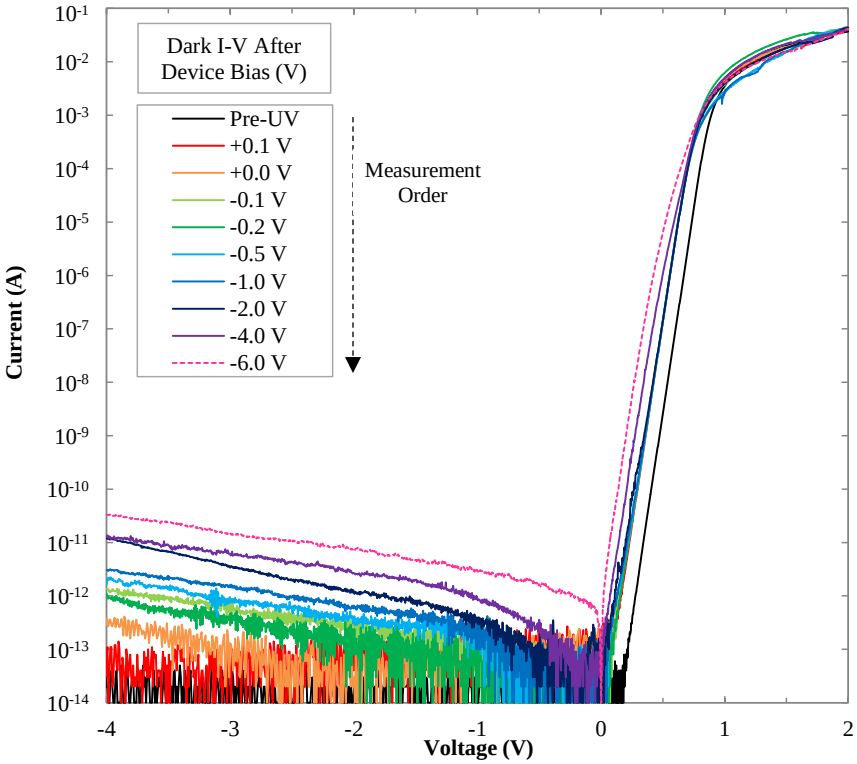

Figure 7.40: 4.0:10 (O_2:Ar) IrO_x Dark I-V After Each UV Photoresponse Bias Test

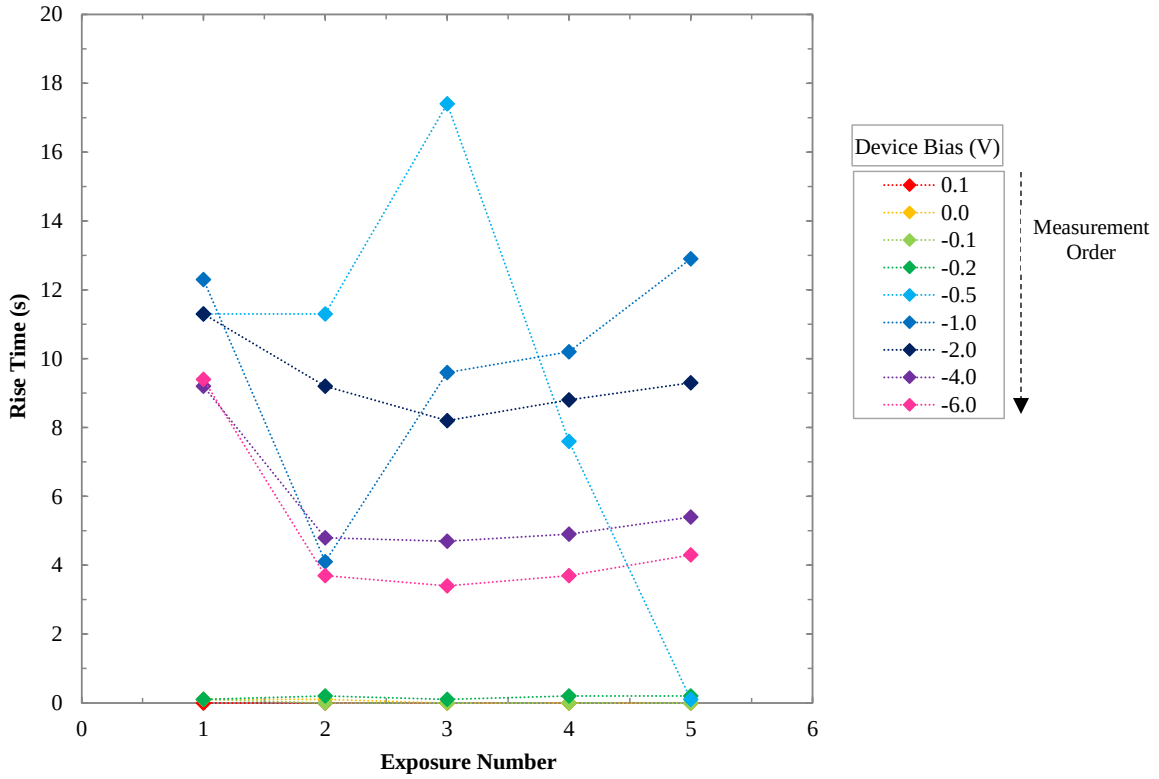

Figure 7.41: 4.0:10 (O_2:Ar) IrO_x 30 s UV Photoresponse with Bias, Rise-Time

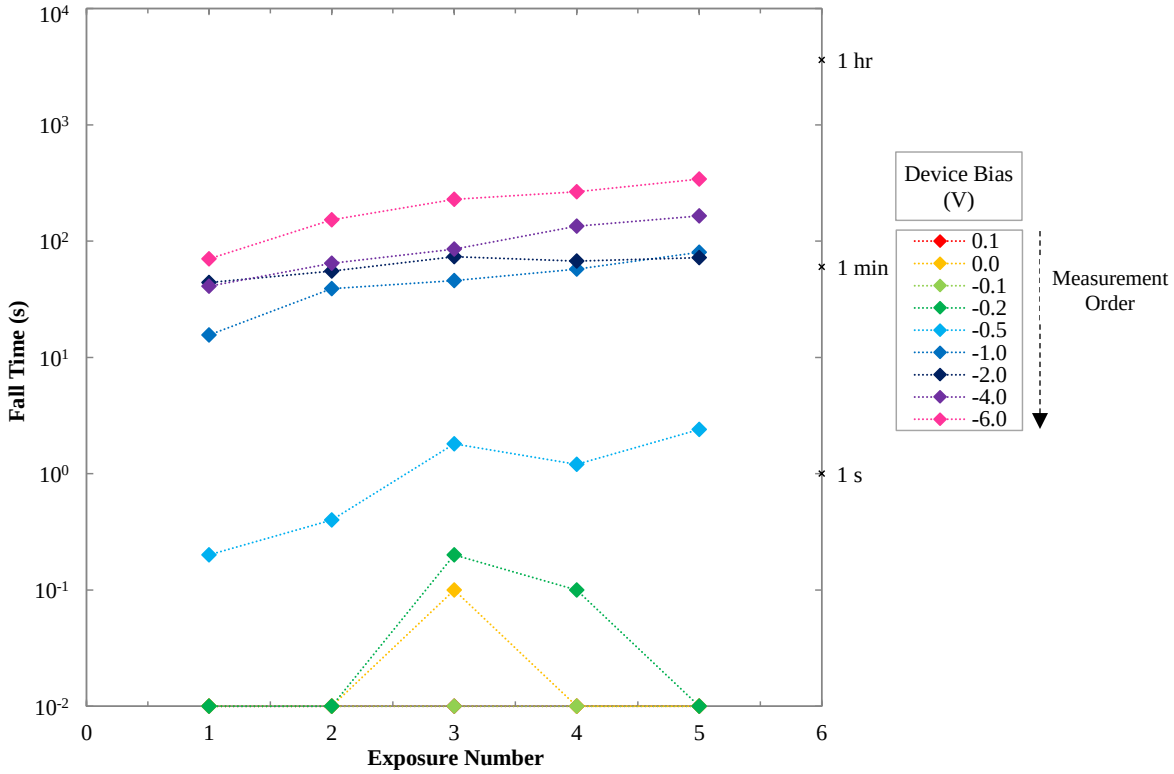

Figure 7.42: 4.0:10 (O_2:Ar) IrO_x 30 s UV Photoresponse with Bias, Fall-Time

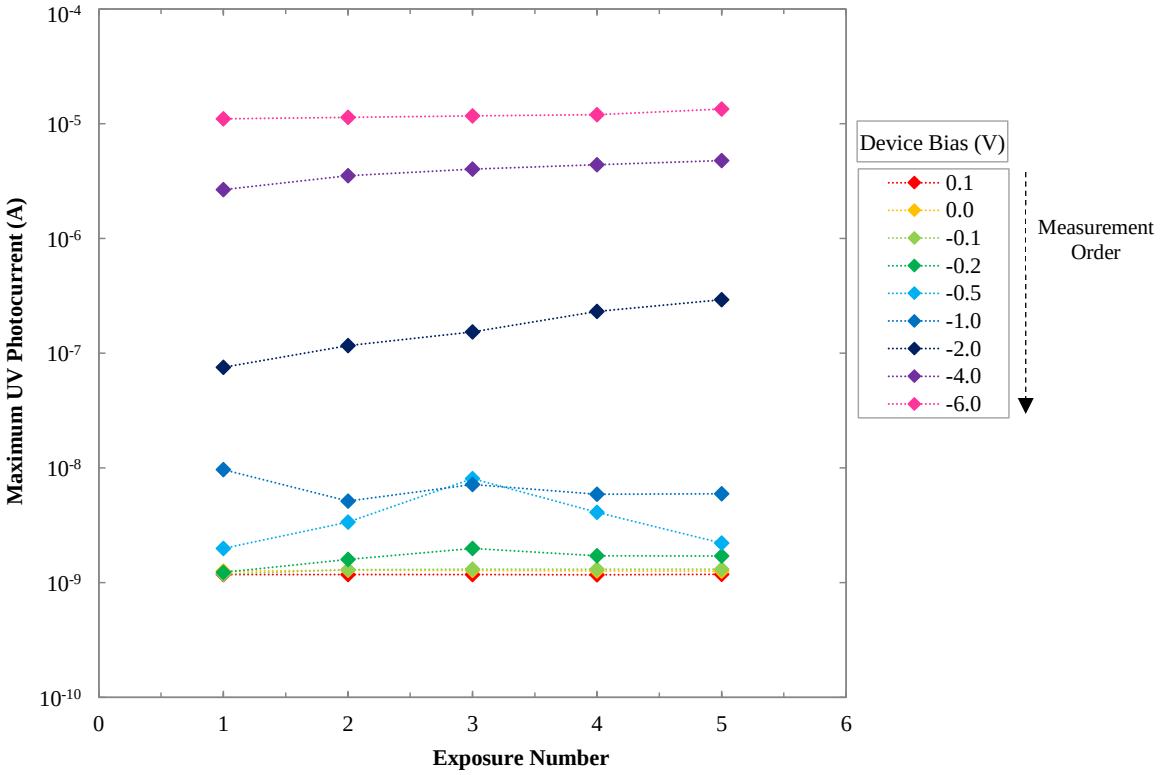

Figure 7.43: 4.0:10 (O_2:Ar) IrO_x 30 s UV Photoresponse with Bias, Maximum Current

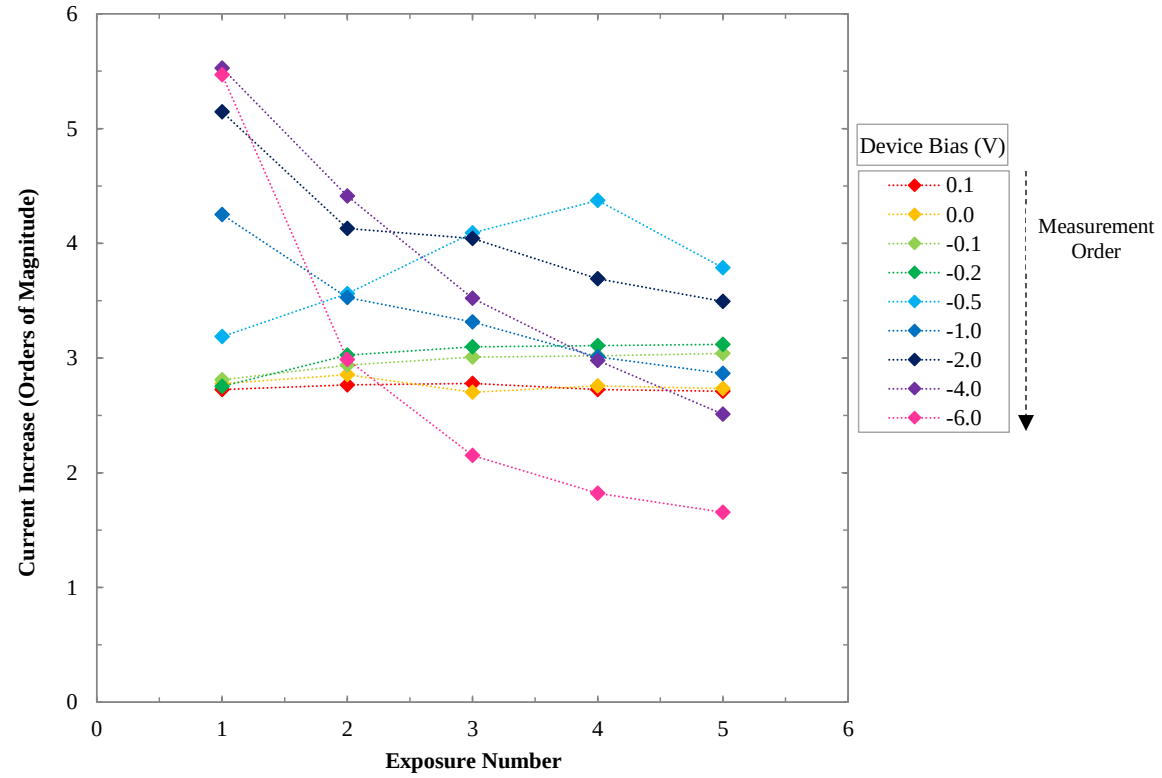

Figure 7.44: 4.0:10 (O_2:Ar) IrO_x 30 s UV Photoresponse with Bias, Current Increase

Figure 7.39 clearly shows the relationship between increasingly negative device bias and the increase in UV photoresponse. The device showed a square-wave response to the UV radiation from 0.1 V to -0.2 V, compared to the AgO_x contact in Figure 7.10, which showed PPC with only -0.1 V. The RuO_x contact was measured with a minimum negative bias of -0.5 V, however there was a significant amount of PPC present in the UV photoresponse, as shown in Figure 7.21. The dark I-V measurements between the UV photoresponse measurements in Figure 7.40 show increasing levels of reverse bias leakage current with subsequent exposures, indicating a long-term effect on the IrO_x contact to the +c-plane (low-lithium) ZnO, which was recoverable over time.

In Figure 7.39, the UV photoresponse of -0.2 V to -1.0 V also showed a significant amount of variation, compared to the UV photoresponse of -2.0 V and below. This unstable photocurrent apparent in the transition between a low-photocurrent response and a high-photocurrent PPC response can also be observed in Figure 7.10, at -1.0 V bias. This indicates a potential transition between different behaviours, such a fast-response and a slow-response, dominating the overall UV photoresponse.

Figure 7.41 shows a steep increase in rise-time for -0.2 V, but a decreasing rise-time for -0.5 V to -6.0 V. Figure 7.42 shows the fall-time increasing by > 3 O_{Mag} from -0.2 V to -6.0 V, showing the significance of the PPC generated with increasingly negative device bias, which also affects maximum photocurrent possible at -6.0 V, as shown in Figure 7.44. Again, increasingly negative device bias shows a trade-off between response time and response signal.

7.5 Ultraviolet Photoresponse of Palladium Oxide Schottky Contacts

The visual and UV photoresponse of 0.5:10 – 7.0:10 (O_2:Ar) RF-sputtered PdO_x Schottky contacts to +c-plane (low-lithium) ZnO were carried out in order to investigate the effect of oxygen incorporation on the photoresponse for this material. The photoresponse measurements consisted of a comparison between visual and UV radiation with a -1.0 V bias, as described in Table 7.1. The second test consisted of 5 pulses of 30 s UV radiation with 30 s darkness between each pulse, with device bias varied, as described in Table 7.4, performed on all 0.5:10 – 7.0:10 (O_2:Ar) PdO_x contacts.

The visual spectrum and UV photoresponse of 30 s illumination for the 1.0:10 – 7.0:10 (O_2:Ar) PdO_x contacts is shown in Figure 7.45, with the UV photoresponse scaled to match the visual spectrum LED incident power. The individual photoresponses of the PdO_x contacts are included in Appendix A7.4, Figures A7.3 – A7.7.

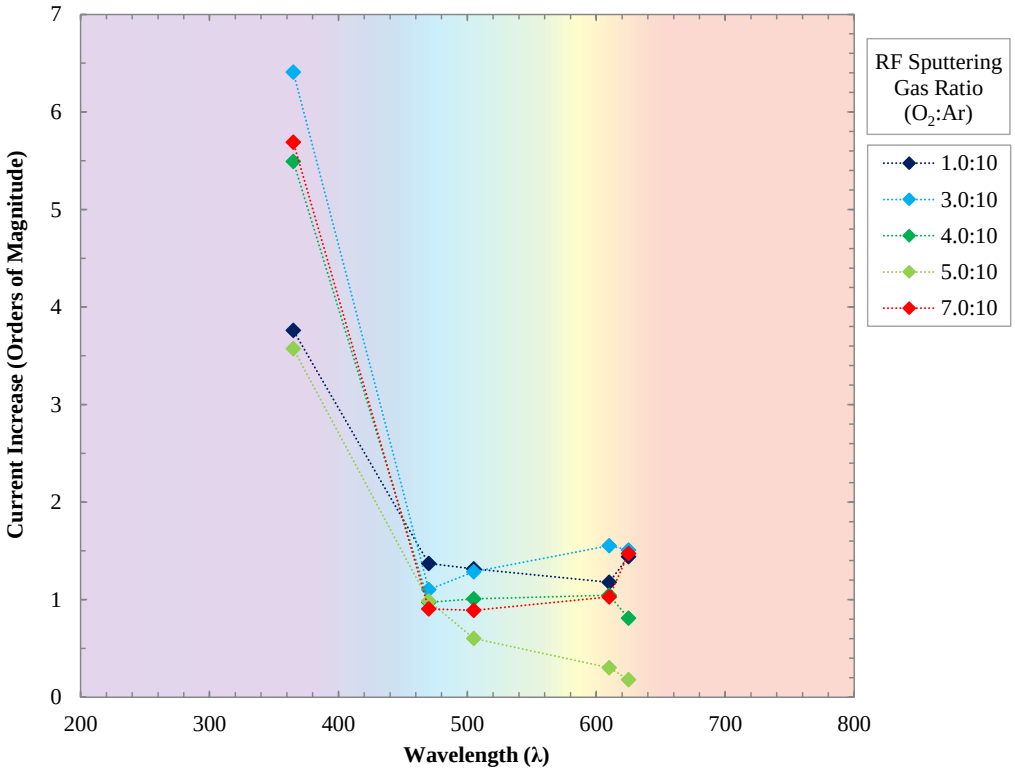

Figure 7.45: 7.0:10 (O_2:Ar) PdO_x 30 s Visual Spectrum and UV Responsivity, -1 V Bias

Figure 7.45 shows significant selectivity of the PdO_x contacts to UV radiation, with 3.8 – 6.4 O_{Mag} current increase to the UV light source, when scaled for incident illumination power (2.5 $mWcm^{-1}$ irradiance), compared to the visual spectrum with 0.54 – 1.5 O_{Mag}. The difference between the UV and averaged visual radiation response increasing from 3.1 to 5.1 O_{Mag} from 1.0:10 to 7.0:10 (O_2:Ar) PdO_x contacts, showing increasing selectivity with increasing oxygen incorporation, indicating significant potential for UV dosimetry.

Due to the significant impact of device bias, the UV photoresponse of all 0.5:10 – 7.0:10 (O_2:Ar) PdO_x contacts was measured with decreasing device bias from 0.1 V to -2.0 – -6.0 V, as shown in Figures 7.46 – 7.51. The full UV photoresponses and the dark I-V characteristics taken between the UV photoresponse measurements of the individual PdO_x contacts are also included in Figures A7.8 – A7.19 of Appendix A7.5, to show the long-term PPC of the device. Comparisons of the full UV photoresponses with 0 V and -4.0 V bias are shown in Figures 7.52 – 7.53. For the analysis of the UV photoresponses, the fifth rise-time, fall-time, maximum UV photocurrent, and current increase of the PdO_x contacts with oxygen incorporation are shown in Figures 7.54 – 7.57. For the analysis of the dark I-V measurements taken between the UV photoresponse measurements, plots of the ideality factor, barrier height, and rectification ratio are shown in Figures 7.58 – 7.60.

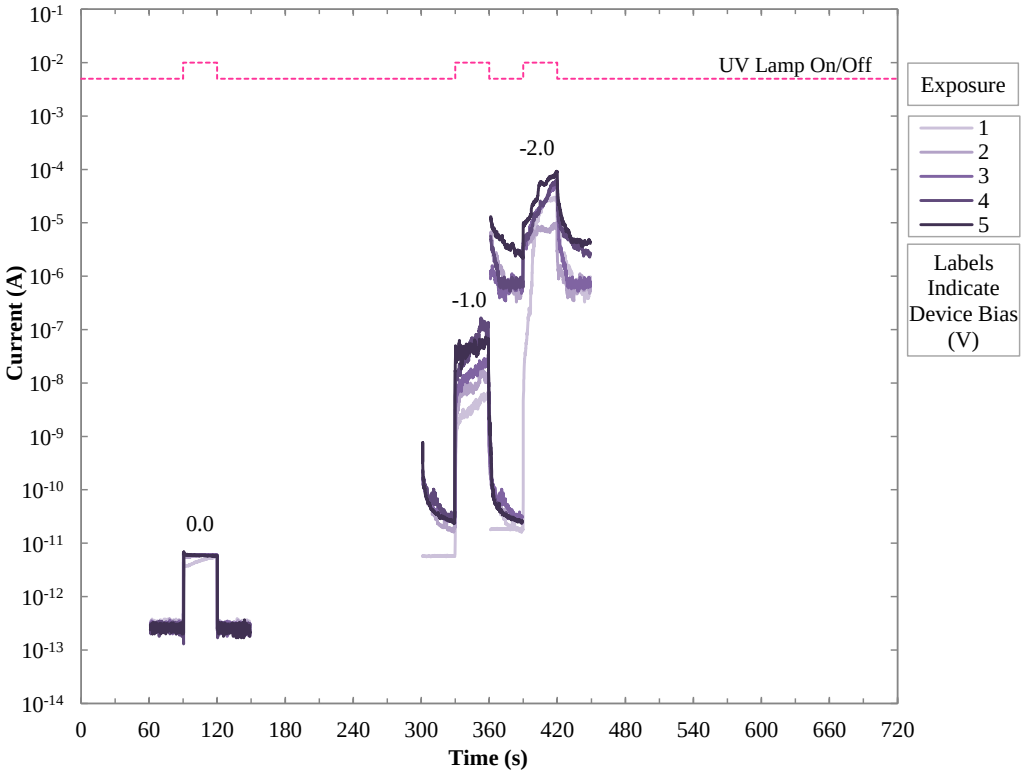

Figure 7.46: 0.5:10 (O_2:Ar) PdO_x 30 s UV Photoresponse with Varied Bias

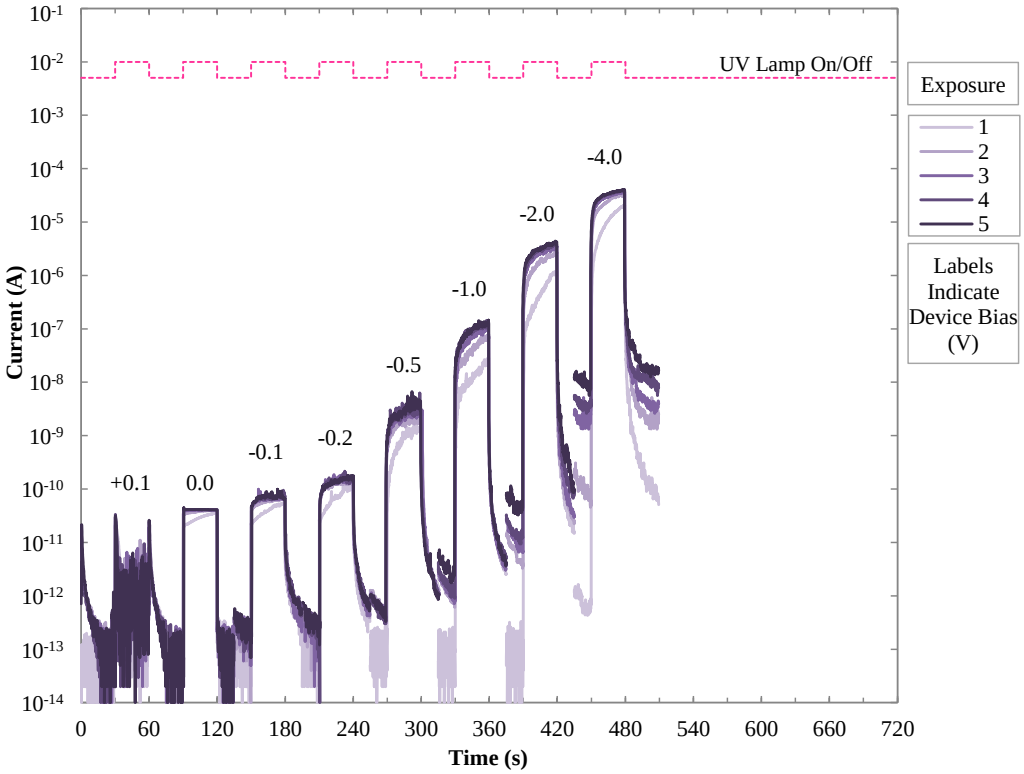

Figure 7.47: 1.0:10 (O_2:Ar) PdO_x 30 s UV Photoresponse with Varied Bias

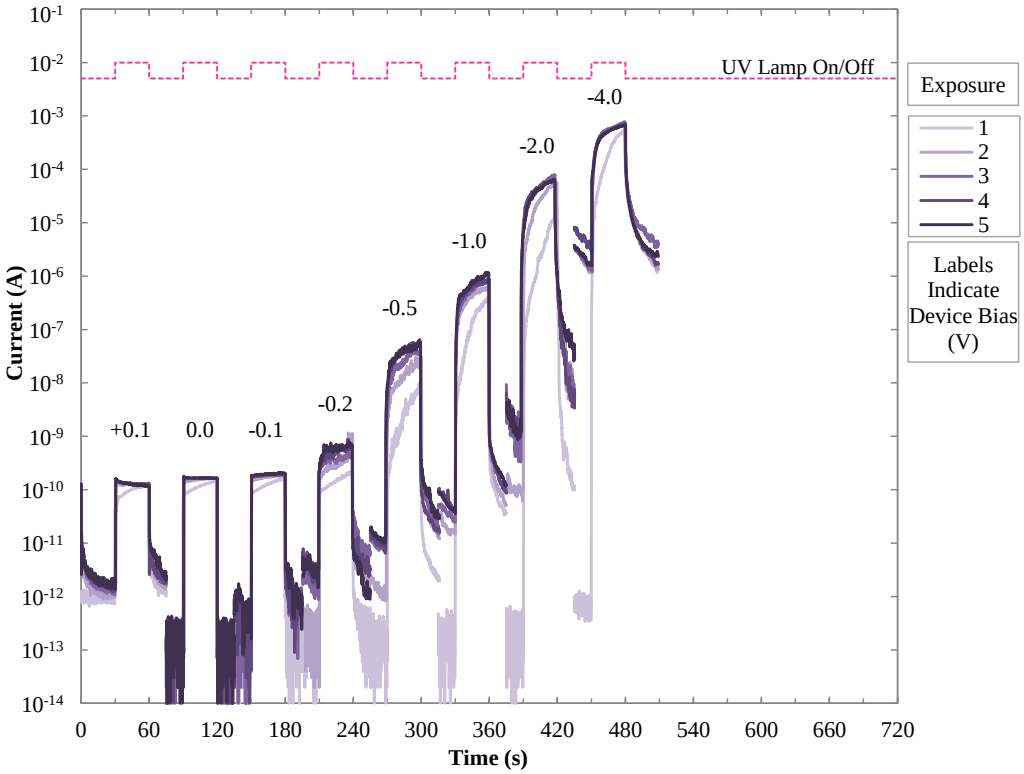

Figure 7.48: 3.0:10 (O_2:Ar) PdO_x 30 s UV Photoresponse with Varied Bias

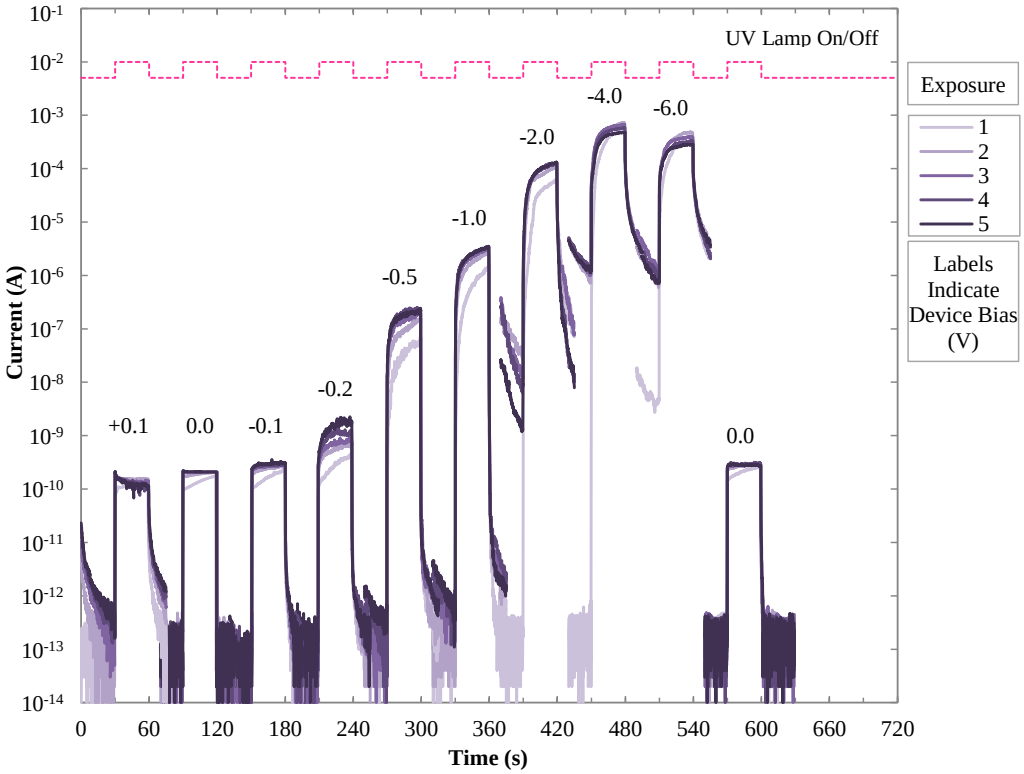

Figure 7.49: 4.0:10 (O_2:Ar) PdO_x 30 s UV Photoresponse with Varied Bias

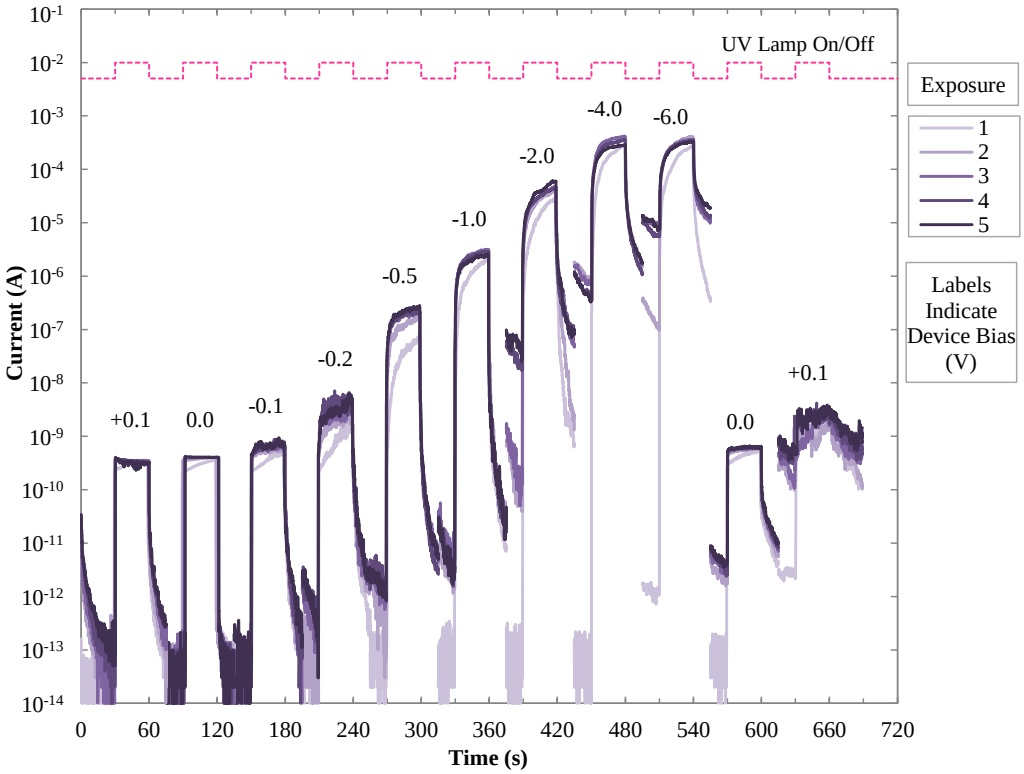

Figure 7.50: 5.0:10 (O_2:Ar) PdO_x 30 s UV Photoresponse with Varied Bias

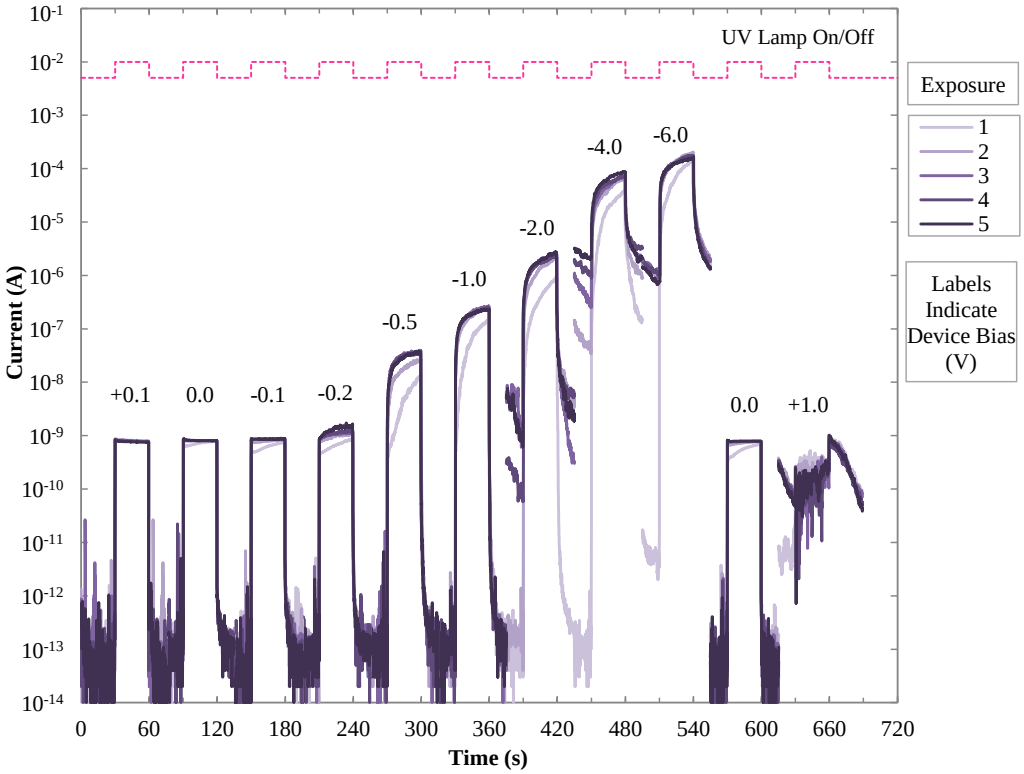

Figure 7.51: 7.0:10 (O_2:Ar) PdO_x 30 s UV Photoresponse with Varied Bias

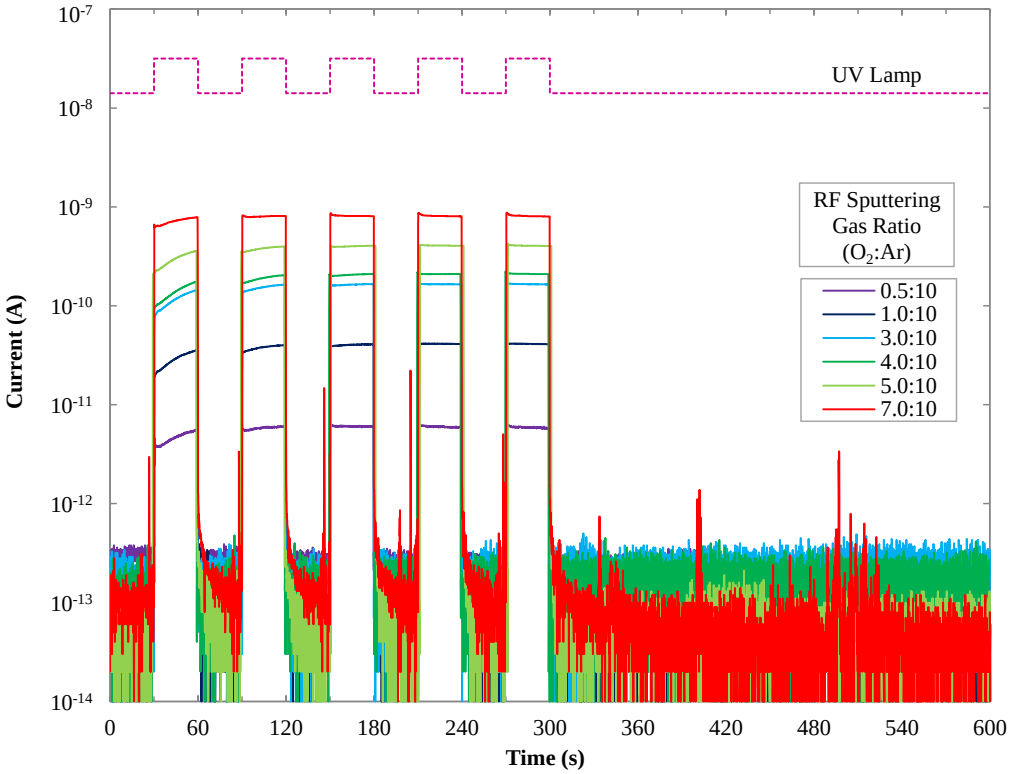

Figure 7.52: 0.5:10 – 7.0:10 (O_2:Ar) PdO_x 30 s UV Photoresponse with 0 V Bias

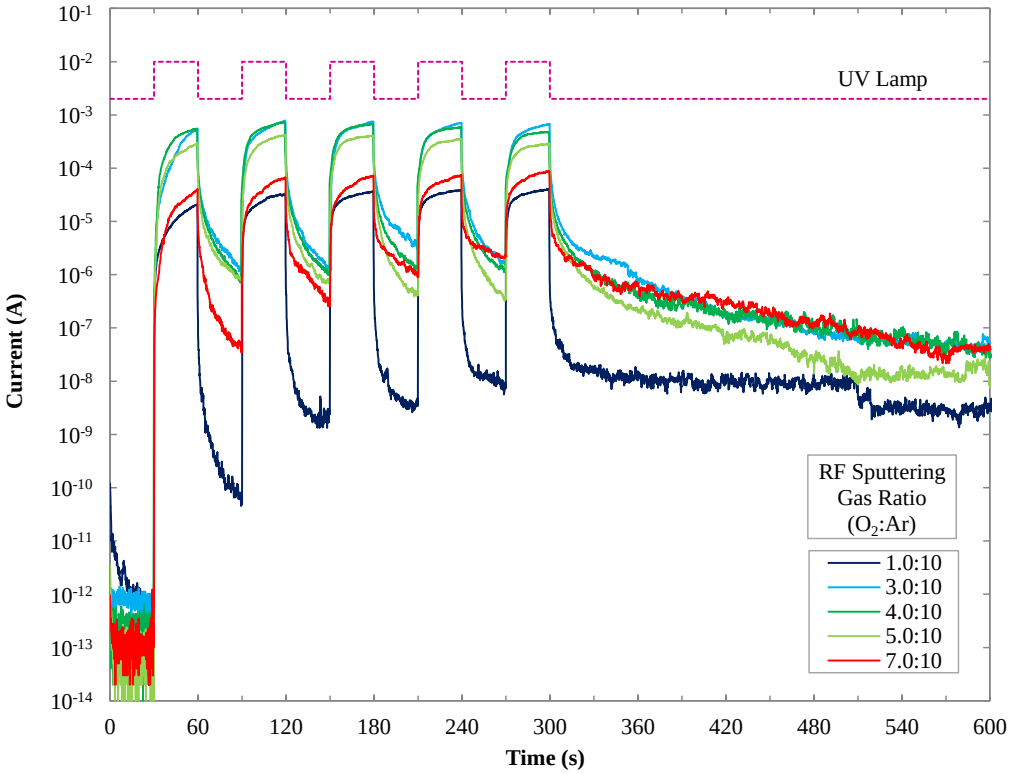

Figure 7.53: 0.5:10 – 7.0:10 (O_2:Ar) PdO_x 30 s UV Photoresponse with -4 V Bias

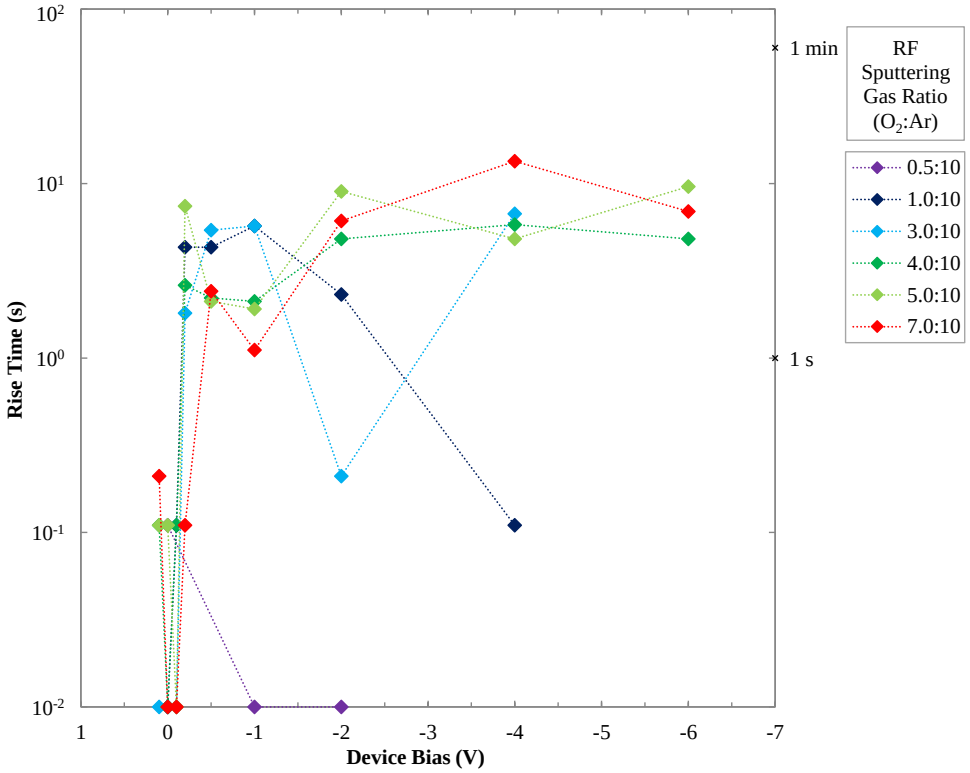

Figure 7.54: PdO_x 30 s UV Photoresponse with Bias (Fifth Pulse), Rise-Time

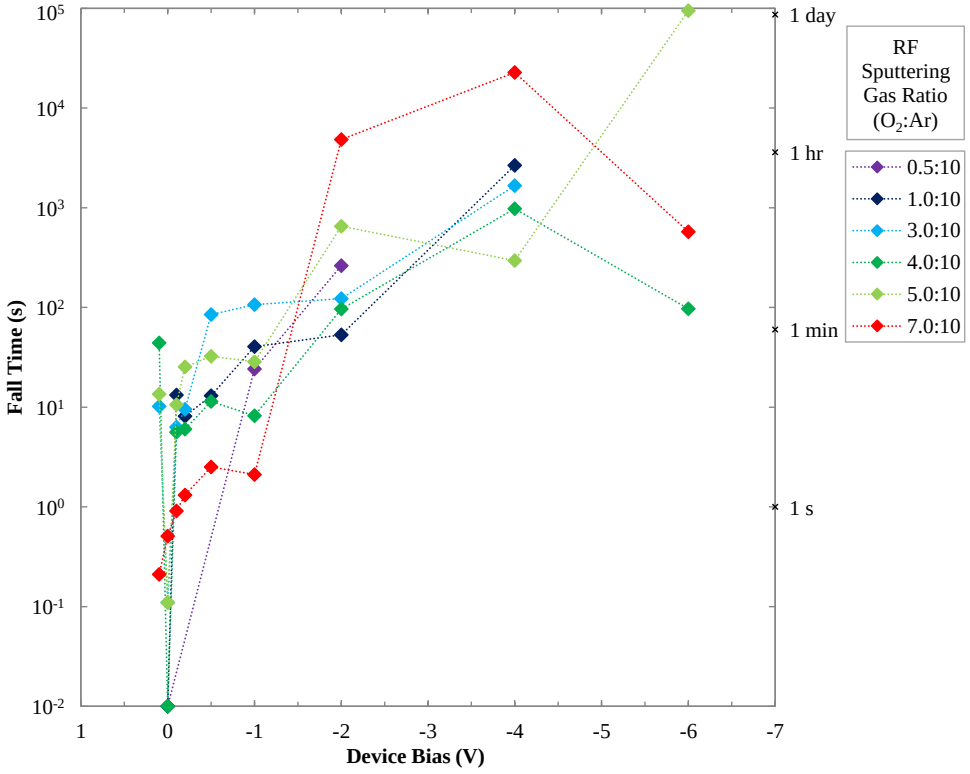

Figure 7.55: PdO_x 30 s UV Photoresponse with Bias (Fifth Pulse), Fall-Time

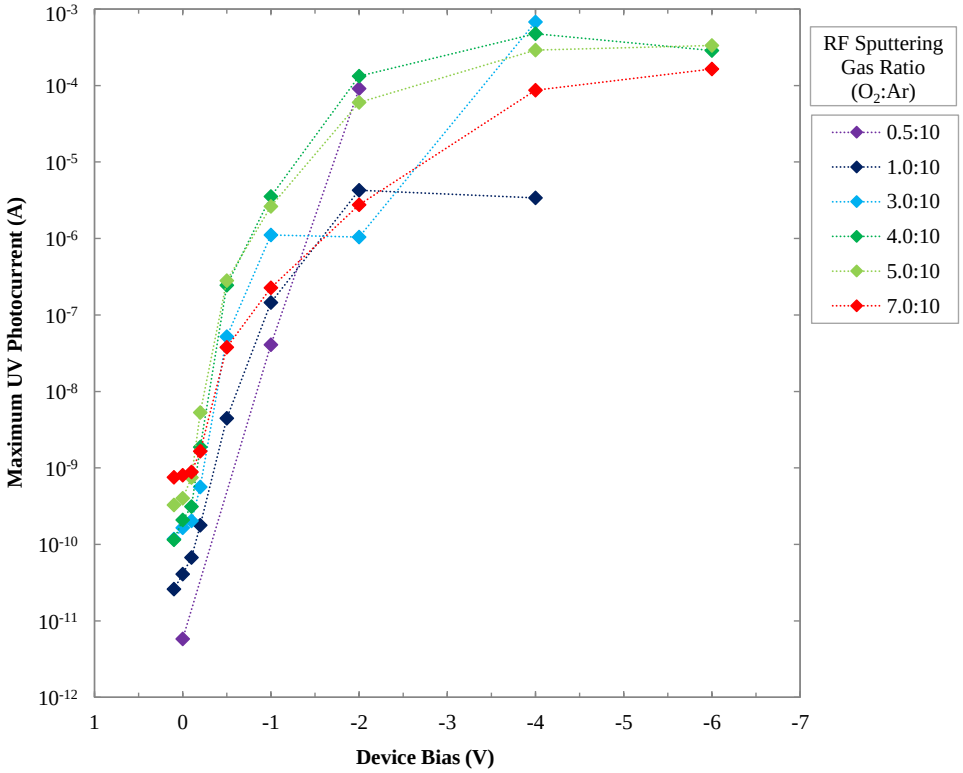

Figure 7.56: PdO_x 30 s UV Photoresponse with Bias (Fifth Pulse), Maximum Current

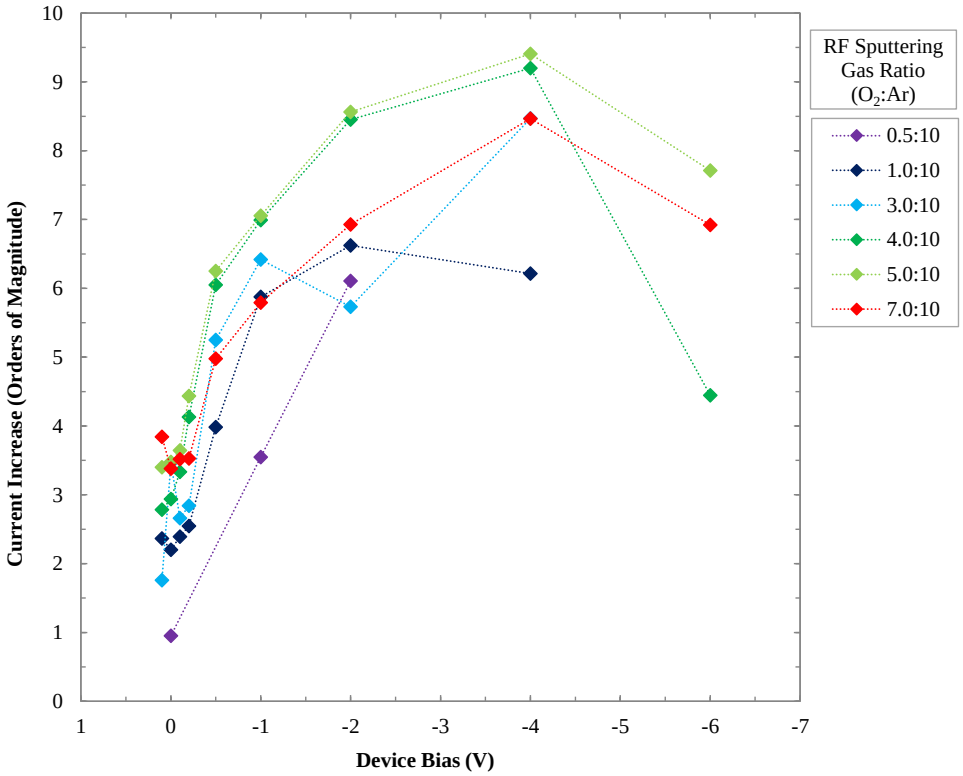

Figure 7.57: PdO_x 30 s UV Photoresponse with Bias (Fifth Pulse), Current Increase

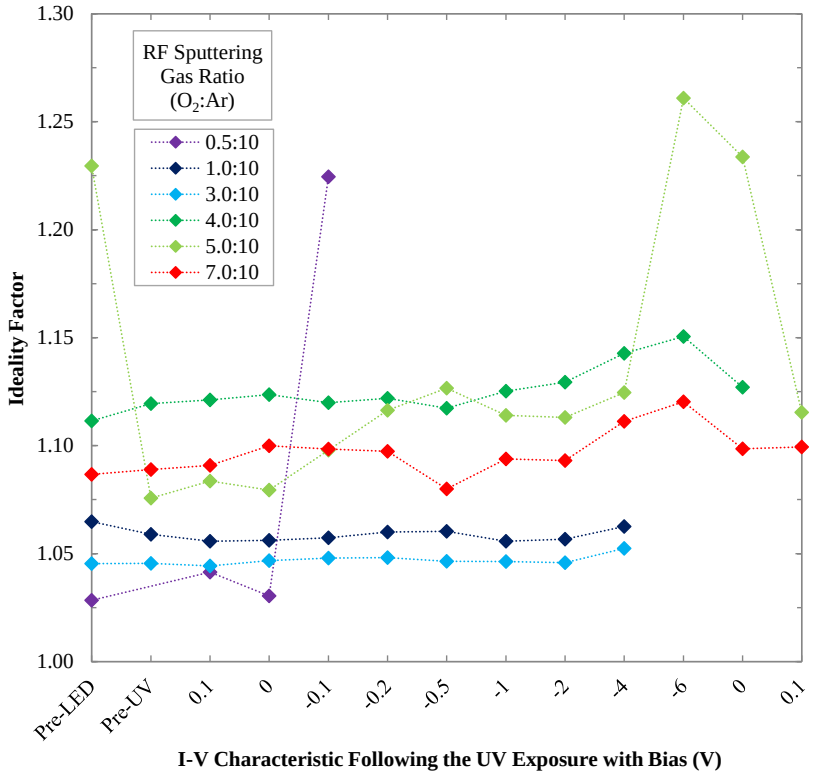

Figure 7.58: PdO_x Dark I-V UV Photoresponse with Bias, Ideality Factors

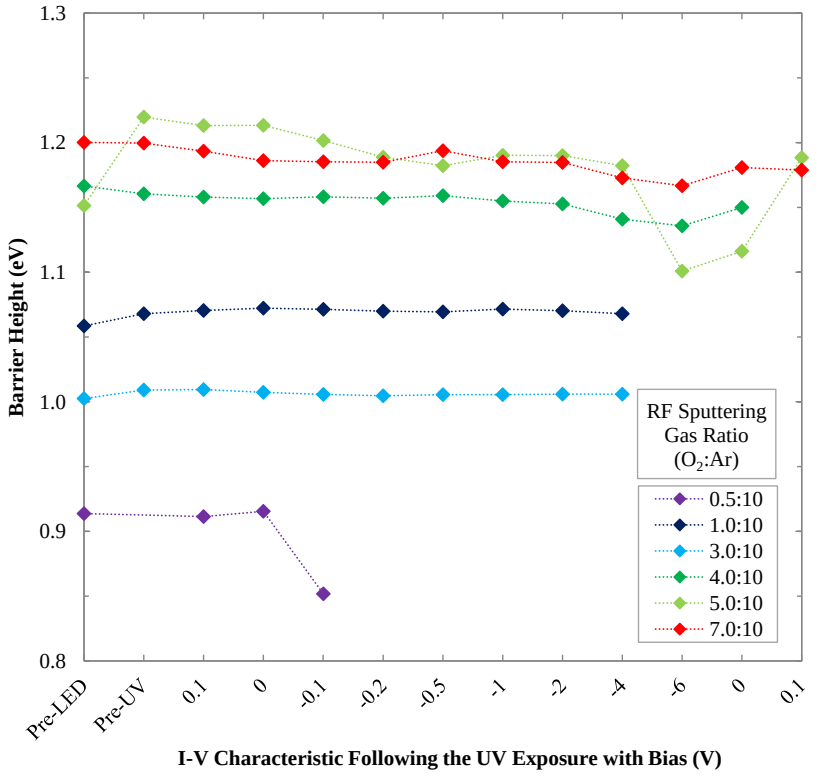

Figure 7.59: PdO_x Dark I-V UV Photoresponse with Bias, Barrier Heights

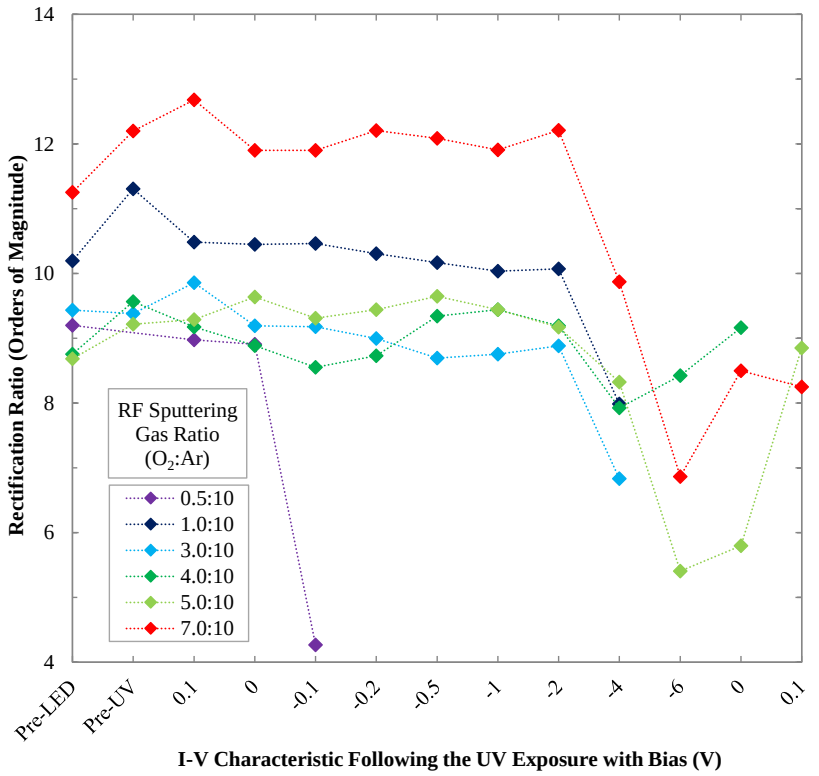

Figure 7.60: PdO_x Dark I-V UV Photoresponse with Bias, Rectification Ratios

The UV photoresponses of the PdO_x contacts in Figures 7.46 – 7.51 show a similar trend of increasing photoresponse with increasingly negative device bias, with the 0.5:10 – 5.0:10 (O_2:Ar) PdO_x devices showing a maximum photocurrent at -4.0 V, with a decrease in the maximum photocurrent at -6.0 V. This trend can also be observed in Figure 7.56. The level of PPC present appears proportionate to the maximum level of photocurrent, as confirmed by the similar trends in Figures 7.55 – 7.56. Figures 7.46 – 7.51 also clearly show the square-wave photoresponse to the UV radiation extending further into the negative-bias measurements with increasing oxygen incorporation. This suggests that the Schottky contacts with increasing levels of oxygen incorporation are more resistant to the production of higher UV photocurrents, and the associated PPC.

Figures 7.50 – 7.52 include 0 V and 0.1 V bias UV photoresponse measurements of the PdO_x contacts after the -6.0 V bias measurements. The 0 V bias results continue to show square-wave behaviour, despite the PPC present in the devices (as shown from the increased reverse-bias leakage current from dark I-V measurements in Figure 7.60, and in A7.14 – A7.19). However, the UV

photoresponse with 0.1 V bias show unstable results, following the -6.0 V bias measurement. This shows the susceptibility of the positive-bias measurements to PPC.

Figure 7.52 shows that the maximum UV photocurrent of the PdO_x contacts at 0 V bias increases with increasing oxygen incorporation, also shown in Figure 7.56. This is significant, as it indicates that PdO_x contacts with higher levels of oxygen incorporation produce greater UV photocurrents with no additional PPC, producing more responsive photodetectors for dosimetry. However, Figure 7.53 shows that the susceptibility to negative-bias induced PPC increases with increasing oxygen incorporation, also shown in the increasing fall-time with oxygen incorporation from Figure 7.56. Although the 7.0:10 (O_2:Ar) PdO_x contact shows the highest resistance to PPC generation with increasingly negative bias, once the PPC is generated with -2.0 V and above, it had the longest recovery time. The rise-time of the PdO_x devices in Figure 7.54 also appears to increase slightly with increasing oxygen incorporation, but was shown to to plateau around 10 s.

The results from the dark I-V measurements taken between UV photoresponse measurements in Figures 7.58 – 7.60 show the decrease barrier height and increase in ideality factor with increasingly negative device bias measurements. This is likely due both to the increasing total UV dose, and level of device bias. The 0.5:10 and 5.0:10 (O_2:Ar) PdO_x contacts show the greatest variation of ideality factor, barrier height and rectification ratio with device bias in Figures 7.58 – 7.60. The 4.0:10 – 7.0:10 (O_2:Ar) PdO_x contacts where the 0 V bias UV photoresponse was performed after the -6.0 V measurements showed a significant recovery of the ideality factor, barrier height, and rectification ratio. This indicates that the long-term effects of PPC could be mitigated by removing the negative bias, applying a positive bias, or exposing the device to UV without an applied bias.

7.6 Ultraviolet Photoresponse of Platinum Oxide Schottky Contacts

The photoresponse of 0.0:10 – 7.0:10 (O_2:Ar) RF-sputtered PtO_x Schottky contacts to +c-plane (low-lithium) ZnO were also carried out. The measurements consisted of visual and UV photoresponse measurements with a -1.0 V bias, described in Table 7.1, and of 5 pulses of 30 s UV radiation separated by 30 s of darkness with device bias varied, as described in Table 7.4.

The visual spectrum and UV photoresponse of 30 s illumination for the 0.0:10 – 7.0:10 (O_2:Ar) PtO_x contacts is shown in Figure 7.61, with the UV photoresponse scaled to match the visual spectrum LED incident power. The individual photoresponses of the PtO_x contacts are included in Appendix A7.6, Figures A7.20 – A7.27.

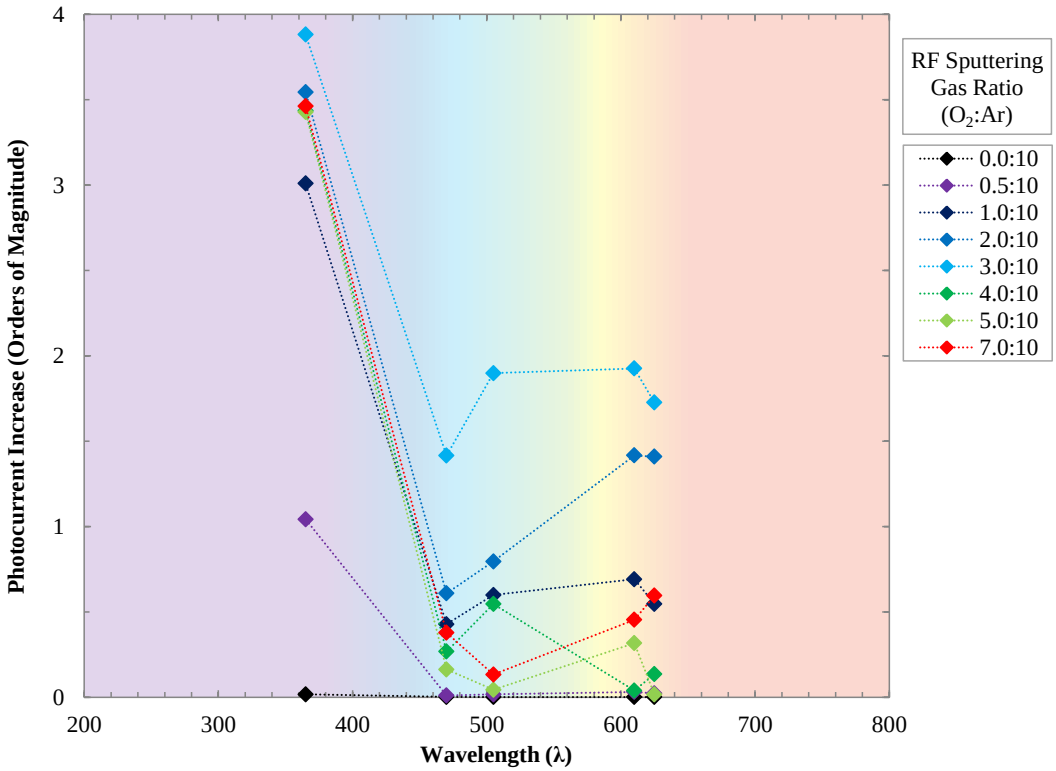

Figure 7.61: PtO_x 30 s Visual Spectrum and UV Responsivity, -1 V Bias

Figure 7.61 shows that the 0.5:10 – 7.0:10 (O_2:Ar) PtO_x contacts have less selectivity between visual and UV radiation than the PdO_x contacts, with 1.0 – 3.9 O_{Mag} current increase to the UV light source, and 0 – 1.9 O_{Mag} for the visual spectrum. Compared to the 6.4 and 1.5 maximum order of magnitude increases for the PdO_x contacts, the PtO_x contacts are more sensitive to photoresponse interference from visual wavelengths, which is undesirable for UV dosimetry. However, increasing levels of oxygen incorporation appear to produce a comparably decreasing photoresponse to the visual spectrum, with a difference between UV and the averaged visual radiation photoresponse of 1.0 to 3.0 O_{Mag} from 0.5:10 to 7.0:10 (O_2:Ar) PtO_x.

The UV photoresponses of the PtO_x contacts with decreasing device bias from 0.1 V to -8.0 V are shown in Figures 7.62 – 7.69. The full UV photoresponses and the dark I-V characteristics taken between the UV photoresponse measurements are included in Figures A7.28 – A7.33 of Appendix A7.7, to show the long-term PPC of the device. Comparisons of the full UV photoresponses with 0 V and -8.0 V bias are shown in Figures 7.70 – 7.71. The fifth rise-time, fall-time, maximum UV photocurrent, current increase from the UV photoresponse measurements, and the ideality factors, barrier heights, and rectification ratios from dark I-V characteristics taken between photoresponse measurements of the 0.5:10 – 7.0:10 (O_2:Ar) PtO_x contacts are shown in Figures 7.72 – 7.78.

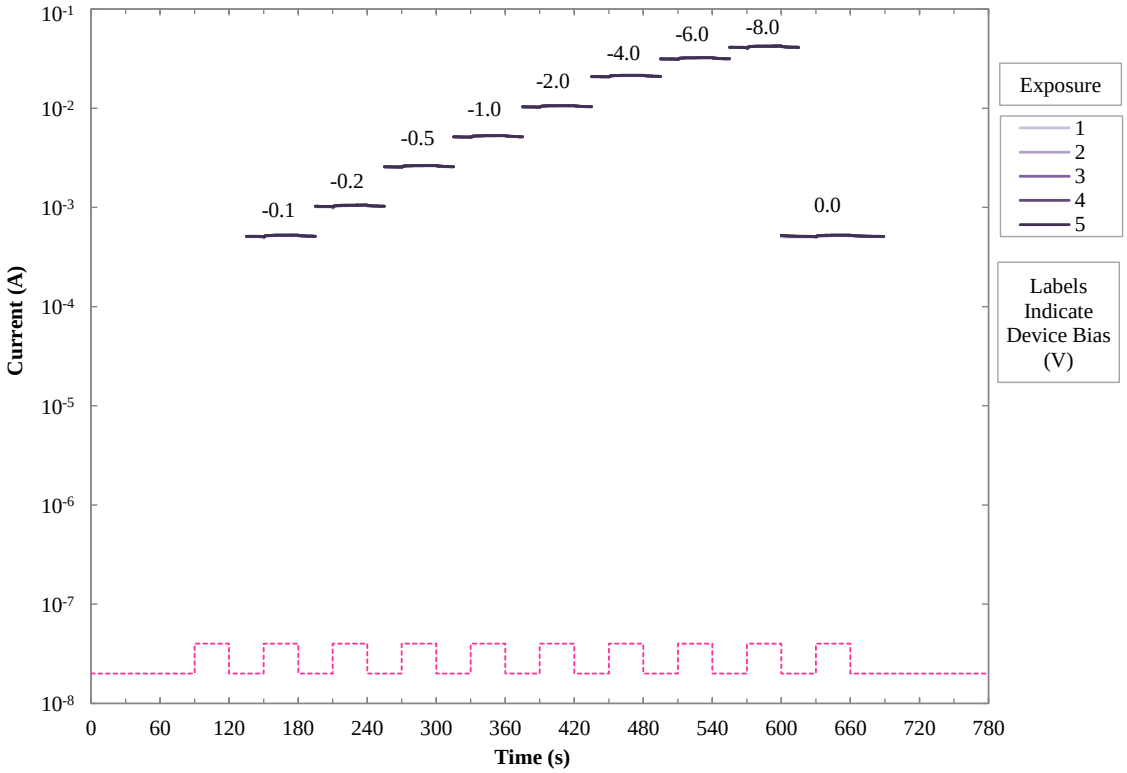

Figure 7.62: 0.0:10 (O_2:Ar) PtO_x 30 s UV Photoresponse with Varied Bias

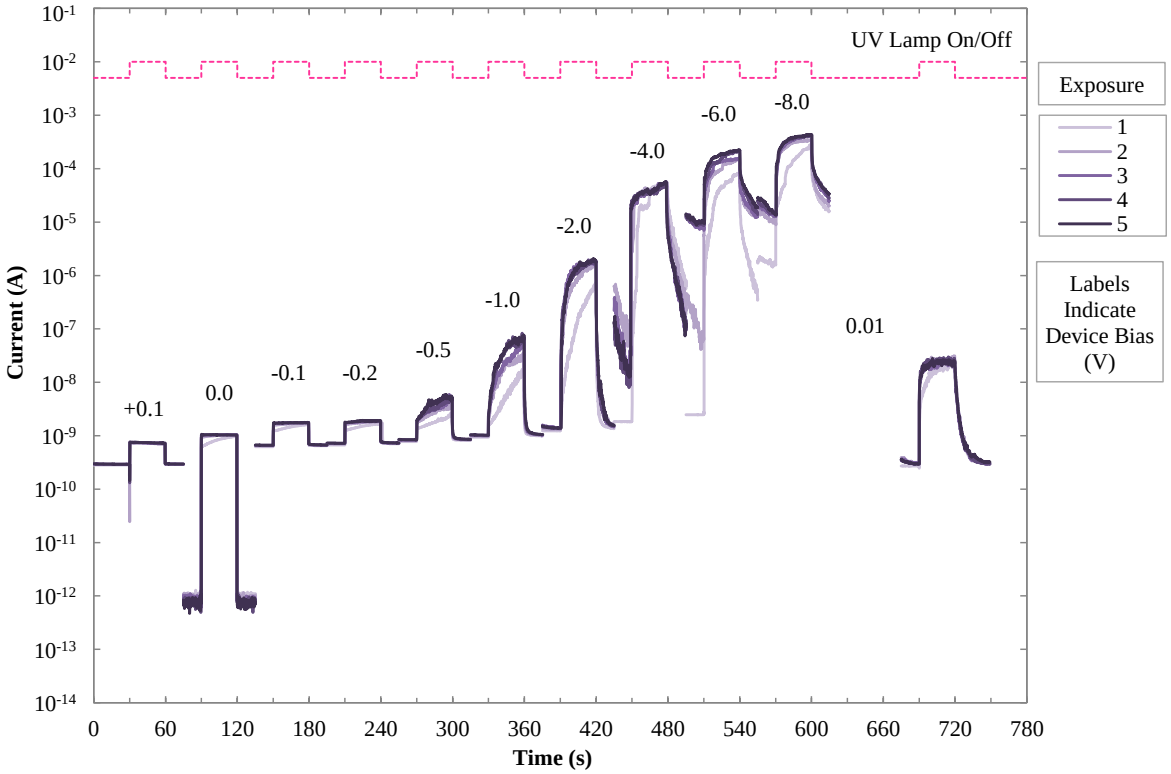

Figure 7.63: 0.5:10 (O_2:Ar) PtO_x 30 s UV Photoresponse with Varied Bias

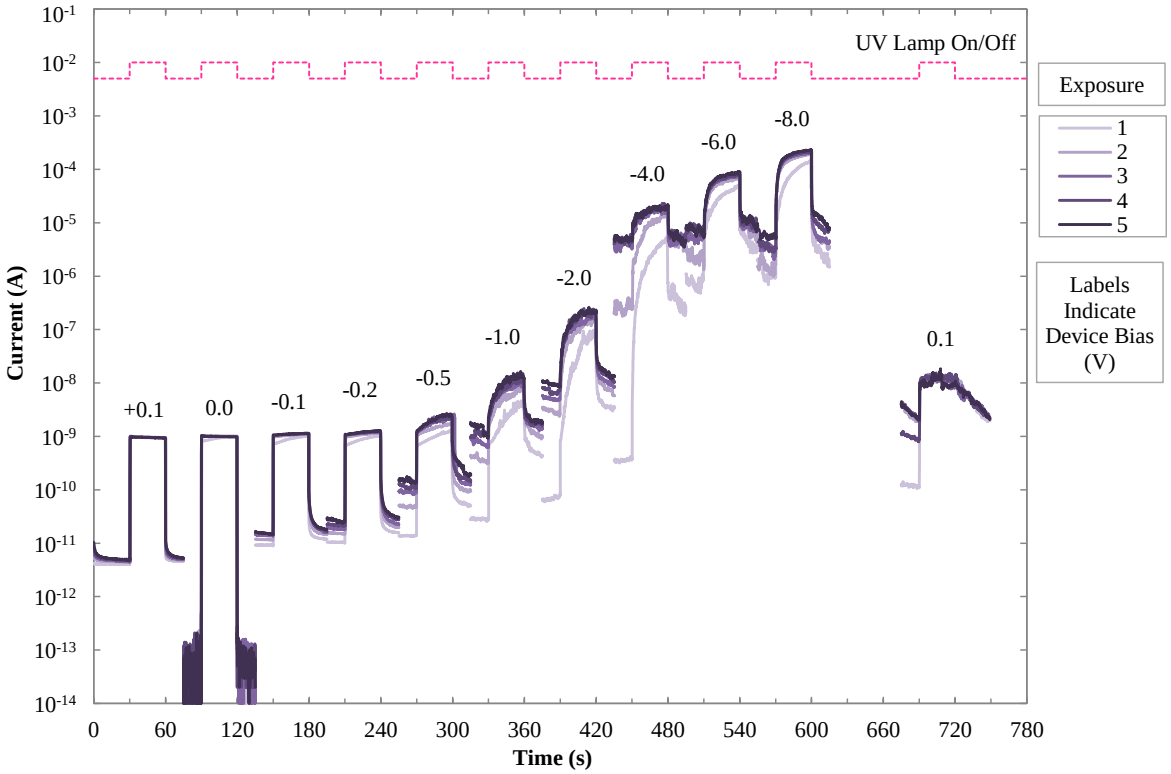

Figure 7.64: 1.0:10 (O_2:Ar) PtO_x 30 s UV Photoresponse with Varied Bias

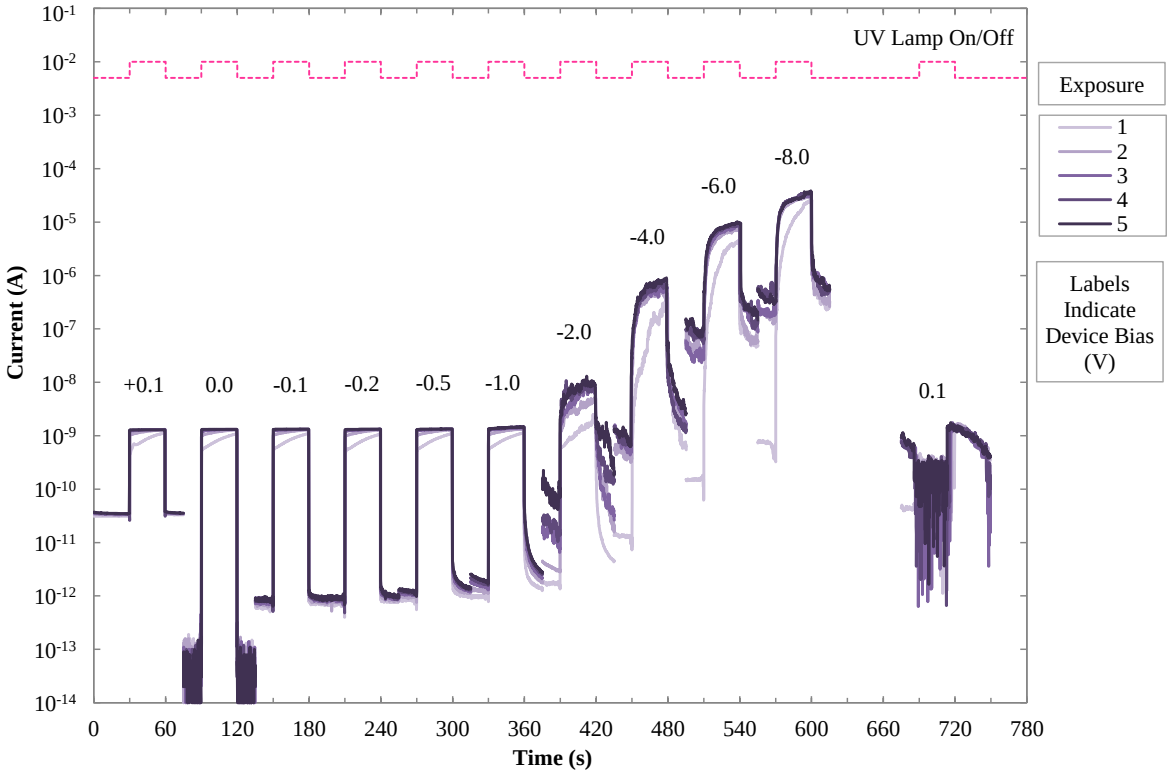

Figure 7.65: 2.0:10 (O_2:Ar) PtO_x 30 s UV Photoresponse with Varied Bias

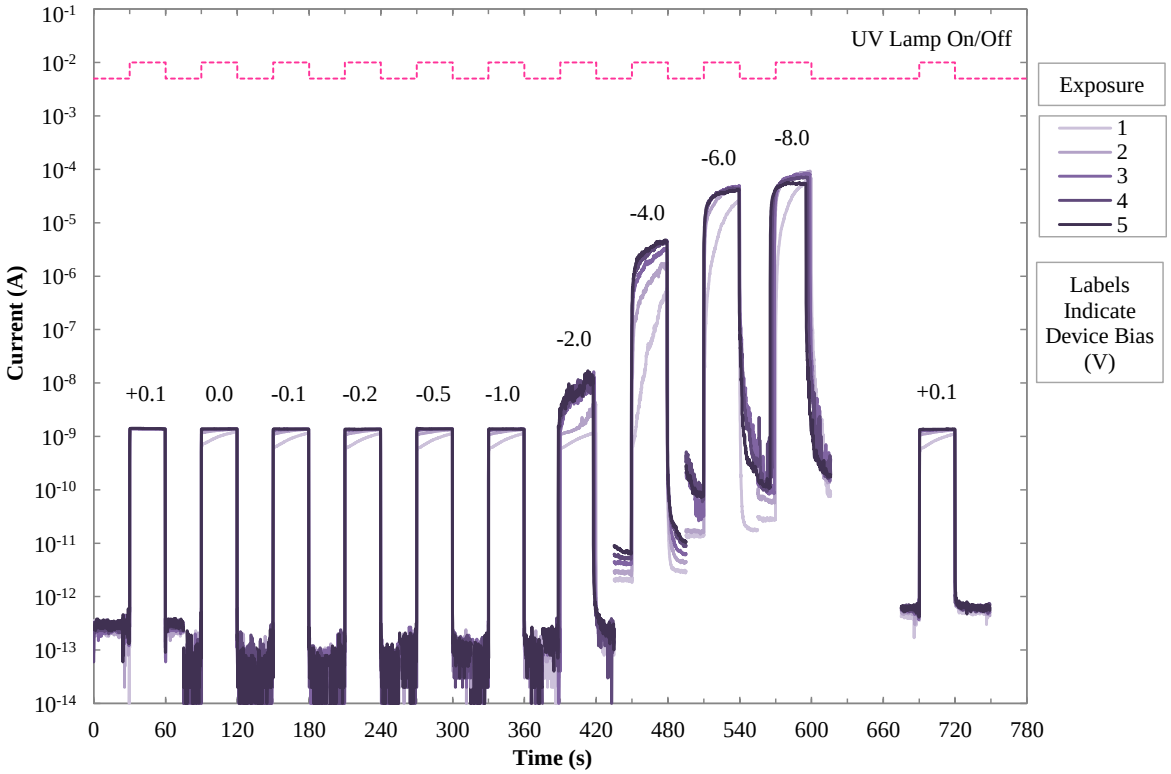

Figure 7.66: 3.0:10 (O_2:Ar) PtO_x 30 s UV Photoresponse with Varied Bias

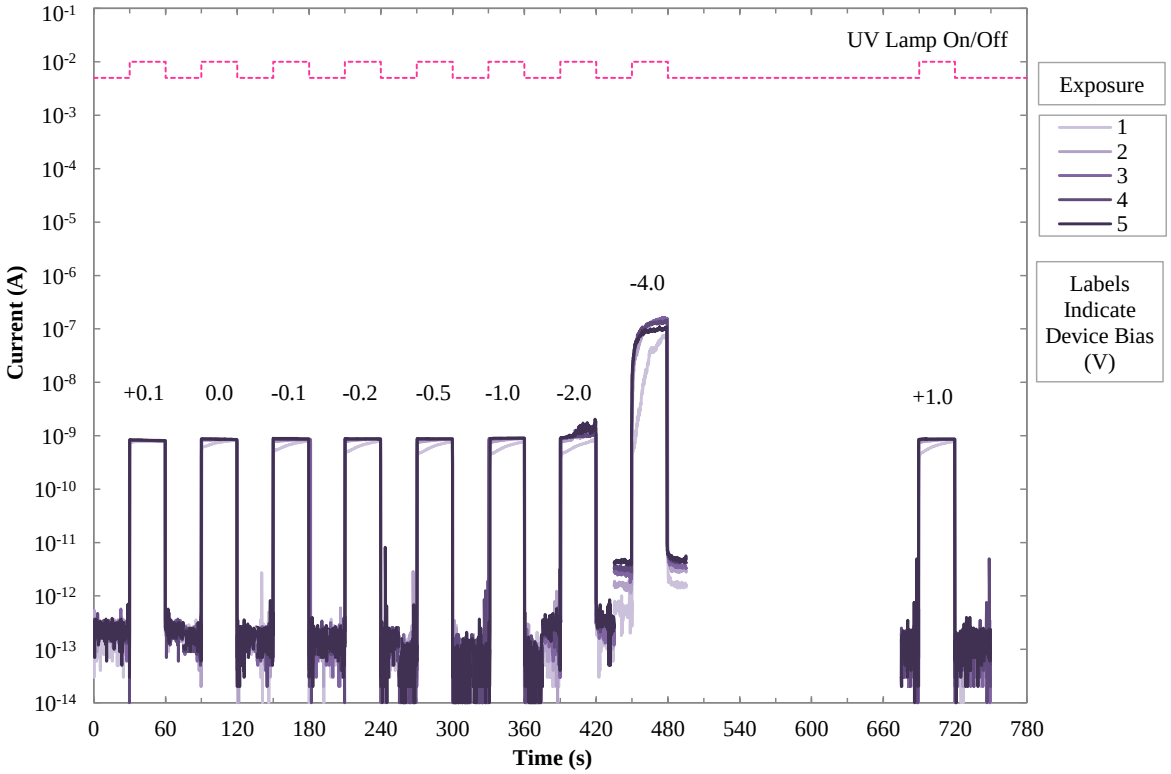

Figure 7.67: 4.0:10 (O_2:Ar) PtO_x 30 s UV Photoresponse with Varied Bias

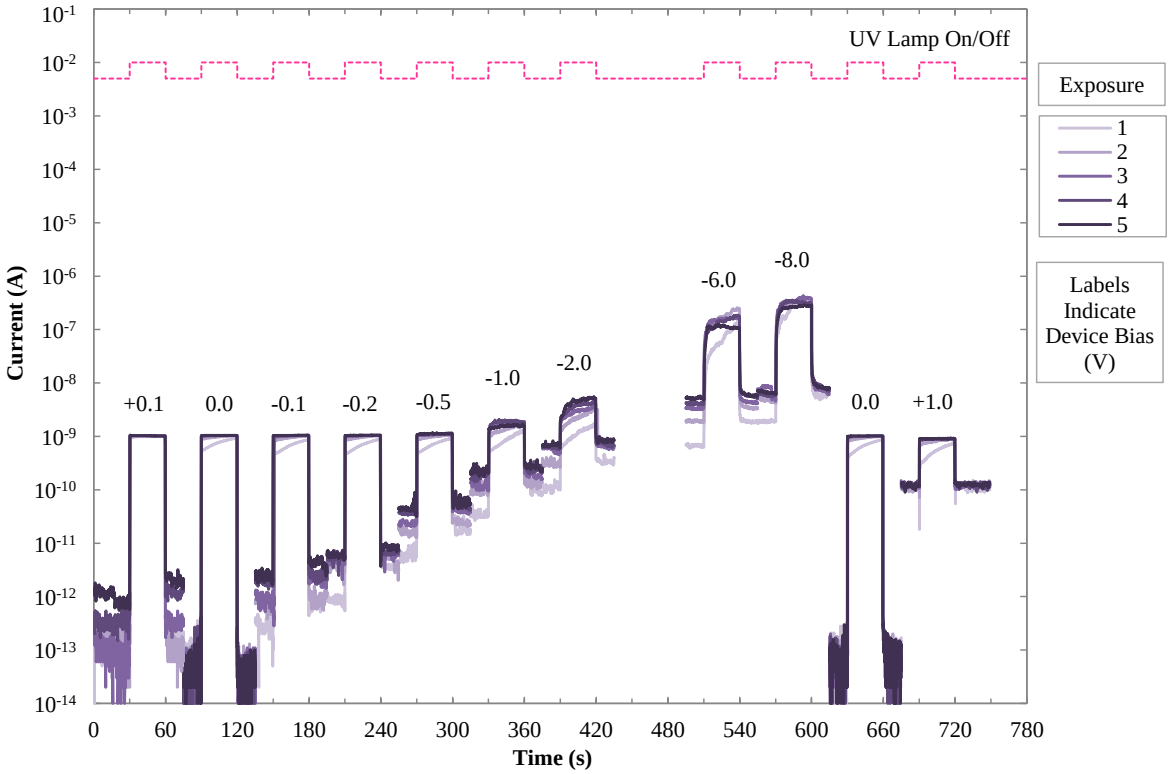

Figure 7.68: 5.0:10 (O_2:Ar) PtO_x 30 s UV Photoresponse with Varied Bias

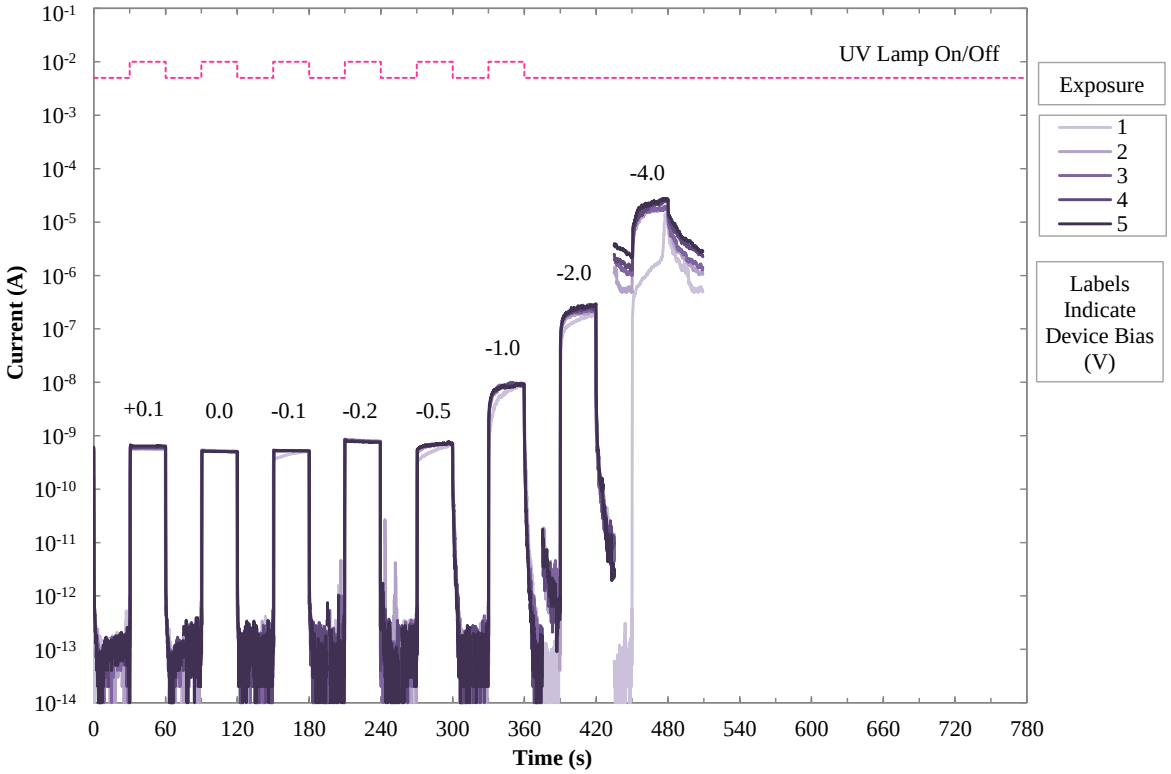

Figure 7.69: 7.0:10 (O_2:Ar) PtO_x 30 s UV Photoresponse with Varied Bias

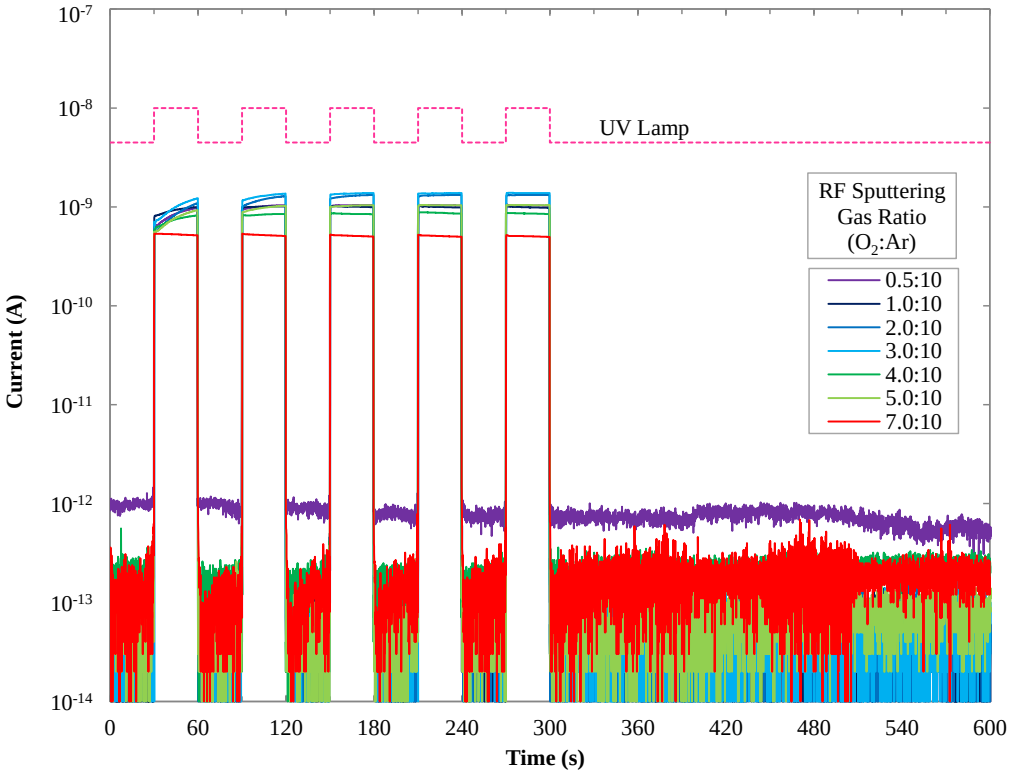

Figure 7.70: 0.5:10 – 7.0:10 (O_2:Ar) PtO_x 30 s UV Photoresponse with 0 V Bias

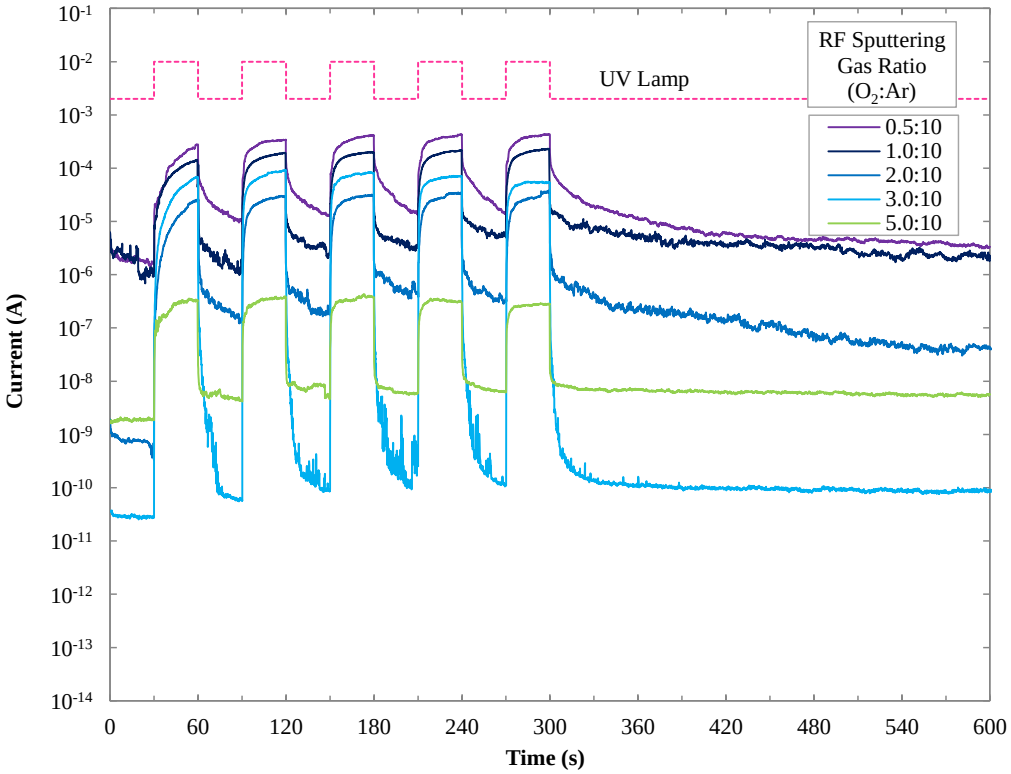

Figure 7.71: 0.5:10 – 5.0:10 (O_2:Ar) PtO_x 30 s UV Photoresponse with -8 V Bias

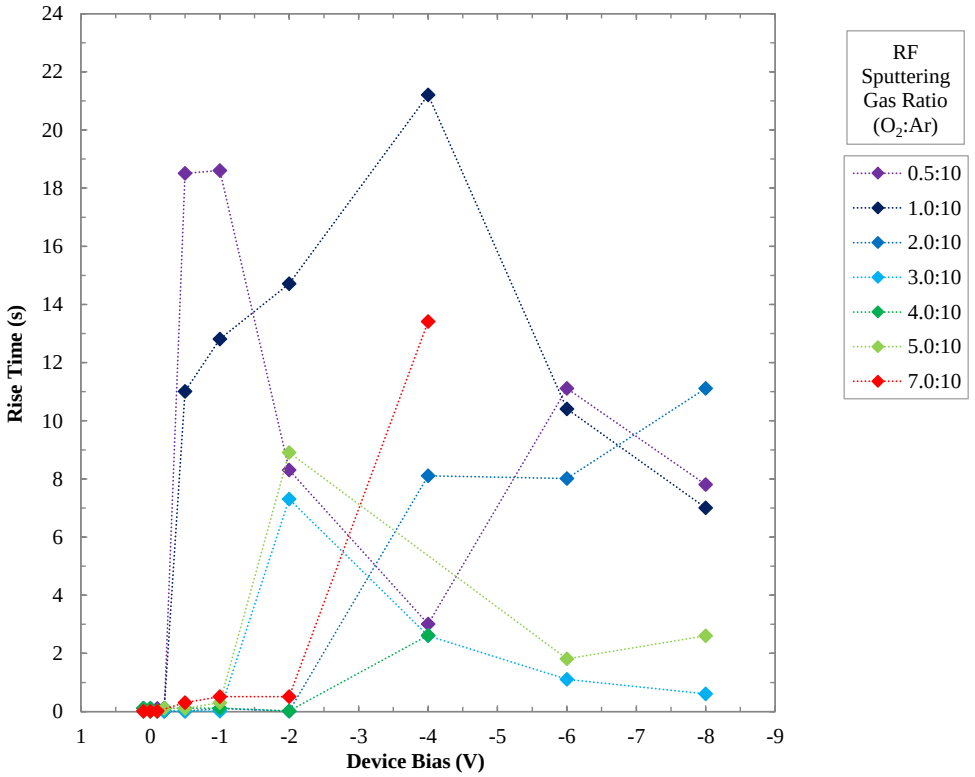

Figure 7.72: PtO_x 30 s UV Photoresponse with Bias (Fifth Pulse), Rise-Time

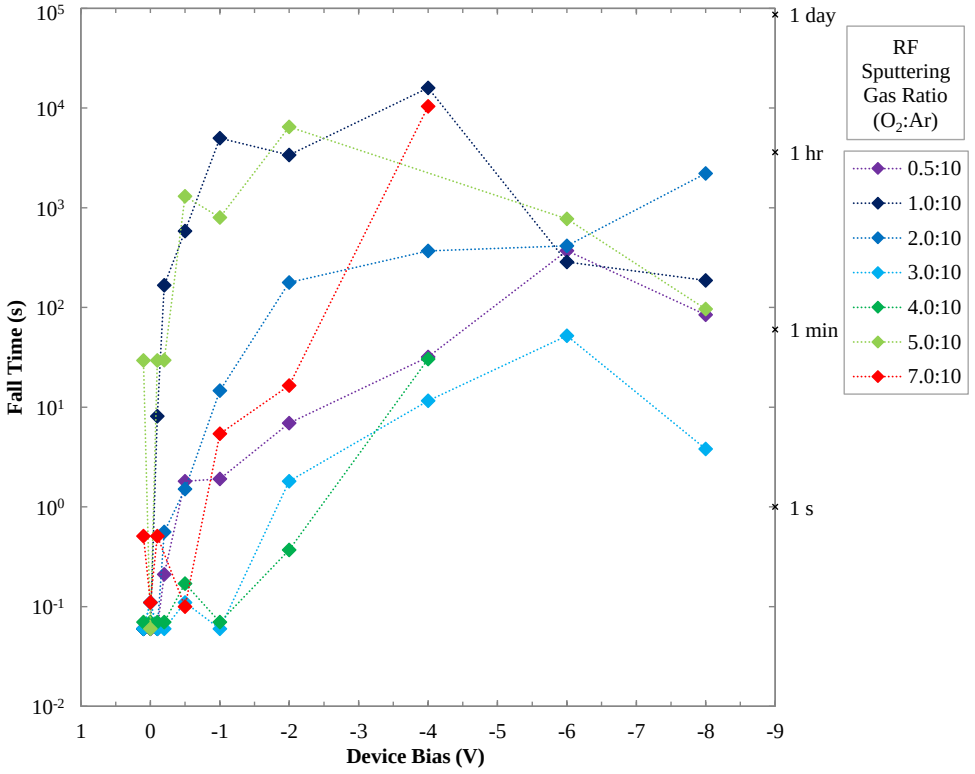

Figure 7.73: PtO_x 30 s UV Photoresponse with Bias (Fifth Pulse), Fall-Time

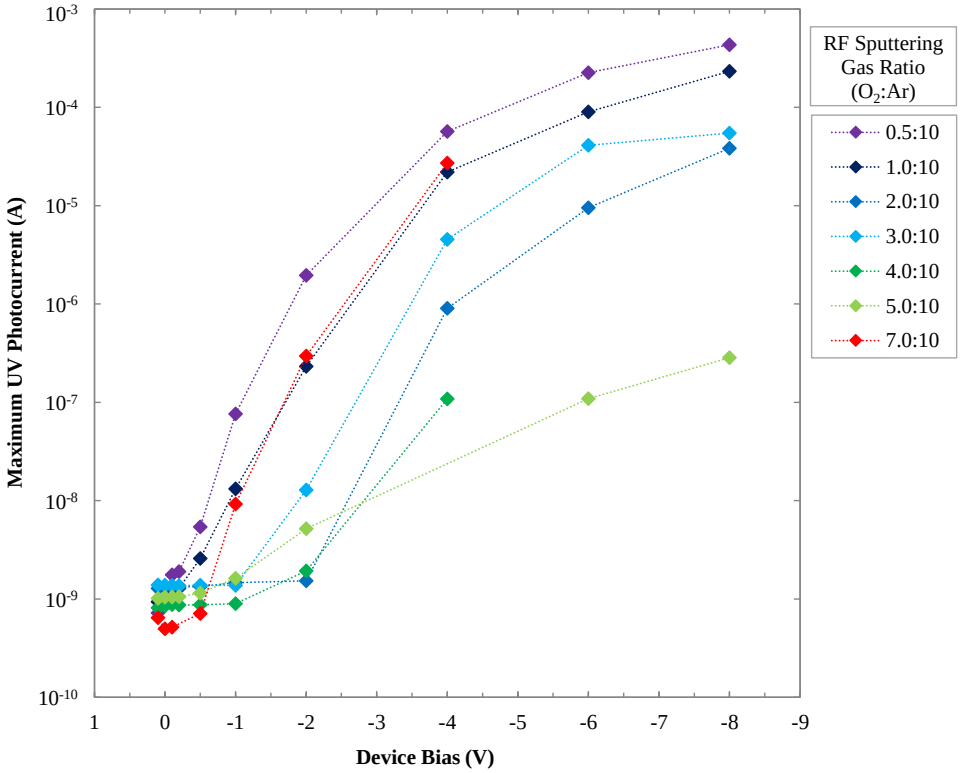

Figure 7.74: PtO_x 30 s UV Photoresponse with Bias (Fifth Pulse), Maximum Current

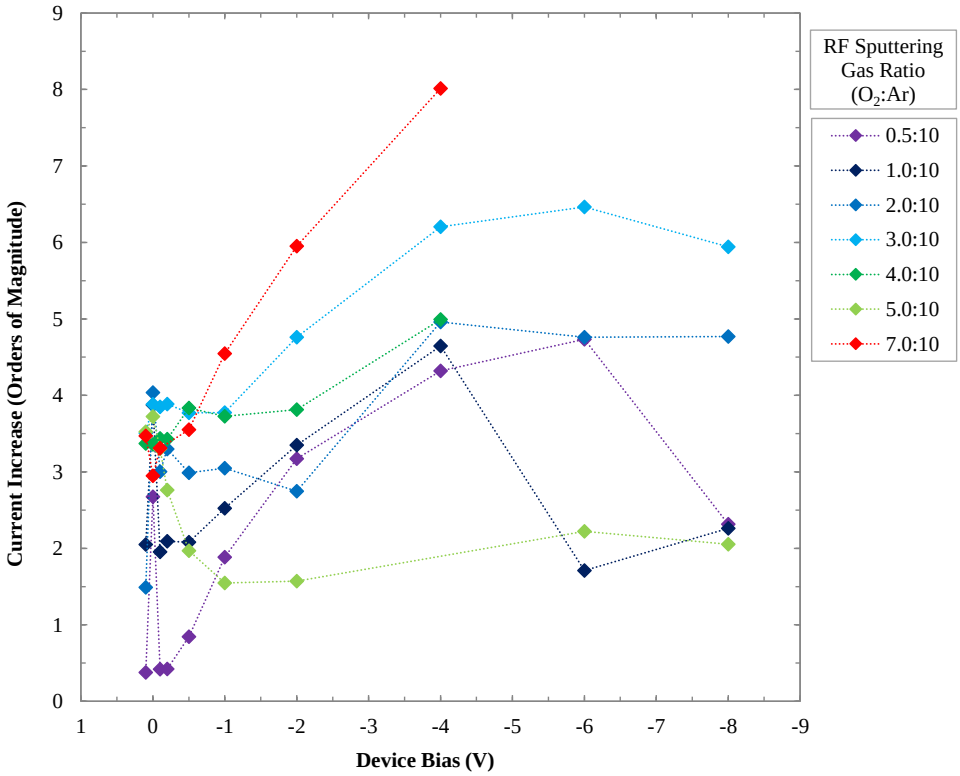

Figure 7.75: PtO_x 30 s UV Photoresponse with Bias (Fifth Pulse), Current Increase

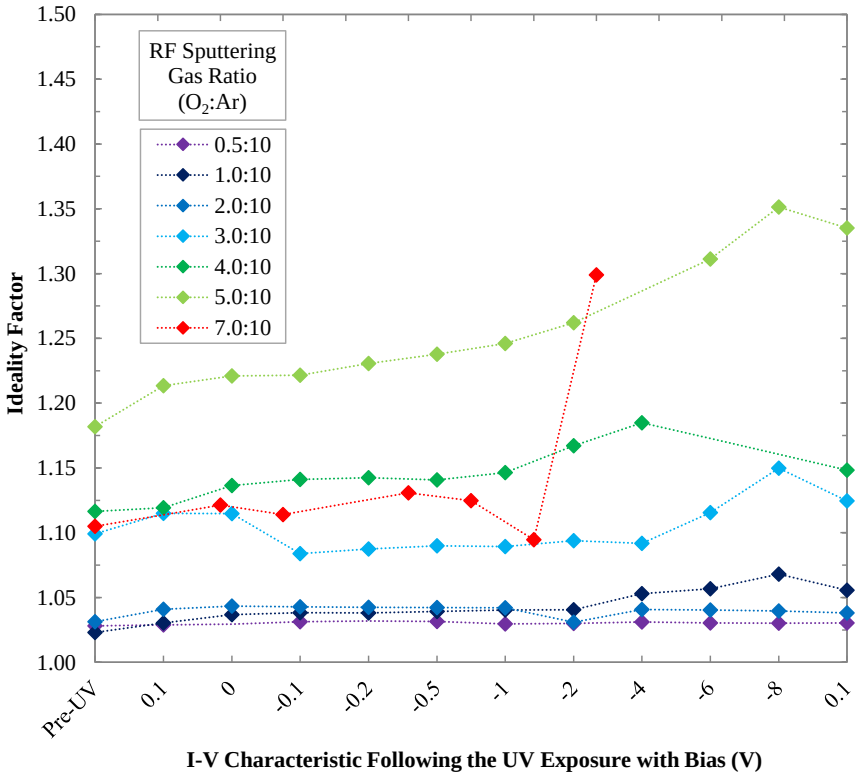

Figure 7.76: PtO_x Dark I-V UV Photoresponse with Bias, Ideality Factors

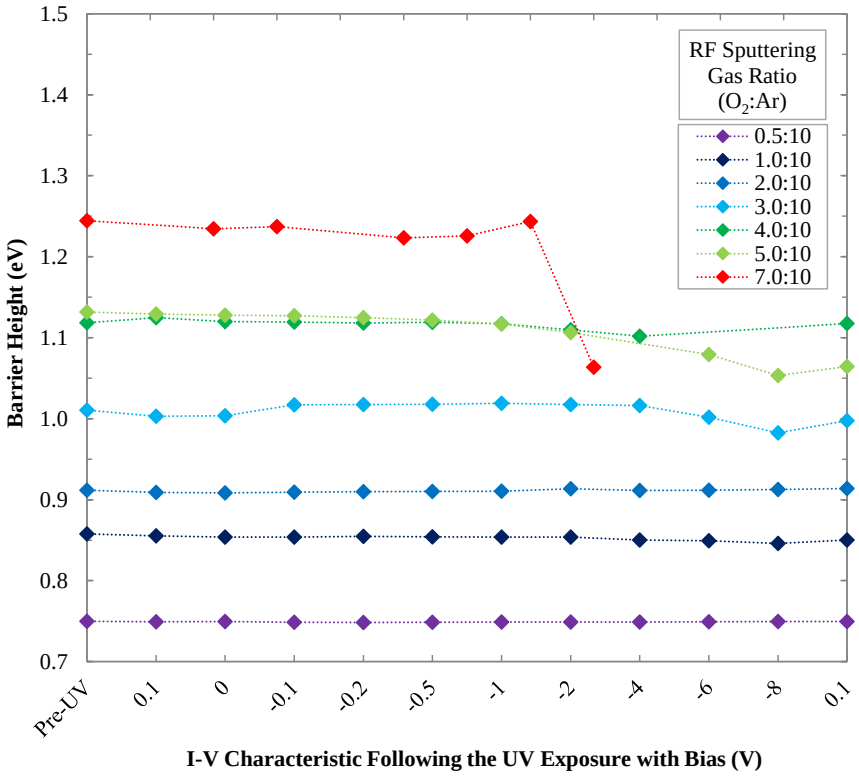

Figure 7.77: PtO_x Dark I-V UV Photoresponse with Bias, Barrier Heights

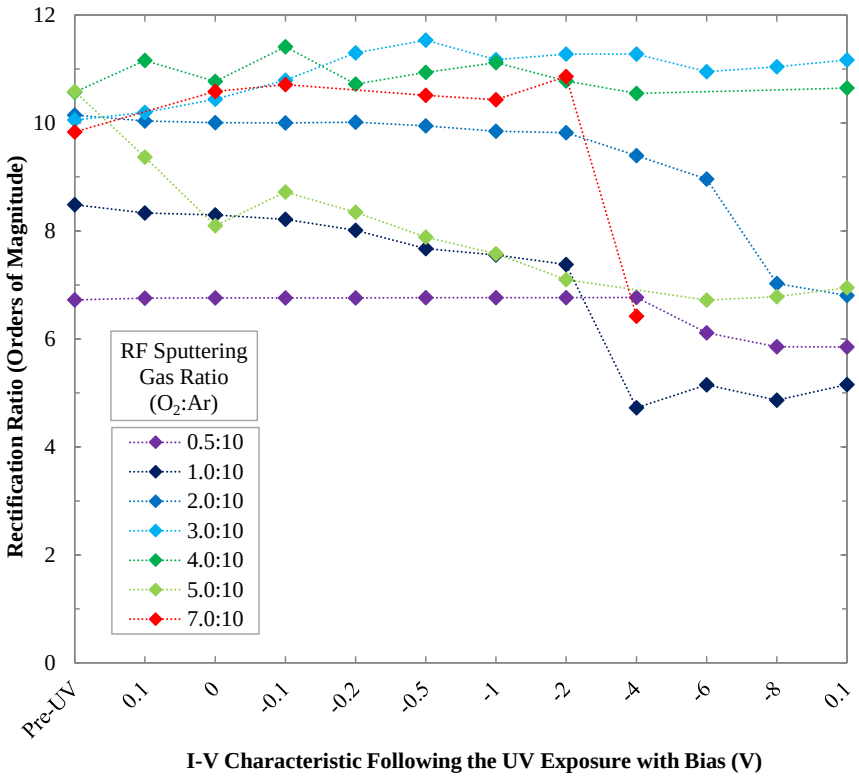

Figure 7.78: PtO_x Dark I-V UV Photoresponse with Bias, Rectification Ratios

Figure 7.71 shows the UV photoresponse of a plain Pt contact. Due to the lack of rectification, the photoresponse increase was less than 0.025 O_{Mag}, as shown in Figure A7.44 of Appendix A7.8, where the UV photoresponse show in 7.71 is normalised for the initial dark current. Due to the low level of photoresponse, the plain Pt contact was not included in further analysis.

The UV photoresponses of the PtO_x contacts in Figures 7.63 – 7.69 show the same trend of increasing photoresponse with increasingly negative device bias, with all contacts showing a maximum UV photocurrent with the most-negative bias used, in contrast to the PdO_x contacts, of which the majority showed a maximum photocurrent at -4.0 V, with a lower photocurrent at -6.0 V.

Figures 7.63 – 7.67 also show the square-wave UV photoresponse extends further into the negative bias tests with increasing oxygen incorporation for the 0.5:10 to 4.0:10 (O_2:Ar) PtO_x contacts, as was observed for the PdO_x contacts, from -0.2 V to -2.0 V bias. However, the 5.0:10 and 7.0:10 (O_2:Ar) PtO_x contacts in Figures 7.68 – 7.69 show the square-wave behaviour only extending to -0.5 V. The oxygen incorporation of the PtO_x films from RBS (Section 5.6) is included in Figure 7.79, and shows that the oxygen incorporation jumps from $x < 2$ to $x > 2$ between 4.0:10 and 5.0:10 (O_2:Ar) PtO_x, which could account for the change in UV photoresponse stability.

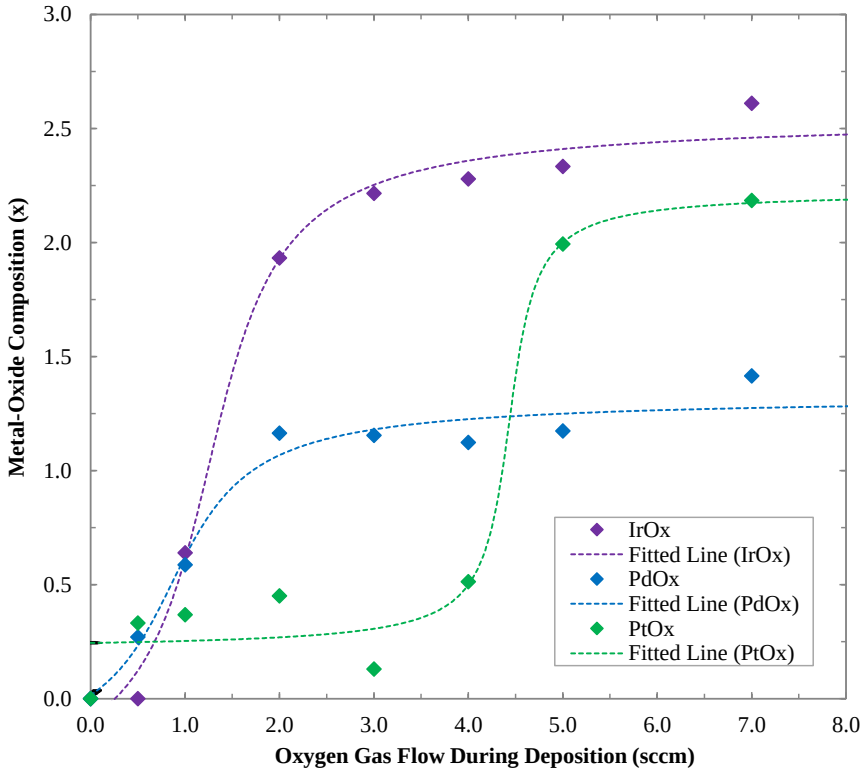

Figure 7.79: Oxygen Incorporation of RF-Sputtered Films with O_2:Ar Ratio from RBS

The UV photoresponse of PtO_x contacts with increasing oxygen incorporation and 0 V bias shown in Figure 7.70 displays a trend of increasing and decreasing UV photocurrent with increasing oxygen incorporation, with a maximum UV photocurrent of 1.39 nA for 3.0:10 (O_2:Ar) PtO_x. Figure 7.71 also shows a trend of decreasing PPC for the PtO_x device biased at -8.0 V with increasing oxygen incorporation, which is shows the opposite of the trend shown for PdO_x in Figure 7.53. The trend of decreasing maximum UV photocurrent with increasing oxygen incorporation of the PtO_x contacts can also be seen in Figure 7.74, however the fall-times of the PtO_x contacts in Figure 7.73 calculated from the UV photoresponse measurements in Figures 7.63 – 7.69 do not show a clear trend with increasing oxygen incorporation. The high fall-time of the 5.0:10 (O_2:Ar) PtO_x contact is due to unexpectedly high levels of PPC generated over successive UV exposures, compared to the rest of the PtO_x contacts, as shown in Figure 7.68. The rise-times of the PtO_x contacts in Figure 7.72 appear to follow a general trend of decreasing rise-time with increasing oxygen incorporation. The rise-times of the PdO_x contacts in Figure 7.54 showed a general trend of increasing rise-time with oxygen incorporation, in contrast.

The dark I-V characteristics did not show a considerable change in the ideality factors or barrier heights of the 0.5:10 – 2.0:10 (O_2:Ar) PtO_x contacts during the UV photoresponse measurements, as

shown in Figures 7.76 – 7.77, however the rectification ratio of all devices decreased with increasingly negative device bias UV photoresponse measurements, as shown in Figure 7.78, due to higher levels of PPC. For the 3.0:10 – 7.0:10 (O_2:Ar) PtO_x contacts, the ideality factors and barrier heights showed a decrease in performance with successive UV photoresponse measurements with increasingly negative device bias, but also showed recovery after the final, positive 0.1 V bias measurement. A similar trend to what was observed from the dark I-V characteristics of the PdO_x contacts, showing potential for the mitigation of PPC with positive device bias between exposures.

The long-term stability of the 7.0:10 (O_2:Ar) PtO_x contact was also tested with 54 pulses of 30 s of UV radiation over a 1-hour period, with a device bias of 0.1 V, shown in Figure 7.80. Dark I-V measurements taken before and after the 1-hour measurement did not show any significant change in ideality factor, barrier height, or rectification ratio, indicating no device degradation from the 1-hour measurement.

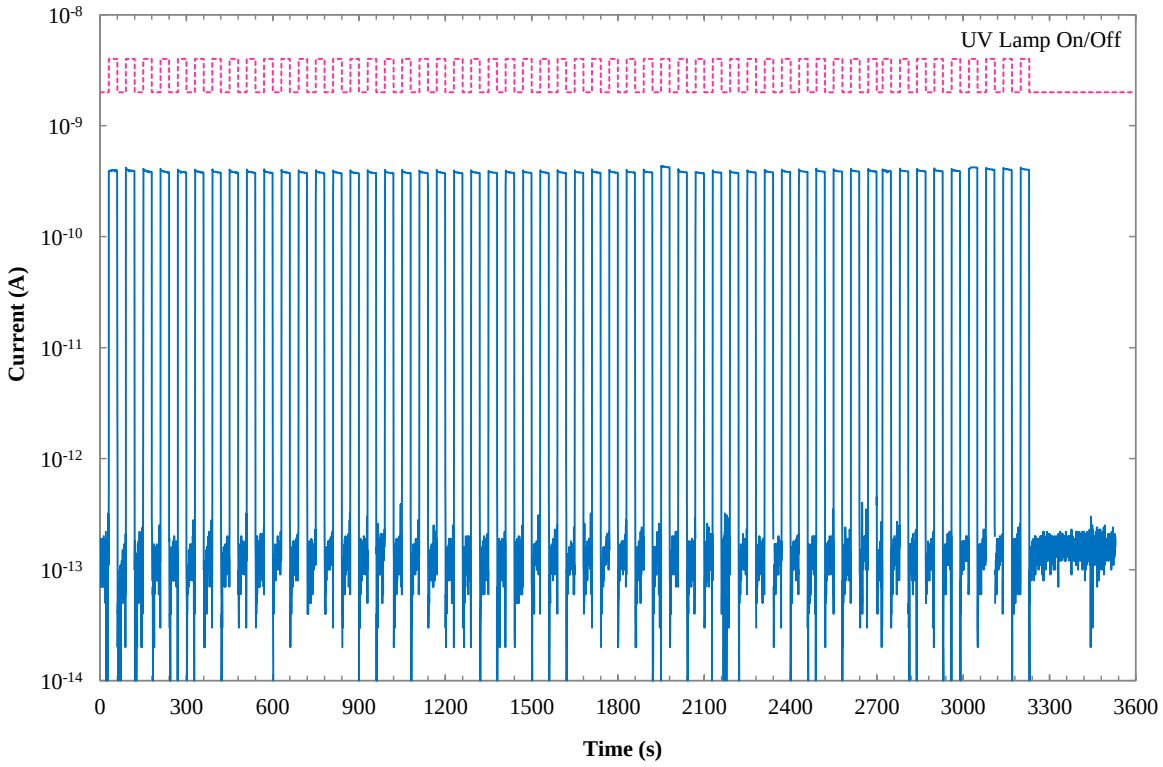

Figure 7.80: 7.0:10 (O_2:Ar) PtO_x 30 s Continual Pulsed UV Photoresponse, 0.1 V Bias

The photoresponse shown in Figure 7.80 shows a high level of stability and responsivity with respect to time, showing no signs of PPC and negligible rise in dark-current. Despite the < 1 nA photocurrent, the current increase is over 3 O_{Mag}. This shows that if the bias is not sufficient to induce PPC during the first few exposures, long-term development of PPC is unlikely.

7.7 Comparison of Ultraviolet Photoresponse of Metal Oxide Contacts with Oxygen Content

The comparison of the UV photoresponses of the RF-sputtered noble metal and metal-oxide Schottky contacts to Zn-polar –c-plane and +c-plane (low-lithium) bulk ZnO consists of the UV photoresponse selectivity (UVPS), and a comparison of the rise-time, fall-time, maximum UV photocurrent and current increase of all devices measured at -1.0 V bias. The UV photoresponse measurements of all devices measured in this chapter included the measurement of 5 pulses of 30 s UV radiation with a device bias of -1.0 V, enabling this comparison.

The UVPS of the IrO_x, PdO_x, and PtO_x devices to UV wavelengths was calculated by averaging the difference in current increase (in O_{Mag}) from the scaled UV photoresponse at -1.0 V to the visual wavelength photoresponse at -1.0 V, as shown in Equation 7.3, where $CI_{UV\text{-}\lambda}$ is the difference in O_{Mag} current increase of the device to UV and a light source of wavelength λ. The selectivity of the devices is plotted against oxygen incorporation in Figure 7.81 from RBS measurements shown in Figure 7.79, from RBS results discussed in Section 5.6.

$$UVPS = \overline{\Delta CI_{UV-Red} + \Delta CI_{UV-Orange} + \Delta CI_{UV-Green} + \Delta CI_{UV-Blue}} \quad (7.3)$$

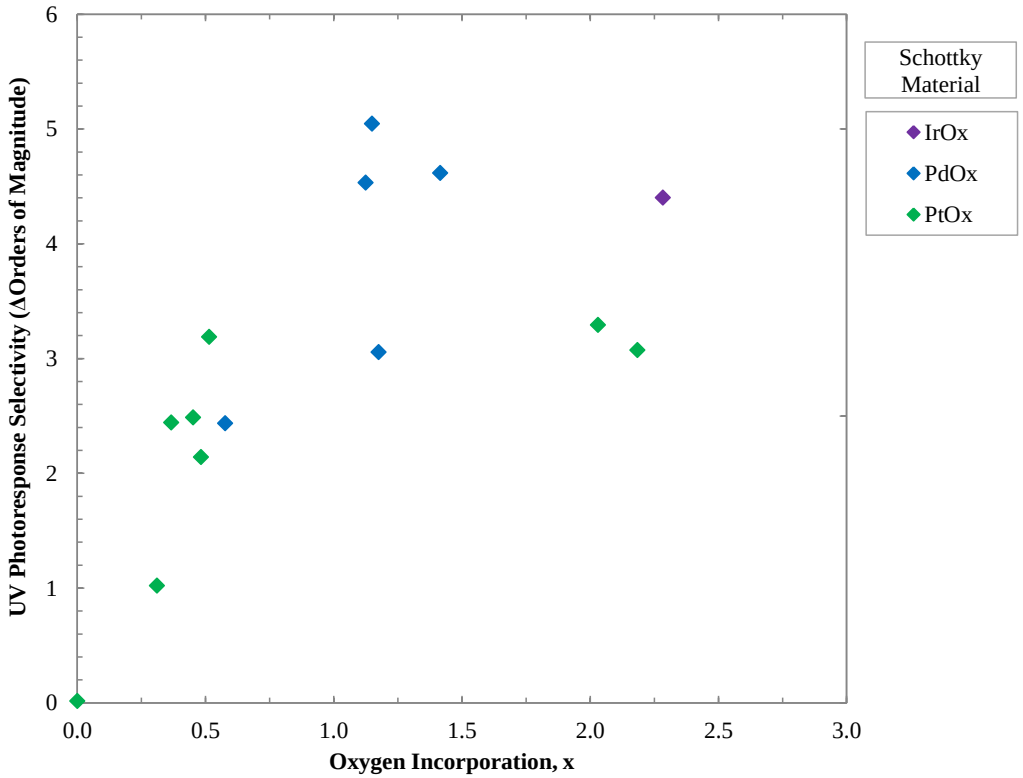

Figure 7.81: UVPS of IrO_x, PdO_x, and PtO_x Contacts with Oxygen Incorporation, -1.0 V

Figure 7.81 shows that the RF-sputtered noble metal-oxide Schottky contacts to ZnO produced up to 5.1 O_{Mag} more photocurrent on average to UV light than to visible light. The UV selectivity of the devices was also observed to increase with increasing oxygen incorporation, reaching a plateau around 4 – 5 O_{Mag}. For the development of UV dosimeters on ZnO, devices with higher UVPS require less filtering of incident light. The IrO_x and PdO_x contacts displayed the highest levels of UVPS, over 4 O_{Mag} above $x > 1$. The PtO_x contacts showed a maximum UVPS of 3.3 for $x = 2$.

While the selectivity of UV photodetectors to visible wavelengths is not reported by standard metric in the literature, 'visible blind' UV photodetectors have been published by Dogar, S., et. al., where the responsivity of ZnO nanowire-gated AlGaN/GaN high electron mobility transistors (HEMTs) UV photodetectors was shown to be at least one order of magnitude lower for wavelengths greater than 400 nm [7.1]. The selectivity of UV photodetectors has also been associated to the device bias by Campos, L. C., et. al., showing greater selectivity between UV and visible wavelengths with device bias [7.2].

Figures 7.82 – 7.83 show the rise-time and fall-time of the noble metal-oxide contacts (-1.0 V bias) with O_2:Ar gas ratio. Plots of the UV photoresponse comparison of the IrO_x, PdO_x, and PtO_x contacts with oxygen incorporation, x, are included in Figures A7.46 – A7.49 of Appendix A7.9.

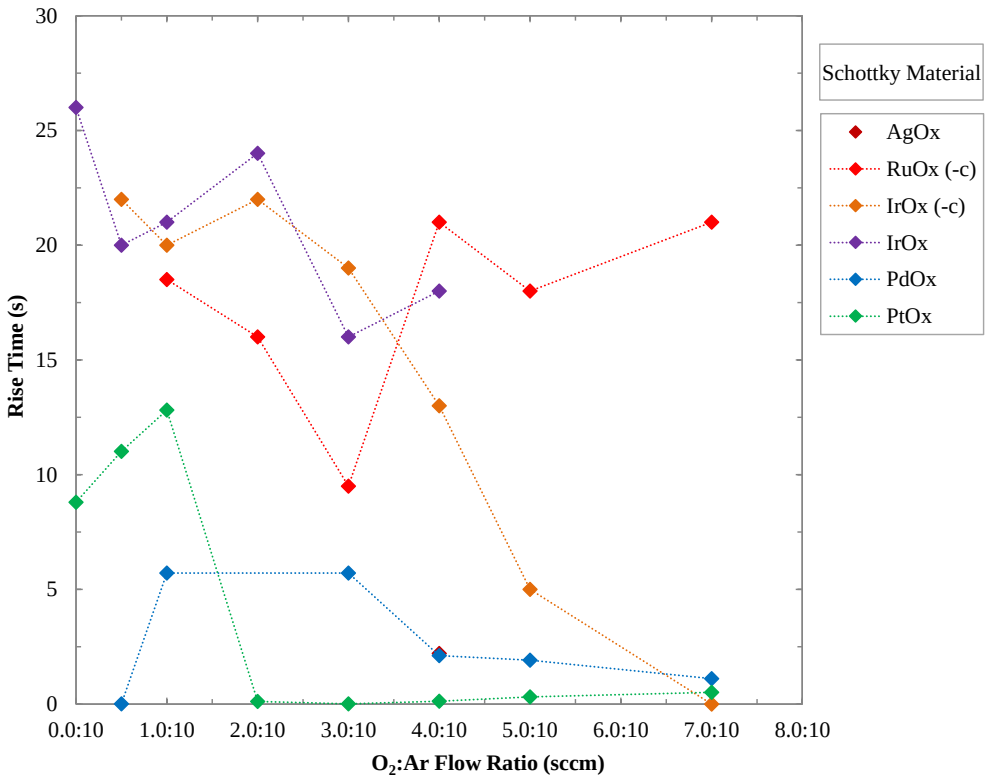

Figure 7.82: UV Photoresponse of All Contacts, -1.0 V, Fifth Exposure, Rise-Time

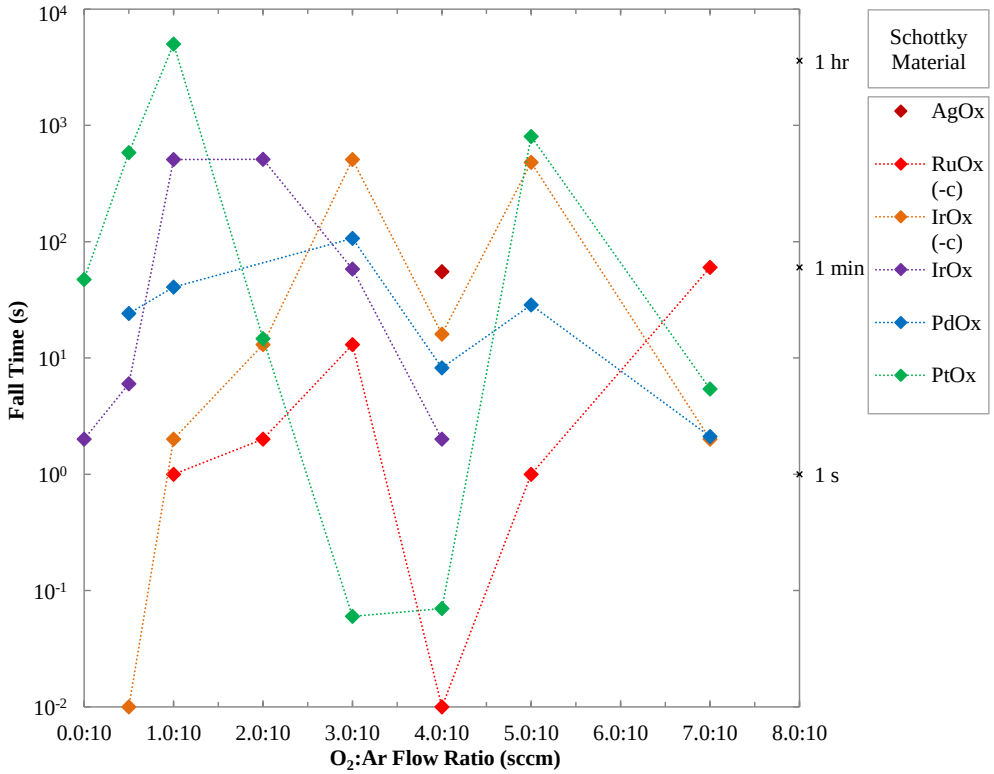

Figure 7.83: UV Photoresponse of All Contacts, -1.0 V, Fifth Exposure, Fall-Time

The rise-time of the devices in Figure 7.82 shows, for a -1.0 V bias, the fifth rise-time of the contacts ranged between 0 s for 0.5:10 (O_2:Ar) PdO_x and 2.0:10 – 4.0:10 (O_2:Ar) PtO_x, to 26 s for Ir. The rise-time of the 4.0:10 (O_2:Ar) AgO_x and PdO_x contacts were both 2.2 s. The IrO_x contacts to both –c-plane and +c-plane (low-lithium) ZnO followed a similar trend with increasing O_2:Ar ratio, implying that the Schottky contact material had a greater impact on rise-time than the ZnO type. There is no clear overall trend in rise-time with increasing O_2:Ar ratio shown in Figure 7.82, as the IrO_x contacts show a decrease, the RuO_x contacts show an increase, and the PdO_x and PtO_x contacts show mixed trends in rise-time with increasing O_2:Ar ratio. The initially high rise-times for the 0.0:10 – 1.0:10 (O_2:Ar) contacts is due to the low levels of UV photocurrent. Rise-time measured with oxygen incorporation, shown in Figure A7.46, shows steep drop-offs in rise-time for IrO_x, PdO_x, and PtO_x at x = 2.0, 1.1, and 0.4, respectively, showing some evidence towards rise-time decreasing with increasing oxygen incorporation.

Figure 7.83 shows, following the fifth pulse of 30 s UV exposure with -1.0 V bias, the fall-time of the devices ranged from 0.01 s (used to plot a measurement of 0 s on the log-plot of fall-time) for 0.5:10 (O_2:Ar) IrO_x and 4.0:10 (O_2:Ar) RuO_x to –c-plane ZnO, to over an hour for 1.0:10 (O_2:Ar) PtO_x. The overall trend of the fall-time with increasing O_2:Ar ratio shows a decreasing rise-time,

with a minimum around 4.0:10 (O_2:Ar), and having low fall-times is essential to producing an accurate UV photodetector. The 3.0:10 – 4.0:10 (O_2:Ar) PtO_x contacts showed the lowest consecutive fall-times, with < 0.1 s. The comparison of the IrO_x, PdO_x, and PtO_x contacts with oxygen incorporation in Figure A7.47 shows trends of increasing fall-times, with sharp drop-offs at x = 2 – 2.5 for IrO_x, x = 1.1 for PdO_x, and x = 0.4 and 2.0 for PtO_x. This could indicate a relation between rise-time, fall-time, and metal-oxide composition.

The rise-times and fall-times of UV photodetectors fabricated with ZnO in the literature ranges from a rise-time of less than 12 ns and a fall-time of less than 50 ns (Ag Schottky contacts to ZnO), to devices that do not show an apparent saturation in UV photocurrent and showed PPC lasting for hours or days [7.3 – 7.8]. The lower limit of the response time of the UV photodetectors, the fast-response, requires the elimination of PPC in the devices, and is the most significant issue facing ZnO-based UV photodetectors [7.3 – 7.8].

The rise-time and fall-time of the UV photoresponse has been modelled by stretched exponentials in literature, as shown for Equations 7.4 – 7.6 of Table 7.6, however these equations did not accurately fit the UV photoresponses measured in this work [7.4, 7.7, 7.9]. This is likely due to the UV response comprising of a slow-response and fast-response that are independent of each other, making a single model difficult to fit to the data from this work. Further work is required to investigate the fit of these decay models to the UV photoresponse data presented in this work, which was discontinued due to time constraints.

Table 7.6: UV PPC Models and Equations

Model	Equation	Equation Number
PPC Build-Up	$I_{PPC\ Build-Up}(t) = I_{Dark} + (I_{Max} - I_{Dark})(1 - \exp[-\alpha t])$	(7.4) [7.4]
PPC Decay	$I_{PPC\ Decay}(t) = I_{Dark} + (I_{Max} - I_{Dark}) \exp\left[-\left({}^{t}/_{\tau}\right)^{\beta}\right], (\beta < 1)$	(7.5) [7.4]
PPC Decay	$I_{PPC\ Decay}(t) = I_{Max} \exp\left[-\left({}^{t}/_{\tau}\right)^{\beta}\right]$	(7.6) [7.7, 7.9]

Figures 7.84 – 7.85 show the comparison of the maximum UV photocurrent and current increase of the metal-oxide contacts with a -1.0 V bias against O_2:Ar gas ratio. Plots of the UV photoresponse comparison with oxygen incorporation, x, are included in Figures A7.46 – A7.49 of Appendix A7.9. A plot of the trade-off between response current and time is shown in Figure 7.86.

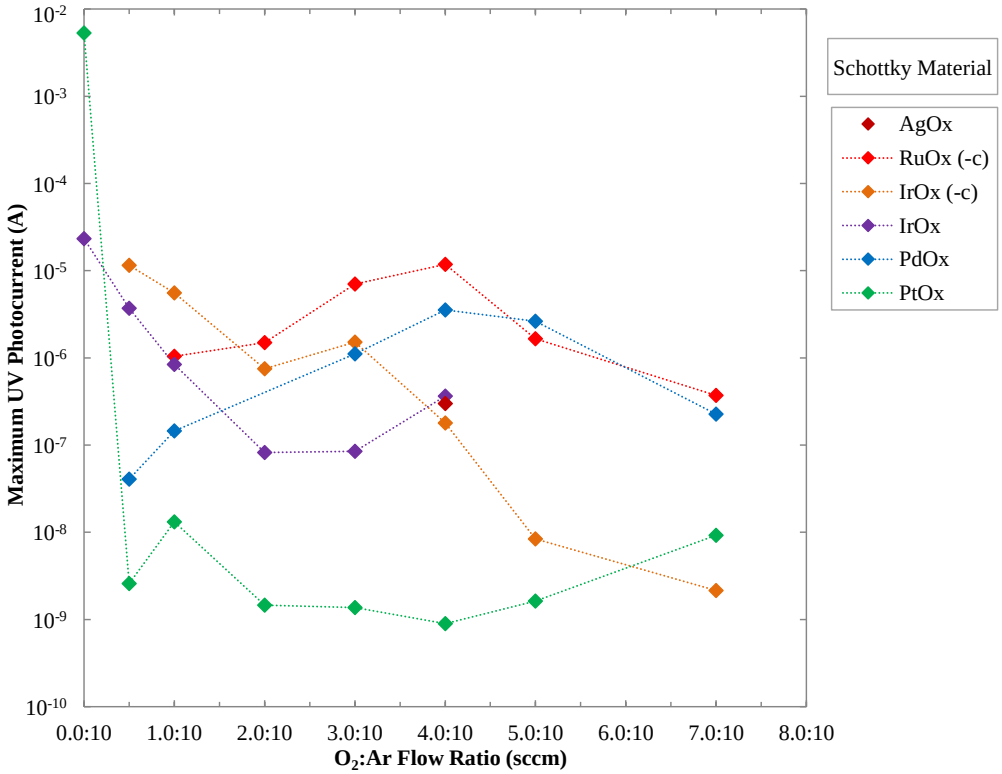

Figure 7.84: UV Photoresponse of All Contacts, -1.0 V, Fifth Exposure, Max. Photocurrent

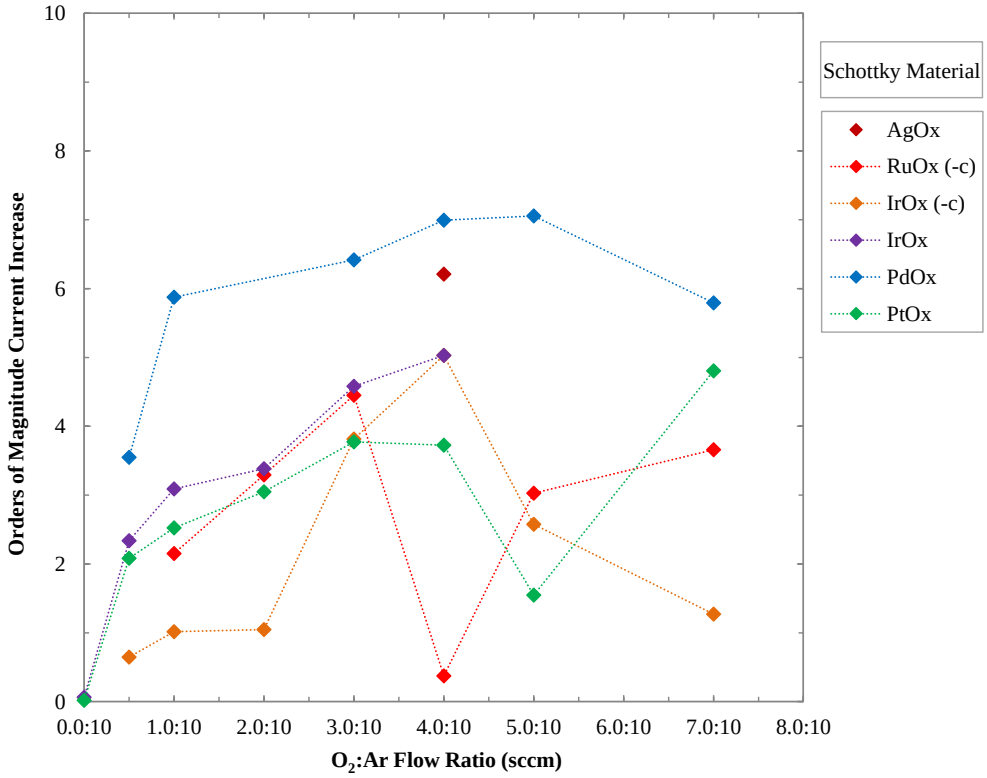

Figure 7.85: UV Photoresponse of All Contacts, -1.0 V, Fifth Exposure, Current Increase

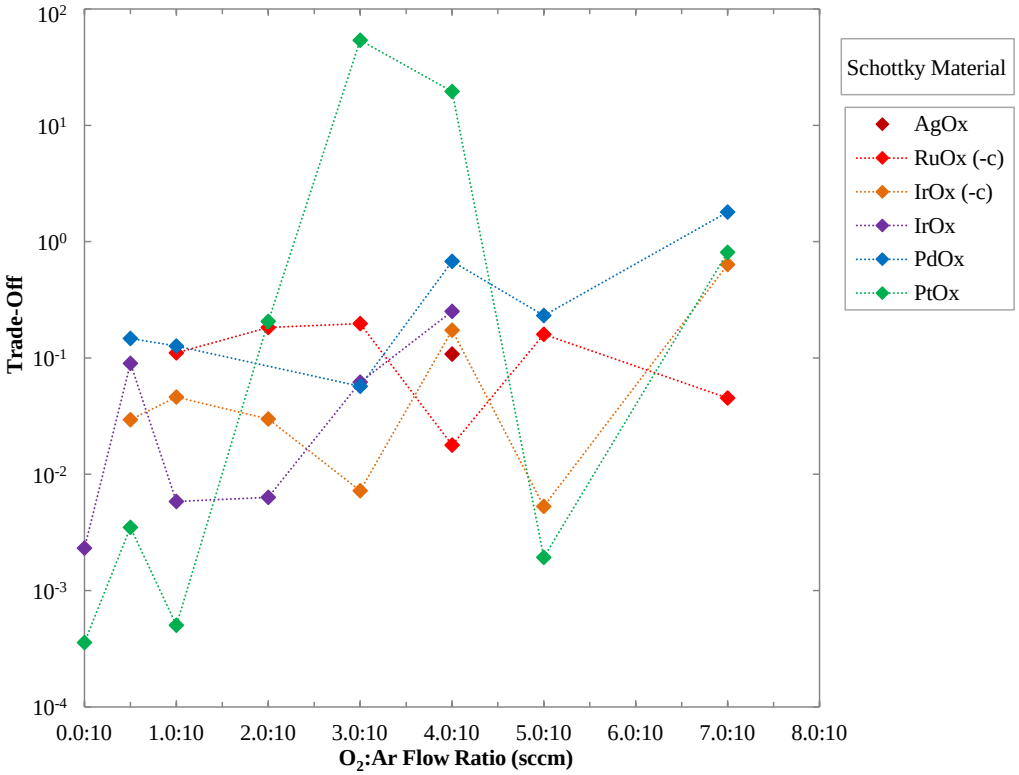

Figure 7.86: Trade-Off (Current Increase Divided by Rise-Time and Fall-Time), All Contacts

The maximum UV photocurrents shown in Figure 7.84 exhibits an overall trend of decreasing current with increasing O_2:Ar ratio, but with significant variation between trends. This is likely due to the trade-off between UV photocurrent and rise-time and fall-time caused by PPC, as well as the increasing contact rectification ratio with increasing oxygen incorporation. The RuO_x and IrO_x contacts to –c-plane ZnO show the highest UV photocurrent response of the metal-oxide contacts, with 11.5 – 11.8 μA, likely due to the higher concentration of impurities in the –c-plane ZnO used.

Figure 7.85 shows the current increase of the noble metal-oxide contacts, in O_{Mag}. With the exception of the IrO_x contacts to –c-plane ZnO, the devices show a trend of a larger current increase with increasing O_2:Ar ratio, with a sudden drop in current increase at 4.0:10 – 7.0:10, followed by further improvement in current increase. The level of UV photocurrent in ZnO-based UV photodetectors in literature ranges between nA and mA, depending on the UV illumination power, wavelength, and duration [7.3 – 7.6, 7.8]. Reduction of PPC has been shown to decrease the amount of UV photocurrent in literature, as shown in this work [7.3 – 7.6, 7.8].

In order to observe the effects of O_2:Ar ratio on the trade-off between UV response current and UV response time (in terms of rise-time and fall-time), a trade-off measurement was calculated for each device using Equation 7.7, where t_{rise} is rise-time and t_{fall} is fall-time. A higher value of

trade-off indicates a device performance more favourable for UV dosimetry; a high increase in current with a low rise-time and low fall-time. Figure 7.86 shows a strong trend of increasing trade-off with increasing O_2:Ar gas flow ratio, showing that the noble metal-oxide Schottky contacts improve in suitability for UV dosimetry applications with increasing levels of oxygen incorporation, as well as improving in selectivity as was shown in Figure 7.81. Despite the overall trend, the 3.0:10 – 4.0:10 (O_2:Ar) PtO_x contacts show the greatest potential for UV photodetection. Figures 7.66 – 7.67 also exhibit the stability of the devices to PPC with increasingly negative device bias, despite the low level of UV photoresponse selectivity shown in 7.81.

$$Trade - off = \frac{CI_{365\,nm}}{(t_{rise} + t_{fall})} \tag{7.7}$$

From the results presented in this work, the 3.0:10 (O_2:Ar) PdO_x Schottky contact was shown to have the greatest potential for UV photodetection applications, with the highest level of selectivity between UV and visible wavelengths measured in this work, 5.1 O_{Mag} greater current increase for UV over the average visible response (see Figures 7.45 and 7.61). The device also showed low values of rise-time and fall-time after 5 consecutive UV exposures, with 0 s and 2.7 s respectively. The 4.0:10 (O_2:Ar) PtO_x Schottky contact to +c-plane (low-lithium) ZnO also showed significant greatest potential for UV photodetection applications, despite the lower UV selectivity.

7.8 Photocurrent and Persistent Photoconductivity Mechanism Analysis

The generation of significant levels of PPC following the UV exposure of ZnO has been widely documented in the literature, as discussed in Section 2.4.6 [7.3 – 7.36]. The two primary causes of PPC in ZnO-based UV photodetectors are widely accepted in the literature as the near-surface desorption and re-adsorption of oxygen, and the metastable ionisation of oxygen vacancies (V_O) [7.3 – 7.36]. Other enviromental impact factors on PPC have also been suggested in the literature, such as the wavelength and intensity of the illumination, ambient gas mixture, humidity, temperature, and the ZnO crystal structure [7.3 – 7.4, 7.9 – 7.16]. Several publications have also investigated the impact of device bias on PPC, which has also been observed in literature as negative bias illumination stress (NBIS) on ZnO and ZnO-based devices in particular [7.8, 7.15 – 7.16].

A model explaining the mechanisms of UV PPC observed in this work is proposed in Sections 7.8.1 – 7.8.5, consisting of the charging and migration of oxygen vacancy (V_O) defect states, the surface desorption and re-adsorption of O_2 and H_2O species, the photoionisation of V_O to V_O^{2+}, and the electromigration of the V_O towards the Schottky interface with device bias [7.3 – 7.36].

7.8.1 Initial UV Photoresponse

It was observed in all the UV photoresponse figures in this work that the first UV photoresponse on initial UV illumination was considerably lower than subsequent UV photoresponses. It is proposed that the initial, slow UV photoresponse is caused by this initial charging and subsequent migration of the V_O defects towards the Schottky interface, where they then can be ionised at an increased rate during subsequent UV exposures [7.3, 7.15, 7.17 – 7.21]. Details of the ionisation and migration mechanisms of the V_O are covered in Sections 7.8.3 – 7.8.4.

7.8.2 Surface Effects

It has been proposed that holes generated in ZnO from UV irradiation migrate towards the surface where they neutralise negatively charged chemisorbed oxygen, water, and hydroxyl groups, allowing them to desorb from the ZnO surface [7.3, 7.6 – 7.7, 7.12 – 7.14, 7.22]. The desorption of these surface species removes some of the photogenerated holes, leaving behind a surplus of photogenerated electrons that contribute towards the long-term decay of PPC once the UV radiation source is removed, as shown in Figure 7.87 [7.3, 7.6 – 7.7, 7.12 – 7.14, 7.22]. Oxygen desorption has also been suggested to occur at grain boundaries within ZnO thin films [7.7, 7.11]. The desorption of chemisorbed surface species changes the surface chemistry of ZnO, reducing downward band bending caused by the chemisorbed species, therefore reducing the depletion region, and increasing conductivity across the device junction [7.13, 7.23 – 7.26].

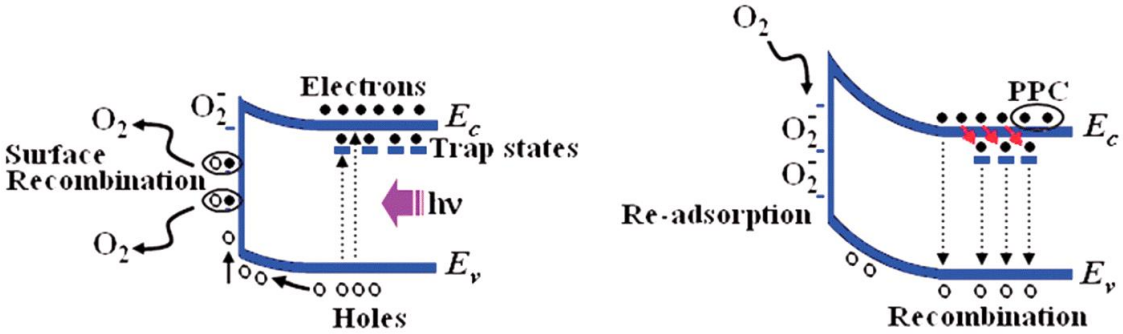

Figure 7.87: ZnO Oxygen Desorption and Re-adsorption of Surface Oxygen [7.6]

The rate of decay of PPC in ZnO has been found to be sensitive to the gas environment, showing different rates of decay in the presence of wet or dry oxygen, pure nitrogen, air, and under vacuum conditions [7.3, 7.13 – 7.14, 7.24, 7.27 – 7.28]. UV photoresponse measurements under

vacuum conditions have shown a significantly longer PPC decay time, supporting the theory of oxygen desorption and re-adsorption from the ZnO surface with UV radiation [7.3, 7.27].

UV photoresponse measurements were made on the 4.0:10 (O_2:Ar) AgO_x Schottky contact fabricated for this work under normal atmospheric conditions, and under a constant flow of N_2 gas, as shown in Figure 7.88. The resulting PPC under N_2 gas shows a dramatically longer decay-time, which decreases rapidly with the removal of the N_2 gas flow and introduction of atmospheric gases at t = 2000 s, as shown in Figure 7.88. This shows considerable support for the theory of surface oxygen desorption by UV radiation and slow re-adsorption post illumination. The comparatively slower rise-time of the UV photoresponse under N_2 gas has also been reported in the literature, but is not well-understood [7.28].

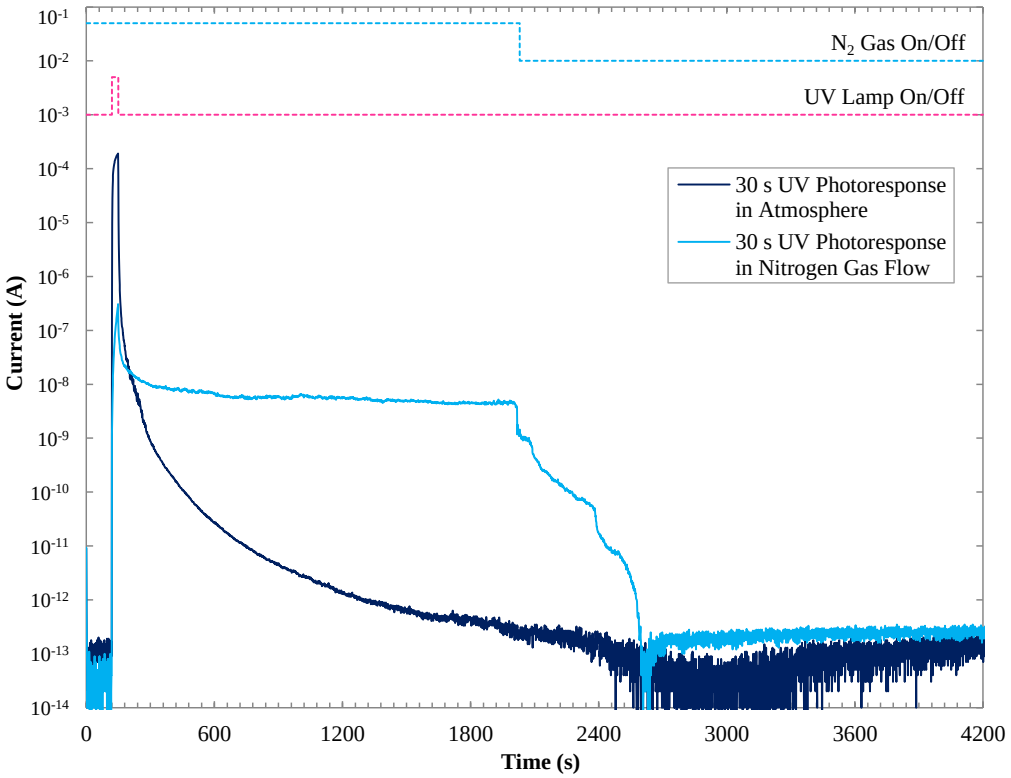

Figure 7.88: UV Photoresponse Under Nitrogen Gas Flow and Atmosphere, -1.0 V Bias

Surface modification with polymer layers has been found to reduce the level of PPC in ZnO-based devices, and decrease the sensitivity of the devices to visible light, however the magnitude of the UV photoresponse using Schottky contacts was decreased from µA to nA [7.22]. Using Schottky contacts rather than ohmic contacts has also been shown to produce significantly less PPC [7.22].

A Pt Schottky contact to a ZnO nanowire with surface modification has shown a fall-time of 10 ms following 10 s illumination under a 365 nm UV light, compared to a Ti/Au ohmic contact to a ZnO nanowire without surface modification, which had a fall-time of over 1500 s after 260 s illumination [7.22]. The modification layers were positive-charged poly(diallydimethylammonium chloride), and negative charged poly(sodium4-styrenesulfonate) [7.22]. Surface modification layers have also been shown to increase downward band-bending of contacts to ZnO, and increase PPC from UV illumination, while reducing the sensitivity of the ZnO to ambient oxygen [7.23]. This shows further evidence of PPC being caused by chemical interactions at the ZnO surface with the application and removal of UV radiation.

The increase in UV photoresponse and PPC with increasingly negative device bias is proposed to be due to the negative bias repelling negatively-charged oxygen species from the ZnO surface, and preventing the re-adsorption of atmospheric oxygen post illumination, and prolonging the effects of UV PPC, as observed in the increased UV PPC with negative bias in this work.

7.8.3 Ionisation of Oxygen Vacancies

It has been widely suggested that a major source of UV-generated PPC in ZnO-based devices is the trapping of photogenerated holes in V_O defects, which become positively ionised, as shown in Equation 7.8 [7.3, 7.15, 7.29]. It has also been proposed that V_O^0 is a ground state which becomes ionised with the absorption of UV radiation, as shown in Equation 7.9 [7.3, 7.8 – 7.9, 7.30 – 7.31]. The ionisation of V_O to V_O^{2+}, through photoionisation or hole-trapping, is understood to produce a strong outward lattice relaxation of the surrounding metal atoms by 23% of the neutral Zn-O bond length, as shown in Figure 7.89 [7.3, 7.8 – 7.9, 7.17 – 7.21, 7.29, 7.31]. As the V_O^{2+} is a negative-U centre, more energy is required to return the V_O^{2+} to the V_O state [7.3, 7.8, 7.17 – 7.18, 7.29 – 7.30, 7.32]. The ionised oxygen vacancy is metastable and therefore able to deeply trap the photogenerated holes, preventing them recombining with the photoelectrons and contributing to the slow-response decay of the PPC [7.3, 7.8, 7.17 – 7.18, 7.29 – 7.30, 7.32].

Ionisation of ZnO Oxygen Vacancies

$$V_O + 2\,h^+ \rightarrow V_O^{2+} \tag{7.8}$$

[7.3]

Excitation of ZnO Oxygen Vacancies

$$V_O + h\nu \rightarrow V_O^{2+} + 2\,e^- \tag{7.9}$$

[7.3]

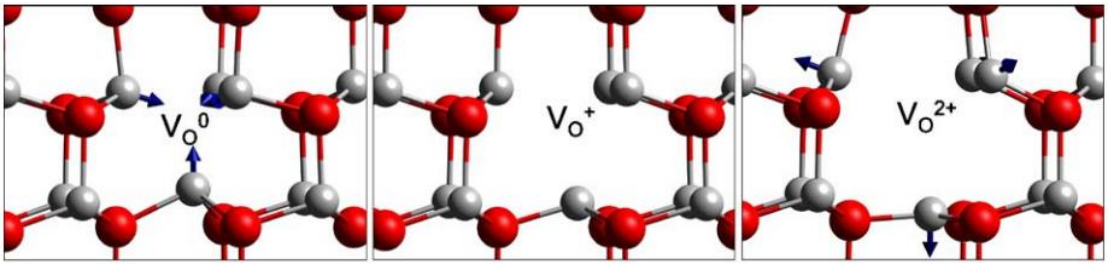

Figure 7.89: Ionisation of ZnO Oxygen Vacancy and Lattice Relaxation [7.18]

Oxygen plasma treatment of a metal-semiconductor-metal (MSM) contact to ZnO has shown a significant reduction in PPC decay time by neutralising oxygen vacancies near the ZnO surface, supporting the involvement of V_O in PPC [7.3, 7.28, 7.33]. Annealing ZnO-based devices in air following UV radiation exposure has also been observed to significantly reduce PPC [7.14].

ZnO films rich in oxygen have been found to have lower maximum UV photocurrent, but faster response-times and lower levels of PPC [7.11]. The oxidised noble metal-oxide Schottky contacts fabricated in this work are expected to result in a decrease in V_O created at the contact interface with increasing oxygen incorporation, as discussed in Chapter 6. This is likely to be the primary cause of the decreasing levels of PPC in the noble metal-oxide contacts with increasing O_2:Ar.

It has been shown in Sections 7.5 – 7.6 that the ability of the devices to resist PPC behaviour, both in terms of increased UV photoresponse and a reduction in t_{rise} and t_{fall}, increased with increasing oxygen incorporation to a point of maximum stability, 3.0:10 (O_2:Ar) for PdO_x and 4.0:10 (O_2:Ar) for PtO_x, that then decreased with increasing oxygen incorporation. As it has also been proposed that the reactively RF-sputtered Schottky contacts have lower levels of V_O near the Schottky contact interface with increasing levels of oxygen incorporation, the initial increase in stability could be due to a lower concentration of V_O near the Schottky contact interface requiring a larger negative device bias to promote the migration of the V_O^{2+}, causing PPC. However, the initial ideality factors of the PdO_x and PtO_x contacts used for the UV photoresponse measurements also showed a minimum at 3.0:10 – 4.0:10 (O_2:Ar), a trend also shown in Chapter 6, which could be impacting the formation of V_O in the ZnO near the Schottky contact interface.

7.8.4 Negative Bias Illumination Stress

Negative bias illumination stress (NBIS) has been widely observed in ZnO and IGZO (InGaZnO) thin film transistors (TFTs) [7.15, 7.34 – 7.36]. NBIS occurs in rectifying contacts as an increase in reverse-bias leakage current or the development of a double-barrier as the result of the application of simultaneous illumination and negative device bias. This is believed to be caused by

migration of oxygen vacancies or hydrogen towards the interface [7.15]. There is great interest in IGZO and ZnO TFTs for use in transparent display devices, prompting the investigation into the effects of visible and UV NBIS [7.15, 7.34 – 7.35]. NBIS has been suggested to be related to the level PPC in IGZO TFTs [7.8]. NBIS has also been reported to cause a negative shift in threshold voltage, V_{th}, in ZnO and IGZO devices, attributed to charge trapping of photogenerated holes at the device interface caused by the negative device bias [7.15, 7.34 – 7.35]. The photogenerated holes were reported to ionise neutral V_O and became deeply trapped, as discussed in Section 7.8.3. NBIS was also suggested to cause migration of the ionised V_O^{2+} towards the interface, causing band-bending and the formation of a potential well at the surface, as shown in Figure 7.90 [7.15].

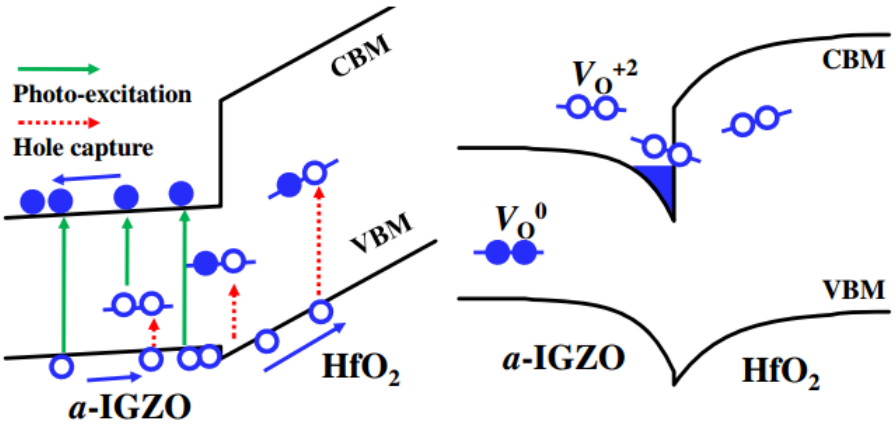

Figure 7.90: NBIS from UV Excitation Ionising Oxygen Vacancies in IGZO [7.15]

7.8.5 Oxygen Vacancy Migration

The migration of oxygen vacancies towards the Schottky contact interface with a negative device bias is proposed as one of the mechanisms involved in the PPC observed in this work [7.3, 7.15, 7.17 – 7.21]. The migration barrier for V_O^{2+}, 1.7 eV, is lower than V_O, 2.4 eV, indicating an increasing migration of oxygen vacancies to the Schottky interface with the ionising of the oxygen vacancies by UV radiation [7.18]. The formation of a depletion region across the Schottky contact and the associated electric field will attract the positively ionised V_O^{2+} towards the Schottky interface [7.37]. This will further accelerate the migration of V_O^{2+} towards the Schottky interface, proportional to the magnitude of the negative device bias.

The effect of positively biasing the Schottky contact during UV photoresponse measurements could be to reduce the accumulation of V_O^{2+} at the Schottky contact surface as the ionised V_O^{2+} defects return to their neutral V_O state. This could explain the lack of observable PPC with

positively-biased devices. However, the UV photocurrent under constant positive bias was also observed to decrease over time with continual exposure to UV radiation, as shown in Figure 7.91. This could be due to the positive bias increasing the rate of re-adsorption of negative oxygen species to the ZnO surface, and by electrons tunnelling through the interface under forward bias [7.8, 7.15]. The electron tunnelling can increase with temperature, which accounts for the faster recovery of PPC following annealing [7.14]. The application of a large positive bias (+10 V) between UV illumination at a negative bias has also been shown to reduce PPC in IGZO TFT UV photodetectors, supporting this theory [7.8].

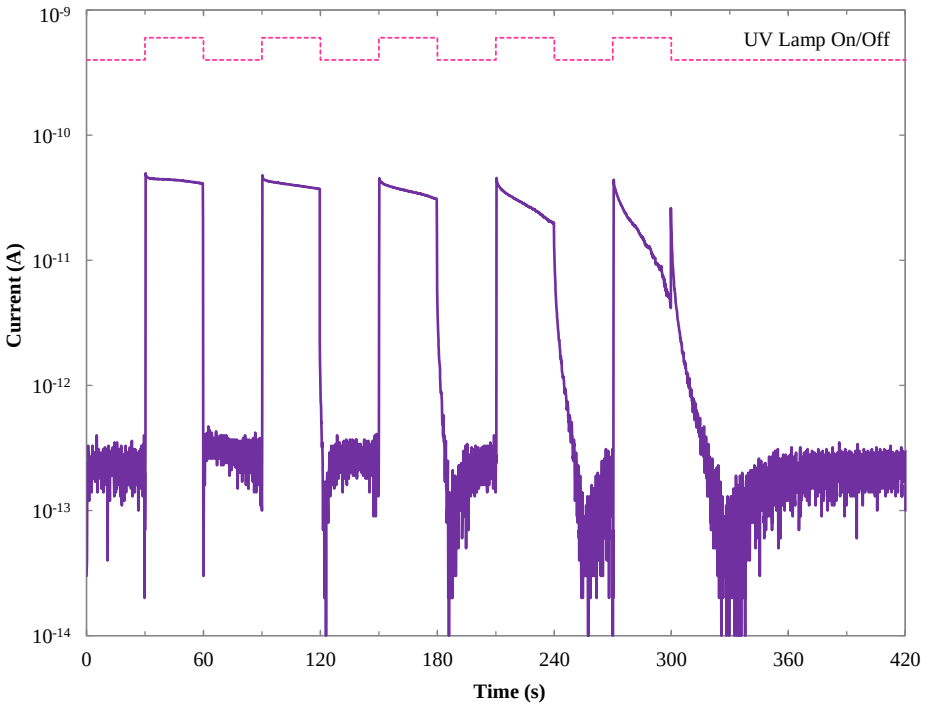

Figure 7.91: UV Photoresponse of 3.0:10 (O_2:Ar) PdO_x Contact to ZnO, +0.1 V Bias

A similar UV photoresponse pattern is shown for a non-ohmic ZnO nanowire contacted by Ti/Au electrodes, biased at +5 V in air with low levels of humidity [7.12 – 7.13]. Overall, this shows that the use of a positive bias to prevent PPC in ZnO-based UV photodetectors could introduce a significant amount of error when used for UV dosimetry. A 0 V bias has been shown to produce the most stable UV photoresponse in this work, and is recommended as the operational bias for the noble metal-oxide Schottky contacts to ZnO.

As discussed in Section 7.8.1, the initial slow rise of UV photocurrent is likely due to the V_O^{2+} initially migrating towards the Schottky contact interface, allowing for faster ionisation of the oxygen vacancies during subsequent UV exposures [7.3, 7.15, 7.17 – 7.21]. The semi-permanent

migration of oxygen vacancies towards the Schottky contact interface would also account for the formation of an apparent double-barrier in the dark I-V characteristics measured between UV photoresponse measurements of increasingly negative device bias performed in this work [7.15].

7.9 Summary

In this chapter, the photoresponses to visible and UV radiation of AgO_x, RuO_x, Ir/IrO_x, PdO_x, and Pt/PtO_x Schottky contacts to bulk hydrothermal c-plane Zn-polar bulk ZnO were investigated, and a model for the mechanisms responsible for UV PPC proposed. The photoresponse measurements performed included multiple pulses of 30 s illumination along with -1.0 V bias, and with varied bias. From these measurements the rise-time, fall-time, maximum UV photocurrent and current increase were calculated. The most significant results were:

- The selectivity of the IrO_x, PdO_x, and PtO_x devices to +c-plane (low-lithium) ZnO showed between 1.0 – 5.1 O_{Mag} greater current increase on average to UV light than visible light when scaled to the same irradiance, as shown in Figure 7.81. The greatest selectivity for each metal-oxide Schottky contact was 4.4, 3.3, and 5.1 O_{Mag} for 4.0:10 (O_2:Ar) IrO_x, 5.0:10 (O_2:Ar) PdO_x, and 3.0:10 (O_2:Ar) PtO_x.

- Noble metal-oxide Schottky contacts with higher oxygen incorporation showed higher levels of UV photoresponse current, partially due to reduced leakage current.

- The 4.0:10 (O_2:Ar) IrO_x contact to +c-plane (low-lithium) ZnO showed lower levels of PPC than the 4.0:10 (O_2:Ar) IrO_x contact to –c-plane ZnO, with fall times of 2 s and 24 s respectively, indicating that the higher concentration of impurities in –c-plane ZnO is increasing the level of PPC generated with UV radiation.

- An hour-long UV photoresponse measurement of the 7.0:10 (O_2:Ar) PtO_x contact with 54 pulses of UV radiation for 30 s and a positive bias of +0.1 V showed no build-up of PPC over time, indicating long-term stability of biased devices with no PPC response to UV.

- The 3.0:10 (O_2:Ar) PdO_x Schottky contact showed the greatest potential for use in UV photodetection, with the highest level of selectivity between UV and visible light,

5.1 O_{Mag}, a reasonable UV photocurrent with 0 V bias of 0.165 nA, and low values of rise-time and fall-time after 5 exposures, 0 s and 2.7 s.

- A 0 V bias has been shown to produce the most stable UV photoresponse in this work, and is recommended as the operational bias for the noble metal-oxide Schottky contacts to ZnO. The maximum UV photoresponse with 0 V bias of each noble metal-oxide were 42.0 pA for 4.0:10 (O_2:Ar) AgO_x, 2.05 nA for 3.0:10 (O_2:Ar) RuO_x, 1.29 nA for 4.0:10 (O_2:Ar) IrO_x, 0.801 nA for 7.0:10 (O_2:Ar) PdO_x, and 1.38 nA for 3.0:10 (O_2:Ar) PtO_x.

- A recoverable double-barrier was formed in the dark I-V characteristics of all noble metal-oxide Schottky contacts following highly-negative device bias UV photoresponse measurements, reducing the barrier height and the rectification ratio of the devices. This has been proposed in this work to be due to NBIS, where the highly negative device bias is proposed in this work to cause the aggregation and trapping of ionised V_O^{2+} at the interface [7.15, 7.17 – 7.21, 7.26].

- Increasing oxygen incorporation in all noble metal-oxide contacts showed an overall trend of a decrease in rise-time and fall-time, and the decrease in maximum UV photocurrent with a -1.0 V bias in Figures 7.82 – 7.84. It is proposed in this work that the increasing oxygen incorporation reduces the levels of PPC, due to the expected reduction of V_O concentration [7.3, 7.8 – 7.9, 7.17 – 7.21, 7.29 – 7.31].

- The device bias required to induce PPC in the oxidised metal-oxide Schottky contacts has been shown in this work to increase with increasing oxygen incorporation. As the contacts with higher levels of oxygen incorporation are expected to have lower concentrations of V_O defects at the interface, a greater negative device bias is likely required to ionise and cause the migration of the V_O defects further away from the surface [7.15, 7.17 – 7.21, 7.26].

REFERENCES

[7.1] Dogar, S., Khan, W., Kim, S.-D., (2016), Ultraviolet photoresponse of ZnO nanostructured AlGaN/GaN HEMTs, *Materials Science in Semiconductor Processing*, 44, pp. 71-77.

[7.2] Campos, L.C., Guimarães, M.H.D., Goncalves, A.M.B., De Oliveira, S., Lacerda, R.G., (2013), ZnO UV photodetector with controllable quality factor and photosensitivity, *AIP Advances*, 3 (2), art. no. 022104.

[7.3] Litton, C.W., Reynolds, D.C., Collins, T.C., (2011), *Zinc Oxide Materials for Electronic and Optoelectronic Device Applications, 1st Edition*, pp. 293-304, West Sussex, United Kingdom: John Wiley & Sons, Ltd.

[7.4] Jiang, H.X., Lin, J.Y., Lin, (2000), Chapter 6 - Persistent photoconductivity in III-nitrides, Manasreh, O., *III-Nitride Semiconductors: Electrical, Structural and Defects Properties*, pp. 151-191, Amsterdam, Netherlands: Elsevier.

[7.5] Liang, S., Sheng, H., Liu, Y., Huo, Z., Lu, Y., Shen, H., (2001), ZnO Schottky ultraviolet photodetectors, *Journal of Crystal Growth*, 225 (2-4), pp. 110-113.

[7.6] Bayan, S., Mohanta, D., (2012), ZnO nanorod-based UV photodetection and the role of persistent photoconductivity, *Philosophical Magazine*, 92 (32), pp. 3909-3919.

[7.7] Li, Z., Guangsheng, F., Xiaoyun, T., Wei, Y., Heju, X., (2009), Persistent photoconductivity in undoped n-type ZnO thin films, *2009 Symposium on Photonics and Optoelectronics, SOPO 2009*, art. no. 5230089.

[7.8] Nathan, A., Lee, S., Jeon, S., Song, I., Chung, U.-I., (2013), Transparent oxide semiconductors for advanced display applications, *Information Display*, 29 (1), pp. 6-11.

[7.9] Kuriyama, K., Matsumoto, K., Suzuki, Y., Kushida, K., Xu, Q., (2009), Persistent photoconductivity and thermally stimulated current related to electron-irradiation induced defects in single crystal ZnO bulk, *Solid State Communications*, 149 (33-34), pp. 1347-1350.

[7.10] Koley, G., Cha, H.-Y., Tilak, V., Eastman, L.F., Spencer, M.G., (2002), Modulation of surface barrier in AlGaN/GaN heterostructures, *Physica Status Solidi (B) Basic Research*, 234 (3), pp. 734-737.

[7.11] Sharma, P., Sreenivas, K., Rao, K.V., (2003), Analysis of ultraviolet photoconductivity in ZnO films prepared by unbalanced magnetron sputtering, *Journal of Applied Physics*, 93 (7), pp. 3963-3970.

[7.12] Li, Y., Della Valle, F., Simonnet, M., Yamada, I., Delaunay, J.-J., (2009), Competitive surface effects of oxygen and water on UV photoresponse of ZnO nanowires, *Applied Physics Letters*, 94 (2), art. no. 023110.

[7.13] Ahn, S.-E., Ji, H.J., Kim, K., Kim, G.T., Bae, C.H., Park, S.M., Kim, Y.-K., Ha, J.S., (2007), Origin of the slow photoresponse in an individual sol-gel synthesized ZnO nanowire, *Applied Physics Letters*, 90 (15), art. no. 153106.

[7.14] Studenikin, S.A., Golego, N., Cocivera, M., (2000), Carrier mobility and density contributions to photoconductivity transients in polycrystalline ZnO films, *Journal of Applied Physics*, 87 (5), pp. 2413-2421.

[7.15] Ryu, B., Noh, H.-K., Choi, E.-A., Chang, K.J., (2010), O-vacancy as the origin of negative bias illumination stress instability in amorphous In-Ga-Zn-O thin film transistors, *Applied Physics Letters*, 97 (2), art. no. 022108.

[7.16] Liao, Z.-M., Lu, Y., Xu, J., Zhang, J.-M., Yu, D.-P., (2009), Temperature dependence of photoconductivity and persistent photoconductivity of single ZnO nanowires, *Applied Physics A: Materials Science and Processing*, 95 (2), pp. 363-366.

[7.17] Janotti, A., Van De Walle, C.G., (2007), Native point defects in ZnO, *Physical Review B - Condensed Matter and Materials Physics*, 76 (16), art. no. 165202.

[7.18] Janotti, A., Van De Walle, C.G., (2005), Oxygen vacancies in ZnO, *Applied Physics Letters*, 87 (12), art. no. 122102, pp. 1-3.

[7.19] Van De Walle, C.G., (2001), Defect analysis and engineering in ZnO, *Physica B: Condensed Matter*, 308-310, pp. 899-903.

[7.20] Shih, A., Zhou, W., Qiu, J., Yang, H.-J., Chen, S., Mi, Z., Shih, I., (2010), Highly stable resistive switching on monocrystalline ZnO, *Nanotechnology*, 21 (12), art. no. 125201.

[7.21] Erhart, P., Albe, K., (2006), First-principles study of migration mechanisms and diffusion of oxygen in zinc oxide, *Physical Review B - Condensed Matter and Materials Physics*, 73 (11), art. no. 115207.

[7.22] Zhou, J., Gu, Y., Hu, Y., Mai, W., Yeh, P.-H., Bao, G., Sood, A.K., Polla, D.L., Wang, Z.L., (2009), Gigantic enhancement in response and reset time of ZnO UV nanosensor by utilizing Schottky contact and surface functionalization, *Applied Physics Letters*, 94 (19), art. no. 191103.

[7.23] McNeill, A.R., Hyndman, A.R., Reeves, R.J., Downard, A.J., Allen, M.W., (2016), Tuning the Band Bending and Controlling the Surface Reactivity at Polar and Nonpolar Surfaces of ZnO through Phosphonic Acid Binding, *ACS Appl. Mater. Interfaces*, 8 (45), pp 31392–31402.

[7.24] Jagadish, C., Pearton, S.J., (2006), *Zinc Oxide Bulk, Thin Films and Nanostructures – Processing, Properties and Applications*, Oxford, U.K: Elsevier Ltd.

[7.25] Heinhold, R., Williams, G.T., Cooil, S.P., Evans, D.A., Allen, M.W., (2013), Influence of polarity and hydroxyl termination on the band bending at ZnO surfaces, *Physical Review B - Condensed Matter and Materials Physics*, 88 (23), art. no. 235315.

[7.26] Coppa, B.J., Fulton, C.C., Kiesel, S.M., Davis, R.F., Pandarinath, C., Burnette, J.E., Nemanich, R.J., Smith, D.J., (2005), Structural, microstructural, and electrical properties of gold films and Schottky contacts on remote plasma-cleaned, n -type ZnO{0001} surfaces, *Journal of Applied Physics*, 97 (10), art. no. 103517.

[7.27] Cammi, D., Ronning, C., (2014), Persistent photoconductivity in ZnO nanowires in different atmospheres, *Advances in Condensed Matter Physics*, art. no. 184120.

[7.28] Liu, M., Kim, H.K., (2004), Ultraviolet detection with ultrathin ZnO epitaxial films treated with oxygen plasma, *Applied Physics Letters*, 84 (2), pp. 173-175.

[7.29] Zhang, S.B., Wei, S.-H., Zunger, A., (2001), Intrinsic n-type versus p-type doping asymmetry and the defect physics of ZnO, *Physical Review B - Condensed Matter and Materials Physics*, 63 (7), art. no. 075205, pp. 0752051-0752057.

[7.30] Yu, K.M., Jeong, S.H., Bae, B.S., Yun, E.-J., (2012), The Effect of UV treatment on the recovery characteristics of a-IGZO-based thin film transistors, *Journal of the Korean Physical Society*, 61 (6), pp. 852-857.

[7.31] Lany, S., Zunger, A., (2005), Anion vacancies as a source of persistent photoconductivity in II-VI and chalcopyrite semiconductors, *Physical Review B - Condensed Matter and Materials Physics*, 72 (3), art. no. 035215.

[7.32] Li, H., Feng, H., Zhang, F., Liu, Y., Xie, E., (2013), The effect of oxygen-rich condition on properties of ZnO:In films by sputtering, *Advanced Materials Research*, 634-638 (1), pp. 2512-2517.

[7.33] Liu, P., She, G., Liao, Z., Wang, Y., Wang, Z., Shi, W., Zhang, X., Lee, S.-T., Chen, D., (2009), Observation of persistent photoconductance in single ZnO nanotube, *Applied Physics Letters*, 94 (6), art. no. 063120.

[7.34] Shin, J.-H., Lee, J.-S., Hwang, C.-S., Park, S.-H.K., Cheong, W.-S., Ryu, M., Byun, C.-W., Lee, J.-I., Chu, H.Y., (2009), Light effects on the bias stability of transparent ZnO thin film transistors, *ETRI Journal*, 31 (1), pp. 62-63.

[7.35] Park, J.S., Kim, T.S., Son, K.S., Maeng, W.-J., Kim, H.-S., Ryu, M., Lee, S.Y., (2011), The effect of UV-assisted cleaning on the performance and stability of amorphous oxide semiconductor thin-film transistors under illumination, *Applied Physics Letters*, 98 (1), art. no. 012107.

[7.36] Noh, H.-K., Chang, K.J., Ryu, B., Lee, W.-J., (2011), Electronic structure of oxygen-vacancy defects in amorphous In-Ga-Zn-O semiconductors, *Physical Review B - Condensed Matter and Materials Physics*, 84 (11), art. no. 115205.

[7.37] Sze, S. M., (2002), *Semiconductor Devices, Physics and Technology, 2nd Ed.*, Hoboken, N.J., U.S.A: John Wiley.

8 Thermal Stability of Schottky Contacts to Zinc Oxide

This chapter contains the results of dark I-V-T characteristics of Schottky contacts on bulk ZnO with temperature between 20 °C and 180 °C, in order to explore the thermal stability of the Schottky contacts and determine the Richardson constant of Tokyo Denpa hydrothermal +c-axis (low-lithium) bulk ZnO. The Schottky Contacts tested consisted of those with PLD IrO_x, and RF-sputtered AgO_x, IrO_x, PdO_x, and PtO_x Schottky contacts.

8.1 Dark I-V Thermal Stability Experiments

The methodology of the I-V characterisation with temperature is described in Sections 4.2.1 and 4.2.5 respectively. Repeat temperature measurements were performed on PLD IrO_x Schottky contacts in order to observe the dark I-V characteristics of the devices with repeated high temperature cycling. Temperature measurements were performed on 4.0:10 (O_2:Ar) RF-sputtered AgO_x Schottky contacts on Zn-polar and O-polar ZnO in order to perform a novel study of the effects of ZnO polarity on thermal stability. The effects of oxygen incorporation on thermal stability were also investigated for RF-sputtered 1.0:10 – 4.0:10 (O_2:Ar) IrO_x, 3.0:10 – 7.0:10 (O_2:Ar) PtO_x, and 7.0:10 (O_2:Ar) PdO_x for a comparison of Schottky material comparison and thermal stability.

8.2 Thermal Stability of Pulsed Laser Deposited Iridium Oxide Schottky Contacts

IrO_x Schottky contacts were fabricated to +c-axis (low-lithium) bulk ZnO using PLD, and capped with 50 nm Au top contacts, as described in Section 3.4. The oxygen incorporation of the PLD IrO_x films is unknown; however the barrier heights (Φ_B), ideality factors (η), and rectification ratios (R_R) of PLD IrO_x were compared to RF-sputtered IrO_x Schottky contacts with increasing levels of oxidation, shown in Figure 8.1. The PLD and RF-sputtered Schottky contacts in Figure 8.1 were deposited on two different samples of +c low-Li ZnO with resistivities of 0.87 Ωcm and 1.18 Ωcm respectively. Samples and fabrication details are included in Appendices A3.2 and A3.4.

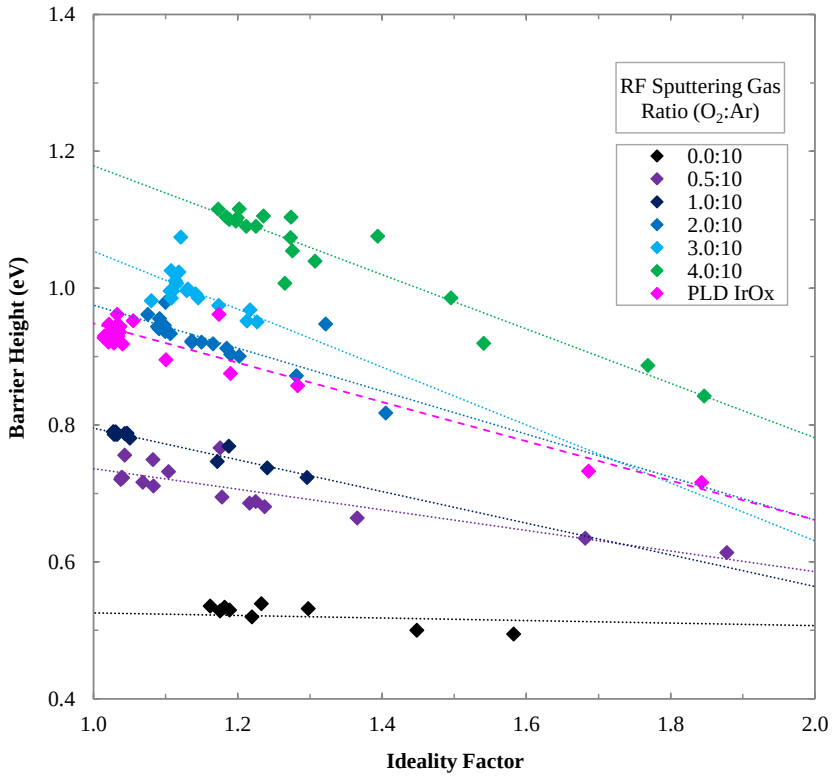

Figure 8.1: Barrier Heights of PLD, RF-sputtered IrO_x Diodes on +c-axis (Low-Li) ZnO

The barrier heights and ideality factors of PLD IrO_x contacts indicate that the equivalent oxygen incorporation of PLD IrO_x was between 1.0:10 (O_2:Ar) and 2.0:10 (O_2:Ar), as interpolated from Figure 8.1. Although detailed analysis has not been performed on the optical and electrical characteristics of the PLD IrO_x thin films, it has been reported that room-temperature PLD deposition of IrO_x produces films with similar resistivities to RF-sputtered IrO_x films [8.1, 8.2].

Varied temperature experiments were performed on PLD and RF-sputtered IrO_x Schottky contacts, with a temperature cycle of 20 °C → 180 °C → 20 °C for both the initial and repeat measurements. The dark I-V characterisation of a single PLD IrO_x contact with increasing and decreasing temperatures is shown in Figures 8.2 and 8.3. The evolution of the ideality factor and barrier height with temperature are shown in Figures 8.4 and 8.5 for both the initial and repeat temperature cycle. Figures 8.2 – 8.5 are the results for a PLD IrO_x contact undergoing temperature cycling, Figures 8.6 – 8.9 are the results for the 2.0:10 (O_2:Ar) RF-sputtered IrO_x Schottky contact undergoing the same temperature cycling. The comparison of the barrier heights and ideality factors of PLD and RF-sputtered IrO_x contacts are shown in Figure 8.10 – 8.11. The dark I-V characteristics for both the initial and repeat temperature measurements of both PLD and RF-sputtered IrO_x contacts, as well as individual plots of the barrier heights and ideality factors of the PLD IrO_x contact, can be found in Appendix A8.1, Figures A8.1 – A8.8.

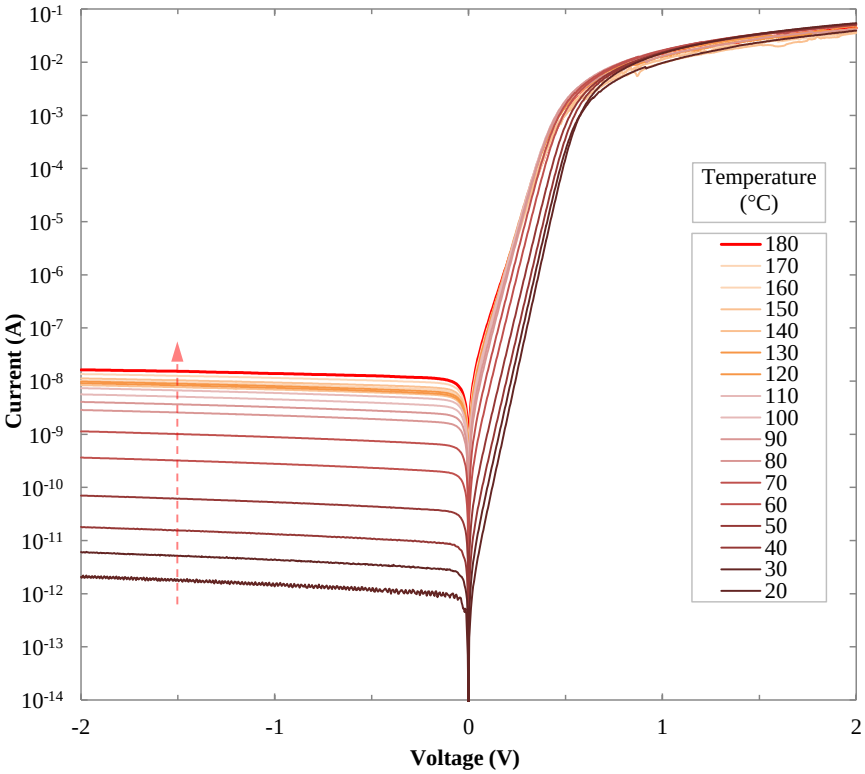

Figure 8.2: Dark I-V Results of PLD IrO_x Contacts (Increasing Temperature)

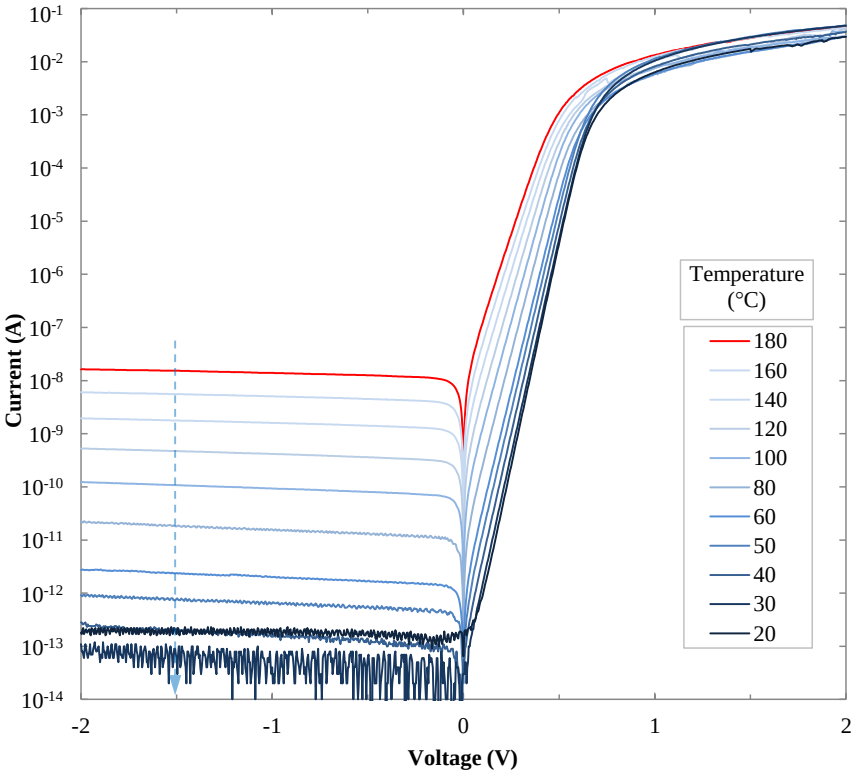

Figure 8.3: Dark I-V Results of PLD IrO_x Contacts (Decreasing Temperature)

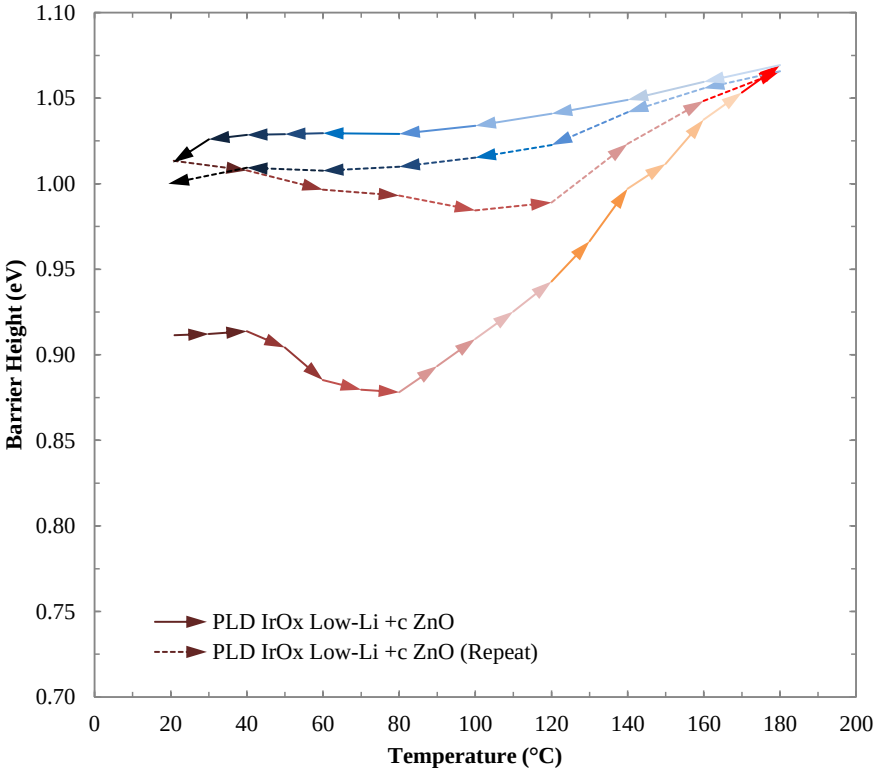

Figure 8.4: Barrier Heights with Temperature of PLD IrO_x Contacts

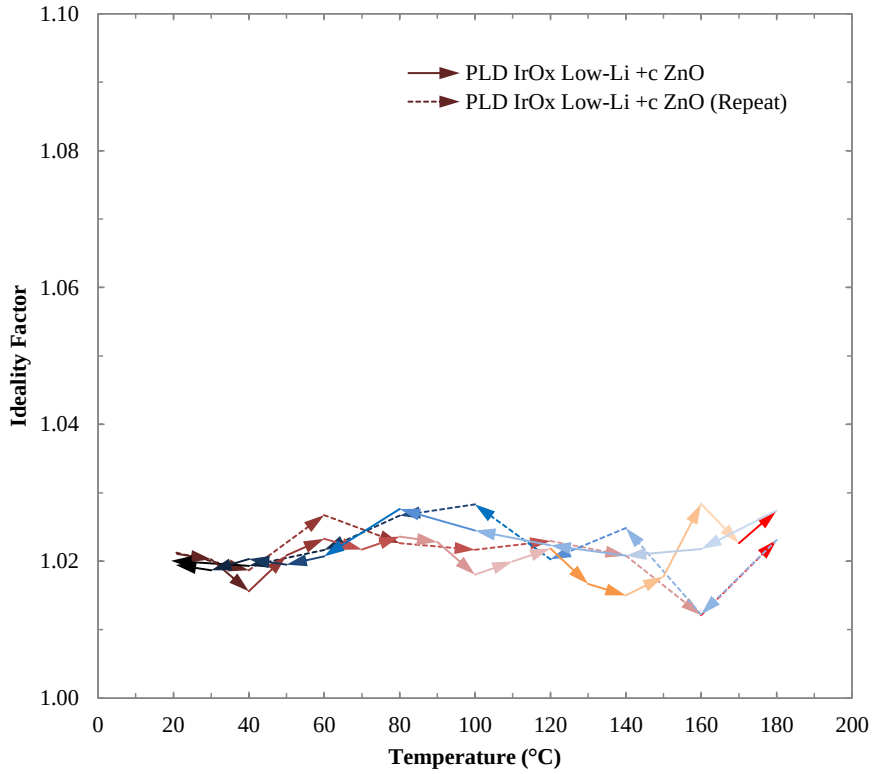

Figure 8.5: Ideality Factors with Temperature of PLD IrO_x Contacts

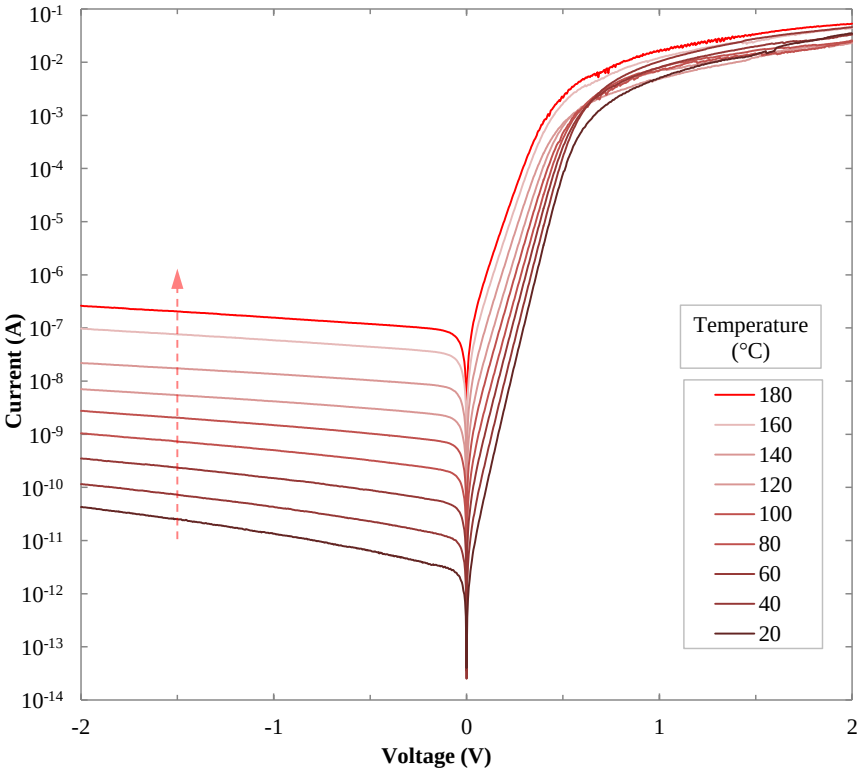

Figure 8.6: Dark I-V Results of 2.0:10 (O_2:Ar) RF-sputtered IrO_x (Increasing Temperature)

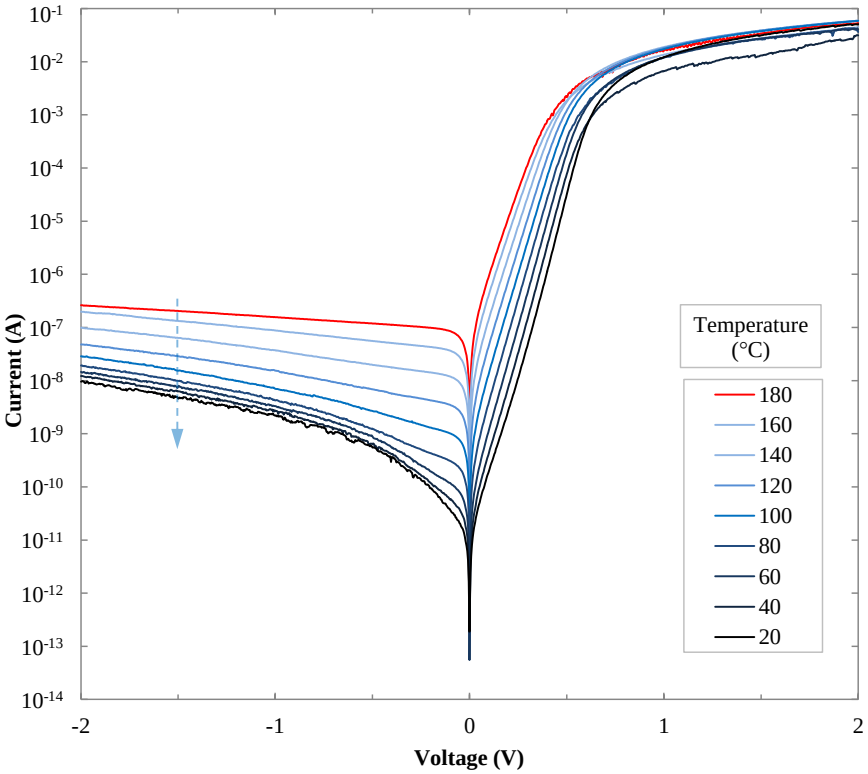

Figure 8.7: Dark I-V Results of 2.0:10 (O_2:Ar) RF-sputtered IrO_x (Decreasing Temperature)

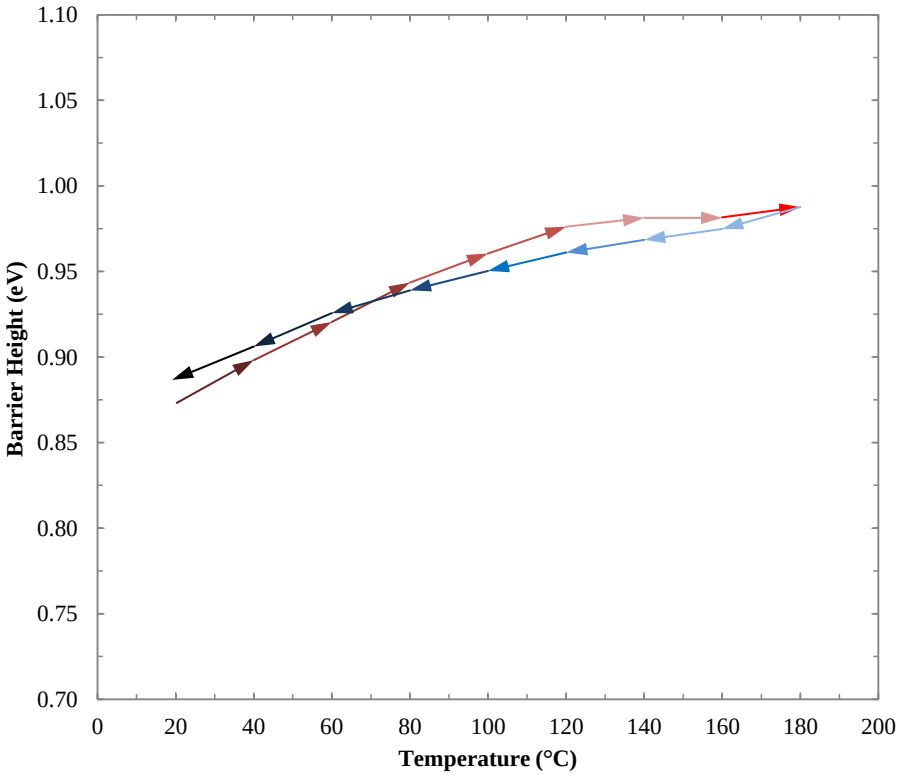

Figure 8.8: Barrier Heights with Temperature of 2.0:10 (O_2:Ar) RF-sputtered IrO_x

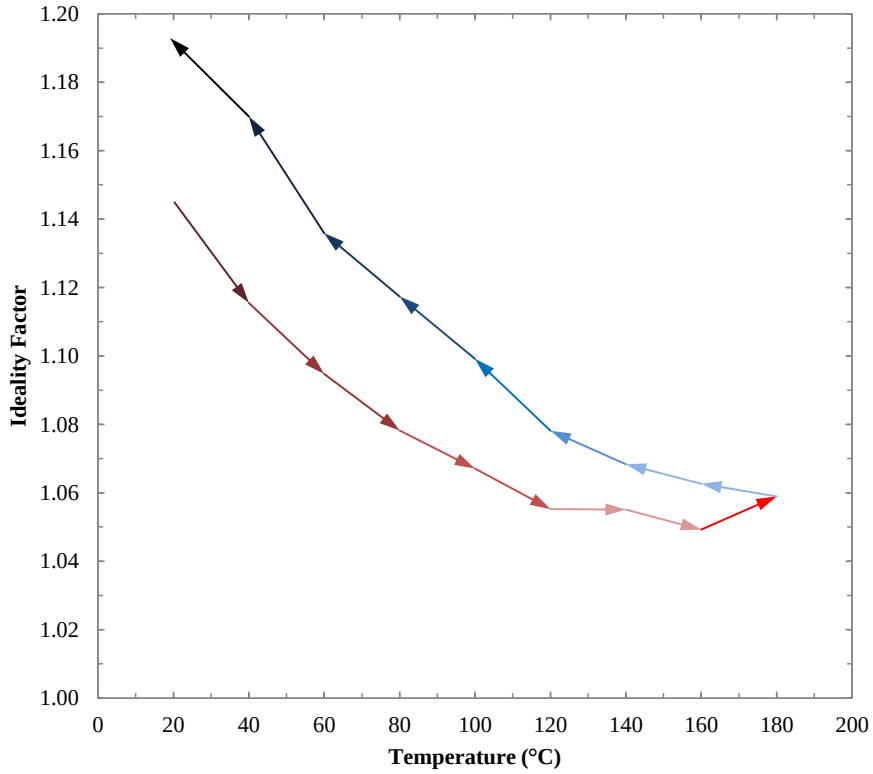

Figure 8.9: Ideality Factors with Temperature of 2.0:10 (O_2:Ar) RF-sputtered IrO_x

Both the PLD and RF-sputtered IrO_x contacts were shown to be stable at temperatures up to 180 °C, with rectification ratios between 3.7 – 7.0 orders of magnitude (O_{Mag}) at 180 °C, as shown in Figures 8.2 – 8.3 and 8.6 – 8.7. The PLD IrO_x contact appeared to improve with the temperature cycle; however the RF-sputtered IrO_x contact appeared to degrade during the temperature test cycle.

The PLD IrO_x contact showed an increase of rectification ratio following the temperature testing cycles, from 10 to 11 O_{Mag}, shown in Figures 8.2 – 8.3 and Appendix A8.1, Figures A8.5 – A8.6. Figure 8.4 shows an increasing barrier height during 80 – 180 °C of the initial temperature cycle, leading to a permanent barrier height increase from 0.911 eV to 1.01 eV at room temperature (20 °C) despite the expected lowering of the barrier height with decreasing temperature. Although the barrier height was observed to increase over 120 – 180 °C during the repeat temperature cycle, there was no permanent change in room temperature barrier height. This indicates that the PLD IrO_x contact was annealed between 40 – 180 °C. The ideality factor of the contacts also showed an improvement (a reduction) following the initial measurement in Figure 8.5. The trends of the ideality factors with temperature of the initial and repeat temperature cycle measurement of the PLD IrO_x contact did not show clear trends with increasing or decreasing temperature, shown in Figure 8.5 and in separate plots in Appendix A8.1, Figures A8.4 and A8.8.

The RF-sputtered IrO_x contact also developed a permanent increase in barrier height following the temperature test cycle, from 0.873 eV to 0.887 eV in Figure 8.8. However, a comparison of Figures 8.6 – 8.7 shows significantly higher reverse leakage current in the device following the temperature cycle, characteristic of an ohmic shunt resistance rather than thermal emission. This has been observed in RF-sputtered PdO_x Schottky contacts to ZnO, and linked to permanent thermal damage to the Schottky contacts [8.3]. This thermal degradation was not observed in the PLD Pd Schottky contacts to ZnO [8.3]. Physical damage to the Schottky contacts from the repeated contacting of the parameter analyser probes is likely to be a source of the observed increase in reverse bias leakage current, by introducing lateral inhomogeneities in the Schottky contact, as described in Section 6.1. However, identical devices across the same sample tested before and after the temperature cycle (during which the sample is repeatedly subject to probe contacting) show a similar increase in reverse leakage current and ideality factor, as shown in Appendix A8.2, Figures A8.9 – A8.10. This makes it unlikely that repeated-measurement probe damage is the cause of the increase in reverse bias leakage current in the devices fabricated and tested in this work.

The RF-sputtered IrO_x contact also developed a permanent increase of ideality factor following the temperature cycle, shown in Figure 8.9, which was also linked to thermal damage. The comparison between Figure 8.5 and 8.9 shows significantly more variation of the RF-sputtered IrO_x contact ideality factor with temperature than the PLD IrO_x contacts.

It can be seen from Figures 8.2 – 8.3, and 8.6 – 8.7, that there is a slight 'bulge' in forward bias current between 0 – 0.2 V with increasing temperatures, compared to the initial log-linear I-V trend of forward bias current at 20 °C in Figures 8.2 and 8.6, characteristic of a slight double-barrier, as described in Section 6.1., and illustrated in Figures A6.1 – A6.3 of Appendices 6.1 – 6.2. This double-barrier could account for the increase in the ideality factor of the RF-sputtered IrO_x contact, as the double-barrier complicates the fitting the linear forward bias region of the dark I-V characteristics described in Section 4.2.2. The double-barrier also appears to remain in the dark I-V characteristics of the RF-sputtered IrO_x contact following the decreasing temperature cycle, seen in Figure 8.7; however the double-barrier appears to disappear with decreasing temperature in the PLD IrO_x contact in Figure 8.3. This indicates that the formation of a double-barrier could be related to the temperature instability of the IrO_x contacts. Differences in Schottky contact crystal structure could account for the differences in stability, however both room temperature depositions of PLD and RF-sputtered IrO_x films have been reported as amorphous, as discussed in Section 5.3 [8.1].

Room temperature, amorphous RF-sputtered IrO_x films have been reported to decrease in resistivity by an order of magnitude when annealed from 25 °C to 200 °C in air, which was associated with the decomposition of Ir_2O_3 (Ir^{3+}) compounds into IrO_2 (Ir^{4+}) [8.2]. This decomposition could be related to the increase barrier height, by increasing the oxygen incorporation in the RF-sputtered IrO_x films from x = 3/2 to x = 2 [8.2]. Further investigations into the differences in film structure and oxygen incorporation of PLD and RF-sputtered IrO_x films should be performed, especially following the effects of annealing at temperatures up to 180 °C, in order to discover the cause of the substantial increase in temperature stability that PLD IrO_x contacts exhibit over RF-sputtered IrO_x contacts.

8.3 Thermal Stability of RF-Sputtered Iridium Oxide Schottky Contacts

Varied temperature experiments were performed on 1.0:10, 2.0:10, 3.0:10, and 4.0:10 (O_2:Ar) RF-sputtered IrO_x Schottky contacts, with a temperature cycle of 20 °C → 180 °C → 20 °C. The comparisons of the 20 °C and 180 °C dark I-V characteristics of the RF-sputtered IrO_x contacts with varied oxygen incorporation for increasing and decreasing temperatures are shown in Figures 8.10 and 8.11 respectively. The comparisons of the barrier heights and ideality factors with temperature of the RF-sputtered IrO_x contacts with varied levels of oxygen incorporation are shown in Figures 8.12 – 8.13. The dark I-V characteristics, barrier heights, and ideality factors for the individual levels of oxygen incorporation with increasing and decreasing temperature are included in Appendix A8.3, Figures A8.11 – A8.26.

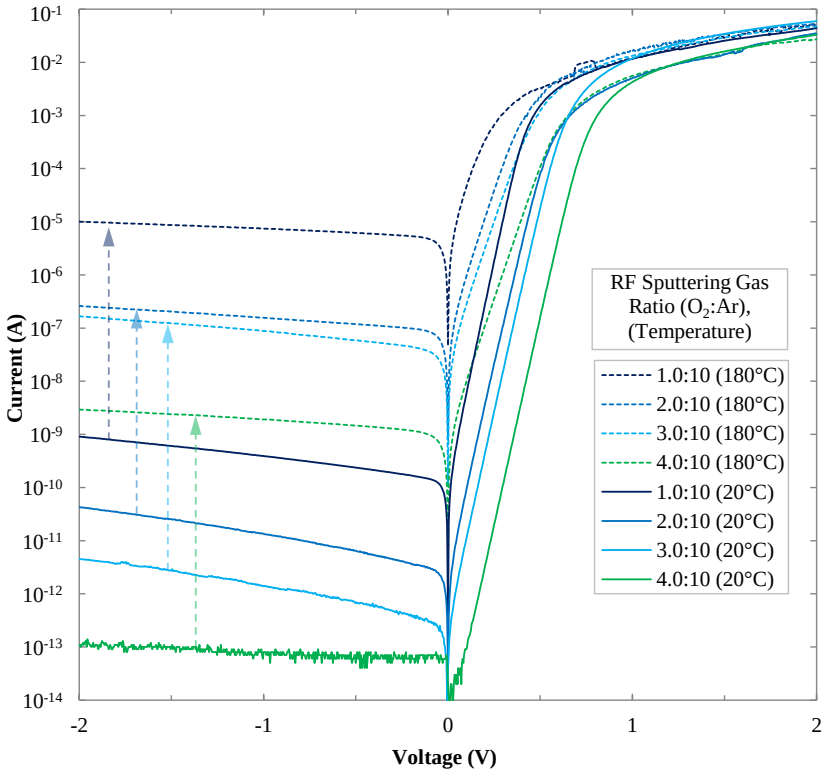

Figure 8.10: Dark I-V of 1.0:10 – 4.0:10 (O_2:Ar) RF-sputtered IrO_x (Increasing Temperature)

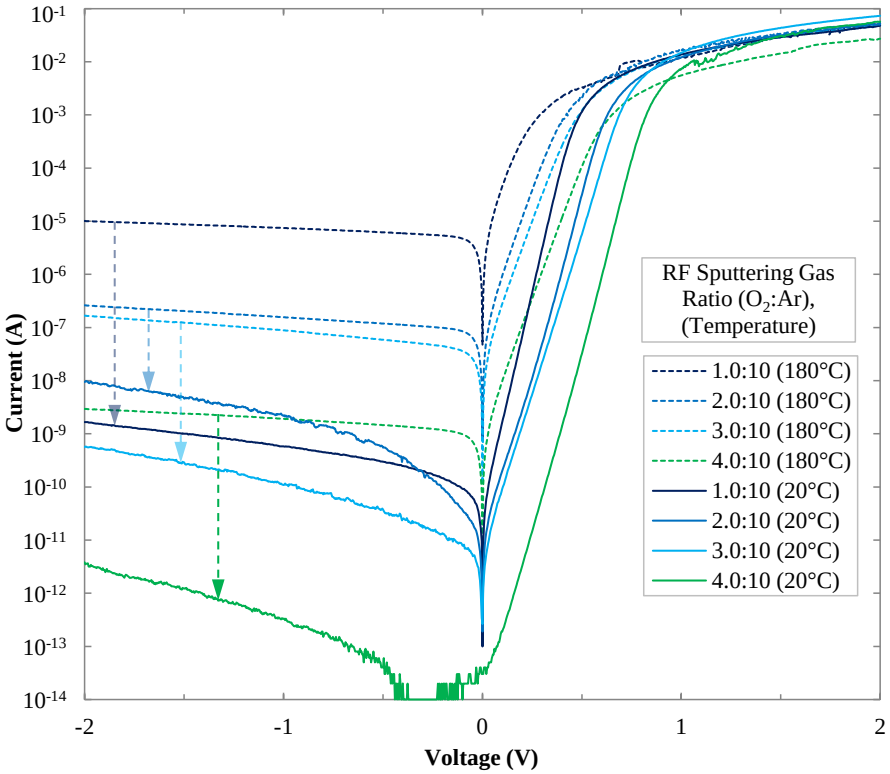

Figure 8.11: Dark I-V of 1.0:10 – 4.0:10 (O_2:Ar) RF-sputtered IrO_x (Decreasing Temperature)

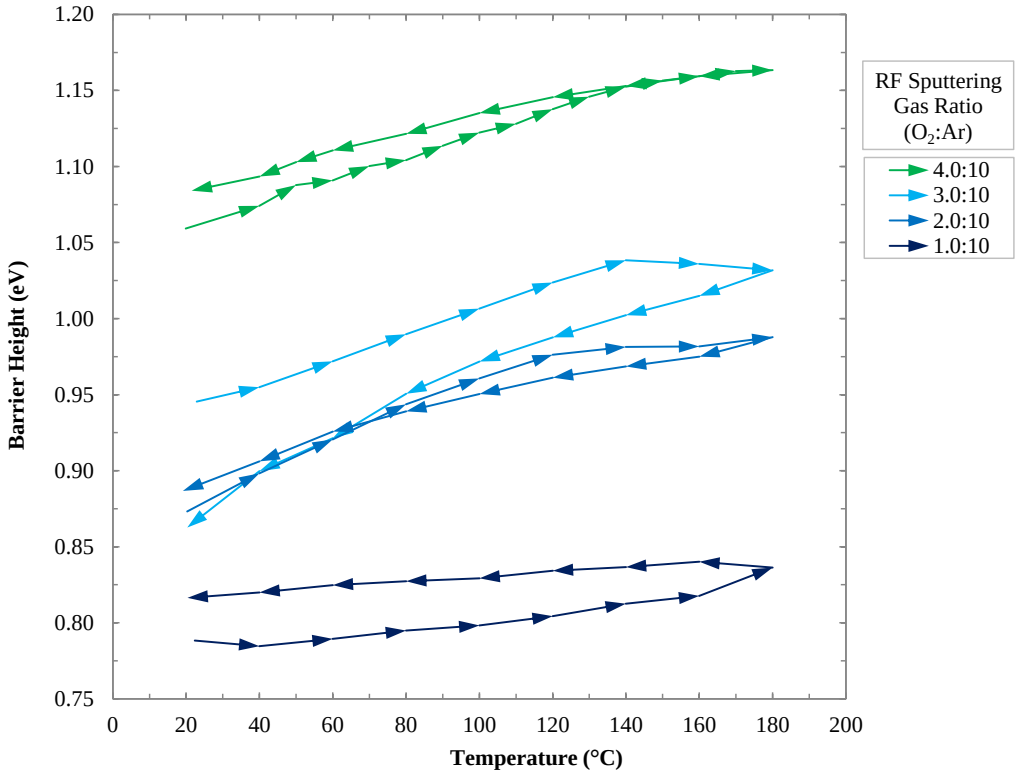

Figure 8.12: Barrier Heights with Temperature of RF-sputtered IrO_x Oxidation Series

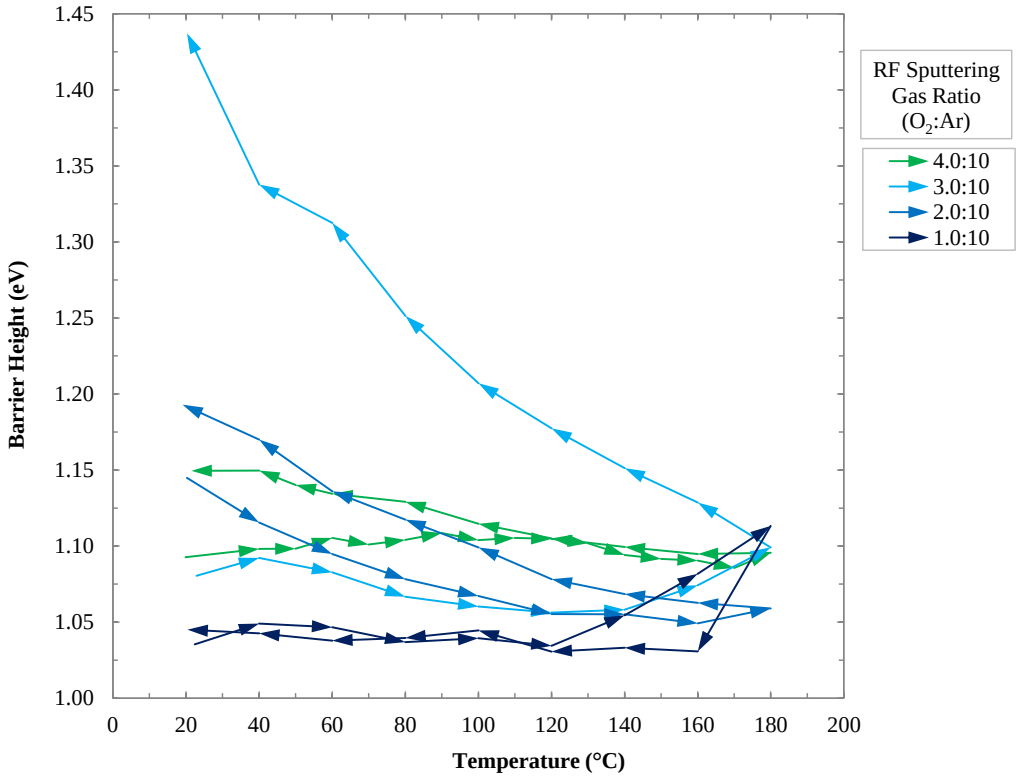

Figure 8.13: Ideality Factors with Temperature of RF-sputtered IrO_x Oxidation Series

It can be observed from Figure 8.10 that the 1.0:10 – 4.0:10 (O_2:Ar) RF-sputtered IrO_x contacts to ZnO were stable at 180 °C, with rectification ratios between 3.7 – 7.0 O_{Mag} from 20 °C to 180 °C. It can also be observed from Figure 8.10 that the forward bias current between 0 – 0.2 V exhibits a double-barrier at 180 °C, compared to the linear trend of the same devices at 20 °C, related to an increase in ohmic shunt resistance, as mentioned in Section 8.2. The same trend can be observed across all temperatures of the individual plots of 1.0:10 – 4.0:10 (O_2:Ar) RF-sputtered IrO_x contacts with temperature, in Appendix A8.3, Figures A8.11 – A8.12, A8.15 – A8.16, A8.19 – A8.20, and A8.23 – A8.24. The persistence in the double-barrier in forward bias current with decreasing temperatures, shown in Figure 8.11, correlates with the significant increase in reverse bias current characteristic of an increase in ohmic shunt resistance, discussed in Section 8.2. This implies that the thermal damage has affected all of the 1.0:10 – 4.0:10 (O_2:Ar) RF-sputtered IrO_x contacts, with no clear trend between oxygen incorporation and leakage current.

Figure 8.12 shows that the temperature test cycle of the 1.0:10, 2.0:10, and 4.0:10 (O_2:Ar) IrO_x contacts resulted in a permanent increase in barrier height. However, the 3.0:10 (O_2:Ar) IrO_x contact showed a permanent decrease in barrier height, correlated with a significant increase in ideality factor, from 1.08 to 1.44, in Figure 8.13. It is unclear from the small sample size of devices tested whether the decrease in barrier height was an outlier due to excessive thermal damage, or characteristic of the level of oxygen incorporation, as the increase in reverse leakage current for 3.0:10 (O_2:Ar) is less than the increase in reverse leakage current for 2.0:10 (O_2:Ar), shown in Figure 8.11. Temperature measurements were not performed on 0.0:10 and 0.5:10 (O_2:Ar) IrO_x contacts due to the low rectification ratio at room temperature resulting in inaccurate calculation of the ideality factor and barrier height at higher temperatures.

8.4 Thermal Stability of RF-Sputtered Platinum Oxide Schottky Contacts

Varied temperature experiments were performed on 3.0:10, 4.0:10, 5.0:10, and 7.0:10 (O_2:Ar) RF-sputtered PtO_x Schottky contacts, with either a temperature cycle of 20 °C → 180 °C → 20 °C, or of 20 °C → 120 °C → 20 °C if the devices appeared unstable at 120 °C. The comparisons of the 20 °C and 120 °C dark I-V characteristics of the RF-sputtered PtO_x contacts with varied oxygen incorporation for increasing and decreasing temperatures, barrier heights, and ideality factors with temperature are shown in Figures 8.14 – 8.17, following the presentation format of the RF-sputtered IrO_x contacts in Section 8.3. The dark I-V characteristics, barrier heights, and ideality factors for the individual levels of oxygen incorporation with increasing and decreasing temperature are included in Appendix A8.4, Figures A8.27 – A8.42.

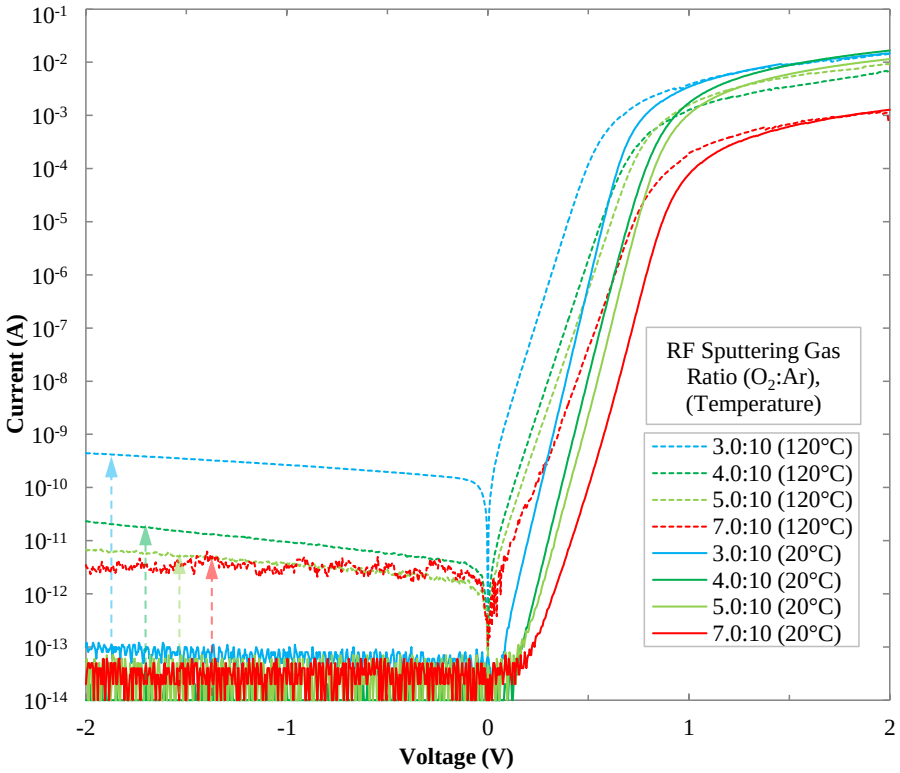

Figure 8.14: Dark I-V of 3.0:10 – 7.0:10 (O_2:Ar) RF-sputtered PtO_x (Increasing Temperature)

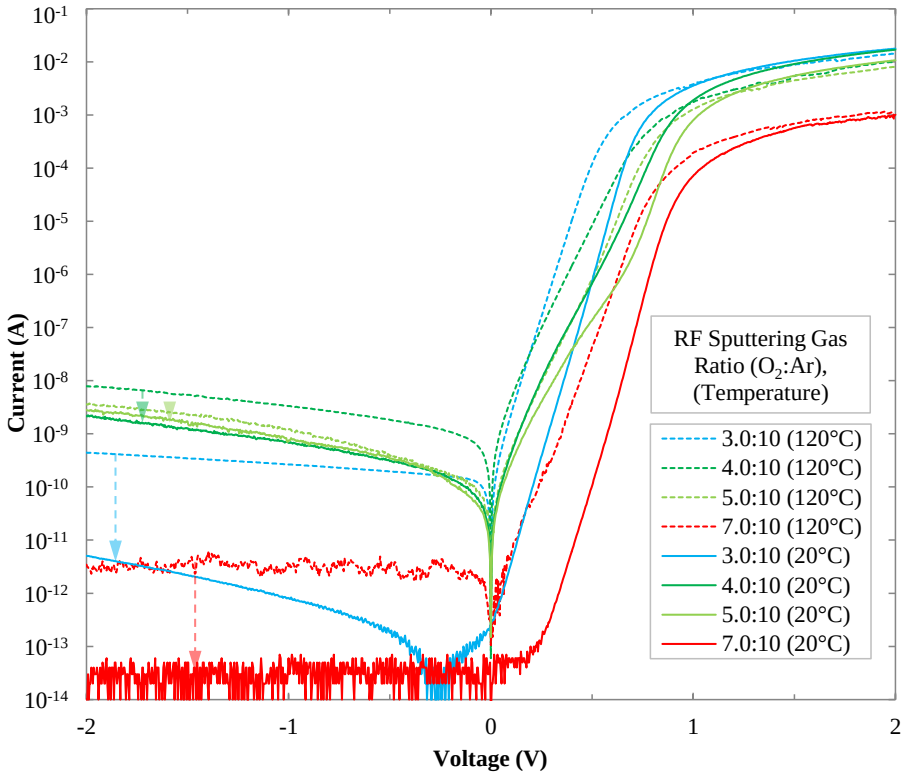

Figure 8.15: Dark I-V of 3.0:10 – 7.0:10 (O_2:Ar) RF-sputtered PtO_x (Decreasing Temperature)

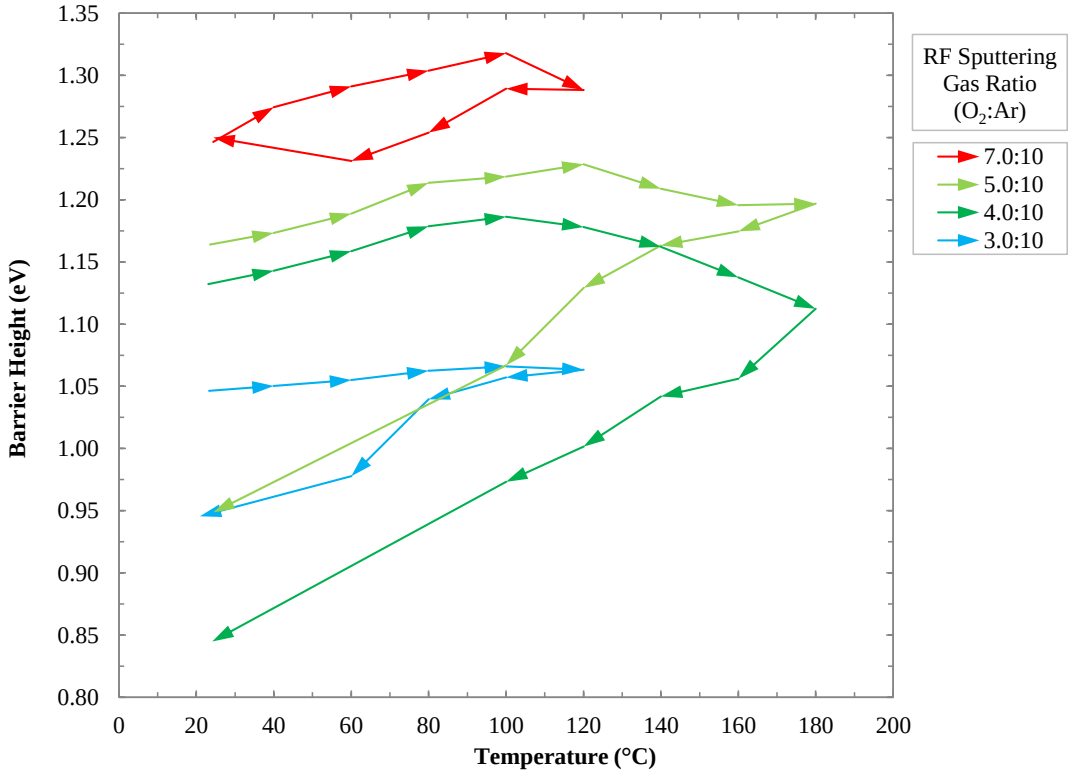

Figure 8.16: Barrier Heights with Temperature of RF-sputtered PtO_x Oxidation Series

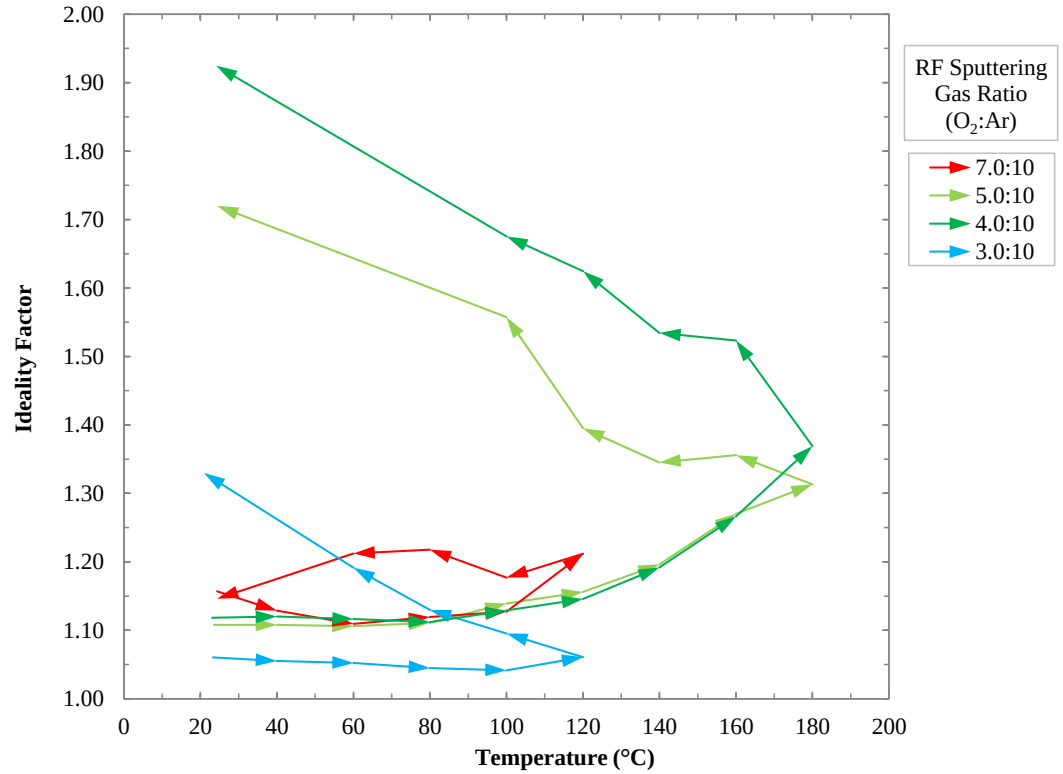

Figure 8.17: Ideality Factors with Temperature of RF-sputtered PtO_x Oxidation Series

Figure 8.14 shows that, at a temperature of 120 °C, the rectification ratios of the 3.0:10 – 7.0:10 (O_2:Ar) RF-sputtered PtO_x contacts range from 7.5 – 9.0 O_{Mag}. At 180 °C, the rectification ratios of the 4.0:10 and 5.0:10 (O_2:Ar) PtO_x contacts was 5.7 and 5.2 O_{Mag}, respectively, however the reverse bias leakage current showed ohmic shunt resistance behaviour at this temperature, shown in Appendix 8.3 (Figures A8.31 and A8.35). In comparison with the RF-sputtered IrO_x Schottky contacts, the PtO_x contacts showed ohmic shunt resistance with both increasing and decreasing temperature, indicating a lower thermal stability than that of IrO_x.

While the barrier heights of the IrO_x contacts in Figures 8.12 show increasing and plateauing barrier height with increasing temperature, Figure 8.16 shows that, above 100 °C, the barrier heights of the PtO_x contacts decreased with increasing temperature. The barrier heights of the PtO_x contacts in Figure 8.16 also decreased with decreasing temperature, resulting in significantly reduced barrier heights of the devices following the temperature test cycle. As the 3.0:10 and 7.0:10 (O_2:Ar) PtO_x contacts were only tested up to 120 °C, the decrease in barrier height and increase in ideality factor were not as significant, shown in Figures 8.16 – 8.17. PLD Pt Schottky contacts to ZnO have been reported to decrease in barrier height from 0.61 eV to 0.46 eV at 200 °C [8.7]. DC sputtered Pt Schottky contacts to ZnO have also been reported to decrease in barrier height at 100 °C [8.8].

A double-barrier is also present in Figures 8.14 – 8.15, significantly larger in the 4.0:10 and 5.0:10 (O_2:Ar) PtO_x contacts. As PtO_x is known to decompose into Pt, rather than PtO_{x-1} with annealing, the annealing process could be forming a layer of Pt within the Schottky contact, creating the observed double-barrier [8.4 – 8.6].

Figure 8.16 shows that higher oxygen incorporation in the 3.0:10 – 7.0:10 (O_2:Ar) PtO_x contacts appears to correlate with an increase in the barrier height gradient with temperature, despite the thermal damage to the devices tested above 100 °C. The recovery of the 7.0:10 (O_2:Ar) PtO_x contact following the temperature test cycle shows almost no double-barrier after the decreasing temperature cycle in Figure 8.15, indicating that increasing oxygen incorporation may contribute to temperature stability. Temperature measurements were not performed on 0.0:10 – 2.0:10 (O_2:Ar) PtO_x contacts due to the low rectification ratio at room temperature, as discussed in Section 8.3.

8.5 Thermal Stability of RF-Sputtered Silver Oxide Schottky Contacts

Varied temperature experiments were performed on 4.0:10 (O_2:Ar) RF-sputtered AgO_x Schottky contacts, with a temperature cycle of 20 °C → 140 °C → 20 °C. The dark I-V characteristics, barrier heights, and ideality factors with temperature are shown in Figures 8.18 – 8.21.

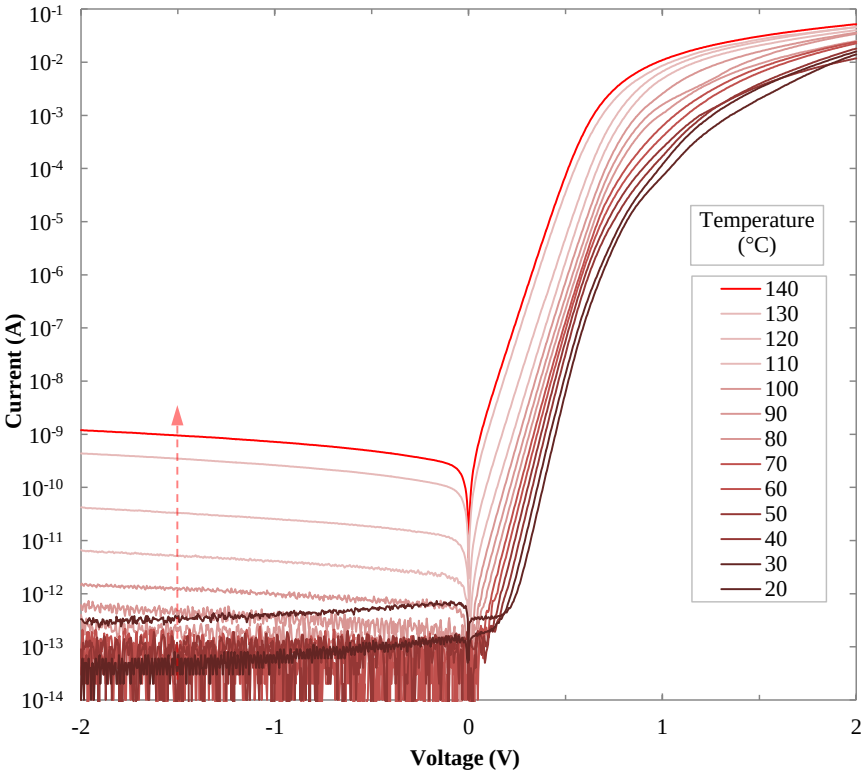

Figure 8.18: Dark I-V of 4.0:10 (O_2:Ar) RF-sputtered AgO_x (Increasing Temperature)

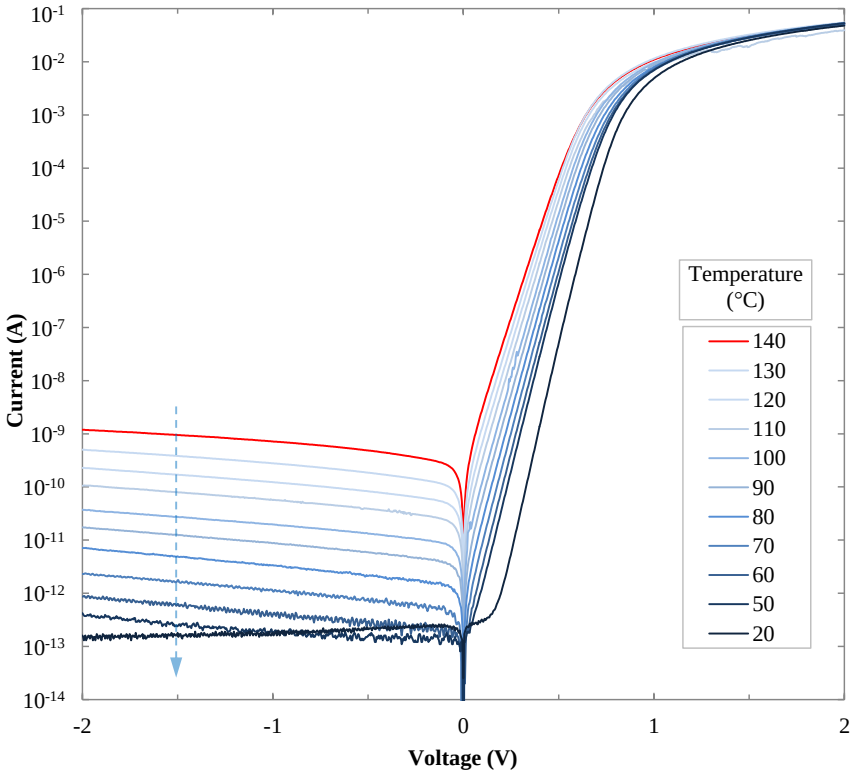

Figure 8.19: Dark I-V of 4.0:10 (O_2:Ar) RF-sputtered AgO_x (Decreasing Temperature)

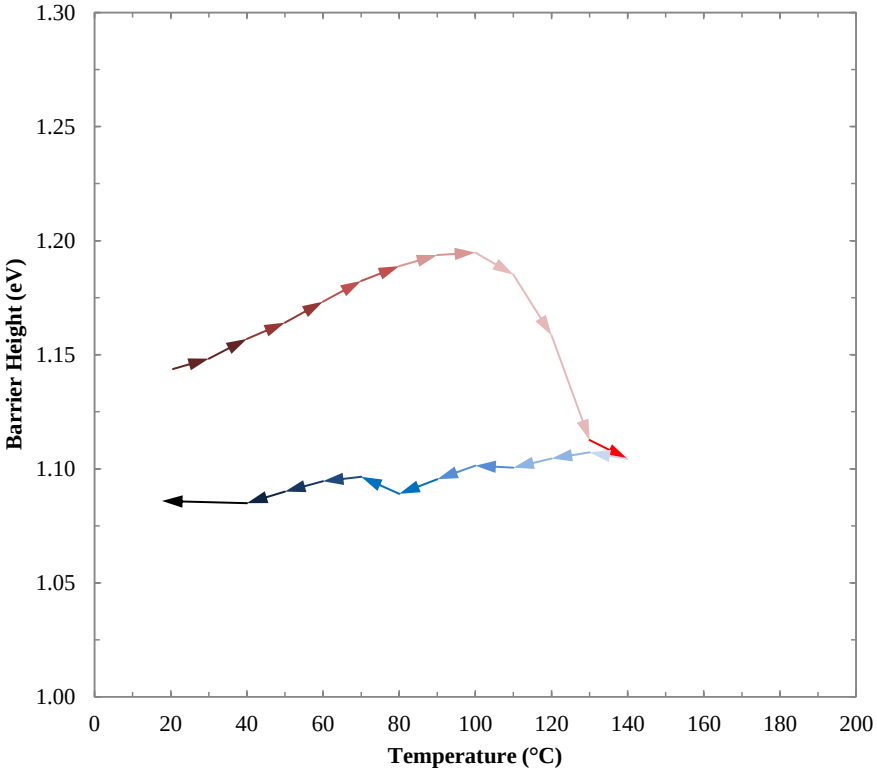

Figure 8.20: Barrier Heights with Temperature of 4.0:10 (O_2:Ar) RF-sputtered AgO_x

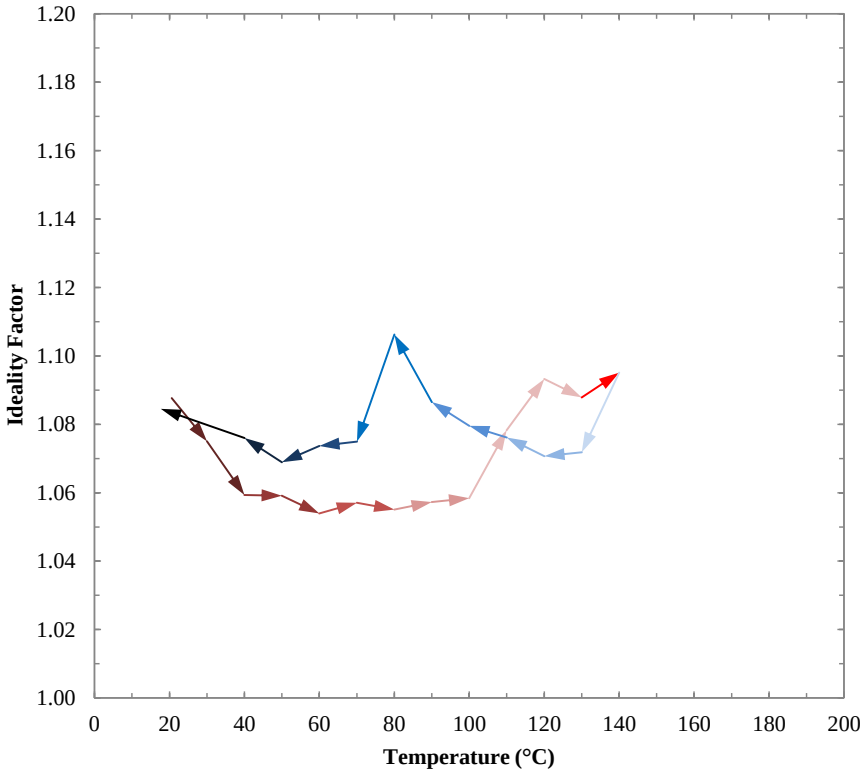

Figure 8.21: Ideality Factors with Temperature of 4.0:10 (O_2:Ar) RF-sputtered AgO_x

Figures 8.18 – 8.19 show that the 4.0:10 (O_2:Ar) RF-sputtered AgO_x Schottky contact at 140 °C had a rectification ratio of 7.6 O_{Mag}, comparable to that of RF-sputtered 4.0:10 (O_2:Ar) IrO_x and PtO_x at 140 °C, with rectification ratios of 8.1 and 7.3 O_{Mag} respectively. AgO_x was the only material to completely in recover rectification ratio following the temperature test cycle. However, the AgO_x devices were only tested to a maximum temperature of 140 °C, as opposed to 180 °C.

In contrast to the dark I-V characteristics with increasing temperature of all of the Schottky contacts in Sections 8.2 – 8.5, the AgO_x contact in Figure 8.18 showed a permanent increase in forward bias current with increasing temperature. Although there was no significant change in the rectification ratio, calculated at ±2.0 V, the 20 °C rectification ratio at ±1.0 V increased from 9.1 O_{Mag} to 11 O_{Mag} following the temperature cycle. There was no apparent double-barrier formed in the forward bias region following the temperature cycle, implying low or no thermal damage. However, this could be due to the low maximum-temperature tested for AgO_x Schottky contacts.

The barrier heights and ideality factors shown in Figures 8.20 – 8.21 show an increase in diode quality from 20 °C to 100 °C, with barrier height increasing and ideality factor decreasing. For temperatures above 100 °C, the barrier height decreases and the ideality factor increases rapidly. The barrier height and ideality factor do not change significantly during the decreasing temperature cycle, with the exception of the dark I-V characteristic at 80 °C. The stability of the ideality factor has been attributed to the lack of double-barrier present during the decreasing temperature cycle. The trends in Figures 8.20 – 8.21 suggest that the 4.0:10 (O_2:Ar) RF-sputtered AgO_x Schottky contacts are only stable up to 100 °C. Published trends of DC sputtered Ag Schottky contacts on ZnO show barrier height and ideality factor improving between temperatures of 20 – 80 °C, followed by decreasing barrier height and increasing ideality between 80 – 150 °C [8.8].

As a full oxidation series was not performed on AgO_x, only one sample was tested for material comparison. The increase in forward bias conductivity, decrease in ideality factor and significant decrease in barrier height were behaviours not observed in the IrO_x and PtO_x Schottky contact tests. This warrants further investigation, specifically of the variation with oxygen incorporation.

8.6 Thermal Stability of RF-Sputtered Palladium Oxide Schottky Contacts

Varied temperature experiments were performed on 7.0:10 (O_2:Ar) RF-sputtered PdO_x Schottky contacts, with an initial temperature cycle of 20 °C → 150 °C → 20 °C, and a repeat temperature cycle of 20 °C → 180 °C → 20 °C. The dark I-V characteristics, comparison barrier heights, and comparison ideality factors with temperature, are shown in Figures 8.22 – 8.27. Barrier heights and ideality factors of the individual contacts are included in Appendix A8.5, Figures A8.43 – A8.46.

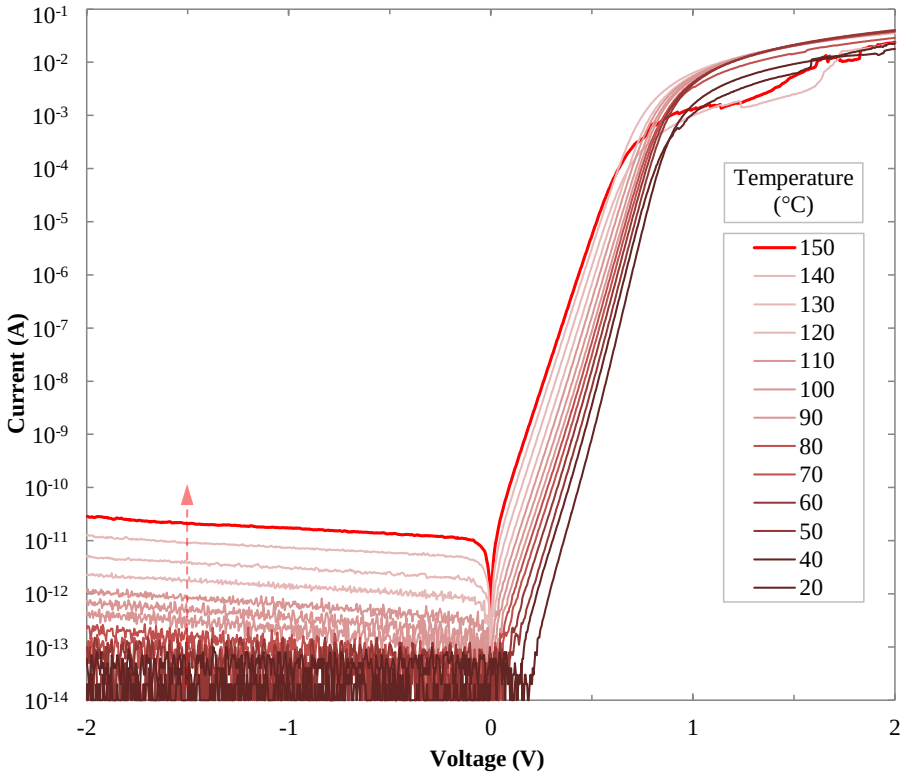

Figure 8.22: Dark I-V of 7.0:10 (O_2:Ar) RF-sputtered PdO_x (Increasing Temperature)

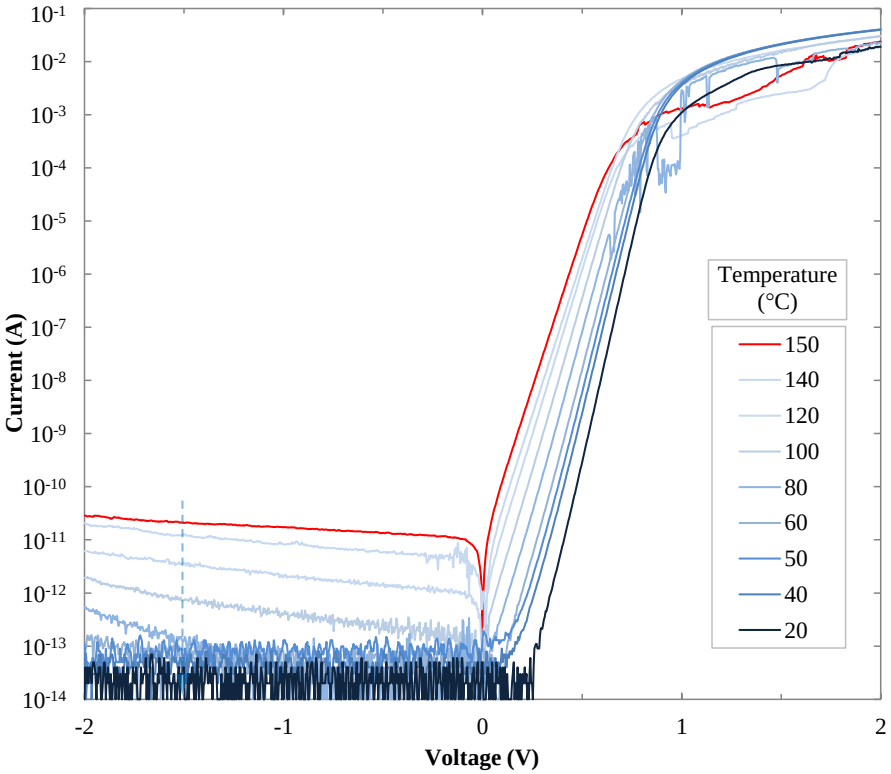

Figure 8.23: Dark I-V of 7.0:10 (O_2:Ar) RF-sputtered PdO_x (Decreasing Temperature)

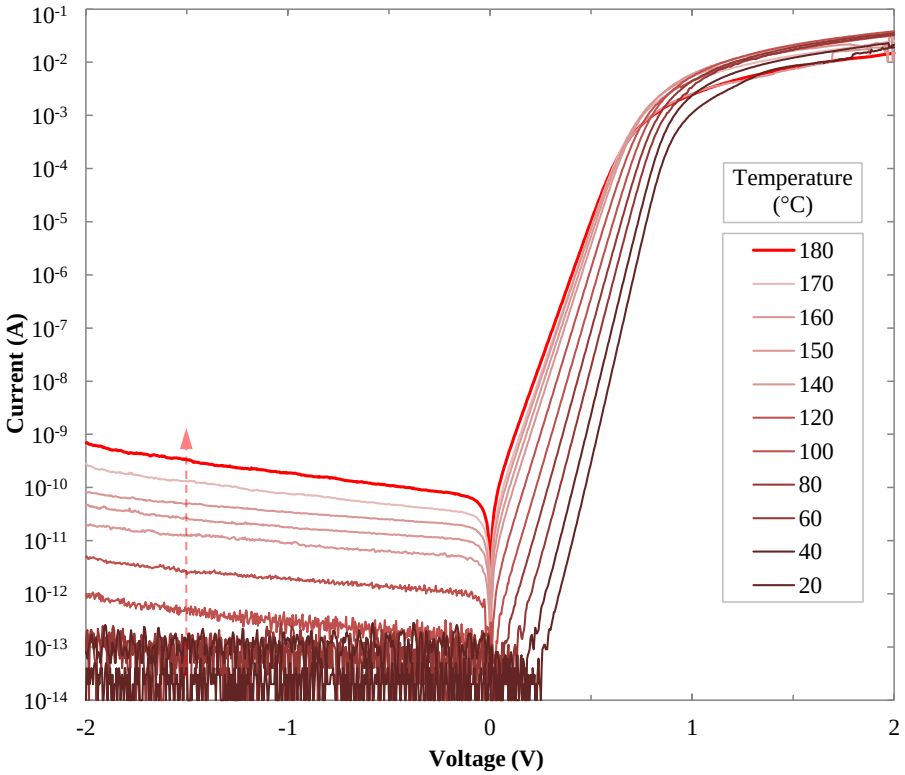

Figure 8.24: 7.0:10 (O_2:Ar) RF-sputtered PdO_x Dark I-V (Increasing Temperature, Repeat)

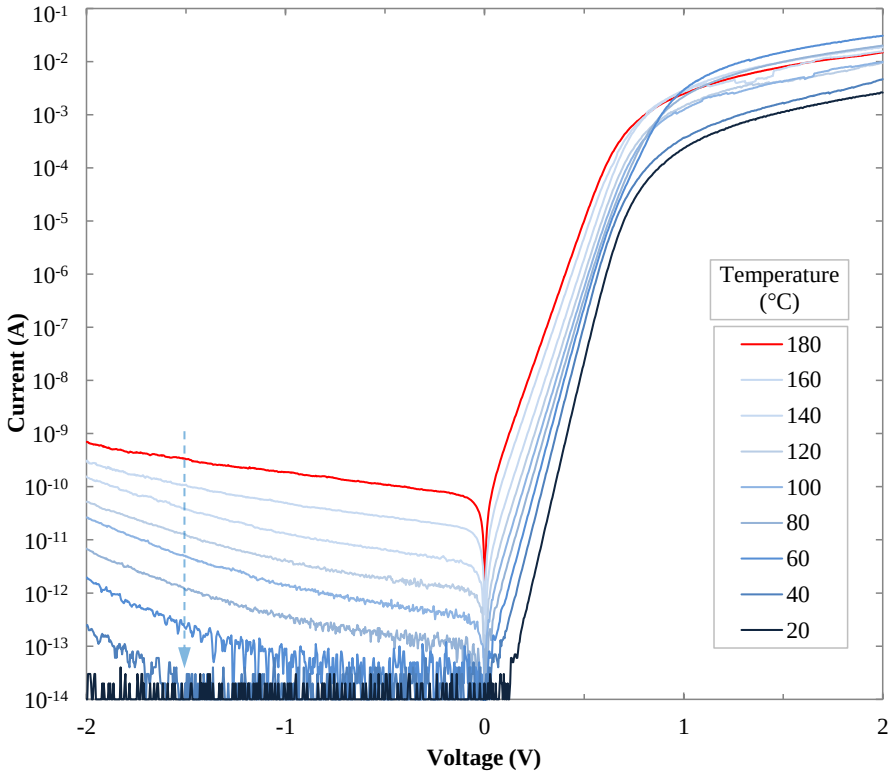

Figure 8.25: 7.0:10 (O_2:Ar) RF-sputtered PdO_x Dark I-V (Decreasing Temperature, Repeat)

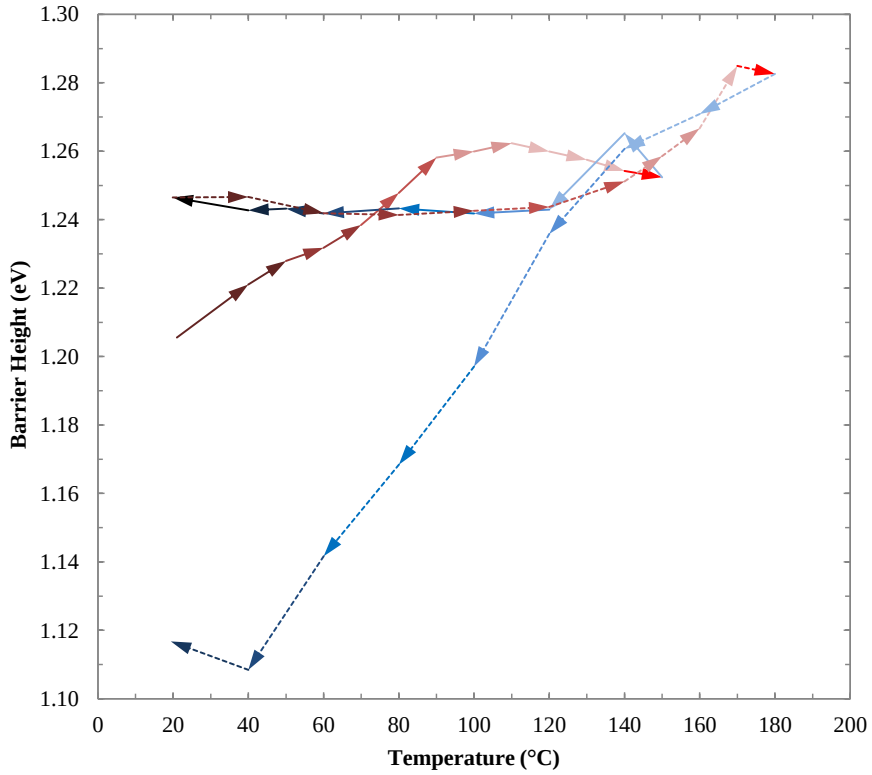

Figure 8.26: Barrier Heights with Temperature of 7.0:10 (O_2:Ar) RF-sputtered PdO_x

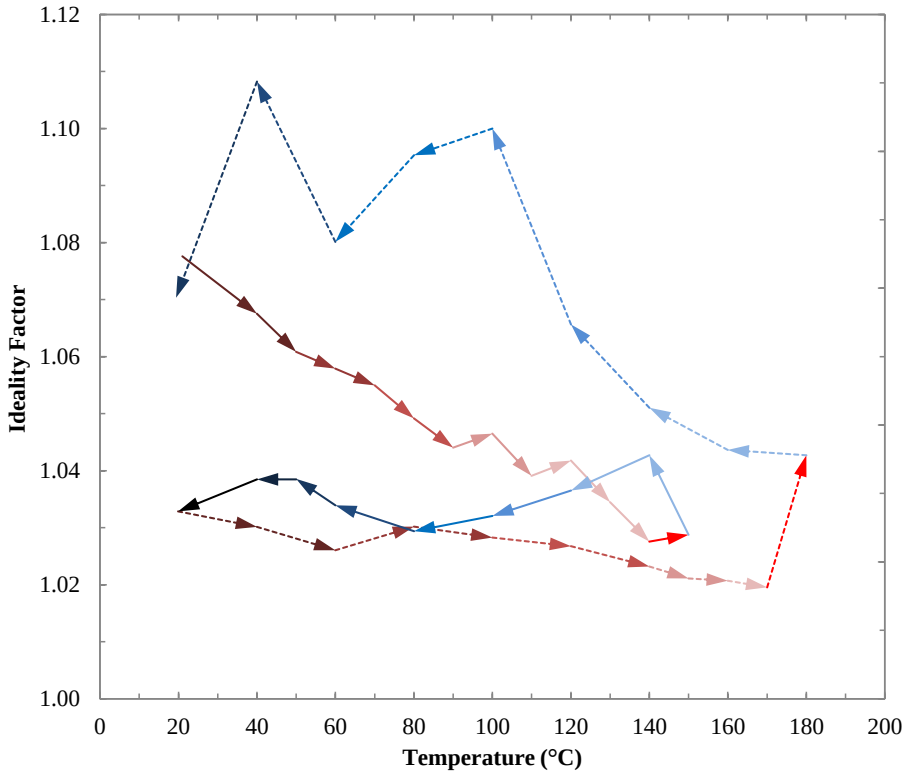

Figure 8.27: Ideality Factors with Temperature of 7.0:10 (O_2:Ar) RF-sputtered PdO_x

The dark I-V characteristics in Figures 8.22 – 8.23 show an unstable forward bias current at temperatures of 80 °C, 120 °C, and 150 °C in Figure 8.22, and at 150 °C and 130 °C in Figure 8.23. This was not a result of the temperature tests, but of poor probe contact to the device during testing, which did not affect the calculations of barrier heights or ideality factors.

The initial temperature test cycle of 20 °C → 150 °C → 20 °C was shown to increase barrier height, 1.21 – 1.25 eV, and decrease ideality factor, 1.08 – 1.03, in Figures 8.26 – 8.27 and in Appendix A8.5 Figures A8.43 – A8.44, displaying the same permanent improvement following annealing as shown for PLD IrO_x and the 7.0:10 (O_2:Ar) RF-sputtered PtO_x Schottky contact. The barrier height appeared to peak at 110 °C, indicating that the 7.0:10 (O_2:Ar) PdO_x contacts were stable up to 110 °C. The ideality factor continued to drop until 140 °C, implying that the improvement in barrier height and improvement in ideality factor may not follow the same mechanism. While a double-barrier be observed in Figure 8.22 with increasing temperature, Figure 8.23 shows a log-linear trend of forward bias current between 0 – 0.5 V. This implies that a double-barrier was not formed and there was no thermal damage to the contacts following the temperature cycle up to 150 °C, despite the barrier height improvement peaking at 110 °C. However, Figure 8.22 shows a slight increase in leakage current above 120 °C for a reverse bias of -1.0 – -2.0 V.

The dark I-V characteristics of the repeat temperature test cycle, shown in Figures 8.24 – 8.25, exhibits a significant increase in reverse bias leakage current above 100 °C, and a permanent increase in reverse-bias leakage current following the temperature cycle, which was difficult to measure for 20 °C due to the measurement low-current limitations of the parameter analyser; 1.0 fA. Despite the increase in rectification ratio, there was no visible double-barrier following the decreasing temperature cycle of the repeat measurement, implying that no permanent double-barrier was formed from thermal degradation.

The trend of the barrier heights and ideality factors of the PdO_x device during the second temperature cycle are at odds with the trends of the initial temperature cycle in Figures 8.26 – 8.27, and detailed in Appendix A8.5, Figures A8.43 – A8.46. The barrier height is shown to peak at 170 °C, rather than 110 °C, followed by a rapid decrease in barrier height with decreasing temperature in Figure 8.26. The ideality factor is also shown to decrease until 170 °C, before increasing rapidly at 180 °C and with decreasing temperature in Figure 8.27. These trends indicate that the PdO_x contacts are thermally stable to 170 °C, compared to the apparent stability of the device to 110 – 140 °C during the initial temperature cycle.

Figure 8.26 shows a steep trend of decreasing barrier height with decreasing temperature for the repeat cycle of the 7.0:10 (O_2:Ar) PdO_x contact. This could be the result of the device exceeding the

maximum stable temperature during the repeat cycle, indicating that the maximum stable temperature of the 7.0:10 (O_2:Ar) PdO_x contact is between 150 - 180 °C.

Temperature measurements of DC sputtered Pd Schottky contacts to ZnO in literature have shown a peak increase of barrier height at 75 °C, and a peak decrease of ideality factor at 100 °C [8.8]. This follows the trend of the maximum barrier height improvement preceding the maximum ideality factor improvement. Dark I-V characteristics of thermally-deposited Pd Schottky contacts to ZnO have also shown a continuous increase in barrier height, 0.67 – 0.89, and decrease in ideality factor, 2.36 – 1.48, over an increasing temperature range of 27 – 150 °C, although permanent changes to the Pd contacts were not reported [8.9].

The temperature measurements have been found to change not only the dark I-V characteristics of the devices, but the trends of future temperature measurements. The maximum thermal stability of the PdO_x device was between 110 – 140 °C, however in order to find the exact temperature of thermal stability, iterative temperature tests with increasing maximum temperature are required. As the temperature measurements require repeated contacting of the Schottky contact surface, a modified contact design is needed for this test, such as a thicker Au capping layer or a wire-bonded contact area, in order to protect the Schottky contact area. This will be especially important for Schottky contacts with a thickness of <100 nm. As the 7.0:10 (O_2:Ar) PdO_x contact showed considerable thermal stability to 150 °C, thermal stability tests of 0.0:10 – 5.0:10 (O_2:Ar) RF-sputtered PdO_x contacts should also be performed, in order to observe any trends of thermal stability with oxygen incorporation, and possible annealing of the films. The temperature tests were required to be the final experiment performed on the contacts, due to potential sample damage.

8.7 Comparison of Metal-Oxide Schottky Contact Thermal Stabilities

As the only RF-sputtered AgO_x and PdO_x devices measured with temperature cycling were deposited with gas flow ratios of 4.0:10 and 7.0:10 (O_2:Ar) respectively, the comparison of metal-oxide temperature stabilities has been divided into two parts. The dark I-V characteristics, barrier heights and ideality factors with temperature of 4.0:10 (O_2:Ar) RF-sputtered IrO_x, PtO_x, and AgO_x Schottky contacts are shown in Figures 8.28 – 8.31 at 20 °C and 140 °C. The dark I-V characteristics, barrier heights and ideality factors of 7.0:10 (O_2:Ar) RF-sputtered PtO_x and PdO_x Schottky contacts are shown in Figures 8.32 – 8.35 at 20 °C and 120 °C. The constituents of Figures 8.28 – 8.35 are included in Appendix A8.3 – A8.5. The PLD IrO_x Schottky contacts are not included in this Section, as the temperature stability of the contacts showed a significant difference from the RF-sputtered IrO_x Schottky contacts with similar initial barrier heights in Section 8.2.

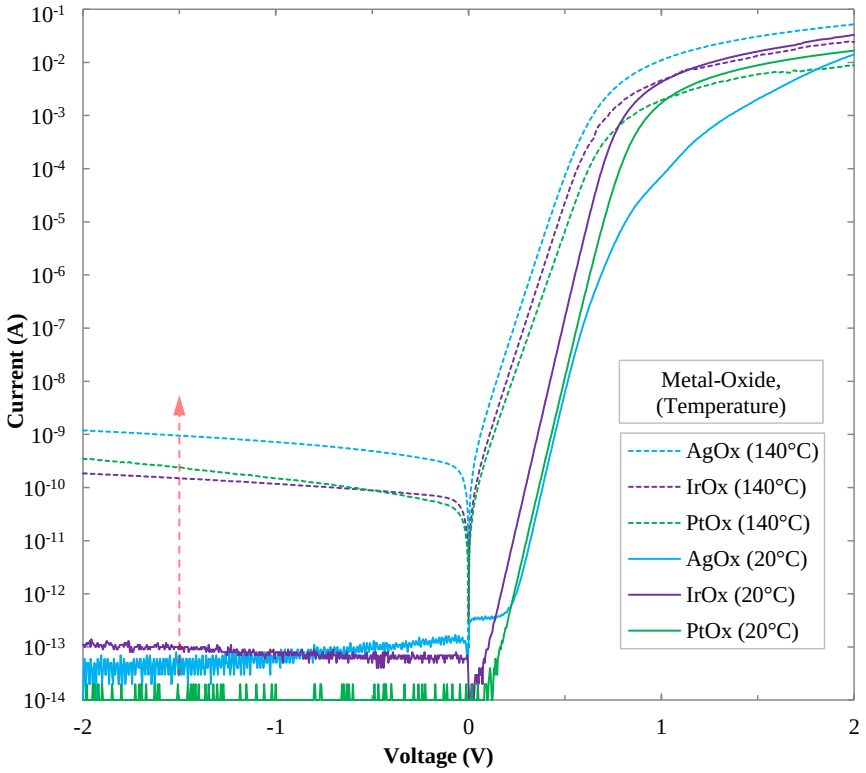

Figure 8.28: 4.0:10 (O_2:Ar) RF-sputtered AgO_x, IrO_x, and PtO_x Dark I-V (Increasing Temp.)

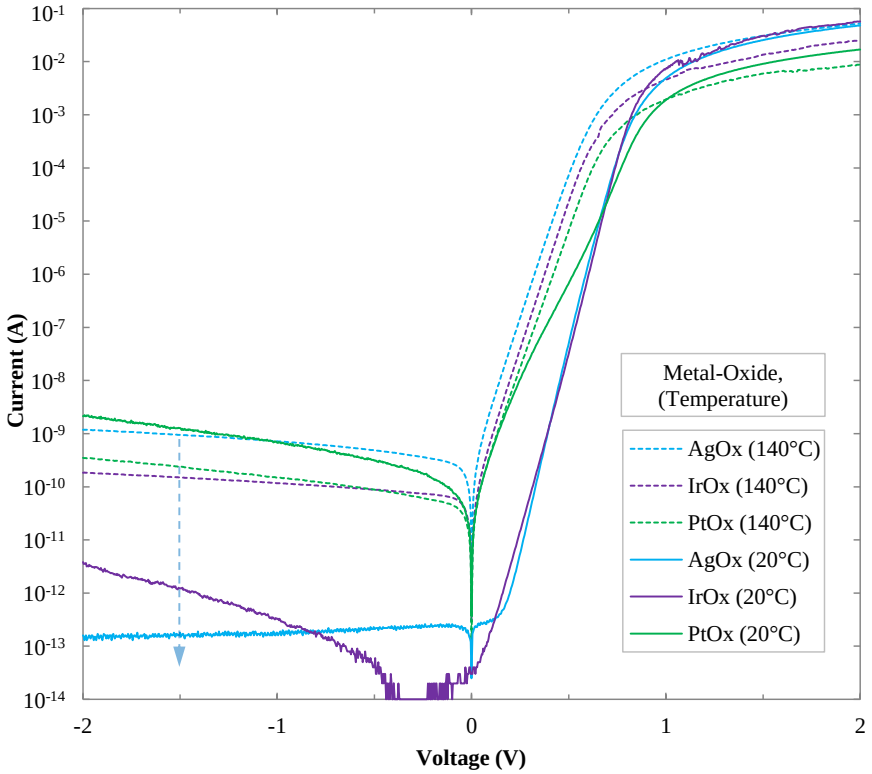

Figure 8.29: 4.0:10 (O_2:Ar) RF-sputtered AgO_x, IrO_x, and PtO_x Dark I-V (Decreasing Temp.)

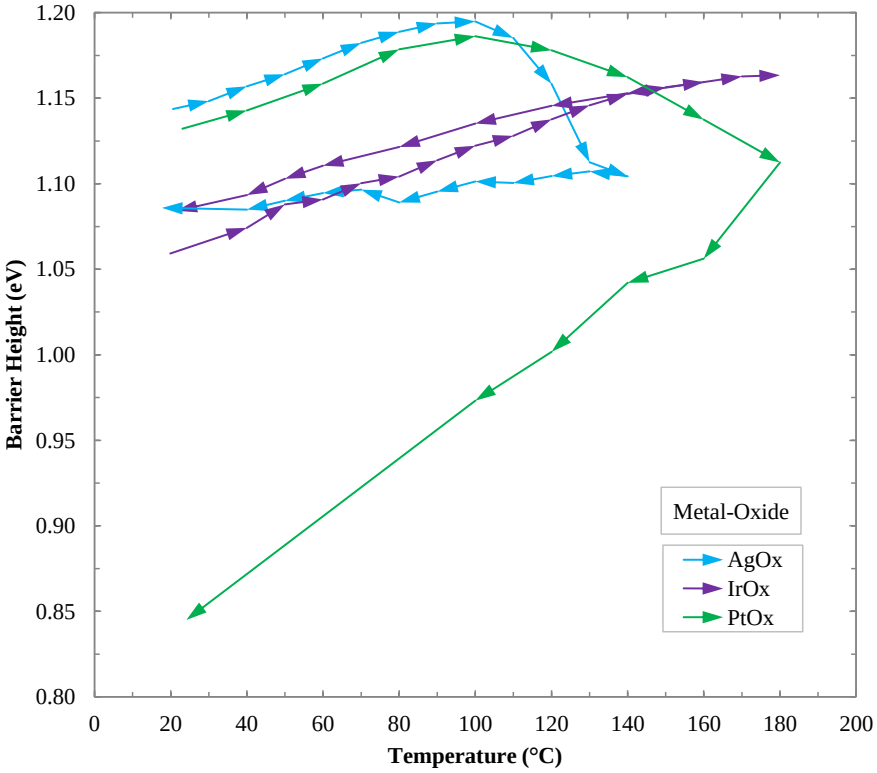

Figure 8.30: Barrier Heights with Temperature of 4.0:10 (O_2:Ar) AgO_x, IrO_x, and PtO_x

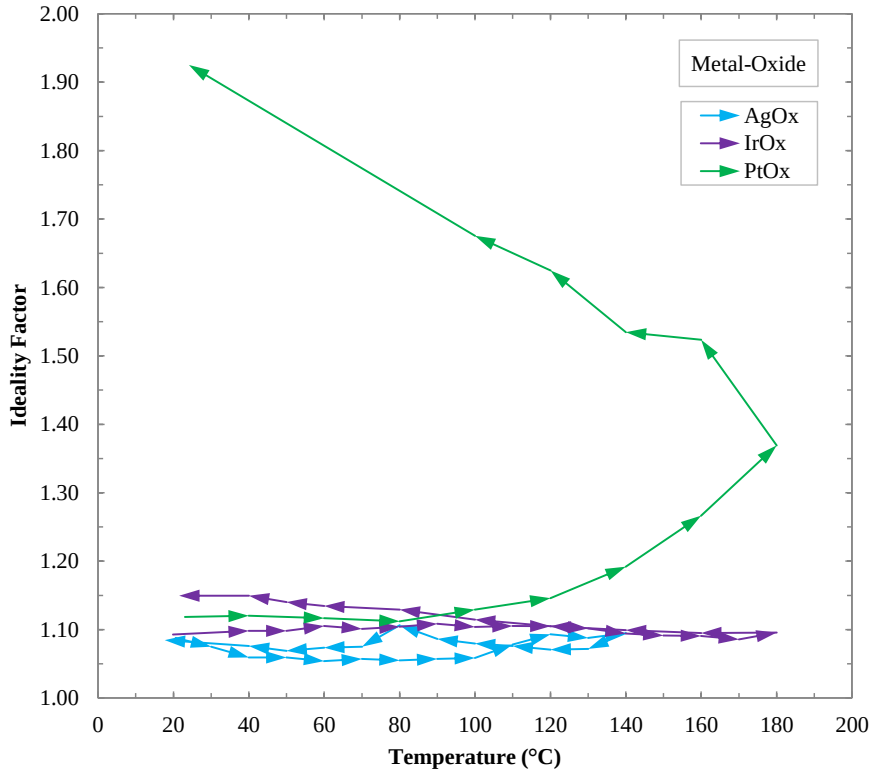

Figure 8.31: Ideality Factors with Temperature of 7.0:10 (O_2:Ar) AgO_x, IrO_x, and PtO_x

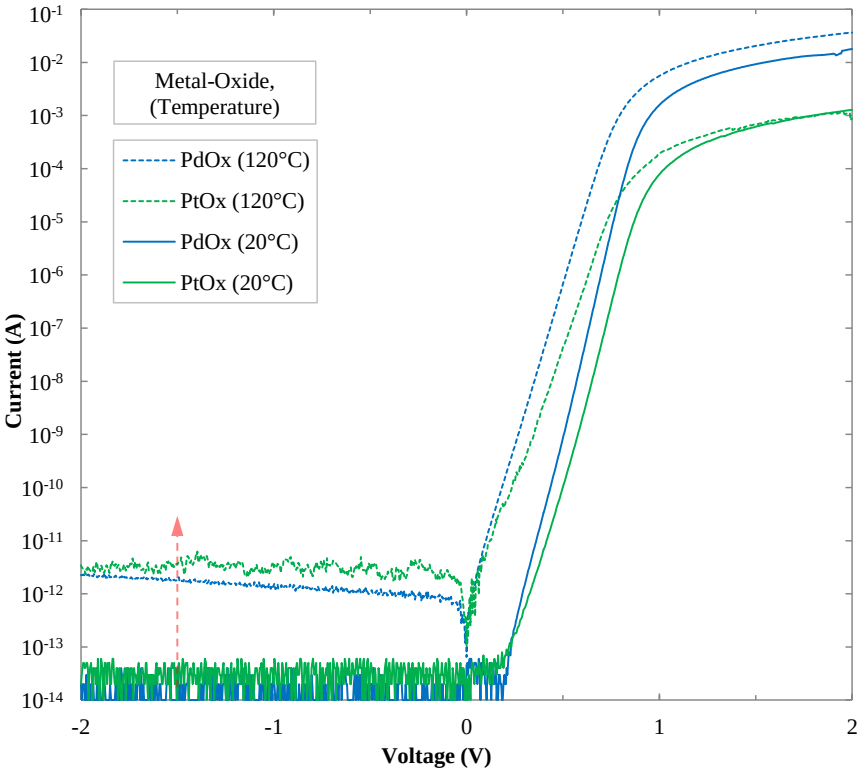

Figure 8.32: 7.0:10 (O_2:Ar) RF-sputtered PdO_x, PtO_x Dark I-V (Increasing Temp.)

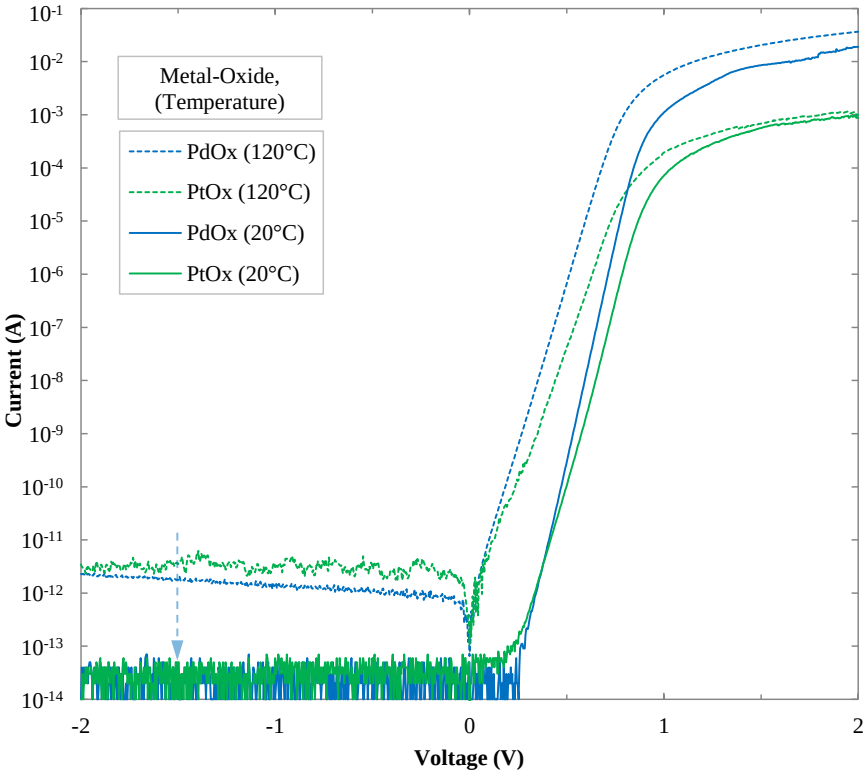

Figure 8.33: 7.0:10 (O_2:Ar) RF-sputtered PdO_x, PtO_x Dark I-V (Decreasing Temp.)

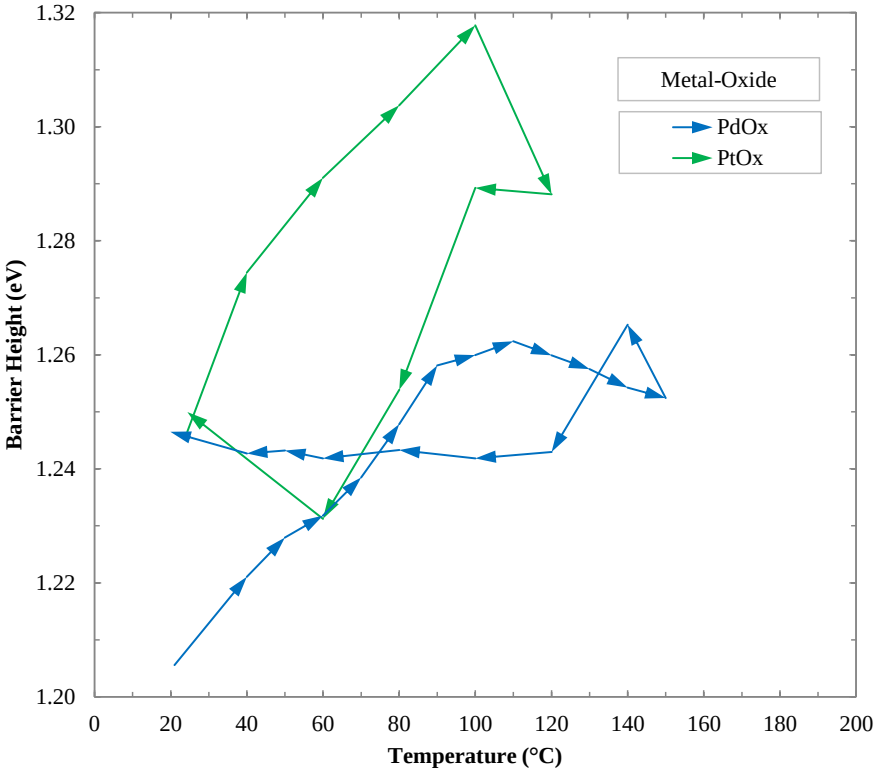

Figure 8.34: Barrier Heights with Temperature of 7.0:10 (O_2:Ar) RF-sputtered PdO_x, PtO_x

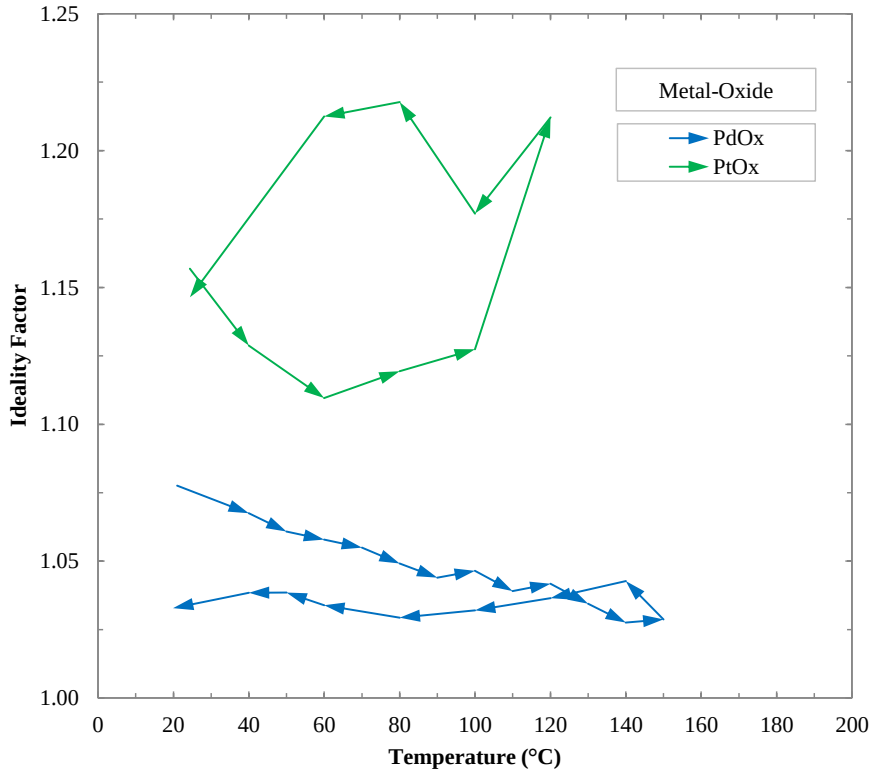

Figure 8.35: Ideality Factors with Temperature of 7.0:10 (O_2:Ar) RF-sputtered PdO_x, PtO_x

The dark I-V characteristics of 4.0:10 (O_2:Ar) RF-sputtered AgO_x, IrO_x, and PtO_x Schottky contacts in Figures 8.28 – 8.29 show that the PtO_x contact underwent a greater level of thermal degradation from the temperature tests. However, the AgO_x contact was only tested to a maximum temperature of 140 °C, compared to the IrO_x and PtO_x contacts, which were tested to 180 °C.

Figures 8.30 – 8.31 show both the AgO_x and PtO_x contacts exhibiting a peak in barrier height with temperature at 100 °C, indicating that the AgO_x contacts may have shown similar thermal degradation if tested to 180 °C. 4.0:10 (O_2:Ar) RF-sputtered AgO_x devices deposited onto molecular beam epitaxy (MBE) ZnO grown by Adam Hyndman, Department of Physics and Astronomy, University of Canterbury, New Zealand. These AgO_x devices have been tested to 160 °C with results included in Appendix 8.6 Figures A8.47 – A8.50. The device shows permanent degradation of the rectification ratio, barrier height, and ideality factor following this temperature cycle, supporting the supposition that the AgO_x contacts explored in Section 8.5 would have suffered similar damage to the PtO_x devices if tested to 180 °C.

It should also be noted that, in Figure 8.18, all temperatures produced a significant increase in the forward bias current of the AgO_x contacts. Post-deposition annealing of the AgO_x contacts to 140 °C should be considered for improved device performance.

The thermal instability of the 4.0:10 (O_2:Ar) PtO_x contacts could be due to the PtO_x decomposing into Pt during the temperature test, forming inhomogeneous Schottky barriers with lower oxygen incorporation within the PtO_x Schottky contact [8.4 – 8.6]. The appearance of a double-barrier in IrO_x following the temperature test cycle could also be caused by the thermal reduction of the film, or a change in crystal structure, although amorphous IrO_2 has been observed to crystallise into rutile IrO_2 at temperatures above 350 °C in air [8.1 – 8.2, 8.10].

The dark I-V characteristics of 7.0:10 (O_2:Ar) RF-sputtered PdO_x and PtO_x Schottky contacts in Figures 8.32 – 8.33 show similar thermal stability between the PdO_x and PtO_x contacts. Both contacts show recoverable rectification ratios when heated to 120 °C. There is a slight increase in the appearance of a double-barrier in the PtO_x contact, following the temperature test cycle. The 7.0:10 (O_2:Ar) PdO_x contact in Figures 8.24 – 8.35 for and Figures A8.35 – A8.36 of Appendix A8.4 for the 5.0:10 (O_2:Ar) PtO_x contact show that the PdO_x contact is significantly more stable up to 180 °C, although a direct comparison cannot be made. However, Figures 8.34 – 8.35 show that the barrier heights and ideality factors of the 7.0:10 (O_2:Ar) PtO_x contact improved following the temperature test cycle, but those of the PdO_x did not. The thermal stability comparison of RF-sputtered PdO_x and PtO_x contacts remains inconclusive, and requires a systematic measurement of thermal stability in order to properly characterise the materials.

In conclusion, the 4.0:10 (O_2:Ar) RF-sputtered IrO_x Schottky contact showed the greatest thermal stability of the 4.0:10 (O_2:Ar) AgO_x, IrO_x, and PtO_x contacts, appearing stable over temperatures up to 180 °C. However, there was a noticeable increase in reverse bias leakage current characteristic of ohmic shunt resistance and the appearance of a double-barrier following the temperature test cycle. As this did not appear in the PLD IrO_x Schottky contacts, it shows that there is potential for IrO_x Schottky contacts on ZnO to be stable up to 180 °C with no thermal damage.

The 7.0:10 (O_2:Ar) RF-sputtered PtO_x Schottky contact appeared more thermally stable than the PtO_x contacts tested with lower levels of oxygen incorporation, and showed a similar thermal stability to the 7.0:10 (O_2:Ar) RF-sputtered PdO_x Schottky contact. In order to properly compare the materials; iterative temperature tests of 20 °C → 30 °C → 20 °C to 20 °C → 180 °C → 20 °C are required of 2.0:10 – 7.0:10 (O_2:Ar) AgO_x, IrO_x, PdO_x, and PtO_x, using a modified Schottky contact architecture capable of repeated probe contact without risking Schottky layer damage.

8.8 Calculation of Experimental Richardson Constant for ZnO

The calculation of the Richardson constant, A^*, for bulk +c-axis Zn-polar (low-lithium) ZnO was performed on PLD IrO_x, 1.0:10 – 4.0:10 (O_2:Ar) RF-sputtered IrO_x, 3.0:10 – 7.0:10 (O_2:Ar) RF-sputtered PtO_x, 4.0:10 (O_2:Ar) RF-sputtered AgO_x, and 7.0:10 (O_2:Ar) RF-sputtered PdO_x, using the method detailed in Section 4.2.5.1. However, there is considerable uncertainty in the results.

The Richardson constant was obtained experimentally using Equation 8.1, and fitting a linear trend to a plot of $\ln\left(\frac{J_s}{T^2}\right)$ against $\frac{1000}{T}$, where J_s is the saturation current per Schottky contact area. The temperatures used range from 20 – 180 °C (293 – 453 K), producing a $\frac{1000}{T}$ range of 3.41 – 2.21 K^{-1}. For reference, ZnO would melt at 0.445 K^{-1} (1975 °C) [8.12]. The Richardson constant is calculated from the intercept, $\ln(A^*)$, therefore error in the fit of the linear trend would cause an exponential error in experimental Richardson constant.

$$\ln\left(\frac{J_s}{T^2}\right) = \frac{-q\Phi_B}{kT} + \ln(A^*) \qquad (8.1)[8.11]$$

Figure 8.36 shows the experimental determination of the 3.0:10 – 7.0:10 RF-sputtered (O_2:Ar) PtO_x Schottky contacts with the linear fit across the decreasing temperature range. For Figure 8.36, the filled data points indicate data points that were used to calculate the linear fit producing the smallest R^2 constant. The corresponding Richardson constant, R^2 value of the linear fit, and barrier height calculation for the results shown in Figure 8.36 are included in Table 8.1.

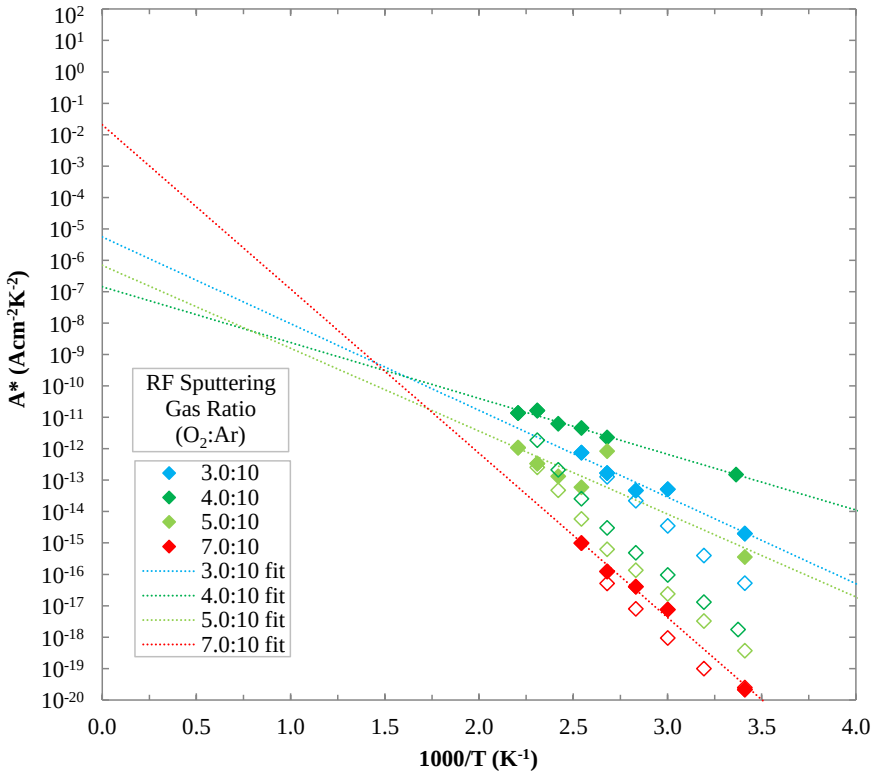

Figure 8.36: Richardson Constants for PtO_x Schottky Contacts with Decreasing Temperature

Table 8.1: Richardson Constants for PtO_x Schottky Contacts in Figure 8.36

Material	RF Sputtering Gas Ratio (O_2:Ar)	Temperature Range of Linear Fit (°C)	Calculated A^* ($Acm^{-2}K^{-2}$)	R^2 of Linear Fit	Calculated Φ_B (eV)
PtO_x	3.0:10	120 – 20	5.53×10^{-6}	0.953	0.548
PtO_x	4.0:10	180 – 20	1.44×10^{-7}	0.985	0.353
PtO_x	5.0:10	180 – 20	6.90×10^{-7}	0.794	0.524
PtO_x	7.0:10	120 – 20	2.06×10^{-2}	0.989	1.04

Figure 8.36 is intended to show the uncertainty involved in calculating the experimental Richardson constant. It was observed that the barrier height of the Schottky contacts was changing with increasing temperature due to annealing of the Schottky contact. As Equation 8.1 assumes a constant barrier height, the linear trend in $\ln\left(\frac{J_S}{T^2}\right)$ against $\frac{1000}{T}$ would not apply with increasing temperature, therefore the temperature range used to calculate the experimental Richardson constant was always the decreasing temperature region of the temperature cycle data. The limited number of data points available to fit the linear trend, combined with the amount of extrapolation necessary to obtain the Richardson constant and the exponential nature of the uncertainties complicated the accurate calculation of the experimental Richardson constant.

The range of Richardson constants able to be obtained from a linear fit of three sequential data points in the decreasing temperature cycle was calculated for the metal-oxide Schottky contacts analysed in this Chapter. Richardson constant with the best linear fit of the range was also calculated, with results included in Table 8.2. It is notable from Table 8.2 that the thermal stability tests on devices that did not show permanent thermal degradation; PLD IrO_x (initial test), PLD IrO_x (repeat test), 7.0:10 (O_2:Ar) PtO_x, 4.0:10 (O_2:Ar) AgO_x, and 7.0:10 (O_2:Ar) PdO_x (initial test), either contain or are within an order of magnitude of the theoretical Richardson constant for ZnO, 32 $Acm^{-2}K^{-2}$ [8.11]. The 7.0:10 (O_2:Ar) PtO_x and PdO_x contacts shows a best fit corresponding to a Richardson constant of 48.1 and 36.4 respectively. Richardson constant plots for the metal-oxide contacts with the best fit from Table 8.2 are included in Figures A8.51 – A8.57 of Appendix 8.7.

Table 8.2: Experimental Richardson Constants for Metal-Oxide Schottky Contacts

Material	RF Sputtering Gas Ratio (O_2:Ar)		A^* Range ($Acm^{-2}K^{-2}$)	Best Fit A^* ($Acm^{-2}K^{-2}$)	Best Fit R^2 Value
IrO_x	PLD	(initial)	1.90×10^{-3} – 30.6	17.5	1.0000
IrO_x	PLD	(repeat)	1.62×10^{-2} – 28.7	8.36×10^{-1}	0.9999
IrO_x	1.0:10		2.80 – 8.85	8.85	1.0000
IrO_x	2.0:10		5.17×10^{-4} – 5.05×10^{-2}	5.05×10^{-2}	1.0000
IrO_x	3.0:10		9.45×10^{-7} – 4.54×10^{-3}	4.54×10^{-3}	0.9999
IrO_x	4.0:10		1.52×10^{-3} – 1.79×10^{-1}	2.56×10^{-2}	0.9999
PtO_x	3.0:10		1.85×10^{-6} – 1.85×10^{-6}	1.85×10^{-6}	0.8997
PtO_x	4.0:10		7.78×10^{-8} – 1.50×10^{-7}	1.50×10^{-7}	0.9985
PtO_x	5.0:10		1.39×10^{-21} – 1.75×10^{-4}	1.75×10^{-4}	0.7709
PtO_x	7.0:10		48.1	48.1	0.9889
AgO_x	4.0:10		2.48×10^{-2} – 709	1.18×10^{-1}	1.0000
PdO_x	7.0:10	(initial)	28.2 – 133	36.4	0.9999
PdO_x	7.0:10	(repeat)	1.13×10^{-7} – 4.73×10^{-2}	3.37×10^{-6}	0.9998

Experimentally-determined Richardson constants have been published for Pd Schottky contacts to ZnO, with values of 7.7 – 167 $Acm^{-2}K^{-2}$ [8.3, 8.9, 8.13 – 8.16]. Experimental Richardson contacts have also been calculated for Ag Schottky contacts to ZnO as 0.15 – 49.0 $Acm^{-2}K^{-2}$, and AgO_x Schottky contacts to ZnO as 10 ± 6 $Acm^{-2}K^{-2}$ [8.11, 8.17 – 8.19]. The range of experimentally determined Richardson constants demonstrates the difficulty of extrapolating the value. However, as this Chapter has demonstrated the potential of Schottky contacts to ZnO to withstand temperatures up to 180 °C, a repeat experiment with a greater number of measurements over the temperature range could provide a more accurate experimental Richardson constant for ZnO.

8.9 Summary

In this chapter, the thermal stability of PLD IrO_x, and RF-sputtered IrO_x, PtO_x, AgO_x, and PdO_x Schottky contacts to bulk hydrothermal +c-axis (low-lithium) ZnO were investigated using dark I-V-T characteristics with temperatures between 20 °C and 180 °C. Experimental Richardson contacts were also calculated from the dark I-V-T characteristics. The most significant results were:

- The PLD IrO_x Schottky contacts were the most thermally-stable, with a rectification ratio of 6.4 O_{Mag} at 180 °C, and no observed thermal degradation in electrical characteristics following a temperature cycle of 20 °C → 180 °C → 20 °C. The room temperature barrier height increased from 0.911 eV to 1.01 eV, indicating beneficial annealing of the contacts between the temperatures 20 – 180 °C.

- The RF-sputtered IrO_x and PtO_x Schottky contacts tested with a temperature cycle of 20 °C → 180 °C → 20 °C suffered significant thermal degradation, developing double-barrier and increased reverse-bias leakage current. However, the RF-sputtered 7.0:10 (O_2:Ar) PtO_x contact showed thermal stability at temperatures up to 120 °C only.

- The RF-sputtered 4.0:10 (O_2:Ar) AgO_x Schottky contact showed stability at temperatures up to 140 °C, but an RF-sputtered AgO_x Schottky contact to MBE ZnO tested to 160 °C suffered permanent degradation, becoming almost ohmic from dark I-V measurements.

- The RF-sputtered 7.0:10 (O_2:Ar) PdO_x Schottky contact showed an improvement in barrier height from 1.21 eV to 1.25 eV following a 20 °C → 150 °C → 20 °C temperature cycle, but decreased to 1.11 eV following a 20 °C → 180 °C → 20 °C temperature cycle.

- An experimental Richardson constant of 36.4 $Acm^{-2}K^{-2}$ was calculated from the best fit of the 7.0:10 (O_2:Ar) PdO_x Schottky contact dark I-V-T measurements with decreasing temperature, which is close to the theoretical Richardson constant, 32 $Acm^{-2}K^{-2}$ [8.11].

- The range of experimental Richardson constants calculated for PLD IrO_x, and RF-sputtered 7.0:10 (O_2:Ar) PtO_x and 4.0:10 (O_2:Ar) AgO_x also either contained or were within an order of magnitude of the theoretical Richardson constant for ZnO [8.11].

REFERENCES

[8.1] Liu, Y., Masumoto, H., Goto, T., (2004), Electrical and optical properties of IrO_2 thin films prepared by laser-ablation, *Materials Transactions*, 45 (10), pp. 3023-3027.

[8.2] Sanjinés, R., Lévy, F., Aruchamy, A., (1989), Thermal Stability of Sputtered Iridium Oxide Films, *Journal of the Electrochemical Society*, 136 (6), pp. 1740-1743.

[8.3] Müller, S., Von Wenckstern, H., Schmidt, F., Splith, D., Heinhold, R., Allen, M., Grundmann, M., (2014), Method of choice for fabrication of high-quality ZnO-based Schottky Contacts, *Journal of Applied Physics*, 116 (19), art. no. 194506.

[8.4] Abe, Y., Yanagisawa, H., Sasaki, K., (1998), Preparation of oxygen-containing Pt and Pt oxide thin films by reactive sputtering and their characterization, *Japanese Journal of Applied Physics, Part 1: Regular Papers and Short Notes and Review Papers*, 37 (8), pp. 4482-4486.

[8.5] Mosquera, A., Horwat, D., Vazquez, L., Gutiérrez, A., Erko, A., Anders, A., Andersson, J., Endrino, J.L., (2012), Thermal decomposition and fractal properties of sputter-deposited platinum oxide thin films, *Journal of Materials Research*, 27 (5), pp. 829-836.

[8.6] Kuribayashi, K., Kitamura, S., (2001), Preparation of Pt-PtO_x thin films as electrode for memory capacitors, *Thin Solid Films*, 400 (1-2), pp. 160-164.

[8.7] Ip, K., Heo, Y.W., Baik, K.H., Norton, D.P., Pearton, S.J., Kim, S., LaRoche, J.R., Ren, F., (2004), Temperature-dependent characteristics of Pt Schottky contacts on n-type ZnO, *Applied Physics Letters*, 84 (15), pp. 2835-2837.

[8.8] Frenzel, H., Lajn, A., von Wenckstern, H., Biehne, G., Hochmuth, H., Grundmann, M., (2009), ZnO-based metal-semiconductor field-effect transistors with Ag-, Pt-, Pd-, and Au-Schottky gates, *Thin Solid Films*, 518 (4), pp. 1119-1123.

[8.9] Somvanshi, D., Jit, S., (2013), Mean barrier height and richardson constant for Pd/ZnO Thin film-based Schottky Contacts grown on n-Si substrates by thermal evaporation method, *IEEE Electron Device Letters*, 34 (10), art. no. 6595016, pp. 1238-1240.

[8.10] Pfeifer, V., Jones, T.E., Velasco Vélez, J.J., Massué, C., Arrigo, R., Teschner, D., Girgsdies, F., Scherzer, M., Greiner, M.T., Allan, J., Hashagen, M., Weinberg, G., Piccinin, S., Hävecker, M., Knop-Gericke, A., Schlögl, R., (2016), The electronic structure of iridium and its oxides, *Surface and Interface Analysis*, 48 (5), pp. 261-273.

[8.11] Sheng, H., Muthukumar, S., Emanetoglu, N.W., Lu, Y., (2002), Schottky diode with Ag on $(11\bar{2}0)$ epitaxial ZnO film, *Applied Physics Letters*, 80 (12), pp. 2132-2134.

[8.12] Özgür, Ü., Alivov, Ya.I., Liu, C., Teke, A., Reshchikov, M.A., Doğan, S., Avrutin, V., Cho, S.-J., Morkǫ, H., (2005), A comprehensive review of ZnO materials and devices, *Journal of Applied Physics*, 98 (4), art. no. 041301, pp. 1-103.

[8.13] Gayen, R.N., Bhattacharyya, S.R., Jana, P., (2014), Temperature dependent current transport of Pd/ZnO nanowire Schottky Contacts, *Semiconductor Science and Technology*, 29 (9), art. no. 095022.

[8.14] Mayimele, M.A., Van Rensburg, J.P.J., Auret, F.D., Diale, M., (2016), Analysis of temperature-dependant current-voltage characteristics and extraction of series resistance in Pd/ZnO Schottky barrier diodes, *Physica B: Condensed Matter*, 480, pp. 58-62.

[8.15] Mayimele, M.A., Diale, M., Mtangi, W., Auret, F.D., (2015), Temperature-dependent current-voltage characteristics of Pd/ZnO Schottky barrier diodes and the determination of the Richardson constant, *Materials Science in Semiconductor Processing*, 34, pp. 359-364.

[8.16] Mtangi, W., Auret, F.D., Nyamhere, C., Janse van Rensburg, P.J., Chawanda, M.D., A., (2009), Analysis of temperature dependent I-V measurements on Pd/ZnO Schottky barrier diodes and the determination of the Richardson constant, *Physica B: Condensed Matter*, 404 (8-11), pp. 1092-1096.

[8.17] Gür, E., Tüzemen, S., Kiliç, B., Cokun, C., (2007), High-temperature Schottky diode characteristics of bulk ZnO, *Journal of Physics Condensed Matter*, 19 (19), art. no. 196206.

[8.18] Kim, H., Sohn, A., Kim, D.-W., (2012), Silver Schottky contacts to Zn-polar and O-polar bulk ZnO grown by pressurized melt-growth method, *Semiconductor Science and Technology*, 27 (3), art. no. 035010.

[8.19] Allen, M.W., Weng, X., Redwing, J.M., Sarpatwari, K., Mohney, S.E., von Wenckstern, H., Grundmann, M., Durbin, S.M., (2009), Temperature-dependent properties of nearly ideal ZnO Schottky Contacts, *IEEE Transactions on Electron Devices*, 56 (9), pp. 2160-2164.

9 Conclusion and Suggestions for Further Investigations

The most significant findings in this work were the dramatic and reproducible increase in the rectifying performance of noble metal Schottky contacts to ZnO with increasing oxygen incorporation, the fabrication of noble metal-oxide Schottky contacts to bulk ZnO with the largest reported barrier heights (up to 1.42 eV), the realisation of a UV Schottky photodetector with a "square-wave" zero-bias photoresponse to repeated cycles of UVA (365 nm) radiation, therefore free of persistent photoconductivity (PPC) and the production of high-temperature noble metal-oxide Schottky contacts to ZnO that were stable up to at least 180 °C. Suggestions for further investigations include varying additional reactive RF-sputtering parameters (e.g. RF-sputtering power and substrate heating), optimising the use of surface passivation coatings to control PPC effects, and using a solar simulator to compare the UV photoresponse of the devices in this work to commercially available GaN UV photodiodes.

9.1 Summary of Work Presented

This work focused primarily on the fabrication of noble metal-oxide Schottky contacts to bulk hydrothermal ZnO towards their ultimate use in UV dosimetry. As discussed in Chapter 2, the high incidence of skin cancers and the negative health effects of vitamin D deficiency worldwide are currently driving the development of more affordable means of personal UV dosimetry than the currently available GaN and AlGaN-based devices [9.1 – 9.5]. ZnO is an earth-abundant semiconductor with a wide direct band gap, 3.37 eV at 300 K, allowing ZnO to operate in the UV spectrum [9.6 – 9.7]. Hydrothermal growth of ZnO has been shown to produce low-cost, large (2-inch) wafers of high-quality single-crystal bulk ZnO [9.7 – 9.9].

Table 9.1 lists the metal and metal-oxide Schottky contacts fabricated in this work using pulsed laser deposition (PLD) and RF-sputtered deposition techniques on wafers of Tokyo Denpa c-plane bulk hydrothermal ZnO, with device geometry shown in Figure 9.1. The fabrication methodologies are covered in Chapter 3, with an image of the photolithography mask used to create the array of Schottky contacts included in Figure A3.1 of Appendix A3.1.

Details of the ZnO wafers listed in Table 9.1 are included in Appendix A3.2, and details of the device fabrication conditions are included in Appendix A3.3. The active area of each Schottky contact in this work was 134000 μm^2, with thicknesses between 50 – 200 nm, and capped with a layer of 50 nm thick Au deposited using electron-beam deposition (EBD). Oxygen incorporation of the RF-sputtered Schottky contacts was varied by increasing the O_2:Ar gas flow ratio during sputtering from 0.0:10 sccm to 10:10 sccm, as detailed in Chapter 3.

Table 9.1: Devices Fabricated and Analysed in This Work

Metal-Oxide	Fabrication Methodology	RF-Sputtering Gas Ratio (O_2:Ar)	Deposition Power	ZnO Wafer Type	ZnO Wafer Number	Wafer Resistivity (Ωcm)
AgO_x	RF-Sputtering	0.0:10 – 4.0:10	50 W	+c-plane Zn-polar (low-lithium)	XGZ-0196-14	1.88
RuO_x	RF-Sputtering	0.5:10 – 7.0:10	50 W	–c-plane Zn-polar	CGZ-1209-5	0.09
IrO_x	PLD	-	26 kV, 10 Hz	+c-plane Zn-polar (low-lithium)	CGZ-1210-5	0.87
IrO_x	RF-Sputtering	0.5:10 – 7.0:10	50 W	–c-plane Zn-polar	CGZ-1209-9	0.10
IrO_x	RF-Sputtering	0.0:10 – 4.0:10	50 W	+c-plane Zn-polar (low-lithium)	XGZ-0196-17	1.18
PdO_x	RF-Sputtering	0.0:10 – 7.0:10	50 W	+c-plane Zn-polar (low-lithium)	XGZ-0196-9	0.85
PtO_x	RF-Sputtering	0.0:10 – 7.0:10	50 W	+c-plane Zn-polar (low-lithium)	XGZ-0196-6	3.69
PtO_x	RF-Sputtering	6.0:10 – 10:10	50 W	+c-plane Zn-polar (low-lithium)	XGZ-0196-19	5.12

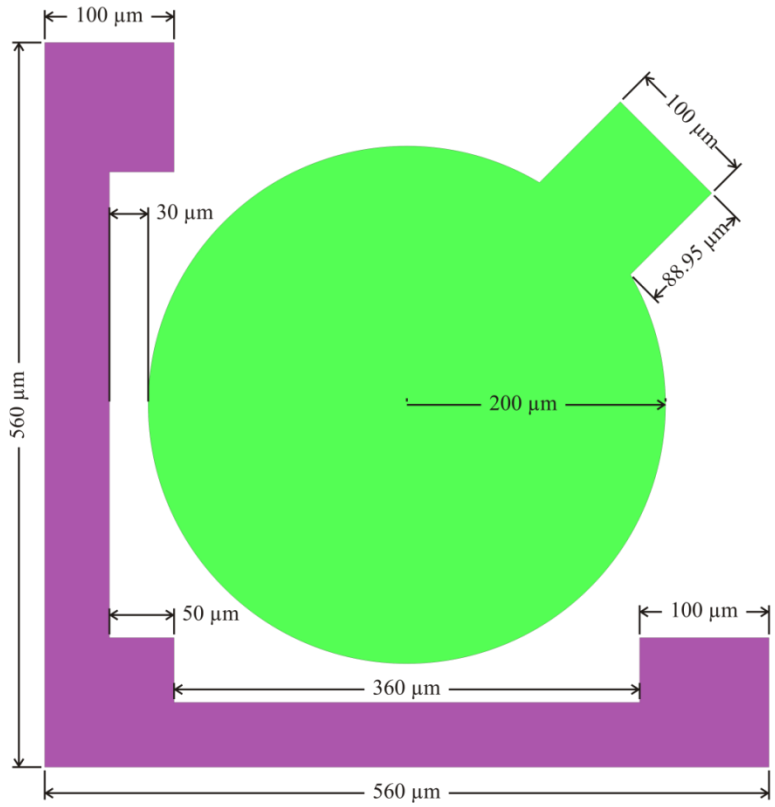

Figure 9.1: Device Dimensions with Schottky Contact in Green, Ohmic Contact in Purple

During the deposition of the RF-sputtered metal/metal-oxide Schottky contacts, thin films were simultaneously deposited onto quartz substrates for thin film analysis, with characterisation methodology detailed in Section 4.1, and results in Chapter 5. X-ray diffraction (XRD) results are courtesy of Adam Hyndman, Department of Physics and Astronomy, University of Canterbury, New Zealand. X-ray photoemission spectroscopy (XPS) results are courtesy of Dr Colin Doyle, Faculty of Engineering, University of Auckland, New Zealand. Rutherford backscattering spectroscopy (RBS) measurements, calculated values, and fitted trends are courtesy of Professor Steven M. Durbin and Robert Makin of the Department of Electrical and Computer Engineering, Western Michigan University, United States of America.

The analysis of the metal/metal-oxide films was used to determine the transparency, crystal structure, growth rate, surface potential, oxygen incorporation, and conductivity of the films. The results of the metal/metal-oxide film analysis were used to create a model of the observed Schottky contact behaviours observed in dark current-voltage (I-V) and dark capacitance-voltage (C-V) characterisation, as detailed in Chapters 6 – 8.

Dark I-V and dark C-V measurements were performed on all Schottky contacts fabricated in this work in order to determine the ideality factors, η, barrier heights, Φ_B, and rectification ratio, R_R, measured in orders of magnitude (O_{Mag}), of the contacts. These quality factors were used to assess the performance of the Schottky contacts, with a low η approaching the theoretical value of 1, and high values of Φ_B and R_R being desirable. Details of the characterisation methodology of the dark I-V and dark C-V measurements are included in Section 4.2, with results analysed in Chapter 6.

The current-time (I-T) photoresponse measurements to visible wavelengths; 625 nm (red), 610 nm (orange), 505 nm (green), and 470 nm (blue), and a UV wavelength of 365 nm were performed in order to measure the current increase and response-time to 30 s exposures of varying wavelengths, with varying device bias. The measured irradiance of the visible and UV radiation was measured as 1.31 $mWcm^{-1}$ and 2.5 Wcm^{-1}, respectively. The full spectral response of the Norland Products Inc. UVA Splice Lamp Model P/N 5200 is included in Appendix A4.6, courtesy of Dr. Salim Elzwawi, Department of Electrical and Computer Engineering, University of Canterbury, New Zealand. The methodology of the photoresponse measurements is detailed in Section 4.2.4, with results analysed in Chapter 7.

The current-voltage-temperature (I-V-T) measurements with temperatures between 20 °C and 180 °C were performed on representative devices on selected arrays of metal-oxide Schottky contacts to determine the temperature stability of the Schottky contacts, and to experimentally determine the Richardson constant, A^*, of the ZnO wafers. The methodology of the temperature stability measurements is detailed in Section 4.2.5, with results analysed in Chapter 8.

9.1.1 Metal-Oxide Films with Varied Oxygen Content Summary

Chapter 5 investigated the optical, structural, and electrical characteristics of RF-sputtered Ag, AgO_x, Ir, IrO_x, Pd, PdO_x, Pt, and PtO_x films. Transmission measurements were performed on all films to determine their optical properties. XRD was performed on the Ir/IrO_x, Pd/PdO_x, and Pt/PtO_x films to investigate the crystal structure of the films. Atomic-force microscopy (AFM) was performed on thin films of Ir/IrO_x, Pd/PdO_x, and Pt/ PtO_x films to determine their growth rate, with simultaneous Kelvin-probe microscopy (KPM) performed to determine the surface potential of the films. XPS and RBS measurements were performed on the Ir/IrO_x, Pd/PdO_x, and Pt/PtO_x films to determine the level of oxygen incorporation. Hall effect measurements were performed on the Ir/IrO_x, Pd/PdO_x, and Pt/PtO_x films to measure film conductivity.

The ~70 nm thick noble metal oxide films deposited by the usual 15 min reactive RF-sputtering showed significant attenuation of UV wavelengths, an undesirable trait for UV sensors, that require

a high degree of selectivity of UV compared to visible wavelengths. However, both IrO_x and PtO_x films showed significantly higher levels of transmission for thinner films as shown in Figure 9.2, in the case of IrO_x. IrO_x Schottky contacts with high levels of rectification have been fabricated with contact thicknesses of only 5 nm, indicating significant potential for transparent thin-film IrO_x Schottky contacts.

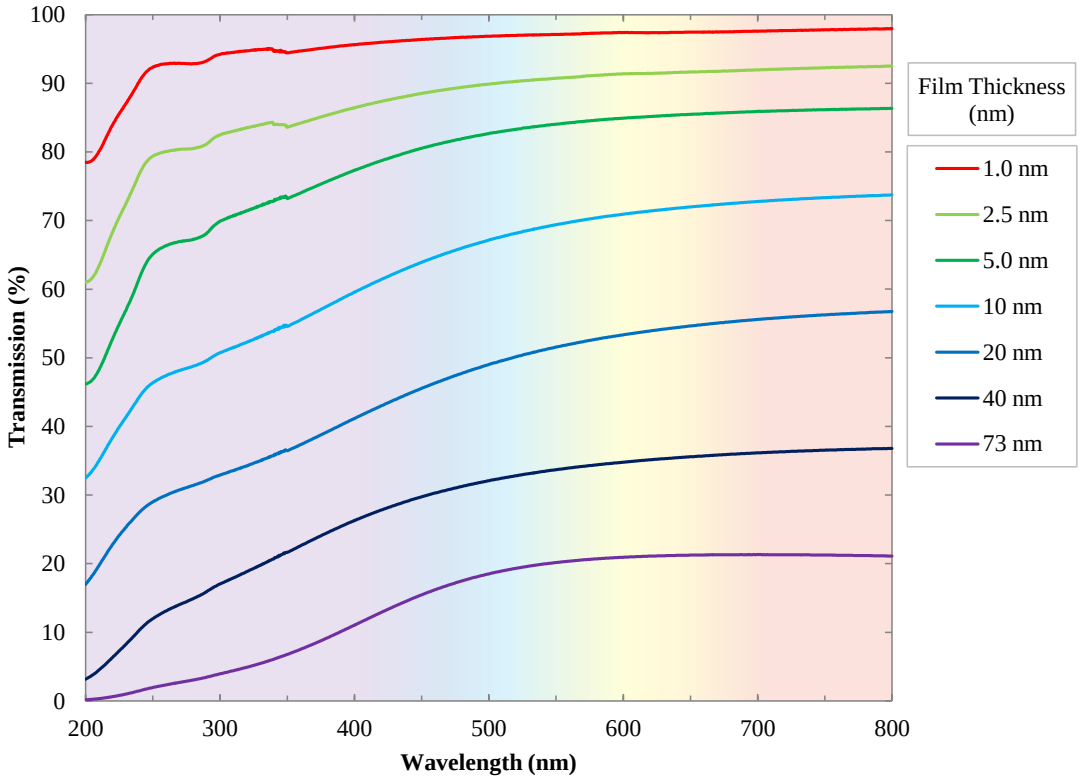

Figure 9.2: Transmission of 3.0:10 (O_2:Ar) RF-Sputtered IrO_x Films, 1.0 – 73 nm Thickness

The grazing incidence XRD (GIXRD) scans of RF-sputtered Ir, Pd, and Pt films showed a polycrystalline structure. GIXRD scans of 1.0:10 (O_2:Ar) IrO_x and PtO_x films appeared amorphous, however the 1.0:10 (O_2:Ar) PdO_x film appeared polycrystalline. Annealing room-temperature RF-sputtered films of IrO_x and PdO_x to 350 – 400 °C and 200 °C, respectively, has been shown to improve film crystallinity [9.10 – 9.11]. However PtO_x has been reported to decompose with annealing, likely due to its positive metal-oxide formation energy [9.6, 9.12].

AFM measurements of Ir/IrO_x and Pt/PtO_x films showed growth rates of 3.0 to 11 nms^{-1} for 0.0:10 to 8.0:10 (O_2:Ar) Ir/IrO_x, and 4.4 to 12 nms^{-1} for 0.0:10 to 8.0:10 (O_2:Ar) Pt/PtO_x. KPM measurements showed a trend of increasing metal-oxide surface potential with increasing oxygen

incorporation, which fits the Schottky-Mott model, predicting the production of higher noble metal oxide Schottky contact potential barriers with increasing oxygen fractions [9.13].

XPS and RBS were used to measure oxygen incorporation of the Ir/IrO_x, Pd/PdO_x, and Pt/PtO_x films. Deconvoluted XPS peaks showed a trend of increasing near-surface oxygen incorporation with increasing RF-sputtering O_2:Ar ratio. RBS was used to calculate the bulk oxygen incorporation of the films, also showing an increasing oxygen incorporation, x, from 0.0:10 to 7.0:10 (O_2:Ar) of x = 0.0 to 2.6 for Ir/IrO_x, x = 0.0 to 1.4 for Pd/PdO_x, and x = 0.0 to 2.2 for Pt/PtO_x, as shown in Figure 9.3, with arctangent trends identified and fitted by Robert Makin.

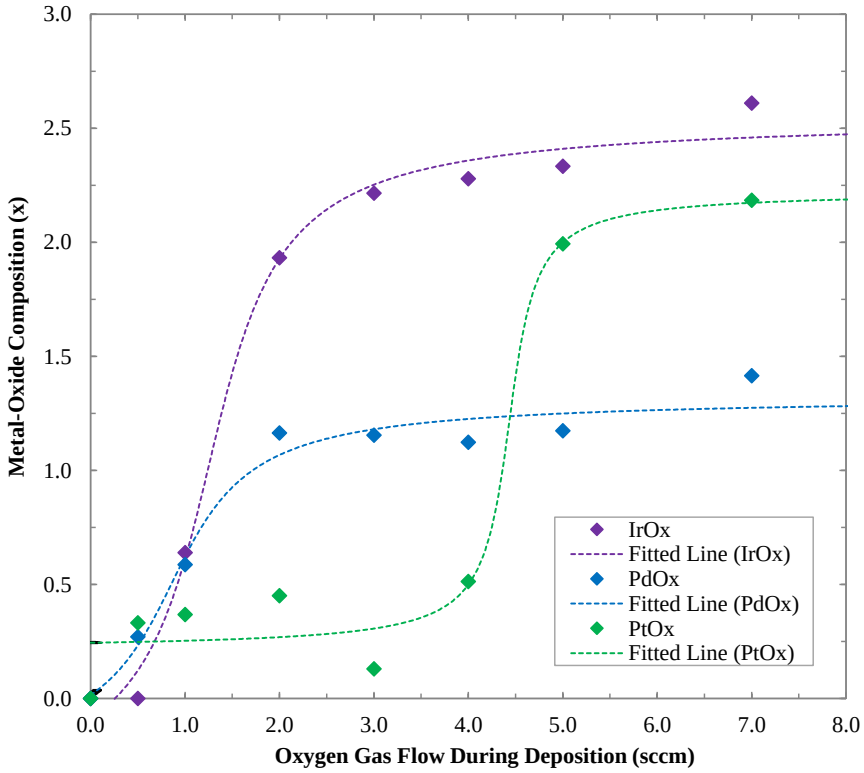

Figure 9.3: Composition of Ir/IrO_x, Pd/PdO_x, and Pt/PtO_x Films from RBS

All Ir/IrO_x films were found to be laterally conductive from measurements performed using Hall effect apparatus, with resistivities of 22 to 600 μΩcm for 0.0:10 to 4.0:10 (O_2:Ar). The lateral resistivities of 0.0:10 to 7.0:10 (O_2:Ar) Pd/PdO_x and Pt/PtO_x films increased with O_2:Ar ratio from 19 μΩcm to 4.14 Ωcm, and 94 μΩcm to 110 Ωcm, respectively, showing a significant dependence between oxygen incorporation and lateral conductivity. However, the increasing lateral resistivity did not affect the forward bias current of the Schottky contacts, as shown in Chapter 6, as this was determined by the vertical current transport through the contacts.

9.1.2 Metal-Oxide Schottky Contacts with Oxygen Content Summary

Chapter 6 investigated the electrical characteristics of the Ag/AgO_x, RuO_x, Ir/IrO_x, Pd/PdO_x, and Pt/PtO_x Schottky contacts to c-plane (Zn-polar) bulk ZnO, as described in Table 9.1. The electrical characteristics of the Ag/AgO_x, RuO_x, Ir/IrO_x, Pd/PdO_x, and Pt/PtO_x Schottky contacts were investigated with increasing oxygen incorporation, and combined with results of the metal-oxide film analysis in Chapter 5 to propose a model for formation mechanisms of the contacts.

All metal/metal-oxide Schottky contacts showed substantial improvement in η, Φ_B, and R_R with increasing oxygen incorporation. Figure 9.4 shows the dark I-V characteristics improving with oxygen incorporation of the Pt/PtO_x contacts, from completely ohmic plain Pt contacts.

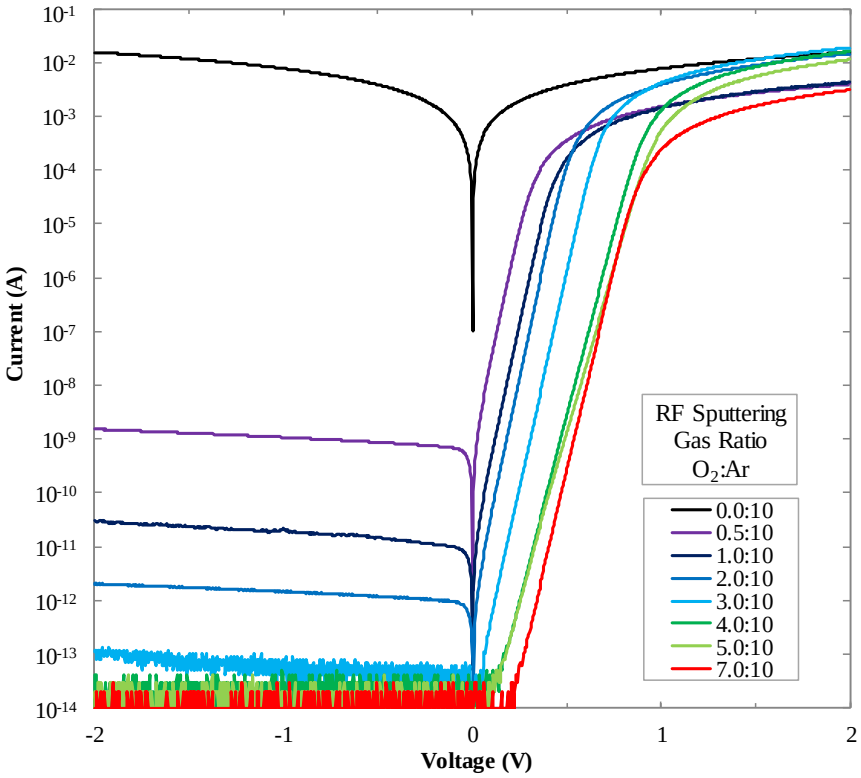

Figure 9.4: RF-Sputtered PtO_x Schottky Contacts Dark I-V Characteristics

The improvement of the dark I-V characteristics of the RF-sputtered Schottky contacts with increasing O_2:Ar ratio is shown in Table 9.2, where the η, Φ_B, and R_R are listed for representative contacts of the lowest and highest ratios of O_2:Ar gas for each metal/metal-oxide contact series. The 6.0:10 – 10:10 (O_2:Ar) series of PtO_x was not included, as there was no significant improvement of barrier height or rectification ratio with O_2:Ar > 7.0:10 for PtO_x. The highest R_R that could be calculated was 12 O_{Mag}, due to the noise floor limit of the parameter analyser, 10 fA.

Table 9.2: Electrical Characteristics of Metal/Metal-Oxide Schottky Contacts with O_2:Ar

Metal/Metal-Oxide	ZnO Wafer Type	Gas Ratio (O_2:Ar)	η	Φ_B (eV)	R_R	Gas Ratio (O_2:Ar)	η	Φ_B (eV)	R_R
Ag/AgO_x	+c-plane (low-Li)	0.0:10	1.11	0.56	4	4.0:10	1.08	1.42	11
RuO_x	–c-plane	0.5:10	1.10	0.68	6	7.0:10	1.05	0.96	10
IrO_x	–c-plane	0.5:10	1.21	0.62	4	7.0:10	1.39	0.97	9
Ir/IrO_x	+c-plane (low-Li)	0.0:10	1.18	0.53	3	4.0:10	1.29	1.12	12+
Pd/PdO_x	+c-plane (low-Li)	0.0:10	>2	0.37	1	7.0:10	1.27	1.27	12+
Pt/PtO_x	+c-plane (low-Li)	0.0:10	>2	0.36	0	7.0:10	1.12	1.22	12+

The 4.0:10 (O_2:Ar) AgO_x contact showed the largest barrier height reported to date, with Φ_B = 1.42 eV, η = 1.09, and R_R = 11 [9.14 – 9.16]. AgO_x Schottky contacts fabricated with only a limited initial supply of oxygen also showed significant improvements of η, Φ_B, and R_R from the plain Ag contacts, implying that the Schottky behaviour is dominated by the species present at the interface.

RuO_x and IrO_x Schottky contacts fabricated on –c-plane ZnO had higher leakage current and lower barrier heights compared to Schottky contacts fabricated on +c-plane (low-lithium) ZnO. This was thought to be due to higher levels of defects and lower resistivities of the –c-plane ZnO, shown in Table 9.1.

Dark C-V measurements of Ir/IrO_x, Pd/PdO_x and Pt/PtO_x Schottky contacts yielded $\Phi_{B,C\text{-}V}$ values that correlated strongly with the Φ_B values measured from dark I-V measurements, indicating a high level of lateral homogeneity in all Schottky contacts [9.17].

Figure 9.5 shows representative η and Φ_B values from the metal/metal-oxide contacts measured in this work, compared to values from metal/metal-oxide contacts to ZnO in the literature [9.14 – 9.16]. A number of AgO_x and PtO_x contacts from this work show significant improvements in the barrier heights of contemporary Schottky contacts to ZnO, which was a primary objective of this work.

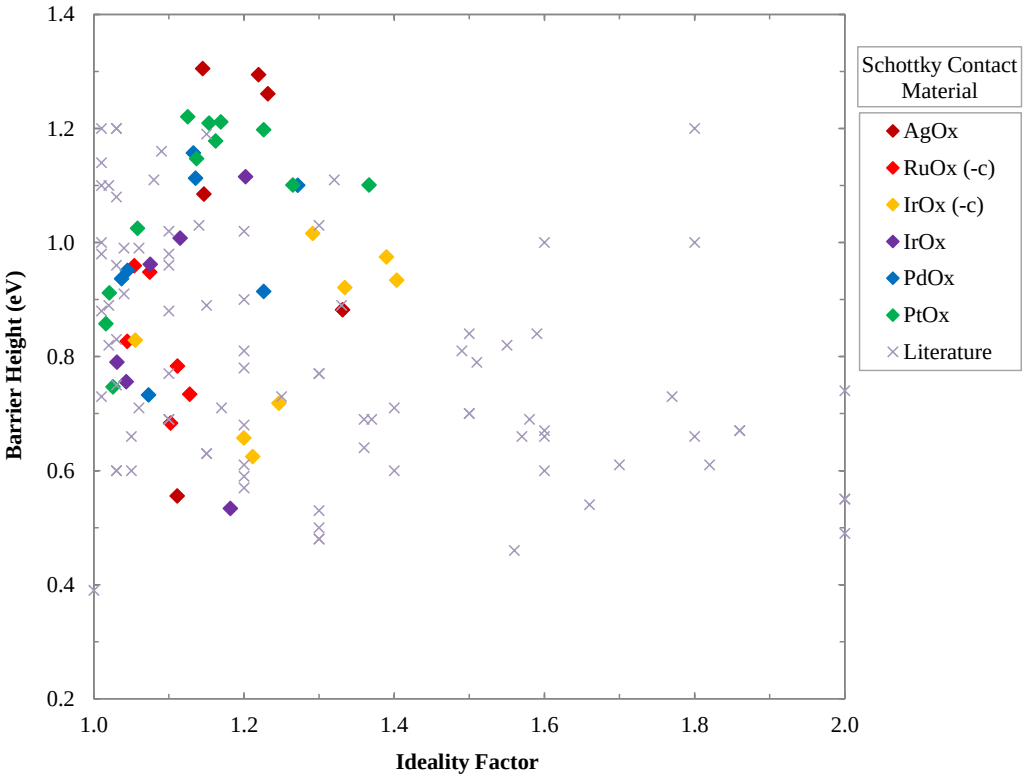

Figure 9.5: Barrier Heights of Schottky Contacts to ZnO: This Work, Literature [9.14 – 9.16]

A model for the mechanisms responsible for the dramatic improvement in the rectifying performance (in particular Φ_B and R_R) of the noble metal-oxide Schottky contacts to ZnO with their degree of oxidation was proposed that is based on the presence of active oxygen species during Schottky contact fabrication. These active oxygen species produces the following beneficial effects: (1) the removal of the terminating surface hydroxyl coverage from the ZnO surface and the associated 2-dimensional surface electron accumulation layer (SEAL), (2) the reduction in the density of oxygen vacancies (V_O) at the ZnO/Schottky contact interface that otherwise tend to pin the ZnO Fermi-level restricting the resulting Schottky barrier, and (3) an increase in the work function and electronegativity of the Schottky contact material with increasing oxygen incorporation, that was supported by KPM measurements [9.16 – 9.26].

Plain (unoxidised) noble metal Schottky contacts to ZnO reported in the literature showed significantly higher values of Φ_B than the devices measured in this work. This is likely due to pre-deposition surface treatments of the ZnO employed in the literature that provide a source of oxygen during the fabrication of the contacts, such as remote O_2/He plasma, ozone and H_2O_2 treatments, that could produce improvements in ZnO Schottky contacts in line with the same mechanisms proposed for the reactively RF-sputtered contacts in this work [9.14 – 9.16].

The RBS measurements of the Ir/IrO_x, Pd/PdO_x and Pt/PtO_x films in Figure 9.2 showed that, while IrO_x and PtO_x had exceeded x = 2 with 7.0:10 (O_2:Ar), PdO_x did not exceed x = 1.4. This implies that higher levels of oxygen incorporation of PdO_x Schottky contacts to ZnO could be possible.

9.1.3 Ultraviolet Photoresponse of Metal-Oxide Schottky Contacts to ZnO Summary

Chapter 7 investigated the photoresponse of the noble metal and noble metal-oxide Schottky contacts to 30 s exposures of visible and UV radiation, with a standard -1.0 V device bias, and varied bias. From these measurements the rise-time, t_{rise}, fall-time, t_{fall}, maximum photocurrent, $I_{maximum}$, and current increase $I_{increase}$ were calculated to characterise device photoresponsivity. $I_{increase}$ was calculated as the ratio of the maximum photocurrent to the initial dark current, in O_{Mag}. Large values of t_{rise} and t_{fall} were associated with persistent photoconductivity (PPC), a significant issue in the development of ZnO-based photodetectors [9.7, 9.27 – 9.38]. The UV photoresponse selectivity (*UVPS)* was calculated as the averaged difference in photocurrent increase between the UV and visible wavelengths.

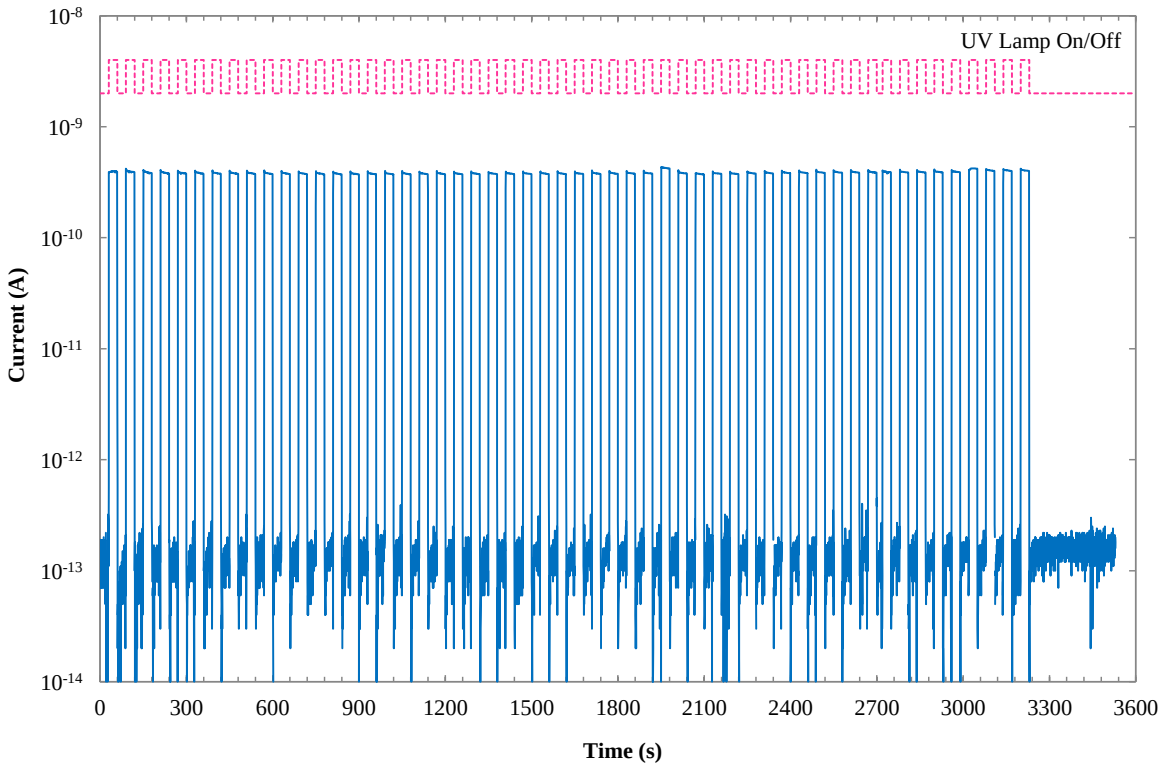

Figure 9.6: 7.0:10 (O_2:Ar) PtO_x 30 s Continual Pulsed UV Photoresponse, 0.1 V Bias

Figure 9.6 shows a square-wave response to UV radiation, with >3 O_{Mag} UV $I_{increase}$ for the 7.0:10 (O_2:Ar) PtO_x Schottky contact. The fast, consistent responsivity of the PtO_x contact shows significant potential for use in UV dosimetry, with a *UVPS* of 3.1 O_{Mag}. Comparatively, the maximum *UVPS* for each metal-oxide was 4.4, 5.1, and 3.3 O_{Mag} for 4.0:10 (O_2:Ar) IrO_x, 5.0:10 (O_2:Ar) PdO_x, and 3.0:10 (O_2:Ar) PtO_x, respectively. The 3.0:10 (O_2:Ar) PdO_x Schottky contact showed the greatest potential for UV dosimetry, with the highest *UVPS* and low t_{rise} and t_{fall}.

Noble metal-oxide Schottky contacts with increasing O_2:Ar ratios showed an overall trend of decreasing t_{rise} and t_{fall}, decreasing $I_{maximum}$, but increasing $I_{increase}$. The increase in $I_{increase}$ is likely related to the increased R_R of the metal-oxide contacts producing lower dark currents. It was also observed that *UVPS* increased with increasing O_2:Ar ratio, which is favourable for UV dosimetry.

The t_{rise}, t_{fall}, $I_{maximum}$, and $I_{increase}$ to UV radiation were also observed to be highly dependent on device bias, with all four figures of merit increasing significantly with increasingly negative device bias. A recoverable double-barrier was also formed in the dark I-V characteristics of all metal-oxide Schottky contacts following UV photoresponse measurements with highly negative device bias.

The device bias of 0 V produced the most stable UV photoresponse in this work. The largest $I_{maximum}$ with 0 V bias of each metal-oxide is shown in Table 9.3., showing 3.0:10 PtO_x to be the most promising contact for UV dosimetry, despite the lower *UVPS* value.

Table 9.3: Largest UV Photoresponse of Metal-Oxide Schottky Contacts with 0 V Bias

Metal-Oxide	ZnO Wafer Type	Gas Ratio (O_2:Ar)	t_{rise} (s)	t_{fall} (s)	$I_{maximum}$ (nA)	$I_{increase}$ (O_{Mag})	*UVPS*
AgO_x	+c-plane (low-Li)	4.0:10	< 0.1	0.7	0.0420	2.6	-
RuO_x	–c-plane	3.0:10	< 0.1	< 0.1	2.05	1.7	-
IrO_x	+c-plane (low-Li)	4.0:10	0.1	< 0.1	1.29	2.9	4.4
PdO_x	+c-plane (low-Li)	7.0:10	0.1	0.3	0.810	3.2	4.6
PtO_x	+c-plane (low-Li)	3.0:10	< 0.1	< 0.1	1.38	3.9	3.3

A comparison of the performance of the AlGaN-based UV-A photodiode listed in Table 2.3 of Section 2.2.1 (a UV sensor comparable to the current sensors used in UV dosimeters developed at the University of Canterbury, New Zealand) and the noble metal-oxide Schottky contacts fabricated in this work is listed in Table 9.4 [9.39]. The comparison shows significantly less responsivity of

the Schottky contacts fabricated in this work, however the responsivity of the AlGaN-based UV-A sensor was assumed to be measured with a 0 V bias, and the UV photocurrent of the noble metal-oxide Schottky contacts has been shown to depend significantly on device bias. The low transmission of the noble metal-oxide Schottky contacts and the 50 nm Au capping layer could also be a source of the reduced responsivity, and should be investigated.

Table 9.4: Comparison of AlGaN-Based UV-A Photodiode to Metal-Oxide Contacts [9.39]

UV Sensor	Gas Ratio (O_2:Ar)	Dark I-V Current at 2 V	Dark I-V Current at -0.1 V	Photocurrent UV-A 365nm, 2.5 $mWcm^{-2}$	Responsivity at 0 V	Active Area (mm^2)
AlGaN-Based UV-A Sensor [9.39]	-	1 mA	1 nA	110 nA	0.14 AW^{-1}	0.076
AgO_x	4.0:10	22 mA	140 fA	41 pA	13 μAW^{-1}	0.134
IrO_x	4.0:10	46 mA	110 fA	1.3 nA	380 μAW^{-1}	0.134
PdO_x	0.5:10	14 mA	1.6 pA	6.2 pA	1.8 μAW^{-1}	0.134
PdO_x	1.0:10	58 mA	70 fA	41 pA	12 μAW^{-1}	0.134
PdO_x	3.0:10	40 mA	20 fA	170 pA	50 μAW^{-1}	0.134
PdO_x	4.0:10	25 mA	10 fA	210 pA	62 μAW^{-1}	0.134
PdO_x	5.0:10	29 mA	60 fA	410 pA	120 μAW^{-1}	0.134
PdO_x	7.0:10	45 mA	22 fA	810 pA	240 μAW^{-1}	0.134
PtO_x	0.0:10	9.5 mA	440 µA	110 nA	34 mAW^{-1}	0.134
PtO_x	0.5:10	6.7 mA	620 pA	1.0 nA	310 μAW^{-1}	0.134
PtO_x	1.0:10	5.1 mA	8.3 pA	1.0 nA	300 μAW^{-1}	0.134
PtO_x	2.0:10	17 mA	470 fA	1.3 nA	390 μAW^{-1}	0.134
PtO_x	3.0:10	12 mA	1.1 pA	1.4 nA	410 μAW^{-1}	0.134
PtO_x	4.0:10	11 mA	300 fA	860 pA	250 μAW^{-1}	0.134
PtO_x	5.0:10	8.4 mA	260 fA	1.0 nA	310 μAW^{-1}	0.134
PtO_x	7.0:10	1.0 mA	950 fA	740 pA	220 μAW^{-1}	0.134

A proposed model of the PPC mechanisms responsible for the dependence of t_{rise}, t_{fall}, $I_{maximum}$, and $I_{increase}$ on oxygen incorporation and device bias in noble metal-oxide Schottky contacts include

(1) the UV-induced desorption of atmospheric surface species, in particular chemisorbed oxygen and water vapour, and (2) the ionisation and migration of metastable V_O defects in ZnO towards the Schottky contact interface [9.27, 9.32 – 9.37]. Noble metal-oxide Schottky contacts with higher levels of oxygen incorporation are expected to have fewer V_O defects at the Schottky contact interface, reducing V_O ionisation and associated PPC [9.35 – 9.36]. The formation of a double-barrier in the dark I-V characteristics is thought to be related to negative bias illumination stress (NBIS), causing the increased aggregation and trapping of ionised V_O defects at the interface, and therefore increasing levels of of t_{rise}, t_{fall}, $I_{maximum}$, and $I_{increase}$ with increasing negative device bias [9.7, 9.37 – 9.38].

9.1.4 Thermal Stability of Schottky Contacts to ZnO Summary

Chapter 8 investigated the thermal stability of RF-sputtered AgO_x, IrO_x, PdO_x, and PtO_x and PLD IrO_x, Schottky contacts to +c-axis (low-lithium) bulk ZnO using dark I-V-T characteristics at temperatures between 20 °C and 180 °C, the methodology detailed in Section 4.2.5. Experimental Richardson contacts were also calculated from the dark I-V-T characteristics.

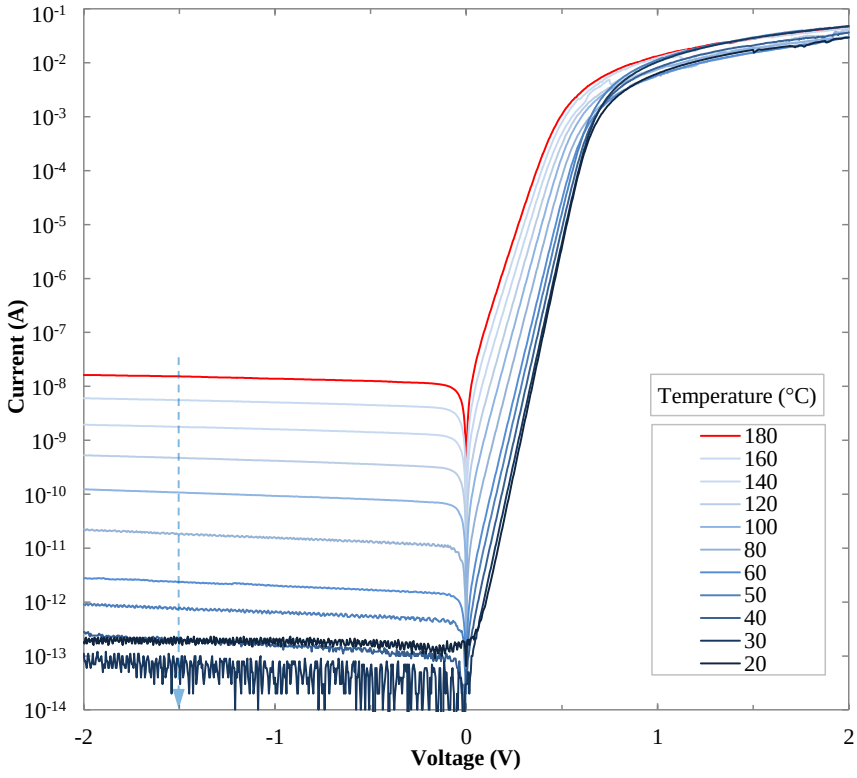

Figure 9.7: Dark I-V-T Results of PLD IrO_x Contacts (Decreasing Temperature)

The PLD IrO_x Schottky contacts to +c-plane (low-lithium) ZnO were found the most thermally-stable devices during a temperature cycle of 20 °C → 180 °C → 20 °C, as shown in Figure 9.7. At 180 °C, the device had Φ_B = 1.07 eV, η = 1.03, and R_R = 6.4, compared to the initial 20 °C measurement, with Φ_B = 0.91 eV, η = 1.02, and R_R = 10. This increase in barrier height indicates that post-fabrication annealing of the contacts can produce useful improvements in Schottky contact quality. RF-sputtered Schottky contacts showed significant thermal degradation after I-V-T measurements at 180 °C, but not at 120 °C.

An experimental Richardson constant of 36.4 $Acm^{-2}K^{-2}$ was calculated from the 7.0:10 (O_2:Ar) PdO_x Schottky contact, very close to the theoretical Richardson constant, 32 $Acm^{-2}K^{-2}$ [9.40]. The range of Richardson constants calculated for PLD IrO_x, and RF-sputtered 7.0:10 (O_2:Ar) PtO_x and 4.0:10 (O_2:Ar) AgO_x Schottky contacts were also reasonably close to the theoretical value of 32 $Acm^{-2}K^{-2}$ [9.40].

9.1.5 Overall Summary

This work investigated the fabrication and characterisation of PLD and RF-sputtered noble metal and noble metal-oxide Schottky contacts of Ag/AgO_x, RuO_x, Ir/IrO_x, Pd/PdO_x, and Pt/PtO_x to bulk c-plane ZnO for ultimate use as photodetectors for UV dosimetry. The oxygen incorporation of the RF-sputtered contacts was varied by increasing the O_2:Ar gas flow during RF-sputtering, as confirmed by RBS measurements. Chapters 5 – 8 investigated the characteristics of thin films of the metal/metal-oxide material used to make the contacts, the electrical characteristics of the contacts, the photoresponse of the contacts to monochromatic light, and the temperature stability of the contacts up to 180 °C.

- Analysis of noble metal/noble metal-oxide films deposited simultaneously with the corresponding RF-sputtered Schottky contacts confirmed an increased oxygen incorporation in the films with increasing RF-sputtering O_2:Ar gas ratio, and also showed an increasing surface potential with increasing oxygen incorporation.

- The noble metal/noble metal-oxide Schottky contacts were shown to improve substantially in Φ_B, and R_R with increasing oxygen incorporation, as shown in Table 9.2, with the 7.0:10 (O_2:Ar) PtO_x (x = 2.2) contacts showing over 12 O_{Mag} rectification, compared to the ohmic nature of plain Pt contacts to the same bulk single

crystal ZnO material. Higher levels of oxygen incorporation above x = 2.2 produced no further improvements in the PtO_x contacts.

- The 4.0:10 (O_2:Ar) AgO_x Schottky contact to +c-plane (low-lithium) ZnO in this work produced the highest barrier height reported in the literature to date, with Φ_B = 1.42 eV, η = 1.09, and R_R = 11 at 20 °C [9.14 – 9.16]. Several other AgO_x and PtO_x contacts in this work showed higher barrier heights to ZnO than values published in literature, as shown in Figure 9.5 [9.14 – 9.16].

- A proposed model for the mechanisms responsible for the very high barrier heights of the noble metal oxide Schottky contact devices fabricated in this work is based on the presence of active oxygen species during reactive RF-sputtering (and reactive PLD) that (1) removes the terminating hydroxyl layers from the ZnO surface, (2) prevents Fermi-level pinning by oxygen vacancies at ~ E_c - 0.8 eV by decreasing the V_O density near the Schottky interface, and (3) increases the work function and electronegativity of the Schottky contacts. [9.16 – 9.26]

- Noble metal-oxide Schottky contacts showed an overall trend of decreasing PPC and an increasing ratio of UV photocurrent to dark I-V current with increasing oxygen incorporation. The level of PPC was found to be strongly dependent on device bias, with increasingly negative device bias causing NBIS and reducing contact performance.

- The 7.0:10 (O_2:Ar) PtO_x Schottky contact to +c-plane (low-lithium) ZnO showed a consistent PPC-free ‘square-wave’ response to 30 s intervals of UV radiation when biased at 0 V, with over 3 O_{Mag} current increase on UV irradiation, and over 3 O_{Mag} average higher current increase to UV radiation than to visible radiation.

- A model of the mechanisms responsible for PPC in the metal-oxide Schottky contacts has been proposed in this work is based on (1) the UV-induced desorption of atmospheric surface species, particularly O_2 and H_2O, and (2) the ionisation of metastable V_O that causes the trapping photogenerated holes [9.27, 9.32 – 9.37].

- The PLD IrO_x Schottky contacts to +c-plane (low-lithium) ZnO were found the most thermally-stable to 180 °C with Φ_B = 1.07 eV, η = 1.03, and R_R = 6.4, and also showed

a permanent increase in barrier height, showing the potential of post-fabrication annealing for device improvement. The RF-sputtered Schottky contacts showed thermal stability up to 120 – 150 °C.

- An experimental Richardson constant of 36.4 $Acm^{-2}K^{-2}$ was calculated from the 7.0:10 (O_2:Ar) PdO_x contact, close to the theoretical Richardson constant, 32 $Acm^{-2}K^{-2}$ [9.40].

9.2 Suggestions for Further Investigations

This work explored RF-sputtered Schottky contacts with varying ratios of O_2:Ar gas flow during sputtering, however the flow rate of Ar gas was kept at a constant 10 sccm, the power of the RF-sputtering was constant 50 W, and no pre-treatments or post-deposition annealing processes were used in the fabrication of the devices. Therefore there is considerable scope for further experimentation. Figure 9.5 shows that the ideality factors of the devices fabricated in this work reached a minimum at barrier heights of 0.8 – 0.9 eV, and then increased with increasing barrier height. This trend can also be seen in several noble metal/metal-oxide Schottky contact series with increasing O_2:Ar ratio in Chapter 6. The oxygen incorporation of RF-sputtered AgO_x contacts should also be investigated with greater detail, as the 4.0:10 (O_2:Ar) AgO_x contact produced the highest barrier heights in this work, with 1.42 eV.

The RBS results shown in Figure 9.3 showed that that IrO_x and PtO_x films exceeded an oxygen incorporation of $x = 2$, however the PdO_x films did not exceed $x = 1.42$, indicating that higher levels of oxygen incorporation in PdO_x may be possible, and that this could produce contacts with higher barrier heights. As the 7.0:10 (O_2:Ar) PdO_x contact showed significant potential as a UV photodetector, and showed high temperature stability up to 150 °C, investigations into higher levels of oxygen incorporation in PdO_x Schottky contacts are strongly suggested.

As the photoresponse measurements performed in this work identified 7.0:10 (O_2:Ar) PdO_x and 3.0:10 (O_2:Ar) PtO_x as the most promising candidates for UV dosimetry, solar simulation tests should be performed on the devices to test the UV dosimetry capability of the devices to broad-spectrum radiation. These results should be compared to the performance of commercially-available GaN photodetectors to determine the viability of the metal-oxide Schottky contacts to bulk ZnO to replace the GaN photodetectors as a cheaper alternative.

REFERENCES

[9.1] Markovic, S.N., Erickson, L.A., Rao, R.D., Weenig, R.H., Pockaj, B.A., Bardia, A., Vachon, C.M., Schild, S.E., McWilliams, R.R., Hand, J.L., Laman, S.D., Kottschade, L.A., Maples, W.J., Pittelkow, M.R., Pulido, J.S., Cameron, J.D., Creagan, E.T., (2007), Malignant melanoma in the 21st century, part 1: Epidemiology, risk factors, screening, prevention, and diagnosis, *Mayo Clinic Proceedings*, 82 (3), pp. 364-380.

[9.2] Godar, D.E., (2005), UV doses worldwide, *Photochemistry and Photobiology*, 81 (4), pp. 736-749.

[9.3] McKenzie, R.L., Liley, J.B., Björn, L.O., (2009), UV radiation: Balancing risks and benefits, *Photochemistry and Photobiology*, 85 (1), pp. 88-98.

[9.4] Holick, M.F., (2007), Medical progress: Vitamin D deficiency, *New England Journal of Medicine*, 357 (3), pp. 266-281.

[9.5] McKenzie, R.L., Liley, B., Johnston, P., Scragg, R., Stewart, A., Reeder, A.I., Allen, M.W., (2013), Small doses from artificial UV sources elucidate the photo-production of vitamin D, *Photochemical and Photobiological Sciences*, 12 (9), pp. 1726-1737.

[9.6] Allen., M., (2008), *Schottky Contact Formation to Bulk Zinc Oxide*, PhD thesis, University of Canterbury, New Zealand.

[9.7] Jagadish, C., Pearton, S.J., (2006), *Zinc Oxide Bulk, Thin Films and Nanostructures – Processing, Properties and Applications*, Oxford, U.K: Elsevier Ltd.

[9.8] Maeda, K., Sato, M., Niikura, I., Fukuda, T., (2005), Growth of 2 inch ZnO bulk single crystal by the hydrothermal method, *Semiconductor Science and Technology*, 20 (4).

[9.9] Ohshima, E., Ogino, H., Niikura, I., Maeda, K., Sato, M., Ito, M., Fukuda, T., (2004), Growth of the 2-in-size bulk ZnO single crystals by the hydrothermal method, *Journal of Crystal Growth*, 260 (1-2), pp. 166-170.

[9.10] Sanjinés, R., Lévy, F., Aruchamy, A., (1989), Thermal Stability of Sputtered Iridium Oxide Films, *Journal of the Electrochemical Society*, 136 (6), pp. 1740-1743.

[9.11] Arai, T., Shima, T., Nakano, T., Tominaga, J., (2007), Thermally-induced optical property changes of sputtered PdO_x films, *Thin Solid Films*, 515 (11), pp. 4774-4777.

[9.12] Mosquera, A., Horwat, D., Vazquez, L., Gutiérrez, A., Erko, A., Anders, A., Andersson, J., Endrino, J.L., (2012), Thermal decomposition and fractal properties of sputter-deposited platinum oxide thin films, *Journal of Materials Research*, 27 (5), pp. 829-836.

[9.13] Sze, S. M.., (2002), *Semiconductor Devices, Physics and Technology, 2nd Ed.*, Hoboken, N.J., U.S.A: John Wiley.

[9.14] Müller, S., Von Wenckstern, H., Schmidt, F., Splith, D., Heinhold, R., Allen, M., Grundmann, M., (2014), Method of choice for fabrication of high-quality ZnO-based Schottky diodes, *Journal of Applied Physics*, 116 (19), art. no. 194506.

[9.15] Özgür, Ü., Alivov, Ya.I., Liu, C., Teke, A., Reshchikov, M.A., Doğan, S., Avrutin, V., Cho, S.-J., Morkǫ, H., (2005), A comprehensive review of ZnO materials and devices, *Journal of Applied Physics*, 98 (4), art. no. 041301, pp. 1-103.

[9.16] Brillson, L.J., Lu, Y., (2011), ZnO Schottky barriers and Ohmic contacts, *Journal of Applied Physics*, 109 (12), art. no. 121301.

[9.17] Werner, J.H., Güttler, H.H., (1991), Barrier inhomogeneities at Schottky contacts, *Journal of Applied Physics*, 69 (3), pp. 1522-1533.

[9.18] McNeill, A.R., Hyndman, A.R., Reeves, R.J., Downard, A.J., Allen, M.W., (2016), Tuning the Band Bending and Controlling the Surface Reactivity at Polar and Nonpolar Surfaces of ZnO through Phosphonic Acid Binding, *ACS Appl. Mater. Interfaces*, 8 (45), pp 31392–31402.

[9.19] Allen, M.W., Swartz, C.H., Myers, T.H., Veal, T.D., McConville, C.F., Durbin, S.M., (2010), Bulk transport measurements in ZnO: The effect of surface electron layers, *Physical Review B - Condensed Matter and Materials Physics*, 81 (7), art. no. 075211.

[9.20] Heinhold, R., Williams, G.T., Cooil, S.P., Evans, D.A., Allen, M.W., (2013), Influence of polarity and hydroxyl termination on the band bending at ZnO surfaces, *Physical Review B - Condensed Matter and Materials Physics*, 88 (23), art. no. 235315.

[9.21] Coppa, B.J., Fulton, C.C., Kiesel, S.M., Davis, R.F., Pandarinath, C., Burnette, J.E., Nemanich, R.J., Smith, D.J., (2005), Structural, microstructural, and electrical properties of gold films and Schottky contacts on remote plasma-cleaned, n -type ZnO{0001} surfaces, *Journal of Applied Physics*, 97 (10), art. no. 103517.

[9.22] Ozawa, K., Mase, K., (2011), Comparison of the surface electronic structures of H-adsorbed ZnO surfaces: An angle-resolved photoelectron spectroscopy study, *Physical Review B - Condensed Matter and Materials Physics*, 83 (12), art. no. 125406.

[9.23] Piper, L.F.J., Preston, A.R.H., Fedorov, A., Cho, S.W., Demasi, A., Smith, K.E., (2010), Direct evidence of metallicity at ZnO $(000\bar{1})$ - (1×1) surfaces from angle-resolved photoemission spectroscopy, *Physical Review B - Condensed Matter and Materials Physics*, 81 (23), art. no. 233305.

[9.24] Allen, M.W., Durbin, S.M., (2008), Influence of oxygen vacancies on Schottky contacts to ZnO, *Applied Physics Letters*, 92 (12), art. no. 122110.

[9.25] Robertson, J., Sharia, O., Demkov, A.A., (2007), Fermi-level pinning by defects in HfO_2 - metal gate stacks, *Applied Physics Letters*, 91 (13), art. no. 132912.

[9.26] Allen, M.W., Durbin, S.M., (2010), Role of a universal branch-point energy at ZnO interfaces, *Physical Review B - Condensed Matter and Materials Physics*, 82 (16), art. no. 165310.

[9.27] Litton, C.W., Reynolds, D.C., Collins, T.C., (2011), *Zinc Oxide Materials for Electronic and Optoelectronic Device Applications, 1st Edition*, West Sussex, United Kingdom: John Wiley & Sons, Ltd.

[9.28] Bayan, S., Mohanta, D., (2012), ZnO nanorod-based UV photodetection and the role of persistent photoconductivity, *Philosophical Magazine*, 92 (32), pp. 3909-3919.

[9.29] Sharma, P., Sreenivas, K., Rao, K.V., (2003), Analysis of ultraviolet photoconductivity in ZnO films prepared by unbalanced magnetron sputtering, *Journal of Applied Physics*, 93 (7), pp. 3963-3970.

[9.30] Kumar, S., Kim, G.-H., Sreenivas, K., Tandon, R.P., (2007), Mechanism of ultraviolet photoconductivity in zinc oxide nanoneedles, *Journal of Physics Condensed Matter*, 19 (47), art. no. 472202.

[9.31] Liao, Z.-M., Lu, Y., Xu, J., Zhang, J.-M., Yu, D.-P., (2009), Temperature dependence of photoconductivity and persistent photoconductivity of single ZnO nanowires, *Applied Physics A: Materials Science and Processing*, 95 (2), pp. 363-366.

[9.32] Yu, K.M., Jeong, S.H., Bae, B.S., Yun, E.-J., (2012), The Effect of UV treatment on the recovery characteristics of a-IGZO-based thin film transistors, *Journal of the Korean Physical Society*, 61 (6), pp. 852-857.

[9.33] Kuriyama, K., Matsumoto, K., Suzuki, Y., Kushida, K., Xu, Q., (2009), Persistent photoconductivity and thermally stimulated current related to electron-irradiation induced defects in single crystal ZnO bulk, *Solid State Communications*, 149 (33-34), pp. 1347-1350.

[9.34] Li, Z., Guangsheng, F., Xiaoyun, T., Wei, Y., Heju, X., (2009), Persistent photoconductivity in undoped n-type ZnO thin films, *2009 Symposium on Photonics and Optoelectronics, SOPO 2009*, art. no. 5230089.

[9.35] Ryu, B., Noh, H.-K., Choi, E.-A., Chang, K.J., (2010), O-vacancy as the origin of negative bias illumination stress instability in amorphous In-Ga-Zn-O thin film transistors, *Applied Physics Letters*, 97 (2), art. no. 022108.

[9.36] Zhang, S.B., Wei, S.-H., Zunger, A., (2001), Intrinsic n-type versus p-type doping asymmetry and the defect physics of ZnO, *Physical Review B - Condensed Matter and Materials Physics*, 63 (7), art. no. 075205, pp. 0752051-0752057.

[9.37] Nathan, A., Lee, S., Jeon, S., Song, I., Chung, U.-I., (2013), Transparent oxide semiconductors for advanced display applications, *Information Display*, 29 (1), pp. 6-11.

[9.38] Cammi, D., Ronning, C., (2014), Persistent photoconductivity in ZnO nanowires in different atmospheres, *Advances in Condensed Matter Physics*, art. no. 184120.

[9.39] Genicom, (2016), *UV-A Sensor GUVA-S12SD*, Retrieved from

http://www.geni-uv.com/download/eng/UV_Sensor/UV-A_Sensor/GUVA-S12SD.pdf

[9.40] Sheng, H., Muthukumar, S., Emanetoglu, N.W., Lu, Y., (2002), Schottky diode with Ag on (11$\bar{2}$0) epitaxial ZnO film, *Applied Physics Letters*, 80 (12), pp. 2132-2134.

Appendix

[A3.1] Mask Images

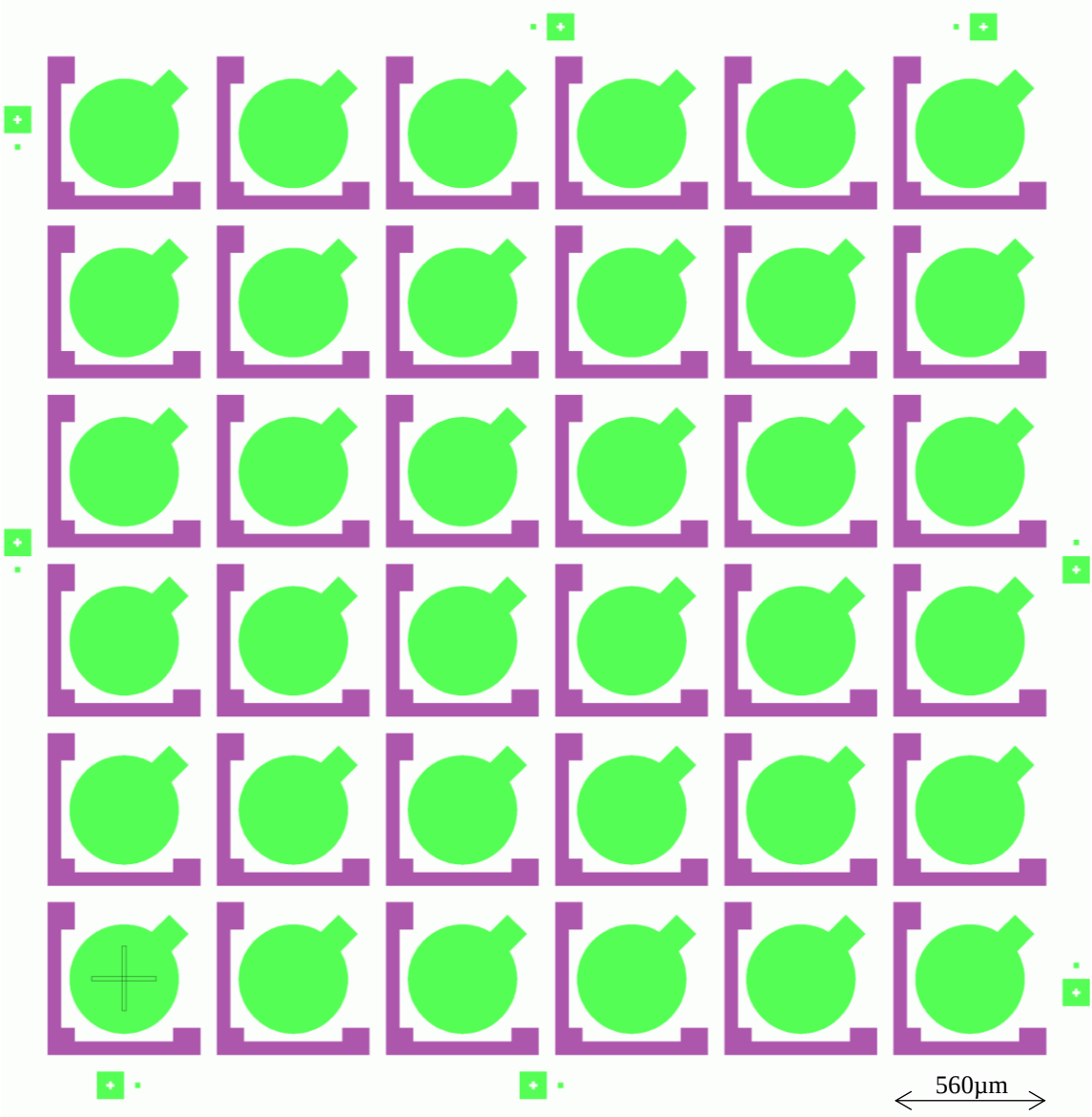

Figure A3.1: Schottky diode masks (purple ohmic mask, green Schottky mask)

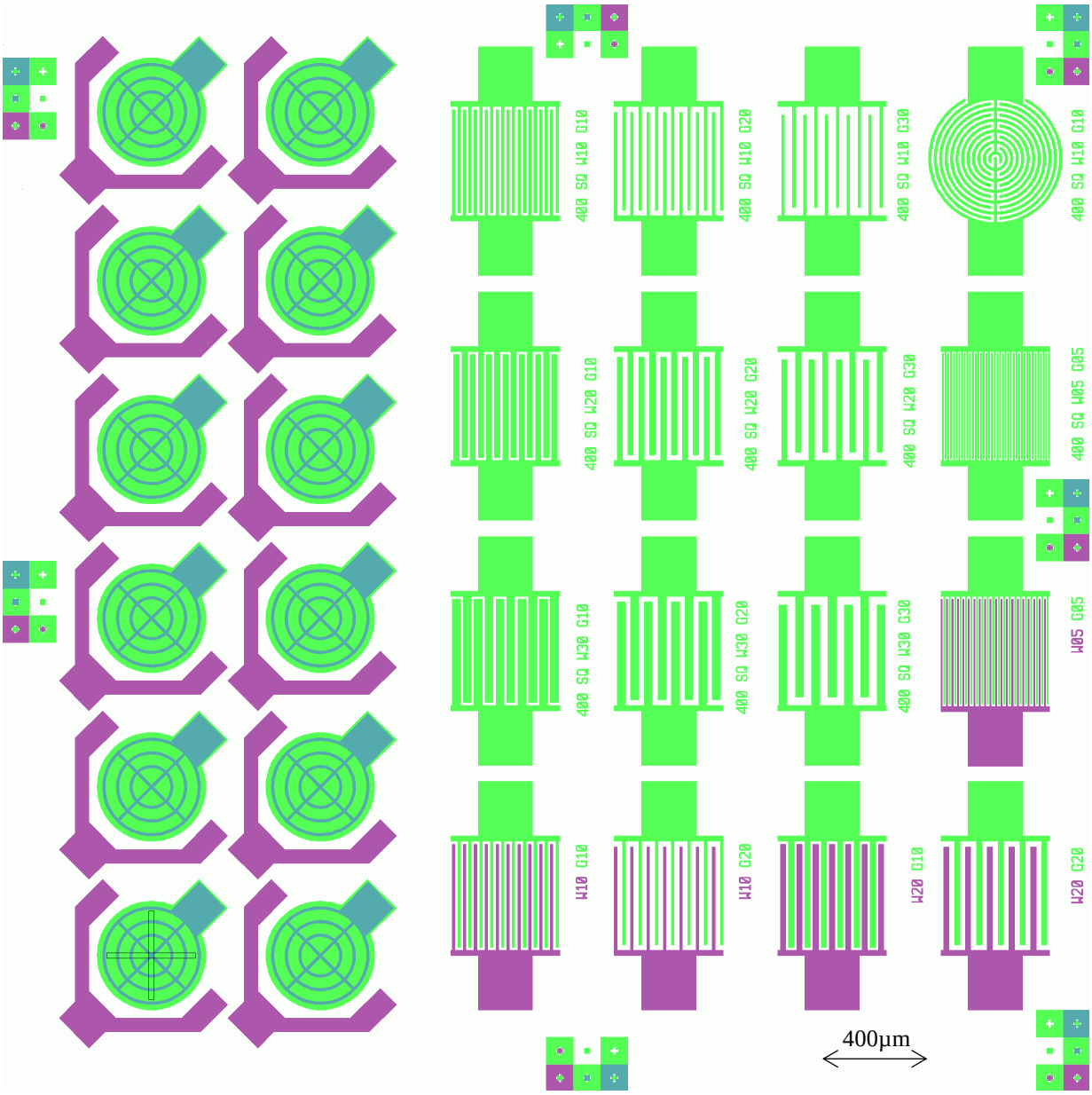

Figure A3.2: Schottky diode, interdigitated diode and interdigitated metal-semiconductor-metal masks (purple ohmic mask, green Schottky mask, blue webbed top contact mask)

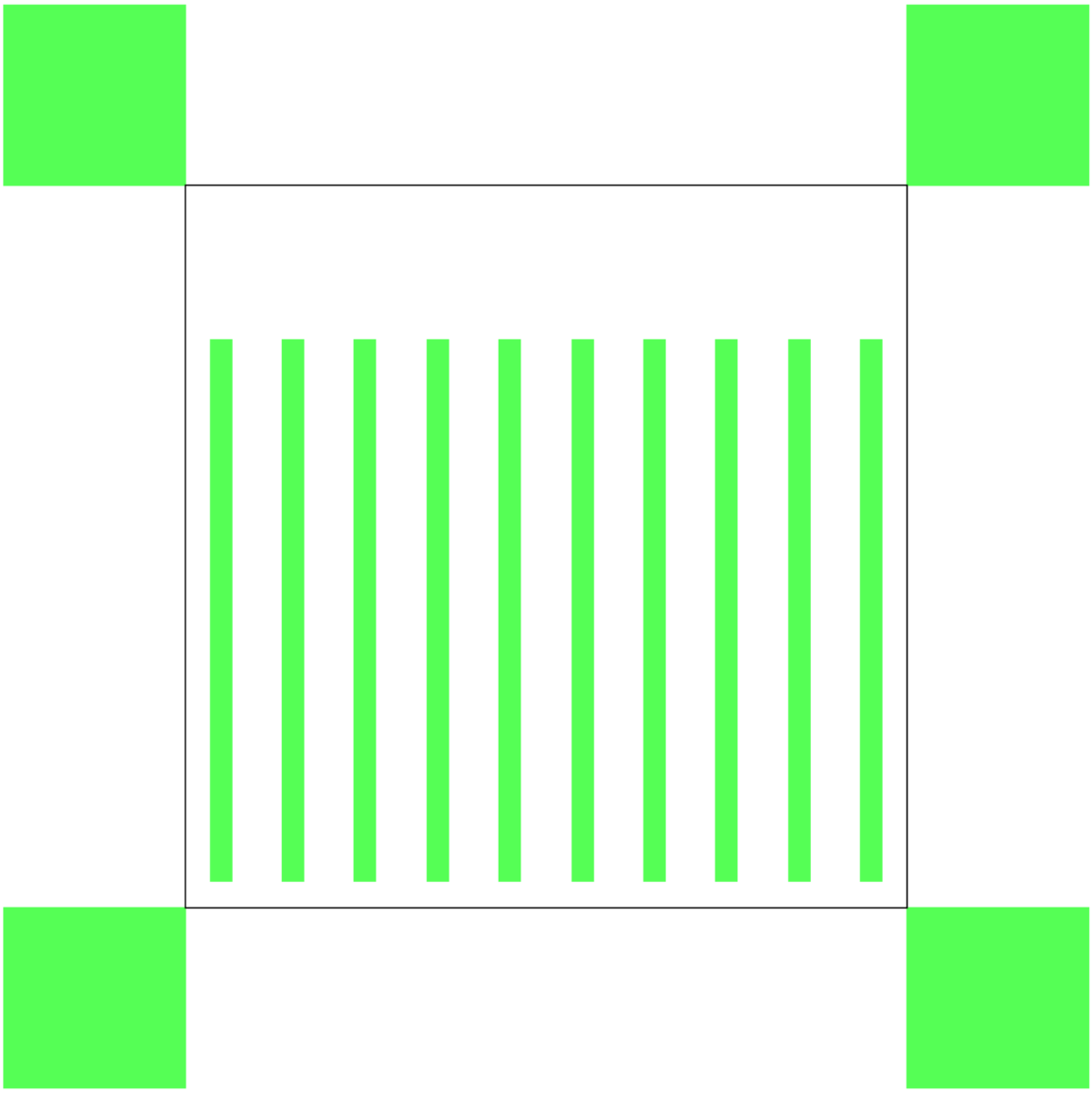

Figure A3.3: Kelvin Probe Mask (green mask, black line outlines position of 100 x 100 mm sample)

[A3.2] List of Bulk ZnO Substrates Used

Tokyo Denpa Co., Ltd Wafer List

Experiment	Crystal Face	Product No.	Wafer No.	Wafer Lot No.
RF-Sputtered_AgOx_I	+c-plane Zn-polar (low lithium)	XGZ-0196	14	JZN-3241-042-15-03
RF-Sputtered _RuOx_I	-c-plane Zn-polar	CGZ1209	5	JZN-3235-044-03-(-1)
PLD_IrOx	+c-plane Zn-polar (low lithium)	CGZ-1210	5	JZN-0119-020-09-02
RF-Sputtered _IrOx_I	+c-plane Zn-polar (low lithium)	CGZ-0937	6	JZN-0313-017-11-02
RF-Sputtered _IrOx_I	-c-plane Zn-polar	CGZ-1209	9	JZN-3235-044-05-(-1)
RF-Sputtered _IrOx_II	+c-plane Zn-polar (low lithium)	XGZ-0196	17	JZN-3241-017-09-02
RF-Sputtered _IrOx_III	+c plane Zn-polar (low lithium)	XGZ-0196	1	JZN-3241-042-04-02
RF-Sputtered _IrOx_III	+c-plane Zn-polar (low lithium)	XGZ-0196	12	JZN-3241-042-14-02
RF-Sputtered _IrOx_III	+c-plane Zn-polar (low lithium)	XGZ-0196	17	JZN-3241-017-09-02
RF-Sputtered _PdOx_I	+c-plane Zn-polar (low lithium)	XGZ-0196	9	JZN-3241-042-10-02
RF-Sputtered _PtOx_I	+c-plane Zn-polar (low lithium)	XGZ-0196	6	JZN-3241-042-09-03
RF-Sputtered _PtOx_II	+c-plane Zn-polar (low lithium)	XGZ-0196	19	JZN-3241-017-13-04
RF-Sputtered _PtOx_III	+c-plane Zn-polar (low lithium)	XGZ-0196	3	JZN-3241-042-06-03

Tokyo Denpa Co., Ltd C-Plane Wafer Details

Product Number	Wafer Number	Size A (mm)	Size B (mm)	Thickness (μm)	Off-Angle (deg) m-axis	Off-Angle (deg) a-axis	Resistivity (Ωcm)	Wafer Lot No.
CGZ-0937	6	10.01	10.01	499	-0.02	0.00	0.85	JZN-0313-017-11-02
CGZ-1209	5	10.04	10.04	549	0.00	0.05	0.09	JZN-3235-044-03-(-1)
CGZ-1209	9	10.04	10.01	549	0.02	-0.02	0.10	JZN-3235-044-05-(-1)
CGZ-1210	5	10.00	10.00	502	-0.02	-0.03	0.87	JZN-0119-020-09-02
XGZ-0196	1	10.04	10.02	515	0.00	-0.07	0.89	JZN-3241-042-04-02
XGZ-0196	3	10.01	9.99	516	-0.02	-0.03	4.13	JZN-3241-042-06-03
XGZ-0196	6	10.02	10.02	515	0.02	-0.05	3.69	JZN-3241-042-09-03
XGZ-0196	9	10.01	10.02	513	0.00	-0.02	0.85	JZN-3241-042-10-02
XGZ-0196	12	10.02	10.03	514	0.03	-0.03	1.39	JZN-3241-042-14-02
XGZ-0196	17	10.02	10.02	500	-0.02	-0.03	1.18	JZN-3241-017-09-02
XGZ-0196	19	10.01	10.03	499	-0.02	0.07	5.12	JZN-3241-017-13-04
XGZ-0196	1	10.04	10.02	515	0.00	-0.07	0.89	JZN-3241-042-04-02

Tokyo Denpa Co., Ltd C-Plane Wafer Orientation

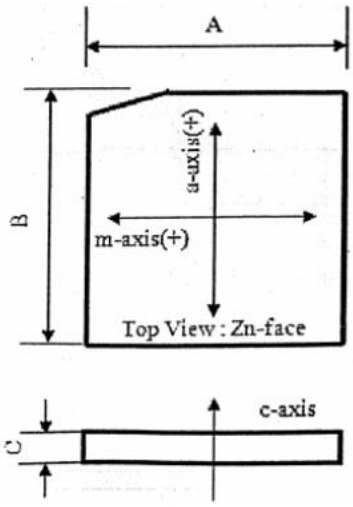

[A3.3] Equipment/Chemical List

Equipment List

AFM	Veeco Dimension 3100 Atomic Force Microscope
Dektak	Veeco DEKTAK 150 Profilometer
Diamond Blade	Dicing Blade Technology resin bond diamond dicing blade
Dicing Saw	J.M. Industries TEMPRESS 602 Dicing Saw
Drying Oven	Contherm Laboratory Drying Oven
Hall Effect System	EGK Corp. HEM-2000 Hall Effect System
Masks	Nanofilm AZ 1518 Soda Lime Low Reflective Chrome Blank Photomasks
Mask Aligner	Karl Süss MA6 Mask Aligner
Mask Writer	Heidelberg Instruments µPG 101 Mask Writer
Parameter Analyser	Hewlett-Packard 4155A Semiconductor Parameter Analyser
Probe Station	Cascade Microtech, Inc. Summit™ 11000 Manual Wafer Prober Cascade Microtech, Inc. 8-inch/200mm Gold-Plated Thermal Chuck Cascade Microtech, Inc. DPP220 Probe Positioner Cascade Microtech, Inc. Model 107-158 5µm Radius Replaceable Coaxial Probe Cascade Microtech, Inc. RRP304-SU-AI Probe Positioner Temptronic Corp. Model TP03000 ThermoChuck® Thermal Chuck Controller
RCL Meter	Philips Fluke PM6303A Automatic RCL Meter
Source Meter	SMU Instruments Keithley 2400 SourceMeter®
Spectrophotometer	Aglient Cary 6000i UV-Vis-NIR Spectrophotometer
Spinner	Headway Research, Inc. PWM32-PS-R790 Spinner System
Sputterer	BOC Edwards Auto 500 RF, DC Sputtering and Electron-Beam Evaporation Centre: NXH54600 220V, 50Hz Auto 306 EB3 Multihearth Electron-Beam Source and Accessories: EB3 3 kW Power Supply and Sweep Control Kurt J. Lesker FAMBATE® Crucible Liners Auto 306 System Model 1706 Vacuum Controller EPM75 Planar Magnetron Sputtering Source EXC300 Pump System Controller EXT55H Compound Turbomolecular Pump FL400 Front Loading Chamber FTM7 Film Thickness Monitor Model 825 Mass Flow Controller RV12 A 655-09-903 Rotary Vane Pump CAL 9900 Autotune PID Temperature Controller Cesar® RF Power Supply: Model 136 13.56MHz, 600W
Ultrasonic Unit	Elma Elmasonic S 60 (H) Ultrasonic Cleaning Unit
Ultraviolet Lamp	Norland Products Inc. UVA Splice Lamp Model P/N 5200 Serial B283

Materials List

AFM Tips	BudgetSensors Tap300AL-G AFM Tips
Glassy Carbon	SPI Glas 11 Grade Glassy (Vitreous) Carbon Plate 25 x 25 x 1 mm
Hall Effect Wire	Single strand of 8 x 0.1 mm Gauge Tinned Copper Hookup Wire
Kelvin Probe Tips	BudgetSensors Tap300E AFM Tips

Photoresist	MicroChemicals GmbH AZ® 1518 Photoresist
Photoresist Developer	MicroChemicals GmbH AZ® 326 MIF Developer
RF Sputtering Gases	BOC Oxygen, High Purity Grade, Compressed
	BOC Argon, Zero Grade, Compressed
Silver Paste	ESL 1109-S Polymer Conductive Silver Paste
Temptronic Coolant	SOLVAY SOLEXIS, Inc. Galden HT 55 Coolant
Thermal Paste	CMR-Direct GE/IMI 7031 Varnish

Kurt J. Lesker Company Sputtering Targets

Target Material	Purity	Diameter (Inches)	Thickness (Inches)	Density (gcm^{-3})	Part #	Lot #
Iridium	99.9%	3.00	0.125	19.36	EJTIRXX303A2	0001366032/VPU110496
Palladium	99.99%	3.00	0.125	-	EJTPDXX403A2	23082/VPU135301
Platinum	99.99%	3.00	0.125	-	EJTPTXX403A2	201735/VPU126085
Silver	99.99%	3.00	0.250	-	EJTAGXX403A4	C926354/591265

Kurt J. Lesker Company Iridium Target, 99.9% Pure, 3.00” diameter x 0.125” thick
Kurt J. Lesker Company Palladium Target, 99.99% Pure, 3.00” diameter x 0.125” thick
Kurt J. Lesker Company Platinum Target, 99.99% Pure, 3.00” diameter x 0.125” thick
Kurt J. Lesker Company Silver Target, 99.99% Pure, 3.00” diameter x 0.250” thick

Department of Physics and Astronomy, University of Canterbury

PLD Laser	Lambda Physik Compex 205 248nm KrF excimer laser
PLD Chamber	Thermionics High Vacuum Chamber
Spectrophotometer	Agilent Cary 6000i UV-Vis-IR Spectrophotometer

[A3.4] PLD and Sputtering Logs

PLD_IrOx

Date	Source	Material	Gas (sccm)	Power	Temp (°C)	Time (min)	Base Pressure (mbar)	Process Pressure (mbar)	Thickness (nm)	Tooling Factor
14/05/13	E-Beam	Ti Au	- -	110 mA 96 mA	20-53 49-53	7:30 1:07	1.9E-5 2.1E-5	1.4E-5 2.7E-5	50 30	1.0 1.0
28/08/13	PLD	IrO_x	O_2	26 kV 10 Hz	-	60:00	1.2E-5	7.5E-5 O_2	-	-
29/08/13	E-Beam	Au	-	70 mA	36-52	3:36	8.5E-6	1.9E-5	40	1.0

RF-Sputtered_AgOx_I (*O_2 valve closed)

Date	Source	Material	Gas (sccm)	Power	Temp (°C)	Time (min)	Base Pressure (mbar)	Process Pressure (mbar)	Thickness (nm)	Tooling Factor
07/11/14	E-Beam	Ti Au	- -	110 mA 60 mA	22-26 30-36	1:40 3:45	7.5E-6 2.9E-6	2.3E-6 1.0E-5	40 50	1.8 1.8
14/11/14	RF	Ag	Ar (10)	50 W	29-36	15:00	3.8E-6	3.0E-3 Ar 3.2E-3 RF	160	4.55
14/11/14	E-Beam	Au	-	66 mA	26-30	2:49	8.5E-6	1.9E-5	50	1.8
14/11/14	RF	AgO_x	Ar (10) O_2 (3.3)*	50 W	24-33	15:00	8.0E-6	0.0E-4 O_2 3.2E-3 Ar 3.4E-3 RF	201.3	4.55
14/11/14	E-Beam	Au	-	60 mA	23-25	1:10	6.0E-6	1.6E-5	40	1.8
15/11/14	RF	AgO_x	Ar (10) O_2 (3.8)*	50 W	18-33	15:00	9.0E-7	0.0E-4 O_2 3.2E-3 Ar 3.2E-3 RF	204.3	4.55
15/11/14	E-Beam	Au	-	60 mA	23-27	3:00	9.0E-6	2.0E-5	40	1.8
15/11/14	RF	AgO_x	Ar (10) O_2 (3.3)	50 W	20-36	15:00	4.2E-6	1.0E-4 O_2 3.4E-3 Ar 3.4E-3 RF	209.6	4.55
15/11/14	E-Beam	Au	-	60 mA	24-28	2:35	8.5E-6	2.1E-5	40	1.8
15/11/14	RF	AgO_x	Ar (10) O_2 (3.8)	50 W	21-34	15:00	8.0E-6	2.0E-4 O_2 3.6E-3 Ar 3.2E-3 RF	208.4	4.55
15/11/14	E-Beam	Au	-	60 mA	33-37	2:48	6.0E-6	1.6E-5	40	1.8
15/11/14	RF	AgO_x	Ar (10) O_2 (4.8)	50 W	19-33	15:00	1.0E-5	8.0E-4 O_2 4.0E-3 Ar 3.8E-3 RF	196.0	4.55
15/11/14	E-Beam	Au	-	60 mA	25-30	2:50	8.5E-6	2.1E-5	40	1.8
16/11/14	RF	AgO_x	Ar (10) O_2 (5.8)	50 W	17-31	15:00	8.0E-7	9.0E-4 O_2 4.2E-3 Ar 4.0E-3 RF	171.2	4.55
16/11/14	E-Beam	Au	-	60 mA	21-25	2:36	8.5E-6	2.1E-5	40	1.8
16/11/14	RF	AgO_x	Ar (10) O_2 (6.8)	50 W	20-33	15:00	4.8E-6	1.2E-3 O_2 4.4E-3 Ar 4.2E-3 RF	156.4	4.55
16/11/14	E-Beam	Au	-	60 mA	30-36	3:14	7.0E-6	2.1E-5	40	1.8

RF-Sputtered_RuOx_I

Date	Source	Material	Gas (sccm)	Power	Temp (°C)	Time (min)	Base Pressure (mbar)	Process Pressure (mbar)	Thickness (nm)	Tooling Factor
19/02/14	E-Beam	Ti Au	- -	130 mA 110 mA	37-45 42-54	6:01 9:24	1.0E-5 8.5E-6	4.0E-6 1.3E-5	30 30	1.3 1.3
22/02/14	RF	RuO_x	Ar (10) O_2 (3.3)	50 W	19-29	15:00	1.0E-5	1.0E-4 O_2 3.4E-3 Ar 3.2E-3 RF	64.0	3.9
22/02/14	E-Beam	Au	-	80 mA	32-62	35:00	1.1E-5	1.9E-5	30	1.3
22/02/14	RF	RuO_x	Ar (10) O_2 (3.8)	50 W	27-36	15:00	1.6E-5	3.0E-4 O_2 3.6E-3 Ar 3.4E-3 RF	84.5	5.1
22/02/14	E-Beam	Au	-	90 mA	25-45	13:00	1.6E-5	1.9E-5	30	1.3
23/02/14	RF	RuO_x	Ar (10) O_2 (4.8)	50 W	31-34	15:00	1.6E-5	5.0E-4 O_2 3.8E-3 Ar 3.6E-3 RF	94.6	6.1
23/02/14	E-Beam	Au	-	90 mA	33-49	13:40	1.4E-5	2.3E-6	30	1.3
23/02/14	RF	RuO_x	Ar (10) O_2 (5.8)	50 W	37-40	15:00	1.3E-5	9.0E-4 O_2 4.0E-3 Ar 3.8E-3 RF	83.8	6.5
23/02/14	E-Beam	Au	-	90 mA	36-51	14:10	1.6E-5	2.4E-5	30	1.3
26/02/14	RF	RuO_x	Ar (10) O_2 (6.8)	50 W	35-40	15:00	1.3E-5	1.2E-3 O_2 4.2E-3 Ar 3.6E-3 RF	74.0	5.4
26/02/14	E-Beam	Au	-	90 mA	37-51	9:25	1.4E-6	2.3E-5	30	1.3
26/02/14	RF	RuO_x	Ar (10) O_2 (7.8)	50 W	36-38	15:00	1.1E-5	1.5E-3 O_2 4.4E-3 Ar 4.2E-3 RF	70.9	12.2
26/02/14	E-Beam	Au	-	90 mA	35-51	9:44	1.1E-5	2.4E-5	30	1.3
26/02/14	RF	RuO_x	Ar (10) O_2 (9.8)	50 W	36-38	15:00	1.5E-5	2.0E-3 O_2 5.0E-3 Ar 4.6E-3 RF	39.6	54.0
26/02/14	E-Beam	Au	-	90 mA	34-51	9:49	1.4E-5	2.4E-5	30	1.3

RF-Sputtered_IrOx_I

Date	Source	Material	Gas (sccm)	Power	Temp (°C)	Time (min)	Base Pressure (mbar)	Process Pressure (mbar)	Thickness (nm)	Tooling Factor
8/11/13	E-Beam	Ti Au	- -	140 mA 120 mA	24-52 49-77	5:23 7:25	1.8E-5 1.5E-5	1.1E-5 2.5E-5	30 30	1.0 1.0
14/11/13	RF	IrO_x	Ar (10) O_2 (3.3)	50 W	34-37	15:00	1.7E-5	1.0E-4 O_2 3.2E-3 Ar 3.2E-3 RF	44.0	1.7
14/11/13	E-Beam	Au	-	100 mA	34-49	2:39	1.7E-5	3.0E-5	30	1.0
13/11/13	RF	IrO_x	Ar (10) O_2 (3.8)	50 W	21-34	15:00	1.8E-5	3.0E-4 O_2 3.4E-4 Ar 3.4E-4 RF	56.8	2.1
13/11/13	E-Beam	Au	-	100 mA	21-36	2:04	1.7E-5	3.0E-6	30	1.0
12/11/13	RF	IrO_x	Ar (10) O_2 (4.7)	50 W	19-34	15:00	1.4E-5	5.0E-4 O_2 3.6E-3 Ar 3.4E-3 RF	45.2	1.6
12/11/13	E-Beam	Au	-	110 mA	34-46	1:35	1.5E-5	3.0E-5	30	1.0
13/11/13	RF	IrO_x	Ar (10) O_2 (5.8)	50 W	34-38	15:00	1.4E-5	9.0E-4 O_2 3.8E-3 Ar 3.6E-3 RF	88.5	3.2

13/11/13	E-Beam	Au	-	100 mA	33-45	2:09	1.6E-5	3.0E-5	30	1.0
14/11/13	RF	IrO_x	Ar (10) O_2 (6.8)	50 W	20-33	15:00	6.0E-6	1.1E-3 O_2 4.0E-3 Ar 3.8E-3 RF	75.0	2.8
14/11/13	E-Beam	Au	-	100 mA	34-47	2:19	1.5E-5	2.8E-5	30	1.0
28/11/13	RF	IrO_x	Ar (10) O_2 (7.8)	50 W	33-36	15:00	1.6E-5	1.6E-3 O_2 4.4E-3 Ar 4.4E-3 RF	82.0	3.2
28/11/13	E-Beam	Au	-	100 mA	21-32	3:28	1.4E-5	2.0E-5	30	1.0
30/11/13	RF	IrO_x	Ar (10) O_2 (9.8)	50 W	21-32	15:00	1.0E-5	2.0E-3 O_2 4.8E-3 Ar 4.8E-3 RF	85.9	3.5
30/11/13	E-Beam	Au	-	100 mA	34-43	3:35	1.1E-5	1.9E-5	30	1.0

RF-Sputtered_IrOx_II

Date	Source	Material	Gas (sccm)	Power	Temp (°C)	Time (min)	Base Pressure (mbar)	Process Pressure (mbar)	Thickness (nm)	Tooling Factor
26/3/14	E-Beam	Ti Au	- -	130 mA 110 mA	33-62 47-58	21:00 8:00	1.0E-5 8.0E-6	8.5E-6 1.0E-5	30 50	1.3 1.3
28/3/14	RF Sputter	Ir	Ar (10)	50 W	20-34	15:00	1.1E-5	2.9E-3 Ar 3.1E-3 RF	37.8	1.5
28/3/14	E-Beam	Au	-	100 mA	22-31	2:00	1.6E-5	2.8E-5	40	1.3
29/3/14	RF Sputter	IrO_x	Ar (10) O_2 (3.3)	50 W	19-32	15:00	1.4E-5	1.0E-4 O_2 3.2E-3 Ar 3.4E-3 RF	47.7	1.8
29/3/14	E-Beam	Au	-	100 mA	32-40	5:00	1.4E-5	2.4E-5	40	1.3
29/3/14	RF Sputter	IrO_x	Ar (10) O_2 (3.8)	50 W	34-37	15:00	1.4E-5	2.0E-4 O_2 3.4E-3 Ar 3.6E-3 RF	70.9	2.6
29/3/14	E-Beam	Au	-	100 mA	34-42	5:00	1.4E-5		40	1.3
31/3/14	RF Sputter	IrO_x	Ar (10) O_2 (4.8)	50 W	19-29	15:00	1.6E-5	6.0E-4 O_2 3.8E-3 Ar 3.4E-3 RF	87.8	3.2
31/3/14	E-Beam	Au	-	100 mA	35-46	6:00	1.7E-5	4.2E-5	40	1.3
2/4/14	RF Sputter	IrO_x	Ar (10) O_2 (5.8)	50 W	19-34	15:00	2.0E-5	9.0E-4 O_2 3.8E-3 Ar 3.6E-3 RF	80.7	3.0
2/4/14	E-Beam	Au	-	100 mA	21-26	7:00	2.0E-5	3.6E-5	40	1.3
4/4/14	RF Sputter	IrO_x	Ar (10) O_2 (6.8)	50 W	20-34	15:00	2.1E-5	1.3E-3 O_2 4.2E-3 Ar 3.8E-3 RF	83.3	3.2
4/4/14	E-Beam	Au	-	90 mA	21-42	8:00	2.1E-5	3.2E-5	40	1.3

RF-Sputtered_IrOx_III

Date	Source	Material	Gas (sccm)	Power	Temp (°C)	Time (min)	Base Pressure (mbar)	Process Pressure (mbar)	Thickness (nm)	Tooling Factor
09/07/14	E-Beam	Ti Au	- -	90 mA 60 mA	26-36 37-49	2:57 5:00	1.4E-5 1.0E-5	2.8E-6 1.7E-5	40 40	2.2 1.5
11/07/14	RF Sputter	IrO_x	Ar (10) O_2 (5.8)	50 W	22-36	15:00	1.6E-5	1.3E-3 O_2 4.4E-3 Ar 4.0E-3 RF	72.6	4.0
11/07/14	E-Beam	Au	-	60 mA	35-42	3:38	8.0E-6	1.9E-5	40	1.5

12/07/14	RF Sputter	IrO_x	Ar (10) O_2 (5.8)	50 W	28-38	8:00	6.5E-6	1.0E-3 O_2 4.0E-3 Ar 3.8E-3 RF	39.9	4.0
12/07/14	E-Beam	Au	-	60 mA	36-44	3:39	1.1E-5	2.0E-5	40	1.5
12/07/14	RF Sputter	IrO_x	Ar (10) O_2 (5.8)	50 W	38-39	4:00	6.5E-6	1.0E-3 O_2 4.0E-3 Ar 3.8E-3 RF	20.2	4.0
12/07/14	E-Beam	Au	-	60 mA	36-44	4:47	1.6E-5		40	1.5
12/07/14	RF Sputter	IrO_x	Ar (10) O_2 (5.8)	50 W	36-37	2:00	8.5E-6	1.3E-3 O_2 4.4E-3 Ar 4.0E-3 RF	10.2	4.0
13/07/14	E-Beam	Au	-	60 mA	36-48	8:36	4.0E-6	7.5E-6	40	1.5
04/08/14	RF Sputter	IrO_x	Ar (10) O_2 (5.8)	50 W	34-36	1:00	6.5E-6	1.0E-3 O_2 4.0E-3 Ar 3.8E-3 RF	5.0	4.0
04/08/14	E-Beam	Au	-	60 mA	35-47	9:23	6.0E-6	1.8E-5	40	1.5
14/08/14	RF Sputter	IrO_x	Ar (10) O_2 (5.8)	50 W	30-32	0:30	2.0E-6	9.0E-4 O_2 4.0E-4 Ar 3.6E-4 RF	2.3	4.0
14/08/14	E-Beam	Au	-	60 mA	36-42	4:36	2.0E-6	7.0E-6	40	1.5
24/08/14	RF Sputter	IrO_x	Ar (10) O_2 (5.8)	50 W	24-25	0:10	5.5E-6	9.0E-4 O_2 4.0E-3 Ar 3.8E-3 RF	1.0	4.0
24/08/14	E-Beam	Au	-	60 mA	20-28	4:03	1.0E-5	2.0E-5	40	1.5
13/07/14	RF Sputter	IrO_x	Ar (10) O_2 (6.8)	50 W	38-41	15:00	6.5E-6	1.4E-3 O_2 4.6E-3 Ar 4.2E-3 RF	77.21	4.0
13/07/14	E-Beam	Au	-	60 mA	38-46	5:48	1.0E-5	1.9E-5	40	1.5
13/07/14	RF Sputter	IrO_x	Ar (10) O_2 (6.8)	50 W	36-39	8:00	5.5E-6	1.4E-3 O_2 4.6E-3 Ar 4.2E-3 RF	39.9	4.0
13/07/14	E-Beam	Au	-	60 mA	26-37	3:37	8.5E-6	1.7E-5	40	1.5
14/07/14	RF Sputter	IrO_x	Ar (10) O_2 (6.8)	50 W	37-38	4:00	1.2E-6	1.3E-3 O_2 4.4E-3 Ar 4.0E-3 RF	20.2	4.0
14/07/14	E-Beam	Au	-	60 mA	29-38	3:26	8.5E-6		40	1.5
14/07/14	RF Sputter	IrO_x	Ar (10) O_2 (6.8)	50 W	26-31	2:00	3.0E-6	1.3E-3 O_2 4.2E-3 Ar 4.0E-3 RF	9.8	4.0
14/07/14	E-Beam	Au	-	60 mA	23-33	3:33	1.7E-5	2.3E-5	40	1.5
04/08/14	RF Sputter	IrO_x	Ar (10) O_2 (6.8)	50 W	36-38	1:00	5.0E-6	1.2E-3 O_2 4.2E-3 Ar 3.8E-3 RF	5.3	4.0
04/08/14	E-Beam	Au	-	60 mA	35-46	8:20	6.0E-6	1.8E-5	40	1.5

RF-Sputtered_PdOx_I

Date	Source	Material	Gas (sccm)	Power	Temp (°C)	Time (min)	Base Pressure (mbar)	Process Pressure (mbar)	Thickness (nm)	Tooling Factor
25/04/14	E-Beam	Ti Au	- -	110 mA 70 mA	25-37 40-47	5:18 4:05	1.1E-6 5.0E-7	2.0E-6 5.0E-6	50 50	1.8 1.8
25/04/14	RF Sputter	Pd	Ar (10)	50 W	27-40	15:00	4.2E-6	3.2E-3 Ar 3.0E-3 RF	80.4	4.3
25/04/14	E-Beam	Au	-	70 mA	41-49	4:12	1.2E-5	2.7E-5	50	1.8
25/04/14	RF Sputter	PdO_x	Ar (10) O_2 (3.3)	50 W	30-43	15:00	8.5E-6	1.0E-4 O_2 3.4E-3 Ar 3.4E-3 RF	95.0	5.4
25/04/14	E-Beam	Au	-	70 mA	30-40	4:23	1.4E-5	2.9E-5	50	1.8

25/04/14	RF Sputter	PdO_x	Ar (10) O_2 (3.8)	50 W	40-46	15:00	7.5E-6	2.0E-4 O_2 3.6E-3 Ar 3.4E-3 RF	106.7	6.2
25/04/14	E-Beam	Au	-	70 mA	30-40	4:13	1.0E-5	2.5E-5	50	1.8
26/04/15	RF Sputter	PdO_x	Ar (10) O_2 (4.8)	50 W	26-40	15:00	1.2E-6	5.0E-4 O_2 3.8E-3 Ar 3.6E-3 RF	133.2	8.0
26/04/15	E-Beam	Au	-	70 mA	29-37	3:47	1.0E-5	2.4E-5	50	1.8
26/04/15	RF Sputter	PdO_x	Ar (10) O_2 (5.8)	50 W	26-39	15:00	7.5E-6	8.0E-4 O_2 4.0E-3 Ar 3.8E-8 RF	135.2	8.8
26/04/15	E-Beam	Au	-	70 mA	29-38	3:54	1.3E-5	2.8E-5	50	1.8
26/04/15	RF Sputter	PdO_x	Ar (10) O_2 (6.8)	50 W	28-41	15:00	8.0E-6	1.1E-3 O_2 4.2E-3 Ar 4.2E-3 RF	114.4	8.7
26/04/15	E-Beam	Au	-	70 mA	29-37	3:44	1.4E-5	3.0E-5	50	1.8
26/04/15	RF Sputter	PdO_x	Ar (10) O_2 (7.8)	50 W	28-40	15:00	7.0E-6	1.5E-3 O_2 4.6E-3 Ar 4.4E-3 RF	95.3	8.7
26/04/15	E-Beam	Au	-	70 mA	30-38	3:35	1.6E-5	3.2E-5	50	1.8
26/04/15	RF Sputter	PdO_x	Ar (10) O_2 (9.8)	50 W	26-42	15:00	8.0E-6	2.2E-3 O_2 5.5E-3 Ar 5.5E-3 RF	65.2	8.8
26/04/15	E-Beam	Au	-	70 mA	34-41	3:18	3.4E-5	5.5E-5	50	1.8

RF-Sputtered_PtOx_I

Date	Source	Material	Gas (sccm)	Power	Temp (°C)	Time (min)	Base Pressure (mbar)	Process Pressure (mbar)	Thickness (nm)	Tooling Factor
02/10/14	E-Beam	Ti	-	110 mA	21-27	1:55	3.2E-6	1.1E-6	40	1.8
		Au	-	70 mA	31-38	1:35	9.0E-7	5.5E-6	40	1.8
06/10/14	RF Sputter	Pt	Ar (10)	50 W	21-34	15:00	4.6E-6	3.3E-3 Ar 3.2E-3 RF	58.8	3.9
06/10/14	E-Beam	Au	-	70 mA	24-27	1:06	8.0E-6	2.3E-5	40	1.8
07/10/14	RF Sputter	PtO_x	Ar (10) O_2 (3.3)	50 W	38-41	15:00	3.0E-6	1.0E-4 O_2 3.2E-3 Ar 3.2E-3 RF	55.6	3.4
07/10/14	E-Beam	Au	-	70 mA	26-30	1:24	6.5E-5	2.5E-5	40	1.8
07/10/14	RF Sputter	PtO_x	Ar (10) O_2 (3.8)	50 W	37-41	15:00	7.0E-6	2.0E-4 O_2 3.4E-3 Ar 3.2E-3 RF	82.6	4.9
07/10/14	E-Beam	Au	-	70 mA	26-33	3:35	7.0E-6	1.8E-5	40	1.8
09/10/14	RF Sputter	PtO_x	Ar (10) O_2 (4.8)	50 W	23-36	15:00	7.0E-6	6.0E-4 O_2 3.8E-3 Ar 3.6E-3 RF	96.2	6.0
09/10/14	E-Beam	Au	-	70 mA	22-31	4:14	5.0E-6	1.7E-6	40	1.8
09/10/14	RF Sputter	PtO_x	Ar (10) O_2 (5.8)	50 W	23-37	15:00	7.0E-6	9.0E-4 O_2 4.0E-3 Ar 3.8E-3 RF	101.3	6.5
09/10/14	E-Beam	Au	-	70 mA	37-40	2:02	6.0E-6	1.6E-5	40	1.8
12/10/14	RF Sputter	PtO_x	Ar (10) O_2 (6.8)	50 W	20-36	15:00	7.0E-6	1.3E-3 O_2 4.4E-3 Ar 4.2E-3 RF	105.9	6.9
12/10/14	E-Beam	Au	-	70 mA	23-27	1:52	7.0E-6	2.0E-5	40	1.8
16/10/14	RF Sputter	PtO_x	Ar (10) O_2 (7.8)	50 W	20-36	15:00	5.5E-6	1.6E-3 O_2 4.8E-3 Ar 4.4E-3 RF	124.8	8.0
16/10/14	E-Beam	Au	-	70 mA	22-27	1:32	8.0E-6	2.5E-5	40	1.8

16/10/14	RF Sputter	PtO_x	Ar (10) O_2 (9.8)	50 W	34-39	15:00	7.0E-6	2.2E-3 O_2 5.5E-3 Ar 4.8E-3 RF	134	10.0
16/10/14	E-Beam	Au	-	70 mA	35-37	1:51	8.0E-6	2.2E-5	40	1.8

RF-Sputtered_PtOx_II

Date	Source	Material	Gas (sccm)	Power	Temp (°C)	Time (min)	Base Pressure (mbar)	Process Pressure (mbar)	Thickness (nm)	Tooling Factor
20/05/15	E-Beam	Ti Au	- -	110 mA 65 mA	25-32 36-43	4:06 4:32	1.7E-5 1.6E-5	8.0E-6 1.9E-5	50 50	1.8 1.8
14/06/15	RF Sputter	PtO_x	Ar (10) O_2 (8.8)	50 W	21-29	5:00	1.6E-5	2.0E-3 O_2 4.8E-3 Ar 4.6E-3 RF	44.8	8.2
14/06/15	E-Beam	Au	-	65 mA	23-28	2:09	9.0E-6	2.5E-5	50	1.8
24/05/15	RF Sputter	PtO_x	Ar (10) O_2 (9.8)	50 W	26-33	5:00	2.4E-5	2.6E-3 O_2 6.0E-3 Ar 5.5E-3 RF	44.5	8.2
24/05/15	E-Beam	Au	-	65 mA	24-33	5:05	2.2E-5	3.8E-5	50	1.8
27/05/15	RF Sputter	PtO_x	Ar (10) O_2 (10.8)	50 W	24-32	5:00	1.5E-5	2.6E-3 O_2 6.0E-3 Ar 5.0E-3 RF	47.8	9.2
27/05/15	E-Beam	Au	-	65 mA	25-35	4:47	2.3E-5	3.6E-5	50	1.8
24/05/15	RF Sputter	PtO_x	Ar (10) O_2 (11.8)	50 W	25-32	5:00	2.1E-5	3.0E-3 O_2 6.0E-3 Ar 5.5E-3 RF	47.1	9.6
24/05/15	E-Beam	Au	-	65 mA	24-33	4:29	2.5E-5	3.8E-5	50	1.8
27/05/15	RF Sputter	PtO_x	Ar (10) O_2 (12.8)	50 W	25-33	5:00	1.8E-5	3.4E-3 O_2 6.5E-3 Ar 6.0E-3 RF	46.4	9.6
27/05/15	E-Beam	Au	-	65 mA	28-35	4:15	3.0E-5	4.8E-5	50	1.8

RF-Sputtered_PtOx_III

Date	Source	Material	Gas (sccm)	Power	Temp (°C)	Time (min)	Base Pressure (mbar)	Process Pressure (mbar)	Thickness (nm)	Tooling Factor
21/10/14	E-Beam	Ti Au	- -	110 mA 70 mA	20-35 35-42	2:00 2:00	3.2E-6 1.0E-6	3.0E-6 4.6E-6	40 40	1.8 1.8
22/10/14	RF Sputter	PtO_x	Ar (10) O_2 (6.8)	50 W	30-37	15:00	5.5E-6	1.3E-3 O_2 4.2E-3 Ar 4.0E-3 RF	105.6	6.9
22/10/14	E-Beam	Au	-	70 mA	36-38	1:47	7.5E-6	2.0E-5	40	1.8
23/10/14	RF Sputter	PtO_x	Ar (10) O_2 (6.8)	50 W	20-30	8:00	4.20E-6	1.2E-3 O_2 4.2E-3 Ar 4.0E-3 RF	55.9	6.9
23/10/14	E-Beam	Au	-	70 mA	23-26	1:46	6.5E-6	1.8E-5	40	1.8
23/10/14	RF Sputter	PtO_x	Ar (10) O_2 (6.8)	50 W	24-30	4:00	6.0E-6	1.2E-3 O_2 4.2E-3 Ar 4.0E-3 RF	27.6	6.9
23/10/14	E-Beam	Au	-	70 mA	23-26	1:47	8.5E-6	2.2E-5	40	1.8
23/10/14	RF Sputter	PtO_x	Ar (10) O_2 (6.8)	50 W	17-26	2:00	2.3E-6	1.3E-3 O_2 4.2E-3 Ar 4.0E-3 RF	14.0	6.9
24/10/14	E-Beam	Au	-	70 mA	18-22	1:51	6.5E-6	1.7E-5	40	1.8

24/10/14	RF Sputter	PtO_x	Ar (10) O_2 (6.8)	50 W	35-37	1:00	6.0E-6	1.2E-3 O_2 4.2E-3 Ar 4.0E-3 RF	7.2	6.9
24/10/14	E-Beam	Au	-	70 mA	22-25	1:57	3.8E-6	1.8E-5	40	1.8
03/11/14	RF Sputter	PtO_x	Ar (10) O_2 (6.8)	50 W	20-28	0:30	5.5E-6	1.2E-3 O_2 4.2E-3 Ar 4.0E-3 RF	3.5	6.9
03/11/14	E-Beam	Au	-	70 mA	25-28	2:18	1.5E-5	2.6E-5	40	1.8
03/11/14	RF Sputter	PtO_x	Ar (10) O_2 (6.8)	50 W	34-35	0:10	3.0E-6	1.2E-3 O_2 4.2E-3 Ar 4.0E-3 RF	1.4	6.9
03/11/14	E-Beam	Au	-	70 mA	23-27	1:45	7.0E-6	2.5E-5	60	1.8

[A4.1] Surface Topography Step-Height from DEKTAK

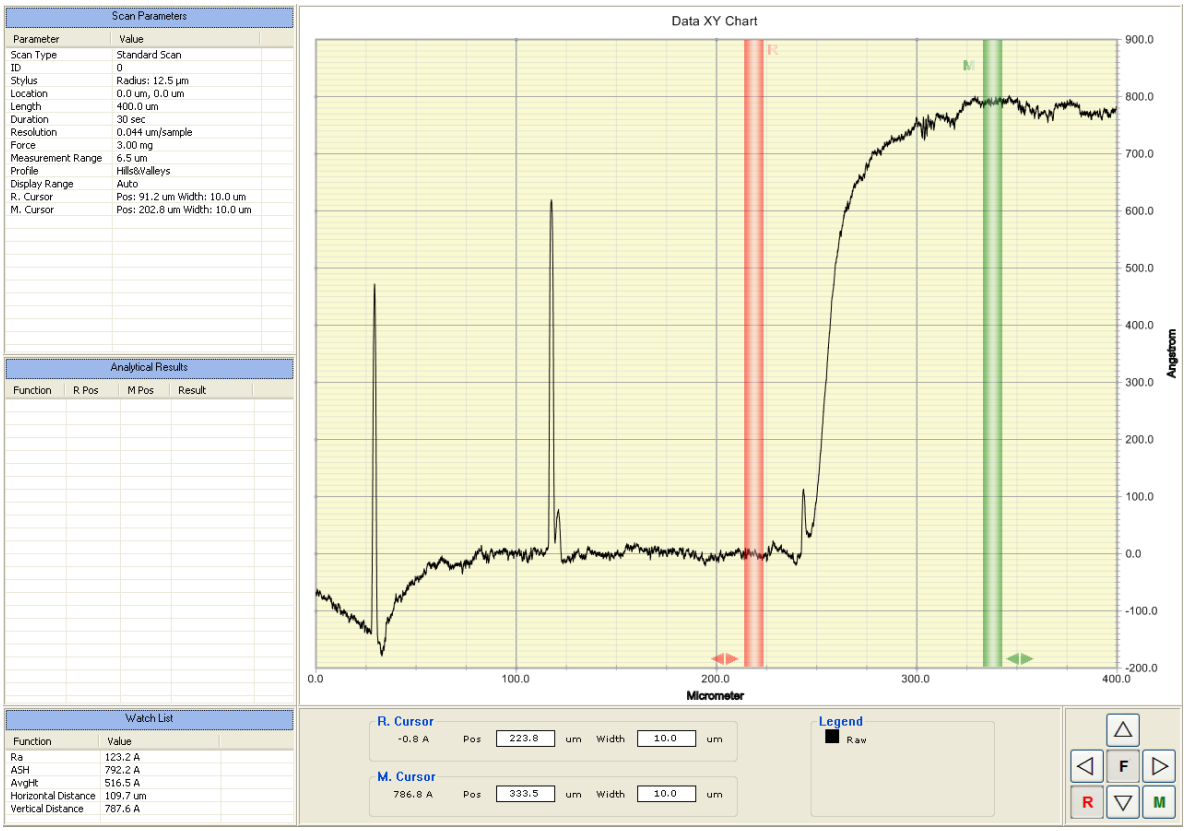

Material: RF sputtered IrO_x (O_2:Ar flow ratio 1.0:10.0 sccm)

Measured height: 78.76 nm (single scan)

Mean height: 70.89 nm (all scans)

[A4.2] Hall Effect Van der Pauw Calculations

Table A4.2: Hall Effect Parameters, Units and Equations [4.8 – 4.9]

Parameter	Symbol	Unit	Equation	Equation Number
Contact Resistance 1→2	R_{12}	Ω	$R_{12} = \frac{V_{12}}{I}$	(A4.1)
Mean Vertical Resistance	$R_{vertical}$	Ω	$R_{vertical} = \frac{(R_{23} + R_{32} + R_{12} + R_{12})}{4}$	(A4.2)
Mean Horizonal Resistance	$R_{horizontal}$	Ω	$R_{horizontal} = \frac{(R_{12} + R_{12} + R_{12} + R_{12})}{4}$	(A4.3)
Hall Voltage Contact 2→4	V_C	V	$V_C = V_{M24} - V_{-M24}$	(A4.4)
Hall Voltage Contact 4→2	V_D	V	$V_D = V_{M42} - V_{-M42}$	(A4.5)
Hall Voltage Contact 1→3	V_E	V	$V_E = V_{M13} - V_{-M13}$	(A4.6)
Hall Voltage Contact 3→1	V_F	V	$V_F = V_{M31} - V_{-M31}$	(A4.7)
Sheet Resistance	Rs	Ω	$e^{-\pi R_{vertical}/R_s} + e^{-\pi R_{horizontal}/R_s} = 1$	(A4.8)
Bulk Resistivity	ρ	Ωcm	$\rho = R_S W$	(A4.9)
Conductivity	σ	$\Omega^{-1}cm^{-1}$	$\sigma = \frac{1}{\rho}$	(A4.10)
Hall Voltage	V_H	V	$V_H = \frac{(\lvert V_C\rvert + \lvert V_D\rvert + \lvert V_E\rvert + \lvert V_F\rvert)}{4}$	(A4.11)
Sheet Carrier Concentration	N_S	cm^{-2}	$N_S = \frac{IB}{q\lvert V_H\rvert}$	(A4.12)
Bulk Carrier Concentration	N_B	cm^{-3}	$N_B = \frac{N_S}{W}$	(A4.13)
Mobility	μ	$cm^2V^{-1}s^{-1}$	$\mu = \frac{1}{qN_S R_S}$	(A4.14)
			$\mu = \frac{\lvert V_H\rvert}{R_S IB}$	(A4.15)
Hall Effect Coefficient	R_H		$R_H = \frac{W\lvert V_H\rvert}{IB}$	(A4.16)
Magnetoresistance	δR	Ω	$\delta R = \frac{V_H}{I}$	(A4.17)
V/H Ratio of Resistance	α		$\alpha = \frac{\sum R_{vertical}}{\sum R_{horizontal}}$	(A4.18)

[A4.3] AFM, KPM Scan Calculations

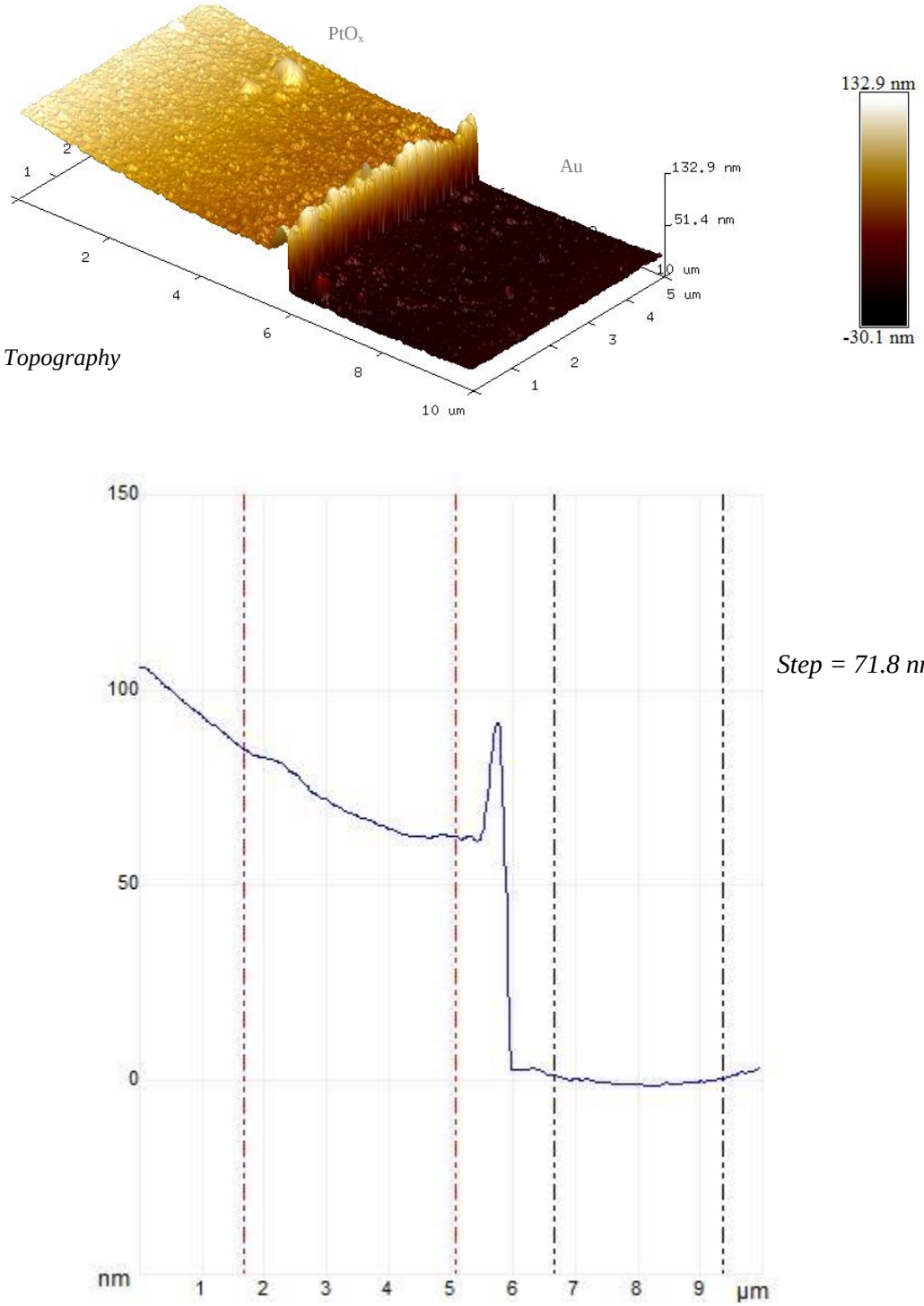

Figure A4.3.1: AFM (above) and Averaged (below) Measurement of RF Sputtered 6.0:10 (O_2:Ar) PtO_x thin film on Au reference

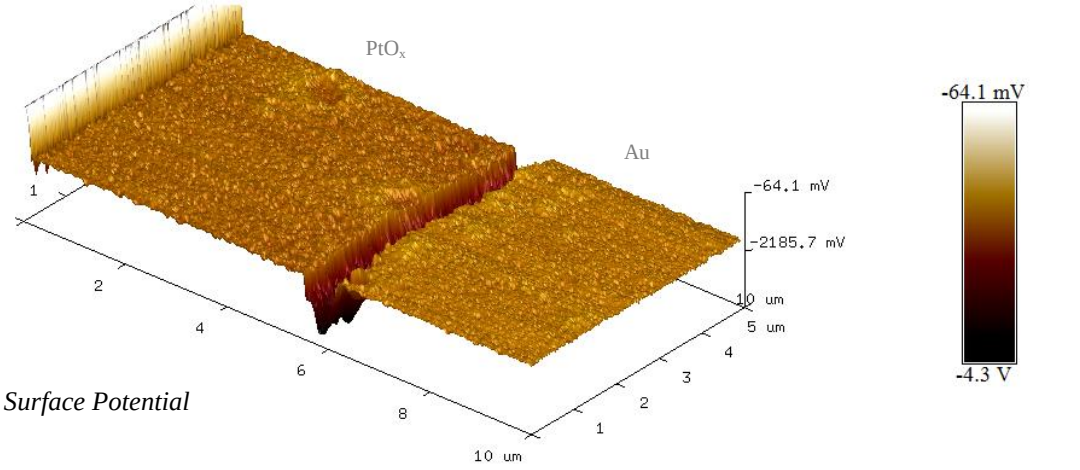

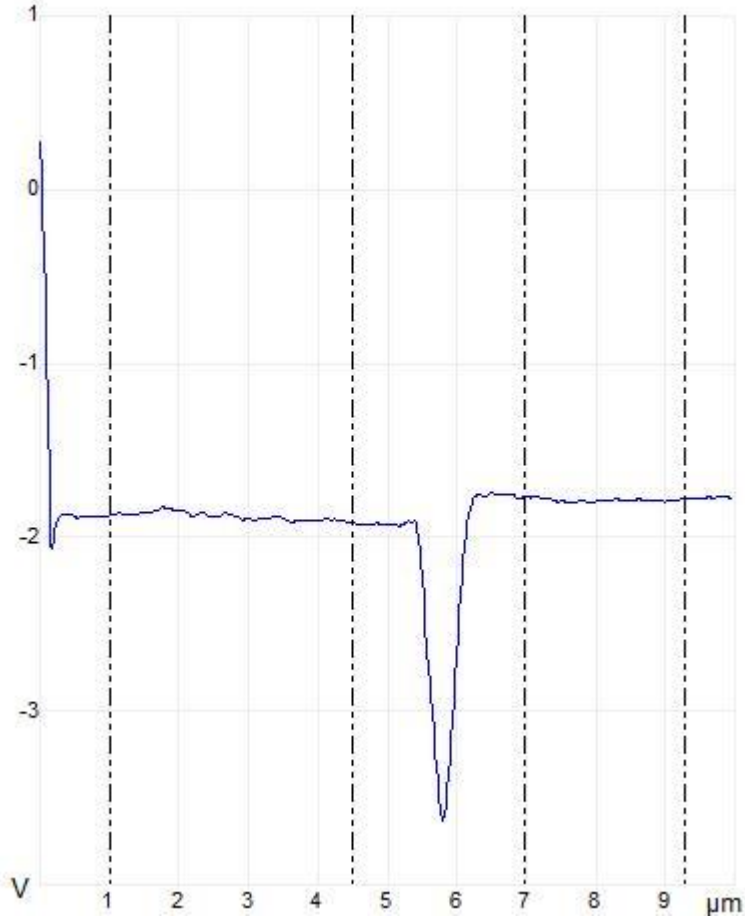

$V_{\Delta CPD}$ = 115 mV

Figure A4.3.2: KPM (above) and Averaged (below) Measurement of RF Sputtered 6.0:10 (O_2:Ar) PtO_x thin film on Au reference

[A4.4] RBS Results for Iridium, Palladium, and Platinum Oxidation Series
Courtesy of Professor Steven M. Durbin and Robert Makin, Department of Electrical and Computer Engineering, Western Michigan University, USA.

Samples Fabricated 23 – 28 October 2015
RBS Performed 23 December 2015

Table A4.5: RBS Results For Iridium, Palladium, and Platinum Oxidation Series

Material	O_2:Ar Gas Flow Ratio During RF Sputtering	Metal Concentration	Oxygen Concentration
Ir	0.0:10	0.000 ± 0.001	1.000 ± 0.001
IrO_x	0.5:10	0.000 ± 0.001	1.000 ± 0.001
IrO_x	1.0:10	0.390 ± 0.002	0.610 ± 0.002
IrO_x	2.0:10	0.659 ± 0.001	0.341 ± 0.001
IrO_x	3.0:10	0.689 ± 0.001	0.311 ± 0.001
IrO_x	4.0:10	0.695 ± 0.001	0.305 ± 0.001
IrO_x	5.0:10	0.700 ± 0.001	0.300 ± 0.001
IrO_x	7.0:10	0.723 ± 0.001	0.277 ± 0.001
Pd	0.0:10	0.000 ± 0.001	1.000 ± 0.001
PdO_x	0.5:10	0.213 ± 0.002	0.787 ± 0.002
PdO_x	1.0:10	0.370 ± 0.002	0.630 ± 0.002
PdO_x	2.0:10	0.538 ± 0.002	0.462 ± 0.002
PdO_x	3.0:10	0.536 ± 0.002	0.464 ± 0.002
PdO_x	4.0:10	0.529 ± 0.002	0.471 ± 0.002
PdO_x	5.0:10	0.540 ± 0.002	0.460 ± 0.002
PdO_x	7.0:10	0.586 ± 0.002	0.414 ± 0.002
Pt	0.0:10	0.000 ± 0.001	1.000 ± 0.001
PtO_x	0.5:10	0.249 ± 0.001	0.751 ± 0.001
PtO_x	1.0:10	0.269 ± 0.002	0.731 ± 0.002
PtO_x	2.0:10	0.311 ± 0.003	0.689 ± 0.003
PtO_x	3.0:10	0.115 ± 0.002	0.885 ± 0.002
PtO_x	4.0:10	0.339 ± 0.002	0.661 ± 0.002
PtO_x	5.0:10	0.666 ± 0.001	0.334 ± 0.001
PtO_x	7.0:10	0.686 ± 0.001	0.314 ± 0.001

[A4.5] XPS Results for Iridium, Palladium, and Platinum Oxidation Series
Results courtesy of Dr Colin Doyle, Faculty of Engineering, University of Auckland, NZ.

Ir, IrO_x Samples Fabricated	28/03/2014 – 04/04/2014
XPS Performed	18/11/2014

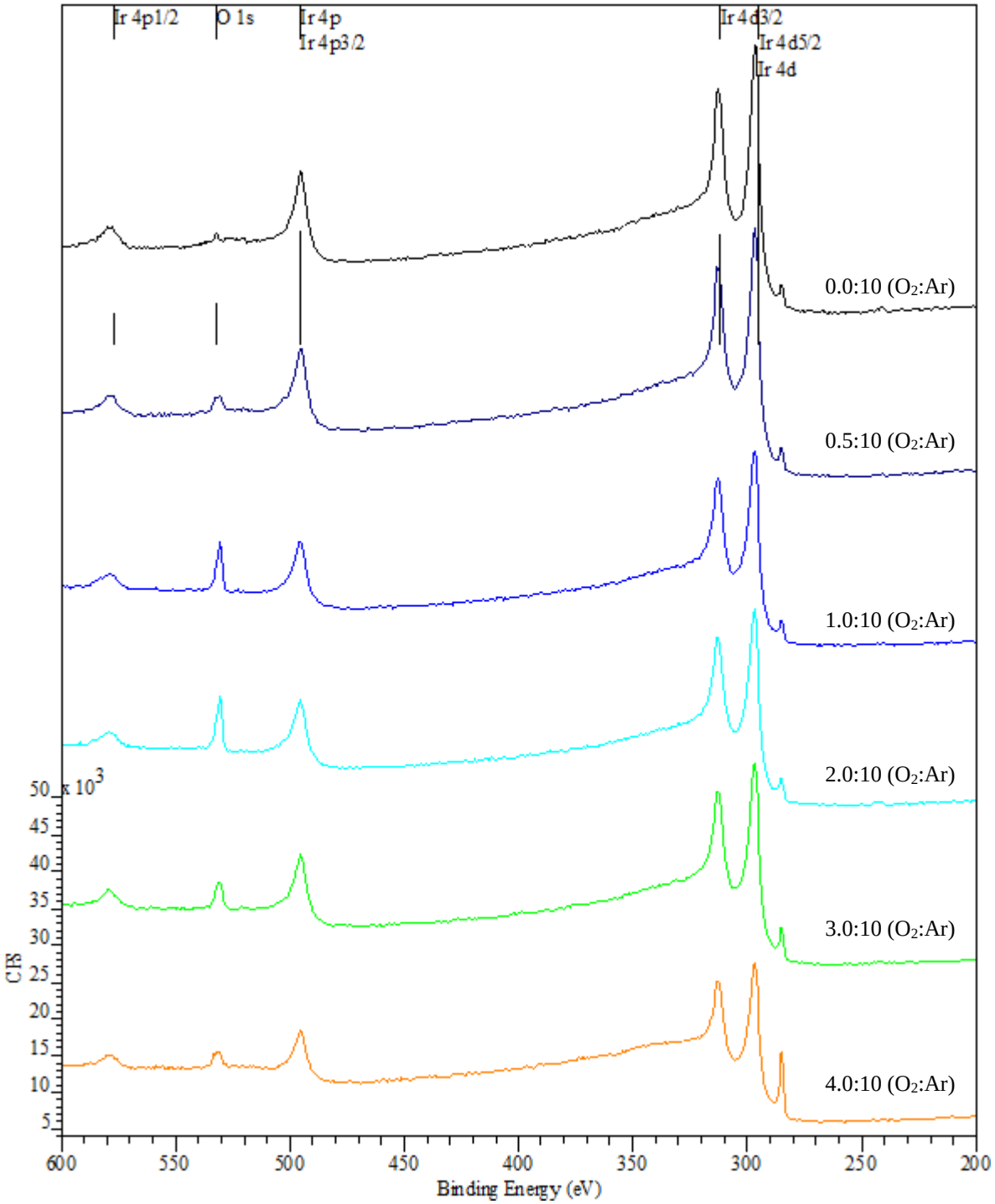

Figure A4.5.1: XPS Spectra of Survey 01 of Iridium Oxide Series

Pt, PtO_x Samples Fabricated 02/10/2014 – 16/10/2014
XPS Performed 18/11/2014

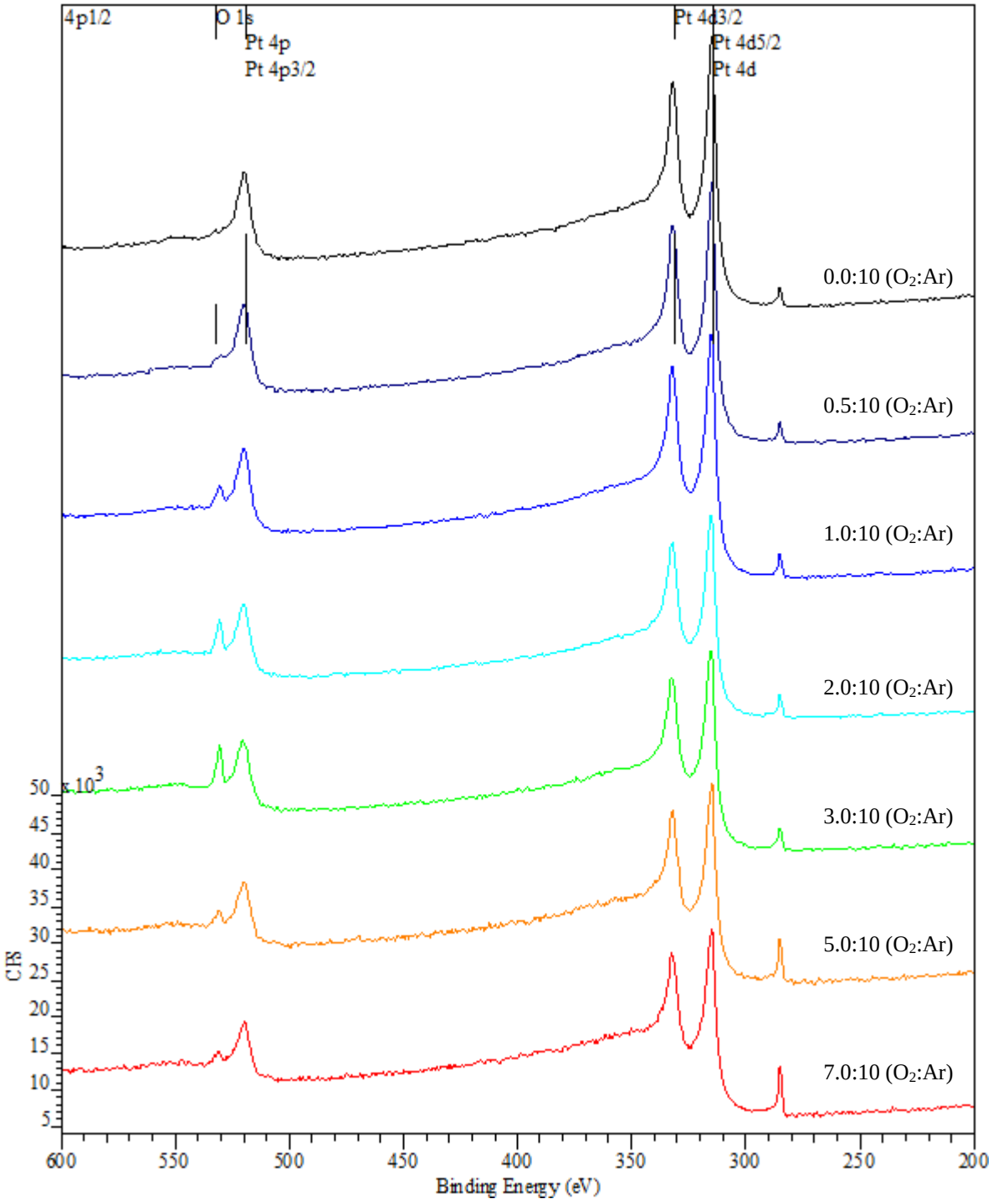

Figure A4.5.2: XPS Spectra of Survey 01 of Platinum Oxide Series

Samples Fabricated 03/07/2015 – 05/07/2015
XPS Performed 31/08/2015

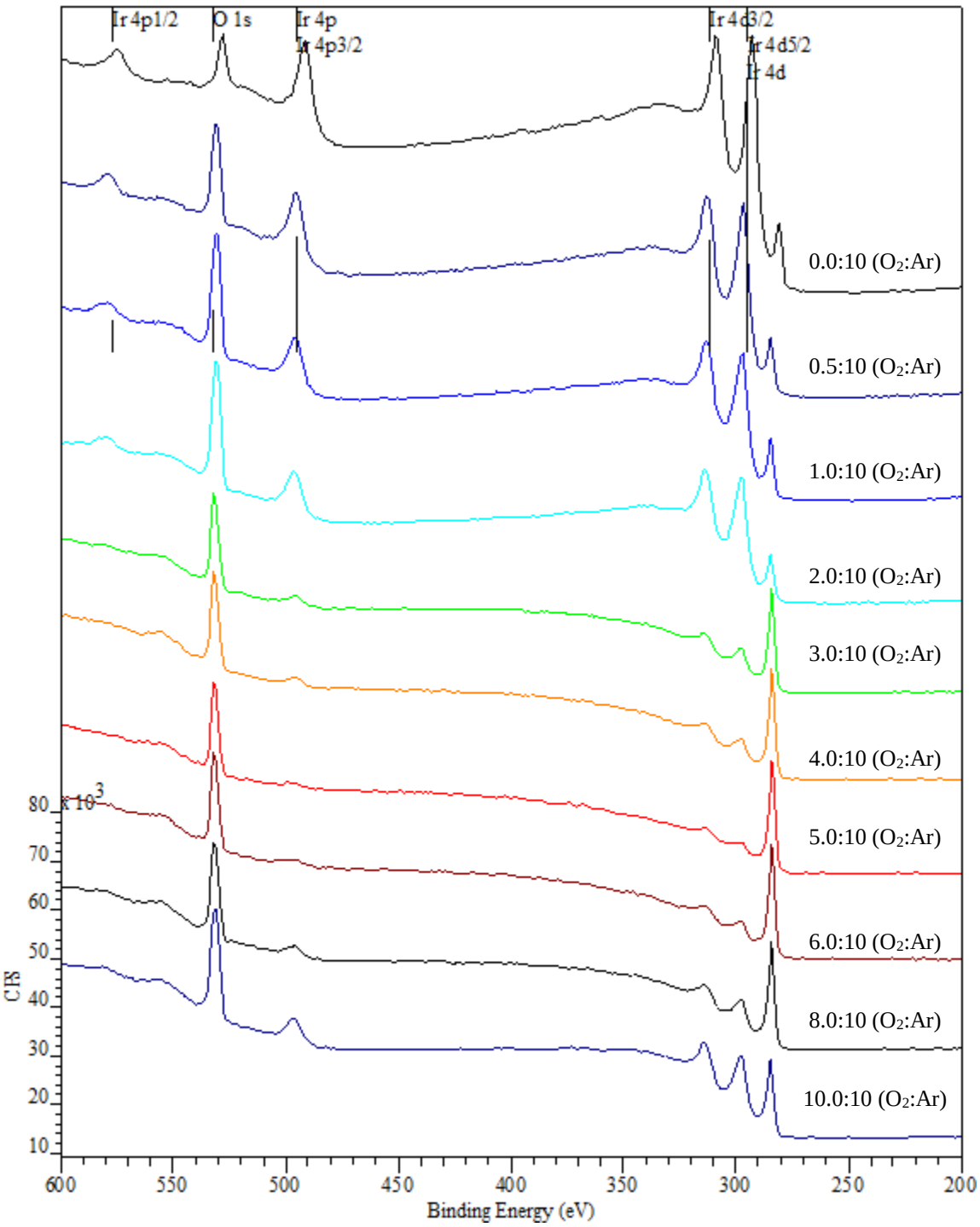

Figure A4.5.3: XPS Spectra of Survey 02 of Iridium Oxide Series

Samples Fabricated 03/07/2015 – 05/07/2015
XPS Performed 31/08/2015

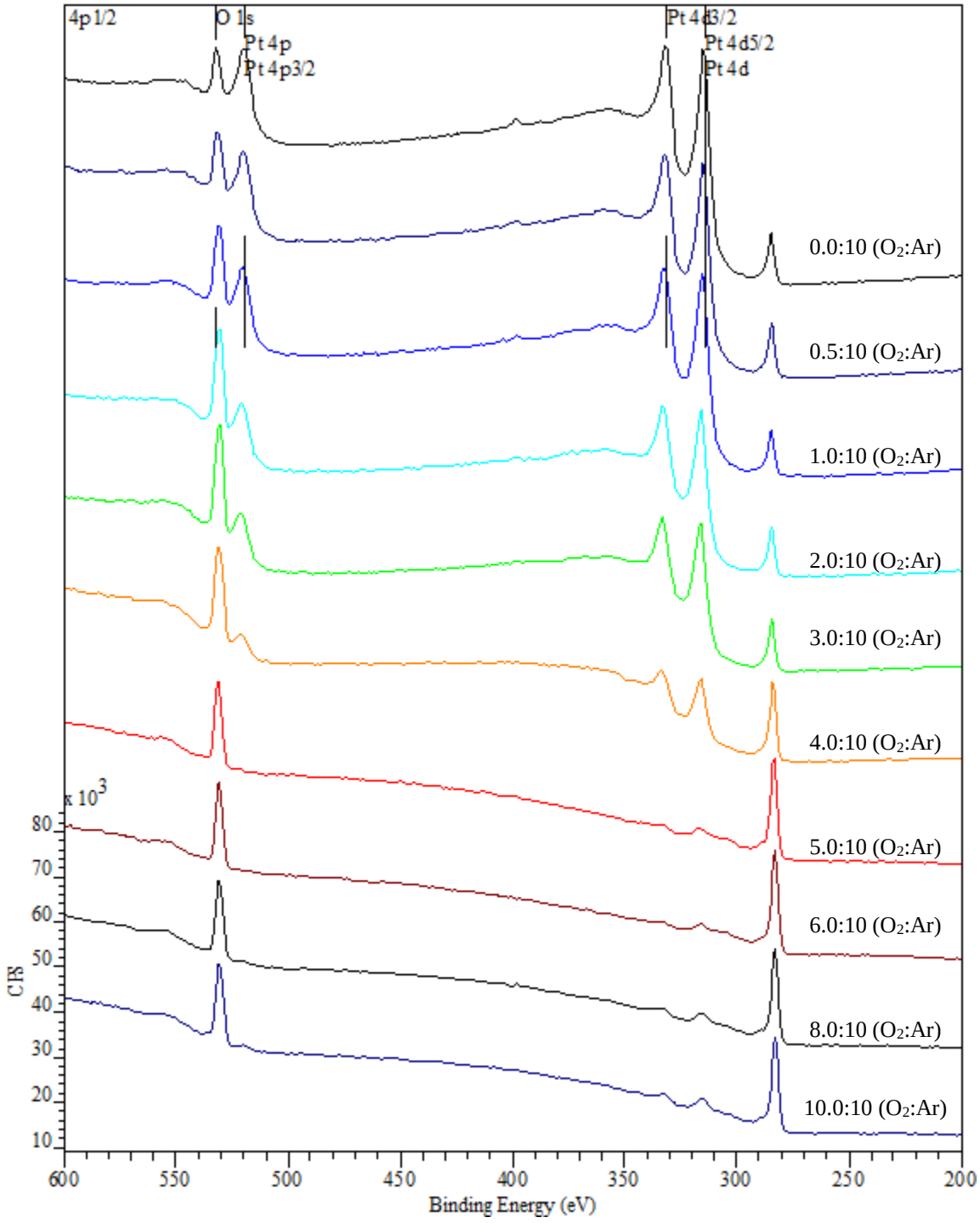

Figure A4.5.4: XPS Spectra of Survey 02 of Platinum Oxide Series

Samples Fabricated 23/10/2015 – 28/10/2015
XPS Performed 02/02/2016

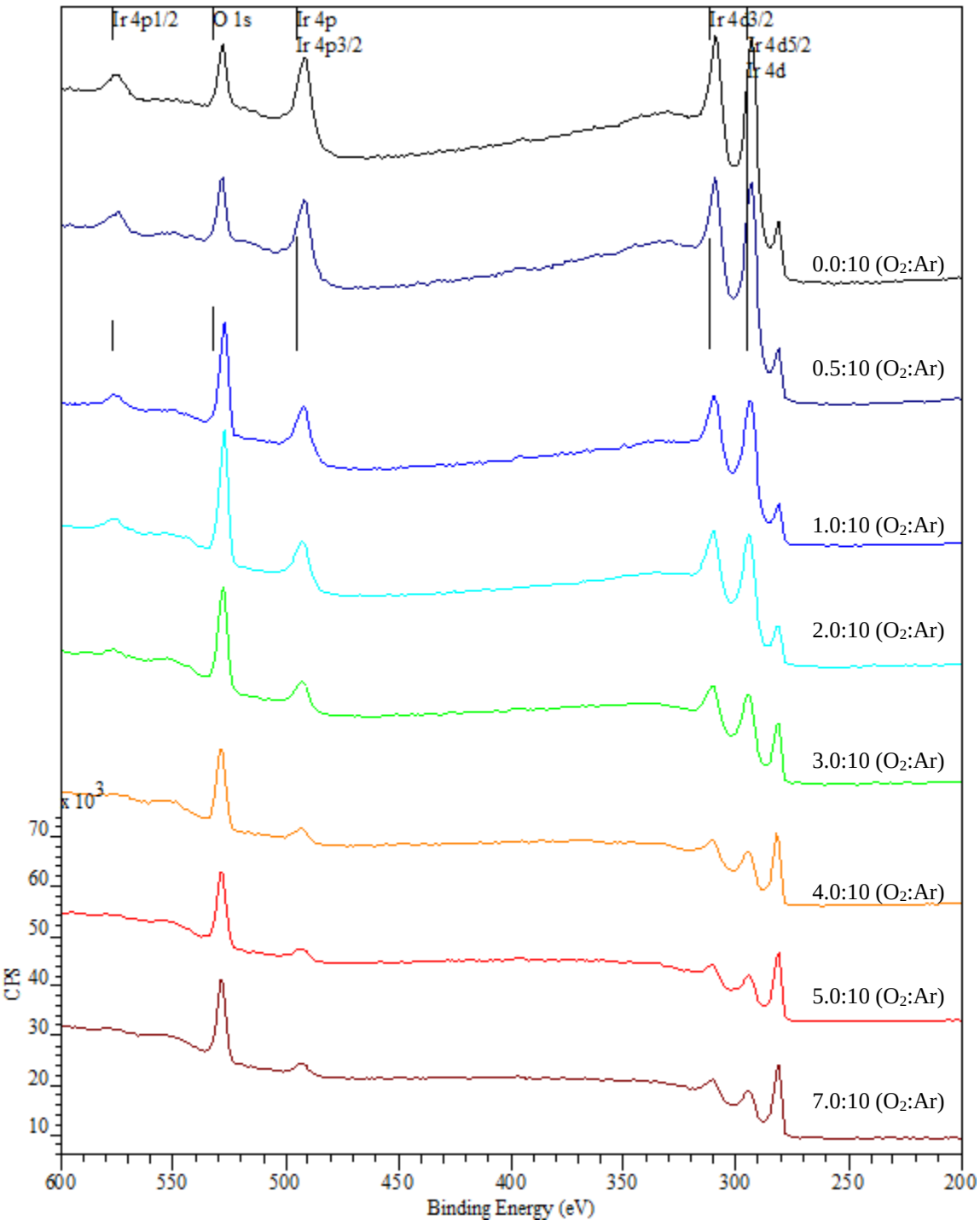

Figure A4.5.5: XPS Spectra of Survey 03 of Iridium Oxide Series

Samples Fabricated 23/10/2015 – 28/10/2015
XPS Performed 02/02/2016

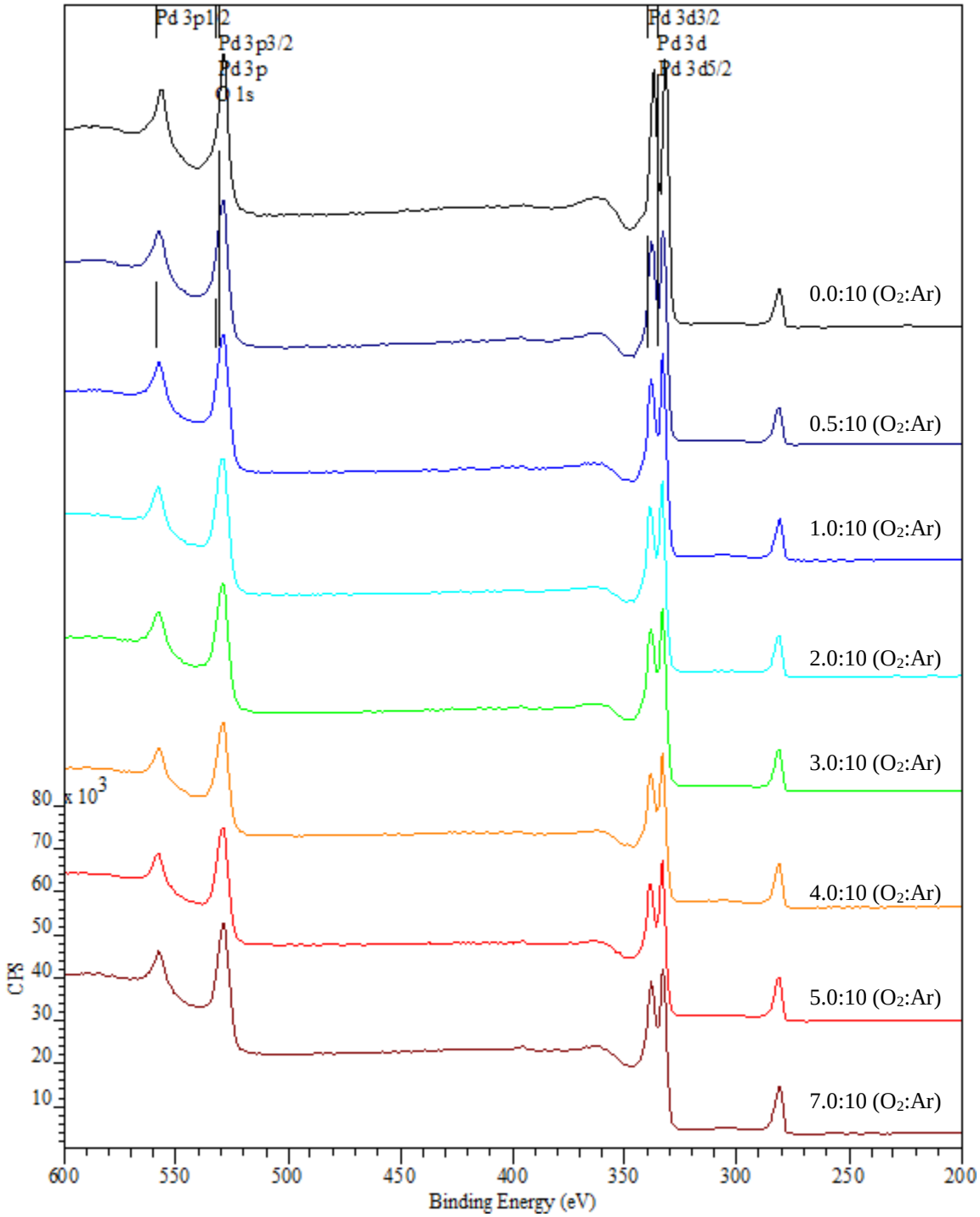

Figure A4.5.6: XPS Spectra of Survey 03 of Palladium Oxide Series

Samples Fabricated 23/10/2015 – 28/10/2015
XPS Performed 02/02/2016

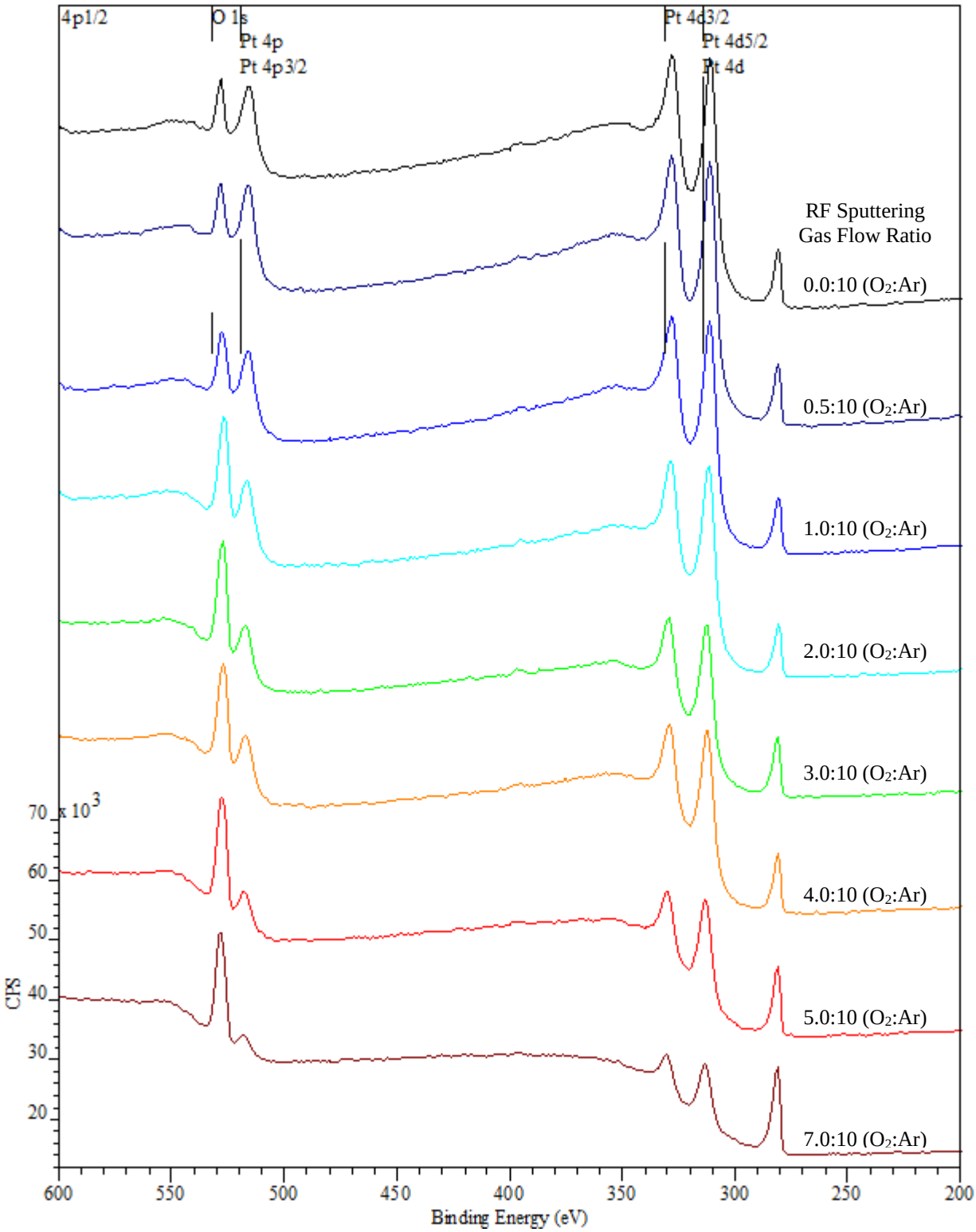

Figure A4.5.7: XPS Spectra of Survey 03 of Platinum Oxide Series

[A4.6] Norland Products Inc. UVA Splice Lamp Model P/N 5200 Spectral Response
Courtesy of Dr. Salim Elzwawi

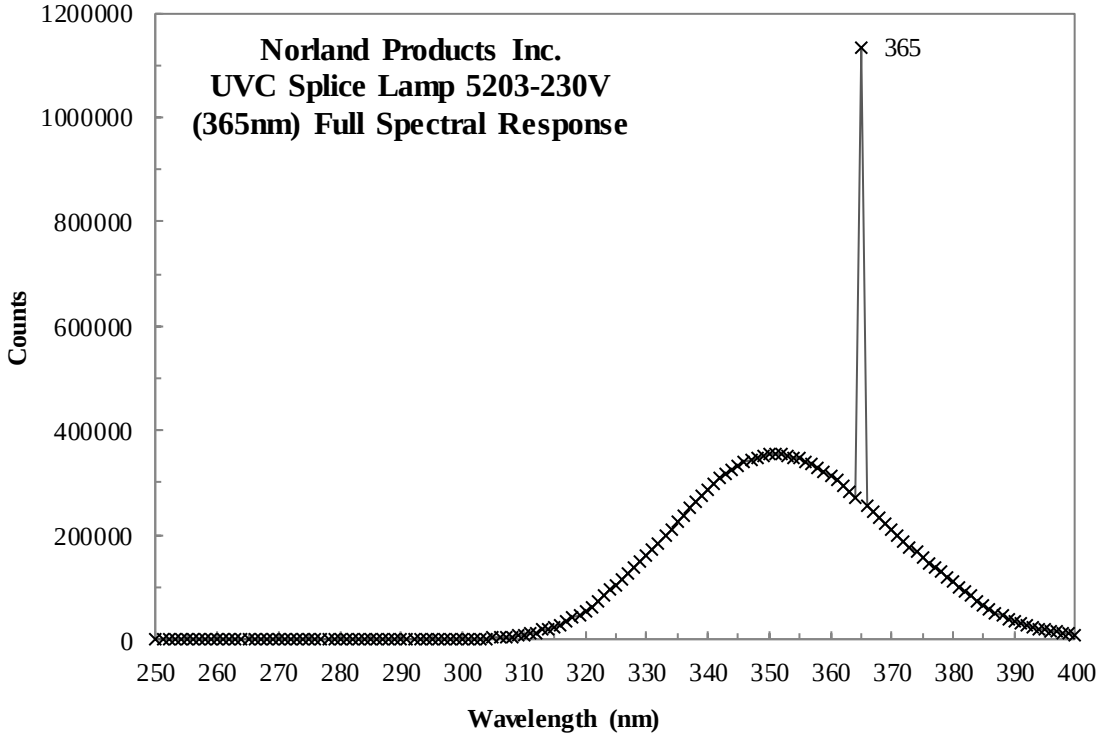

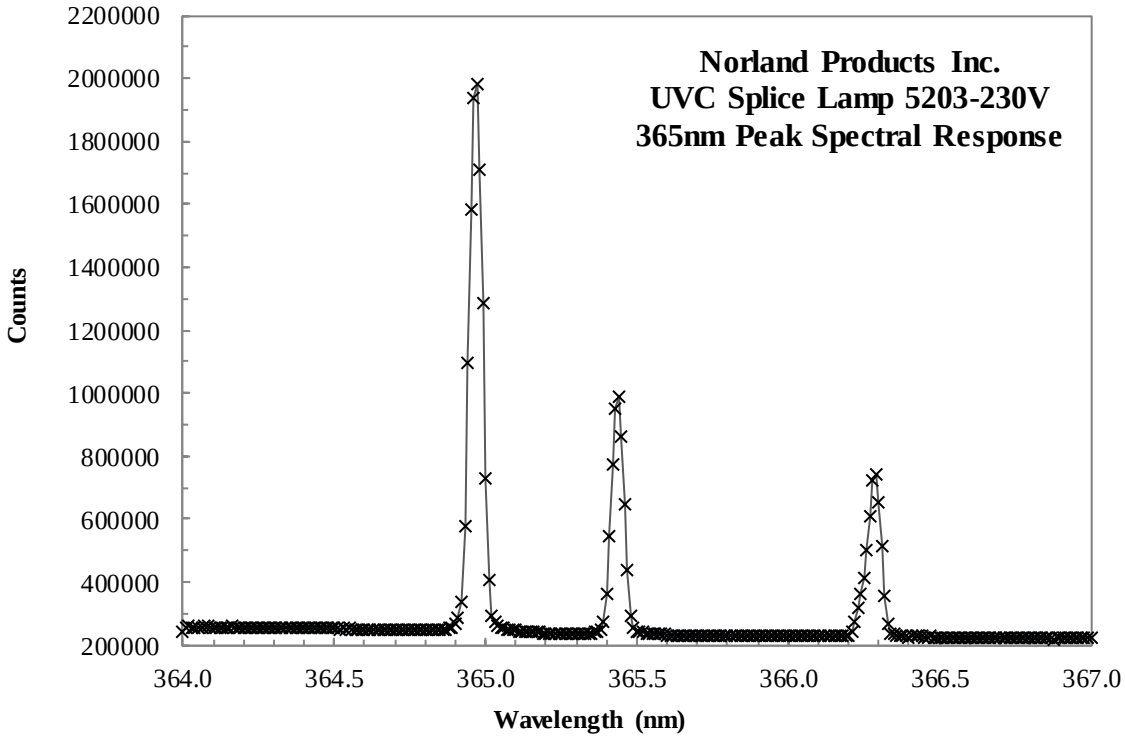

[A5.1] Transmission Spectra for Metal and Metal Oxide Thin Films (and Gold Capping Layers)

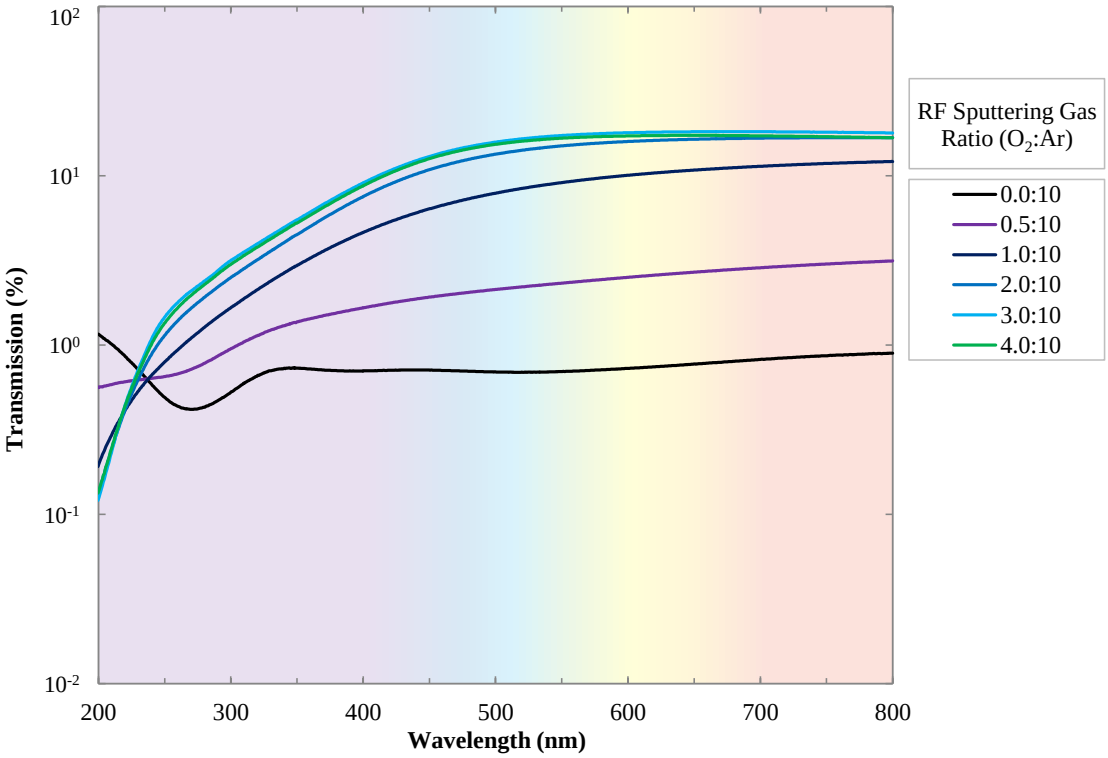

Figure A5.1: Transmission of IrO_x Films 0.0:10 – 4.0:10 (O_2:Ar)

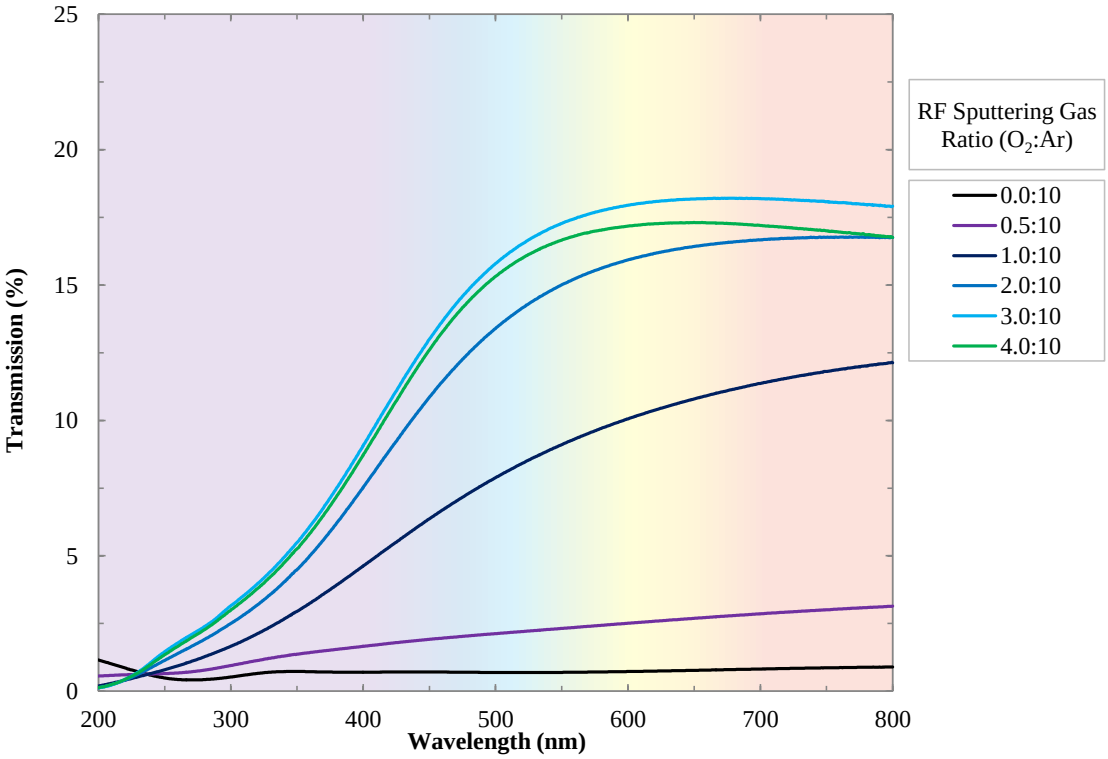

Figure A5.2: Transmission of IrO_x Films 0.0:10 – 4.0:10 (O_2:Ar) (Linear Scale)

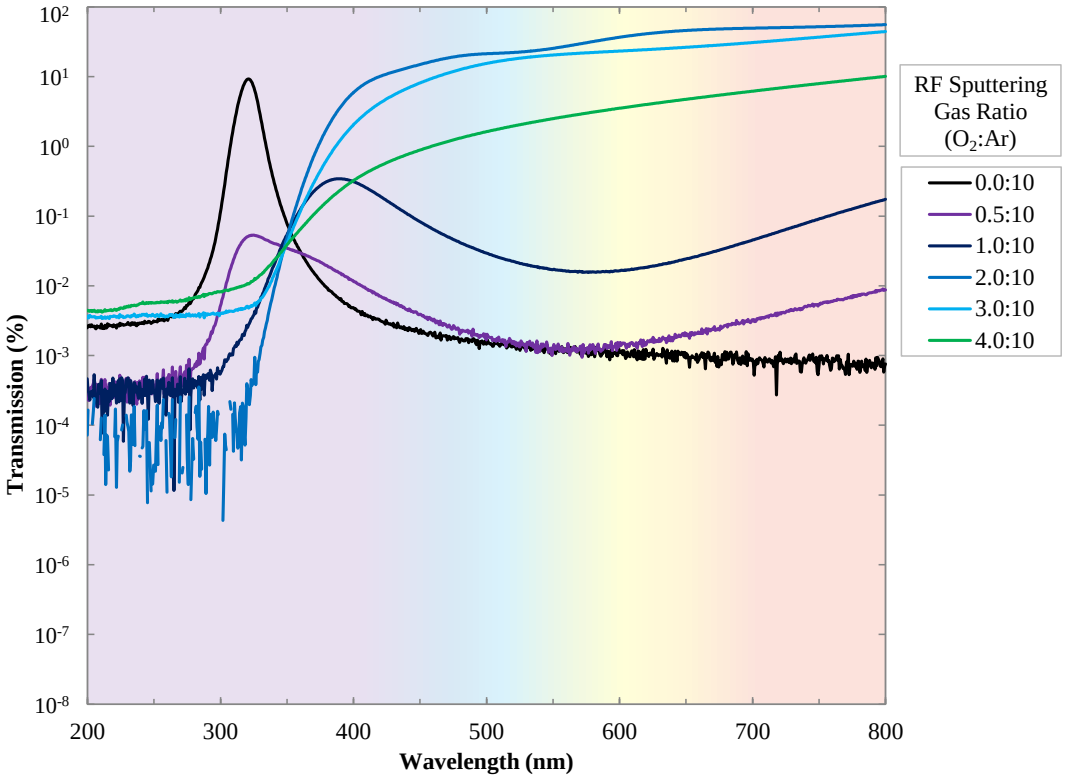

Figure A5.3: Transmission of AgO_x Films 0.5:10 – 4.0:10 (O_2:Ar)

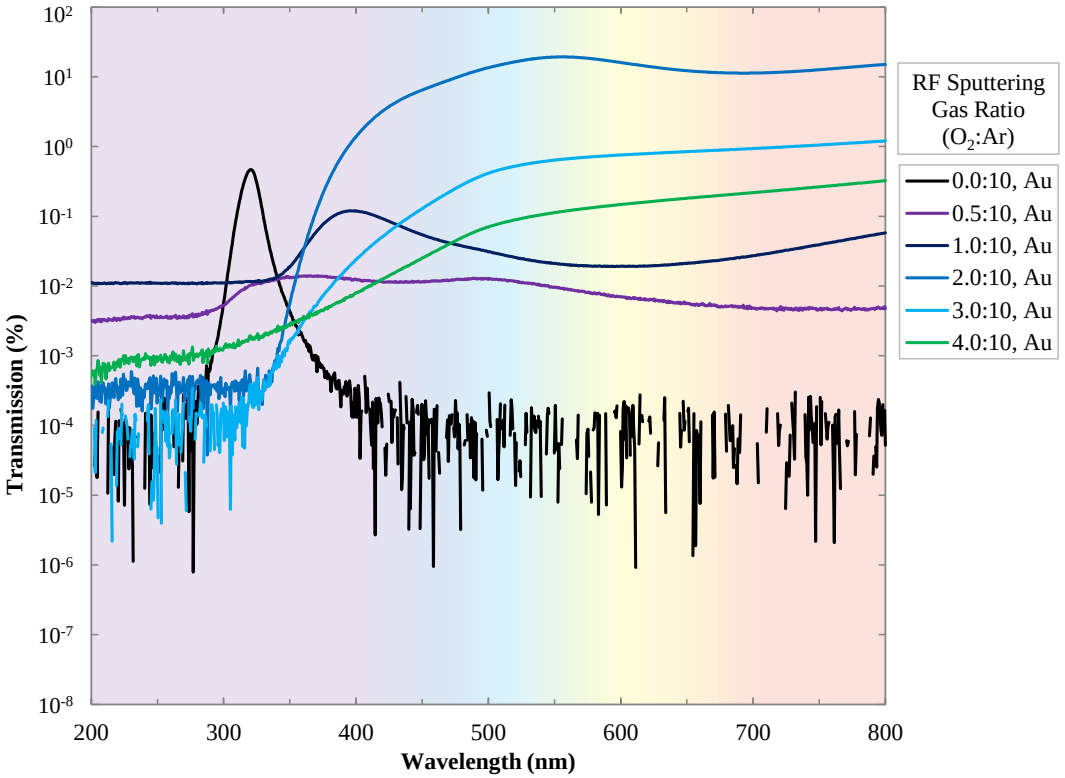

Figure A5.4: Transmission of AgO_x/Au Films 0.5:10 – 4.0:10 (O_2:Ar)

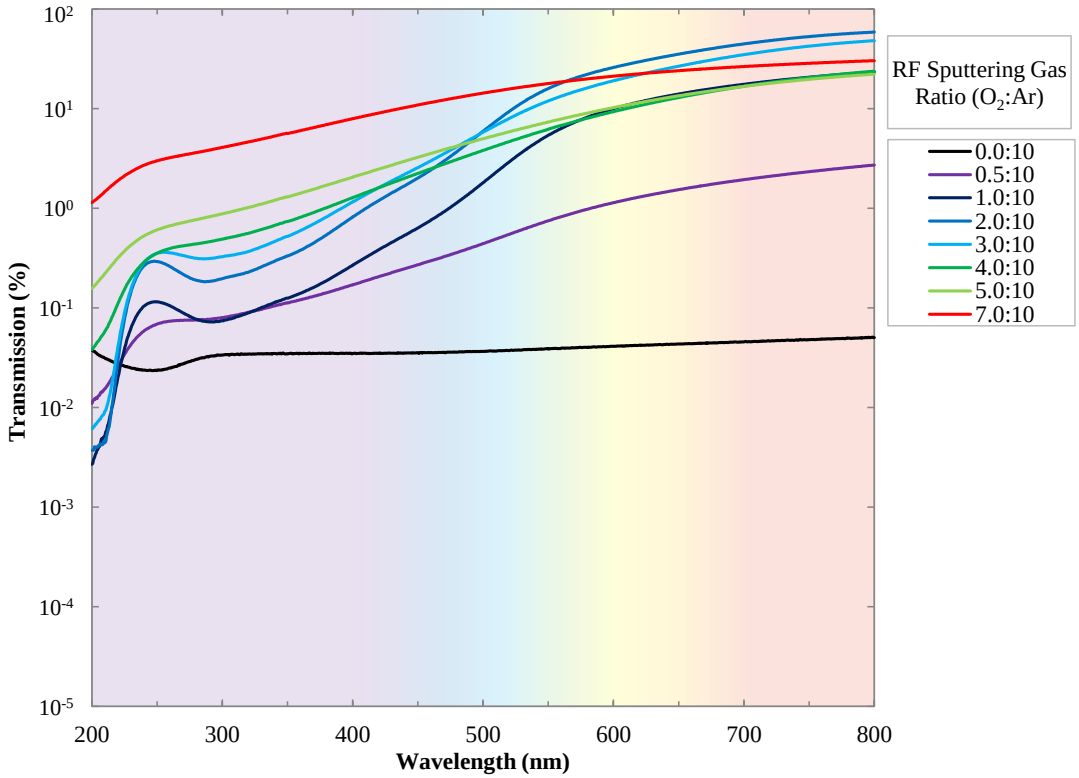

Figure A5.5: Transmission of PdO_x Films 0.0:10 – 7.0:10 (O_2:Ar)

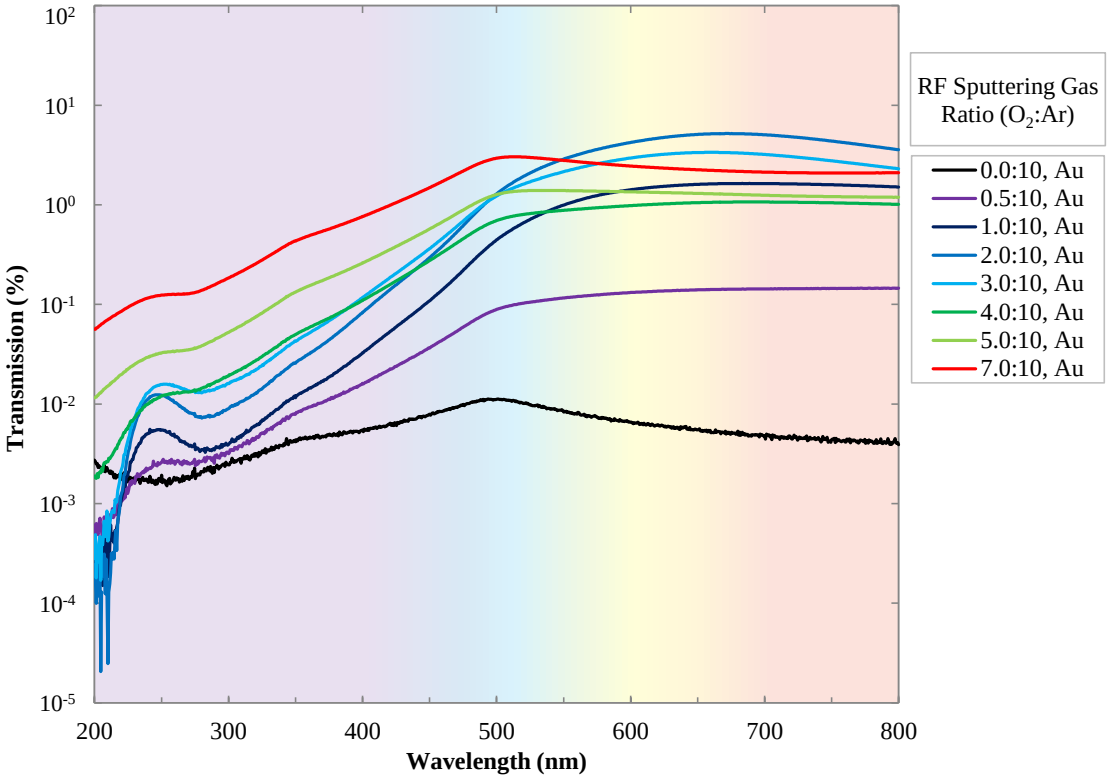

Figure A5.6: Transmission of PdO_x/Au Films 0.0:10 – 7.0:10 (O_2:Ar)

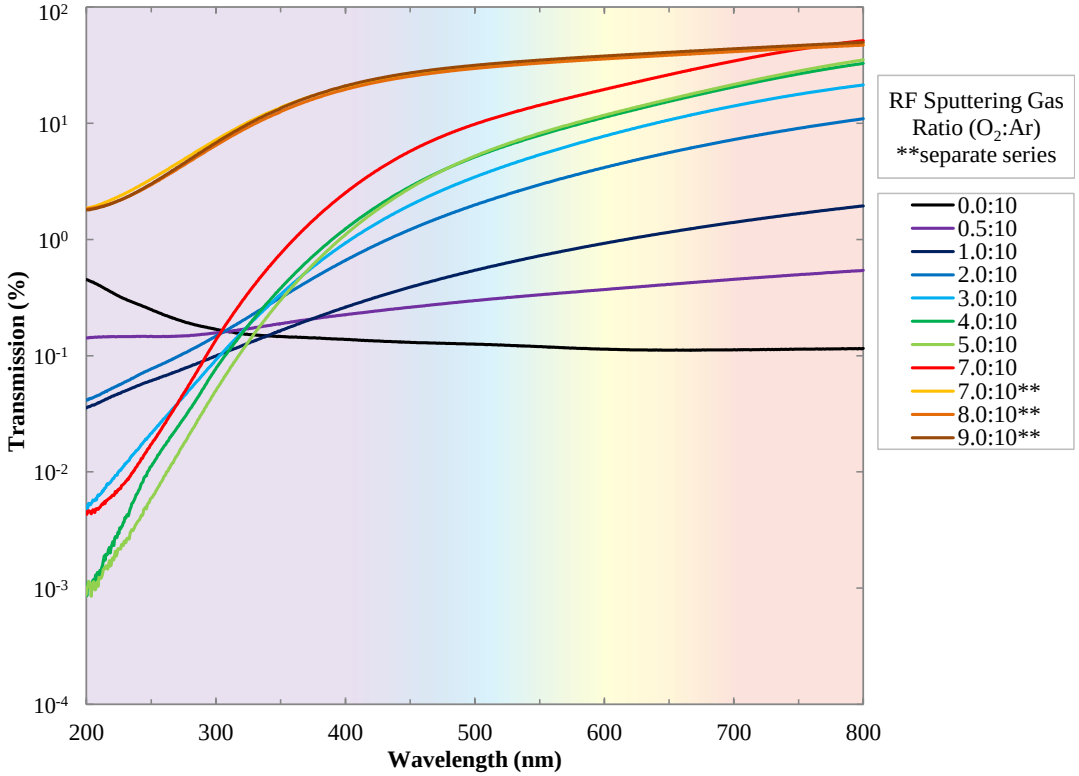

Figure A5.7: Transmission of PtO_x Films 0.0:10 – 9.0:10 (O_2:Ar)

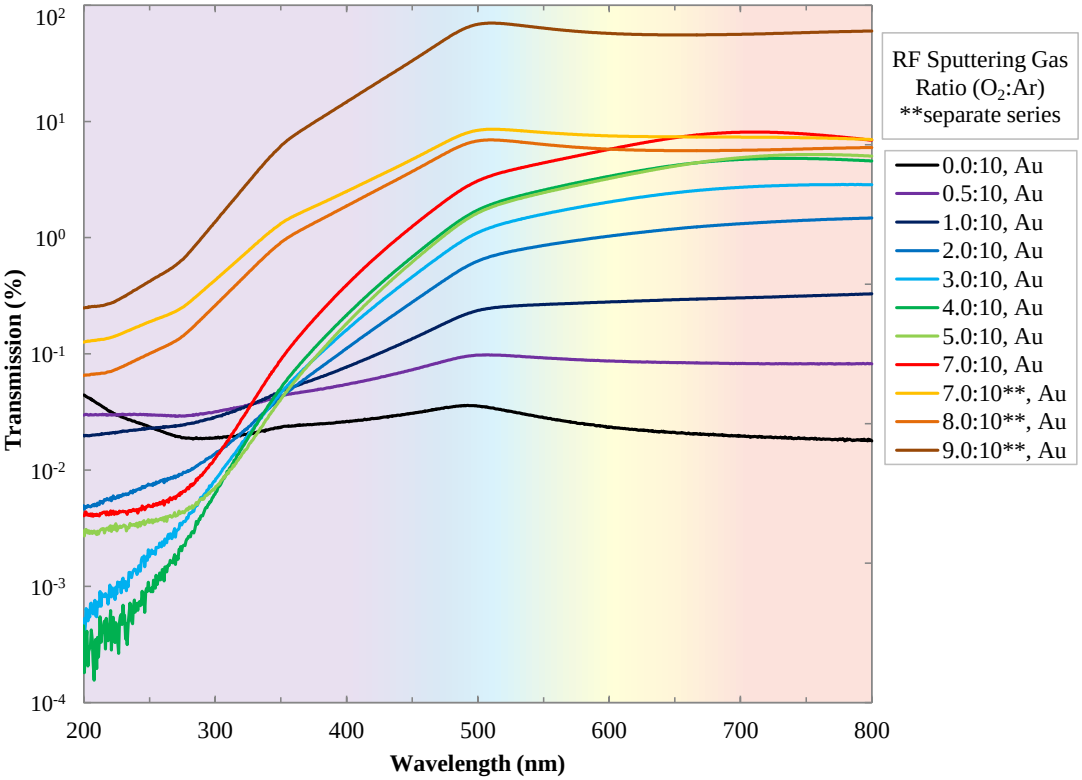

Figure A5.8: Transmission of PtO_x/Au Films 0.0:10 – 9.0:10 (O_2:Ar)

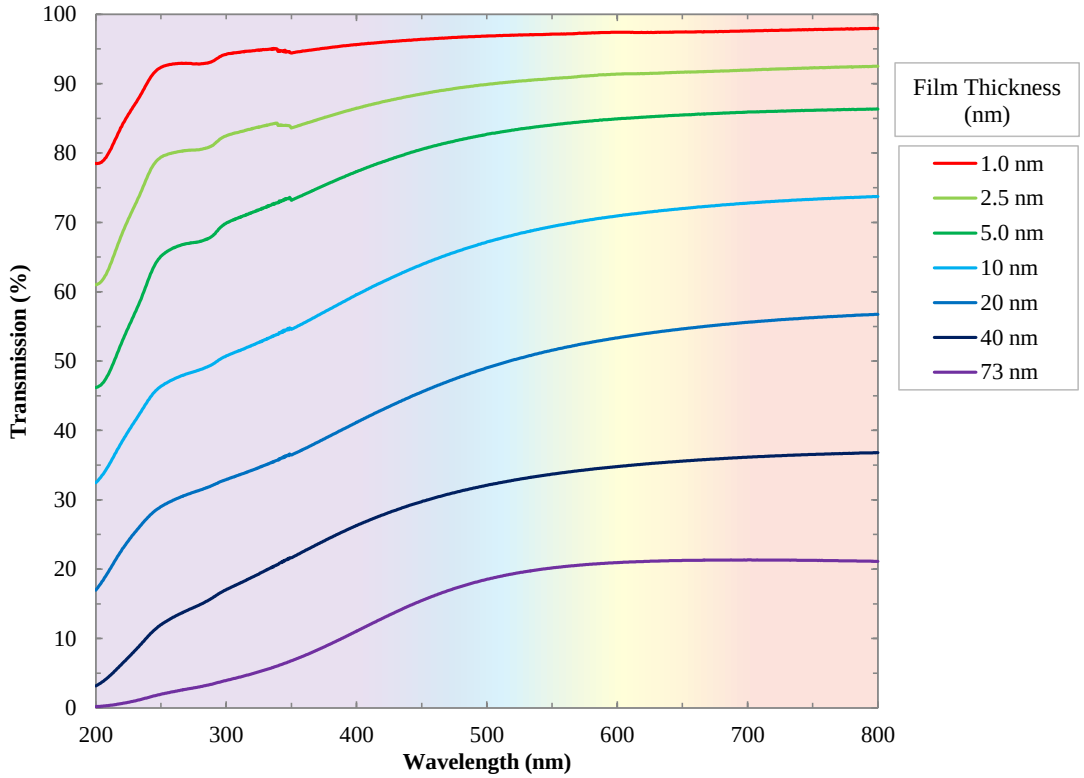

Figure A5.9: Transmission of IrO_x Films 3.0:10 (O_2:Ar) 73 – 1.0 nm Thickness (Linear)

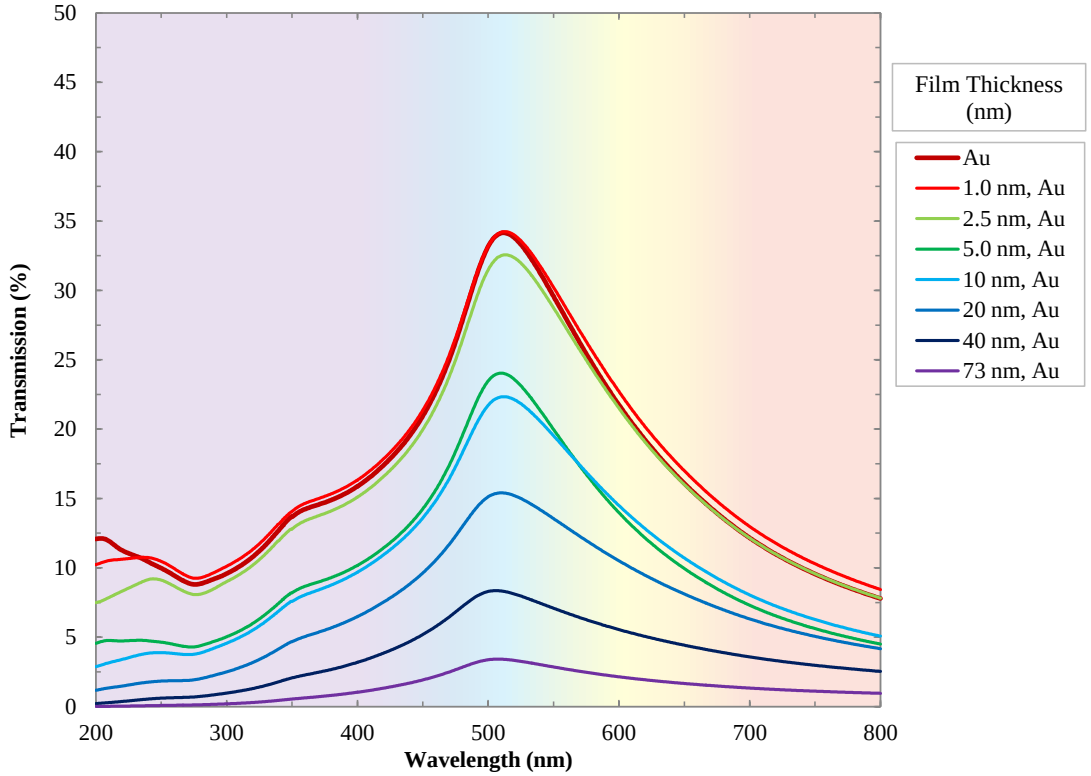

Figure A5.10: Transmission of IrO_x/Au Films 3.0:10 (O_2:Ar) 73 – 1.0 nm Thickness (Linear)

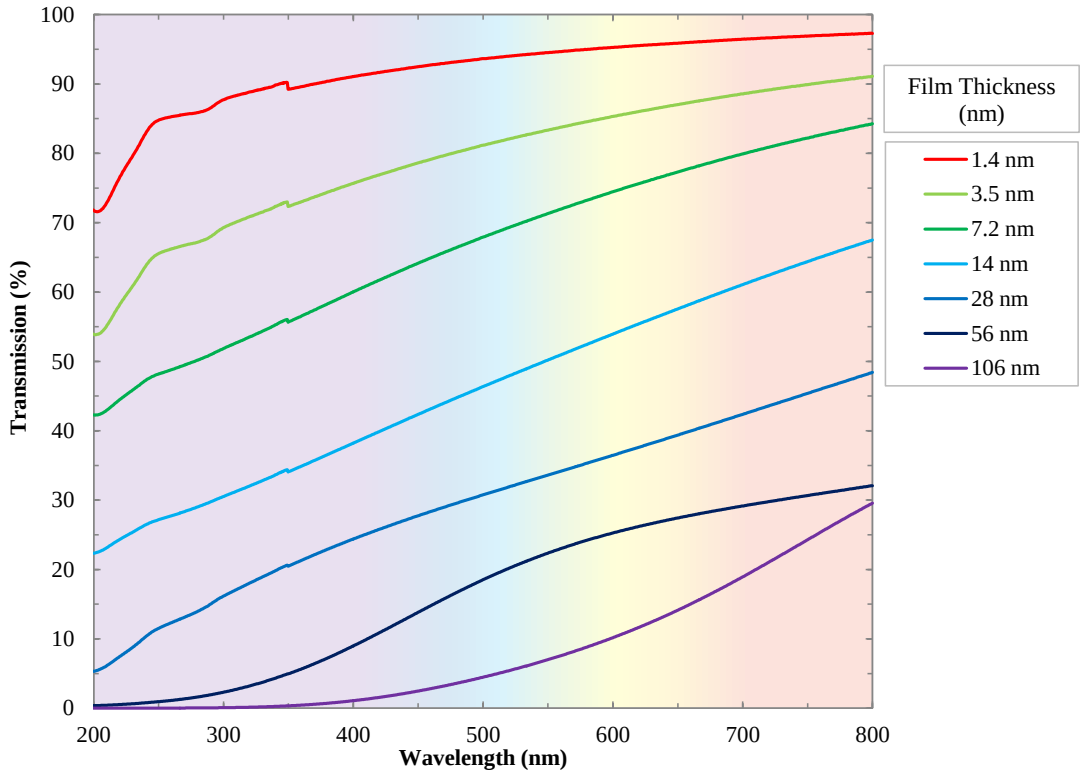

Figure A5.11: Transmission of PtO_x Films 4.0:10 (O_2:Ar) 106 – 1.4 nm Thickness (Linear)

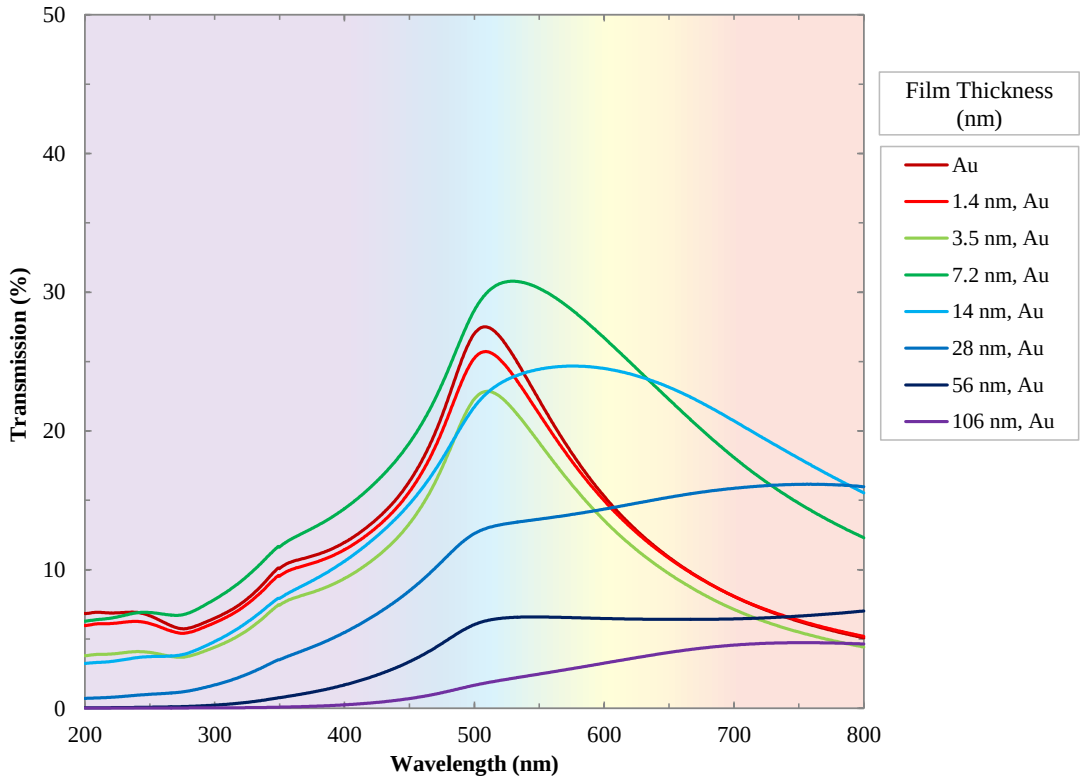

Figure A5.12: Transmission of PtO_x/Au Films 4.0:10 (O_2:Ar) 106 – 1.4 nm Thickness (Linear)

[A6.1] Schottky Contact Dark I-V Characteristics: Double-Barrier Example

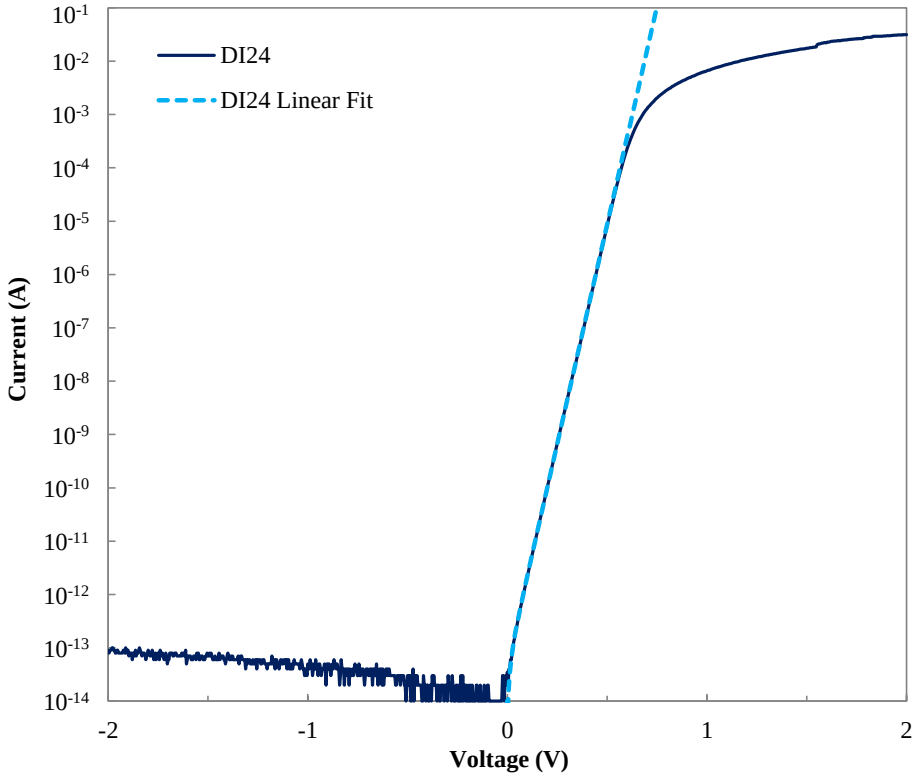

A6.2: Dark I-V Characteristics of 3.0:10 (O_2:Ar) PdO_x Contact DI24 with Least Squares Fit

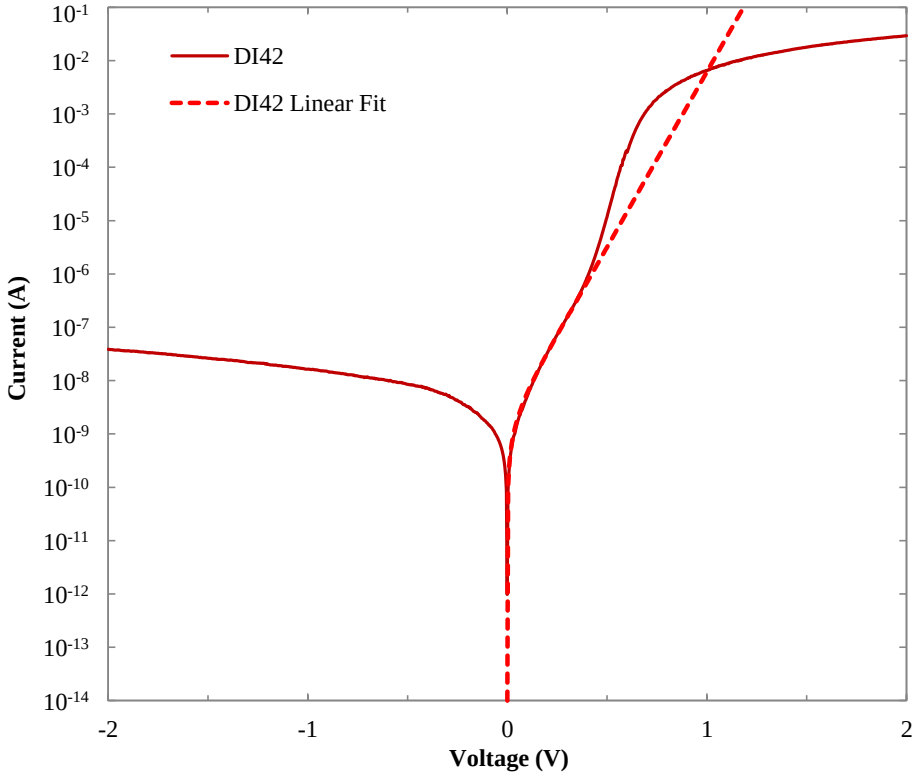

A6.3: Dark I-V Characteristics of 3.0:10 (O_2:Ar) PdO_x Contact DI42 with Least Squares Fit

[A6.2] Complete Dark I-V Characteristics for 1.0:10 (O_2:Ar) AgO_x Schottky Contacts

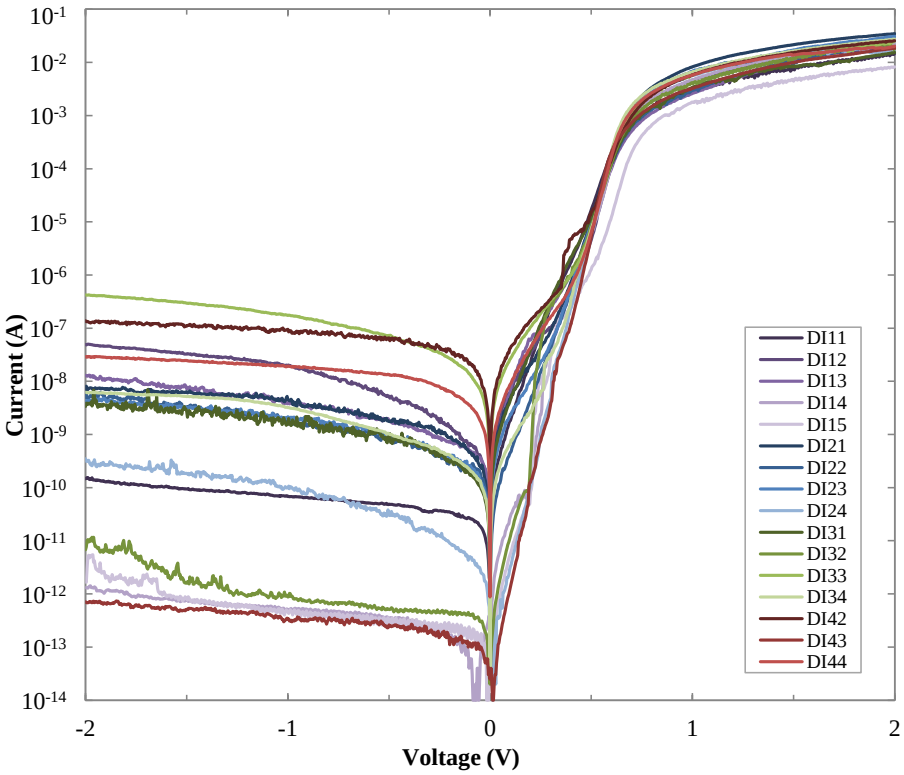

A6.3: Dark I-V Characteristics of Complete Set of 1.0:10 (O_2:Ar) AgO_x Schottky Contacts

[A6.3] Statistical Analysis of the Electrical Characteristics of the Schottky Contacts in This Work

AgO_x Schottky Contact Barrier Height (Φ_B)

ZnO Type	Schottky Contact Material	Gas Ratio	Calculated Ideal (eV)	Maximum (eV)	Minimum (eV)	Mean (eV)	Std. Dev. (eV)
+c-plane (low-Li)	Ag	0.0:10	0.563	0.562	0.489	0.545	0.0184
+c-plane (low-Li)	AgO_x	0.5:10*	-	0.647	0.489	0.562	0.0442
+c-plane (low-Li)	AgO_x	1.0:10*	-	1.147	1.058	1.099	0.0237
+c-plane (low-Li)	AgO_x	0.5:10	1.134	1.112	1.001	1.052	0.0277
+c-plane (low-Li)	AgO_x	1.0:10	1.008	1.050	0.801	0.899	0.0673
+c-plane (low-Li)	AgO_x	2.0:10	1.377	1.404	1.188	1.285	0.0729
+c-plane (low-Li)	AgO_x	3.0:10	1.383	1.414	1.212	1.308	0.0428
+c-plane (low-Li)	AgO_x	4.0:10	1.364	1.420	1.083	1.247	0.0671

AgO_x Schottky Contact Ideality (η)

ZnO Type	Schottky Contact Material	Gas Ratio	Calculated Ideal R^2	Maximum	Minimum	Mean	Std. Dev.
+c-plane (low-Li)	Ag	0.0:10	0.7244	1.845	1.095	1.228	0.1941
+c-plane (low-Li)	AgO_x	0.5:10*	-	4.121	1.354	2.582	0.8254
+c-plane (low-Li)	AgO_x	1.0:10*	-	1.241	1.127	1.152	0.0299
+c-plane (low-Li)	AgO_x	0.5:10	0.9335	1.371	1.188	1.220	0.0442
+c-plane (low-Li)	AgO_x	1.0:10	0.9469	1.653	0.939	1.317	0.1881
+c-plane (low-Li)	AgO_x	2.0:10	0.9416	1.474	1.051	1.219	0.1681
+c-plane (low-Li)	AgO_x	3.0:10	0.6540	1.399	1.077	1.206	0.0715
+c-plane (low-Li)	AgO_x	4.0:10	0.8170	1.840	1.087	1.309	0.1599

RuO_x Schottky Contact Barrier Height (Φ_B)

ZnO Type	Schottky Contact Material	Gas Ratio	Calculated Ideal (eV)	Maximum (eV)	Minimum (eV)	Mean (eV)	Std. Dev. (eV)
–c-plane	RuO_x	0.5:10	-	0.711	0.442	0.604	0.1028
–c-plane	RuO_x	1.0:10	-	0.739	0.720	0.726	0.0061
–c-plane	RuO_x	2.0:10	-	0.827	0.784	0.799	0.0153
–c-plane	RuO_x	3.0:10	-	0.834	0.781	0.818	0.0137
–c-plane	RuO_x	4.0:10	-	0.615	0.549	0.567	0.0163
–c-plane	RuO_x	5.0:10	-	1.018	0.729	0.932	0.0602
–c-plane	RuO_x	7.0:10	-	0.959	0.811	0.922	0.0469

RuO_x Schottky Contact Ideality (η)

ZnO Type	Schottky Contact Material	Gas Ratio	Calculated Ideal R^2	Maximum	Minimum	Mean	Std. Dev.
–c-plane	RuO_x	0.5:10	-	5.827	1.102	3.188	2.1248
–c-plane	RuO_x	1.0:10	-	1.128	1.106	1.120	0.0084
–c-plane	RuO_x	2.0:10	-	1.236	1.111	1.132	0.0401
–c-plane	RuO_x	3.0:10	-	1.094	1.043	1.051	0.0133
–c-plane	RuO_x	4.0:10	-	1.153	1.109	1.126	0.0093
–c-plane	RuO_x	5.0:10	-	3.153	1.068	1.218	0.4997
–c-plane	RuO_x	7.0:10	-	1.657	1.054	1.161	0.2024

IrO_x Schottky Contact Barrier Height (Φ_B)

ZnO Type	Schottky Contact Material	Gas Ratio	Calculated Ideal (eV)	Maximum (eV)	Minimum (eV)	Mean (eV)	Std. Dev. (eV)
–c-plane	IrO_x	0.5:10	-	0.642	0.624	0.630	0.0072
–c-plane	IrO_x	1.0:10	0.698	0.662	0.654	0.659	0.0026
–c-plane	IrO_x	2.0:10	0.755	0.730	0.712	0.720	0.0058
–c-plane	IrO_x	3.0:10	0.986	0.921	0.619	0.884	0.0933
–c-plane	IrO_x	4.0:10	1.060	1.059	1.016	1.037	0.0160
–c-plane	IrO_x	5.0:10	1.195	0.953	0.874	0.931	0.0208
–c-plane	IrO_x	7.0:10	1.170	1.017	0.968	0.990	0.0162

IrO_x Schottky Contact Ideality (η)

ZnO Type	Schottky Contact Material	Gas Ratio	Calculated Ideal R^2	Maximum	Minimum	Mean	Std. Dev.
–c-plane	IrO_x	0.5:10	-	1.230	1.203	1.215	0.0078
–c-plane	IrO_x	1.0:10	0.5368	1.212	1.183	1.199	0.0097
–c-plane	IrO_x	2.0:10	0.2122	1.310	1.232	1.252	0.0193
–c-plane	IrO_x	3.0:10	0.9990	2.807	1.334	1.502	0.4593
–c-plane	IrO_x	4.0:10	0.9416	1.291	1.223	1.254	0.0251
–c-plane	IrO_x	5.0:10	0.9439	1.612	1.386	1.424	0.0668
–c-plane	IrO_x	7.0:10	0.8525	1.439	1.341	1.381	0.0316

IrO_x Schottky Contact Barrier Height (Φ_B)

ZnO Type	Schottky Contact Material	Gas Ratio	Calculated Ideal (eV)	Maximum (eV)	Minimum (eV)	Mean (eV)	Std. Dev. (eV)
+c-plane (low-Li)	Ir	0.0:10	0.526	0.539	0.368	0.484	0.0597
+c-plane (low-Li)	IrO_x	0.5:10	0.736	0.766	0.613	0.704	0.0420
+c-plane (low-Li)	IrO_x	1.0:10	0.795	0.790	0.723	0.777	0.0213
+c-plane (low-Li)	IrO_x	2.0:10	0.975	0.979	0.817	0.925	0.0358
+c-plane (low-Li)	IrO_x	3.0:10	1.054	1.075	0.951	0.996	0.0286
+c-plane (low-Li)	IrO_x	4.0:10	1.179	1.116	0.842	1.048	0.0825
+c-plane (low-Li)	IrO_x	PLD	-	0.965	0.934	0.947	0.0099

IrO_x Schottky Contact Ideality (η)

ZnO Type	Schottky Contact Material	Gas Ratio	Calculated Ideal R^2	Maximum	Minimum	Mean	Std. Dev.
+c-plane (low-Li)	Ir	0.0:10	0.9090	9.495	1.162	3.214	3.0635
+c-plane (low-Li)	IrO_x	0.5:10	0.7485	1.878	1.038	1.216	0.2414
+c-plane (low-Li)	IrO_x	1.0:10	0.9349	1.296	1.028	1.081	0.0888
+c-plane (low-Li)	IrO_x	2.0:10	0.6203	1.405	1.075	1.159	0.0898
+c-plane (low-Li)	IrO_x	3.0:10	0.3912	1.227	1.080	1.137	0.0423
+c-plane (low-Li)	IrO_x	4.0:10	0.9028	1.846	1.173	1.329	0.1972
+c-plane (low-Li)	IrO_x	PLD	-	1.013	1.006	1.007	0.0018

PdO_x Schottky Contact Barrier Height (Φ_B)

ZnO Type	Schottky Contact Material	Gas Ratio	Calculated Ideal (eV)	Maximum (eV)	Minimum (eV)	Mean (eV)	Std. Dev. (eV)
+c-plane (low-Li)	Pd	0.0:10	0.462	0.446	0.370	0.403	0.0266
+c-plane (low-Li)	PdO_x	0.5:10	0.738	0.743	0.624	0.707	0.0327
+c-plane (low-Li)	PdO_x	1.0:10	0.955	0.975	0.921	0.945	0.0116
+c-plane (low-Li)	PdO_x	2.0:10	0.941	0.951	0.887	0.914	0.0192
+c-plane (low-Li)	PdO_x	3.0:10	0.951	0.994	0.696	0.929	0.0588
+c-plane (low-Li)	PdO_x	4.0:10	1.183	1.155	1.029	1.123	0.0234
+c-plane (low-Li)	PdO_x	5.0:10	1.212	1.231	0.896	1.146	0.0670
+c-plane (low-Li)	PdO_x	7.0:10	1.231	1.206	1.101	1.164	0.0263

PdO_x Schottky Contact Ideality (η)

ZnO Type	Schottky Contact Material	Gas Ratio	Calculated Ideal R^2	Maximum	Minimum	Mean	Std. Dev.
+c-plane (low-Li)	Pd	0.0:10	0.8690	17.239	3.943	11.587	4.4141
+c-plane (low-Li)	PdO_x	0.5:10	0.8709	1.991	1.057	1.314	0.3092
+c-plane (low-Li)	PdO_x	1.0:10	0.2420	1.168	1.041	1.072	0.0414
+c-plane (low-Li)	PdO_x	2.0:10	0.1980	1.335	1.119	1.197	0.0605
+c-plane (low-Li)	PdO_x	3.0:10	0.8955	2.432	1.033	1.120	0.3095
+c-plane (low-Li)	PdO_x	4.0:10	0.6943	1.296	1.095	1.126	0.0407
+c-plane (low-Li)	PdO_x	5.0:10	0.8613	1.997	1.128	1.204	0.1904
+c-plane (low-Li)	PdO_x	7.0:10	0.7051	1.271	1.109	1.145	0.0475

PtO_x Schottky Contact Barrier Height (Φ_B)

ZnO Type	Schottky Contact Material	Gas Ratio	Calculated Ideal (eV)	Maximum (eV)	Minimum (eV)	Mean (eV)	Std. Dev. (eV)
+c-plane (low-Li)	Pt	0.0:10	0.4146	0.406	0.360	0.373	0.0126
+c-plane (low-Li)	PtO_x	0.5:10	0.751	0.773	0.663	0.735	0.0266
+c-plane (low-Li)	PtO_x	1.0:10	0.8467	0.858	0.693	0.809	0.0511
+c-plane (low-Li)	PtO_x	2.0:10	0.9237	0.944	0.745	0.900	0.0436
+c-plane (low-Li)	PtO_x	3.0:10	1.0170	1.027	0.802	0.941	0.0700
+c-plane (low-Li)	PtO_x	4.0:10	1.2179	1.147	1.004	1.084	0.0466
+c-plane (low-Li)	PtO_x	5.0:10	1.2985	1.175	1.050	1.105	0.0379
+c-plane (low-Li)	PtO_x	7.0:10	1.3042	1.281	1.100	1.202	0.0556

PtO_x Schottky Contact Ideality (η)

ZnO Type	Schottky Contact Material	Gas Ratio	Calculated Ideal R^2	Maximum	Minimum	Mean	Std. Dev.
+c-plane (low-Li)	Pt	0.0:10	0.2964	33.534	10.788	31.475	5.0643
+c-plane (low-Li)	PtO_x	0.5:10	0.9257	1.620	1.025	1.104	0.1626
+c-plane (low-Li)	PtO_x	1.0:10	0.9252	1.798	1.016	1.187	0.2473
+c-plane (low-Li)	PtO_x	2.0:10	0.7597	1.744	1.018	1.104	0.1669
+c-plane (low-Li)	PtO_x	3.0:10	0.8808	2.004	1.048	1.294	0.2537
+c-plane (low-Li)	PtO_x	4.0:10	0.9020	1.528	1.183	1.309	0.1020
+c-plane (low-Li)	PtO_x	5.0:10	0.7042	1.503	1.283	1.387	0.0635
+c-plane (low-Li)	PtO_x	7.0:10	0.8280	1.434	1.125	1.210	0.1037

PtO_x Schottky Contact Barrier Height (Φ_B)

ZnO Type	Schottky Contact Material	Gas Ratio	Calculated Ideal (eV)	Maximum (eV)	Minimum (eV)	Mean (eV)	Std. Dev. (eV)
+c-plane (low-Li)	Pt	6.0:10	1.2081	1.175	1.058	1.132	0.0267
+c-plane (low-Li)	PtO_x	7.5:10	1.2627	1.204	1.133	1.175	0.0185
+c-plane (low-Li)	PtO_x	8.0:10	1.2426	1.220	1.144	1.176	0.0164
+c-plane (low-Li)	PtO_x	9.0:10	1.2579	1.220	1.168	1.191	0.0118
+c-plane (low-Li)	PtO_x	10:10	1.2818	1.223	1.183	1.201	0.0104

PtO_x Schottky Contact Ideality (η)

ZnO Type	Schottky Contact Material	Gas Ratio	Calculated Ideal R^2	Maximum	Minimum	Mean	Std. Dev.
+c-plane (low-Li)	Pt	6.0:10	0.8552	1.365	1.121	1.187	0.0603
+c-plane (low-Li)	PtO_x	7.5:10	0.6438	1.338	1.190	1.242	0.0409
+c-plane (low-Li)	PtO_x	8.0:10	0.6231	1.290	1.140	1.199	0.0385
+c-plane (low-Li)	PtO_x	9.0:10	0.3994	1.248	1.162	1.215	0.0240
+c-plane (low-Li)	PtO_x	10:10	0.5048	1.208	1.153	1.173	0.0158

[A7.1] 4.0:10 (O_2:Ar) AgO_x UV Photoresponse: Repeated 30 s UV Exposure with Bias

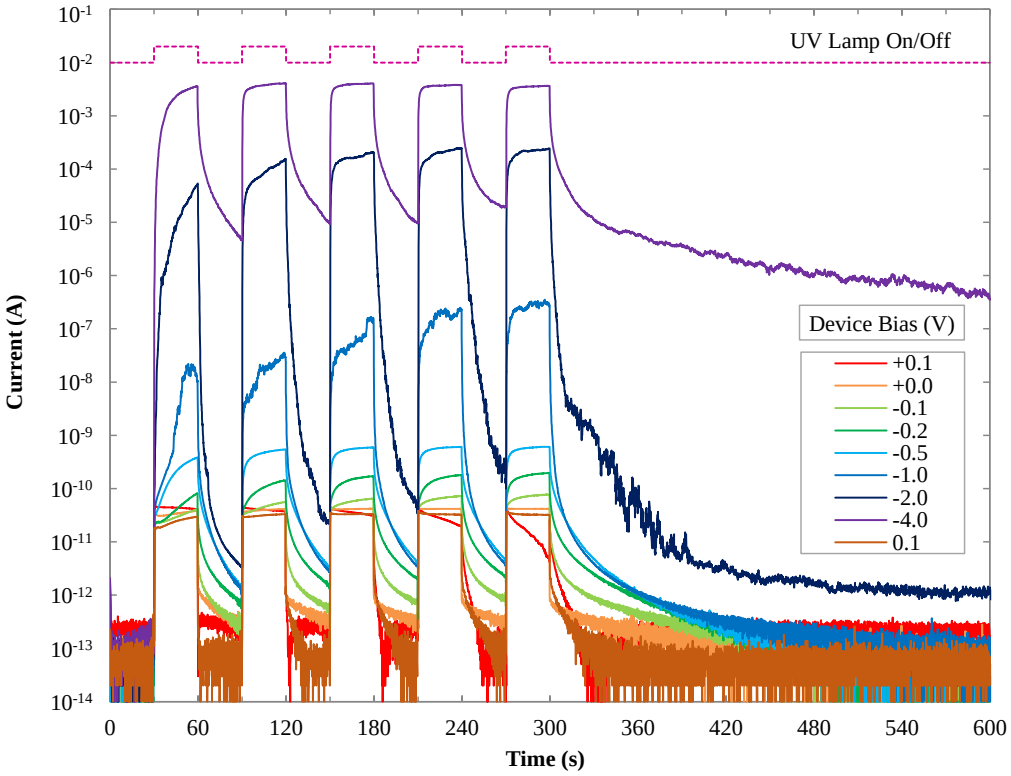

Figure A7.1: 4.0:10 (O_2:Ar) AgO_x 30 s UV Pulsed Photoresponse, Varied Bias

[A7.2] 3.0:10 (O_2:Ar) RuO_x UV Photoresponse: Repeated 30 s UV Exposure with Bias

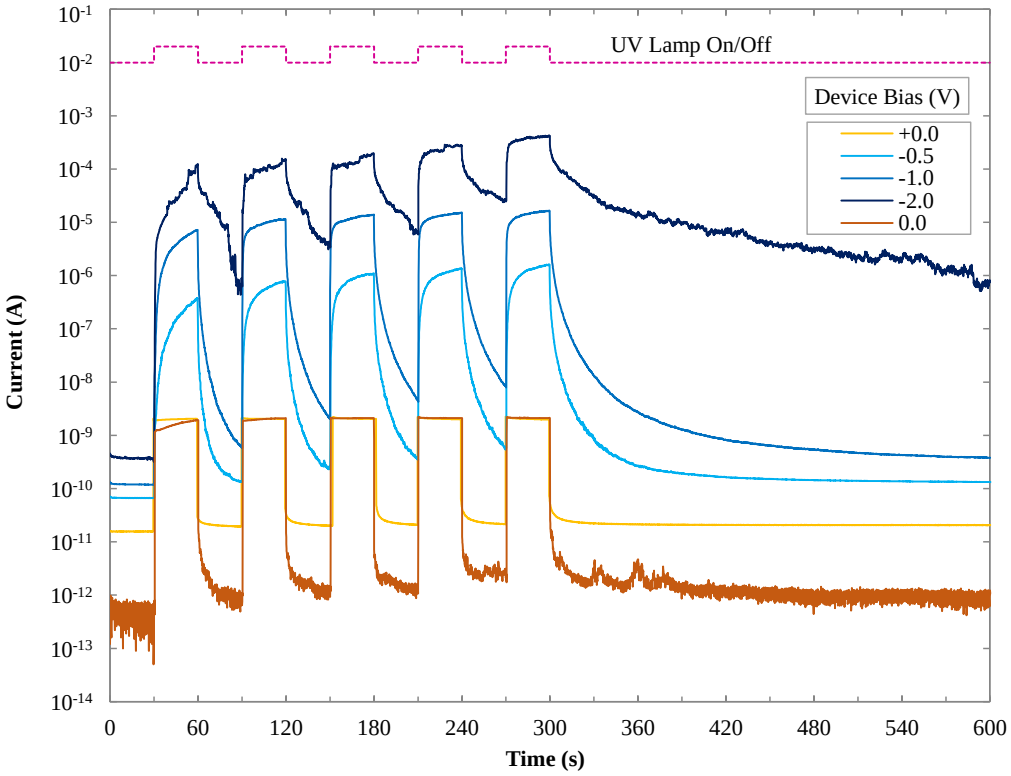

Figure A7.2: 3.0:10 (O_2:Ar) RuO_x 30 s UV Pulsed Photoresponse, Varied Bias

[A7.3] 4.0:10 (O_2:Ar) IrO_x to +c-plane (low-lithium) ZnO, UV Photoresponse: Repeated 30 s UV Exposure with Bias

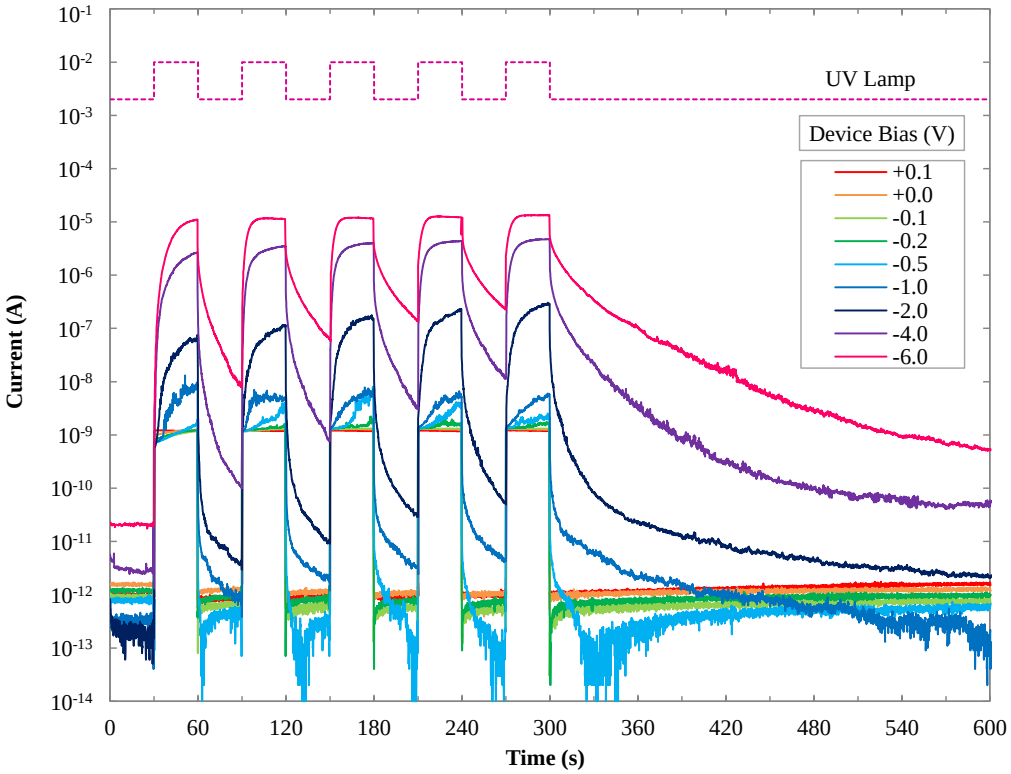

Figure A7.3: 4.0:10 (O_2:Ar) IrO_x (+c-plane low-Li) 30 s UV Photoresponse with Varied Bias

[A7.4] PdO_x Visual and UV Photoresponse Measurements: Repeated 30 s UV Exposure

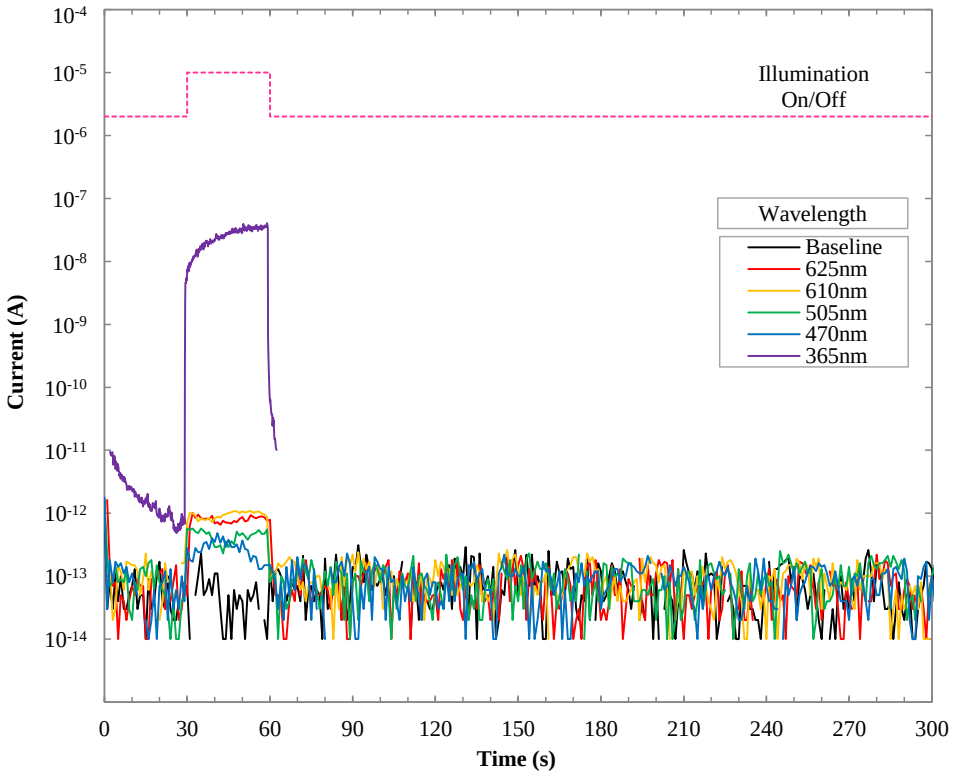

Figure A7.4: 1.0:10 (O_2:Ar) PdO_x 30 s Visual Spectrum and UV Photoresponse, -1 V Bias

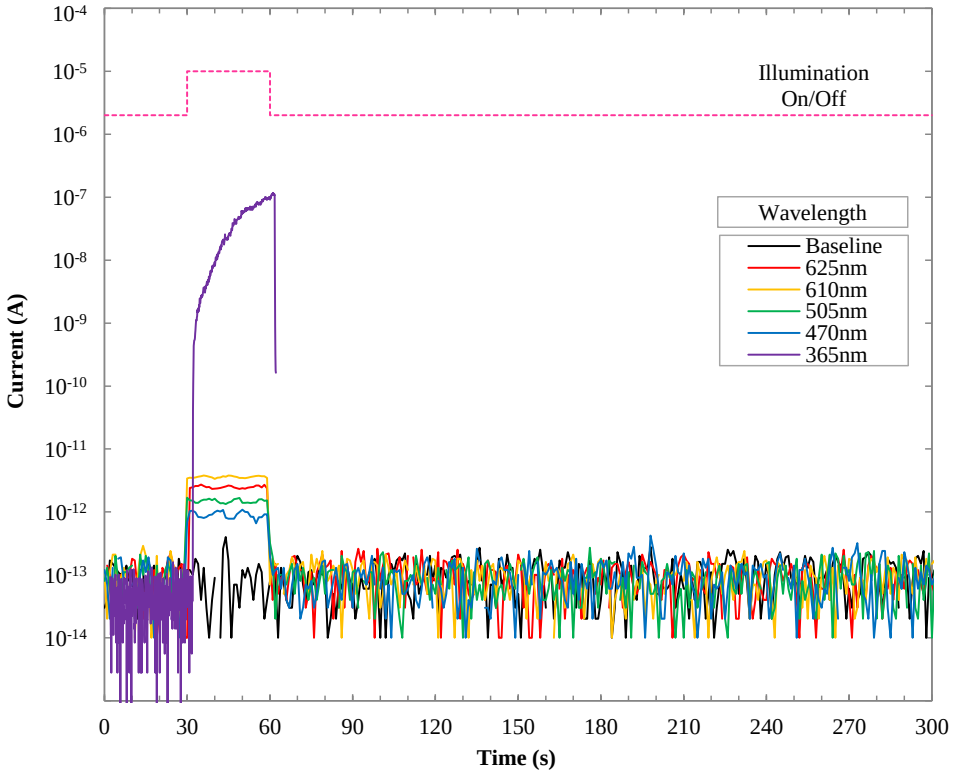

Figure A7.5: 3.0:10 (O_2:Ar) PdO_x 30 s Visual Spectrum and UV Photoresponse, -1 V Bias

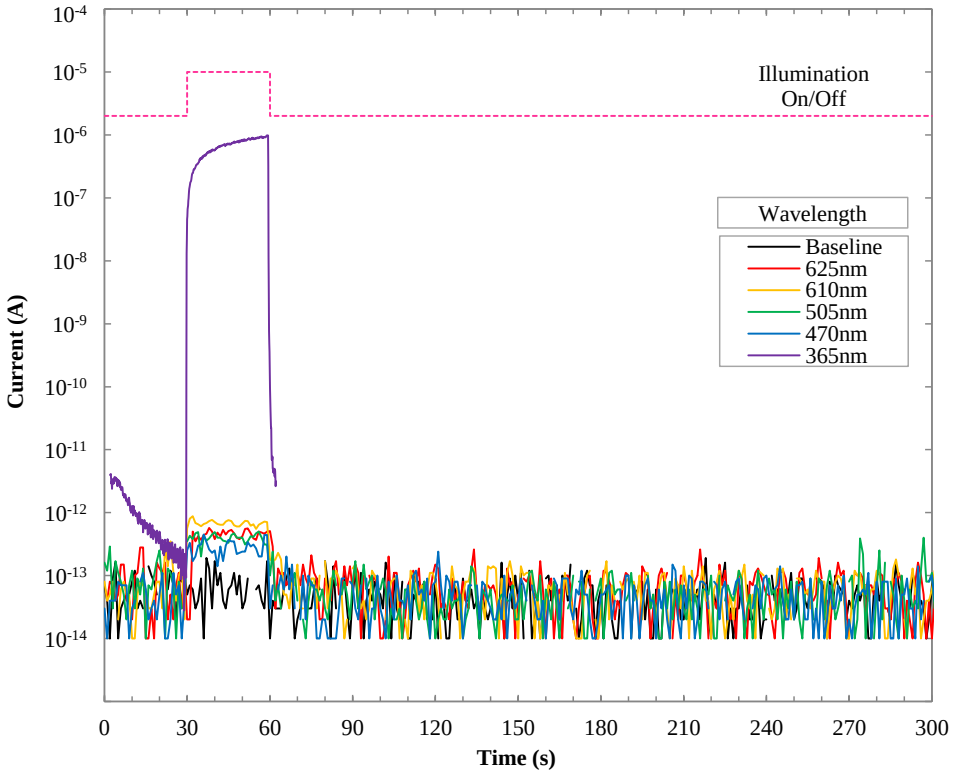

Figure A7.6: 4.0:10 (O_2:Ar) PdO_x 30 s Visual Spectrum and UV Photoresponse, -1 V Bias

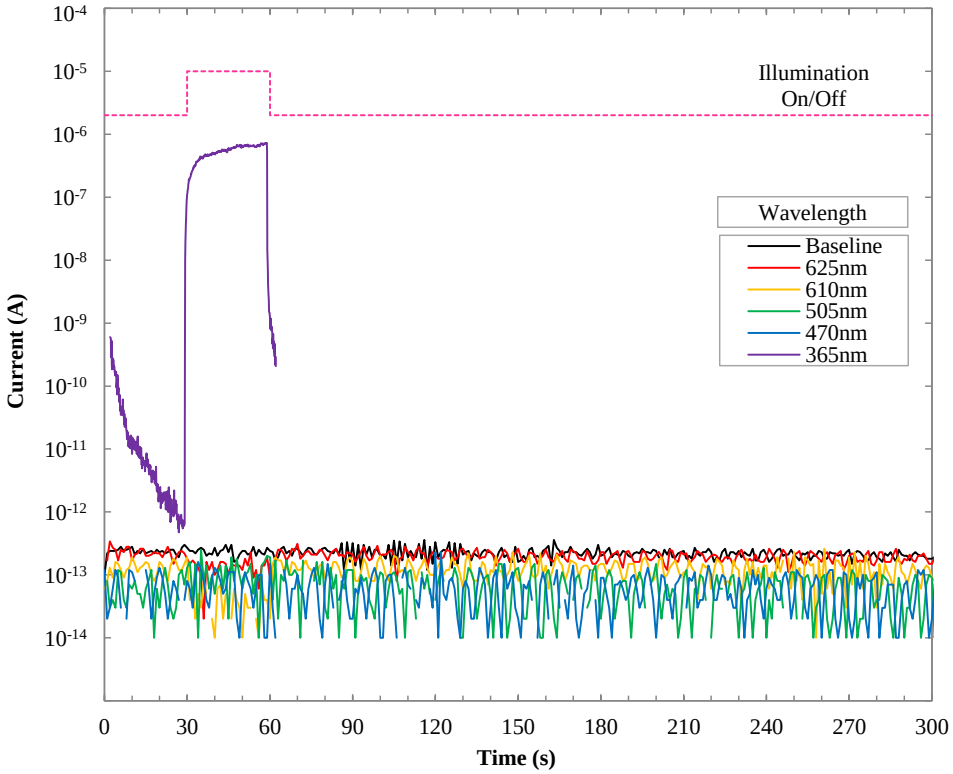

Figure A7.7: 5.0:10 (O_2:Ar) PdO_x 30 s Visual Spectrum and UV Photoresponse, -1 V Bias

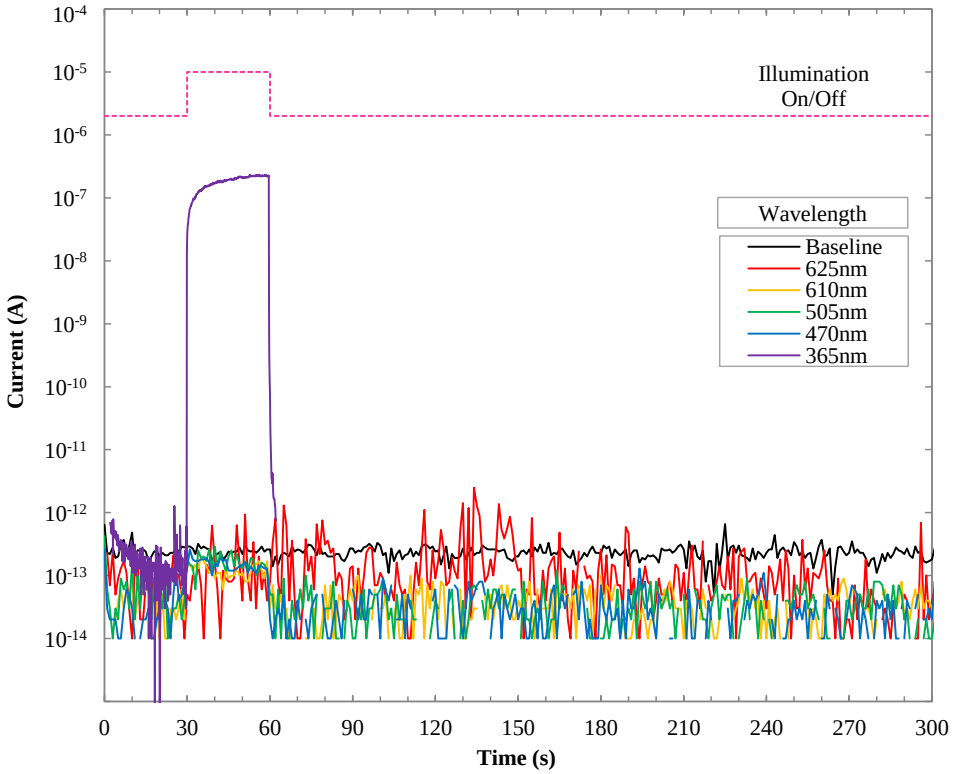

Figure A7.8: 7.0:10 (O_2:Ar) PdO_x 30 s Visual Spectrum and UV Photoresponse, -1 V Bias

[A7.5] PdO_x UV Photoresponse Measurements: Repeated 30 s UV Exposure with Bias

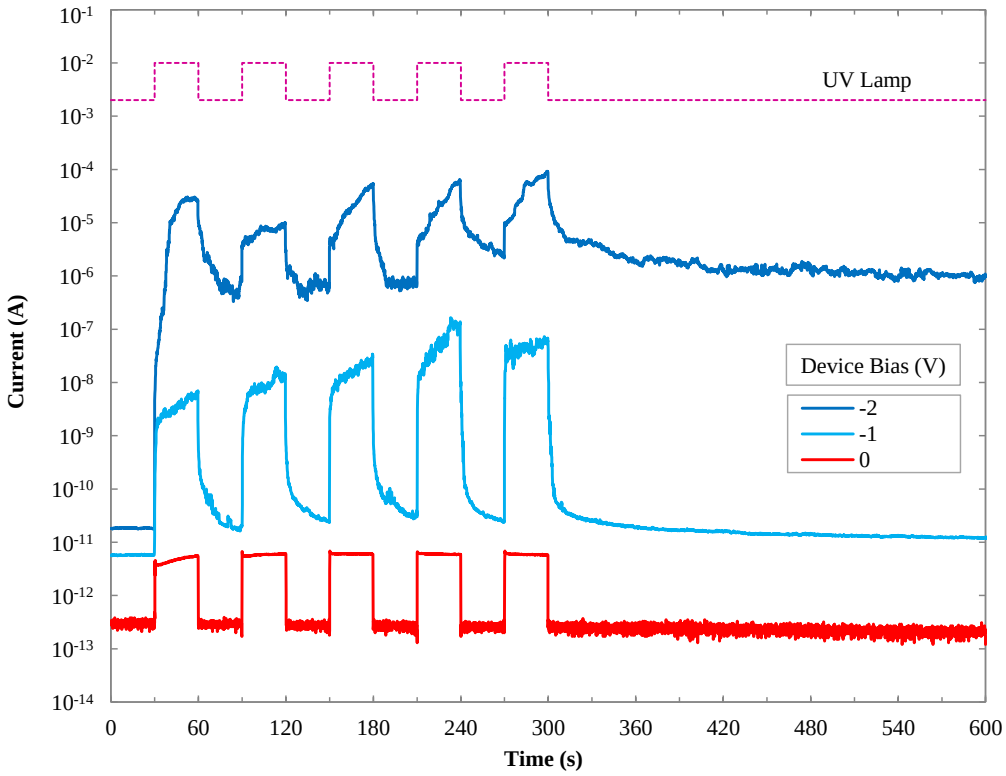

Figure A7.9: 0.5:10 (O_2:Ar) PdO_x 30 s UV Photoresponse with Bias

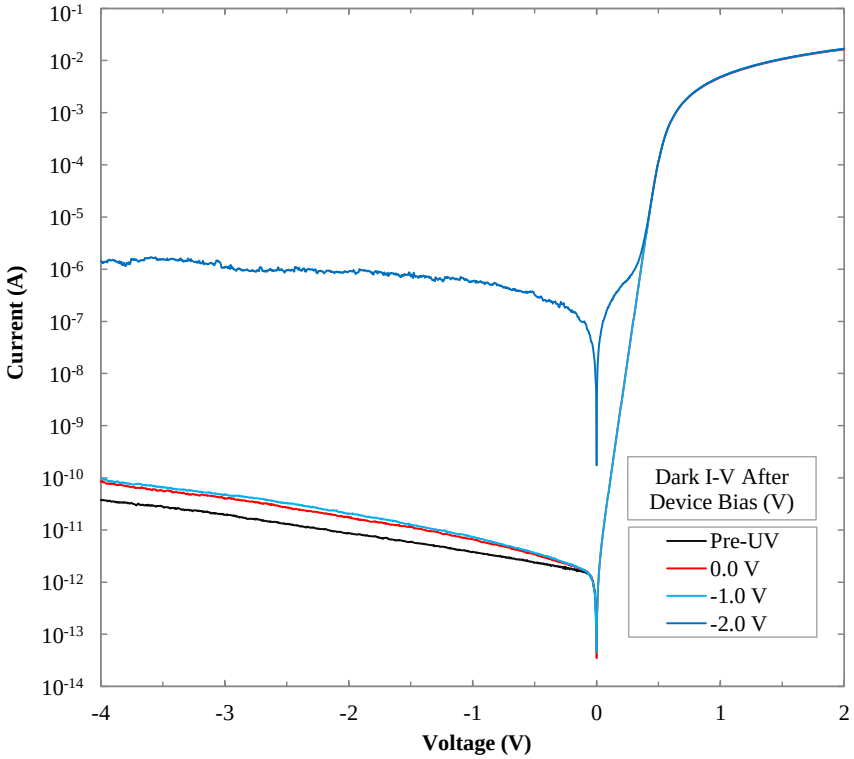

Figure A7.10: 0.5:10 PdO_x Dark I-V After Each UV Photoresponse Bias Test

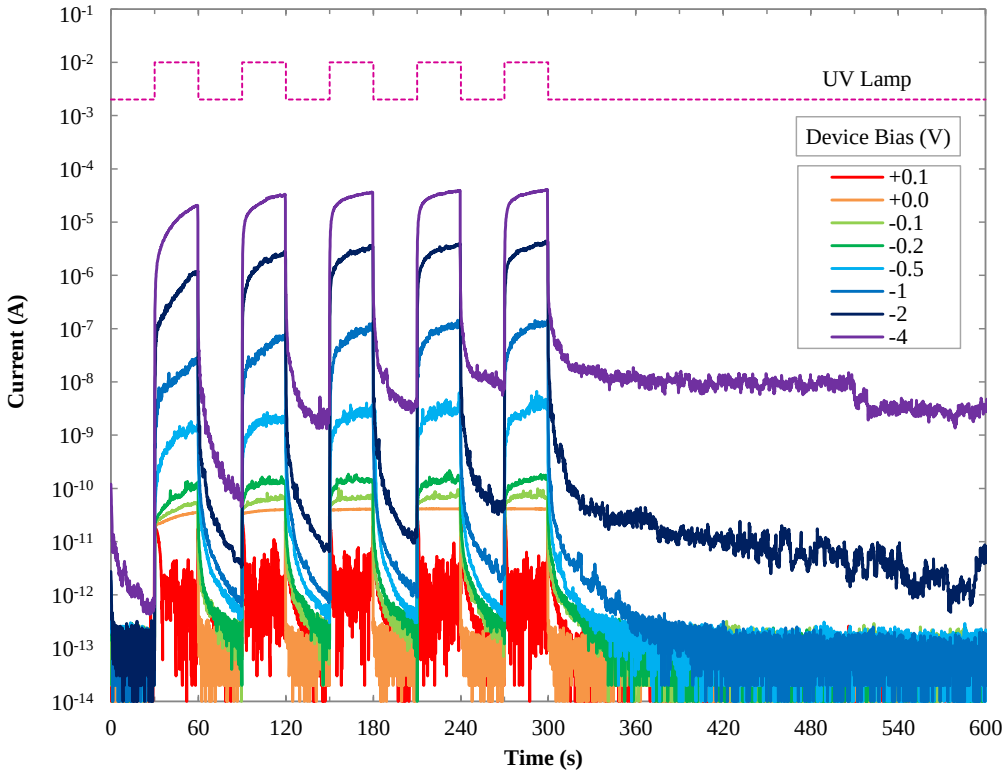

Figure A7.11: 1.0:10 (O_2:Ar) PdO_x 30 s UV Photoresponse with Varied Bias

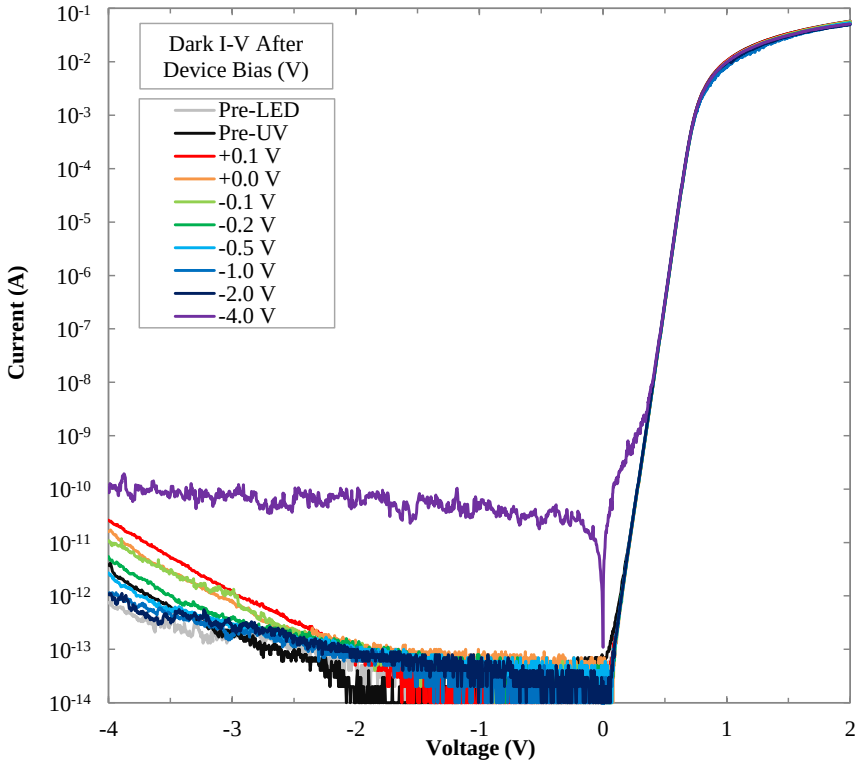

Figure A7.12: 1.0:10 PdO_x Dark I-V After Each UV Photoresponse Bias Test

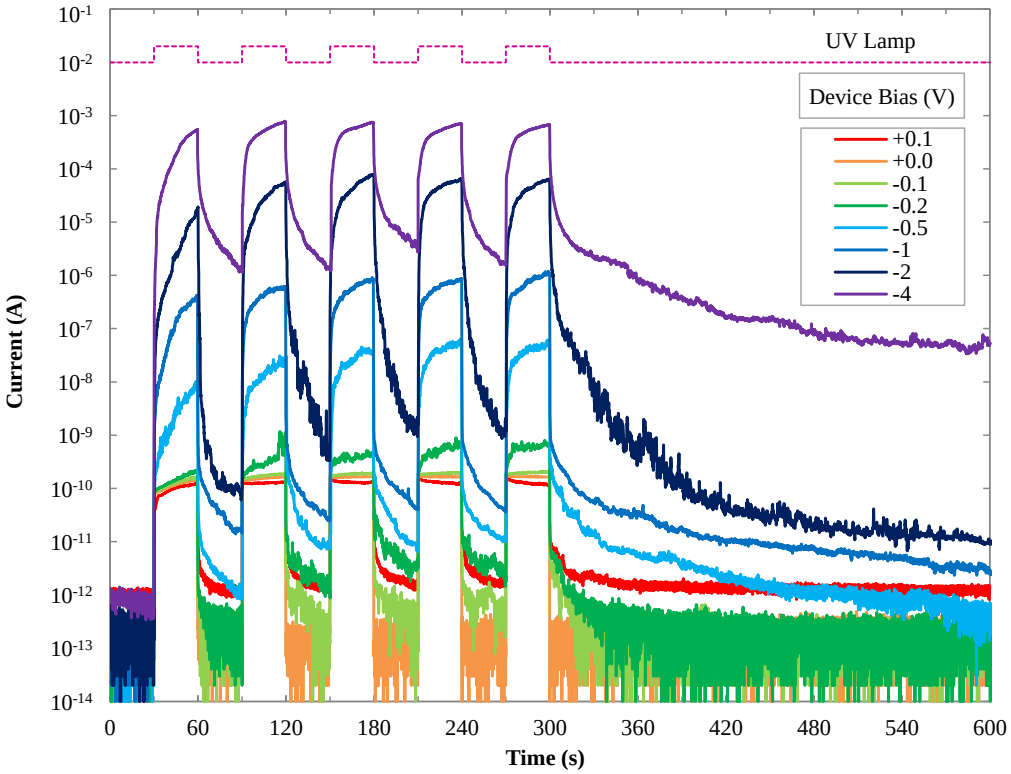

Figure A7.13: 3.0:10 (O_2:Ar) PdO_x 30 s UV Photoresponse with Varied Bias

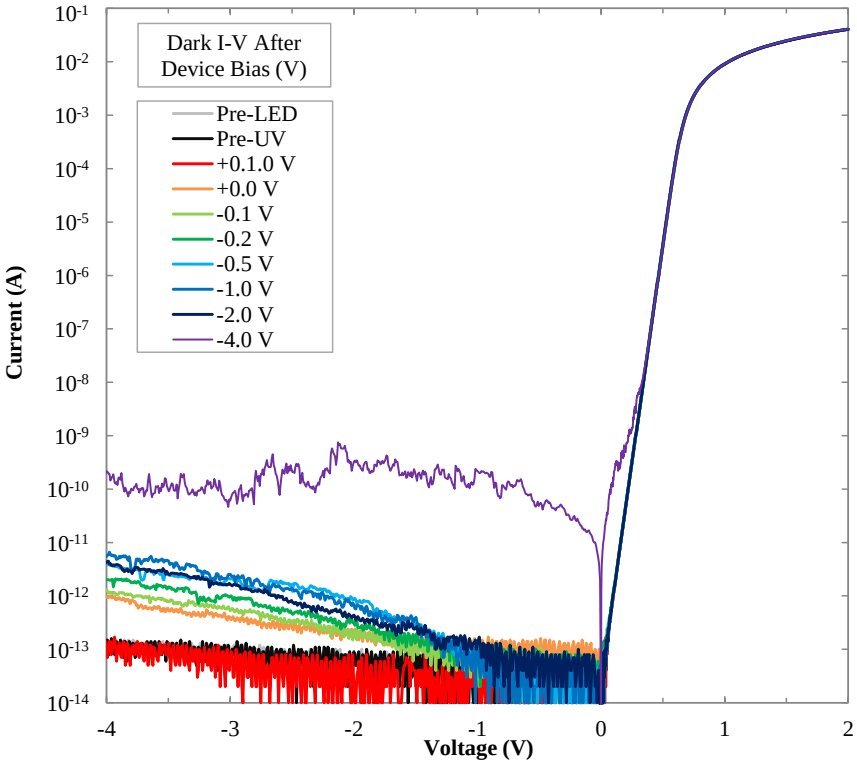

Figure A7.14: 3.0:10 PdO_x Dark I-V After Each UV Photoresponse Bias Test

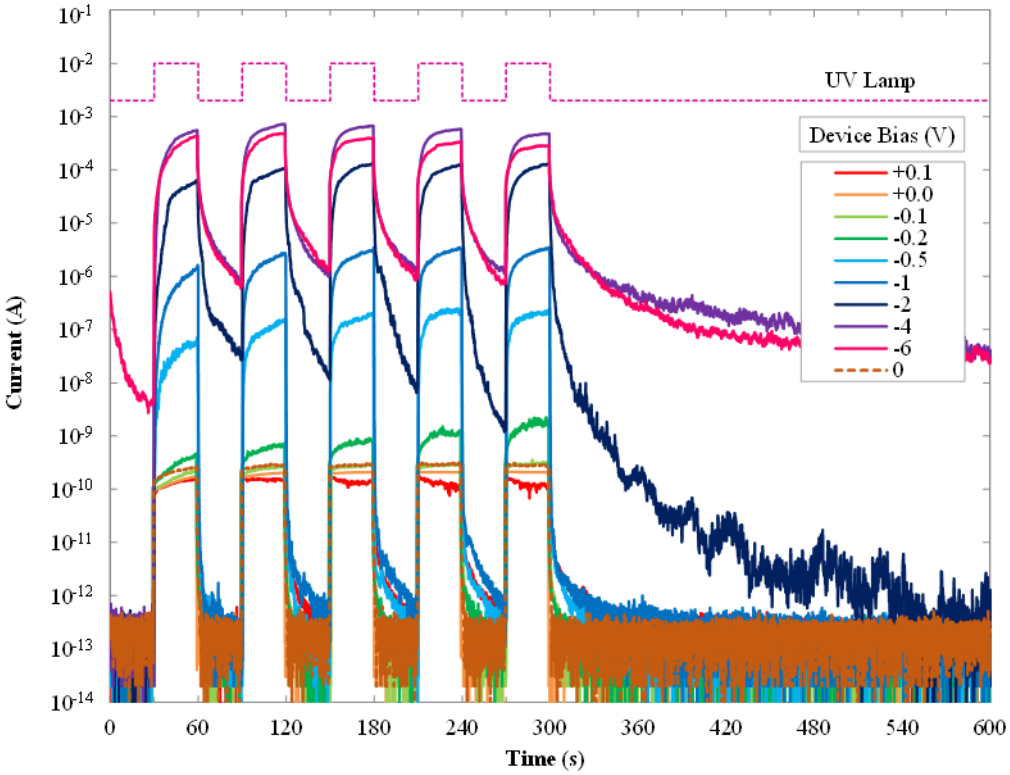

Figure A7.15: 4.0:10 (O_2:Ar) PdO_x 30 s UV Photoresponse with Bias

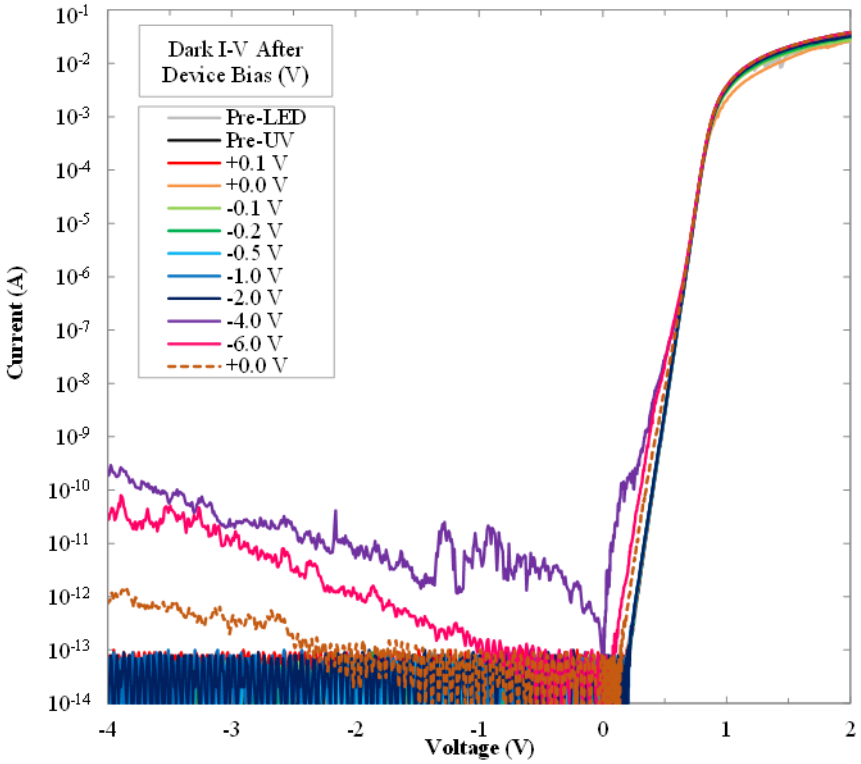

Figure A7.16: 4.0:10 PdO_x Dark I-V After Each UV Photoresponse Bias Test

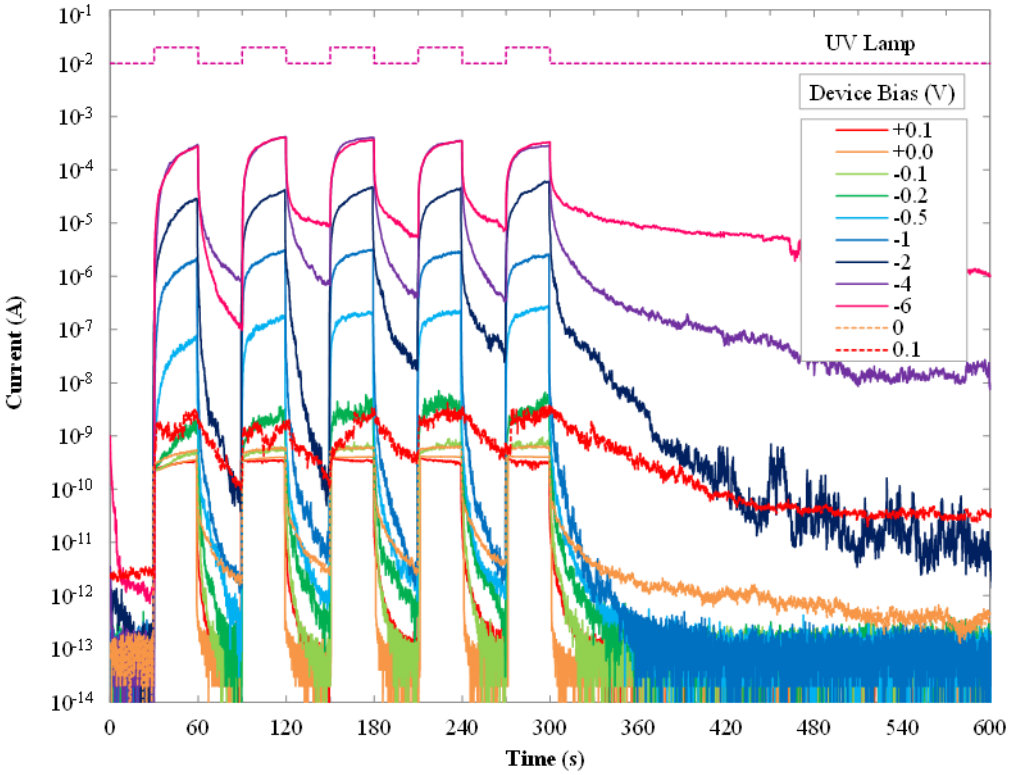

Figure A7.17: 5.0:10 (O_2:Ar) PdO_x 30 s UV Photoresponse with Varied Bias

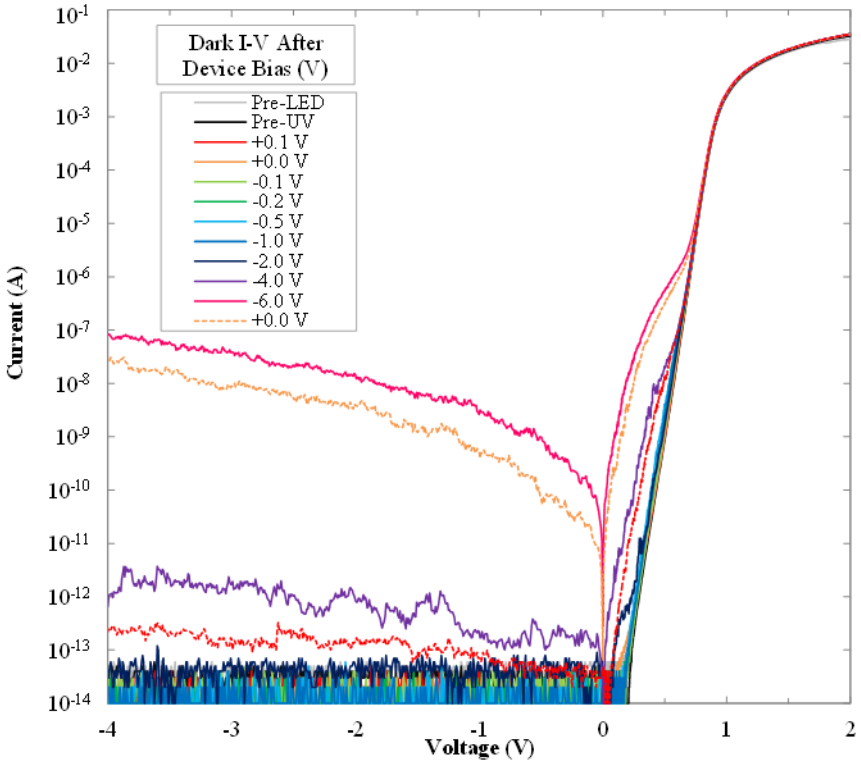

Figure A7.18: 5.0:10 PdO_x Dark I-V After Each UV Photoresponse Bias Test

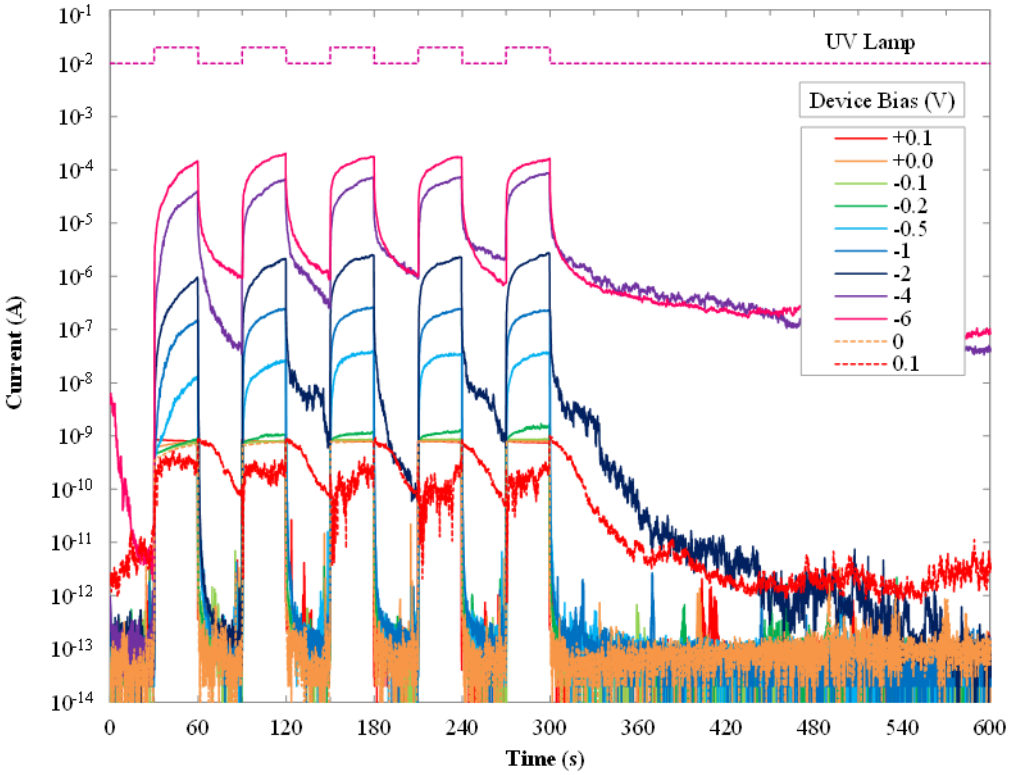

Figure A7.19: 7.0:10 (O_2:Ar) PdO_x 30 s UV Photoresponse with Varied Bias

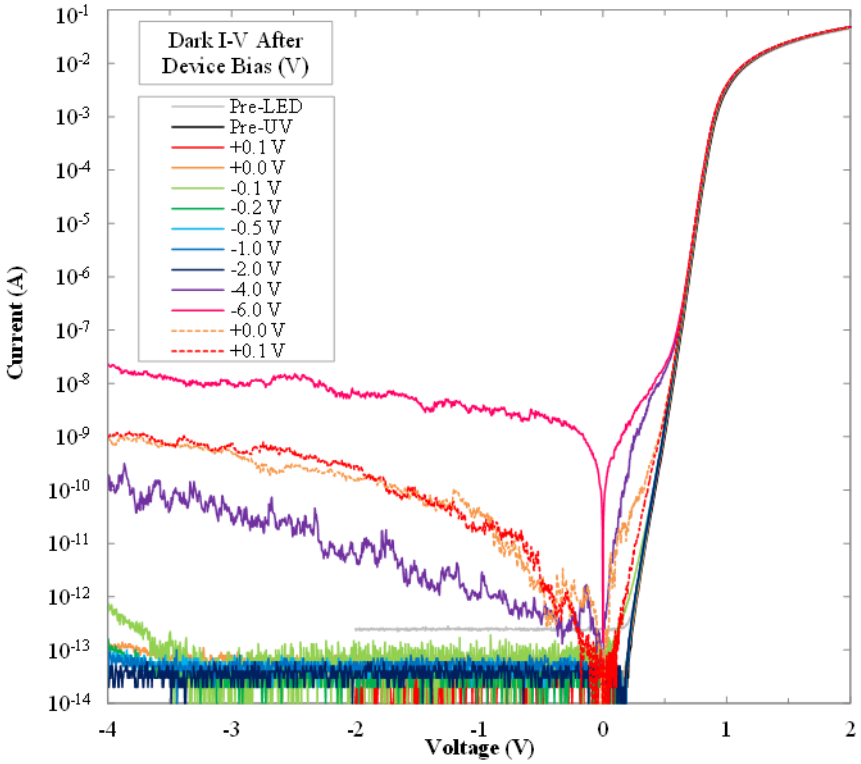

Figure A7.20: 7.0:10 PdO_x Dark I-V After Each UV Photoresponse Bias Test

[A7.6] PtO_x Visual and UV Photoresponse Measurements: Repeated 30 s UV Exposure

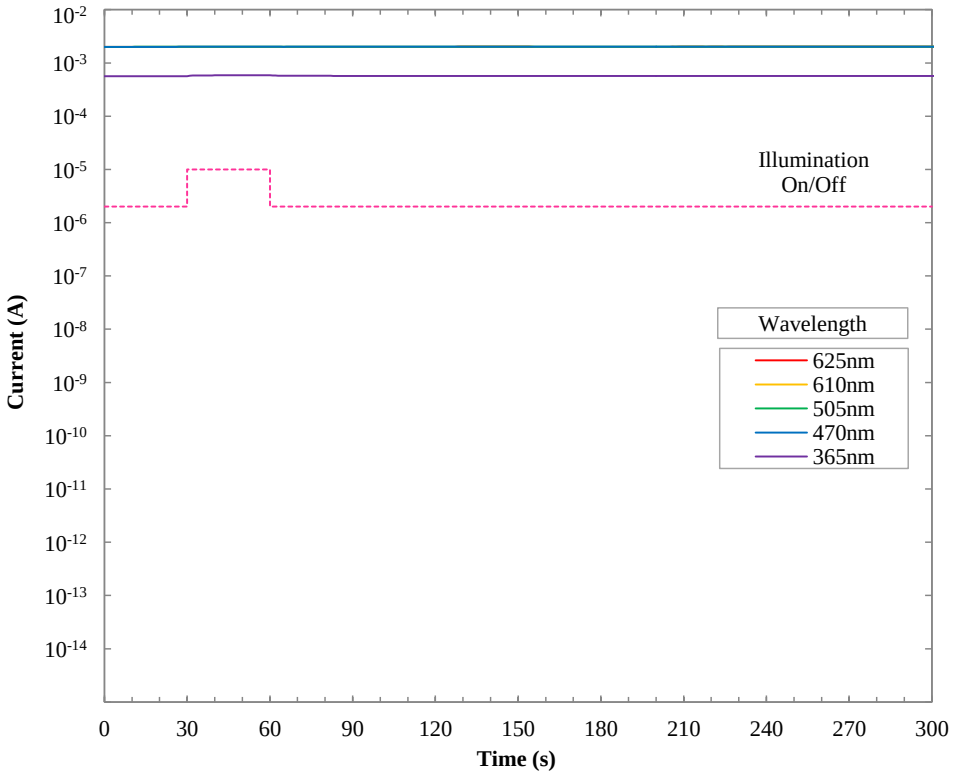

Figure A7.21: 0.0:10 (O_2:Ar) PtO_x 30 s Visual Spectrum and UV Photoresponse, -1 V Bias

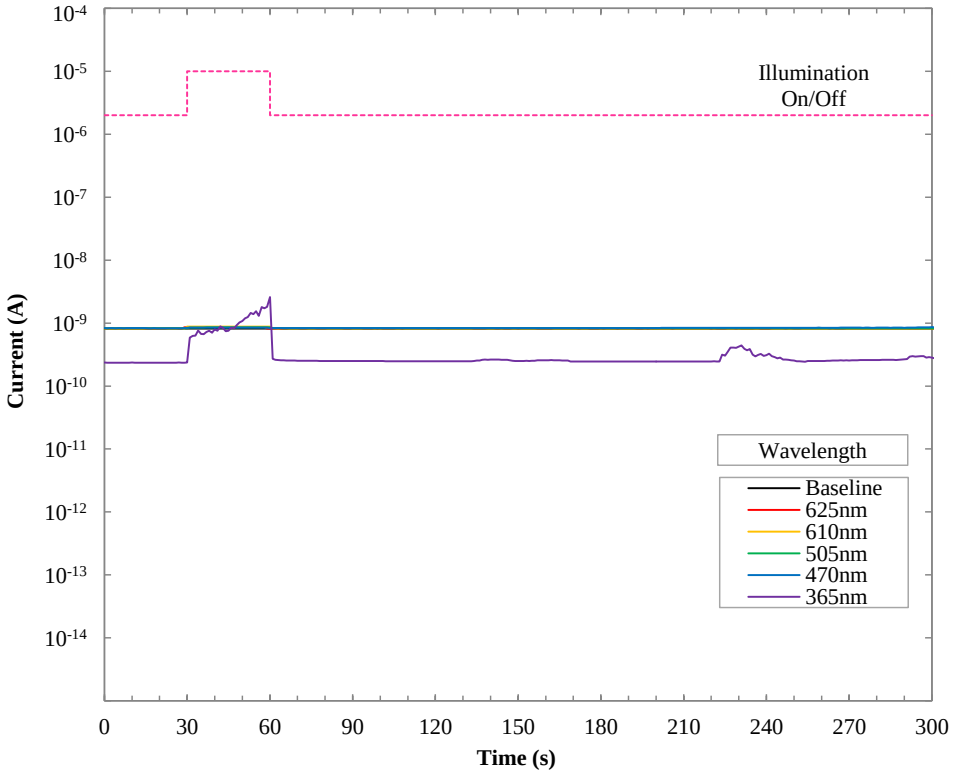

Figure A7.22: 0.5:10 (O_2:Ar) PtO_x 30 s Visual Spectrum and UV Photoresponse, -1 V Bias

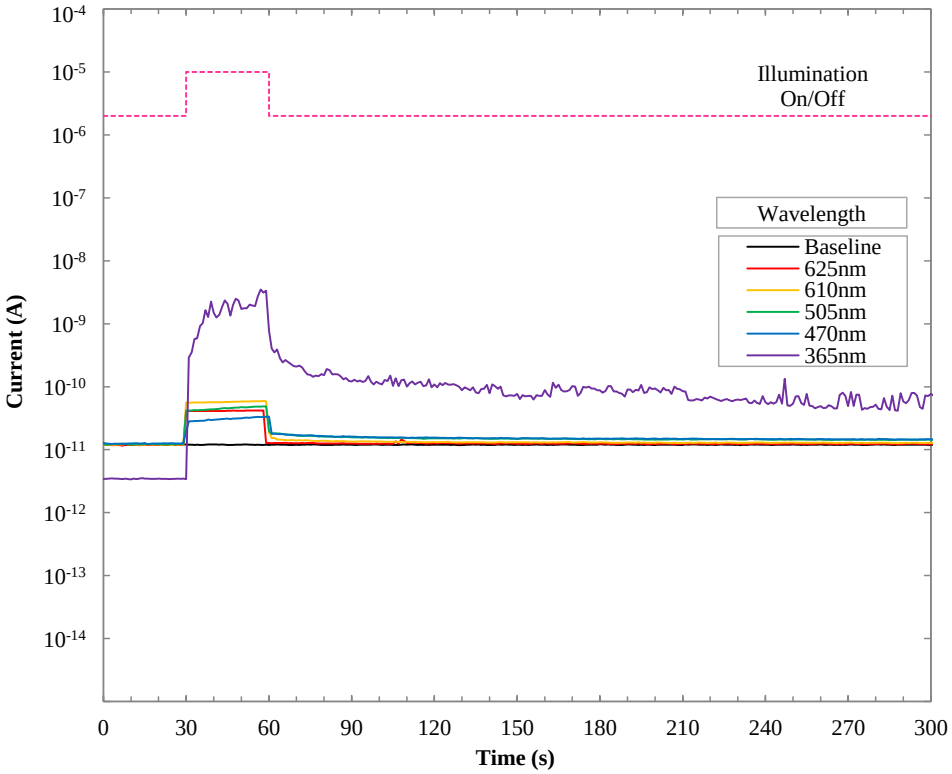

Figure A7.23: 1.0:10 (O_2:Ar) PtO_x 30 s Visual Spectrum and UV Photoresponse, -1 V Bias

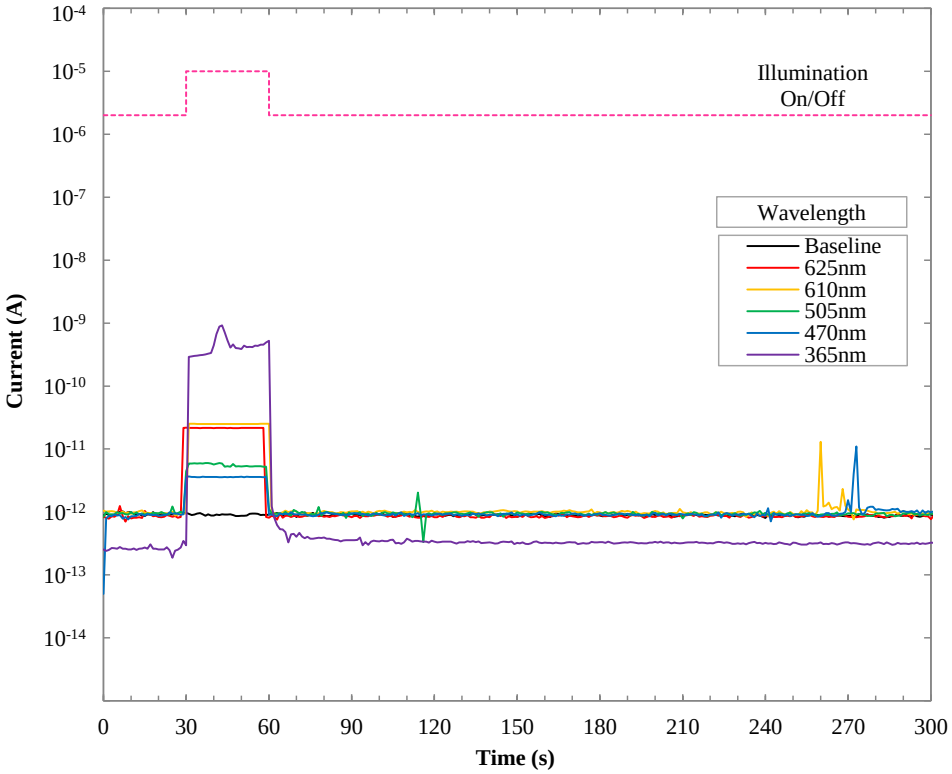

Figure A7.24: 2.0:10 (O_2:Ar) PtO_x 30 s Visual Spectrum and UV Photoresponse, -1 V Bias

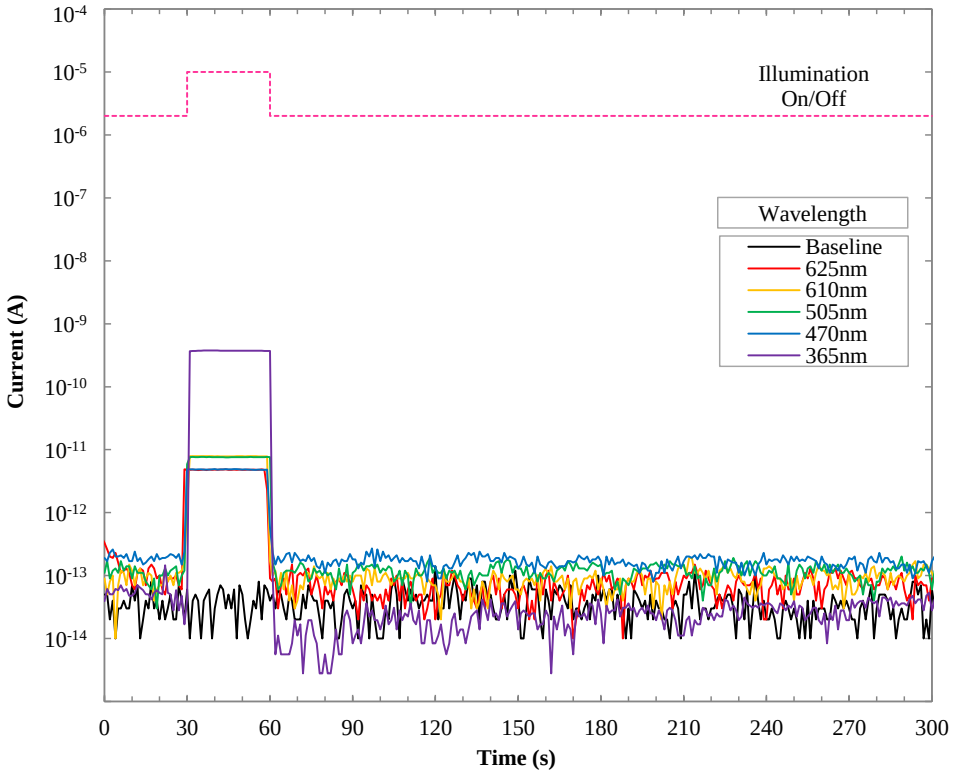

Figure A7.25: 3.0:10 (O_2:Ar) PtO_x 30 s Visual Spectrum and UV Photoresponse, -1 V Bias

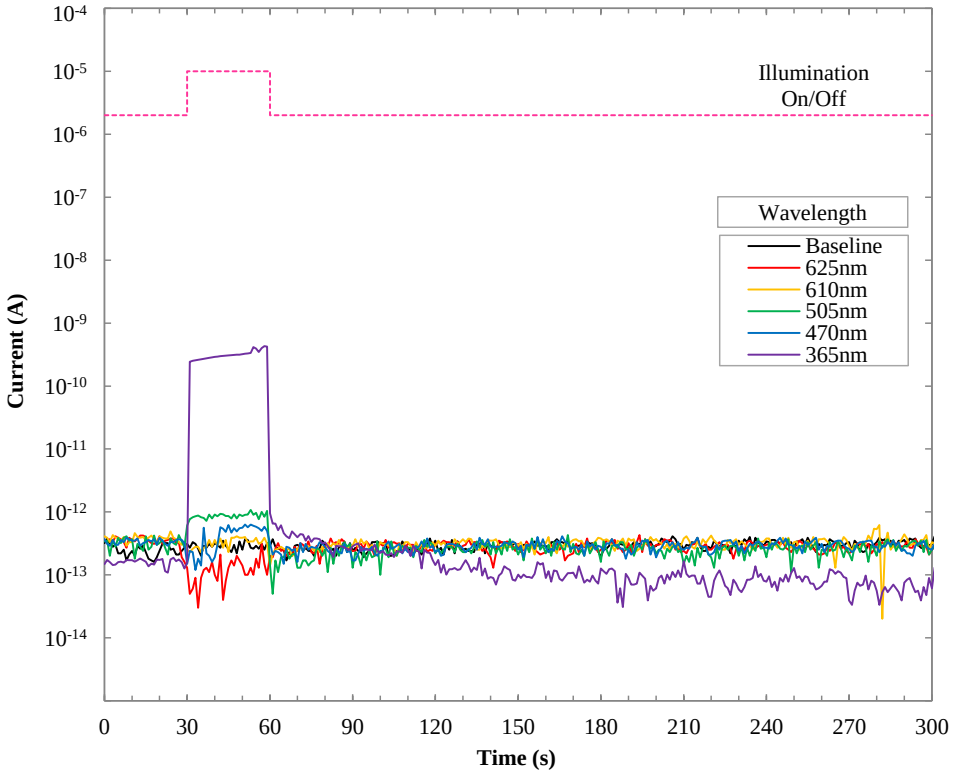

Figure A7.26: 4.0:10 (O_2:Ar) PtO_x 30 s Visual Spectrum and UV Photoresponse, -1 V Bias

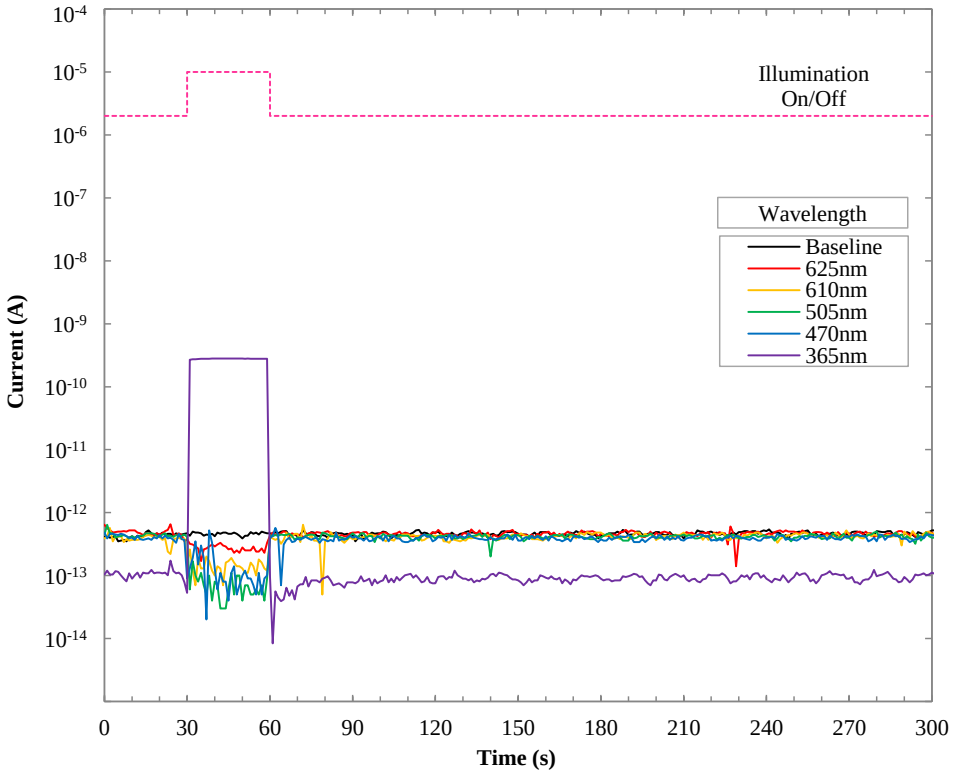

Figure A7.27: 5.0:10 (O_2:Ar) PtO_x 30 s Visual Spectrum and UV Photoresponse, -1 V Bias

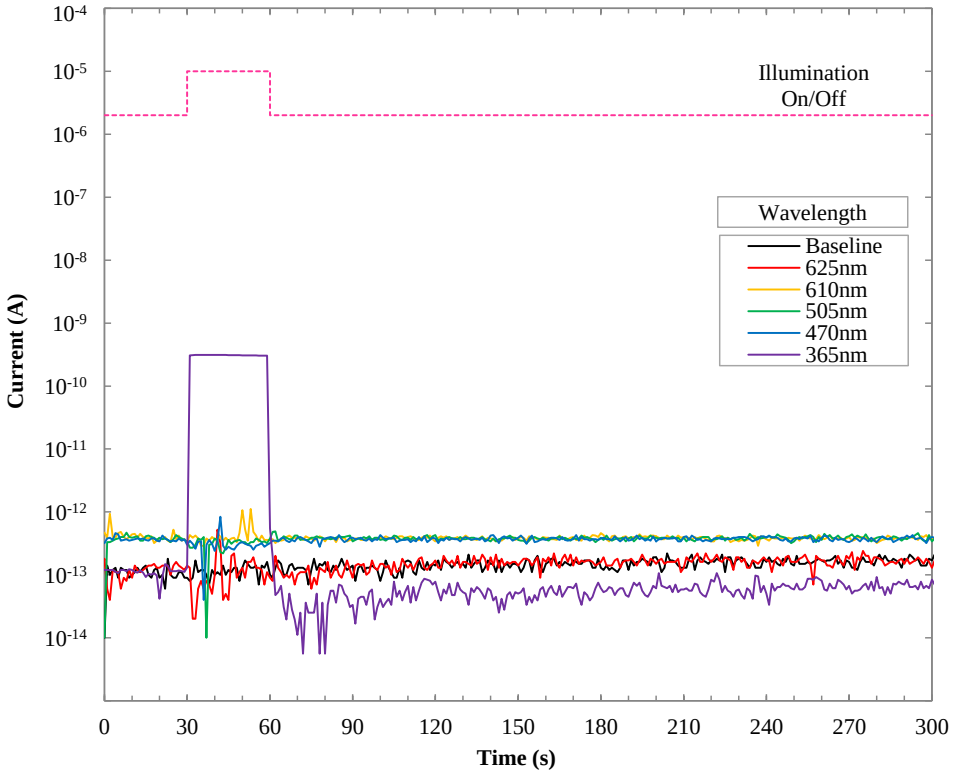

Figure A7.28: 7.0:10 (O_2:Ar) PtO_x 30 s Visual Spectrum and UV Photoresponse, -1 V Bias

[A7.7] PtO_x UV Photoresponse Measurements: Repeated 30 s UV Exposure with Bias

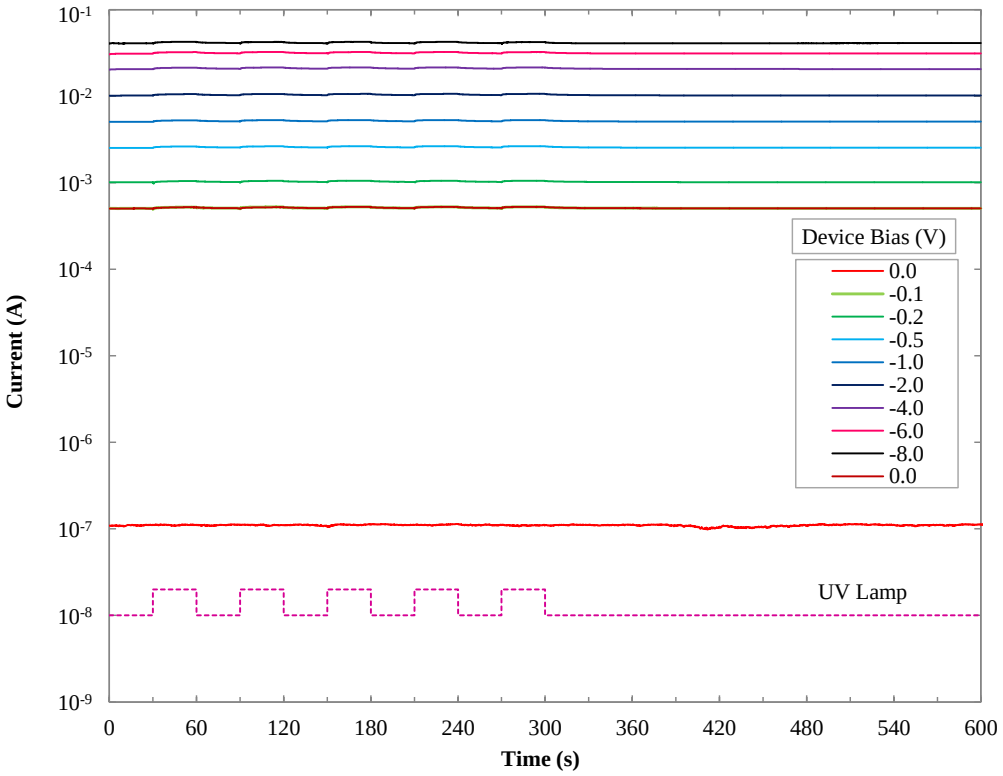

Figure A7.29: 0.0:10 (O_2:Ar) PtO_x 30 s UV Photoresponse with Bias

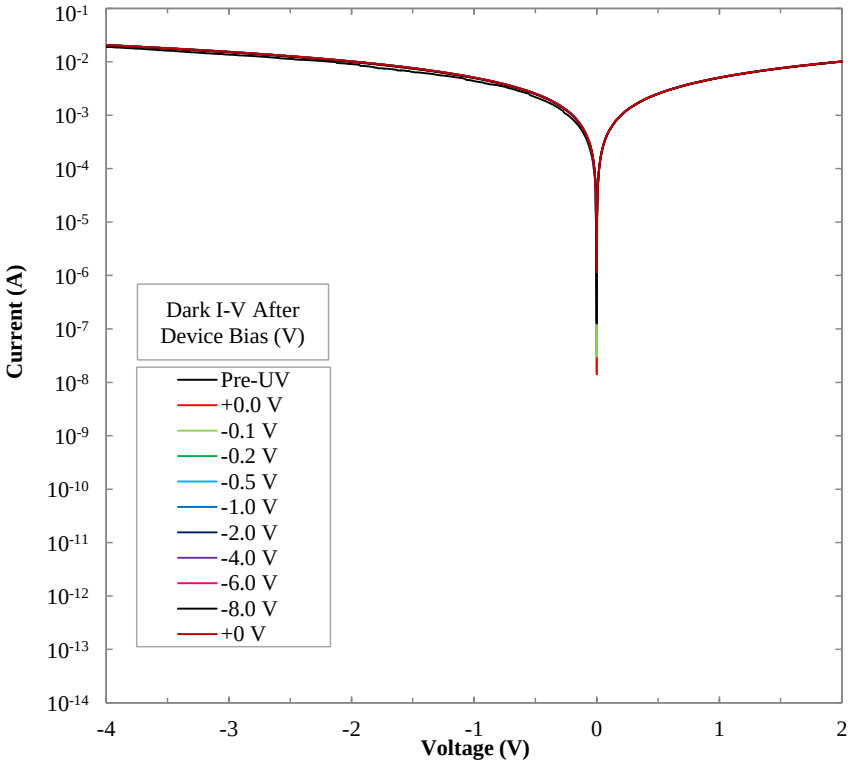

Figure A7.30: 0.0:10 PtO_x Dark I-V After Each UV Photoresponse Bias Test

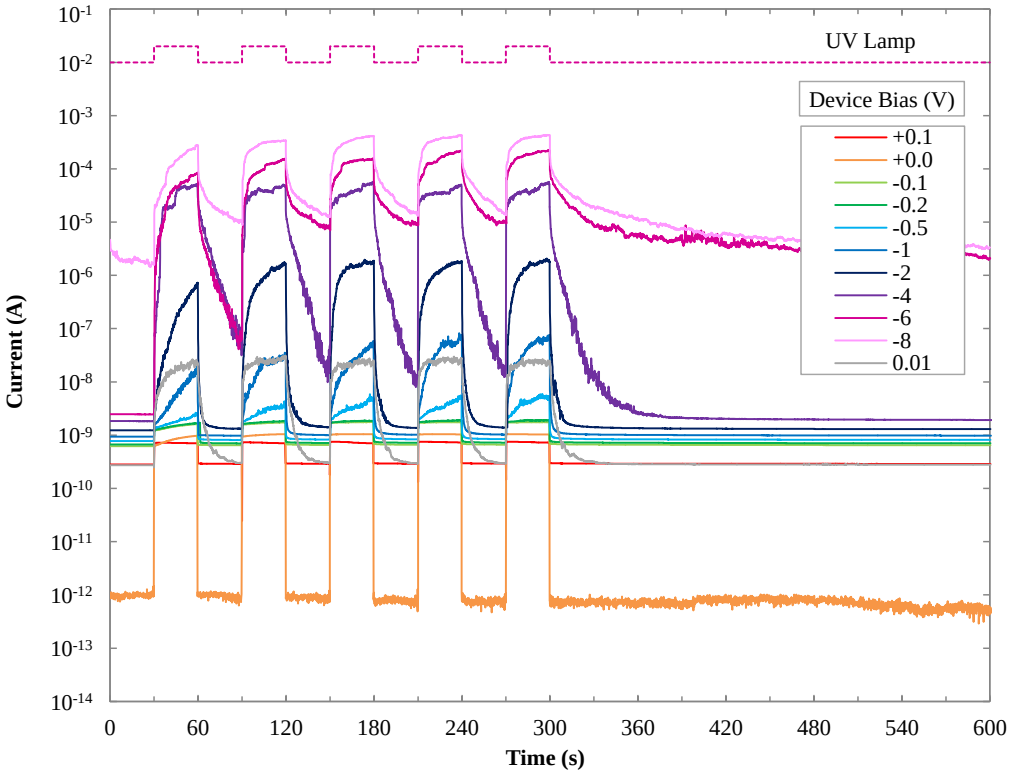

Figure A7.31: 0.5:10 (O_2:Ar) PtO_x 30 s UV Photoresponse with Bias

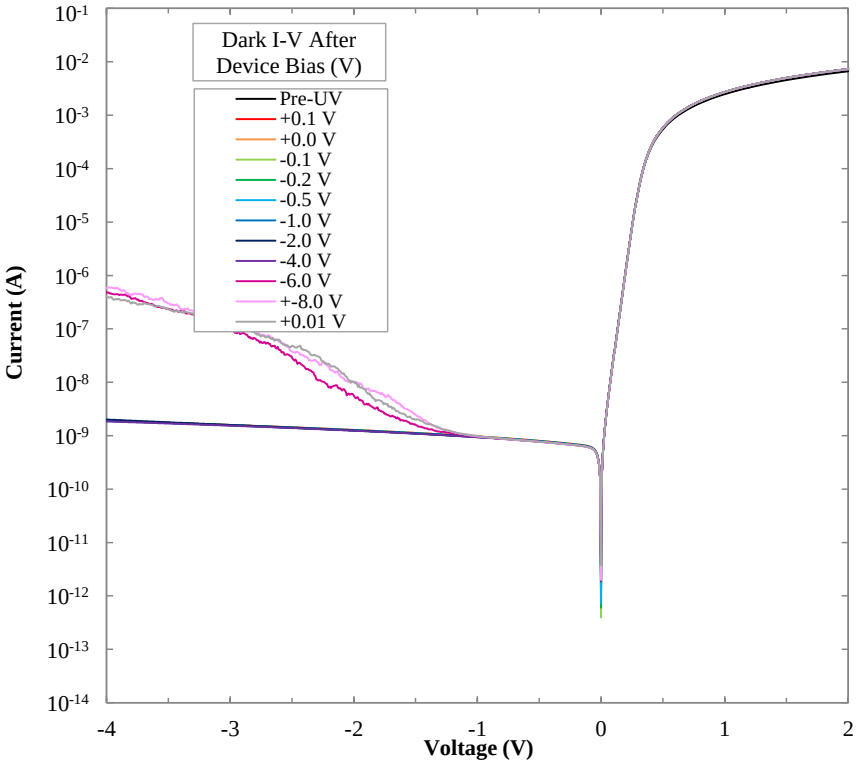

Figure A7.32: 0.5:10 PtO_x Dark I-V After Each UV Photoresponse Bias Test

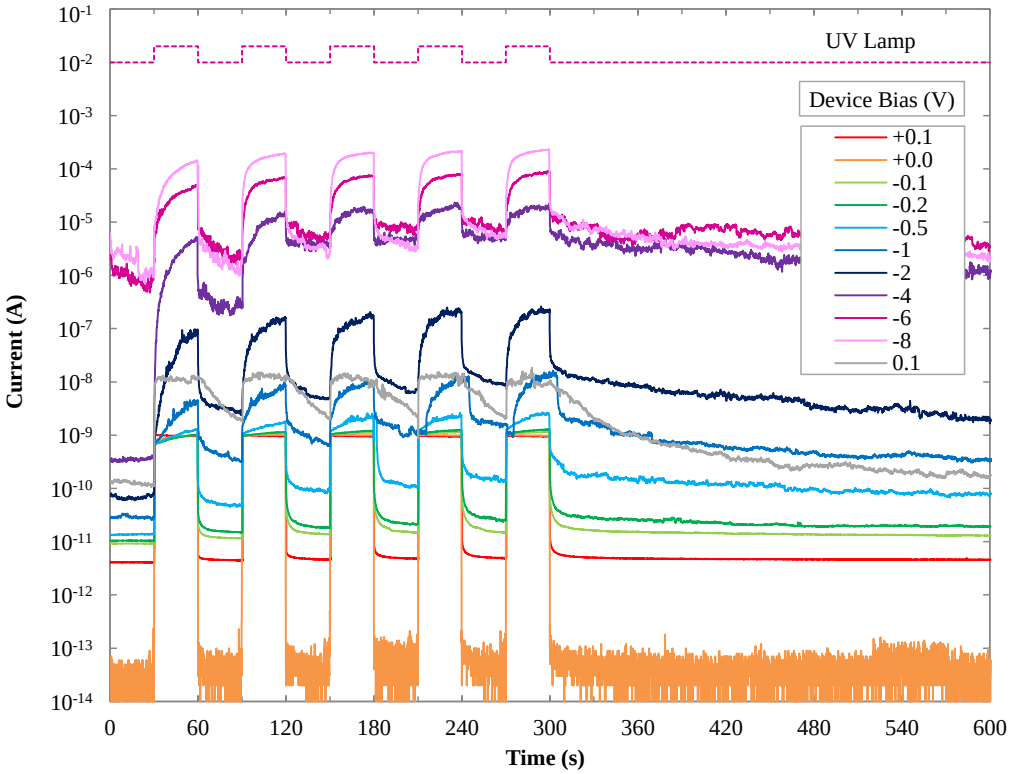

Figure A7.33: 1.0:10 (O_2:Ar) PtO_x 30 s UV Photoresponse with Bias

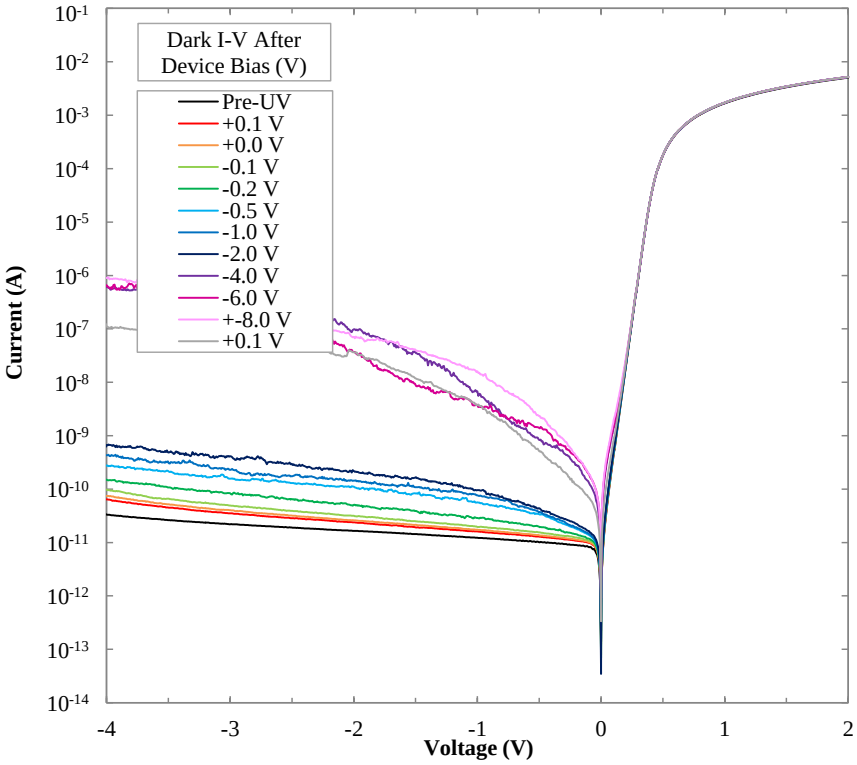

Figure A7.34: 1.0:10 PtO_x Dark I-V After Each UV Photoresponse Bias Test

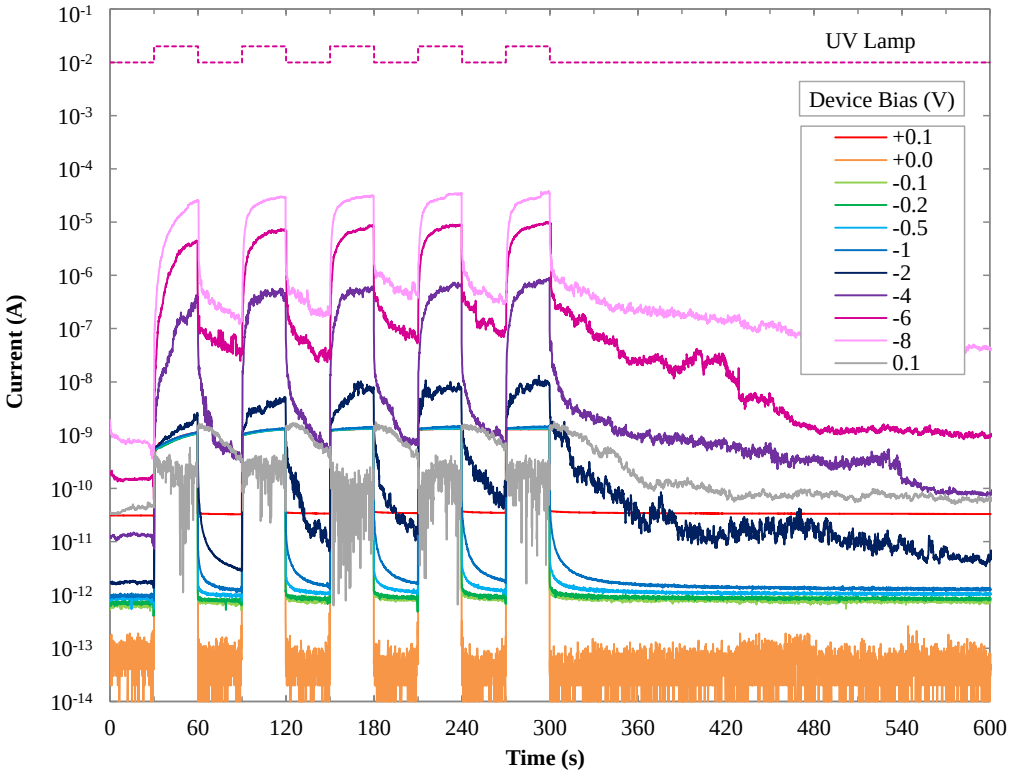

Figure A7.35: 2.0:10 (O_2:Ar) PtO_x 30 s UV Photoresponse with Varied Bias

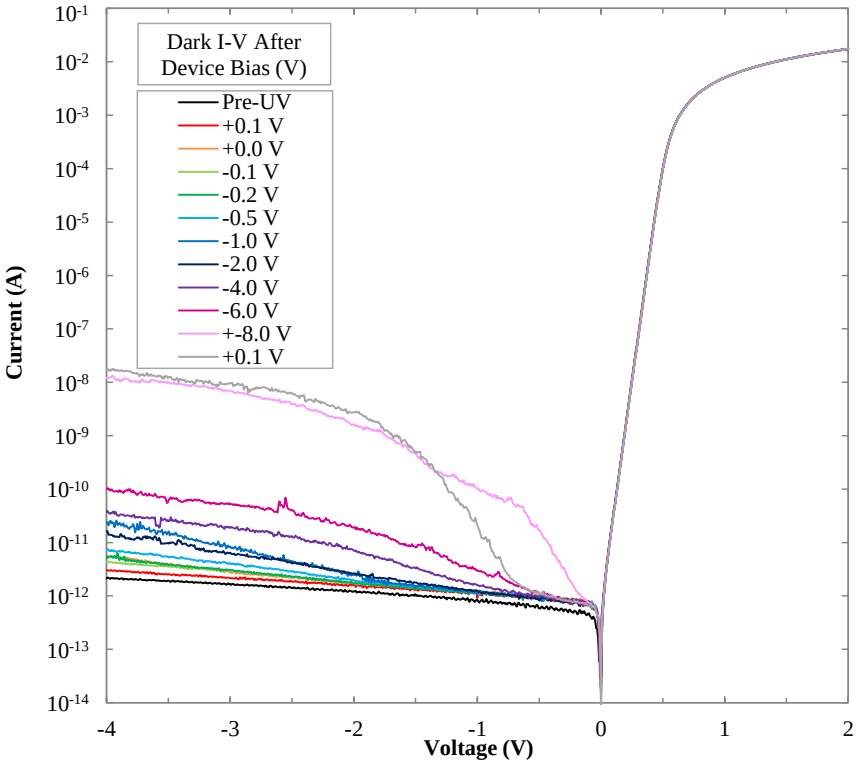

Figure A7.36: 2.0:10 PtO_x Dark I-V After Each UV Photoresponse Bias Test

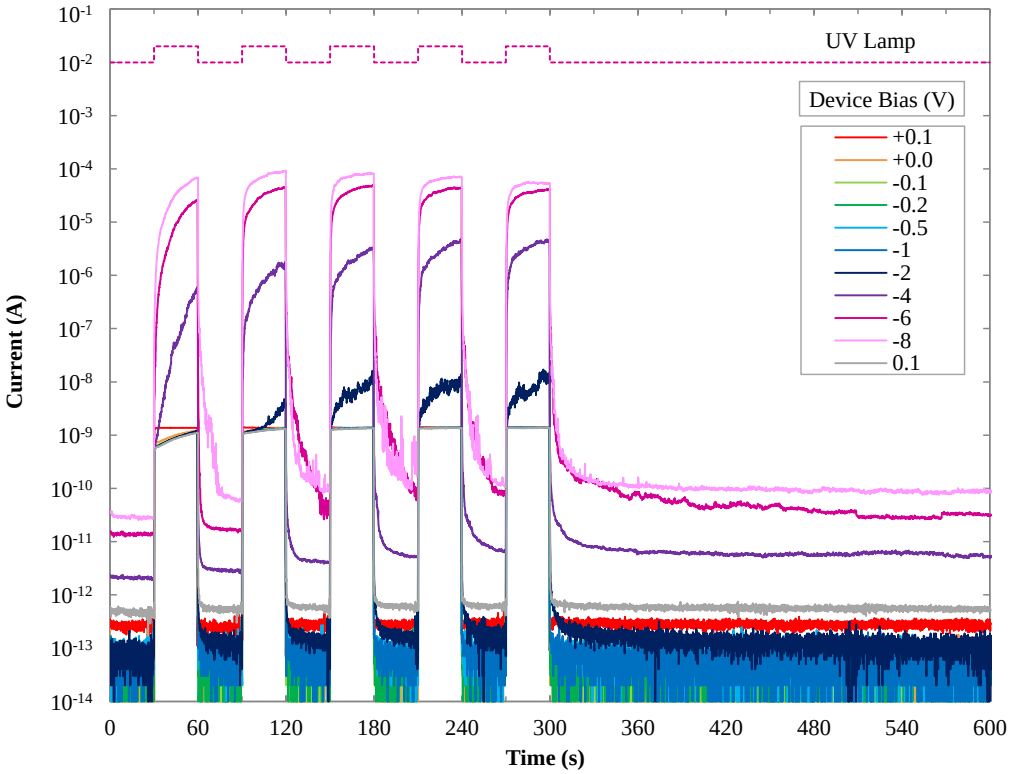

Figure A7.37: 3.0:10 (O_2:Ar) PtO_x 30 s UV Photoresponse with Varied Bias

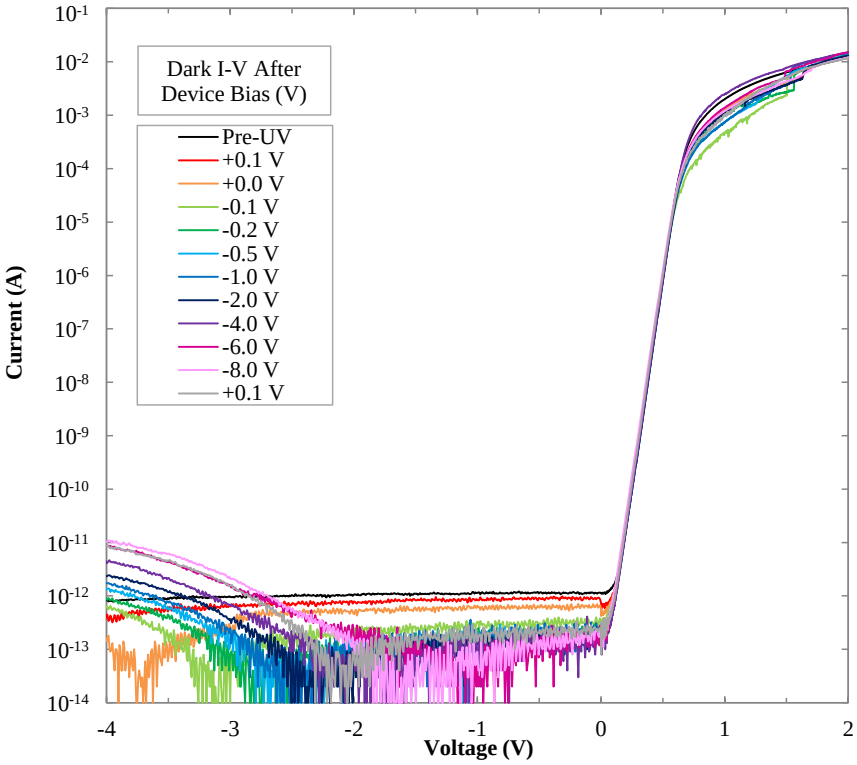

Figure A7.38: 3.0:10 PtO_x Dark I-V After Each UV Photoresponse Bias Test

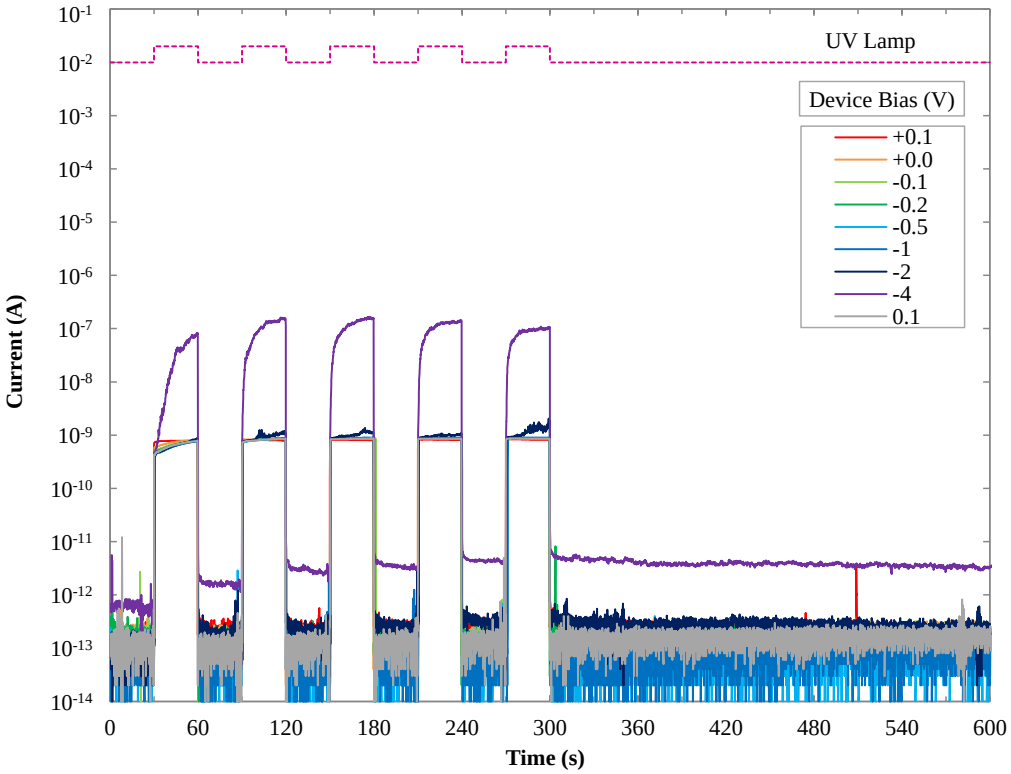

Figure A7.39: 4.0:10 (O_2:Ar) PtO_x 30 s UV Photoresponse with Bias

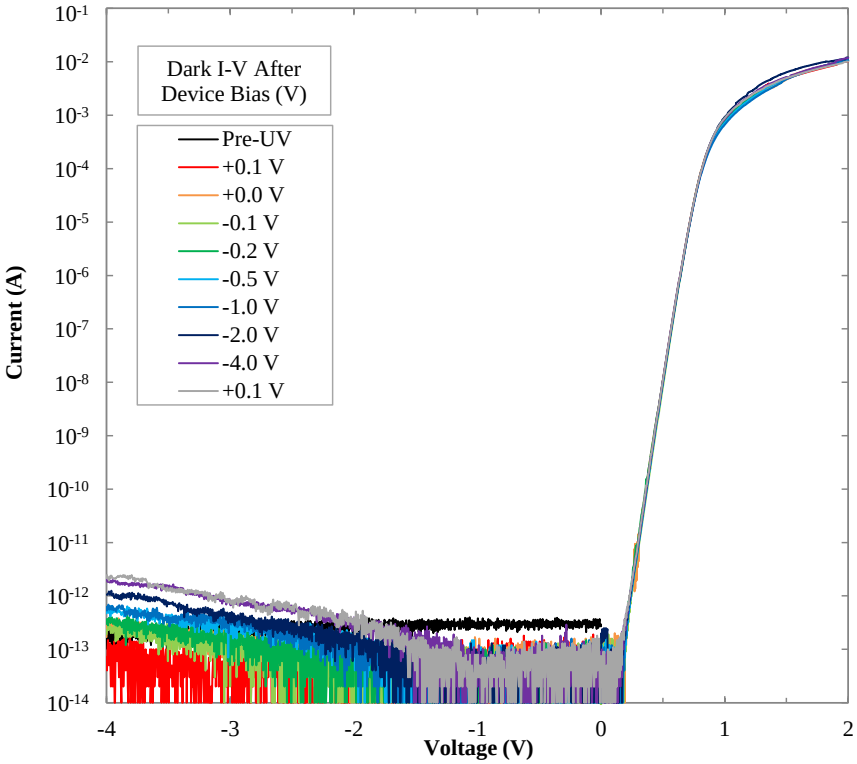

Figure A7.40: 4.0:10 PtO_x Dark I-V After Each UV Photoresponse Bias Test

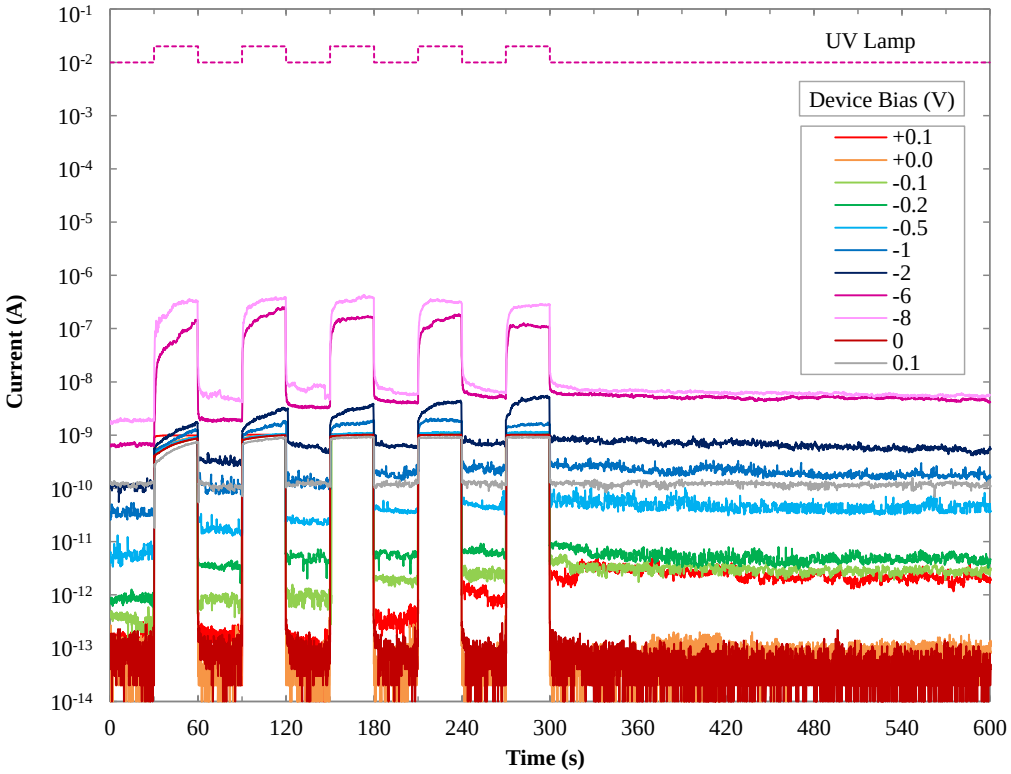

Figure A7.41: 5.0:10 (O_2:Ar) PtO_x 30 s UV Photoresponse with Varied Bias

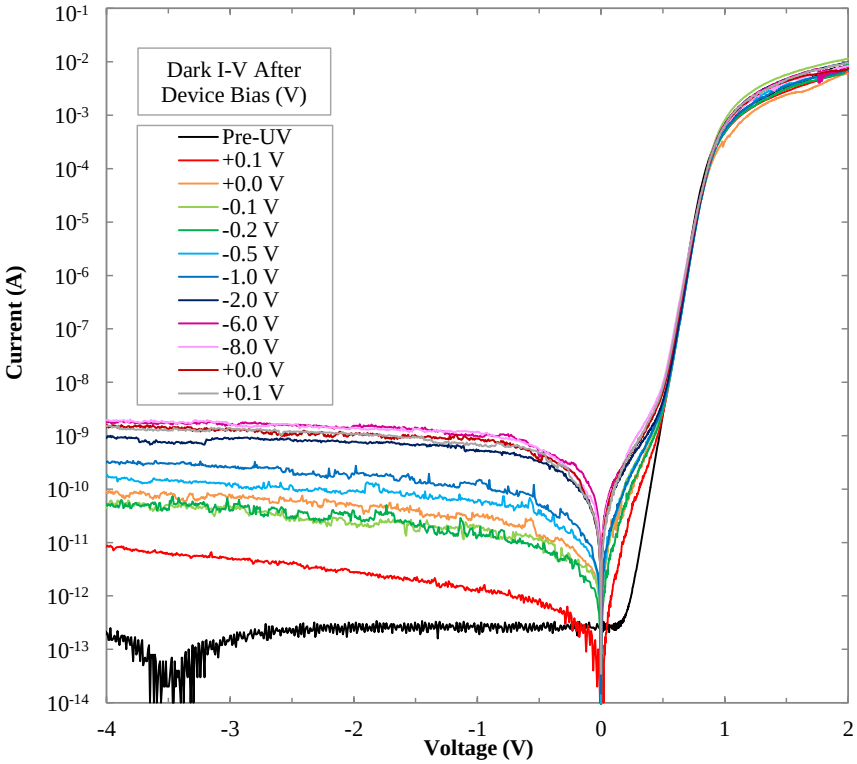

Figure A7.42: 5.0:10 PtO_x Dark I-V After Each UV Photoresponse Bias Test

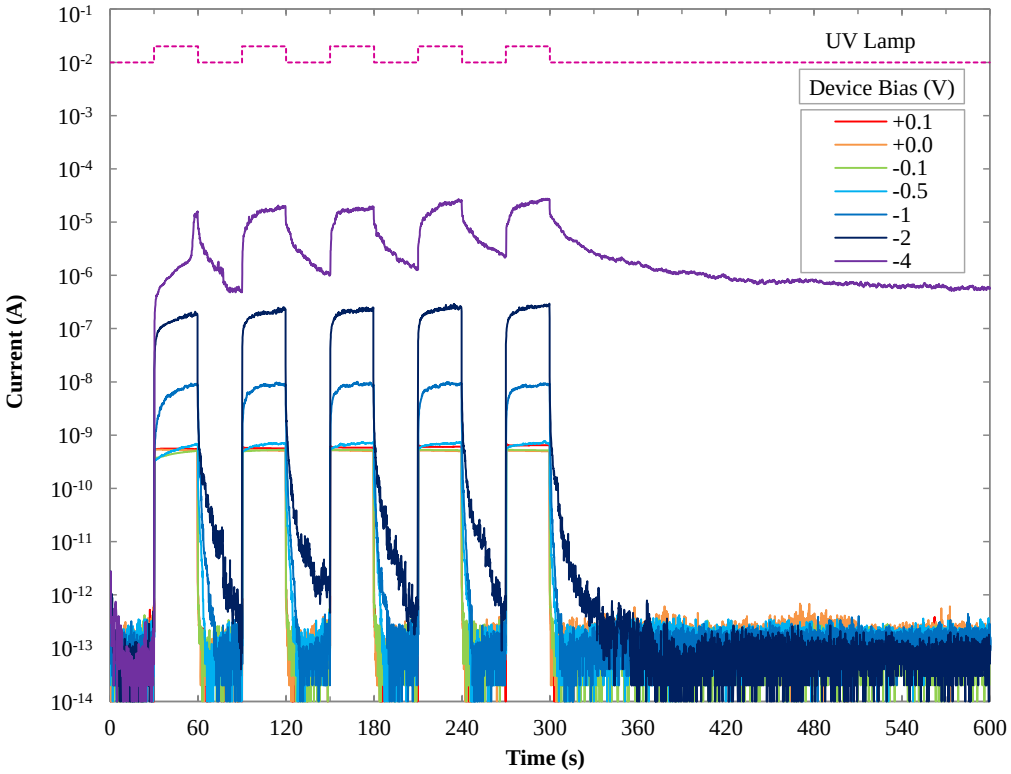

Figure A7.43: 7.0:10 (O_2:Ar) PtO_x 30 s UV Photoresponse with Varied Bias

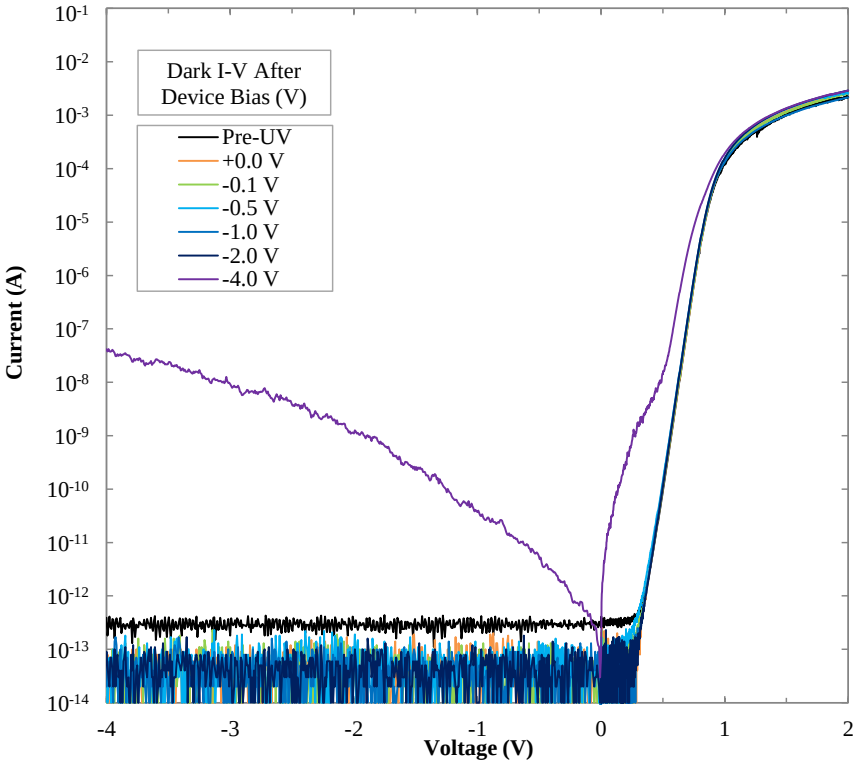

Figure A7.44: 7.0:10 PtO_x Dark I-V After Each UV Photoresponse Bias Test

[A7.8] 0.0:10 (O_2:Ar) PtO_x UV Photoresponse: Current Normalised ($I_{Normal} = I_{Measured}/I_{Initial\ Dark}$)

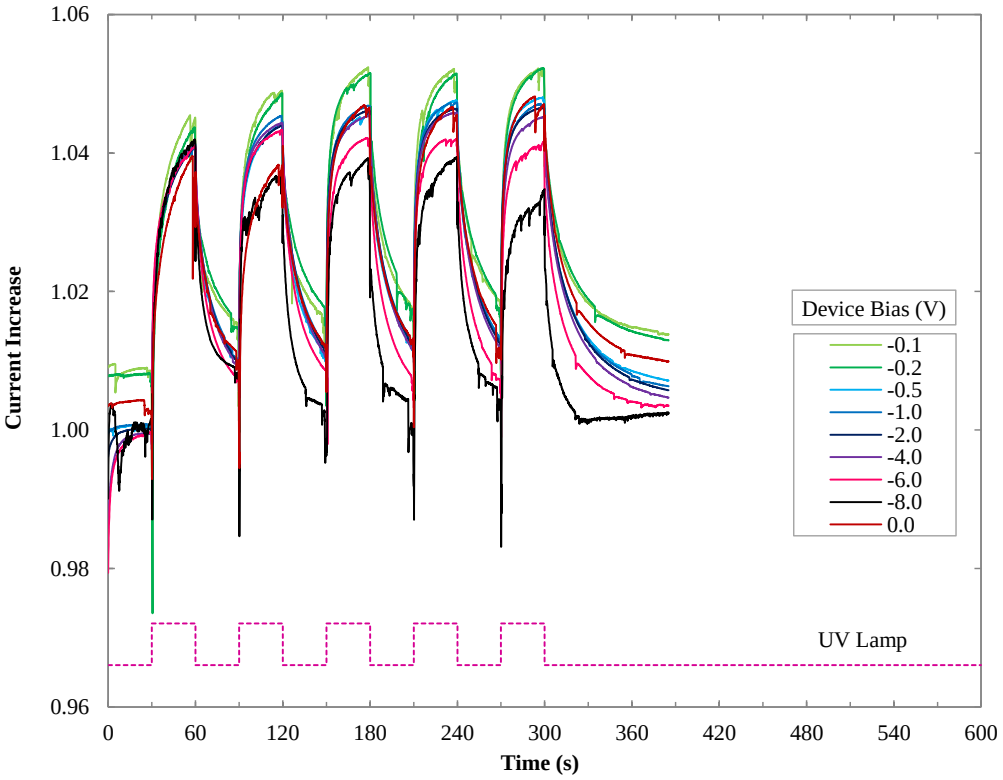

Figure A7.45: 0.0:10 (O_2:Ar) PtO_x 30 s UV Photoresponse Current Increase with Bias

[A7.9] IrO_x, PdO_x, PtO_x UV Photoresponse (Fifth Exposure) Comparison, Oxygen Incorporation

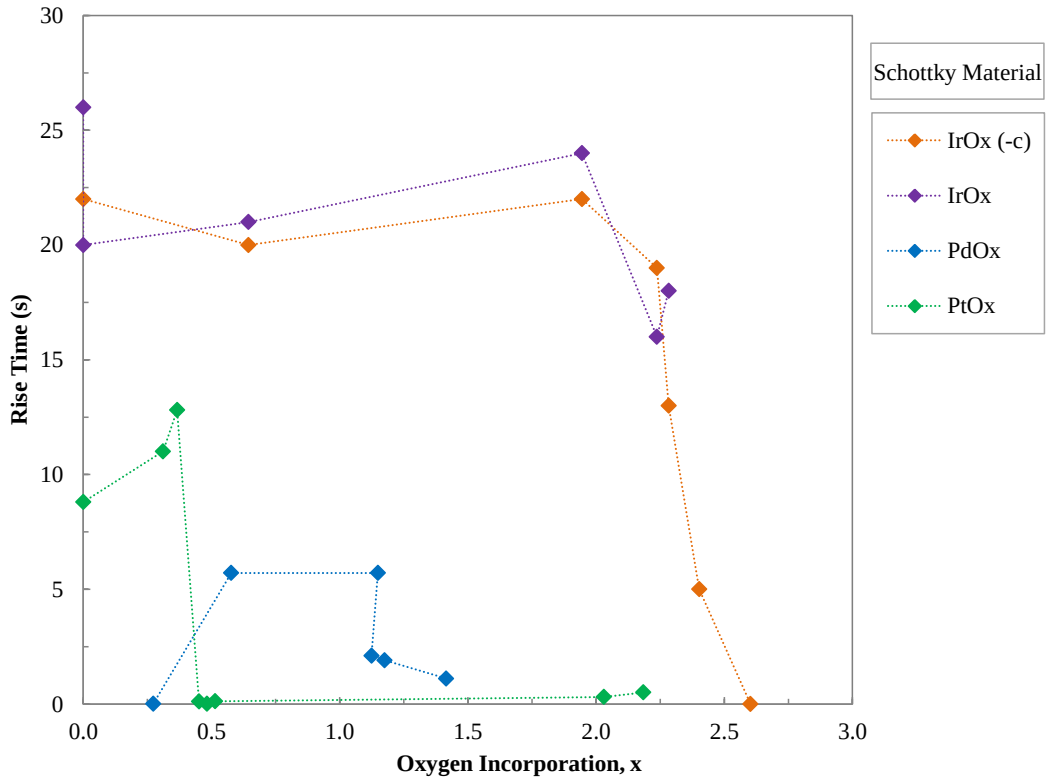

Figure A7.46: UV Photoresponse of Ir/IrO_x, PdO_x, and Pt/PtO_x, -1.0 V, Rise-Time

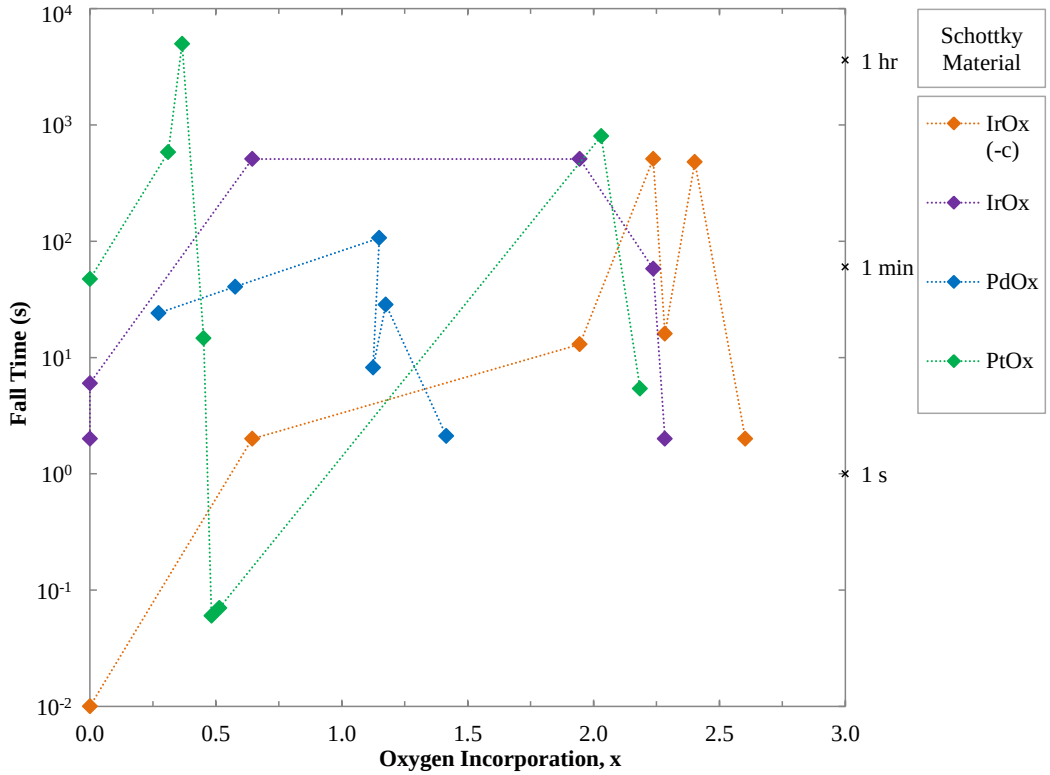

Figure A7.47 UV Photoresponse of Ir/IrO_x, PdO_x, and Pt/PtO_x, -1.0 V, Fall-Time

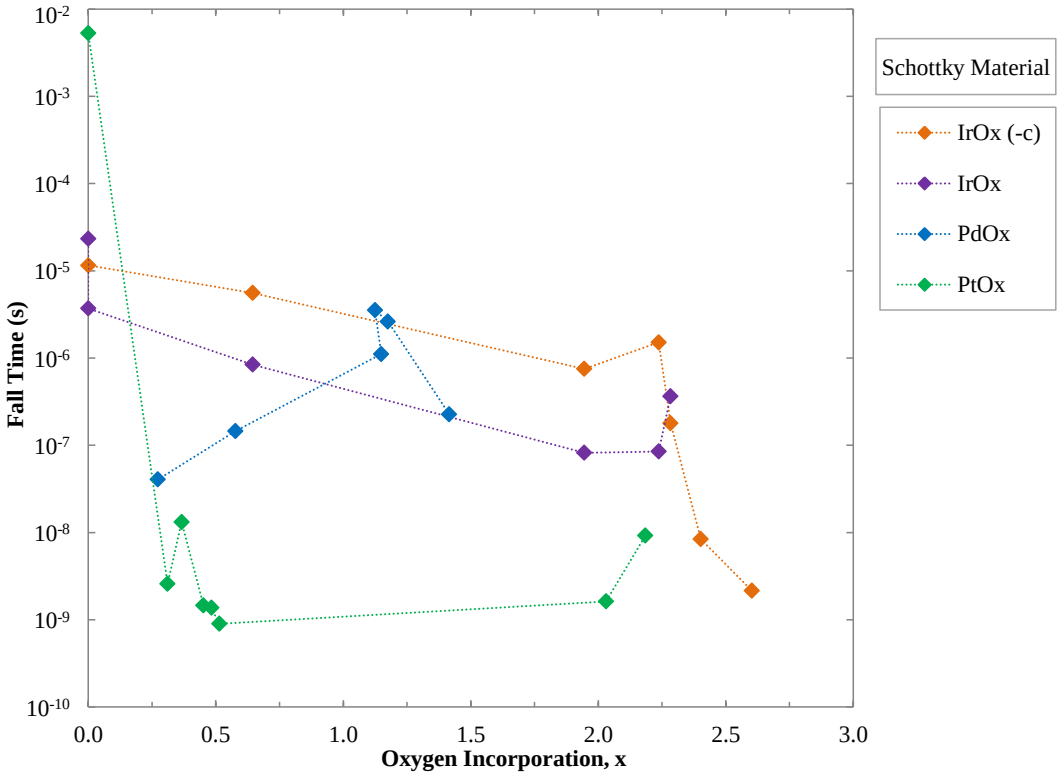

Figure A7.48: UV Photoresponse of Ir/IrO_x, PdO_x, and Pt/PtO_x, -1.0 V, Max. Photocurrent

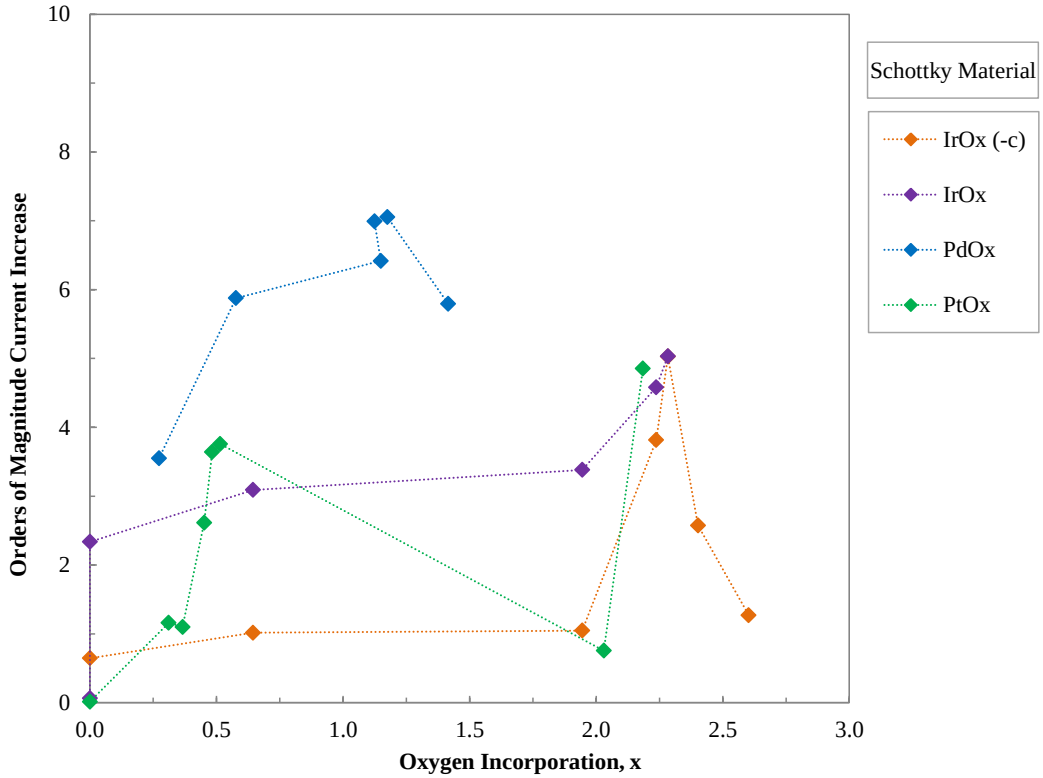

Figure A7.49: UV Photoresponse of Ir/IrO_x, PdO_x, and Pt/PtO_x, -1.0 V, Current Increase

[A8.1] Temperature Test Cycle Results of PLD IrO_x Schottky Contacts on +c-axis Low-Li ZnO

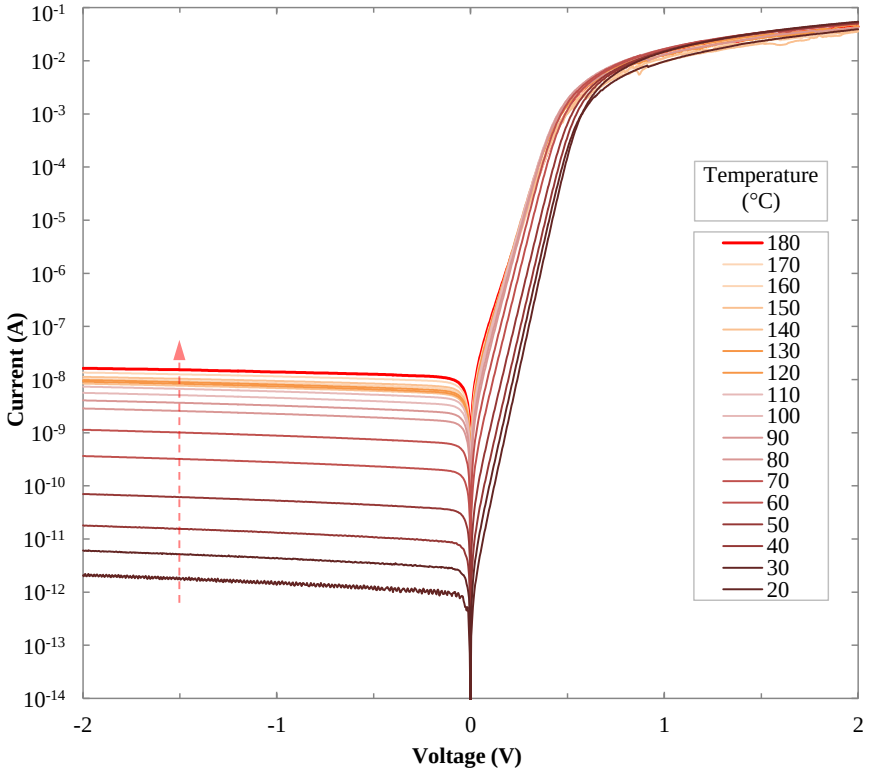

Figure A8.1: Dark I-V Results of PLD IrO_x Contacts (Increasing Temperature)

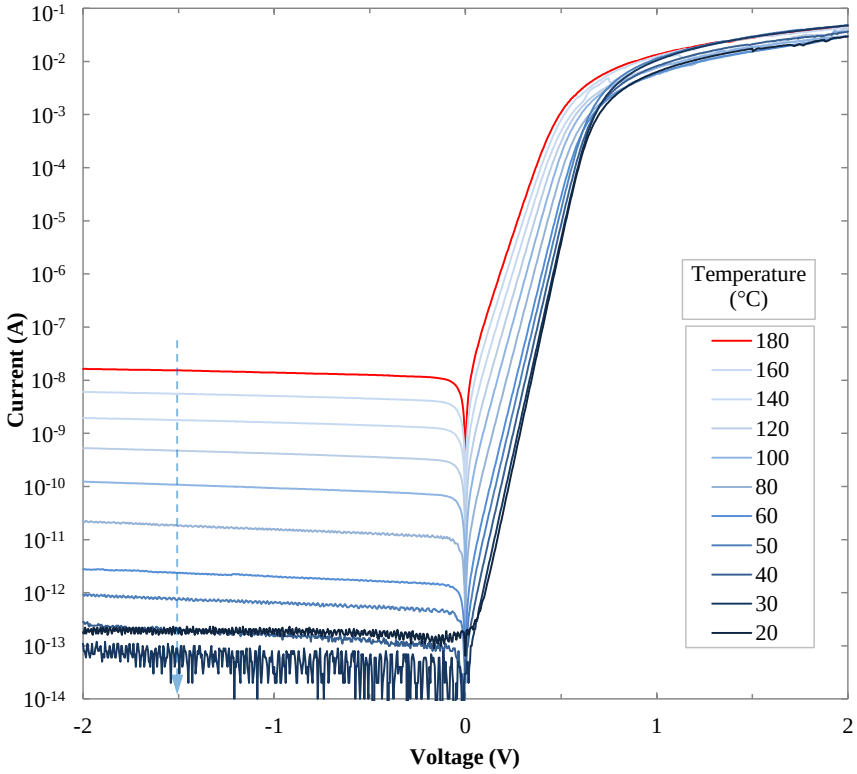

Figure A8.2: Dark I-V Results of PLD IrO_x Contacts (Decreasing Temperature)

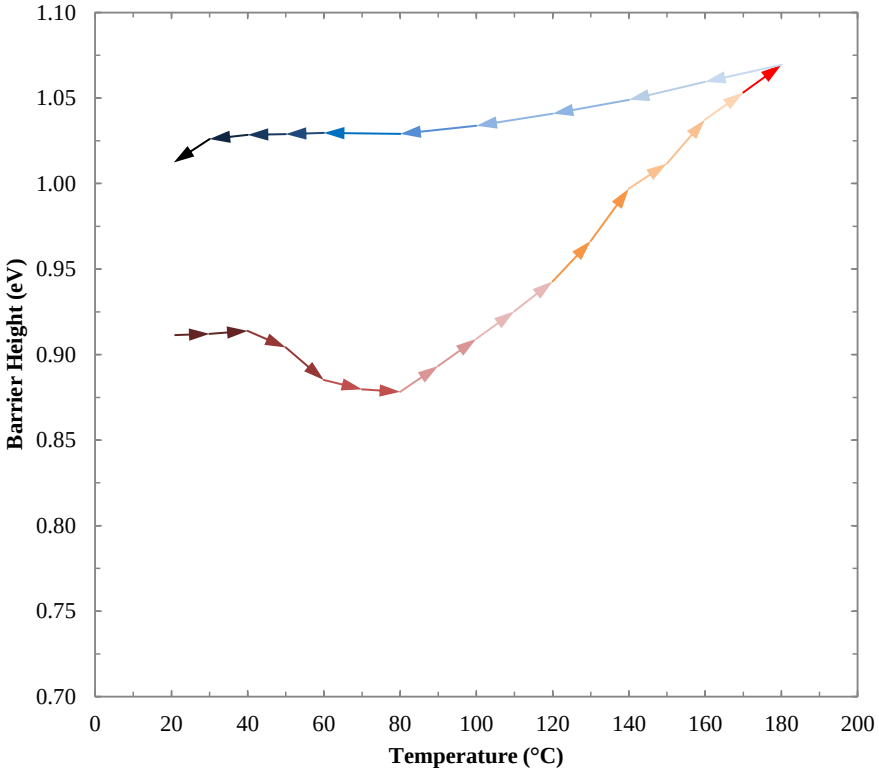

Figure A8.3: Barrier Heights with Temperature of PLD IrO_x Contacts

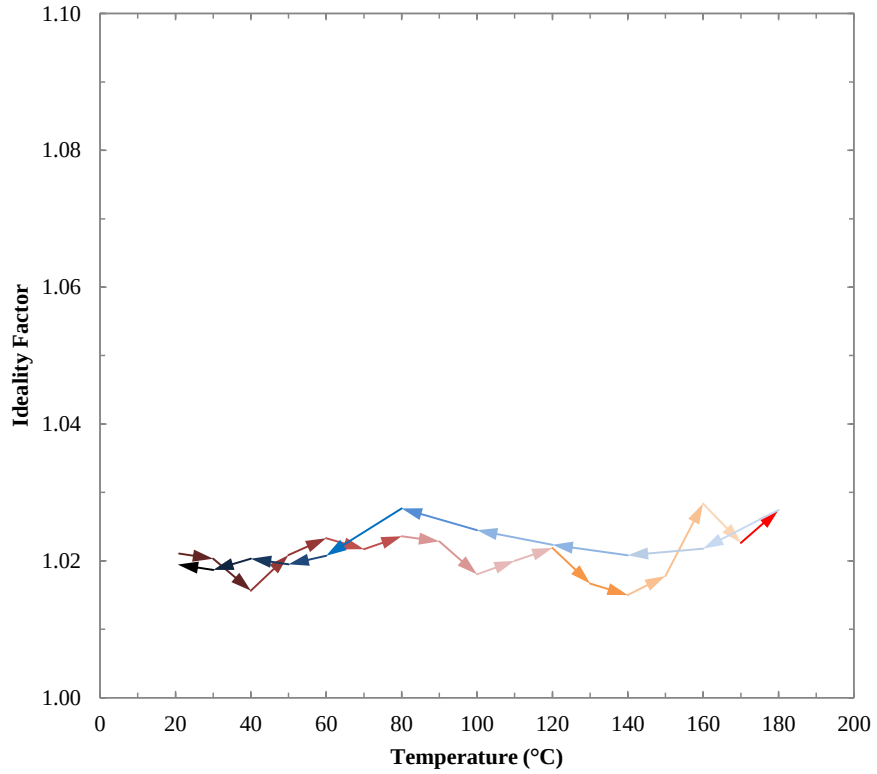

Figure A8.4: Ideality Factors with Temperature of PLD IrO_x Contacts

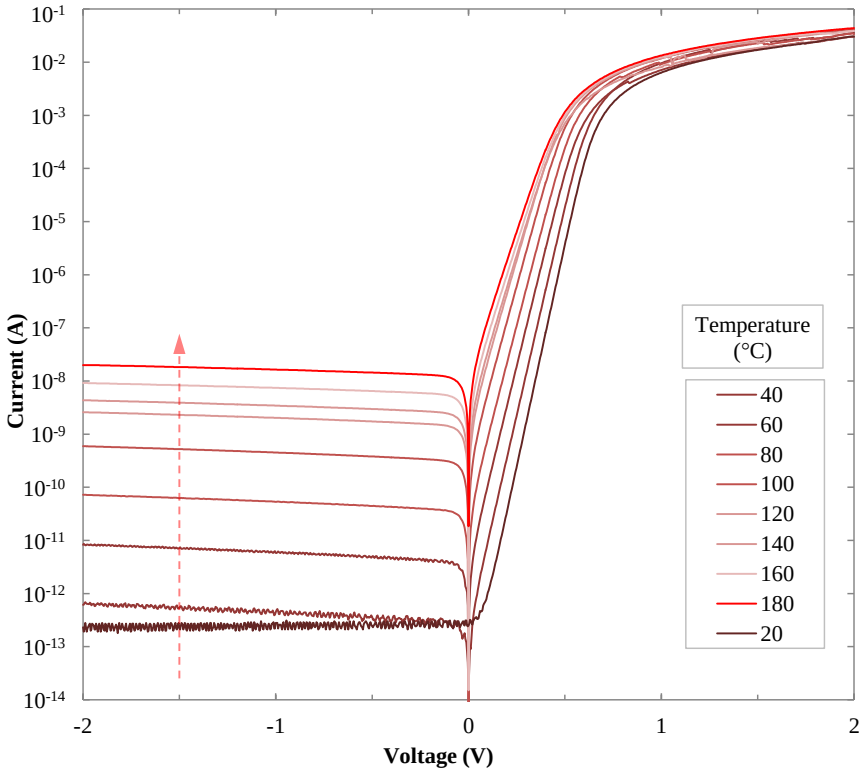

Figure A8.5: Dark I-V Results of PLD IrO_x Contacts (Increasing Temperature, Repeat)

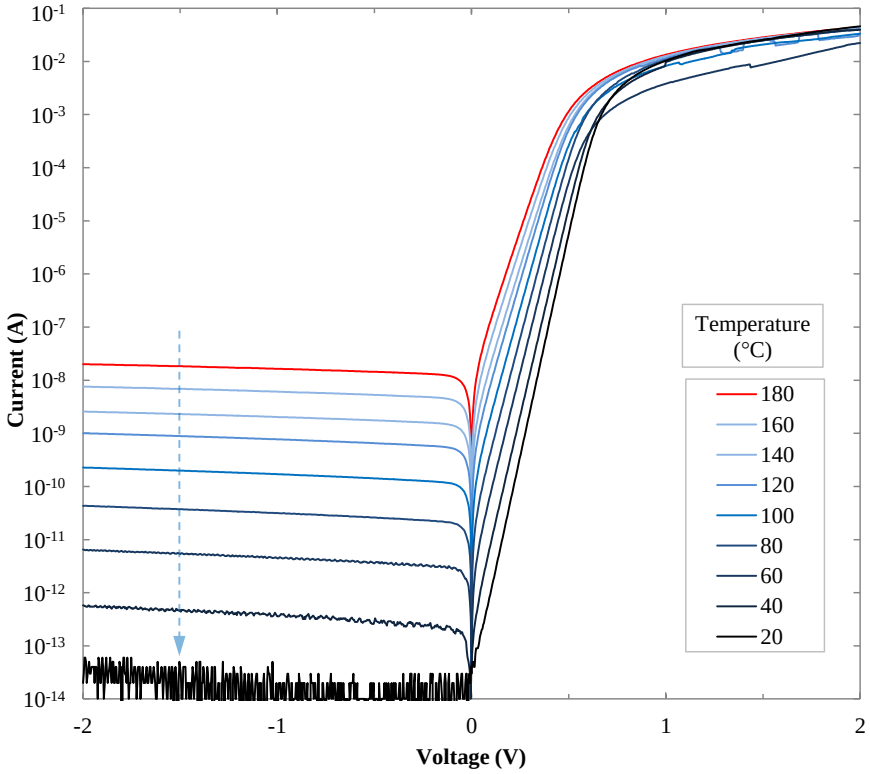

Figure A8.6: Dark I-V Results of PLD IrO_x Contacts (Decreasing Temperature, Repeat)

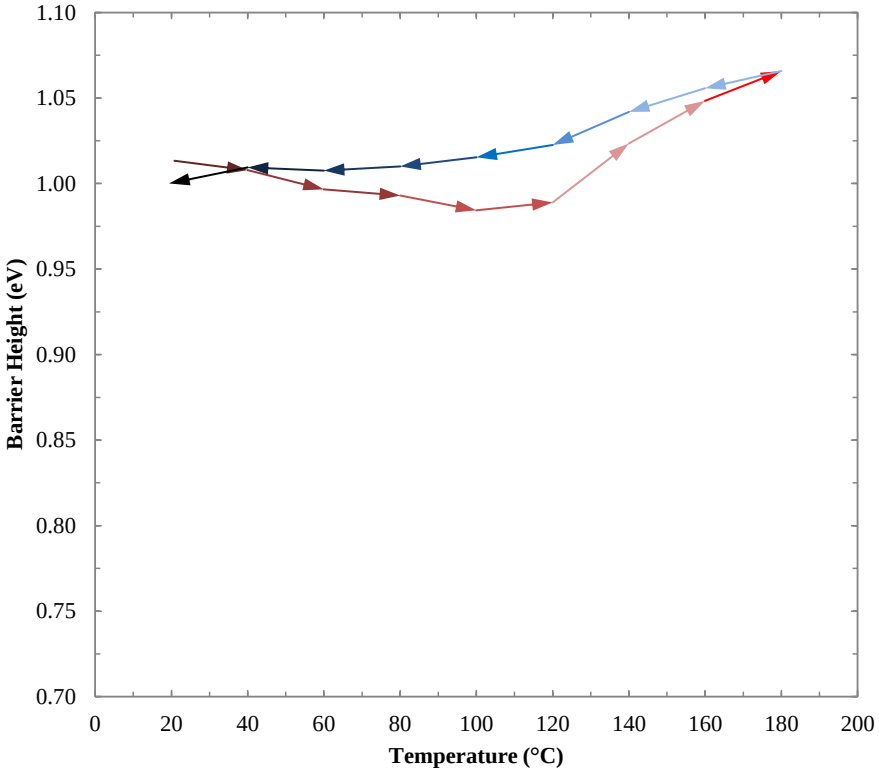

Figure A8.7: Barrier Heights with Temperature of PLD IrO_x (Repeat)

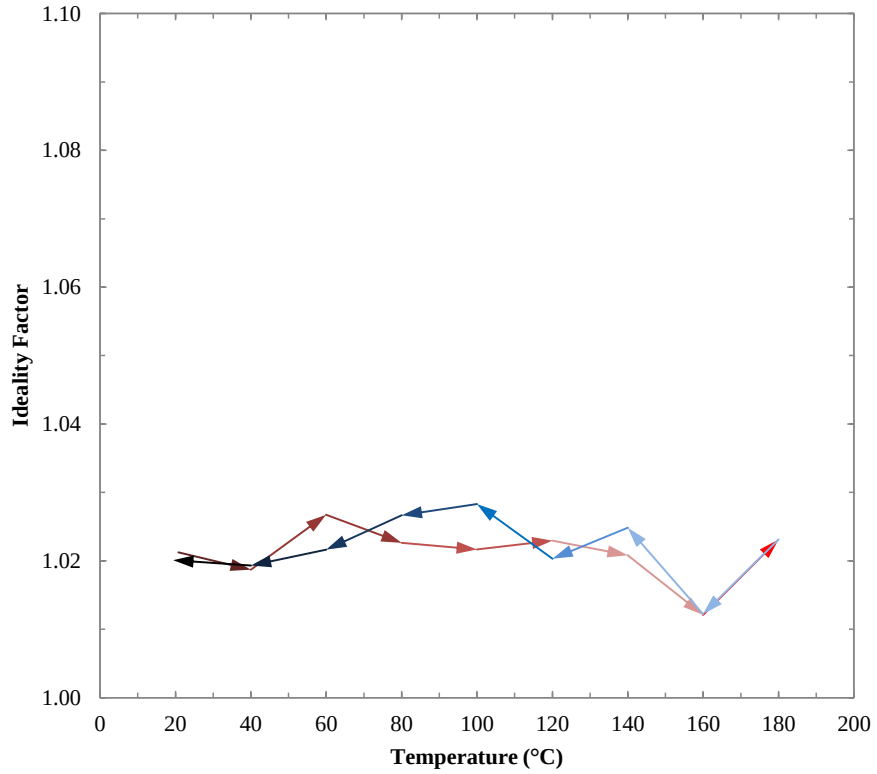

Figure A8.8: Ideality Factors with Temperature of PLD IrO_x (Repeat)

[A8.2] Dark I-V of 2.0:10 (O_2:Ar) RF-sputtered IrO_x Contacts Before, After Temperature Cycles

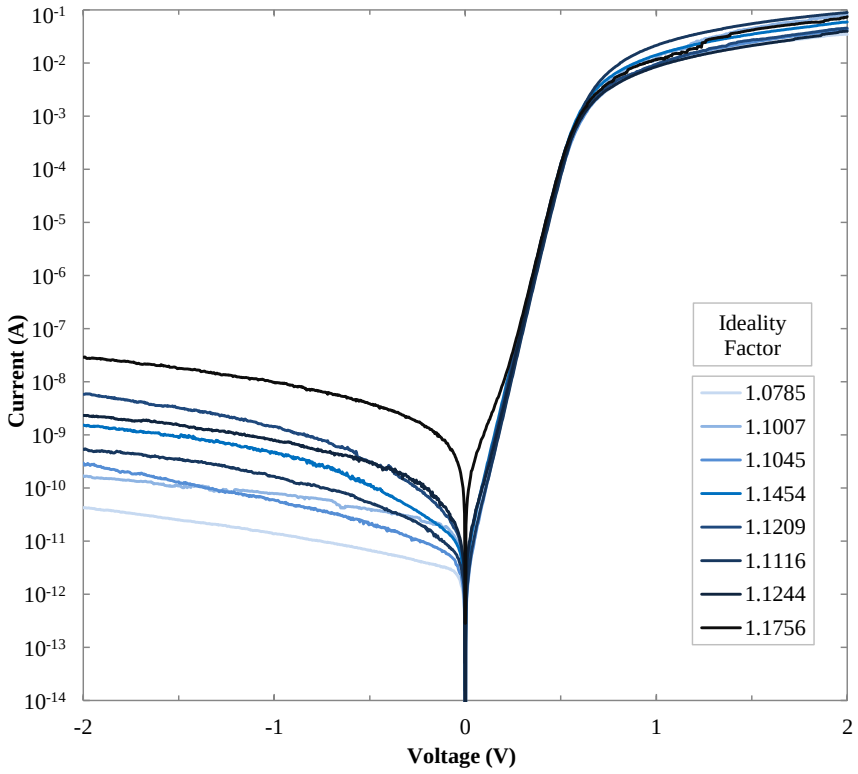

Figure A8.9: Dark I-V of 2.0:10 (O_2:Ar) RF-sputtered IrO_x Devices, Pre-Temperature Test

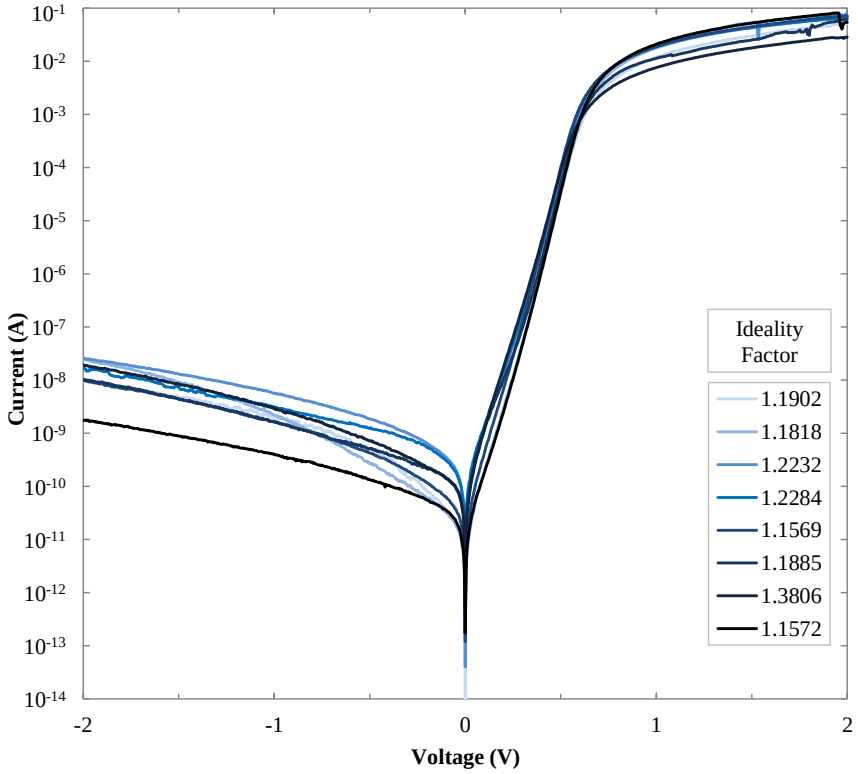

Figure A8.10: Dark I-V of 2.0:10 (O_2:Ar) RF-sputtered IrO_x Devices, Post-Temperature Test

[A8.3] Temperature Test Cycle Results of 1.0:10 – 4.0:10 (O_2:Ar) RF-sputtered IrO_x Contacts

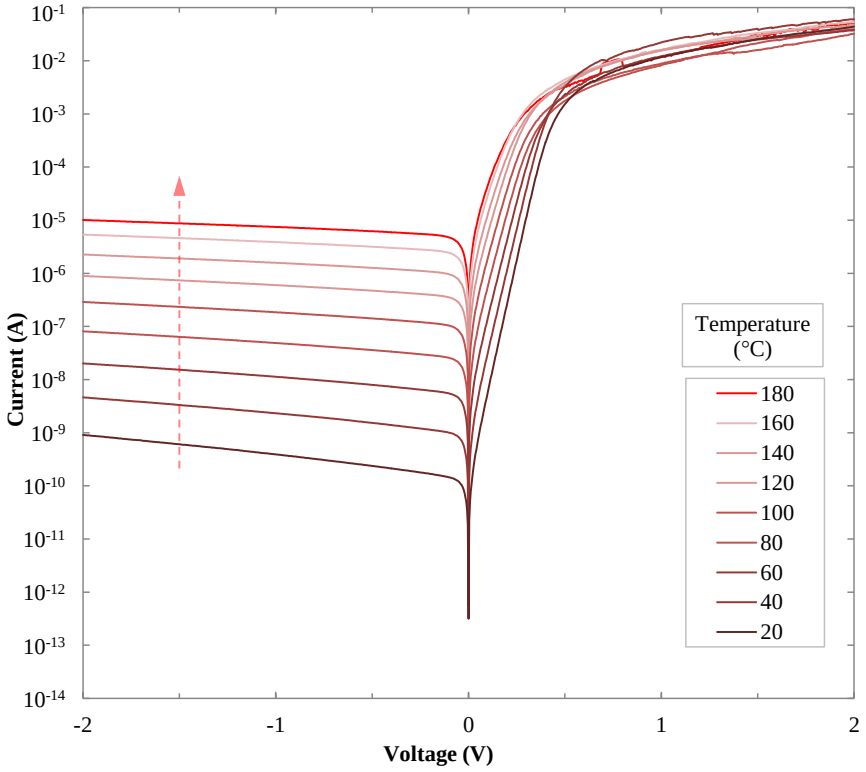

Figure A8.11: 1.0:10 (O_2:Ar) RF-sputtered IrO_x Dark I-V Results (Increasing Temperature)

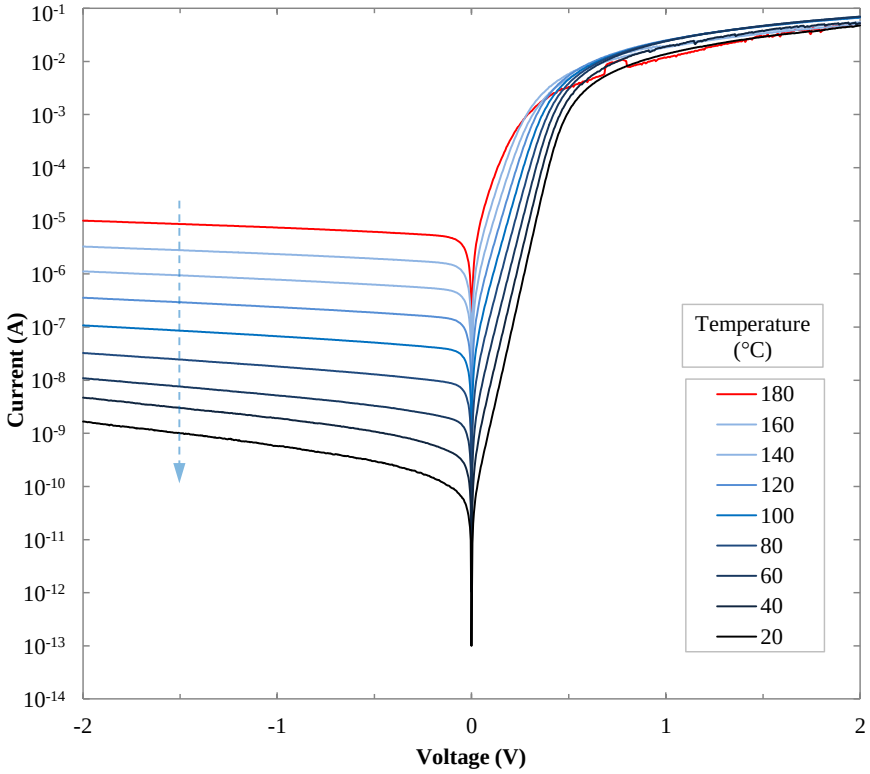

Figure A8.12: 1.0:10 (O_2:Ar) RF-sputtered IrO_x Dark I-V Results (Decreasing Temperature)

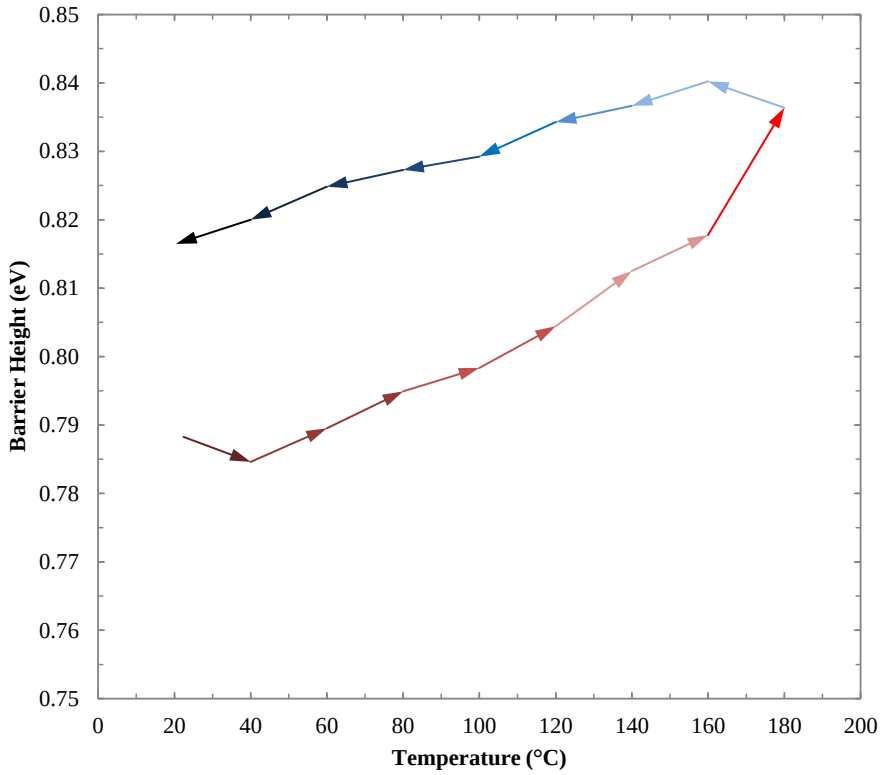

Figure A8.13: Barrier Heights with Temperature of 1.0:10 (O_2:Ar) RF-sputtered IrO_x

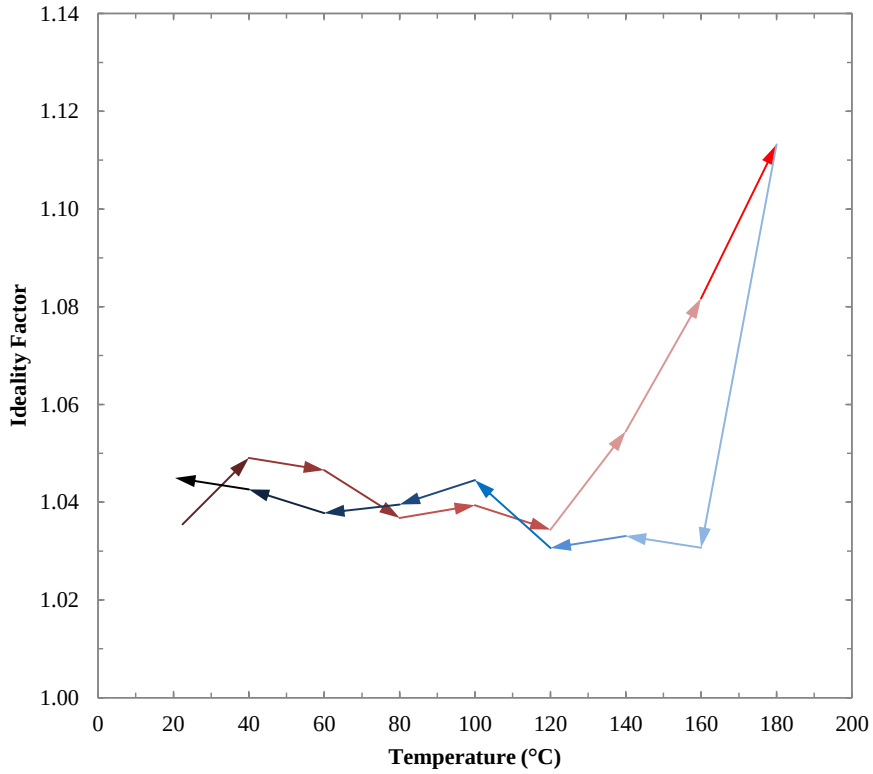

Figure A8.14: Ideality Factors with Temperature of 1.0:10 (O_2:Ar) RF-sputtered IrO_x

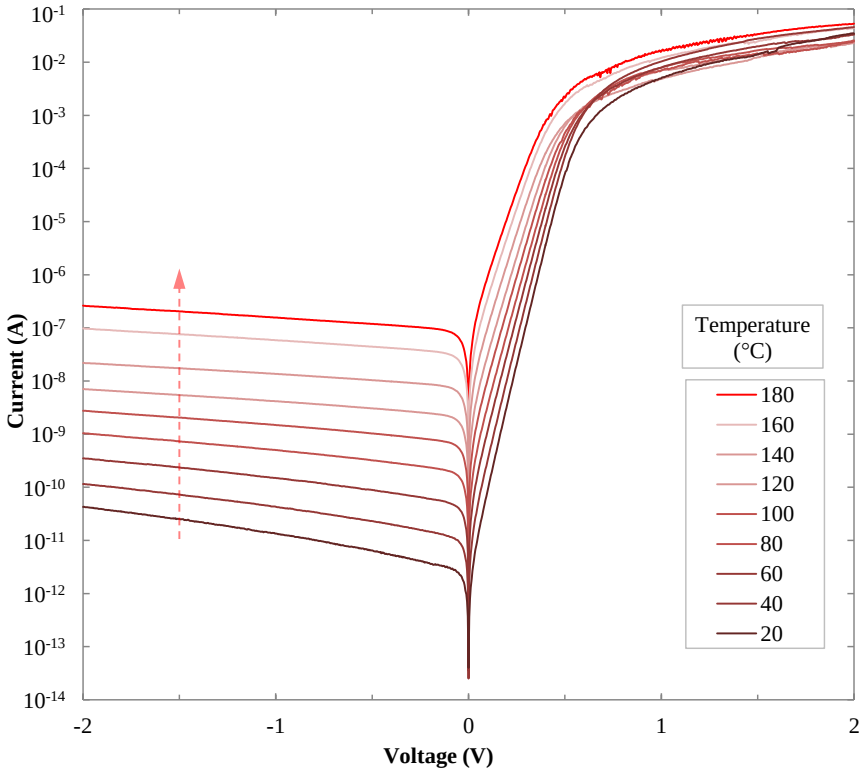

Figure A8.15: 2.0:10 (O_2:Ar) RF-sputtered IrO_x Dark I-V Results (Increasing Temperature)

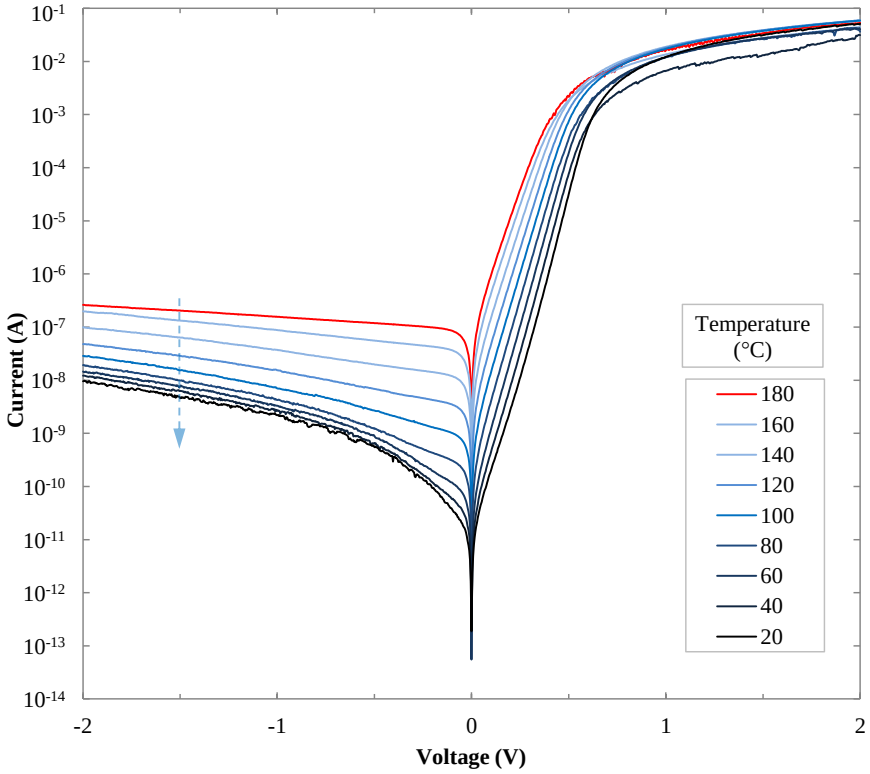

Figure A8.16: 2.0:10 (O_2:Ar) RF-sputtered IrO_x Dark I-V Results (Decreasing Temperature)

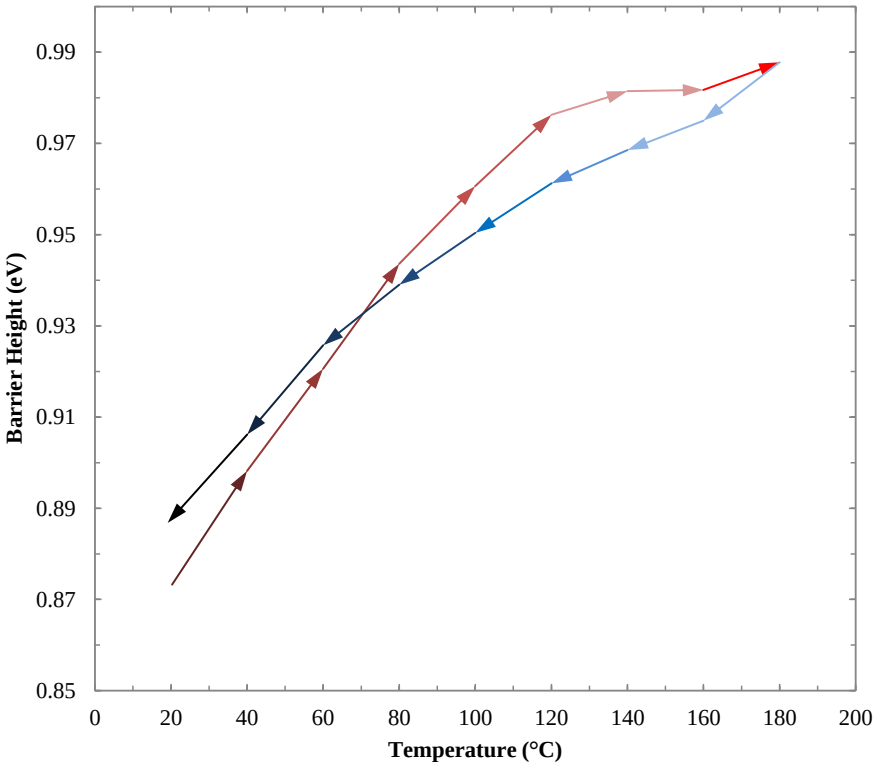

Figure A8.17: Barrier Heights with Temperature of 2.0:10 (O_2:Ar) RF-sputtered IrO_x

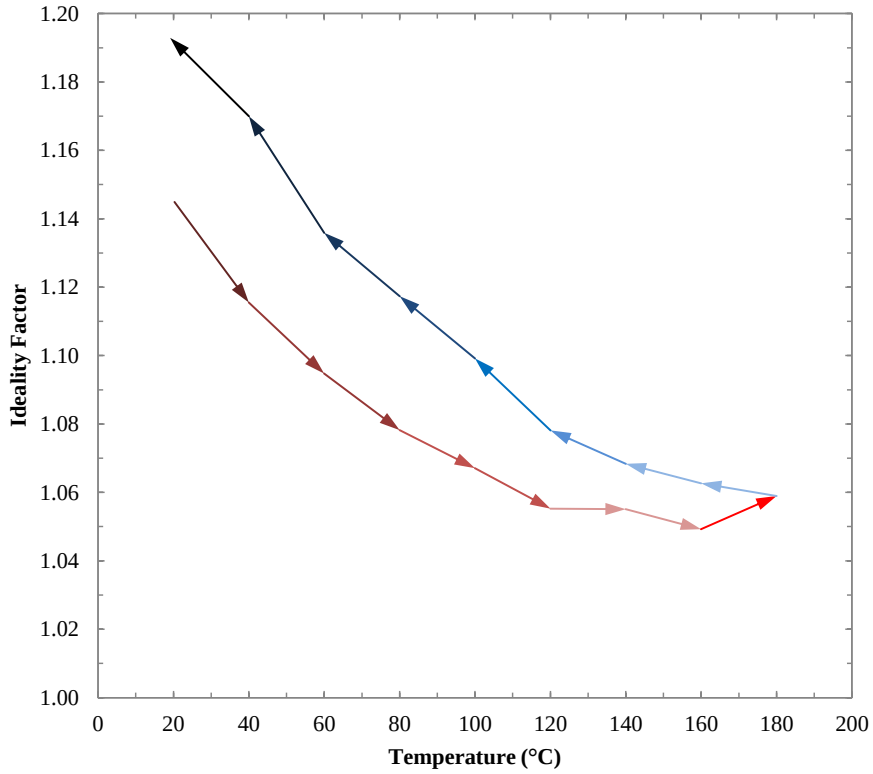

Figure A8.18: Ideality Factors with Temperature of 2.0:10 (O_2:Ar) RF-sputtered IrO_x

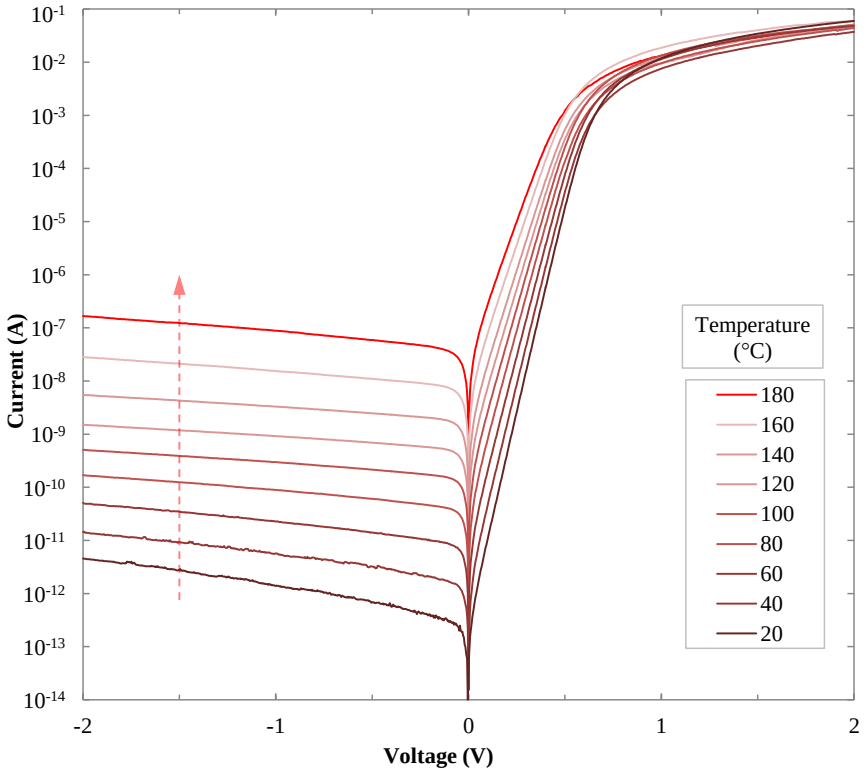

Figure A8.19: 3.0:10 (O_2:Ar) RF-sputtered IrO_x Dark I-V Results (Increasing Temperature)

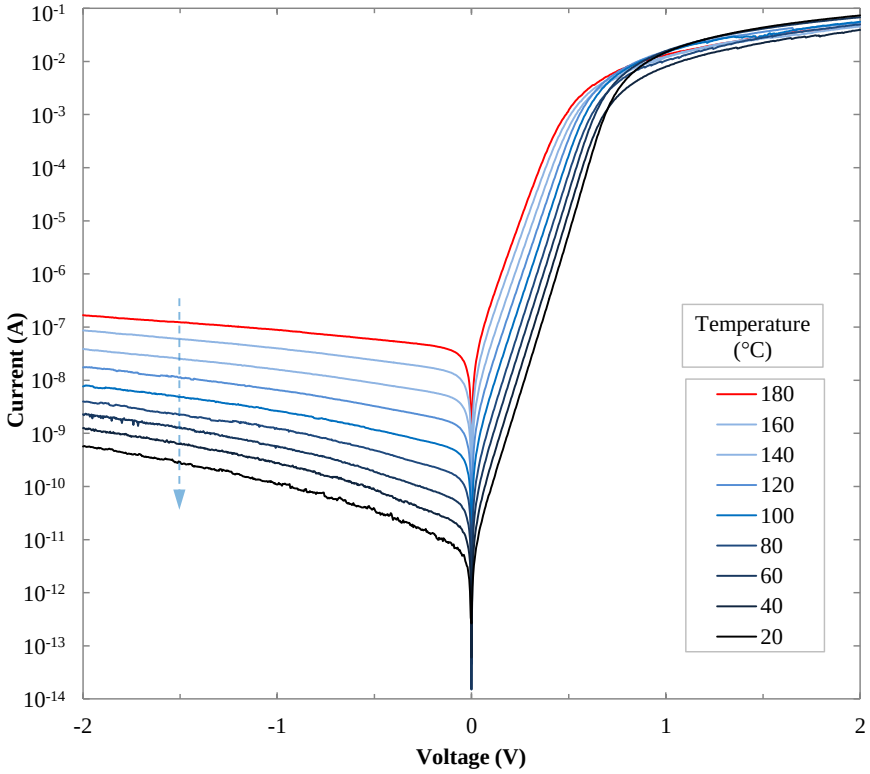

Figure A8.20: 3.0:10 (O_2:Ar) RF-sputtered IrO_x Dark I-V Results (Decreasing Temperature)

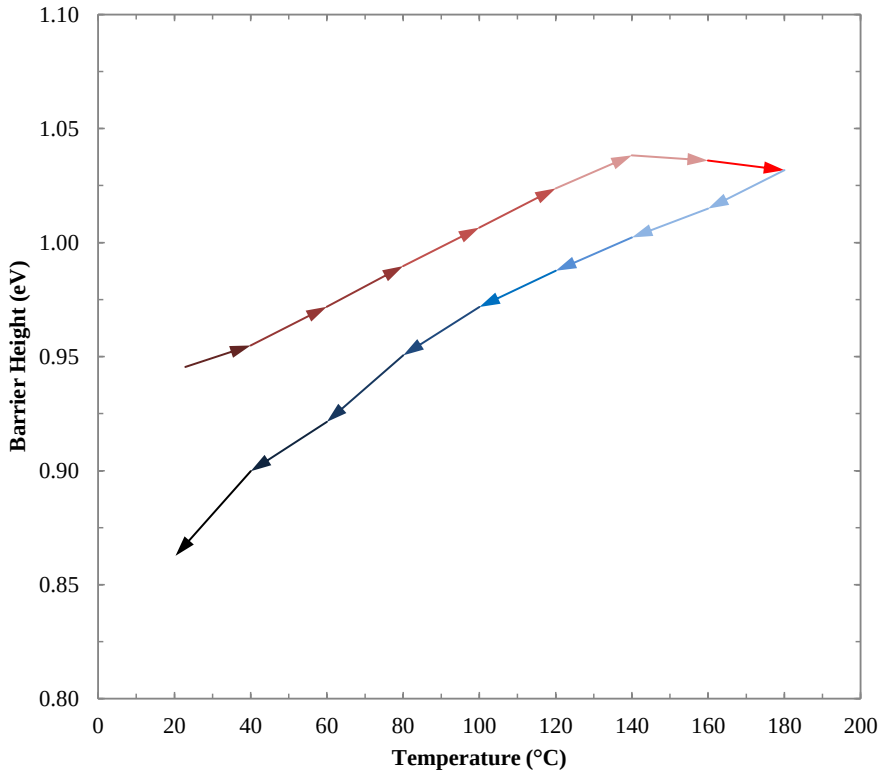

Figure A8.21: Barrier Heights with Temperature of 3.0:10 (O_2:Ar) RF-sputtered IrO_x

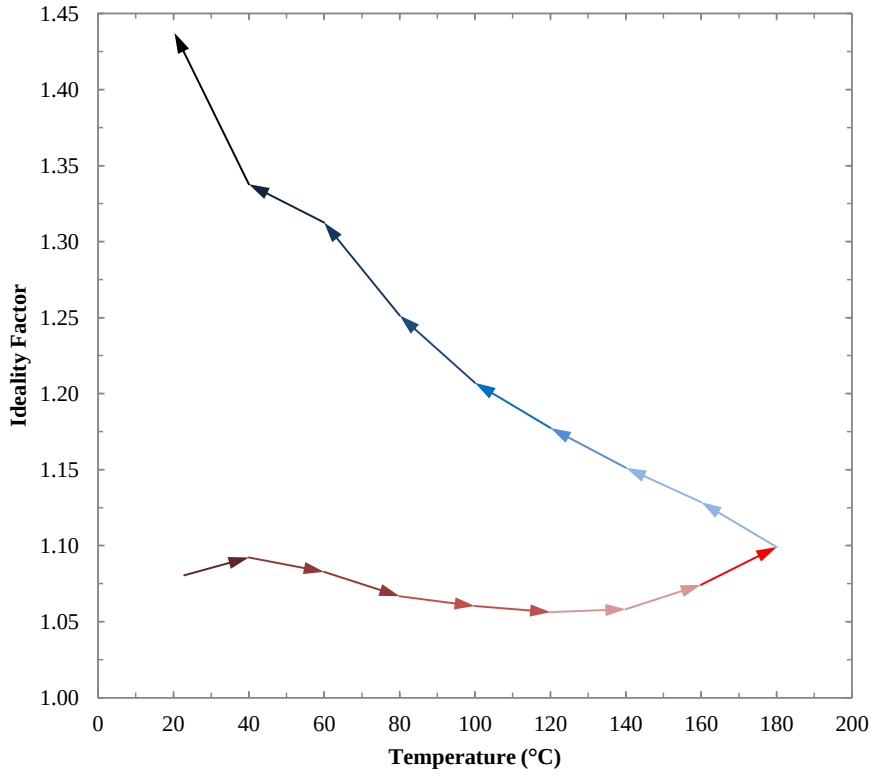

Figure A8.22: Ideality Factors with Temperature of 3.0:10 (O_2:Ar) RF-sputtered IrO_x

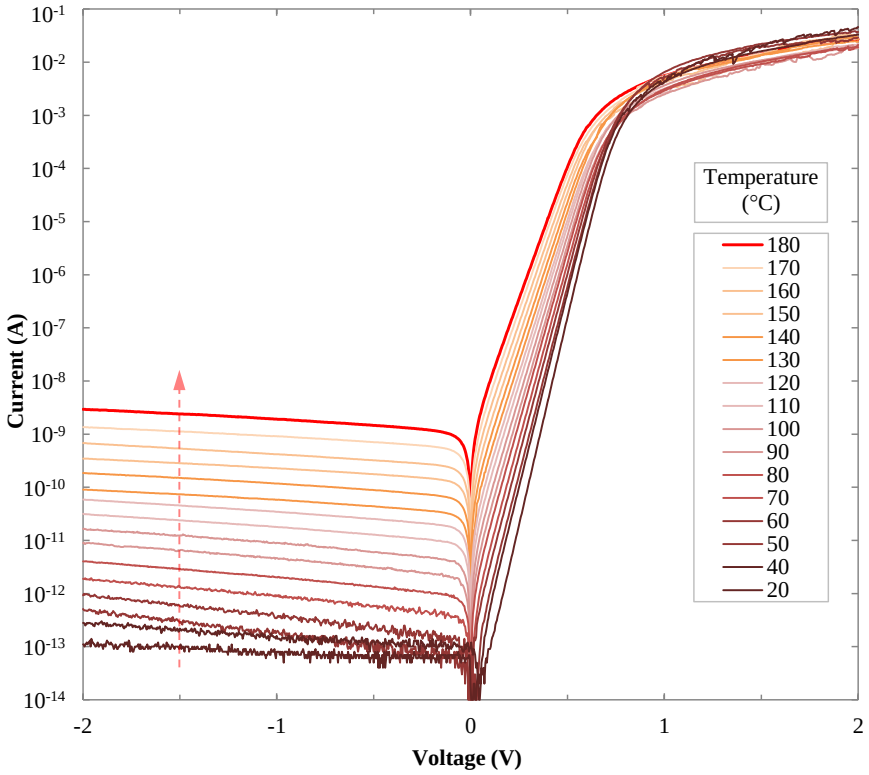

Figure A8.23: 4.0:10 (O_2:Ar) RF-sputtered IrO_x Dark I-V Results (Increasing Temperature)

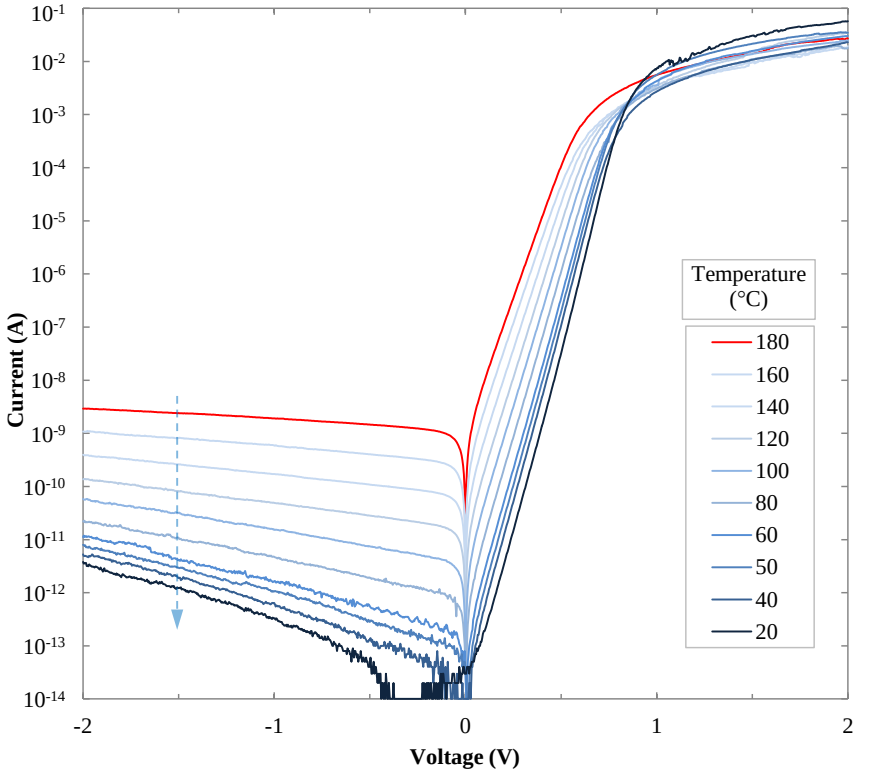

Figure A8.24: 4.0:10 (O_2:Ar) RF-sputtered IrO_x Dark I-V Results (Decreasing Temperature)

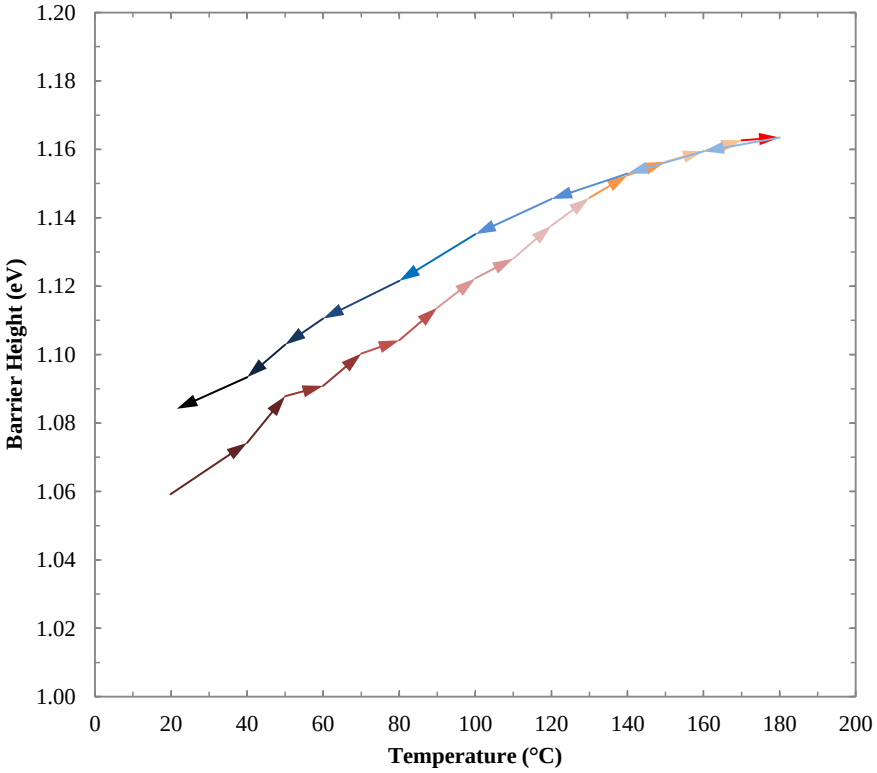

Figure A8.25: Barrier Heights with Temperature of 4.0:10 (O_2:Ar) RF-sputtered IrO_x

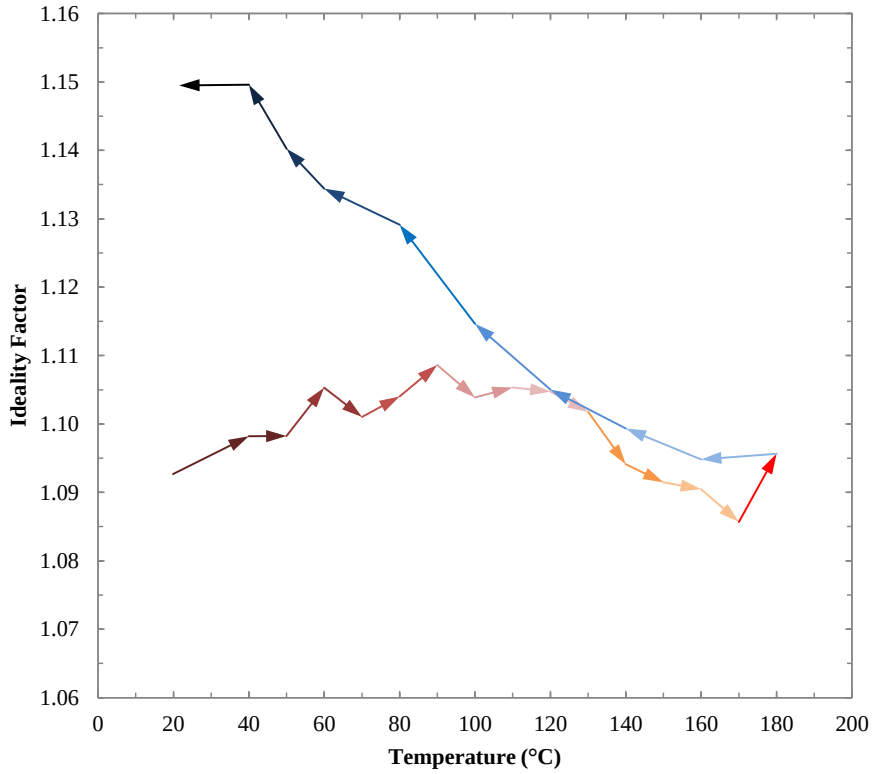

Figure A8.26: Ideality Factors with Temperature of 4.0:10 (O_2:Ar) RF-sputtered IrO_x

[A8.4] Temperature Test Cycle Results of 3.0:10 – 7.0:10 (O_2:Ar) RF-sputtered PtO_x Contacts

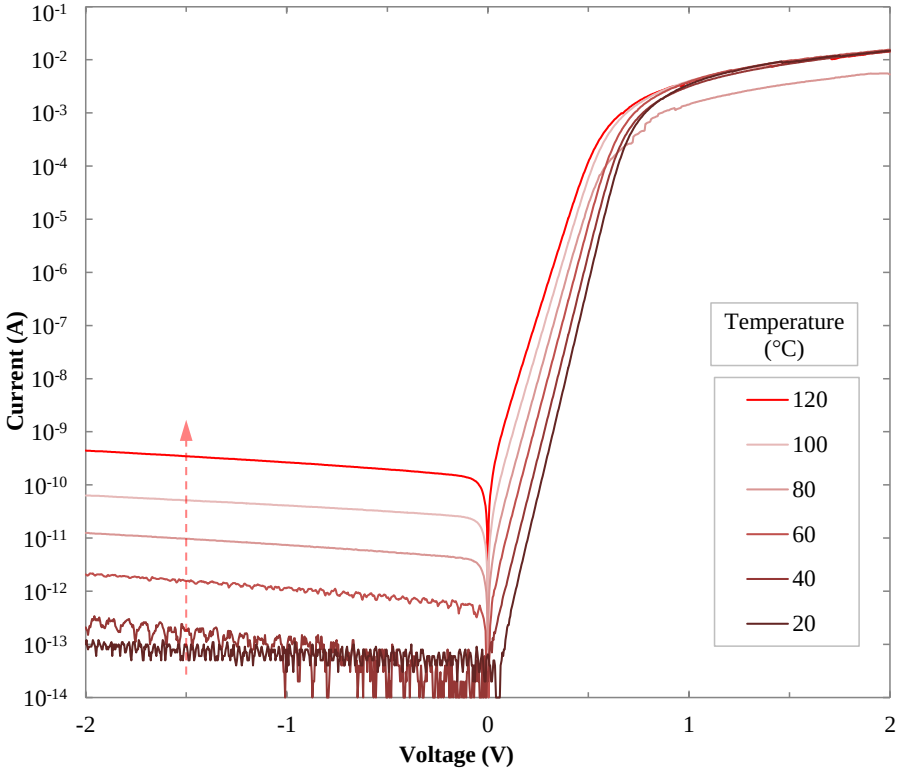

Figure A8.27: Dark I-V of 3.0:10 (O_2:Ar) RF-sputtered PtO_x (Increasing Temperature)

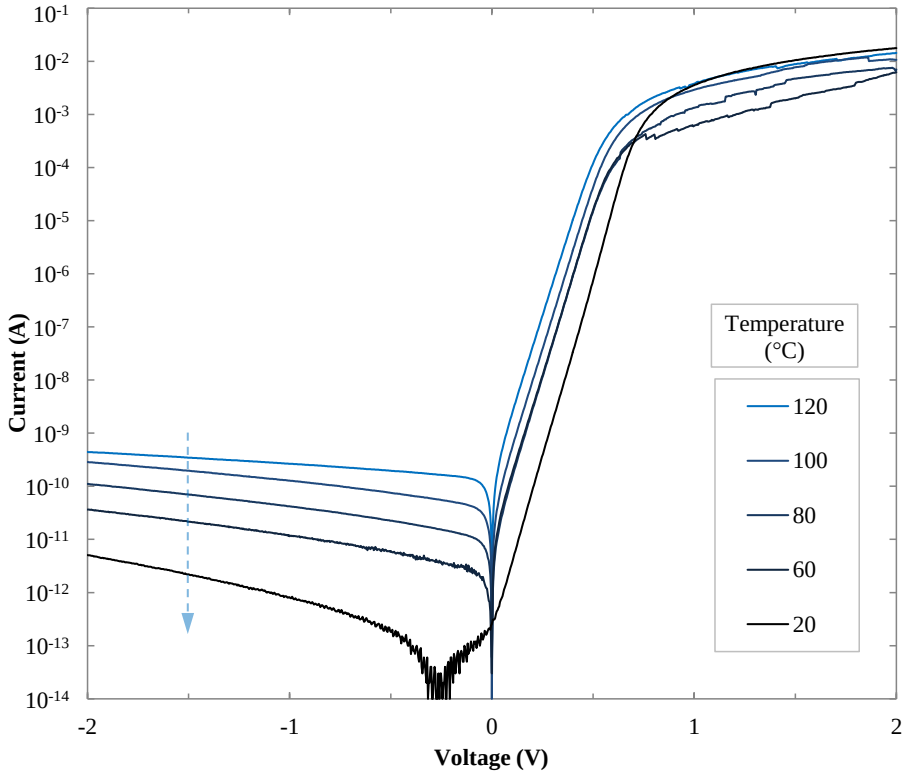

Figure A8.28: Dark I-V of 3.0:10 (O_2:Ar) RF-sputtered PtO_x (Decreasing Temperature)

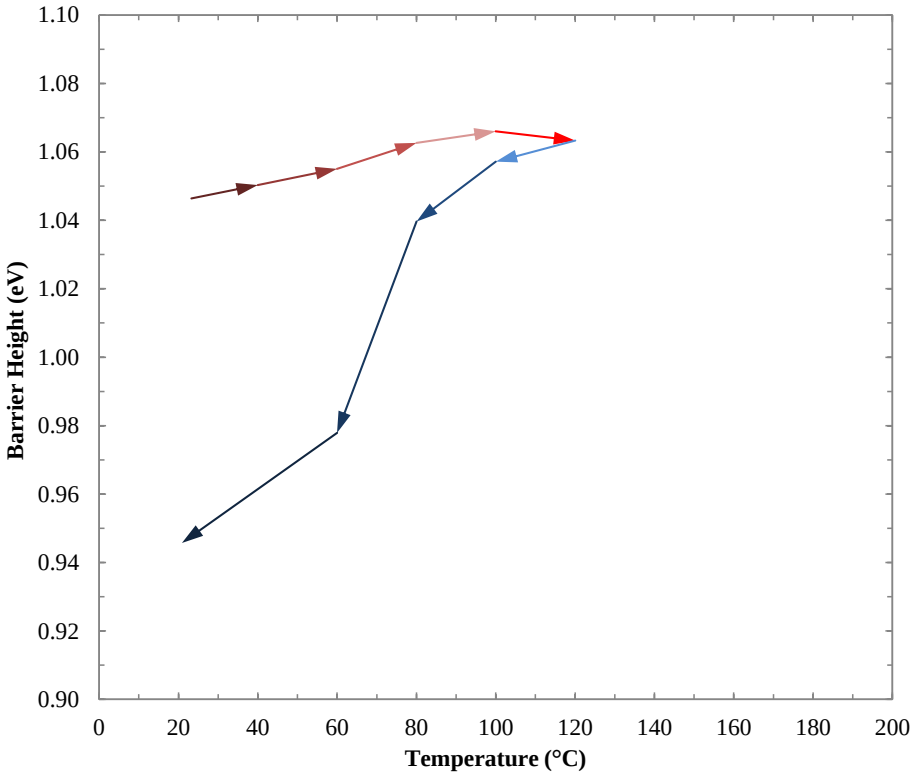

Figure A8.29: Barrier Heights with Temperature of 3.0:10 (O_2:Ar) RF-sputtered PtO_x

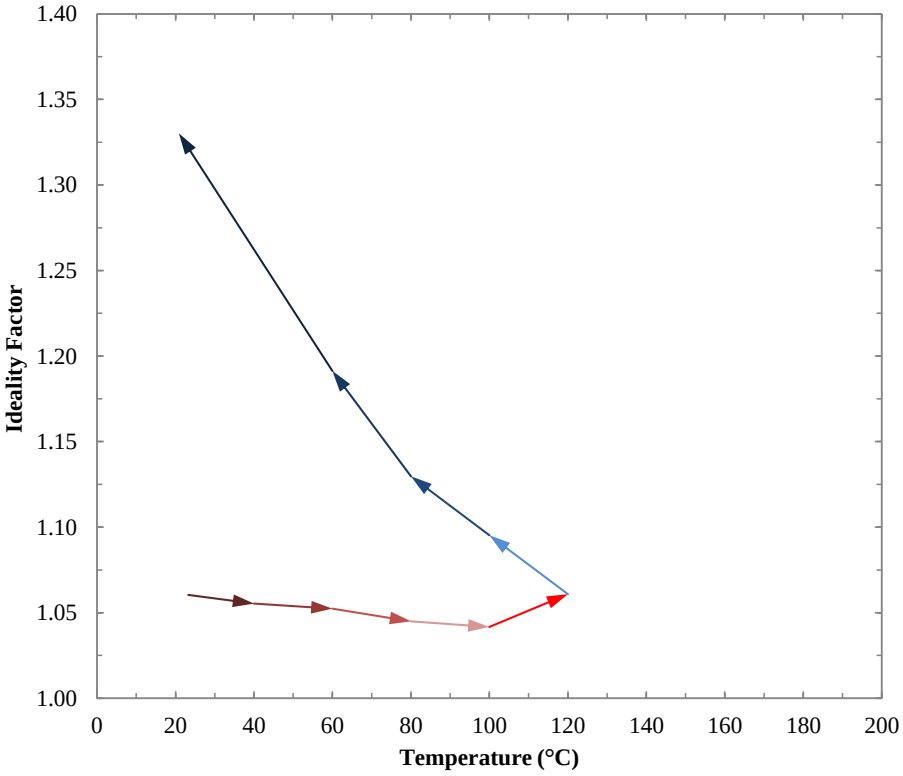

Figure A8.30: Ideality Factors with Temperature of 3.0:10 (O_2:Ar) RF-sputtered PtO_x

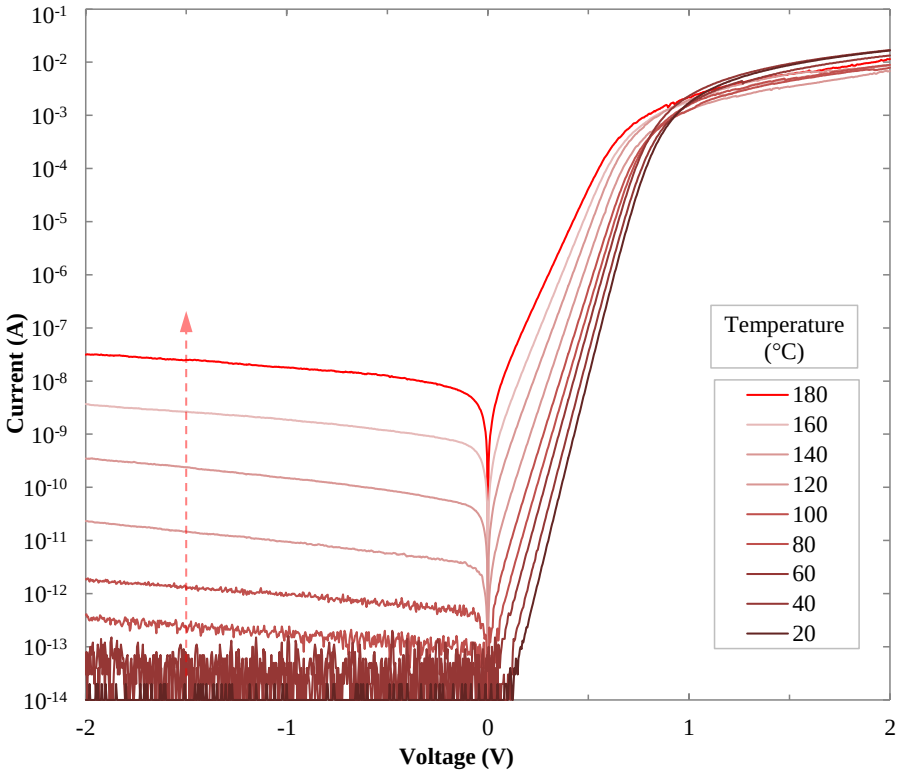

Figure A8.31: Dark I-V of 4.0:10 (O_2:Ar) RF-sputtered PtO_x (Increasing Temperature)

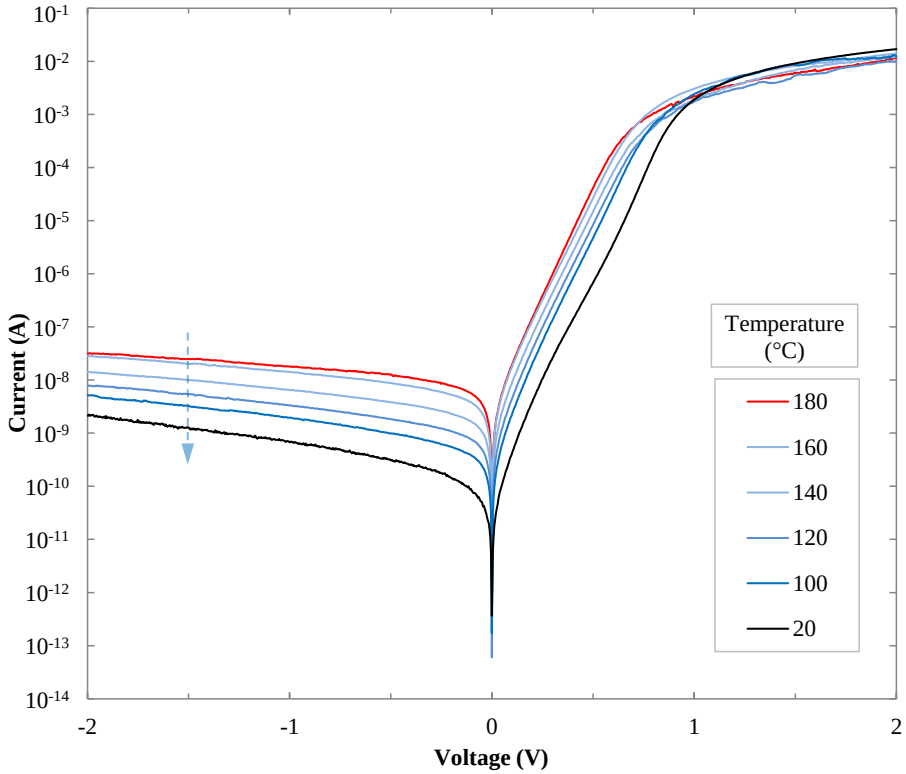

Figure A8.32: Dark I-V of 4.0:10 (O_2:Ar) RF-sputtered PtO_x (Decreasing Temperature)

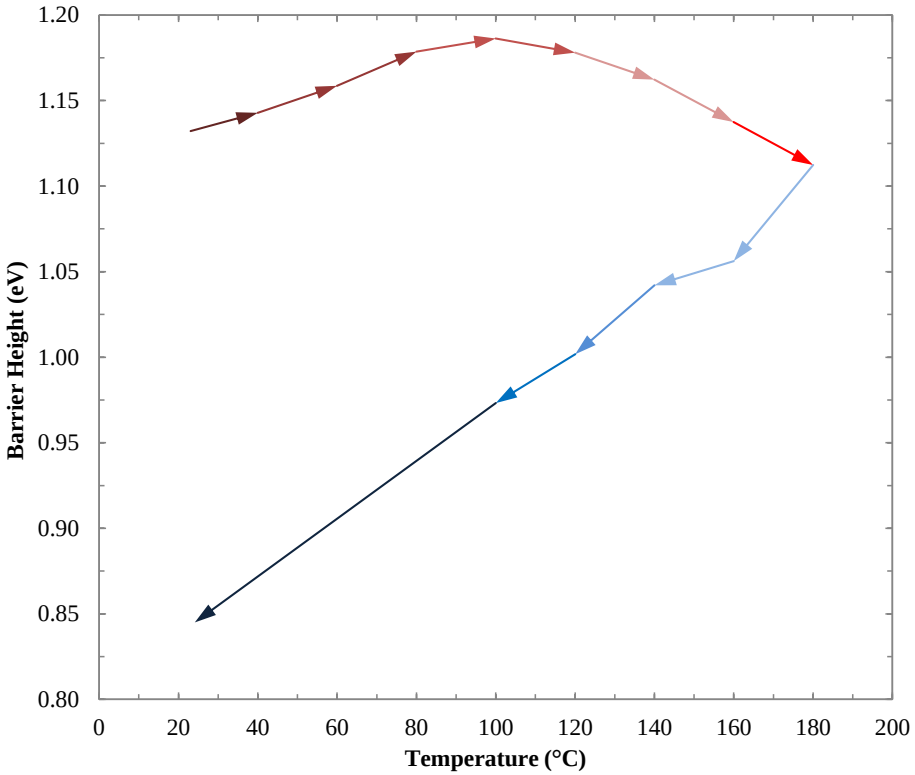

Figure A8.33: Barrier Heights with Temperature of 4.0:10 (O_2:Ar) RF-sputtered PtO_x

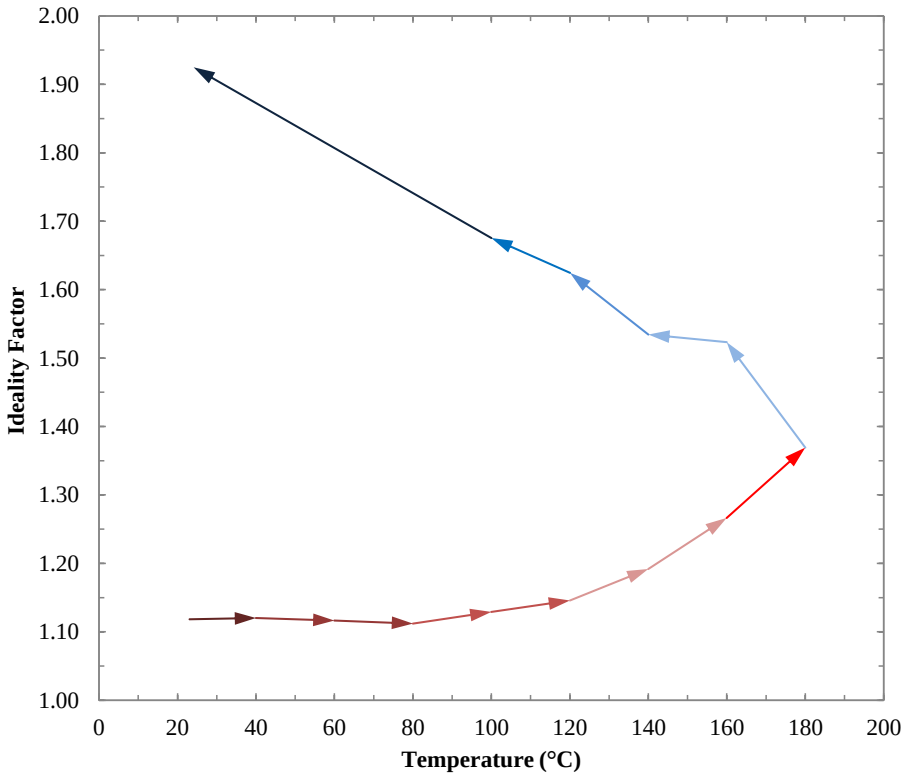

Figure A8.34: Ideality Factors with Temperature of 4.0:10 (O_2:Ar) RF-sputtered PtO_x

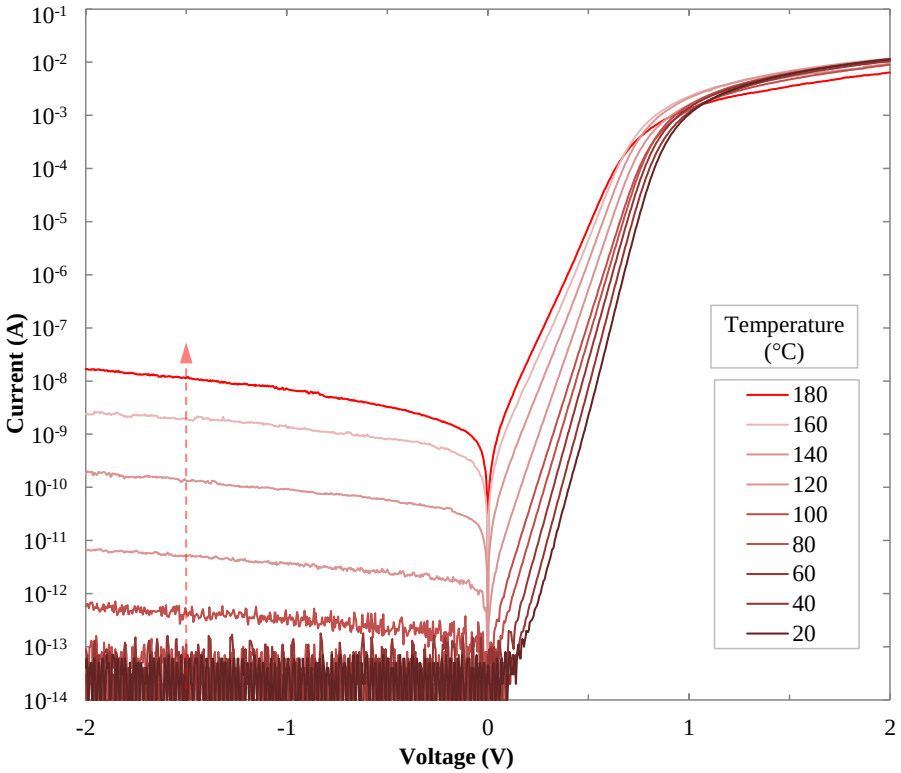

Figure A8.35: Dark I-V of 5.0:10 (O_2:Ar) RF-sputtered PtO_x (Increasing Temperature)

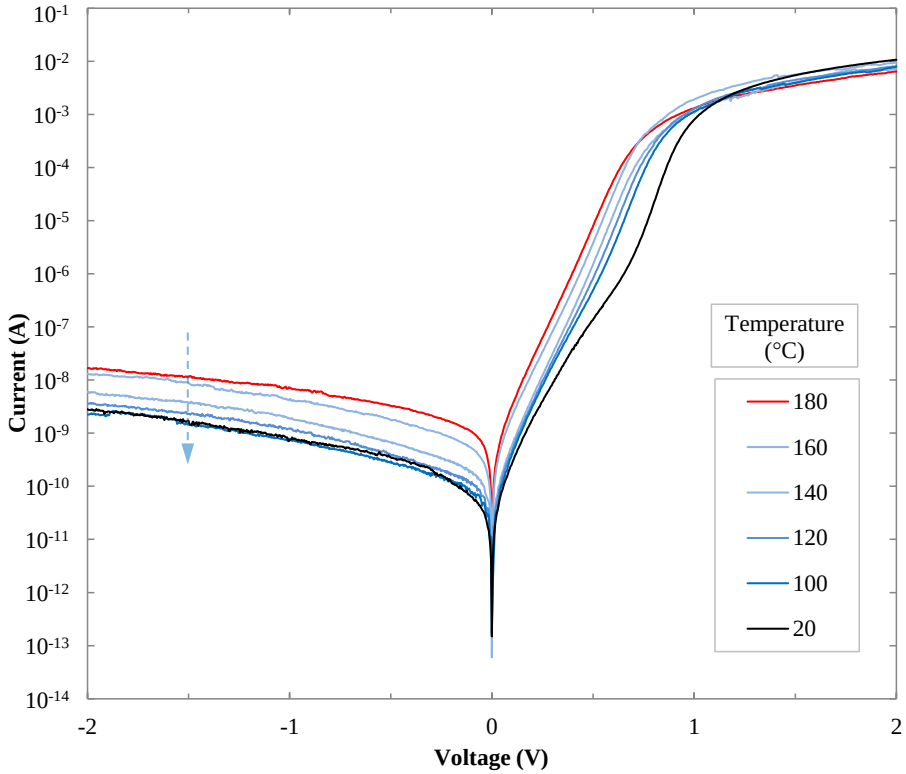

Figure A8.36: Dark I-V of 5.0:10 (O_2:Ar) RF-sputtered PtO_x (Decreasing Temperature)

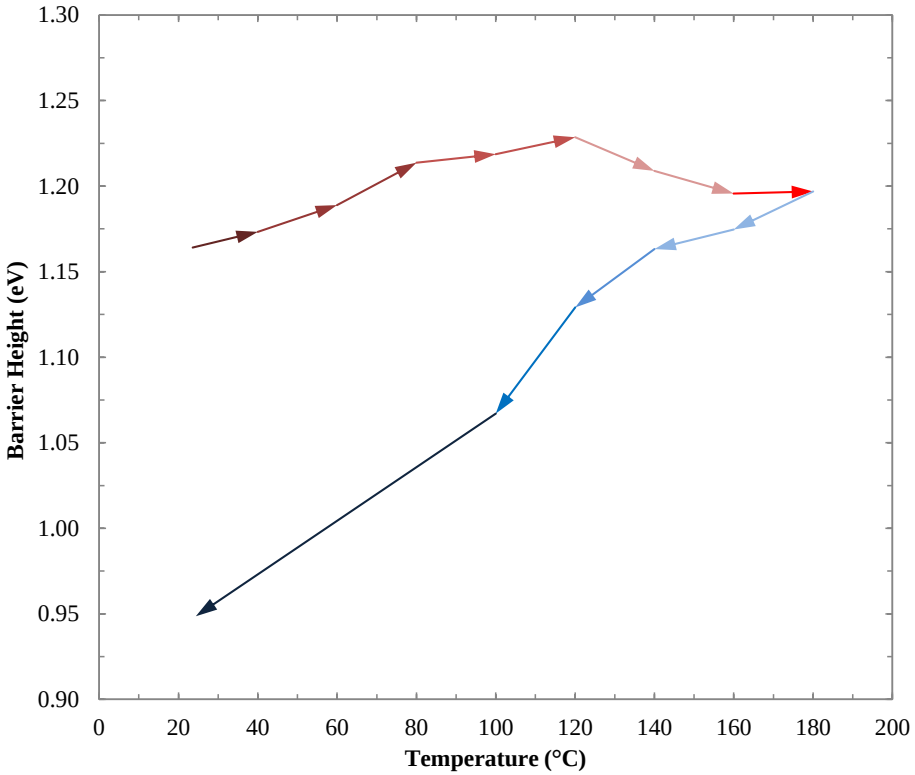

Figure A8.37: Barrier Heights with Temperature of 5.0:10 (O_2:Ar) RF-sputtered PtO_x

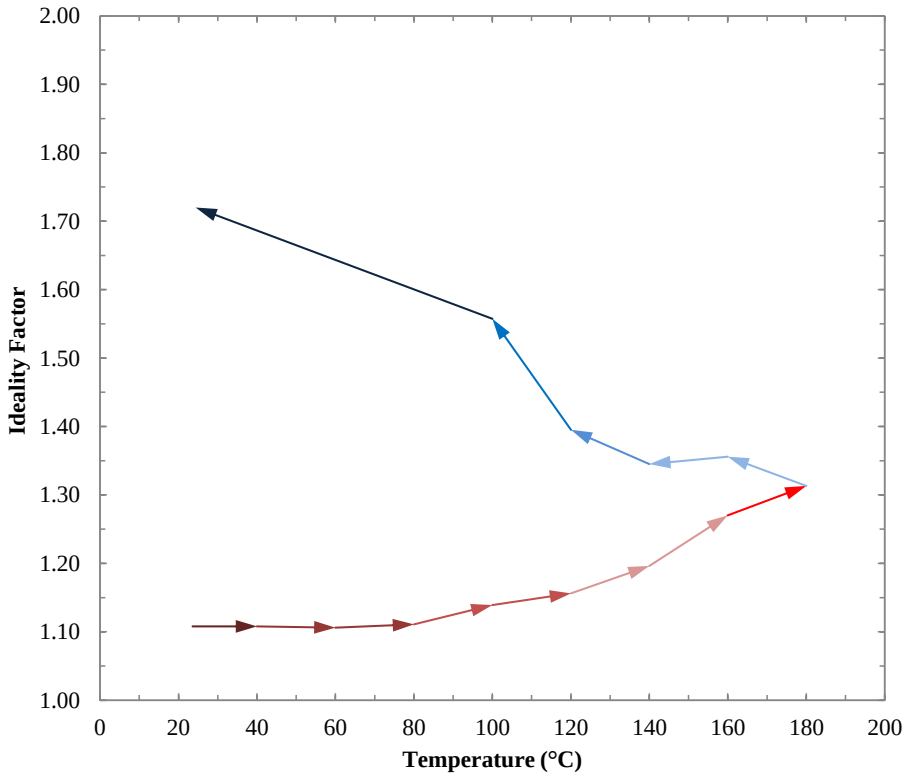

Figure A8.38: Ideality Factors with Temperature of 5.0:10 (O_2:Ar) RF-sputtered PtO_x

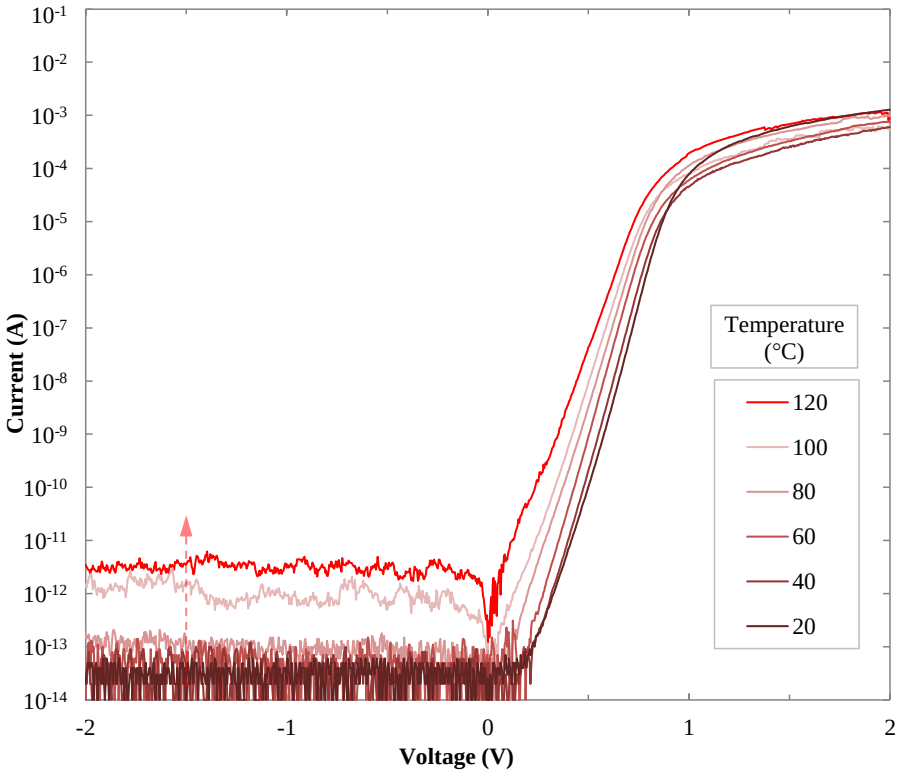

Figure A8.39: Dark I-V of 7.0:10 (O_2:Ar) RF-sputtered PtO_x (Increasing Temperature)

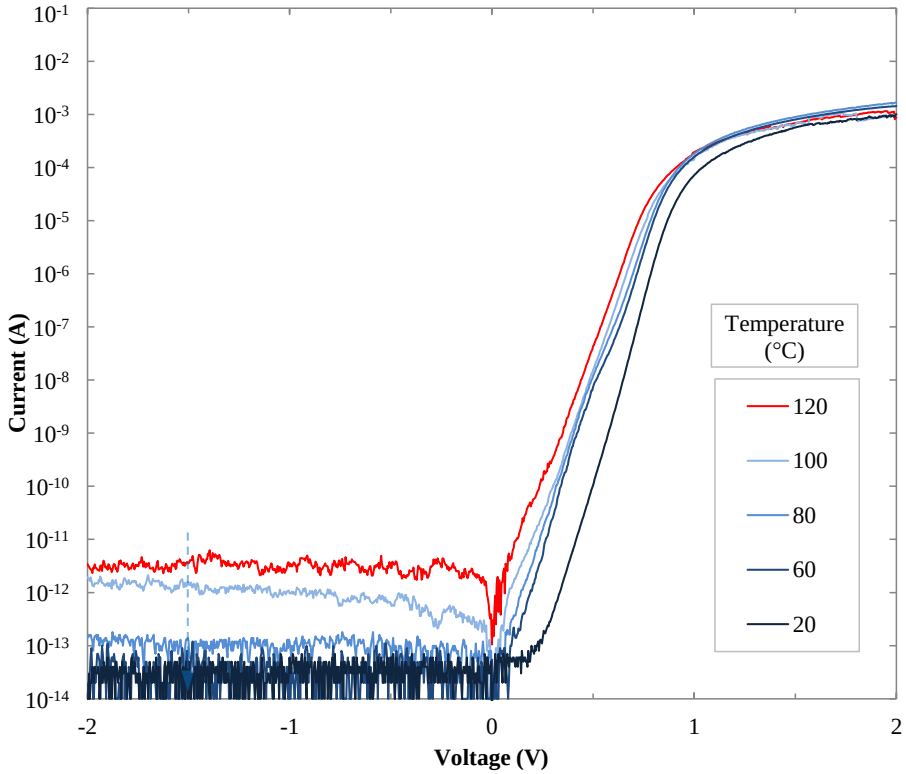

Figure A8.40: Dark I-V of 7.0:10 (O_2:Ar) RF-sputtered PtO_x (Decreasing Temperature)

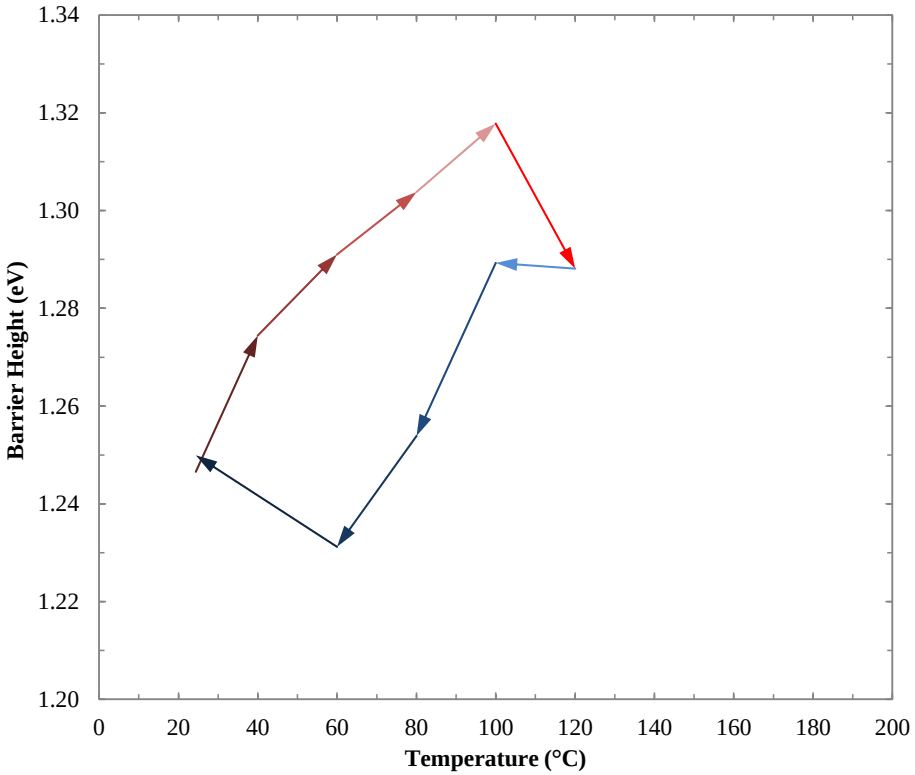

Figure A8.41: Barrier Heights with Temperature of 7.0:10 (O_2:Ar) RF-sputtered PtO_x

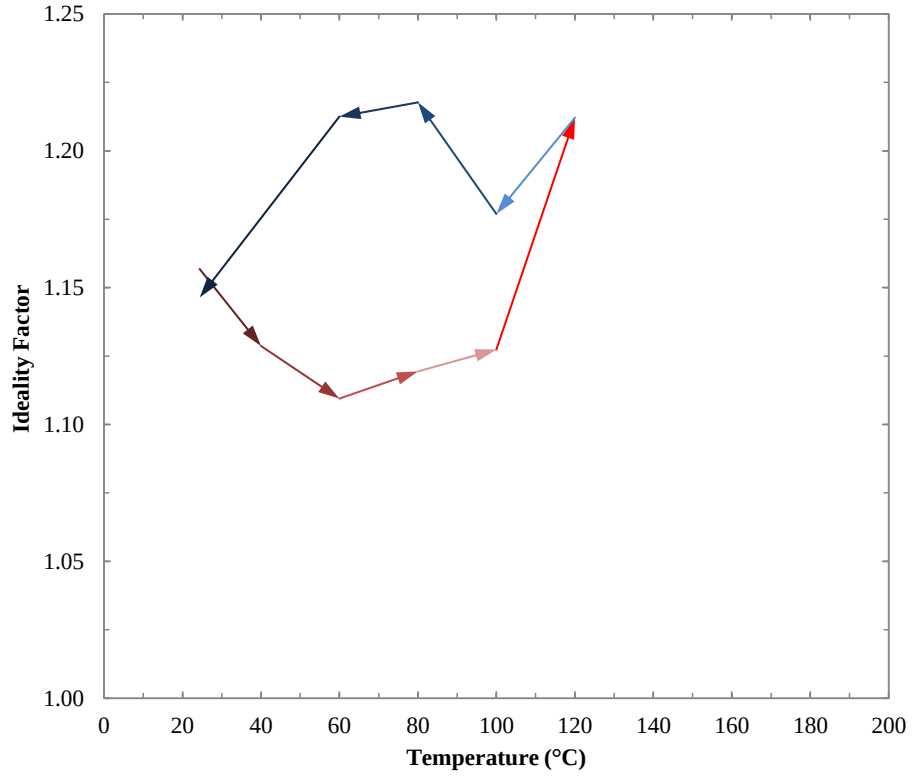

Figure A8.42: Ideality Factors with Temperature of 7.0:10 (O_2:Ar) RF-sputtered PtO_x

[A8.5] Barrier Heights and Ideality Factors with Temperature of PdO_x (Initial and Repeat Cycle)

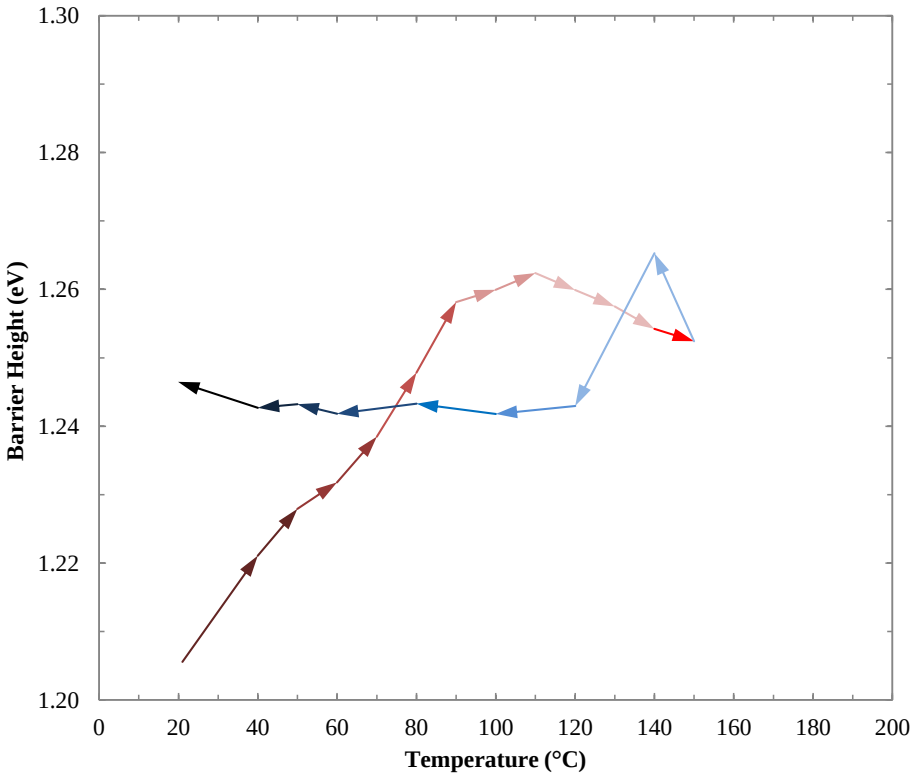

Figure 8.43: Barrier Heights with Temperature of 7.0:10 (O_2:Ar) RF-sputtered PdO_x

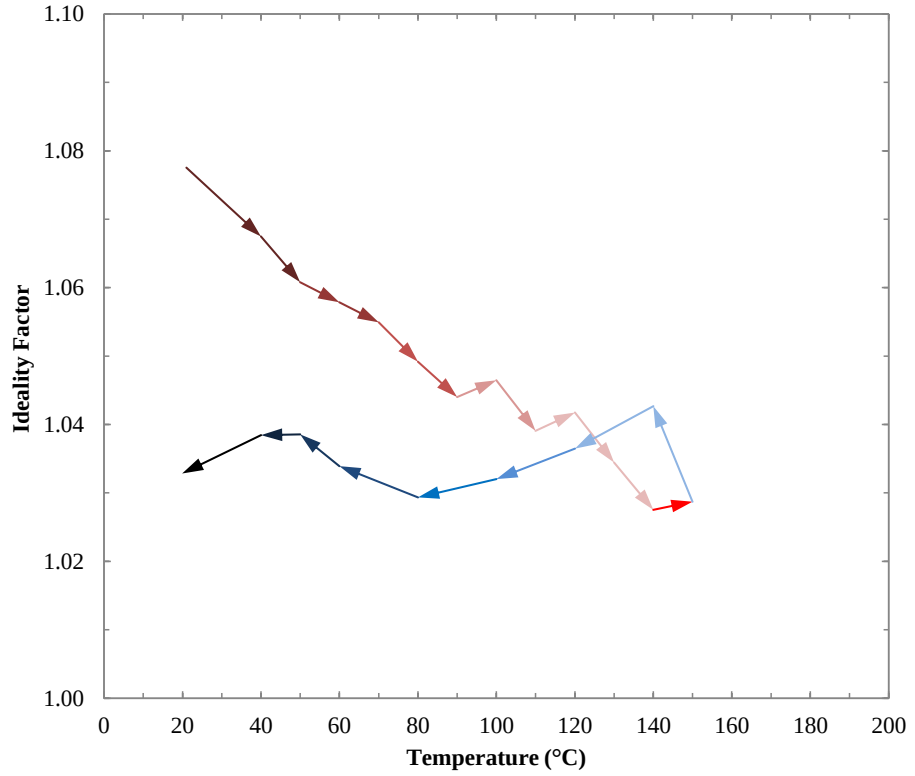

Figure 8.44: Ideality Factors with Temperature of 7.0:10 (O_2:Ar) RF-sputtered PdO_x

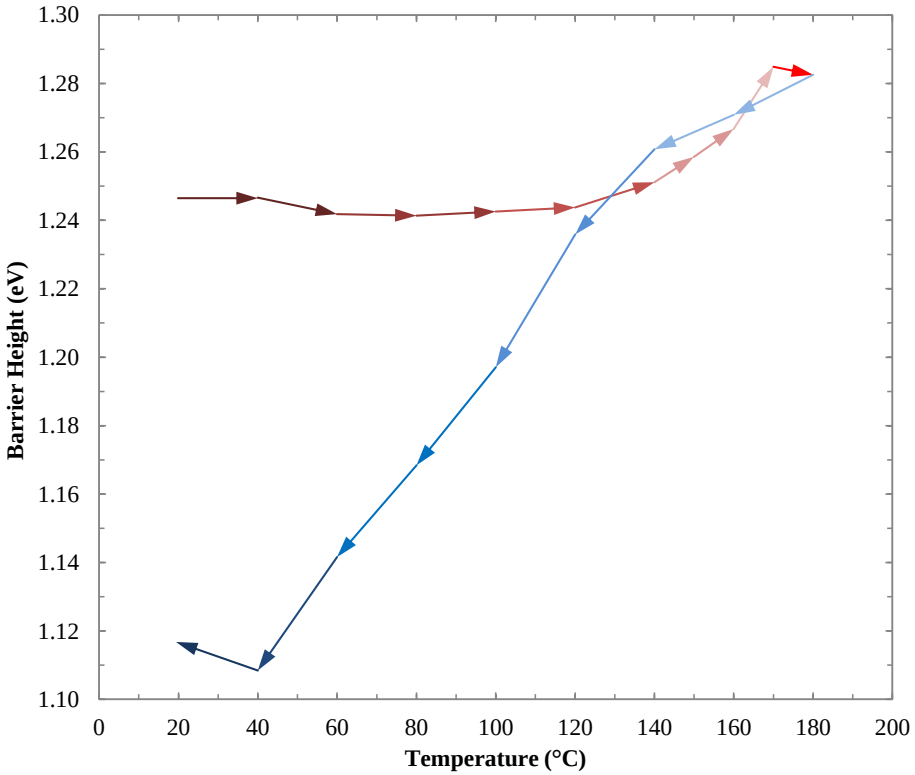

Figure 8.45: Barrier Heights with Temperature of 7.0:10 (O_2:Ar) RF-sputtered PdO_x (Repeat)

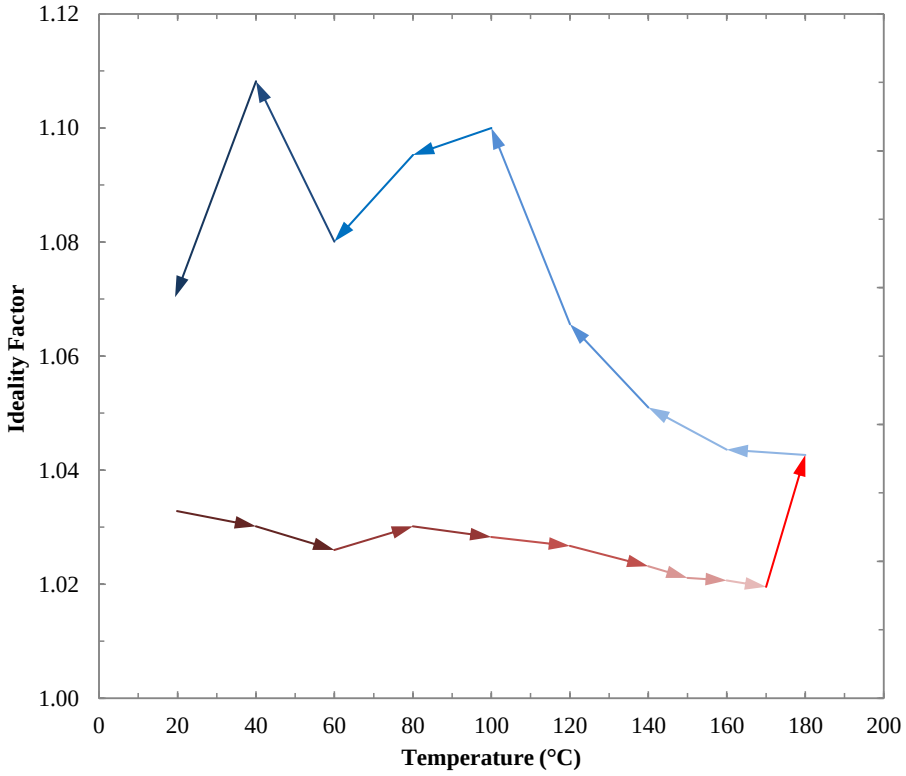

Figure 8.46: Ideality Factors with Temperature of 7.0:10 (O_2:Ar) RF-sputtered PdO_x (Repeat)

[A8.6] RF-sputtered 4.0:10 (O_2:Ar) AgO_x on Molecular Beam Epitaxy (MBE) ZnO

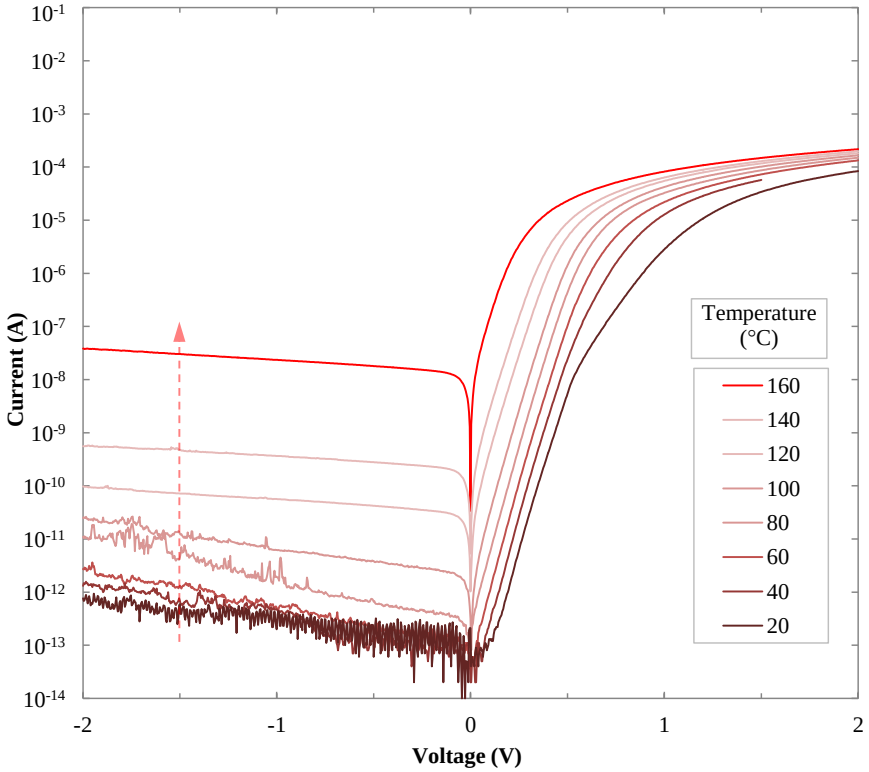

Figure A8.47: 4.0:10 (O_2:Ar) RF-sputtered AgO_x on MBE ZnO Dark I-V (Increasing Temp.)

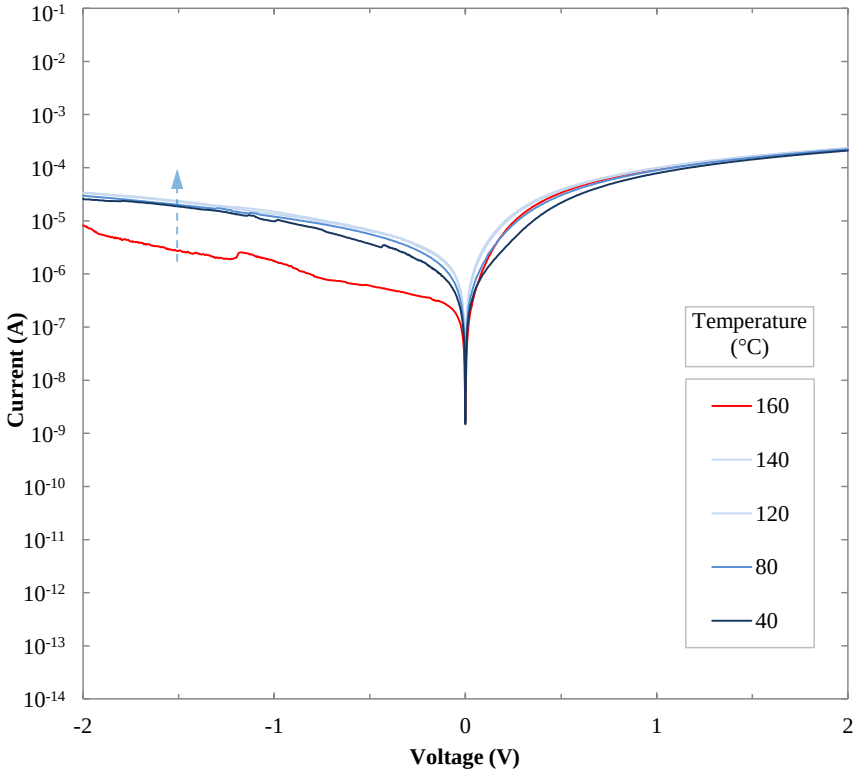

Figure A8.48: 4.0:10 (O_2:Ar) RF-sputtered AgO_x on MBE ZnO Dark I-V (Decreasing Temp.)

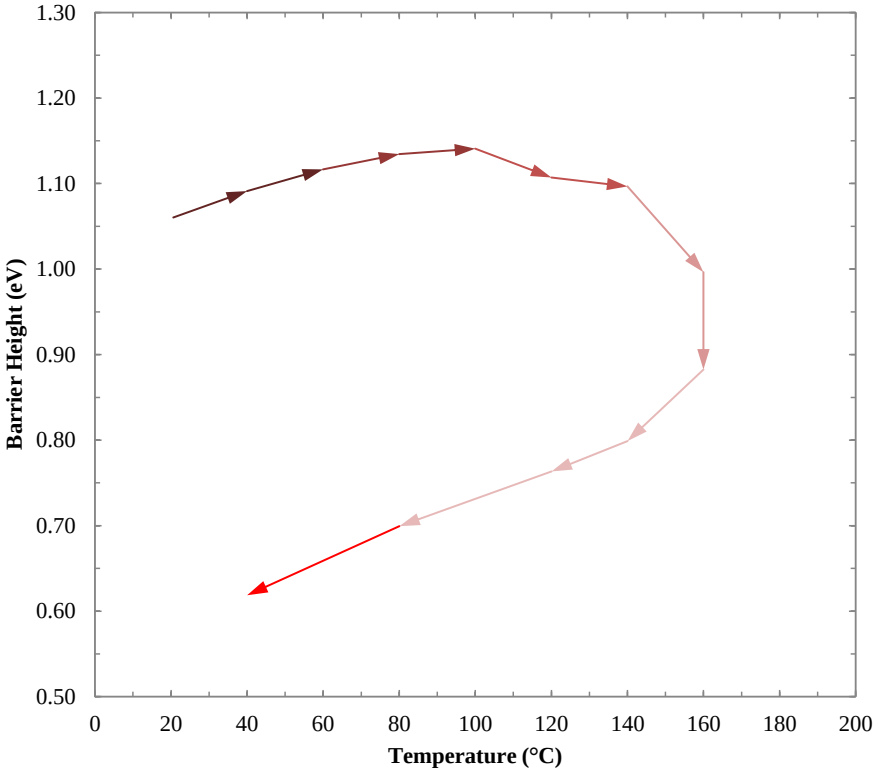

Figure A8.49: Barrier Heights with Temp. of 4.0:10 (O_2:Ar) RF-sputtered AgO_x on MBE ZnO

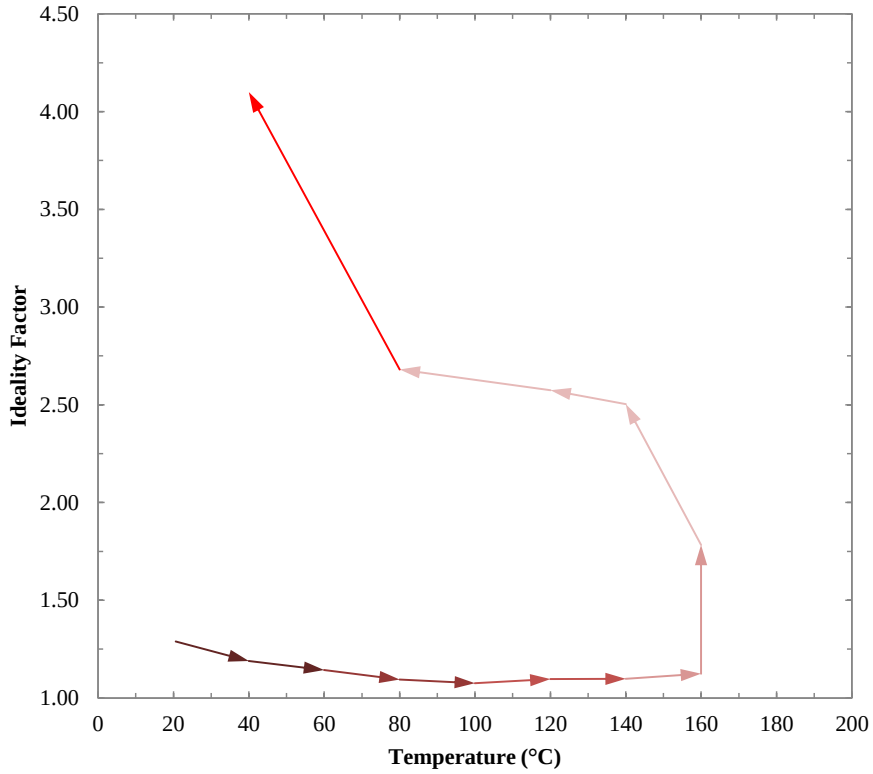

Figure A8.50: Ideality Factors with Temp. of 4.0:10 (O_2:Ar) RF-sputtered AgO_x on MBE ZnO

[A8.7] Richardson Plots for Calculating the Richardson Constant of the Bulk ZnO Material

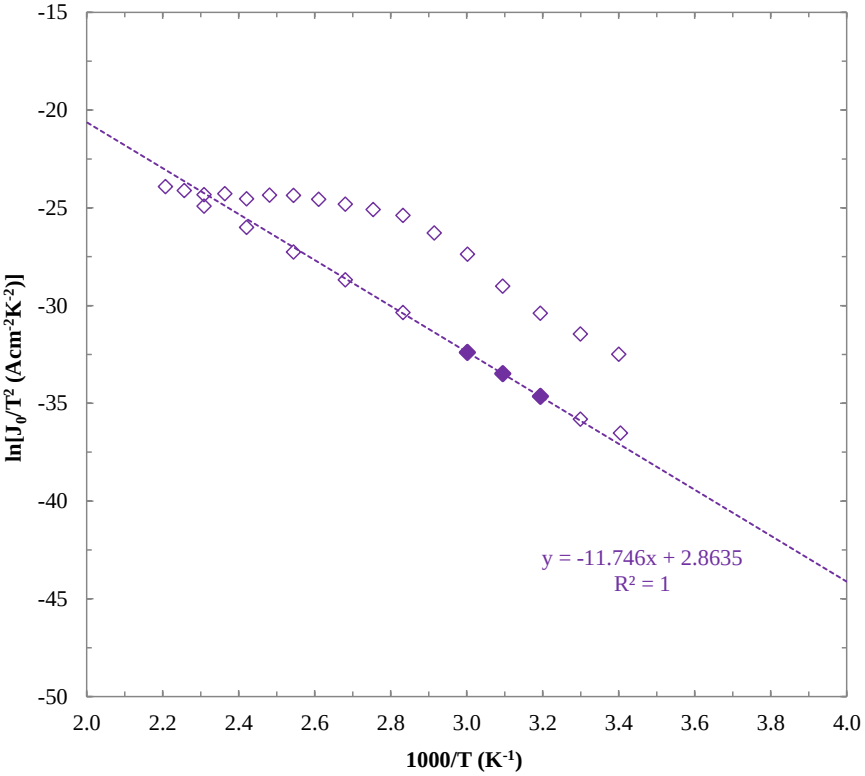

Figure A8.51: Richardson Plot of PLD IrO_x (Initial Measurement)

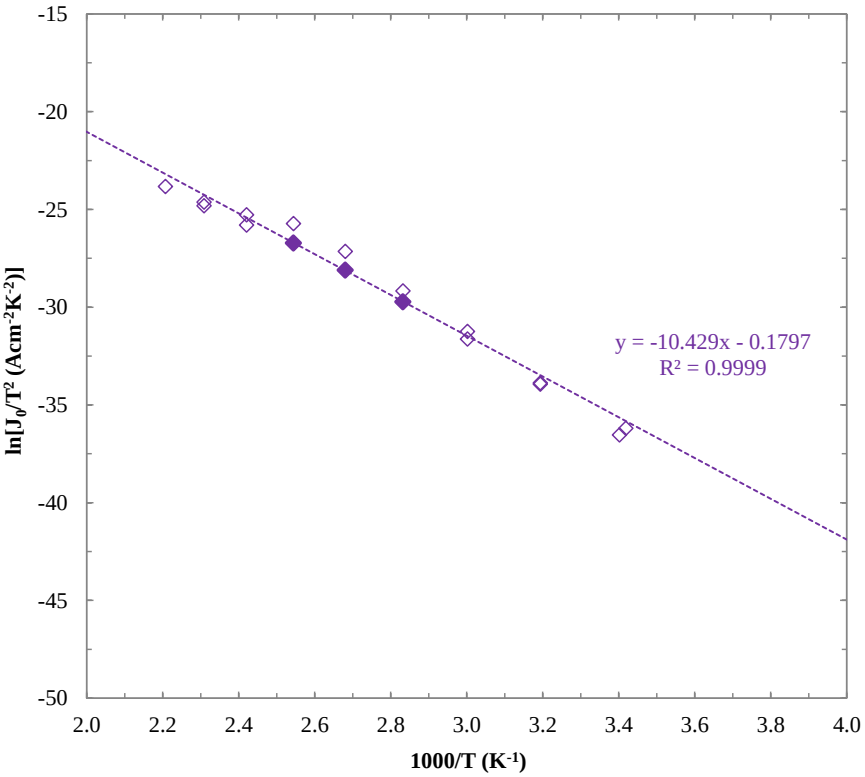

Figure A8.52: Richardson Plot of PLD IrO_x (Repeat Measurement)

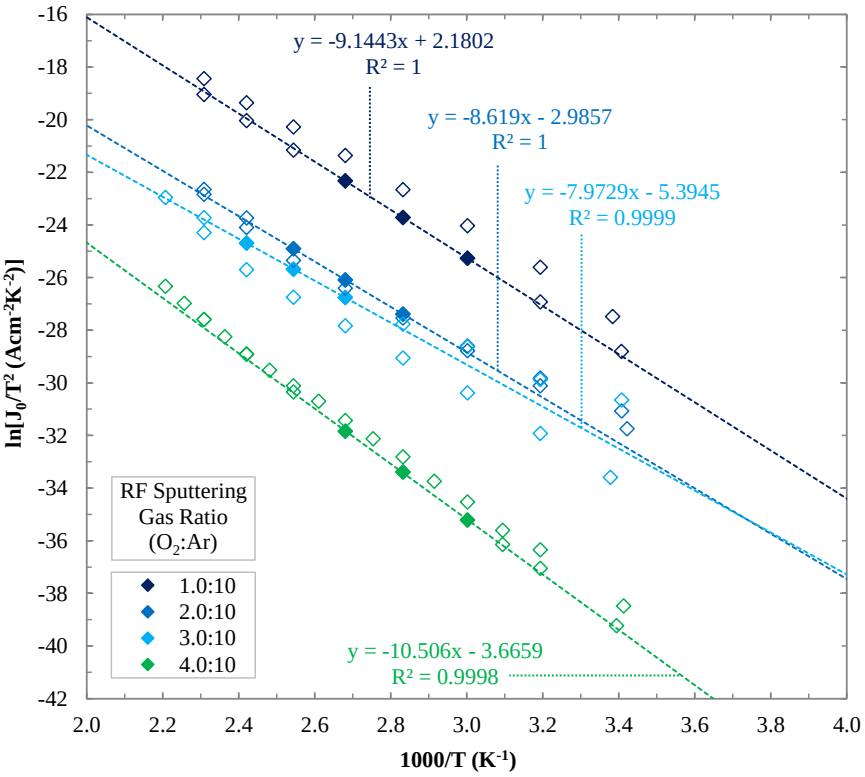

Figure A8.53: Richardson Plot of 1.0:10 – 4.0:10 (O_2:Ar) RF-sputtered IrO_x

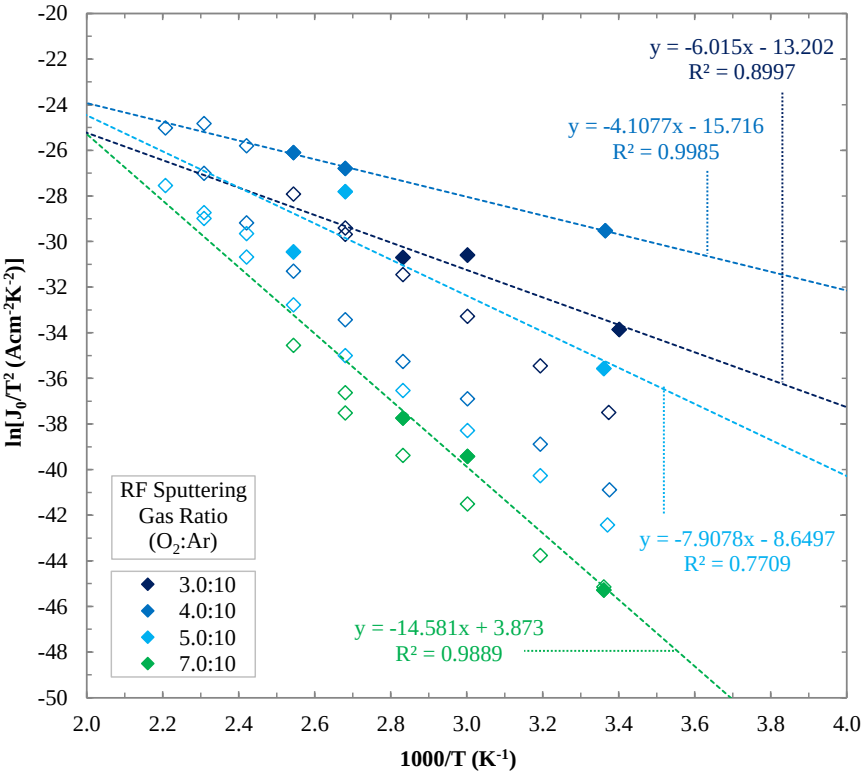

Figure A8.54: Richardson Plot of 3.0:10 – 7.0:10 (O_2:Ar) RF-sputtered PtO_x

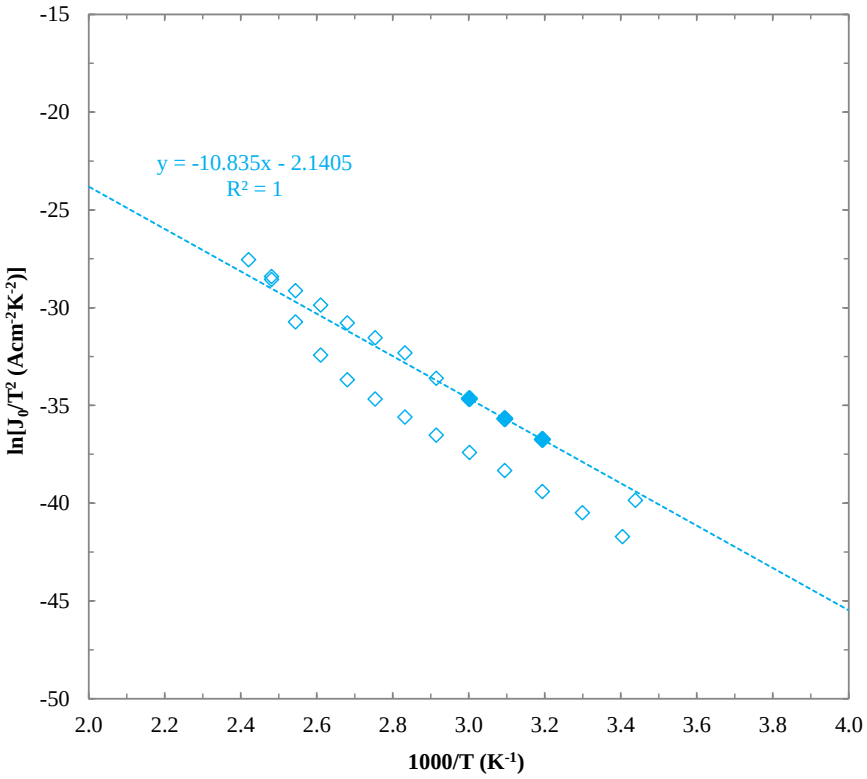

Figure A8.55: Richardson Plot of 4.0:10 (O_2:Ar) RF-sputtered AgO_x

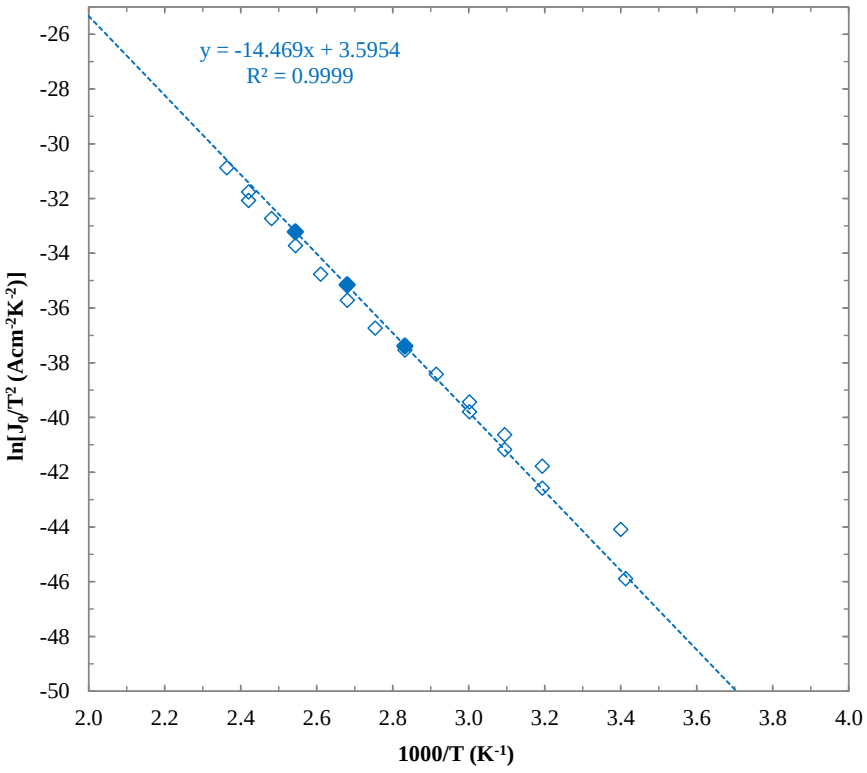

Figure A8.56: Richardson Plot of 7.0:10 (O_2:Ar) RF-sputtered PdO_x

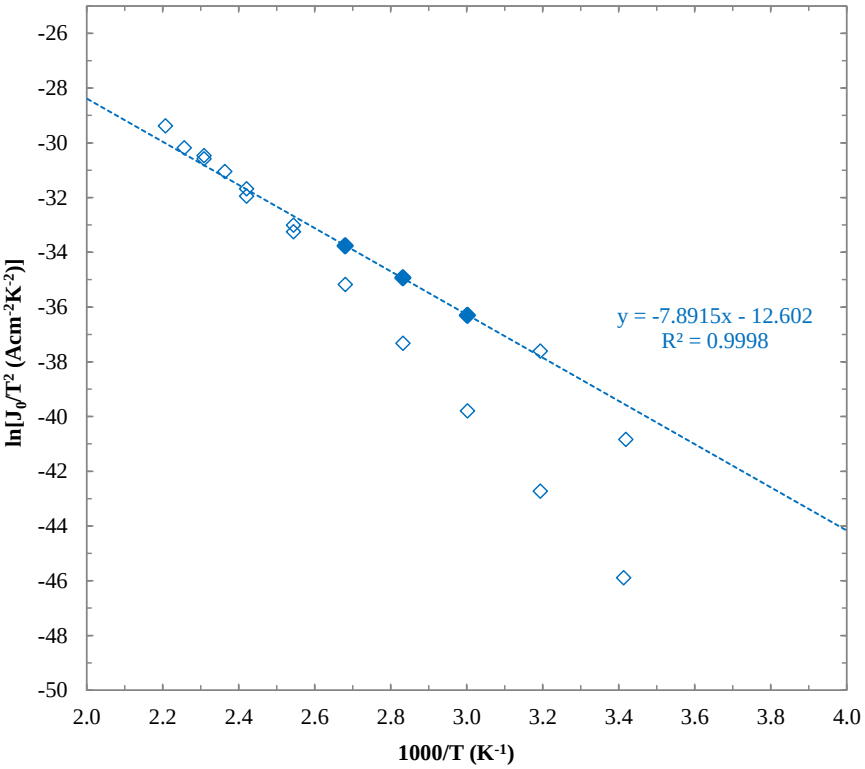

Figure A8.57: Richardson Plot of 7.0:10 (O_2:Ar) RF-sputtered PdO_x